Transactions of the ASME®

Transactions of the ASME, Journal of Applied Mechanics (ISSN 0021-8936) is published bimonthly (Jan., Mar., May, July, Sept., Nov.) The American Society of Mechanical Engineers, Three Park Avenue, New York, NY 10016. Periodicals postage paid at New York, NY and additional mailing office. POSTMASTER: Send address changes to Transactions of the ASME, Journal of Applied Mechanics, c/o THE AMERICAN SOCIETY OF MECHANICAL ENGINEERS, 22 Law Drive, Box 2300, Fairfield, NJ 07007-2300. **CHANGES OF ADDRESS** must be received at Society headquarters seven weeks before they are to be effective. Please send old label and new address. **STATEMENT from By-Laws.** The Society shall not be responsible for statements or opinions advanced in papers or . . . printed in its publications (B7.1, Para. 3).

Journal of Applied Mechanics

Published Bimonthly by The American Society of Mechanical Engineers

VOLUME 68 • NUMBER 6 • NOVEMBER 2001

(**Contents continued on inside back cover**)

This journal is printed on acid-free paper, which exceeds the ANSI Z39.48-1992 specification for permanence of paper and library materials. ♾™
♻ 85% recycled content, including 10% post-consumer fibers.

(Contents continued)

Journal of Applied Mechanics Volume 68, Number 6 NOVEMBER 2001

BRIEF NOTES

DISCUSSION

ANNOUNCEMENTS AND SPECIAL NOTES

Owen Richmond
1928–2001

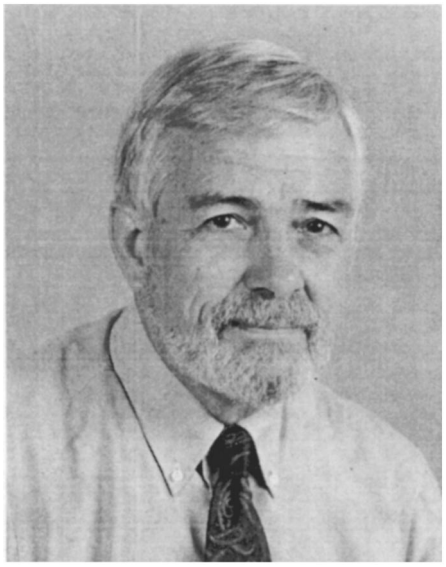

The mechanics and materials community lost a research leader and a national advocate for the disciplines. Owen Richmond died April 17, 2001, in Pittsburgh, PA, following a battle with pulmonary fibrosis, a degenerative lung condition. Owen had an impact on applied mechanics and its application to materials property determination, description, and materials processing. He had a clear vision of the whole of mechanics and materials and the ability to use that vision to extend the realm of the possible. But, more important, Owen was a positive influence on the lives of those who were fortunate enough to know him.

Owen was born on April 1, 1928, in Geneva, IL. His birth date was a source of amusement to him. He would remark that he could be viewed as an ''April Fool.'' He was far from that. Owen grew up in Wasco, IL, a small community west of Chicago. He carried the traits of his Midwestern roots with him throughout his life. He was thoughtful and determined. Owen was also a warm and generous person. He was always willing to share his ideas and to help others understand complicated mechanics and materials problems. Owen was a constant source of encouragement and enthusiasm for younger colleagues in both academia and industry. He encouraged them to develop their own vision and voice and to use it to identify research areas that would have real impact. He took great pleasure in helping colleagues to establish a research presence or to obtain a grant to pursue an idea. Owen was a facilitator.

Owen graduated from Bradley University, Peoria, IL, in 1949 with a degree in general engineering. Perhaps it was this initial training in general engineering that set the course for his future vision of mechanics and materials. Owen continued his education at the University of Illinois, Urbana, IL. He received his M. S. degree in Civil Engineering in 1950. As part of his graduate program, Owen was required to write a research paper. Having grown tired of drafting and design codes, he wrote a paper entitled ''Atomic Theory of Strength of Materials.'' After graduation, he had the opportunity to pursue an interest in architecture with the firm of Emerson, Gregg, and Briggs in Peoria.

The Korean War interrupted Owen's civilian engineering career. He was drafted into the Army and taught recruits how to tie knots at Fort Belvoir, VA. Owen attributed this experience to awakening his interest in topology. The Research and Development Laboratory at Fort Belvoir was looking for a person to investigate the effects of atomic blasts on structures designed to protect people. Owen got the job. He would remark that this was the result of having the right words on his resume. Owen continued to work as a civilian employee on this project for two years after his discharge. He participated in several tests of structures at the Nevada Test Site. This marked the beginnings of Owen's interest in the connection of design and theory to experimentation.

In the fall of 1954, Owen returned to academic pursuits. He began his Ph.D. studies at The Pennsylvania State University in engineering mechanics. Owen worked on the application of plasticity theory to metalworking. He was awarded the degree in 1958 with a thesis entitled ''A Hyperbolic Theory of Plasticity.'' This work marked the beginning of a long interest in using Tresca-type material descriptions to solve problems in metalworking. Owen also used numerical methods to investigate this problem. This may have been the only time that he actually computed results. Owen was not averse to computing; he was simply willing to allow others the enjoyment of doing the computation.

October 1957 marked the beginning of a 25-year career with U.S. Steel's Research Laboratory in Monroeville, PA. Owen began as a scientist in the Mechanical Metallurgy section. He participated in fundamental research on the structure of materials, material design, behavior, and performance. Owen was able to use his skills in mechanics to address problems that aided the advancement of these investigations. Owen designed and analyzed experiments on the creep and the stress relaxation of metals. This work sparked his interest in developing constitutive equations that incorporated the underlying mechanisms responsible for the deformation. It also increased his resolve that good theory and good experiments go hand in hand.

Owen also believed that fundamental work should be motivated by, and connected to, problems of industrial importance. His early work on wire drawing was the result of this belief. Owen developed a theory of streamlined dies. These die shapes produced products that had zero redundant work during deformation and produced wire with increased performance. This was demonstrated in careful experiments with colleagues. The theory was predicted on Tresca's theory of yield and low for a perfectly plastic material. Owen viewed the Tresca model for materials behavior as a homogenization of Schmid's Law for a crystal with an infinity of slip systems or a polycrystalline material with randomly oriented small crystals. Owen used this initial work to develop a theory of ideal forming. Ideal forming uses material models and deformations that require minimum work or energy of deformation. This was an area of increasing importance to Owen in later years. In one of his last conversations, Owen remarked that now that he was retired, he was forming a company to develop and market ideal forming tools.

Owen also began thinking about the relationship between chemical and mechanical interactions in materials. This work was motivated by a problem of residual stress formation from species diffusion. Out of this work came other work dealing with lattice strains produced by solutes and the beginnings of chemical-mechanical integration. This formed the basis of a program on alloy design that included both mechanical and chemical interactions.

Owen was active in the academic community as well. He taught courses in elasticity and plasticity at Carnegie Institute of Technology (Carnegie Mellon University). Here, he developed friendships and collegial associations that lasted for decades. He also spent an industrial sabbatical leave, 1962–1963, as a visiting scientist in the Department of Mechanical Engineering at Stanford University. Owen developed a strong sense that universities and industry needed to collaborate, and that out of these collaborations, synergies would develop that were beneficial to both groups. He collaborated with a number of institutions both nationally and internationally throughout his career.

In 1966, Owen was asked to organize the Mechanical Sciences Division of US Steel's Edgar C. Bain Laboratory for Fundamental Research. He assembled a team of researchers consisting of materials scientists, experimental and applied mechanicians, and mathematicians. Owen was a consummate manager. He once remarked that his father had told him ''Always try to say yes, then your no's will mean so much more.'' Owen provided the guidance and resources for his colleagues to do research that was both interesting and meaningful to the corporation. Out of this environment came fundamental work on the pressure dependence of yielding in metals, the non-normality of plastic flow, the localization of deformation into shear bands, the flow of granular materials, crazing in polymers, basic understanding of the development of stress and air gap formation in casting, tribological studies of interfaces, finite strain elastoplastic analyses of forming processes, and quantitative descriptions of material structure and failure. Through all of this work, Owen was a force in developing theories and corroborating them with experimental findings.

Owen joined the staff of the Alcoa Technical Center in 1983 and was quickly promoted to a Senior Fellow. He took this position after considering opportunities in academia. He felt that the industrial research laboratory afforded him a greater opportunity to strengthen interdisciplinary research efforts in materials and mechanics. The position would also allow opportunities to integrate research across pertinent length scales to predict material properties. Owen received the singular distinction of being named Corporate Fellow and laboratory director in charge of basic research. Under Owen's leadership, Alcoa began and strengthened research programs for atomic-scale simulation of materials, process tribology, polymer processing, composite processing, laser processing of materials, process metallurgy, and deformation process modeling.

Owen's interests returned to a focus of his early career, design. He initiated a program to strengthen and incorporate a comprehensive view of materials and product design. The outgrowth of this effort was his view that products should be designed by considering process, structure, properties, and also performance. This introduced a product's life cycle into the design process. Owen viewed this as an optimization problem and talked about a holistic physico-economic design process. He had hoped to develop these ideas in a monograph.

Owen was instrumental in organizing the Alcoa Technical Symposia celebrating the centenary of the founding of Alcoa in 1888. These symposia brought together researchers from around the world to discuss problems that had impact on the materials industry. Owen retired from the Technical Center in December 1998.

Owen received several significant awards during his career. In 1989, he received the Francis Frary Award from Alcoa Chairman Paul O'Neill for his outstanding contributions to Alcoa science and engineering. Owen received the 1990 ASME Applied Mechanics Division Award for his work in advancing the discipline of applied mechanics. ASME again recognized Owen in 1994 with the Nadai award for this contributions to the advancement of materials engineering in the areas of processing, casting, the effects of pressure on yielding, and the fostering of collaboration between industry and academia. In 1993, Owen's alma mater, Penn State, honored him with its highest award, the Outstanding Engineering Alumni of the Engineering Science and Mechanics Department. Owen was elected to the U.S. National Academy of Engineering in 1997. Owen also served as an industrial advisor to several prominent research universities in the U.S.

Owen took his science seriously, but not too seriously. One fall afternoon, a memorandum arrived in mailboxes across the Technical Center. It was written in Owen's all too familiar hand. The memo began to describe the construction of Voronoi tessellations. This is a topological idea that Owen had adopted to describe the distribution of particles and voids in materials. However, the application was to the raking of leaves that had fallen in his yard. Once again, Owen had seen an application that was beyond the norm.

Owen was looking forward to spending more time with his wife, Ann, and his four children in retirement. He especially wanted to spend time with his seven grandchildren. Owen was an avid baseball fan and supporter of the Chicago Cubs. He planned a family reunion at Garfield Farm, La Fox, IL, in 2000 to coincide with his golden wedding anniversary and a Cubs' home stand. Upon examining the Cubs' web site for the dates of the reunion, he thought the series was sold out. He contacted a number of friends to see if the Cubs' front office could be persuaded to find tickets for him and the grandchildren. Later he discovered that it was only the bleachers that were sold out. Owen was devoted to his favorite sport, his family, and his grandchildren.

Owen's scientific achievements are impressive, but even more impressive were his human qualities. He was a deeply moral man but never overbearing. He cared about people and about using mechanics to make people's lives better. He was also a dear friend to many.

He will be missed.

R. E. Smelser, University of Idaho
L. Anand, Massachusetts Institute of Technology
L. G. Hector, Jr., GM Research & Development

M. Amabili[1]
Professor,
Dipartimento di Ingegneria Industriale,
Università di Parma,
Parco Area delle Scienze 181/Z,
Parma I-43100, Italy
e-mail: marco@me.unipr.it
Mem. ASME

F. Pellicano
Professor,
Dipartimento di Scienze dell'Ingegneria,
Università di Modena e Reggio Emilia,
Via Campi 213B,
Modena I-41100, Italy

M. A. Païdoussis
Thomas Workman Emeritus Professor,
Department of Mechanical Engineering,
McGill University,
817 Sherbrooke Street, W.
Montreal, Quebec H3A 2K6, Canada
Fellow ASME

Nonlinear Stability of Circular Cylindrical Shells in Annular and Unbounded Axial Flow

The stability of circular cylindrical shells with supported ends in compressible, inviscid axial flow is investigated. Nonlinearities due to finite-amplitude shell motion are considered by using Donnell's nonlinear shallow-shell theory; the effect of viscous structural damping is taken into account. Two different in-plane constraints are applied at the shell edges: zero axial force and zero axial displacement; the other boundary conditions are those for simply supported shells. Linear potential flow theory is applied to describe the fluid-structure interaction. Both annular and unbounded external flow are considered by using two different sets of boundary conditions for the flow beyond the shell length: (i) a flexible wall of infinite extent in the longitudinal direction, and (ii) rigid extensions of the shell (baffles). The system is discretized by the Galerkin method and is investigated by using a model involving seven degrees-of-freedom, allowing for traveling-wave response of the shell and shell axisymmetric contraction. Results for both annular and unbounded external flow show that the system loses stability by divergence through strongly subcritical bifurcations. Jumps to bifurcated states can occur well before the onset of instability predicted by linear theory, showing that a linear study of shell stability is not sufficient for engineering applications. [DOI: 10.1115/1.1406957]

1 Introduction

The theories available for the stability of circular cylindrical shells in unbounded air flow do not agree sufficiently well with the experimental results, as pointed out by Horn et al. [1], and even today no satisfactory design criterion is available. Moreover, for subsonic Mach numbers, highly divergent and catastrophic instabilities occurred in experiments with clamped-clamped copper shells in fully developed turbulent flow ([1]). On the other hand, Païdoussis and his co-workers developed several linear theoretical models, first for inviscid annular flow ([2,3]) and then for viscous annular flow ([4,5]). Additional results for inviscid annular flow were obtained by Horáček [6]. However, experiments with rubber shells in annular air flow ([7]) show that the onset of instability (divergence) predicted by linear theory is not conservative, by a margin of more than 30 percent for clamped-clamped shells. Since the fluid-structure interaction models used in the study of Païdoussis and his co-workers are fairly accurate, the reason for disagreement between theoretical and experimental results is suspected to be associated with the use of linear theory in the modelling of shell deformations. This is a common limitation of almost all the previous studies. In fact, experiments show that divergence of shells with supported ends involves deformations at least of the order of the shell thickness. For such deformations, geometric nonlinearities must be taken into account.

Only a few researchers used a geometrically nonlinear shell model to investigate the aeroelastic stability of cylindrical shells in axial flow, but in all cases the flow considered was supersonic. These studies are due to Librescu [8,9], Olson and Fung [10], and Evensen and Olson [11], and they utilized simple modal expansions that were incapable of completely describing the nonlinear behavior of a circumferentially closed shell. A literature review of work on nonlinear dynamics of shells *in vacuo* and filled with or surrounded by quiescent fluid is given by Amabili et al. [12] and will not be repeated here. One important conclusion reached in that study, however, is the following: Since most analyses involve some kind of Galerkin-type expansion, the choice of appropriate comparison functions is as always important, but in the case of nonlinear shell motions it is *crucial*, for the presence of opposing effects due to quadratic and cubic nonlinearities.

The nonlinear stability of supported, circular cylindrical shells in compressible, inviscid axial, subsonic flow is investigated in the present study for the first time. The present approach is based on the geometrically nonlinear shell model developed by Amabili et al. [13] to study stability of shells *containing* incompressible flow.

2 Equation of Motion and Boundary Conditions

A cylindrical coordinate system $(O;x,r,\theta)$ is chosen, with the origin O placed at the center of one end of the shell. The displacements of points in the middle surface of the shell are denoted by u, v and w, in the axial, circumferential, and radial directions, respectively. Using Donnell's nonlinear shallow-shell theory, the equation of motion for large amplitude transverse vibrations of a very thin, circular cylindrical shell is given by ([13])

$$D\nabla^4 w + ch\dot{w} + \rho h\ddot{w} = f + P + \frac{1}{R}\frac{\partial^2 F}{\partial x^2} + \frac{1}{R^2}\left(\frac{\partial^2 F}{\partial \theta^2}\frac{\partial^2 w}{\partial x^2} - 2\frac{\partial^2 F}{\partial x \partial \theta}\frac{\partial^2 w}{\partial x \partial \theta} + \frac{\partial^2 F}{\partial x^2}\frac{\partial^2 w}{\partial \theta^2}\right), \quad (1)$$

where $D = Eh^3/[12(1-\nu^2)]$ is the flexural rigidity, E is Young's modulus, ν the Poisson ratio, h the shell thickness, R the mean shell radius, ρ the mass density of the shell, c the damping parameter, P the radial pressure applied to the surface of the shell by the external flowing fluid, and f a possible, external radial excitation ($f=0$ is taken in most of the present study). The radial deflection w is positive inward, the overdot denotes a time derivative and F is the in-plane Airy stress function, given by

[1]To whom correspondence should be addressed.

Contributed by the Applied Mechanics Division of THE AMERICAN SOCIETY OF MECHANICAL ENGINEERS for publication in the ASME JOURNAL OF APPLIED MECHANICS. Manuscript received by the ASME Applied Mechanics Division, Jan. 20, 2000; final revision, May 10, 2001. Associate Editor: D. A. Siginer. Discussion on the paper should be addressed to the Editor, Professor Lewis T. Wheeler, Department of Mechanical Engineering, University of Houston, Houston, TX 77204-4792, and will be accepted until four months after final publication of the paper itself in the ASME JOURNAL OF APPLIED MECHANICS.

$$\frac{1}{Eh}\nabla^4 F = -\frac{1}{R}\frac{\partial^2 w}{\partial x^2} + \frac{1}{R^2}\left[\left(\frac{\partial^2 w}{\partial x \partial \theta}\right)^2 - \frac{\partial^2 w}{\partial x^2}\frac{\partial^2 w}{\partial \theta^2}\right]. \quad (2)$$

In Eqs. (1) and (2), the biharmonic operator is defined as $\nabla^4 = [\partial^2/\partial x^2 + \partial^2/(R^2\partial\theta^2)]^2$. Donnell's nonlinear shallow-shell equations are accurate only for modes of high circumferential wave number n; specifically, $1/n^2 \ll 1$ must be satisfied, so that $n \geqslant 5$ is required in order to have fairly good accuracy. Donnell's nonlinear shallow-shell equations are obtained by neglecting the in-plane and rotary inertia and transverse shear deformation, giving accurate results only for very thin shells, i.e., $h \ll R$. In-plane displacements are infinitesimal, i.e., $|u| \ll h$, $|v| \ll h$, while w is of the same order of the shell thickness; the curvature changes are expressed by linear functions of w only.

In this study, attention is focused on both (i) a finite, simply supported, circumferentially closed circular cylindrical shell of length L, and (ii) an infinitely long shell, periodically supported. In the latter case, the portion of the shell considered lies between two supports, L apart, while the effect of the part of the shell beyond is only considered as a constraint; only modes that are antisymmetric with respect to each support are considered in this case (lower frequency modes).

In both cases the following boundary conditions must be satisfied:

$$w = 0 \quad \text{and} \quad M_x = -D\{(\partial^2 w/\partial x^2) + \nu[\partial^2 w/(R^2\partial\theta^2)]\} = 0 \quad \text{at } x = 0, L, \quad (3)$$

where M_x is the bending moment per unit length. Two different in-plane boundary conditions are considered:

$$\text{Case 1: } N_x = 0 \quad \text{at } x = 0, L \quad \text{and} \quad v = 0 \quad \text{at } x = 0, L, \quad (4a)$$

$$\text{Case 2: } u = 0 \quad \text{at } x = 0, L \quad \text{and} \quad v = 0 \quad \text{at } x = 0, L; \quad (4b)$$

moreover, u, v, and w must be continuous in θ. The flexural deformation w is expanded by using the linear shell eigenmodes for zero flow as the base; in particular, the flexural response with n nodal diameters and m longitudinal half-waves can be written as follows ([13]):

$$w(x,\theta,t) = \sum_{m=1}^{2} [A_{m,n}(t)\cos(n\theta) + B_{m,n}(t)\sin(n\theta)]\sin(\lambda_m x) + \sum_{m=1}^{3} A_{(2m-1),0}(t)\sin(\lambda_{(2m-1)}x), \quad (5)$$

where $\lambda_m = m\pi/L$ and t is the time; $A_{m,n}(t)$, $B_{m,n}(t)$ and $A_{m,0}(t)$ are unknown functions of t. Equation (5) was obtained by supposing that the nonlinear interaction among ''linear modes'' of the chosen base involves only the asymmetric modes ($n > 0$) having a given n value, and axisymmetric modes ($n = 0$) with an odd m value. Only asymmetric modes with one and two axial half-waves are included; additional modes increase the accuracy of the analysis. Axisymmetric modes are fundamental for describing the nonlinearity correctly.

3 Fluid-Shell Interaction

The shell is considered immersed in annular compressible fluid flow, limited by an external rigid cylinder of radius R_1; the case of a radially unbounded external fluid is obtained in the limit of $R_1 \to \infty$. The cases with $R_1 < R$ (internal annular flow) and $R_1 \to 0$ (internal flow) are also described by the present model. The fluid-structure interaction is described by linear potential flow theory; thus, the fluid is assumed to be inviscid, and the flow isentropic and irrotational. The effect of fluid flow nonlinearities has been found to be negligible in Ref. [14]. In contrast, viscous effects can be significant, especially for annular flow in narrow gaps ([4,5]). Gravity effects, such as prestress in the shell due to the fluid weight, are neglected. The irrotationality property is the condition for the existence of a scalar potential function Ψ from which the velocity may be written as

$$\mathbf{v} = -\nabla\Psi = -\nabla(-Ux + \Phi). \quad (6)$$

In Eq. (6) the potential Ψ is assumed to comprise two components: The first one due to the mean flow associated with the undisturbed axial flow velocity U, and the second one is the unsteady perturbation potential Φ associated with shell motion. For small perturbations, Φ must satisfy

$$\nabla^2\Phi - \frac{1}{c^2}\left(\frac{\partial^2\Phi}{\partial t^2} + 2U\frac{\partial^2\Phi}{\partial t \partial x} + U^2\frac{\partial^2\Phi}{\partial x^2}\right) = 0, \quad (7)$$

where c is the sound speed in the fluid, and the Laplace operator in cylindrical coordinates is

$$\nabla^2\Phi = \frac{\partial^2\Phi}{\partial x^2} + \frac{\partial\Phi}{\partial r^2} + \frac{1}{r\partial}\frac{\partial\Phi}{\partial r} + \frac{1}{r^2}\frac{\partial^2\Phi}{\partial\theta^2} = 0.$$

The perturbed pressure P may be related to the velocity potential by Bernoulli's equation for unsteady fluid flow; hence we can write ([2])

$$P = \overline{P} + p = \overline{P} + \rho_F\left(\frac{\partial\Phi}{\partial t} + U\frac{\partial\Phi}{\partial x}\right), \quad (8)$$

where $\overline{P}$ is the mean pressure, p is the perturbation pressure, and ρ_F is the fluid mass density.

3.1 Model With Separation of Variables. The fluid domain is assumed to be an annular cylinder of infinite extent in the axial direction, delimited internally by a periodically supported shell of infinite length and externally by a rigid cylinder, so that it is possible to employ the method of separation of variables to obtain the velocity potential. Here the mathematical trick is to consider the function w and the fluid domain defined for any $x \in (-\infty, \infty)$. This means that w is a periodic function with main period $2L$, and the same is satisfied for the velocity potential and the perturbation pressure. This type of solution was used by Païdoussis and Denise [15] for shells with incompressible flow, either internal or external. If there is no cavitation, at the fluid-shell interface we can write

$$\left(\frac{\partial\Phi}{\partial r}\right)_{r=R} = \left(\frac{\partial w}{\partial t} + U\frac{\partial w}{\partial x}\right), \quad (9)$$

and at the fluid/rigid-cylinder interface

$$\left(\frac{\partial\Phi}{\partial r}\right)_{r=R_1} = 0. \quad (10)$$

The problem is solved by separation of variables, and the perturbation pressure at the shell wall is given by

$$p_{r=R} = \rho_F \frac{K_n'(\mu R_1)I_n(\mu R) - I_n'(\mu R_1)K_n(\mu R)}{\mu[K_n'(\mu R_1)I_n'(\mu R) - I_n'(\mu R_1)K_n'(\mu R)]} \times \left(\frac{\partial}{\partial t} + U\frac{\partial}{\partial x}\right)^2 w, \quad (11)$$

where $\mu^2 = \alpha^2 - (U/c)^2[\alpha + (\omega/U)]^2$, $\alpha = m\pi/L$, I_n and K_n are the modified Bessel functions of order n of first and second kind, respectively. For flow unbounded in the radial direction ($R_1 \to \infty$), Eq. (11) simplifies to

$$p_{r=R} = \rho_F \frac{K_n(\mu R)}{\mu K_n'(\mu R)}\left(\frac{\partial}{\partial t} + U\frac{\partial}{\partial x}\right)^2 w. \quad (12)$$

3.2 Fourier Transform Model. This model was applied by Dowell and Widnall [16] to evaluate unsteady aerodynamic forces on shells in axial flowing fluid and extended to annular compressible flow by Païdoussis et al. [2]. In this case, rigid baffles (extensions), of the same external diameter as the shell, limit internally (in the radial direction) the fluid domain; these baffles are indefi-

nitely long in the axial direction and are connected to the shell, one at $x=0$ and the other at $x=L$. Externally, the fluid domain is confined by a rigid cylinder at $r=R_1$.

Assuming no cavitation, the boundary condition at the fluid-shell interface is

$$\left(\frac{\partial\Phi}{\partial r}\right)_{r=R}=\left(\frac{\partial w}{\partial t}+U\frac{\partial w}{\partial x}\right) \quad \text{for } 0\leqslant x\leqslant L,$$
$$=0 \quad \text{for } x<0 \quad \text{and} \quad x>L \tag{13}$$

and at the fluid/rigid-cylinder interface

$$\left(\frac{\partial\Phi}{\partial r}\right)_{r=R_1}=0. \tag{14}$$

Assuming $w=A(t)\sin(m\pi x/L)\cos(n\theta)$ and noting that all the terms in the assumed mode expansion of w may be written in similar form, the perturbation pressure at the shell wall is obtained by using Fourier transform ([2])

$$p_{r=R}=\rho_F\frac{L}{2}\cos(n\theta)\int_{-\infty}^{\infty}\frac{m[1-(-1)^m e^{-j\alpha L}]}{m^2\pi^2-\alpha^2L^2}\frac{K_n'(\mu R_1)I_n(\mu R)-I_n'(\mu R_1)K_n(\mu R)}{\mu[K_n'(\mu R_1)I_n'(\mu R)-I_n'(\mu R_1)K_n'(\mu R)]}[\ddot{A}(t)+2j\alpha U\dot{A}(t)-\alpha^2U^2A(t)]e^{j\alpha x}d\alpha \tag{15}$$

where α is the transform variable, $j=\sqrt{-1}$ and μ has been defined in Section 3.1. The expression for p for unbounded flow is immediately obtainable by substituting the appropriate functional of Bessel functions, similarly to Eqs. (11) and (12).

4 Airy Stress Function and Solution

The expansion used for the transverse displacement w satisfies identically the boundary conditions given by Eqs. (3); moreover, it satisfies exactly the continuity of circumferential displacement ([13]),

$$\int_0^{2\pi}\frac{\partial v}{\partial\theta}d\theta=0. \tag{16}$$

The boundary conditions for either set of Eqs. (4) give complicated expressions when transformed into equations involving w. Therefore, they are modified into simpler integral expressions that satisfy Eqs. (4) on the average ([17]), namely

$$\int_0^{2\pi}N_xRd\theta=0, \quad \text{at } x=0,L \quad (\text{Case } 1) \tag{17a}$$

$$\int_0^{2\pi}\int_0^{L}\frac{\partial u}{\partial x}dxRd\theta=\int_0^{2\pi}[u(L,\theta)-u(0,\theta)]Rd\theta$$
$$=0; \quad (\text{Case } 2) \tag{17b}$$

and in both cases

$$\int_0^{2\pi}\int_0^{L}N_{x\theta}dxRd\theta=0. \tag{18}$$

Equation (17a) assures a zero axial force N_x on the average at $x=0$, L, while Eq. (17b) states that the axial displacement u is zero on the average at $x=0$, L. Equation (18) is satisfied when $v=0$ on the average at $x=0$, L and u is continuous in θ on the average. Replacement of Eqs. (4) by (17) and (18) simplifies computations, but it introduces an approximation (boundary conditions are exactly satisfied at n discrete points, where n is the number of circumferential waves).

Substituting the expansion of w, Eq. (5), in the right-hand side of Eq. (2), a partial differential equation for the stress function F is obtained, the solution of which may be written as

$$F=F_h+F_p, \tag{19}$$

where F_h is the homogeneous and F_p is the particular solution. The latter is given by

$$F_p=\sum_{m=0}^{M}\sum_{n=0}^{N}\{[F_{1mn}\cos(n\theta)+F_{2mn}\sin(n\theta)]\sin(\lambda_m x)$$
$$+[F_{3mn}\cos(n\theta)+F_{4mn}\sin(n\theta)]\cos(\lambda_m x)\}, \tag{20a}$$

where the functions of time F_{jmn}, $j=1,\ldots 4$, are given in Amabili et al. [13]. The homogeneous solution may be assumed to be of the form ([12,13,18])

$$F_h=\frac{1}{2}\overline{N}_xR^2\theta^2+\frac{1}{2}x^2\left\{\overline{N}_\theta-\frac{1}{2\pi RL}\int_0^L\int_0^{2\pi}\left[\frac{\partial^2F_p}{\partial x^2}\right]Rd\theta dx\right\}$$
$$-\overline{N}_{x\theta}xR\theta, \tag{20b}$$

where $\overline{N}_x$, $\overline{N}_\theta$, and $\overline{N}_{x\theta}$ are the average in-plane force resultants (per unit length), as a consequence of the in-plane constraints on the average, defined as

$$\overline{N}_\#=\frac{1}{2\pi L}\int_0^{2\pi}\int_0^{L}N_\#dxd\theta, \quad \#=x,\theta,x\theta. \tag{21}$$

Equation (20b) is chosen so as to satisfy on the average the boundary conditions imposed. Boundary conditions (17,18) allow us to express the in-plane restraint stresses $\overline{N}_x$, $\overline{N}_\theta$, and $\overline{N}_{x\theta}$ in terms of w and its derivatives.

By using the Galerkin method, seven second-order ordinary, coupled nonlinear differential equations are obtained for the variables $A_{1,n}(t)$, $B_{1,n}(t)$, $A_{2,n}(t)$, $B_{2,n}(t)$, $A_{1,0}(t)$, $A_{3,0}(t)$, and $A_{5,0}(t)$, by successively weighting the original Eq. (1) with the functions that describe the shape of the seven modes retained in Eq. (9). The Galerkin projection of Eq. (1) has been performed by using the *Mathematica* computer software.

5 Numerical Results for Annular Air Flow

Numerical results were obtained for a case already theoretically (with a linear theory) and experimentally studied by one of the authors ([7]): a circular cylindrical shell made of rubber, in annular incompressible air-flow, with $R=0.0247$ m, $L/R=5.5$, $h/R=0.05$, $R_1/R=1.25$, $E=2.43\times10^6$ Pa, $\rho=1220$ kg/m^3, $\rho_F=1.25$ kg/m^3, and $\nu=0.47$. Supports at both ends approximated clamped ends. The static pressure inside and outside the shell was equal during experiments, so that $\overline{P}=0$ has been taken; the added mass effect of stationary air inside the shell is taken into account, even if small. A modal damping coefficient $\zeta=ch\pi L/(\omega_{1,n}m_1)=0.01$ is assumed, where $\omega_{1,n}$ is the linear natural frequency of the first asymmetric longitudinal mode at zero flow velocity ($\omega_{1,n}=280.21$ for the separation-of-variables fluid model and 279.58 rad/s for the Fourier model) and

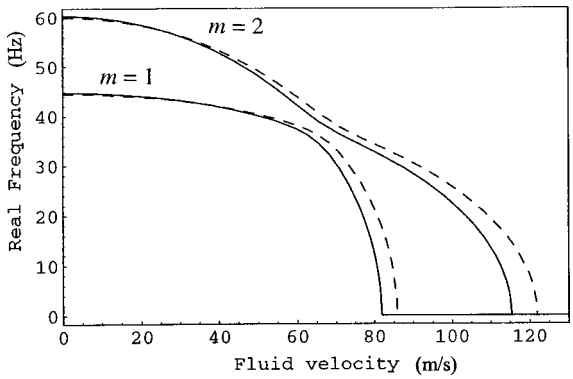

Fig. 1 Frequency obtained from the linearized equations without viscous damping (ζ=0) versus the flow velocity: ——, fluid model with separation of variables; — — —, fluid model with Fourier transform method

$$m_1 = \rho_S h \pi L/2 + \rho_F \pi (L/2) \times \left\{ \frac{K_n'(\mu R_1) I_n(\mu R) - I_n'(\mu R_1) K_n(\mu R)}{\mu [K_n'(\mu R_1) I_n'(\mu R) - I_n'(\mu R_1) K_n'(\mu R)]} + \frac{I_n(\mu R)}{\mu I_n'(\mu R)} \right\}$$

for the separation-of-variables fluid model; an analogous expression of m_1 is obtained for the Fourier transform model. For this case the shell is extremely flexible and the difference between simply supported and clamped edges is small; in this numerical simulation, simple supports are assumed at the shell ends ($N_x = 0$). The system is studied for the circumferential wave number $n = 3$, which is associated with the lowest flow velocity for instability, according to experiments. This value is strictly outside the usual range of applicability of Donnell's shallow-shell theory ($n \geqslant 5$); however, results are of interest for possible comparison with experiments.

Results obtained by linearizing the equations of motion are shown in Fig. 1 for both fluid-structure interaction models; zero structural damping is initially assumed. The natural frequencies of the first two modes are given *versus* the flow velocity. Increasing the flow velocity from zero, the modes become complex. The shell loses stability by divergence at $U \cong 80$ m/s; the buckled shape displays two longitudinal half-waves. Beyond this point, the shell remains unstable; no restabilization is observed. Results obtained with the two different models of fluid-structure interaction are quite close. The less conservative separation-of-variables model will be used in the studies that follow.

Experimental results in El Chebair et al. [7] are in good agreement with the linear theoretical results at zero flow velocity. However, experiments show violent divergence at 49 m/s, i.e., *well before* the value predicted ($\cong$80 m/s), accompanied by large deformation of the shell. Moreover, the shape of the buckled shell at 49 m/s shows one axial half-wave ($n = 3$; $m = 1$), very large deformation and contraction of the circumference in a cross section of the shell. Even if the effect of viscosity is included in the model ([7]), the theoretical predictions are significantly larger than experimental results.

5.1 Nonlinear Results. Results in this section have been computed with the separation-of-variables flow model and with modal damping $\zeta = 0.01$. Solutions of the nonlinear equations of motion have been obtained numerically by using the software *Auto* ([19]) and direct integration of the equations of motion. No periodic solutions have been found, which agrees with the experimental results. In particular, two types of static solutions (divergence) have been detected: (i) solutions of the type $B_{1,n}/A_{1,n} = -B_{2,n}/A_{2,n}$, i.e., when the first and second asymmetric longitudinal modes are in antiphase in θ (i.e., they are described by the same function in θ), and (ii) solutions of the type $B_{1,n}/A_{1,n} = -A_{2,n}/B_{2,n}$, i.e., when the first and second asymmetric longi-

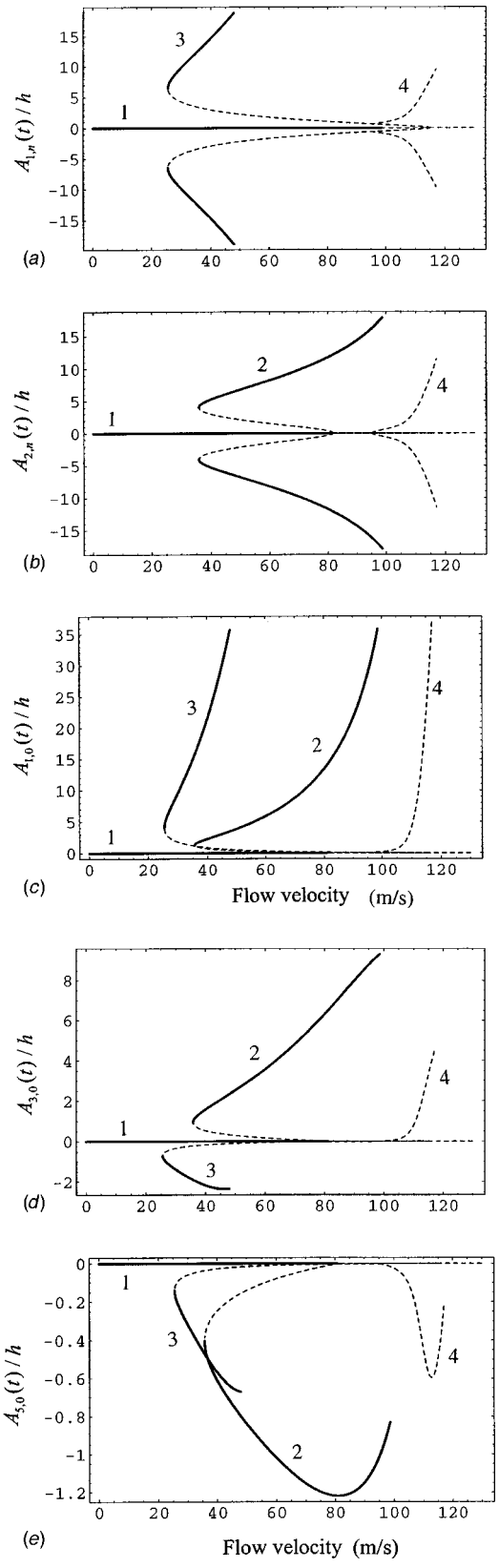

Fig. 2 Amplitude of nonoscillatory solutions versus the flow velocity (rubber shell); in-antiphase modes. ——, stable branches; — — —, unstable branches. (*a*) Amplitude of the first longitudinal mode $A_{1,n}/h$; (*b*) amplitude of the second longitudinal mode $A_{2,n}/h$; (*c*) amplitude of the first axisymmetric mode $A_{1,0}/h$; (*d*) amplitude of the third axisymmetric mode $A_{3,0}/h$; (*e*) amplitude of the fifth axisymmetric mode $A_{5,0}/h$.

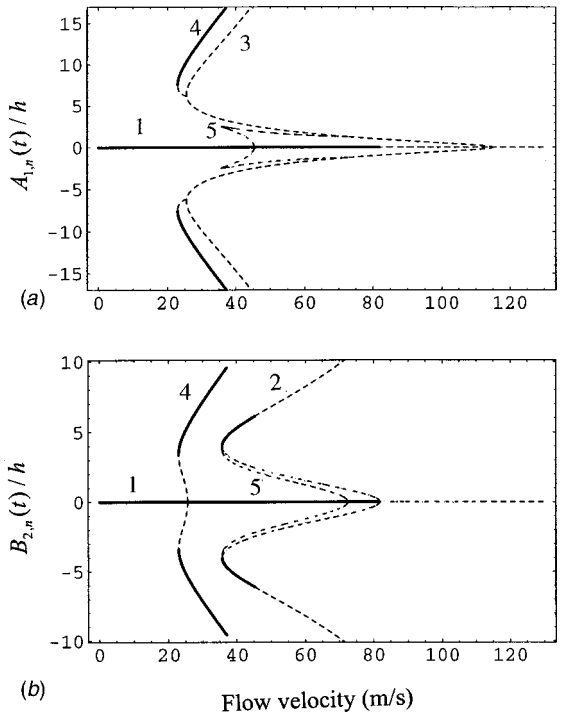

Fig. 3 Amplitude of nonoscillatory solutions versus the flow velocity (rubber shell); modes orthogonal in θ. ——, stable branches; — — —, unstable branches. (*a*) Amplitude of the first longitudinal mode $A_{1,n}/h$; (*b*) amplitude of the second longitudinal mode $A_{2,n}/h$.

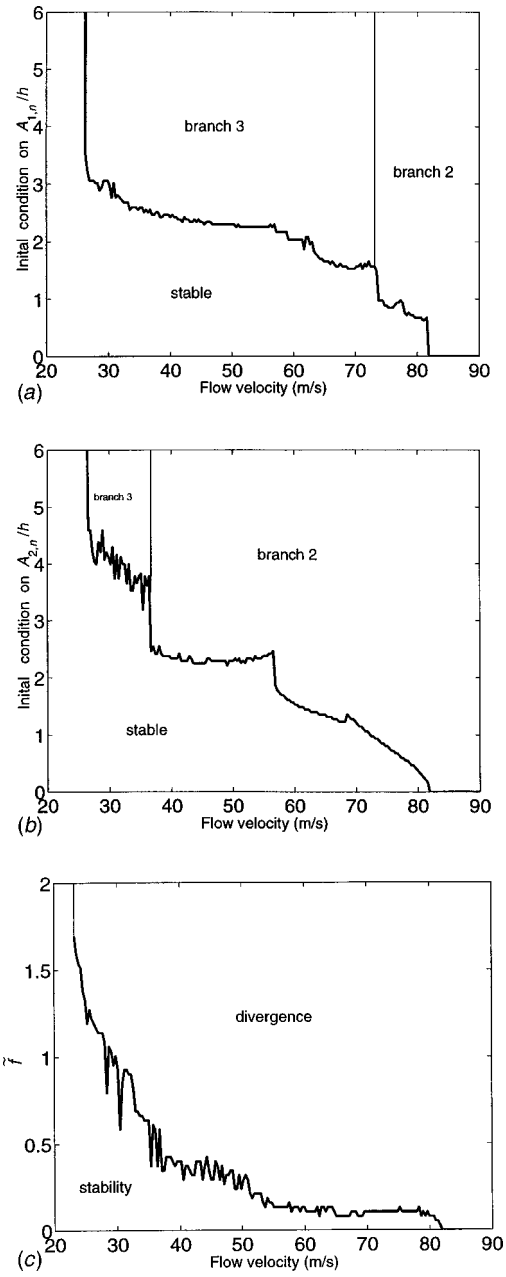

Fig. 4 Basin of attraction of undisturbed and bifurcated solutions; minimum amplitude necessary for divergence is indicated with a thick solid line. (*a*) Shell with antiphase modes, static displacement with first axial-mode shape; (*b*) shell with antiphase modes, static displacement with second axial-mode shape; (*c*) shell with seven degrees-of-freedom at first-axial-mode, resonant modal excitation.

tudinal modes are orthogonal in θ. When all seven generalized coordinates are retained in the equations of motion, the system does not possess a preferential angular coordinate θ to locate the deformation.

In Figs. 2 and 3 the various branches represent the bifurcated solutions of the equilibrium position of the shell. In particular, branch 2 bifurcates from branch 1 (undeformed configuration) for a flow velocity of 81.8 m/s (threshold of instability predicted by linear theory); it is strongly subcritical and is associated to a mode shape with two longitudinal half-waves. Branch 3, which is also strongly subcritical, bifurcates from branch 1 for a flow velocity of 115 m/s and is associated with a mode shape with a single longitudinal half-wave. Other branches involve a combination of the two longitudinal modes, giving a coupled mode divergence. Figure 2(*a*) shows that branch 3 is stable for flow velocities larger than 25.5 m/s; analogously, branch 2 is stable for flow velocities larger than 35.7 m/s. These results indicate that, for flow velocities larger than 25.5 m/s, at least two (four starting at 35.7 m/s) equilibrium positions coexist with the original undeformed configuration of the shell. Similar results are shown in Fig. 3, obtained by considering modes orthogonal in θ. Branch 2, related to a mode with two longitudinal half-waves, is stable for flow velocities between 35.8 and 45.3 m/s, while the coupled-mode divergence, branch 4, is stable for flow velocity larger than 22.9 m/s. Branch 2 loses stability through the bifurcation that gives rise to coupled-mode divergence (branch 5). Branch 3, relative to a mode with one longitudinal half-wave, is never stable. These nonlinear results show that, if the shell is given enough perturbation, the solution can jump from the undeformed original configuration to a bifurcated solution for flow velocity larger than 22.9 m/s. The loss of stability occurs as a violent divergence, with very large shell deformations.

In order to investigate the perturbation necessary to jump to bifurcated branches from the trivial equilibrium and the shape of the buckled shell, the basin of attraction of the trivial configuration and bifurcated solutions is given in Fig. 4. This study has been performed by direct integration of the equations of motion, using an adaptive step-size fourth-fifth order Runge-Kutta method. Figures 4(*a*) and 4(*b*) show the behavior of the shell as a function of flow velocity and with static perturbation of the first and second longitudinal mode shape, respectively. The minimum amplitude necessary for divergence is indicated by a thick solid line in the figure. In particular, for $U=49$ m/s almost the same static displacement with the shape of the first or second longitudinal mode is necessary to have divergence; however, a different shape gives a jump to a different branch. For the shell model with all seven degree-of-freedom active and a static perturbation of the

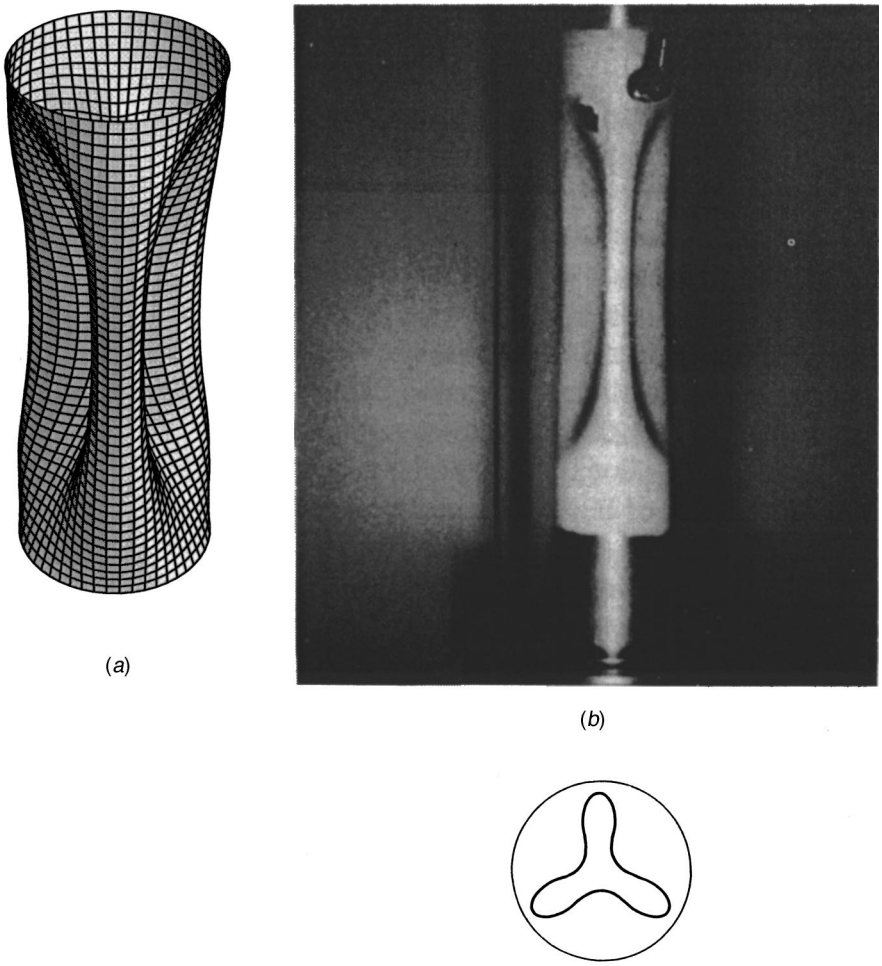

(*a*)

(*b*)

Fig. 5 Post-divergence shape of the rubber shell for mode ($n=3$, $m=1$). (*a*) Computed shape for flow velocity 30 m/s; (*b*) experimental shape, from Ref. [7].

first longitudinal mode, the result is very close to that in Fig. 4(*a*), with the difference that a jump to branch 4 is always obtained. The basin of attraction has been investigated in Fig. 4(*c*) by giving a dynamic perturbation. A modal excitation $f = f_{1,n}\cos(n\theta)\sin(\pi x/L)\cos(\omega t)$ is given to the first longitudinal mode, at the linear resonant radian frequency (therefore the frequency is changed with flow velocity). The minimum force amplitude $\tilde{f} = f_{1,n}/\{h\omega_{1,n}^2 m_1[2/(\pi L)]\}$ necessary for divergence is indicated. This force decreases with flow velocity much more than a static perturbation, as can be seen by comparing Figures 4(*a–c*); in particular, around 50 m/s only a small excitation is necessary to precipitate divergence. This result is in good agreement with the experiments of El Chebair et al. [7]. Moreover, as a consequence of the softening type nonlinear behavior of the shell, a reduced frequency of excitation will result in jumps much easier; this nonlinear behavior is enhanced with flow velocity ([20]).

Table 1 Comparison of linear, nonlinear and experimental ([7]) results for instability of the rubber shell

	Type of Instability	"Helicoidal" Solution
Linear	divergence, mode ($n=3$, $m=2$)	81.8 m/s
Nonlinear	divergence, mode ($n=3$, $m=1$)	between 25.5 and 81.8 m/s
Experimental	divergence, mode ($n=3$, $m=1$)	49 m/s

The computed shape of the shell after divergence is shown in Fig. 5(*a*) for $U=30$ m/s; it corresponds to the stable point of branch 3 in Fig. 2 for $U=30$ m/s, i.e., to mode ($n=3$, $m=1$). At this velocity, the internal faces of the shell start to touch each other as a consequence of the large axisymmetric contraction. Therefore, this shape is not significantly changed by increasing the flow velocity. The experimental shape obtained by El Chebair et al. [7] is shown in Fig. 5(*b*) and is in excellent agreement with Fig. 5(*a*). Figures 5(*a*,*b*) also justify the necessity of a nonlinear shell model to describe the dynamics with such large deformations.

The predictions of divergence computed by using linear and nonlinear theories are compared to the experimental value in Table 1. It must be observed that the stability limit, according to the nonlinear theory, can only be given as a range of values if the level of perturbation is not exactly known. Summarizing, results show that the onset of instability predicted by nonlinear theory given enough disturbance is 22.9 m/s for coupled-mode divergence (or 25.5 m/s for divergence in the first mode) instead of the linear threshold of 81.8 m/s: a difference of more than three times!

6 Numerical Results for Shell in Unbounded Water Flow

The system analyzed is a circular cylindrical shell simply supported at the ends ($N_x=0$), immersed in unbounded flowing water ($c=\infty$) and with $L/R=2$, $h/R=0.01$, $E=206\times10^9$ Pa,

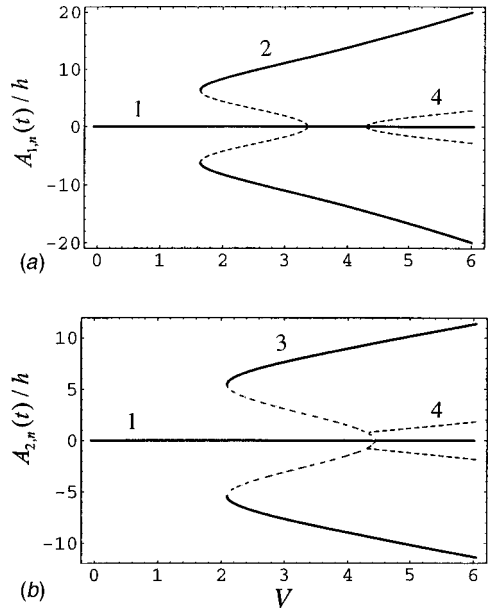

Fig. 6 Amplitude of nonoscillatory solutions versus the nondimensional external axial flow velocity; in-antiphase modes. ——, stable branches; — — —, unstable branches. (*a*) Amplitude of the first longitudinal mode $A_{1,n}/h$; (*b*) amplitude of the second longitudinal mode $A_{2,n}/h$.

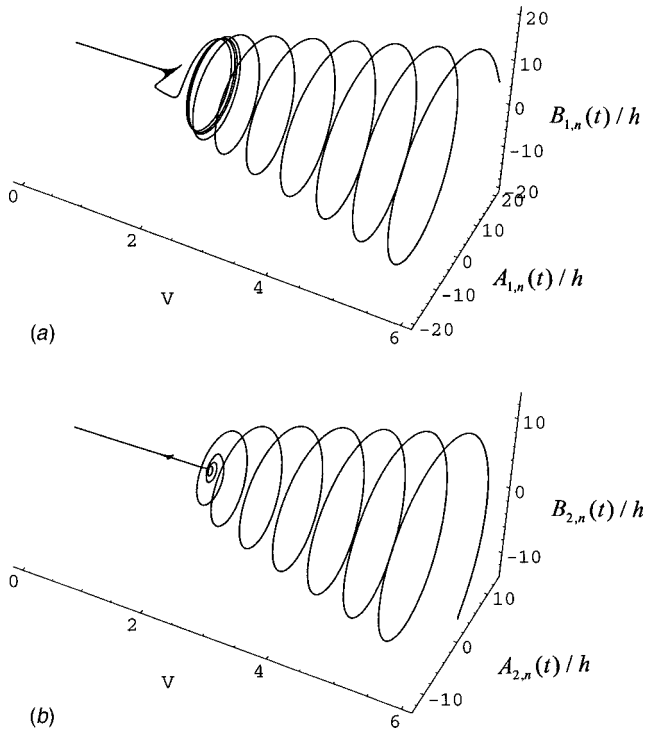

Fig. 8 Behavior of the system starting from a point where the system is subjected to coupled-mode divergence at $V=6$, and then slowly decreasing the nondimensional flow velocity V. Generalized coordinates: (*a*) $A_{1,n}$ and $B_{1,n}$ versus V; (*b*) $A_{2,n}$ and $B_{2,n}$ versus V.

$\rho=7850$ kg/m^3, $\rho_F=1000$ kg/m^3, and $\nu=0.3$. It is studied for $n=5$, which is the first mode to become unstable according to linear theory. A modal damping $\zeta=ch\pi L/2=0.01$ is assumed and the separation-of-variables flow model is used; the mean pressure is $P=0$. A nondimensional fluid velocity $V=U/\{(\pi^2/L)\times[D/(\rho h)]^{1/2}\}$ is introduced for convenience ([21]).

Figures 6 and 7 present the bifurcated solutions of the equilibrium position of the system. In particular, branch 2 bifurcates from branch 1 for $V=3.36$ and is associated with a mode shape with a single longitudinal half-wave; branch 3 bifurcates from branch 1 for $V=4.44$ and is associated to a mode shape with two longitudinal half-waves. Branch 4 involves a combination of the two longitudinal modes, giving coupled-mode divergence. Figure 6(*a*) shows that branch 2 is stable for flow velocities larger than 1.64; analogously, see Fig. 6(*b*), branch 3 is stable for flow velocities larger than 2.09. These results indicate that for flow velocities larger than 1.64, at least two (four starting at 2.09) solutions coexist with the original undeformed configuration of the shell. More complex results are shown in Fig. 7 in which modes orthogonal in θ are considered. Branch 4 corresponds to a stable coupled-mode divergence, emerging at $V=2.63$ and is stable for $V>2.37$. Actually in Fig. 7 this coupled-mode solution is indicated to be stable only for a small part, but all points of the curve are stable for a fixed velocity; i.e., when the velocity is changed, the solution is stable only if all seven degrees of freedom are evaluated, and this solution evolves on an axisymmetric surface, rotating around the velocity axis in a kind of helicoidal motion. The reason for this peculiar behavior is due to the relationship $B_{1,n}/A_{1,n}=-A_{2,n}/B_{2,n}$ between the generalized coordinates related to asymmetric modes. These results show that the onset of instability predicted by nonlinear theory, given enough disturbance, is $V=1.64$, instead of the linear threshold of 3.36. The difference is of the order of 1:2.

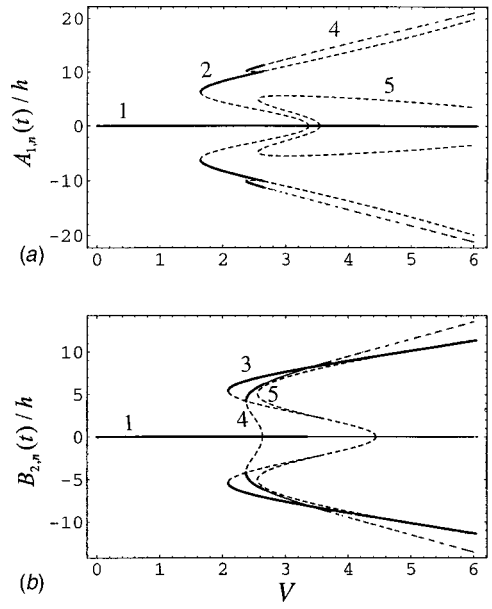

Fig. 7 Amplitude of nonoscillatory solutions versus the nondimensional external axial flow velocity; modes orthogonal in θ. ——, stable branches; — — —, unstable branches. (*a*) Amplitude of the first longitudinal mode $A_{1,n}/h$; (*b*) amplitude of the second longitudinal mode $B_{2,n}/h$.

In order to simulate the dynamical behavior of the complete system, the equations of motion have been integrated numerically, starting from one of the fixed points obtained at $V=6$ and then slowly decreasing the flow velocity. An adaptive step-size fourth-fifth order Runge-Kutta integration algorithm was used. The result in Fig. 8 shows that all seven generalized coordinates are different from zero for a large range of flow velocities. It is interesting to observe that, for $V>2.37$, the solution belongs to an axisymmetric surface that rotates around its axis in helicoidal fashion. This axisymmetric surface is obtained by rotation of branch "4" in Fig. 7 around the V-axis. For $1.64<V<2.37$, the system follows the

first-mode divergence without rotating any more. At $V=1.64$ the system regains the stable undeformed configuration. The results obtained can be compared with those of Amabili et al. [13] for the same shell with internal water flow. The qualitative behavior of the system is the same, but the shell is slightly more stable.

7 Conclusions

The results obtained for both annular and unbounded external axial flow show that the onset of instability, given enough perturbation, is much lower (two, three times, or even more) than the instability limit predicted by linear theories. This is due to the large shell deformation associated with divergence of the shell that, as indicated by calculations and experiments, are at least of the same order of magnitude as the shell thickness. The present study explains the discrepancy between linear theories and experimental results and shows the necessity of using a nonlinear theory, since non-negligible perturbations, e.g., due to flow excitation, are always present in applications. In order to obtain more accurate results, more than two longitudinal modes should be used in the mode expansion; however, the qualitative results are unchanged.

Acknowledgments

The authors acknowledge the financial support of the Italian Space Agency, the NSERC of Canada and FCAR of Québec.

References

[1] Horn, W., Barr, G., Carter, L., and Stearman, R., 1974, ''Recent Contributions to Experiments on Cylindrical Shell Panel Flutter,'' AIAA J., **12**, pp. 1481–1490.
[2] Païdoussis, M. P., Chan, S. P., and Misra, A. K., 1984, ''Dynamics and Stability of Coaxial Cylindrical Shells Containing Flowing Fluid,'' J. Sound Vib., **97**, pp. 201–235.
[3] Païdoussis, M. P., Misra, A. K., and Nguyen, V. B., 1992, ''Internal- and Annular-Flow-Induced Instabilities of a Clamped-Clamped or Cantilevered Cylindrical Shell in a Coaxial Conduit: The Effects of System Parameters,'' J. Sound Vib., **159**, pp. 193–205.
[4] Païdoussis, M. P., Misra, A. K., and Chan, S. P., 1985, ''Dynamics and Stability of Coaxial Cylindrical Shells Conveying Viscous Fluid,'' ASME J. Appl. Mech., **52**, pp. 389–396.
[5] Nguyen, V. B., Païdoussis, M. P., and Misra, A. K., 1994, ''A CFD-Based Model for the Study of the Stability of Cantilevered Coaxial Cylindrical Shells Conveying Viscous Fluid,'' J. Sound Vib., **176**, pp. 105–125.
[6] Horáček, J., 1993, ''Approximate Theory of Annular Flow-Induced Instabilities of Cylindrical Shells,'' J. Fluids Struct., **7**, pp. 123–135.
[7] El Chebair, A., Païdoussis, M. P., and Misra, A. K., 1989, ''Experimental Study of Annular-Flow-Induced Instabilities of Cylindrical Shells,'' J. Fluids Struct., **3**, pp. 349–364.
[8] Librescu, L., 1965, ''Aeroelastic Stability of Orthotropic Heterogeneous Thin Panels in the Vicinity of the Flutter Critical Boundary. Part I: Simply Supported Panels,'' J. Mec., **4**, pp. 51–76.
[9] Librescu, L., 1967, ''Aeroelastic Stability of Orthotropic Heterogeneous Thin Panels in the Vicinity of the Flutter Critical Boundary. Part II,'' J. Mec., **6**, pp. 133–152.
[10] Olson, M. D., and Fung, Y. C., 1967, ''Comparing Theory and Experiment for the Supersonic Flutter of Circular Cylindrical Shells,'' AIAA J., **5**, pp. 1849–1856.
[11] Evensen, D. A., and Olson, M. D., 1968, ''Circumferentially Travelling Wave Flutter of a Circular Cylindrical Shell,'' AIAA J., **6**, pp. 1522–1527.
[12] Amabili, M., Pellicano, F., and Païdoussis, M. P., 1998, ''Nonlinear Vibrations of Simply Supported, Circular Cylindrical Shells, Coupled to Quiescent Fluid,'' J. Fluids Struct., **12**, pp. 883–918.
[13] Amabili, M., Pellicano, F., and Païdoussis, M. P., 1999, ''Non-Linear Dynamics and Stability of Circular Cylindrical Shells Containing Flowing Fluid. Part I: Stability,'' J. Sound Vib., **225**, pp. 655–699.
[14] Lakis, A. A., and Laveau, A., 1991, ''Non-Linear Dynamic Analysis of Anisotropic Cylindrical Shells Containing a Flowing Fluid,'' Int. J. Solids Struct., **28**, pp. 1079–1094.
[15] Païdoussis, M. P., and Denise, J.-P., 1972, ''Flutter of Thin Cylindrical Shells Conveying Fluid,'' J. Sound Vib., **20**, pp. 9–26.
[16] Dowell, E. H., and Widnall, S. E., 1966, ''Generalized Aerodynamic Forces on an Oscillating Cylindrical Shell,'' Q. Appl. Math., **24**, pp. 1–17.
[17] Dowell, E. H., and Ventres, C. S., 1968, ''Modal Equations for the Nonlinear Flexural Vibrations of a Cylindrical Shell,'' Int. J. Solids Struct., **4**, pp. 975–991.
[18] Amabili, M., Pellicano, F., and Païdoussis, M. P., 2000, ''Non-Linear Dynamics and Stability of Circular Cylindrical Shells Containing Flowing Fluid, Part III: Truncation Effect Without Flow and Experiments,'' J. Sound Vib., **237**, pp. 617–640.
[19] Doedel, E. J., Champneys, A. R., Fairgrieve, T. F., Kuznetsov, Y. A., Sandstede, B., and Wang, X., 1998, *AUTO 97: Continuation and Bifurcation Software for Ordinary Differential Equations (with HomCont)*, Concordia University, Montreal, Canada.
[20] Amabili, M., Pellicano, F., and Païdoussis, M. P., 2000, ''Non-Linear Dynamics and Stability of Circular Cylindrical Shells Containing Flowing Fluid, Part IV: Large-Amplitude Vibrations With Flow,'' J. Sound Vib., **237**, pp. 641–666.
[21] Weaver, D. S., and Unny, T. E., 1973, ''On the Dynamic Stability of Fluid-Conveying Pipes,'' ASME J. Appl. Mech., **40**, pp. 48–52.

X. Xin[1]
Department of Civil and Environmental Engineering,
University of Missouri,
Columbia, MO 65211
e-mail: xxin@model1.civil.missouri.edu

C. Chicone
Professor,
Department of Mathematics,
University of Missouri,
Columbia, MO 65211

Z. Chen
Associate Professor,
Department of Civil and Environmental Engineering,
University of Missouri,
Columbia, MO 65211
Mem. ASME

Analyical Solutions for Failure Evolution With a Nonlinear Local Damage Model

The partitioned-modeling and similarity methods are applied in this paper to derive a closed-form solution for localized dynamic failure problems, with a nonlinear local damage model. The initial point of the localization is taken as the point at which the type of governing differential equation transforms from being hyperbolic to elliptic for dynamic case due to material damage. The evolution of localization is represented by a moving material surface of discontinuity between the elliptic domain and hyperbolic domain. A closed-form solution for a static loading case is also given as a complementary note to show evolution of the localized failure. The effects of model parameters on the structural response are investigated, and the evolution of relevant field variables is illustrated to demonstrate the essential feature of the localized failure evolution.
[DOI: 10.1115/1.1406956]

1 Introduction

There exist two different approaches to model the evolution of material failure, i.e., continuous and discontinuous ones, after the onset of failure is identified. Decohesion models and fracture mechanics models are representative of discontinuous approaches, in which strong discontinuities are introduced into a continuum body such that the mathematical model is well posed for a set of given boundary and/or initial data. On the other hand, nonlocal (integral or strain gradient) models, the Cosserat continuum models and rate-dependent models are among the continuous approaches proposed to regularize the localization problems, in which the higher-order terms in space and/or time are introduced into the strain-stress relations so that the mathematical model is well posed in a higher-order sense for given boundary and/or initial data.

The use of higher-order terms in space makes it difficult to perform large-scale computer simulation, due to the limitation of current computational capability. As can be found by reviewing the existing nonlocal models, the nonlocal terms are usually included in the limit surface so that a single higher-order governing differential equation will appear in the problem domain. If we can find an alternative approach to replace the single higher-order equations in the single domain with lower-order equations in subdomains, parallel computing might be used for the large-scale simulation of localization problems. To demonstrate the proposed approach, a one-dimensional wave propagation problem is considered here.

It is known that waves can propagate in a continuum only if the material tangent stiffness tensor is positive definite. The wave equation appears to lose its hyperbolicity with the advent of material softening if a local model is used ([1,2]). As shown by Bazant and Belytschko [3], the softening region in a local continuum tends to localize into a single surface at which the strain becomes infinite instantaneously. As a result, if a local model is used, the strain-softening process dissipates no energy over a finite interval of time in the problem domain, which is not representative of the physics involved. With the use of a partitioned-modeling approach, however, the evolution of localization can be predicted with the use of local models.

The basic idea of the partitioned-modeling approach is to apply different local constitutive models inside and outside the localization domain whose boundary is a moving material surface of discontinuity that is associated with the local changes of material properties. The initial point of localization is taken as the point at which the type of governing differential equation transforms from being hyperbolic to elliptic. The partitioned-modeling approach has been applied to both quasi-static and dynamic localization problems (e.g., [4–8]). To provide a rigorous mathematical treatment, a similarity method has been used with a linear local elastoplastic model to solve the localization problem that involves moving boundary conditions ([7]), without invoking any jump or discontinuity conditions in advance, as required in the previous work ([5,9]). To find a closed-form solution, the key assumption made in the analytical approach was that the speed of the moving surface is constant. To explore the applicability of the similarity method to other problems, a closed-form solution is obtained in this paper for a nonlinear local damage model.

A recent study of the failure wave propagation in shocked glasses implies that the microfissuring at one location might induce local deformation heterogeneities that in turn initiate microfissuring in the adjacent material and so on ([10]). Hence, a diffusion equation governing the progressive percolation of heterogeneous microdamage appears to capture the essence of the dynamic failure evolution in shocked glasses, as verified with the experimental data available. In fact, the use of jump conditions could also result in a diffusion equation governing the failure wave speed, through a mathematical argument ([6]). However, a closed-form solution cannot be obtained for the nonlinear diffusion equation governing the evolution of microdamage that depends on the stress state and internal state variables in general. In order to obtain a closed-form solution in this paper, the diffusion speed of the moving material surface is simplified to be constant. This can be thought as a special case of diffusion: i.e., the time-average of a real diffusion process. Due to the limitation of current experimental facilities, it is still a challenging task to quantitatively determine how the internal energy dissipates and diffuses in real time associated with the evolution of dynamic failure. Although the propagation of a failure interface has been demonstrated in the open literature, the speed appears to decrease with propagation distance in some impact experiments (e.g., [11]) and

[1]To whom correspondence should be addressed.

Contributed by the Applied Mechanics Division of THE AMERICAN SOCIETY OF MECHANICAL ENGINEERS for publication in the ASME JOURNAL OF APPLIED MECHANICS. Manuscript received by the ASME Applied Mechanics Division, Nov. 9, 1999; final revision, Nov. 10, 2000. Editor: J. W. Ju. Discussion on the paper should be addressed to the Editor, Professor Lewis T. Wheeler, Department of Mechanical Engineering, University of Houston, Houston, TX 77204-4792, and will be accepted until four months after final publication of the paper itself in the ASME JOURNAL OF APPLIED MECHANICS.

to be constant in other impact experiments (e.g., [12]), due to the difference in experimental techniques. The lack of consistency in existing experimental data, therefore, does not warrant to quantitatively evaluate the speed of the failure interface. The proposed mathematical approach for modeling dynamic failure evolution with local constitutive models provides not only a qualitative means to explore the energy dissipation and diffusion process, but also a useful tool to verify the numerical solutions.

2 Partitioned-Modeling Approach With a Nonlinear Local Damage Model

The proposed analytical approach is illustrated here by solving a one-dimensional problem of dynamic failure evolution, with the use of a rate-independent nonlinear local damage constitutive model (Fig. 1). In this problem, a tensile bar of length L with mass density ρ is fixed at the left end $x=0$. Letting E denote Young's modulus, σ the normal stress, ε the normal strain, σ_0 the elastic limit stress with $\varepsilon_0=\sigma_0/E$, and b the model parameter, the damage model is described as follows.

A strain-based damage surface is defined as

$$f^d=\varepsilon-\varepsilon_0(1+bD) \tag{1}$$

where D is the damage parameter which can be calculated through the damage consistency condition:

$$D=\frac{\varepsilon-\varepsilon_0}{b\varepsilon_0}, \quad \text{if } \varepsilon\geqslant\varepsilon_0. \tag{2}$$

D is zero for the undamaged material, and it can grow until $D=1$ with $\varepsilon=\varepsilon_F=(b+1)\varepsilon_0$. The elastodamage secant stiffness takes the form of

$$E^{ed}=E(1-D)=\frac{(b+1)\varepsilon_0-\varepsilon}{b\varepsilon_0}E, \quad \text{if } \varepsilon\geqslant\varepsilon_0. \tag{3}$$

The stress is then given by

$$\sigma=\begin{cases} E\varepsilon, & \text{if } \varepsilon<\varepsilon_0 \text{ (elastic regime)}, \quad (4a)\\ \dfrac{(b+1)\varepsilon_0\varepsilon-\varepsilon^2}{b\varepsilon_0}E, & \text{if } \varepsilon\geqslant\varepsilon_0 \text{ (damaging regime)}. \quad (4b)\end{cases}$$

By taking $d\sigma/d\varepsilon=0$, we get $\varepsilon_L=(b+1)\varepsilon_0/2$ that corresponds to the ultimate limit stress $\sigma_L=(b+1)^2\sigma_0/(4b)$, as can be shown by substituting ε_L into Eq. (4*b*). Note that $\varepsilon_F=2\varepsilon_L$ in this nonlinear damage model.

The corresponding tangent modulus takes the forms of

$$\frac{d\sigma}{d\varepsilon}=\begin{cases} E, & \text{if } \varepsilon<\varepsilon_0 \text{ (elastic regime)}, \quad (5a)\\ -\dfrac{2E}{b\varepsilon_0}(\varepsilon-\varepsilon_L), & \text{if } \varepsilon\geqslant\varepsilon_0 \text{ (damaging regime)}. \quad (5b)\end{cases}$$

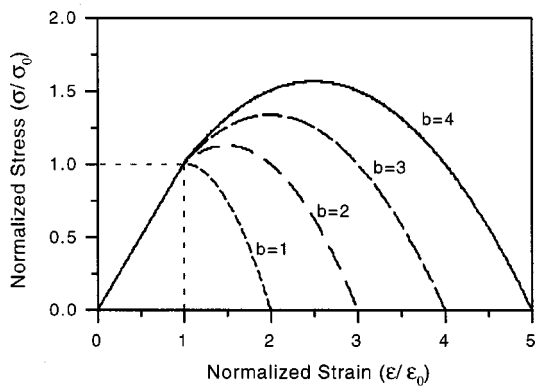

Fig. 1 A nonlinear local elastodamage model

In order to initiate localized damage in the bar at the fixed end $x=0$, a constant stress σ_a within the range $(0.5\sigma_L,\sigma_L)$ is applied at the free end $x=L$. Thus, an elastic stress wave will propagate along the bar from $x=L$ to $x=0$. Generally, the equation of motion for one-dimensional wave propagation can be written as

$$\frac{\partial^2 u}{\partial t^2}-\frac{1}{\rho}\frac{d\sigma}{d\varepsilon}\frac{\partial^2 u}{\partial x^2}=0 \tag{6}$$

where t denotes time, and u displacement.

Before the wave front reaches the rigid boundary at $x=0$, the stress is below the limit stress. The material behavior is elastic and the tangent modulus is positive. Therefore, the differential equation governing the elastic wave domain is hyperbolic: $u_{tt}-v_e^2u_{xx}=0$, with $v_e=(E/\rho)^{1/2}$ being the uniaxial elastic wave speed. When the wavefront reaches the rigid boundary at $t=t_L=L/v_e$, stress will be doubled and exceed the limit stress. As a result, the material will undergo damage with a negative tangent modulus. Thus, a new domain, i.e., a dynamic localization domain, is produced, in which the type of governing differential equation transforms from being hyperbolic to elliptic. If nothing is added to regularize the solution, a zero measure of the elliptic domain would occur for the local model. However, the boundary between the elliptic and hyperbolic domain is assumed here to be governed by a diffusion equation which is the transition type between hyperbolic and elliptic PDE's ([13]). As can be seen, the initiation of localization is accompanied by the initiation of a material boundary across which the type of governing differential equation changes due to the material damage. This material boundary will move along the bar during the evolution process of localization. The physics behind the evolution of localization is related here to the progressive percolation of heterogeneous flow or microdamage, starting from a critical state.

Two facts based on experimental observations should be elucidated here. First, the size of the localization zone is finite. Second, this finite localization zone is not formed instantaneously. Instead, it is formed over a finite time span. In other words, the evolution of localization, which is represented by a moving material boundary between the elliptic and the hyperbolic domain, has a finite speed. To obtain a closed-form solution, this speed is assumed here to be a constant v_b, as discussed in the last section. Based on the experimental data available, however, it appears that v_b should depend on the stress state and internal state variables in general.

In summary, the whole solution domain is partitioned by a moving boundary $\partial\Omega_I=x_b(t)$ after the limit state is reached. At any given time $t>t_L$, the whole domain consists of two subdomains: an elliptic domain Ω_I and a hyperbolic domain $(\Omega_{II}+\Omega_{III})$, as shown in Fig. 2. Therefore, we can apply different

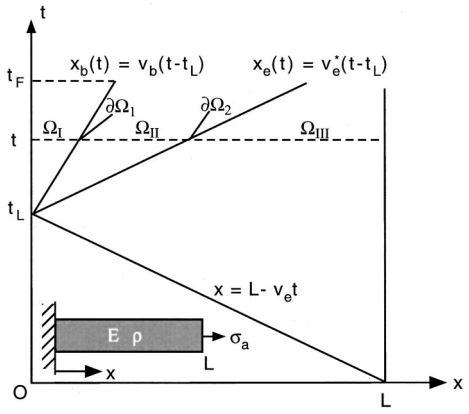

Fig. 2 After the limit state is reached, the whole solution domain is partitioned by a moving boundary $(\partial\Omega_I)$ into two domains: an elliptic domain (Ω_I) and hyperbolic domain $(\Omega_{II}+\Omega_{III})$

local constitutive models to the elliptic and the hyperbolic domains, respectively, and obtain an analytical solution for the whole domain.

3 Analytical Solutions in Partitioned Domains for a Dynamic Case

3.1 Solution in Elliptic Domain (Ω_I). After substituting Eq. (5*b*) into Eq. (6), the differential equation governing the localization zone is given by

$$\frac{\partial^2 u^-}{\partial t^2}+\frac{2E}{b\varepsilon_0\rho}\left(\frac{\partial u^-}{\partial x}-\varepsilon_L\right)\frac{\partial^2 u^-}{\partial x^2}=0, \quad x\in[0,x_b(t)] \quad \text{and} \quad t\in[t_L,t_F] \tag{7}$$

where the superscripts $^-$ and $^+$ denote the field variables to the left and right of the moving material boundary, respectively. The location of the moving material boundary $x_b(t)$ is defined as

$$x_b(t)=v_b(t-t_L), \quad t\in[t_L,t_F]. \tag{8}$$

Since ε_L is a constant, Eq. (7) can be equivalently rewritten as

$$\frac{\partial^2 u^-}{\partial t^2}+\frac{E}{b\varepsilon_0\rho}\frac{\partial}{\partial x}\left(\frac{\partial u^-}{\partial x}-\varepsilon_L\right)^2=0. \tag{9}$$

Then, taking derivative with respect to x for each item in Eq. (9), we have

$$\frac{\partial^2}{\partial t^2}\left(\frac{\partial u^-}{\partial x}-\varepsilon_L\right)+\frac{E}{b\varepsilon_0\rho}\frac{\partial^2}{\partial x^2}\left(\frac{\partial u^-}{\partial x}-\varepsilon_L\right)^2=0. \tag{10}$$

Equation (10) is the differential equation governing the evolution of the strain field after the limit state is reached. Let $a=2E/(\rho b\varepsilon_0)=2v_e^2/(b\varepsilon_0)$, and define a new function

$$\varphi^-(x,t):=\frac{\partial u^-}{\partial x}-\varepsilon_L=\varepsilon^--\varepsilon_L. \tag{11}$$

Then, Eq. (10) becomes

$$\frac{\partial^2}{\partial t^2}\varphi^-+\frac{a}{2}\frac{\partial^2}{\partial x^2}(\varphi^-)^2=0. \tag{12}$$

It can be rewritten as follows:

$$\varphi^-_{tt}+a((\varphi^-_x)^2+\varphi^-\varphi^-_{xx})=0. \tag{13}$$

The following set of data is prescribed for Eq. (13):

$$\varphi^-(x=x_b(t),t)=0, \quad t\in[t_L,t_F], \tag{14a}$$

$$\varphi^-(x=0,t=t_F)=\varepsilon_F-\varepsilon_L=\varepsilon_L, \tag{14b}$$

which represents the condition at the moving boundary $x_b(t)$ (the initiation of localization), and the boundary condition at the fixed end when $t=t_F$, the time at which the final rupture occurs. In this paper, t_F is considered to be an independent parameter, which should be related to the strain rate in the post-limit regime. In fact, $(\varepsilon_F-\varepsilon_0)/(t_F-t_L)$ yields the average strain rate at $x=0$ during the evolution of damage.

The general solution of Eq. (13) can be obtain by variable transformations (Appendix), and is given as follows:

$$\varphi^-(x,t)=\pm[2(k(x-c(t-t_L))+l)]^{1/2}-c^2/a. \tag{15}$$

Substituting Eqs. (8) and (14*a*) in Equation (*A*2) (Appendix) we have

$$0=\varphi^-(v_b(t-t_L),t)=f(v_b(t-t_L)-c(t-t_L)). \tag{16a}$$

The only choice for the above condition to hold leads to $c=v_b$, because t is a variable. In other words, the response in the elliptic domain is instantaneous. At $x=0$, $t=t_L$, we have

$$0=\varphi^-(0,t_L)=\pm(2l)^{1/2}-v_b^2/a, \tag{16b}$$

that is $l=v_b^4/(2a^2)$. Therefore, the solution of Eq. (10) becomes

$$\varphi^-(x,t)=\pm[2k(x-v_b(t-t_L))+(v_b^2/a)^2]^{1/2}-v_b^2/a. \tag{17}$$

Using the condition of final state, $\varphi^-(x=0,t=t_F)=\varepsilon_L$, we obtain

$$k=-\frac{(b+1)\varepsilon_0^2}{4v_b(t_F-t_L)}\left[\frac{b+1}{2}+b\left(\frac{v_b}{v_e}\right)^2\right]. \tag{18}$$

Finally, the evolution of the strain field in the localization domain is described by

$$\varepsilon^-(x,t)=\frac{b+1}{2}\varepsilon_0-\frac{b\varepsilon_0}{2}\left(\frac{v_b}{v_e}\right)^2+\frac{\varepsilon_0}{2}F, \quad x\in[0,x_b(t)] \quad \text{and} \quad t\in[t_L,t_F] \tag{19a}$$

with

$$F=\left[b^2\left(\frac{v_b}{v_e}\right)^4-\frac{(b+1)}{v_b(t_F-t_L)}\left(b+1+2b\left(\frac{v_b}{v_e}\right)^2\right)(x-v_b(t-t_L))\right]^{1/2}.$$

The corresponding strain rate thus takes the form of

$$\dot{\varepsilon}^-(x,t)=\frac{(b+1)\varepsilon_0}{4F(t_F-t_L)}\left[b+1+2b\left(\frac{v_b}{v_e}\right)^2\right], \quad x\in[0,x_b(t)] \quad \text{and} \quad t\in[t_L,t_F]. \tag{19b}$$

3.2 Solution in Damaged Hyperbolic Domain (Ω_{II}). The governing differential equation for the hyperbolic domain Ω_{II} is similar to Eq. (7) except that the tangent modulus is positive due to $\varepsilon-\varepsilon_L<0$ in Eq. (5*b*), namely,

$$\frac{\partial^2 u^+}{\partial t^2}+\frac{2E}{b\varepsilon_0\rho}\left(\frac{\partial u^+}{\partial x}-\varepsilon_L\right)\frac{\partial^2 u^+}{\partial x^2}=0 \quad x\in[x_b(t),x_e(t)] \quad \text{and} \quad t\in[t_L,t_F] \tag{20}$$

where $b>1$. For $b\leqslant 1$, $\varepsilon_L=\varepsilon_0$, so that no damaged hyperbolic (damage hardening) domain exists.

Following the same derivations as in the previous section, Eq. (20) can be rewritten into a form similar to Eq. (12), i.e.,

$$\frac{\partial^2}{\partial t^2}\varphi^++\frac{a}{2}\frac{\partial^2}{\partial x^2}(\varphi^+)^2=0 \tag{21}$$

where

$$\varphi^+:=\frac{\partial u^+}{\partial x}-\varepsilon_L=\varepsilon^+-\varepsilon_L.$$

By the concepts of the domain of dependence and the range of influence ([14]), the post-limit response through the moving material boundary $\partial\Omega_1$ only affects the solution at the points between the moving boundaries $\partial\Omega_1=x_b(t)$ and $\partial\Omega_2=x_e(t)$ that are originated at the point $(0,t_L)$ (Fig. 2). Therefore, the hyperbolic domain can be further partitioned into two subdomains: $\Omega_{II}=\{(x,t):x\in[x_b(t),x_e(t)],t\in[t_L,t_F]\}$ and $\Omega_{III}=\{(x,t):x\in[x_e(t),L],t\in[t_L,t_F]\}$, where the subdomain Ω_{II} is under the influence of post-limit response but the subdomain Ω_{III} is not.

Because of the evolution of the localization zone and the propagation of the reflected wave, the boundaries at both the left and right side of the subdomain Ω_{II} are moving with time. The left boundary $\partial\Omega_I$ (onset failure surface) is assumed to be moving at a constant speed v_b, and it is characterized by a bounded strain ε_u that must be not larger than ε_L. The right boundary $\partial\Omega_2$ (damaged wave front) is moving with speed v_e^* and is characterized by ε_0. Thus, for the subdomain Ω_{II}, we have the following set of prescribed boundary conditions:

$$\varepsilon^+(x=x_b(t),t)=\varepsilon_u, \quad t\in[t_L,t_F], \tag{22a}$$

$$\varepsilon^+(x=x_e(t),t)=\varepsilon_0, \quad t\in[t_L,t_F]. \tag{22b}$$

The positions of the left and right boundaries, for time $t>t_L$ are determined by Eq. (8) and the following equation:

$$x_e(t)=v_e^*(t-t_L), \text{ with } v_e^*=v_e(1-1/b)^{1/2} \quad \text{and} \quad t\in[t_L,t_F], \tag{23}$$

respectively, where v_e^* is the speed of the damaged wavefront, which follows from the fact that the tangent modulus $d\sigma/d\varepsilon=E(1-1/b)$ at $\varepsilon=\varepsilon_0$.

To solve this boundary value problem with the moving boundary conditions, a similarity method ([15,16]) can be used. The similarity transformations assume the form

$$\theta(\eta)=\varphi^+, \quad \eta=\frac{x-x_b(t)}{x_e(t)-x_b(t)}=\frac{x-v_b(t-t_L)}{(v_e^*-v_b)(t-t_L)},$$
$$x\in[x_b(t),x_e(t)] \quad \text{and} \quad t\in[t_L,t_F] \tag{24}$$

where $x-x_b(t)$ is the distance from x to the moving material boundary $\partial\Omega_1$, and $x_e(t)-x_b(t)$ is the current total length of the domain Ω_{II}.

Here, it is reasonable to suppose that θ is not a function of t and x separately, but rather it is a function of their dimensionless ratio η. Using this assumption, Eq. (21) can be recast into an equation for the unknown η. To do this we first represent the partial derivatives of φ^+ with respect to t and x in terms of the derivatives of θ with respect to η, which can be found, using the chain rule, to be

$$\frac{\partial^2}{\partial t^2}\varphi^+=\frac{1}{(v_e^*-v_b)^2(t-t_L)^2}\left[\frac{x^2}{(t-t_L)^2}\frac{d\theta^2}{d\eta^2}+\frac{2x(v_e^*-v_b)}{(t-t_L)}\frac{d\theta}{d\eta}\right], \tag{25a}$$

$$\frac{\partial^2}{\partial x^2}(\varphi^+)^2=\frac{2}{(v_e^*-v_b)^2(t-t_L)^2}\left[\theta\frac{d^2\theta}{d\eta^2}+\left(\frac{\partial\theta}{\partial\eta}\right)^2\right]. \tag{25b}$$

Substituting Eq. (25) into (21) and recalling that

$$\frac{x}{(t-t_L)}=(v_e^*-v_b)\eta+v_b \tag{26}$$

from Eq. (24), we can reduce the second-order PDE (21) to a second-order ODE as follows:

$$[(v_b+(v_e^*-v_b)\eta)^2+a\theta]\frac{d^2\theta}{d\eta^2}+a\left(\frac{d\theta}{d\eta}\right)^2+2(v_e^*-v_b)[v_b+(v_e^*-v_b)\eta]\frac{d\theta}{d\eta}=0. \tag{27}$$

Equation (27) has the simple form

$$\frac{d}{d\eta}\left\{[(v_b+(v_e^*-v_b)\eta)^2+a\theta]\frac{d\theta}{d\eta}\right\}=0; \tag{28}$$

and therefore, we have

$$[(v_b+(v_e^*-v_b)\eta)^2+a\theta]\frac{d\theta}{d\eta}=C_1 \tag{29}$$

for some constant C_1. Since the symmetric condition at $x=0$ when $t=t_L$ is $\varphi_x(x=0,t=t_L)=0$, we have $d\theta/d\eta(\eta=0)=0$ so that $C_1=0$. We have the trivial solution $d\theta/d\eta=0$, namely, $\theta=$constant. The nontrivial solution can be obtained from the following equation:

$$[v_b+(v_e^*-v_b)\eta]^2+a\theta=0. \tag{30}$$

The general solution of Eq. (30) is given by

$$\theta=-\frac{1}{a}[v_b+(v_e^*-v_b)\eta]^2. \tag{31}$$

Substituting Eq. (24) into (31) gives

$$\varepsilon^+(x,t)=\frac{b+1}{2}\varepsilon_0-\frac{b\varepsilon_0}{2}\left[\frac{x}{v_e(t-t_L)}\right]^2,$$
$$x\in[x_b(t),x_e(t)] \quad \text{and} \quad t\in[t_L,t_F]. \tag{32}$$

The corresponding strain rate is given by

$$\dot\varepsilon^+(x,t)=\frac{b\varepsilon_0x^2}{v_e^2(t-t_L)^3}, \quad x\in[x_b(t),x_e(t)] \quad \text{and} \quad t\in[t_L,t_F]. \tag{33}$$

3.3 Solution in Undamaged Hyperbolic Domain (Ω_{III}). To obtain the strain distribution directly, the governing differential equation for the subdomain Ω_{III} is expressed in a strain-based form as follows:

$$\frac{\partial^2\varepsilon^+}{\partial t^2}-\frac{E}{\rho}\frac{\partial^2\varepsilon^+}{\partial x^2}=0 \quad x\in[x_e(t),L] \quad \text{and} \quad t\in[t_L,t_F] \tag{34}$$

with the boundary conditions

$$\varepsilon^+(x=x_e(t),t)=\varepsilon_u\leqslant\varepsilon_0, \quad t\in[t_L,t_F], \tag{35a}$$

$$\varepsilon^+(x=L,t)=\varepsilon_a=\sigma_a/E, \quad t\in[t_L,t_F], \tag{35b}$$

where ε_u is a bounded strain which must be not larger than ε_0. In this case, the similarity transformations take the following form:

$$\theta(\eta)=\frac{\varepsilon^+}{\varepsilon_a}, \quad \eta=\frac{x-v_e^*(t-t_L)}{L-v_e^*(t-t_L)}, \quad x\in[x_e(t),L] \quad \text{and}$$
$$t\in[t_L,t_F] \tag{36}$$

where $L-v_e^*(t-t_L)$ is the current total length of the domain Ω_{III} and ε_a is the strain corresponding to the incident elastic stress wave.

The solution is found to be

$$\varepsilon^+(x,t)=\sigma_a/E, \quad x\in[x_e(t),L] \quad \text{and} \quad t\in[t_L,t_F]. \tag{37}$$

The corresponding stress field in each subdomain can be calculated by using Eq. (4).

3.4 Discussion and Demonstration. There is a jump in strain rate across the moving material boundary $\partial\Omega_1=x_b(t)$, i.e.,

$$\dot\varepsilon^-(x=x_b^-(t),t)\neq\dot\varepsilon^+(x=x_b^+(t),t), \quad t\in[t_L,t_F]. \tag{38a}$$

This fact is easily seen because it follows from Eq. (19*b*) that

$$\dot\varepsilon^-(x=x_b^-(t),t)=\frac{(b+1)\varepsilon_0}{4b(t_F-t_L)}\left[(b+1)\left(\frac{v_e}{v_b}\right)^2+2b\right],$$
$$t\in[t_L,t_F], \tag{38b}$$

while the use of Eq. (33) results in

$$\dot\varepsilon^+(x=x_b^+(t),t)=\frac{b\varepsilon_0}{(t-t_L)}\left(\frac{v_b}{v_e}\right)^2, \quad t\in[t_L,t_F]. \tag{38c}$$

There is also a jump in strain rate across the moving boundary $\partial\Omega_2=x_e(t)$, i.e.,

$$\dot\varepsilon^+(x=x_e^-(t),t)\neq\dot\varepsilon^+(x=x_e^+(t),t), \quad t\in[t_L,t_F], \tag{39a}$$

because it follows from Eq. (33) that

$$\dot\varepsilon^+(x=x_e^-(t),t)=\frac{(b-1)\varepsilon_0}{(t-t_L)}, \quad t\in[t_L,t_F], \tag{39b}$$

while the use of Eq. (37) yields

$$\dot\varepsilon^+(x=x_e^+(t),t)=0, \quad t\in[t_L,t_F]. \tag{39c}$$

At the moving boundary $x_b(t)=v_b(t-t_L)$, the normalized strain and stress jumps are given by

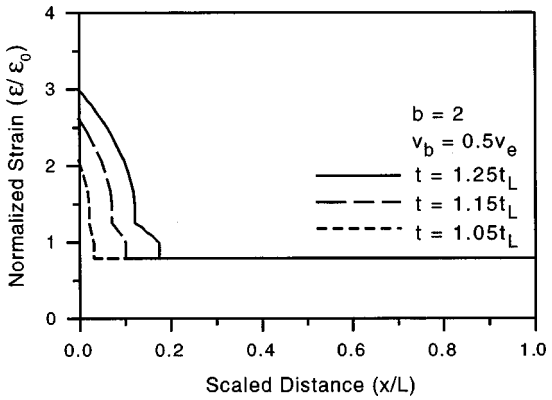

Fig. 3 Evolution of localization along the bar

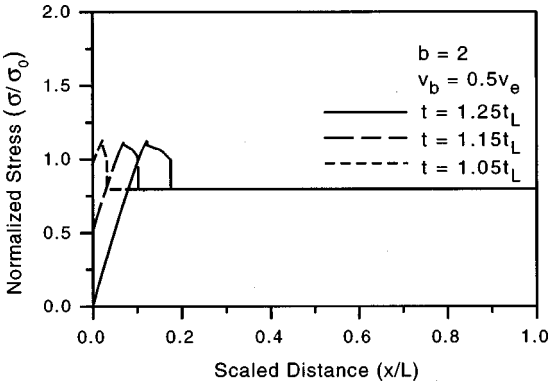

Fig. 4 Normalized stress profiles corresponding to Fig. 3

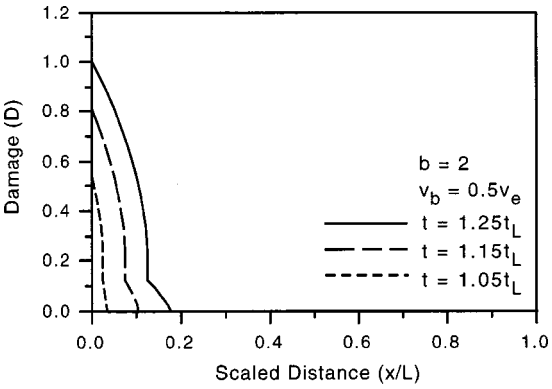

Fig. 5 Damage evolution corresponding to Fig. 3

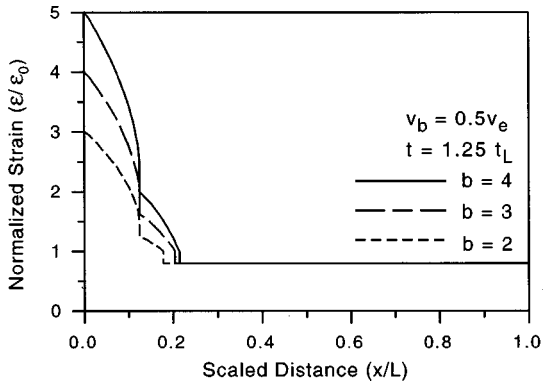

Fig. 6 Strain profiles for different b at $t=1.25t_L$

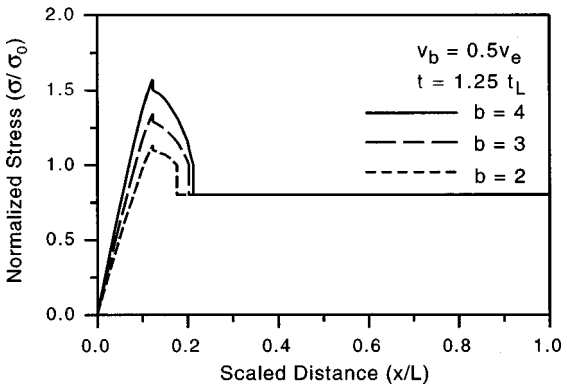

Fig. 7 Stress profiles for different b at $t=1.25t_L$

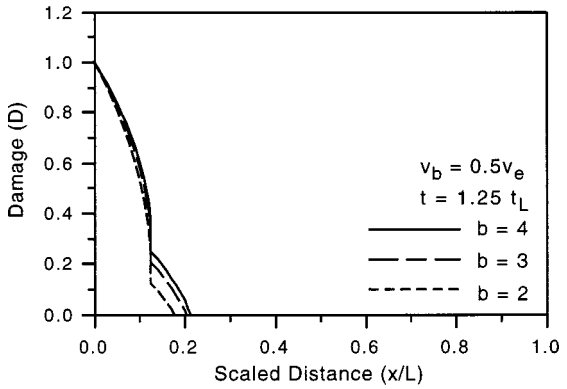

Fig. 8 Damage profiles for different b at $t=1.25t_L$

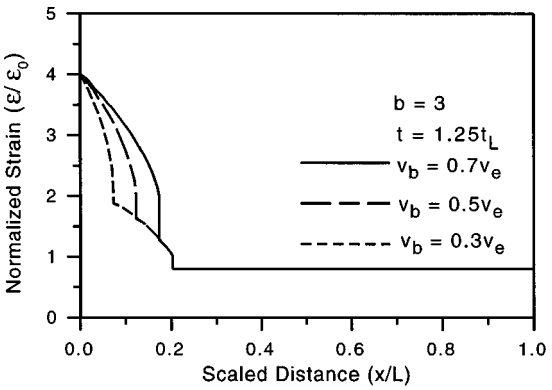

Fig. 9 Strain profiles for different v_b at $t=1.25t_L$

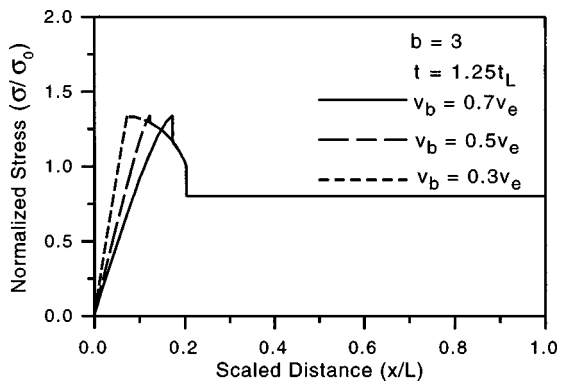

Fig. 10 Stress profiles for different v_b at $t=1.25t_L$

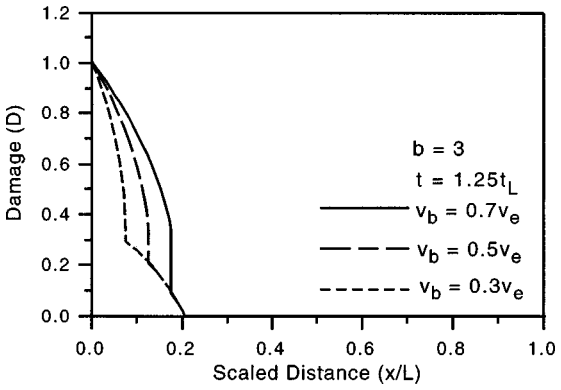

Fig. 11 Damage profiles for different v_b at $t=1.25t_L$

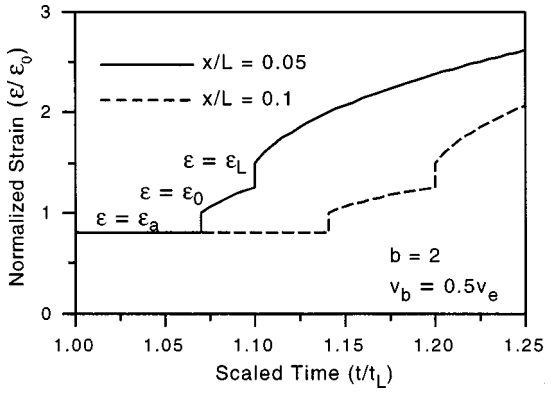

Fig. 12 Strain history at $x/L=0.05$ and 0.1 after localization occurs

$$\frac{\Delta\varepsilon}{\varepsilon_0}=\frac{\varepsilon^+-\varepsilon^-}{\varepsilon_0}=-\frac{b}{2}\left(\frac{v_b}{v_e}\right)^2 \quad \text{and} \quad \frac{\Delta\sigma}{\sigma_0}=\frac{\sigma^+-\sigma^-}{\sigma_0}=\frac{b}{4}\left(\frac{v_b}{v_e}\right)^4. \tag{40}$$

The analytical solutions are illustrated in Figs. 3–12, with an assumption of $t_F=1.25t_L$. The strain and stress are normalized with respect to ε_0 and σ_0, respectively. Figures 3, 4, and 5, respectively, show the evolution of dynamic failure. The effects of the model parameter b on the strain, stress, and damage fields are displayed in Figs. 6, 7, and 8. The influences of the speed of the moving material surface on the evolution of localization are also illustrated in Figs. 9, 10, and 11. The jumps in the strain rate can be seen in Fig. 12.

4 Analytical Solutions in Partitioned Domains for a Static Case

To demonstrate the applicability of the proposed approach to other cases, the analytical solutions for quasi-static failure evolution with the same nonlinear local damage model as in the dynamic case are discussed in this section. Similar to the dynamic problem, a tensile bar of length L is fixed at the left end $x=0$. The one-dimensional governing differential equation for the quasi-static case can be written as follows:

$$\frac{d\sigma}{d\varepsilon}\frac{\partial^2 u}{\partial x^2}=0 \tag{41}$$

where $u(x,t)$ denotes displacement, with t parameterizing the loading process. As illustrated in Fig. 13, the static bar is defined on a closed rectangle in the xt-plane. Assuming an initial imperfection is located at $x=0$, the strain localization is initiated at $x=0$ when $\sigma=\sigma_L$ at time $t=t_L$. The loss of ellipticity is then

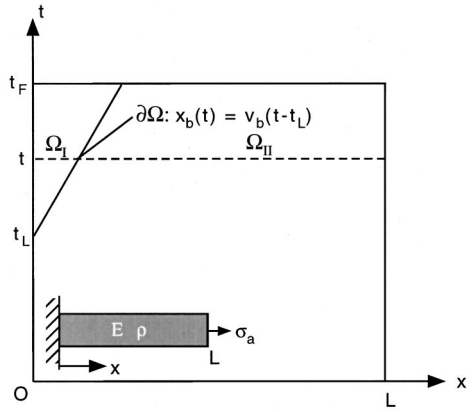

Fig. 13 After the limit state is reached, the whole solution domain for a static bar is partitioned by a moving boundary ($\partial\Omega$) into two elliptic domains: Ω_I and Ω_{II}

regularized by the initiation of a moving material boundary, across which different elliptic equations hold in the subdomain Ω_I and subdomain Ω_{II}, respectively. Using the partitioned-modeling approach discussed in previous sections, we can apply different local constitutive models to each such domain, and obtain analytical solutions for the whole domain by enforcing the displacement continuity across the interface between two subdomains.

4.1 Solution Inside the Localization Domain (Ω_I). After substituting Eq. (5*b*) into Eq. (41), the differential equation governing the localization zone is given by

$$\left(\frac{\partial u^-}{\partial x}-\varepsilon_L\right)\frac{\partial^2 u^-}{\partial x^2}=0 \quad x\in[0,x_b(t)] \quad \text{and} \quad t\in[t_L,t_F] \tag{42}$$

where the superscripts $^-$ and $^+$ denote the field variables to the left and right of the moving boundary $\partial\Omega=x_b(t)$, respectively. The location of the moving boundary $x_b(t)$ is defined by Eq. (8).

Since ε_L is a constant, Eq. (42) can be rewritten as

$$\left(\frac{\partial u^-}{\partial x}-\varepsilon_L\right)\frac{\partial}{\partial x}\left(\frac{\partial u^-}{\partial x}-\varepsilon_L\right)=0. \tag{43}$$

By solving the equation $\partial u^-/\partial x-\varepsilon_L=0$, we get only a trivial solution $\partial u^-/\partial x=\varepsilon_L$ that excludes the evolution of localization. The meaningful solution can be obtained by solving the following equation:

$$\frac{\partial}{\partial x}\left(\frac{\partial u^-}{\partial x}-\varepsilon_L\right)=0, \tag{44}$$

with the following conditions:

$$\varepsilon^-(x=0,t=t_L)=\varepsilon_L \tag{45a}$$

$$\varepsilon^-(x=0,t=t_F)=\varepsilon_F. \tag{45b}$$

The general solution to Eq. (44) can be expressed as

$$u^-(x,t)=\varepsilon_L x+f(t)x+C. \tag{46}$$

Since for any time t at the fixed end, we have $u^-(x=0,t)=0$, so it follows that $C=0$.

The final solution of the original problem is then found to be

$$u^-(x,t)=\varepsilon_L x+\frac{\varepsilon_F-\varepsilon_L}{t_F-t_L}(t-t_L)x, \tag{47}$$

which satisfies both the governing differential equation and the boundary conditions. Substituting $\varepsilon_L=(b+1)\varepsilon_0/2$ and $\varepsilon_F=(b+1)\varepsilon_0$ into (47), we have

$$u^-(x,t)=\frac{(b+1)\varepsilon_0}{2}\left(1+\frac{t-t_L}{t_F-t_L}\right)x. \tag{48}$$

As characterized by an elliptic equation, the strain field is instantaneously uniformly distributed over the whole localization zone, and increases with time only:

$$\varepsilon^-(x,t)=\frac{(b+1)\varepsilon_0}{2}\left(1+\frac{t-t_L}{t_F-t_L}\right). \tag{49}$$

The strain rate inside the localization zone is constant for this simple quasi-static bar problem and given by

$$\dot{\varepsilon}^-(x,t)=\frac{(b+1)\varepsilon_0}{2(t_F-t_L)}. \tag{50}$$

4.2 Solution Outside the Localization Domain (Ω_{II}). The governing differential equation outside the localization domain, i.e., inside Ω_{II}, is similar to Eq. (42) except that the tangent modulus is positive due to $\varepsilon-\varepsilon_L<0$ in Eq. (5*b*), namely,

$$\left(\frac{\partial u^+}{\partial x}-\varepsilon_L\right)\frac{\partial^2 u^+}{\partial x^2}=0 \quad x\in[x_b(t),L] \quad \text{and} \quad t\in[t_L,t_F]. \tag{51}$$

Similarly, Eq. (51) can be rewritten as follows:

$$\left(\frac{\partial u^+}{\partial x}-\varepsilon_L\right)\frac{\partial}{\partial x}\left(\frac{\partial u^+}{\partial x}-\varepsilon_L\right)=0. \tag{52}$$

One possible solution to Eq. (52) can be obtained by solving the equation

$$\frac{\partial u^+}{\partial x}-\varepsilon_L=0, \tag{53}$$

with the result being

$$u^+(x,t)=\varepsilon_L x+f(t)=\frac{(1+b)\varepsilon_0}{2}x+f(t). \tag{54}$$

Since at any time t, the displacement continuity holds across the moving boundary $x_b(t)=v_b(t-t_L)$, that is,

$$u^-(x=x_b^-(t),t)=u^+(x=x_b^+(t),t). \tag{55}$$

Substituting solutions (48) and (54) into Eq. (55), we have

$$\frac{(b+1)\varepsilon_0}{2}\left(1+\frac{t-t_L}{t_F-t_L}\right)v_b(t-t_L)=\frac{(b+1)\varepsilon_0}{2}v_b(t-t_L)+f(t). \tag{56}$$

So

$$f(t)=\frac{(b+1)\varepsilon_0 v_b}{2}\frac{(t-t_L)^2}{t_F-t_L}. \tag{57}$$

The solution in Ω_{II} then takes the form of

$$u^+(x,t)=\frac{(1+b)\varepsilon_0}{2}\left(x+\frac{v_b(t-t_L)^2}{t_F-t_L}\right). \tag{58}$$

Therefore, the strain field is constant outside the localization zone, namely

$$\varepsilon^+(x,t)=\frac{\partial u^+}{\partial x}=\frac{(1+b)}{2}\varepsilon_0, \tag{59}$$

which satisfies the initial condition $\varepsilon^+(x,t=t_L)=\varepsilon_L$.

Another possible solution may be obtained by solving the equation

$$\frac{\partial}{\partial x}\left(\frac{\partial u^+}{\partial x}-\varepsilon_L\right)=0. \tag{60}$$

The general solution of Eq. (60) can be expressed as

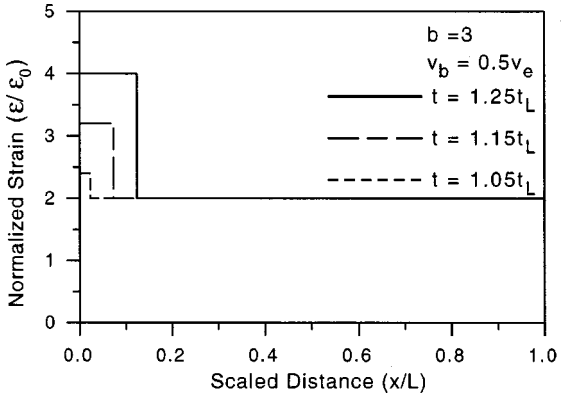

Fig. 14 Evolution of localization along the bar

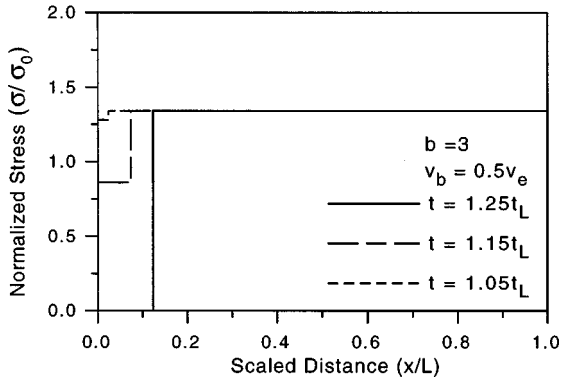

Fig. 15 Normalized stress profiles corresponding to Fig. 14

$$u^+(x,t)=\varepsilon_L x+f(t)x+C=\left(\frac{(1+b)\varepsilon_0}{2}+f(t)\right)x+C. \tag{61}$$

With the use of the initial condition at the fixed end at $t=t_L$, we have $u^+(x=0,t=t_L)=0$, so it follows that $C=0$. Using the continuity condition (55) again, we have

$$\frac{(b+1)\varepsilon_0}{2}\left(1+\frac{t-t_L}{t_F-t_L}\right)v_b(t-t_L)=\left(\frac{(b+1)\varepsilon_0}{2}+f(t)\right)v_b(t-t_L), \tag{62}$$

which yields

$$f(t)=\frac{(b+1)\varepsilon_0}{2}\frac{t-t_L}{t_F-t_L}. \tag{63}$$

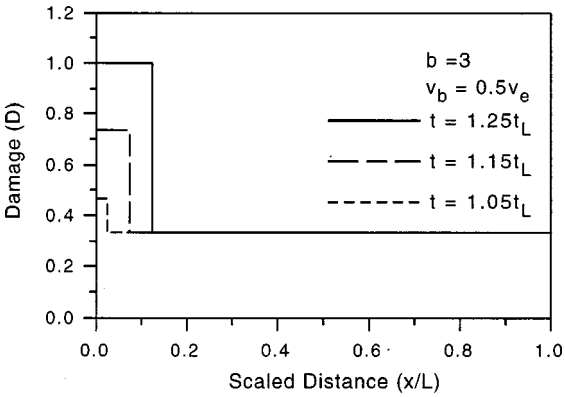

Fig. 16 Damage evolution corresponding to Fig. 14

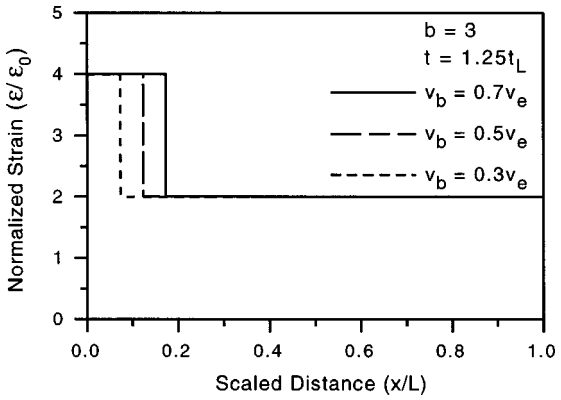

Fig. 17 Strain profiles for different v_b at $t=1.25t_L$

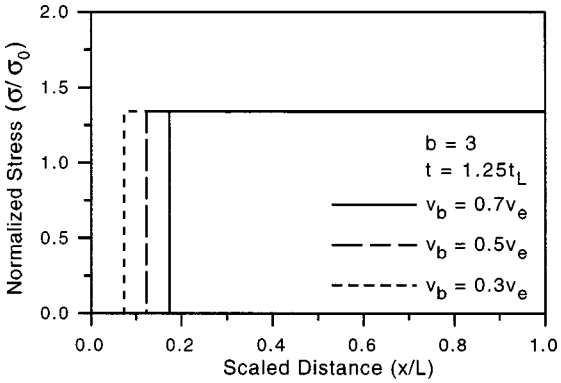

Fig. 18 Stress profiles for different v_b at $t=1.25t_L$

Therefore, we have

$$u^+(x,t)=\frac{(b+1)\varepsilon_0}{2}\left(1+\frac{t-t_L}{t_F-t_L}\right)x. \tag{64}$$

The corresponding strain field is then given by

$$\varepsilon^+(x,t)=\frac{(b+1)\varepsilon_0}{2}\left(1+\frac{t-t_L}{t_F-t_L}\right)\geqslant\varepsilon_L, \quad t\in[t_L,t_F], \tag{65}$$

which is in conflict with the condition that outside the localization zone the strain field should not exceed the limit strain ε_L. In fact, Eq. (65) is the same as Eq. (49), which implies that the whole bar enters the post-limit regime without localization. Therefore the final solutions outside the localization zone should be given by Eqs. (58) and (59).

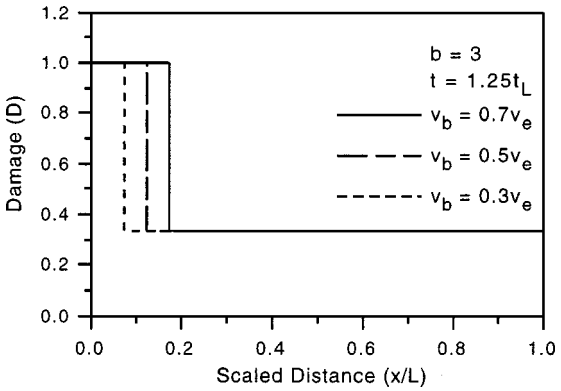

Fig. 19 Damage profiles for different v_b at $t=1.25t_L$

4.3 Discussion and Demonstration. At the moving boundary $x_b(t)=v_b(t-t_L)$, the normalized strain and stress jump are given by

$$\frac{\Delta\varepsilon}{\varepsilon_0}=\frac{\varepsilon^+-\varepsilon^-}{\varepsilon_0}=-\frac{b+1}{2}\frac{t-t_L}{t_F-t_L} \quad \text{and} \quad \frac{\Delta\sigma}{\sigma_0}=\frac{\sigma^+-\sigma^-}{\sigma_0}$$
$$=\frac{(b+1)^2}{4b}\left(\frac{t-t_L}{t_F-t_L}\right)^2. \tag{66}$$

Note that the jumps in the static case depend on the loading process instead of being constant as in the dynamic case, shown in Eq. (40). The analytical solutions are illustrated in Figs. 14–16, with the assumptions of $t_F=1.25t_L$ and $v_b=0.5v_e$. The change of the model parameter b would result in the change of the limit state. The effects of the speed of the moving boundary v_b on the evolution of localization are illustrated in Figs. 17, 18, and 19. As can be seen, the essential features of quasi-static evolution of localization can be quantitatively predicted by the proposed approach. Note that the apparent quasi-static equilibrium does not hold through the whole bar because of the strain jump from the damage model.

5 Concluding Remarks

Instead of invoking nonlocal models, a rigorous partitioned-modeling approach is employed to obtain, via a similarity method, a closed-form solution for a dynamic damaged bar with the use of a nonlinear local damage model. The similarity method is a suitable tool to solve the problem involving moving boundary conditions. It may reduce the second-order PDE to a second-order ODE and map the moving boundary conditions to fixed boundary conditions. It is shown that the predictions of the model continuously depend on the model parameters. The analytical solutions for the localized failure problem, under the given set of boundary and initial data, and the material properties, are unique and stable according to the theory of differential equations. The proposed approach can also be used to obtain a closed-form solution for a quasi-static damage bar.

To obtain a closed-form solution, the major assumption made in this paper is that the material surface of discontinuity is moving at a constant speed. Based on the experimental data available, however, the evolution of localization appears to be an energy dissipation and diffusion process, which should be dependent on the stress state and internal state variables. The similarity method used here may be used for a specific three-dimensional case, such as the localization evolution starting from the center of an isotropic sphere under dynamic loading. For a general case, however, a numerical procedure must be invoked. With the assumption that the evolution of microcracking in space is of diffusion nature, a computational procedure is being developed to simulate the nonlinear damage diffusion process associated with the evolution of dynamic material failure. As a result, the movement of the failure interface will be determined by a nonlinear diffusion equation for given stress state and internal variables. The closed-form solution obtained here could be used to verify the computational procedure in simple cases. If the evolution of localization can be predicted via local models in subdomains in general, parallel computing might be used incrementally for the large-scale simulation of structural failure problems without invoking high-order models.

Acknowledgments

This work was sponsored in part by the Air Force Office of Scientific Research, USAF with Major M. Chipley being program director, and by the National Science Foundation with Dr. K. Chong being program director. The authors are grateful to the reviewers for discerning comments on this paper.

Appendix

From a series of derivations, we obtain the following nonlinear PDE for strain evolution:

$$\varphi_{tt}+a(\varphi_x^2+\varphi\varphi_{xx})=0. \tag{A1}$$

Suppose Eq. (*A*1) has an existing solution in the form of a traveling wave, that is,

$$\varphi(x,t)=f(x-c(t-t_L)) \quad \text{for } t\geqslant t_L, \tag{A2}$$

where $f=f(\xi)$ and c is the wave speed. Substituting (A2) into (A1), we have

$$c^2f''(\xi)+a[f'(\xi)^2+f(\xi)f''(\xi)]=0. \tag{A3}$$

This ODE can be solved after using some variable transformations. Equation (*A*3) can be rewritten as

$$\left(\frac{c^2}{a}+f(\xi)\right)f''(\xi)+f'(\xi)^2=0. \tag{A4}$$

Using the new variable

$$z:=\frac{c^2}{a}+f(\xi) \tag{A5}$$

the ODE (A4) is recast in the form

$$zz''+(z')^2=0. \tag{A6}$$

To solve it, we set $w=z'$ to obtain the first order system

$$z'=w, \tag{A7}$$

$$w'=\frac{w^2}{z}. \tag{A8}$$

Remove the independent variable ξ by

$$\frac{dw}{dz}=-\frac{w}{z} \tag{A9}$$

and separate the variables to obtain the solution

$$\ln|w|=-\ln|z|+k, \tag{A10}$$

or equivalently

$$|w|=\frac{k}{|z|}. \tag{A11}$$

Therefore, we have

$$z'=w=\frac{k}{z}, \tag{A12}$$

so

$$zz'=\frac{d}{d\xi}\left(\frac{1}{2}z^2\right)=k \tag{A13}$$

and

$$\frac{1}{2}z^2=k\xi+l. \tag{A14}$$

This gives

$$z=\pm[2(k\xi+l)]^{1/2}. \tag{A15}$$

Using Eq. (*A*5), we obtain the general solution for Eq. (*A*3), namely,

$$f(\xi)=\pm[2(k\xi+l)]^{1/2}-c^2/a. \tag{A16}$$

By converting back to the original variables through (A2), the final solution is given by

$$\varphi(x,t)=\pm[2(k(x-c(t-t_L))+l)]^{1/2}-c^2/a. \tag{A17}$$

References

[1] Sandler, I. S., 1984, "Strain Softening for Static and Dynamic Problems," *Constitutive Equations: Macro and Computational Aspects*, K. J. William, ed., ASME, New York, pp. 217–231.

[2] Valanis, K. C., 1985, "On the Uniqueness of Solutions of the Initial Value Problems in Softening Materials," ASME J. Appl. Mech., **52**, pp. 649–653.

[3] Bazant, Z. P., and Belytschko, T. B., 1985, "Wave Propagation in a Strain-Softening Bar: Exact Solution," J. Eng. Mech., **111**, pp. 381–389.

[4] Chen, Z., 1993, "A Partitioned-Solution Method With Moving Boundaries for Nonlocal Plasticity," *Modern Approaches to Plasticity*, D. Kolymbas, ed., Elservier, New York, pp. 449–468.

[5] Chen, Z., and Sulsky, D., 1995, "A Partitioned-Modeling Approach With Moving Jump Conditions for Localization," Int. J. Solids Struct., **32**, pp. 1893–1905.

[6] Chen, Z., and Xin, X., 1999, "An Analytical and Numerical Study of Failure Waves," Int. J. Solids Struct., **36**, pp. 3977–3991.

[7] Xin, X., and Chen, Z., 2000, "An Analytical Solution With Local Elastoplastic Models for the Evolution of Dynamic Softening," Int. J. Solids Struct., **37**, pp. 5855–5872.

[8] Xin, X., and Chen, Z., 2000, "An Analytical and Numerical Study to Simulate the Evolution of Dynamic Failure With Local Elastodamage Models," International Journal of Damage Mechanics, **9**, pp. 305–328.

[9] Armero, F., 1997, "On the Characterization of Localized Solutions in Inelastic Solids: An Analysis of Wave Propagation in a Softening Bar," UCB/SEMM-97/18, University of California, Berkeley, CA.

[10] Feng, R., and Chen, Z., 1999, "Propagation of Heterogeneous Microdamage in Shocked Glasses," *Applied Mechanics in the Americas*, Vol. 7, P. Goncalves, I. Jasiuk, D. Pamplona, C. Steele, H. Weber, and L. Bevilacqua, eds., American Academy of Mechanics, Northwestern University, Evanston, IL, pp. 691–694.

[11] Kanel, G. I., Rasorenov, S. V., and Fortov, V. E., 1991, "The Failure Waves and Spallations in Homogeneous Brittle Materials," *Shock Compression of Condensed Matter*, S. C. Schmidt, R. D. Dick, J. W. Forbes, and D. G. Tasker, eds., Elsevier, New York, pp. 451–454.

[12] Kanel, G. I., Rasorenov, S. V., Utkin, A. V., He, H., Jing, F., and Jin, X., 1998, "Influence of the Load Conditions on the Failure Wave in Glasses," High Press. Res., **16**, pp. 27–44.

[13] John, F., 1982, *Partial Differential Equations*, Springer-Verlag, New York.

[14] McOwen, R. C., 1996, *Partial Differential Equations: Methods And Applications*, Prentice-Hall, Englewood Cliffs, NJ.

[15] Bluman, G. W., and Kumei, S., 1989, *Symmetries and Differential Equations*, Springer-Verlag, New York.

[16] Olver, P. J., 1993, *Applications of Lie Group to Differential Equations*. Springer-Verlag, New York.

The Instability and Vibration of Rotating Beams With Arbitrary Pretwist and an Elastically Restrained Root

S. M. Lin
Professor,
Mechanical Engineering Department,
Kun Shan University of Technology,
Tainan, Taiwan 710-03, Republic of China

The governing differential equations and the boundary conditions for the coupled bending-bending-extensional vibration of a rotating nonuniform beam with arbitrary pretwist and an elastically restrained root are derived by Hamilton's principle. The semi-analytical solution procedure for an inextensional beam without taking account of the coriolis forces is derived. The coupled governing differential equations are transformed to be a vector characteristic governing equation. The frequency equation of the system is derived and expressed in terms of the transition matrix of the vector governing equation. A simple and efficient algorithm for determining the transition matrix of the general system with arbitrary pretwist is derived. The divergence in the Frobenius method does not exist in the proposed method. The frequency relations between different systems are revealed. The mechanism of instability is discovered. The influence of the rotatory inertia, the coupling effect of the rotating speed and the mass moment of inertia, the setting angle, the rotating speed and the spring constants on the natural frequencies, and the phenomenon of divergence instability are investigated. [DOI: 10.1115/1.1408615]

1 Introduction

Rotating beams, which have importance in many practical applications such as turbine blades, helicopter rotor blades, airplane propellers, and robot manipulators have been investigated for a long time. An interesting review of the subject can be found in the papers by Leissa [1], Ramamurti and Balasubramanian [2], Rosen [3] and Lin [4]. Much attention has been focused on the investigation of the unpretwisted beam. Most of research of the vibration problem of rotating pretwisted beam have been studied by using numerical method because of its complexity. No analytical solution for the vibration of a rotating pretwisted beam has been presented.

Considering the Bernoulli-Euler unpretwisted beam theory, the influence of tip mass, rotating speed, hub radius, setting angle, taper ratio, and elastic root restraints on the natural frequencies of transverse vibrations of a rotating beam were investigated by many investigators. Lee and Kuo [5] obtained the exact solution for the free vibrations of rotating unpretwisted beam with bending rigidity and mass density varying in arbitrary polynomial forms by taking the Frobenius method. Lee and Lin [6] studied the free vibration of unpretwisted Timoshenko beams. The two coupled characteristic differential equations governing the bending response uncouple into one complete fourth-order ordinary differential equation with variable coefficients in the angle of rotation. The four fundamental solutions of the uncoupled fourth-order ordinary differential equation were obtained using the Frobenius method. The frequency equation was expressed in terms of the four fundamental solutions. Similarly, one can decouple the two coupled governing characteristic differential equations of a rotating pretwisted beam into one complete eighth-order ordinary differential equation by taking many procedures of differentation. The variation of the coefficients of the uncoupled governing characteristic equation will be very large. Taking the Frobenius method, the corresponding eight fundamental solutions of the eighth-order ordinary differential equation can be expressed in power series. However, the fundamental solutions will be divergent because the region of convergence of a power series is usually limited.

Considering the Timoshenko unpretwisted beam theory, the influence of shear deformation and rotatory inertia on the bending vibrations of a rotating beam were investigated by numerous authors. Lee and Lin [6] studied numerically the coupling effect of the rotating speed and the mass moment of inertia on the natural frequencies and the phenomenon of divergence instability. Lin [4] obtained the generalized Green function of an nth-order ordinary differential equation. This Green function was used to obtain the closed-form solution for the forced vibration of a rotating Timoshenko beam. The prediction to the frequencies and the mechanism of divergence instability of a rotating beam have not been investigated.

For a nonrotating pretwisted beam, approximation methods are very useful tools to investigate the free vibrations of pretwisted beams where it is difficult to obtain exact solutions even for the simplest cases. These methods are the finite element method ([7]), the Rayleigh-Ritz method ([8]), the Reissner method ([9]) the Galerkin method ([10]), and the transfer matrix method ([11,12]). Lin [12] derived the exact field transfer matrix of a nonuniform nonrotating pretwisted beam with arbitrary pretwist and studied the performance of a beam with elastic boundary conditions. However, the exact field transfer matrix of a rotating pretwisted beam can not be derived in a similar way.

For a rotating pretwisted beam, Rao and Carnegie [13] used the Holzer-Myklestad approach to determine the natural frequencies and mode shapes of a cantilever pretwisted blade. Subrahmanyam and Kaza [14] studied the vibrations of a cantilever tapered pretwisted beam by using the Ritz method and the finite difference method. Subrahmanyam, Kulkarni, and Rao [15] used the Reissner method to study the vibration of a rotating pretwisted cantile-

Contributed by the Applied Mechanics Division of THE AMERICAN SOCIETY OF MECHANICAL ENGINEERS for publication in the ASME JOURNAL OF APPLIED MECHANICS. Manuscript received by the ASME Applied Mechanics Division, December 12, 1999; final revision, August 23, 2000. Associate Editor: R. C. Benson. Discussion on the paper should be addressed to the Editor, Professor Lewis T. Wheeler, Department of Mechanical Engineering, University of Houston, Houston, TX 77204-4792, and will be accepted until four months after final publication of the paper itself in the ASME JOURNAL OF APPLIED MECHANICS.

ver Timoshenko beam. Sisto and Chang [16] proposed a finite element method for a vibration analysis of rotating pretwisted beam. Young and Lin [17] studied the stability of a cantilever tapered pretwisted beam with varying speed by using the Galerkin method. Kar and Neogy [18] used the Ritz method to study the stability of a rotating pretwisted cantilever beam. Hernried [19] used the finite difference method to determine the natural frequencies of a rotating pretwisted nonuniform cantilever beam. Moreover, the author used the mode-superposition method to determine the forced vibration of the beam. Surace, Anghel, and Mares [20] derived the approximate method based on the use of structural influence function to determine the natural frequencies of a rotating cantilever pretwisted Bernoulli-Euler beam. As a result, no analytical solution has been given to the coupled bending-bending vibrations of a rotating nonuniform beam with arbitrary pretwist and an elastically restrained root.

In this paper, the governing differential equations for the coupled bending-bending-extensional vibration of a rotating nonuniform beam with arbitrary pretwist, an elastically restrained root, setting angle, hub radius, and rotating at a constant angular velocity, are derived by using Hamilton's principle. For an inextensional beam, without taking account of the coriolis force's effect, the three coupled governing differential equations are reduced to two coupled equations and the centrifugal force is obtained. The reduced coupled governing differential equations are transformed to a vector characteristic differential equation. The frequency equation of the system is derived and expressed in terms of the transition matrix of the vector governing equation. A simple and efficient algorithm for determining the semi-analytical transition matrix of the general system with nonuniform pretwist is derived. The frequency relation and the mechanism of instability of unpretwisted and pretwisted rotating beams are investigated. The influence of the rotatory inertia, the coupling effect of the rotating speed and the mass moment of inertia, the setting angle, the rotating speed and the spring constants on the natural frequencies, and the phenomenon of divergence instability are investigated.

2 Pretwisted Beam

2.1 Governing Equations and Boundary Conditions. Consider the coupled bending-bending-extensional vibration of a pretwisted and doubly symmetric nonuniform beam elastically restrained, mounted with setting angle θ on a hub with radius R, rotating with constant angular velocity Ω, as shown in Fig. 1. The displacement fields of the beam are

$$u=u_0(x,t)-z\frac{\partial w}{\partial x}-y\frac{\partial v}{\partial x},\quad v=v(x,t),\quad w=w(x,t), \tag{1}$$

where x, y, and z are the fixed frame coordinates. t is the time variable. The velocity vector of a point (x, y, z) in the beam is given by

$$\mathbf{V}=\left[\frac{\partial u}{\partial t}+\Omega\sin\theta(z+w)+\Omega\cos\theta(y+v)\right]\mathbf{i}+\left[\frac{\partial v}{\partial t}-\Omega\cos\theta(x+R+u)\right]\mathbf{j}+\left[\frac{\partial w}{\partial t}-\Omega\sin\theta(x+R+u)\right]\mathbf{k}. \tag{2}$$

The potential energy $\overline{U}$ and the kinetic energy $\overline{T}$ of the beam are

$$\overline{U}=\frac{1}{2}\int_0^L\int_A\sigma_{xx}\varepsilon_{xx}dAdx+\frac{1}{2}K_{z\theta}\left[\frac{\partial w(0,t)}{\partial x}\right]^2+\frac{1}{2}K_{zT}w^2(0,t)+\frac{1}{2}K_{y\theta}\left[\frac{\partial v(0,t)}{\partial x}\right]^2+\frac{1}{2}K_{yT}v^2(0,t), \tag{3}$$

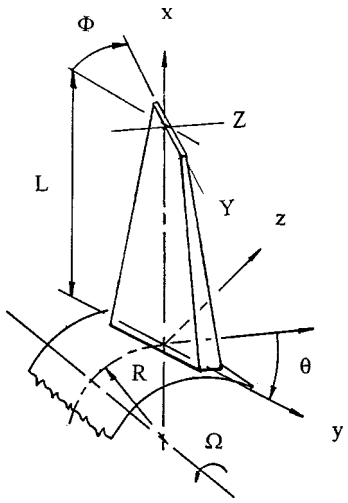

Fig. 1 Geometry and coordinate system of a rotating pretwisted beam

$$\overline{T}=\frac{1}{2}\int_0^L\int_A\left[\left(\frac{\partial u}{\partial t}\right)^2+\left(\frac{\partial v}{\partial t}\right)^2+\left(\frac{\partial w}{\partial t}\right)^2\right]\rho dAdx, \tag{4}$$

where A is the cross-sectional area of the beam. K_{yT}, $K_{y\theta}$, K_{zT}, and $K_{z\theta}$ are the translational and rotational spring constants at the left end of the beam in the y and z-directions, respectively. L is the length of the beam. ρ is the mass density per unit volume. σ_{xx}, ε_{xx} are the normal stress and strain in the x-direction, respectively. Application of Hamilton's principle yields the following governing differential equations:

$$-\frac{\partial^2}{\partial x^2}\left(EI_{yy}\frac{\partial^2 w}{\partial x^2}+EI_{yz}\frac{\partial^2 v}{\partial x^2}\right)+\frac{\partial}{\partial x}\left(N\frac{\partial w}{\partial x}\right)+\frac{\partial}{\partial x}\left(J_y\frac{\partial^3 w}{\partial t^2\partial x}+J_x\frac{\partial^3 v}{\partial t^2\partial x}\right)-\Omega^2\frac{\partial}{\partial x}\left(J_y\frac{\partial w}{\partial x}+J_x\frac{\partial v}{\partial x}\right)-\rho A\left(\frac{\partial^2 w}{\partial t^2}-\Omega\sin\theta\frac{\partial u_0}{\partial t}\right)+\rho A\Omega\sin\theta\left(\frac{\partial u_0}{\partial t}+\Omega\sin\theta w+\Omega\cos\theta v\right)=0, \tag{5}$$

$$-\frac{\partial^2}{\partial x^2}\left(EI_{yz}\frac{\partial^2 w}{\partial x^2}+EI_{zz}\frac{\partial^2 v}{\partial x^2}\right)+\frac{\partial}{\partial x}\left(N\frac{\partial v}{\partial x}\right)+\frac{\partial}{\partial x}\left(J_x\frac{\partial^3 w}{\partial t^2\partial x}+J_z\frac{\partial^3 v}{\partial t^2\partial x}\right)-\Omega^2\frac{\partial}{\partial x}\left(J_x\frac{\partial w}{\partial x}+J_z\frac{\partial v}{\partial x}\right)-\rho A\left(\frac{\partial^2 v}{\partial t^2}-\Omega\cos\theta\frac{\partial u_0}{\partial t}\right)+\rho A\Omega\cos\theta\left(\frac{\partial u_0}{\partial t}+\Omega\sin\theta w+\Omega\cos\theta v\right)=0, \tag{6}$$

$$\frac{\partial N}{\partial x}-\rho A\frac{\partial^2 u_0}{\partial t^2}-2\rho A\Omega\left(\sin\theta\frac{\partial w}{\partial t}+\cos\theta\frac{\partial v}{\partial t}\right)+\rho A\Omega^2(x+u_0)=0, \tag{7}$$

and the associated boundary conditions:
at $x=0$:

$$u_0=0, \tag{8}$$

$$EI_{yy}\frac{\partial^2 w}{\partial x^2}+EI_{yz}\frac{\partial^2 v}{\partial x^2}-K_{z\theta}\frac{\partial w}{\partial x}=0, \tag{9}$$

$$\frac{\partial}{\partial x}\left(EI_{yy}\frac{\partial^2 w}{\partial x^2}+EI_{yz}\frac{\partial^2 v}{\partial x^2}\right)-N\frac{\partial w}{\partial x}-J_y\frac{\partial^3 w}{\partial x\partial t^2}-J_x\frac{\partial^3 v}{\partial x\partial t^2}+\Omega^2\left(J_y\frac{\partial w}{\partial x}+J_x\frac{\partial v}{\partial x}\right)+K_{zT}w=0, \tag{10}$$

$$EI_{yz}\frac{\partial^2 w}{\partial x^2}+EI_{zz}\frac{\partial^2 v}{\partial x^2}-K_{y\theta}\frac{\partial v}{\partial x}=0, \tag{11}$$

$$\frac{\partial}{\partial x}\left(EI_{yz}\frac{\partial^2 w}{\partial x^2}+EI_{zz}\frac{\partial^2 v}{\partial x^2}\right)-N\frac{\partial v}{\partial x}-J_x\frac{\partial^3 w}{\partial x\partial t^2}-J_z\frac{\partial^3 v}{\partial x\partial t^2}+\Omega^2\left(J_x\frac{\partial w}{\partial x}+J_z\frac{\partial v}{\partial x}\right)+K_{yT}w=0, \tag{12}$$

at $x=L$:

$$N(L)=0, \tag{13}$$

$$EI_{yy}\frac{\partial^2 w}{\partial x^2}+EI_{yz}\frac{\partial^2 v}{\partial x^2}=0, \tag{14}$$

$$\frac{\partial}{\partial x}\left(EI_{yy}\frac{\partial^2 w}{\partial x^2}+EI_{yz}\frac{\partial^2 v}{\partial x^2}\right)-N\frac{\partial w}{\partial x}-J_y\frac{\partial^3 w}{\partial x\partial t^2}-J_x\frac{\partial^3 v}{\partial x\partial t^2}+\Omega^2\left(J_y\frac{\partial w}{\partial x}+J_x\frac{\partial v}{\partial x}\right)=0, \tag{15}$$

$$EI_{yz}\frac{\partial^2 w}{\partial x^2}+EI_{zz}\frac{\partial^2 v}{\partial x^2}=0, \tag{16}$$

$$\frac{\partial}{\partial x}\left(EI_{yz}\frac{\partial^2 w}{\partial x^2}+EI_{zz}\frac{\partial^2 v}{\partial x^2}\right)-N\frac{\partial v}{\partial x}-J_x\frac{\partial^3 w}{\partial x\partial t^2}-J_z\frac{\partial^3 v}{\partial x\partial t^2}+\Omega^2\left(J_x\frac{\partial w}{\partial x}+J_z\frac{\partial v}{\partial x}\right)=0, \tag{17}$$

where E is Young's modulus. I is the area moment inertia of the beam. J_x, J_y, and J_z are mass moment of inertia per unit length about the x, y and z-axes, respectively. N is the centrifugal force. It is observed that in Eq. (7) the centrifugal force N is related to u_0, v, and w. The centrifugal force N is the parameter of Eqs. (5) and (6) in terms of u_0, v, and w. Thus the system is nonlinear. It is hard to obtain the solution of the system. But if an inextensional beam without the Coriolis force effect is considered, the system becomes linear and the corresponding solution can be easily obtained. Moreover, the lateral vibration of a blade subjected to low rotational speed is dominant and the effect of the Coriolis force may be neglected [14].

For an inextensional beam, without taking account of the Coriolis force effect, the centrifugal force in Eqs. (7) and (13) can be expressed as

$$N(x)=\Omega^2\int_x^L \rho A(R+x)dx. \tag{18}$$

In terms of the following dimensionless quantities,

$$B_{ij}=E(x)I_{ij}(x)/[E(0)I_{yy}(0)],\quad i,j=x,y,z\quad g_i=J_i(x)/J_y(0),$$
$$m=\rho(x)A(x)/[\rho(0)A(0)],\quad n(\xi)=\alpha^2\int_\xi^1 m(\chi)(r+\chi)d\chi,$$
$$r=R/L,\quad V=v/L,$$
$$W=w/L,\quad \alpha^2=\rho(0)A(0)\Omega^2L^4/[E(0)I_{yy}(0)],$$
$$\beta_1=K_{z\theta}L/[E(0)I_{yy}(0)],\quad \beta_2=K_{zT}L/[E(0)I_{yy}(0)],$$
$$\beta_3=K_{y\theta}L/[E(0)I_{yy}(0)],\quad \beta_4=K_{yT}L/[E(0)I_{yy}(0)],$$
$$\eta=J_y(0)/[\rho(0)A(0)L^2],\quad \Lambda^2=\rho(0)A(0)\omega^2L^4/[E(0)I_{yy}(0)],$$
$$\xi=x/L,\quad \tau=t/L^2\sqrt{E(0)I_{yy}(0)/\rho(0)A(0)},$$
$$\gamma_{i1}=\frac{\beta_i}{1+\beta_i},\quad \gamma_{i2}=\frac{1}{1+\beta_i}, \tag{19}$$

the dimensionless governing characteristic differential equations of motion for harmonic vibration with circular frequency ω are written as

$$-\frac{d^2}{d\xi^2}\left(B_{yy}\frac{d^2W}{d\xi^2}+B_{yz}\frac{d^2V}{d\xi^2}\right)+\frac{d}{d\xi}\left(n\frac{dW}{d\xi}\right)-\eta(\alpha^2+\Lambda^2)\frac{d}{d\xi}\left(g_y\frac{dW}{d\xi}+g_x\frac{dV}{d\xi}\right)+m(\alpha^2\sin^2\theta+\Lambda^2)W+m\alpha^2\sin\theta\cos\theta V=0, \tag{20}$$

$$-\frac{d^2}{d\xi^2}\left(B_{yz}\frac{d^2W}{d\xi^2}+B_{zz}\frac{d^2V}{d\xi^2}\right)+\frac{d}{d\xi}\left(n\frac{dV}{d\xi}\right)-\eta(\alpha^2+\Lambda^2)\frac{d}{d\xi}\left(g_x\frac{dW}{d\xi}+g_z\frac{dV}{d\xi}\right)+m(\alpha^2\cos^2\theta+\Lambda^2)V+m\alpha^2\sin\theta\cos\theta W=0,\quad \xi\in(0,1) \tag{21}$$

and the associated dimensionless elastic boundary conditions are given as follows:
at $\xi=0$:

$$\gamma_{12}\left(B_{yy}\frac{d^2W}{d\xi^2}+B_{yz}\frac{d^2V}{d\xi^2}\right)-\gamma_{11}\frac{dW}{d\xi}=0, \tag{22}$$

$$\gamma_{22}\left\{\frac{d}{d\xi}\left(B_{yy}\frac{d^2W}{d\xi^2}+B_{yz}\frac{d^2V}{d\xi^2}\right)-n\frac{dW}{d\xi}+\eta(\alpha^2+\Lambda^2)\times\left(g_y\frac{dW}{d\xi}+g_x\frac{dV}{d\xi}\right)\right\}+\gamma_{21}W=0, \tag{23}$$

$$\gamma_{32}\left(B_{yz}\frac{d^2W}{d\xi^2}+B_{zz}\frac{d^2V}{d\xi^2}\right)-\gamma_{31}\frac{dV}{d\xi}=0, \tag{24}$$

$$\gamma_{42}\left\{\frac{d}{d\xi}\left(B_{yz}\frac{d^2W}{d\xi^2}+B_{zz}\frac{d^2V}{d\xi^2}\right)-n\frac{dV}{d\xi}+\eta(\alpha^2+\Lambda^2)\times\left(g_x\frac{dW}{d\xi}+g_z\frac{dV}{d\xi}\right)\right\}+\gamma_{41}V=0 \tag{25}$$

at $\xi=1$:

$$B_{yy}\frac{d^2W}{d\xi^2}+B_{yz}\frac{d^2V}{d\xi^2}=0, \tag{26}$$

$$\frac{d}{d\xi}\left(B_{yy}\frac{d^2W}{d\xi^2}+B_{yz}\frac{d^2V}{d\xi^2}\right)+\eta(\alpha^2+\Lambda^2)\left(g_y\frac{dW}{d\xi}+g_x\frac{dV}{d\xi}\right)=0, \tag{27}$$

$$B_{yz}\frac{d^2W}{d\xi^2}+B_{zz}\frac{d^2V}{d\xi^2}=0, \tag{28}$$

$$\frac{d}{d\xi}\left(B_{yz}\frac{d^2W}{d\xi^2}+B_{zz}\frac{d^2V}{d\xi^2}\right)+\eta(\alpha^2+\Lambda^2)\left(g_x\frac{dW}{d\xi}+g_z\frac{dV}{d\xi}\right)=0. \tag{29}$$

It should be noted that considering the velocity field (2) results in the coupling effect of the rotating speed and the mass moment of inertia, $\eta(\alpha^2+\Lambda^2)d(g_ydW/d\xi+g_xdV/d\xi)/d\xi$ and $\eta(\alpha^2+\Lambda^2)d(g_xdW/d\xi+g_zdV/d\xi)/d\xi$. However, if the displacements of any point in the cross section of the beam is the same as that of the center of the cross section, i.e., $u=u_0(x,t)$, $v=v(x,t)$, and $w=w(x,t)$, these effects cannot be considered ([17]). Furthermore, when the setting angle is zero, the governing equations become the same as those given by Rosen [3].

It can be observed that the second terms in Eqs. (20) and (21) present the effect of the centrifugal force n to increase the stiffness of the beam. Because the second and third terms in Eqs. (20) and (21) are positive and negative, respectively, the coupling effect of the rotating speed and the mass moment of inertia, i.e., the third terms in Eqs. (20) and (21), presents an axial compressive force to decrease the stiffness of the beam. Moreover, because the coupling effect includes the product of the rotating speed α and the rotatory inertia η, the coupling effect on the frequencies is great for the system with large parameters α and η.

2.2 Solution Method.

2.2.1 Transformed Vector Governing Equation. Defining the state variables as

$$x_1=W,\quad x_2=\frac{dW}{d\xi},\quad x_3=\frac{d^2W}{d\xi^2},\quad x_4=\frac{d^3W}{d\xi^3},$$
$$x_5=V,\quad x_6=\frac{dV}{d\xi},\quad x_7=\frac{d^2V}{d\xi^2},\quad x_8=\frac{d^3V}{d\xi^3}, \tag{30}$$

Eqs. (20) and (21) can be written as, respectively,

$$a_1\frac{dx_4}{d\xi}+a_2\frac{dx_3}{d\xi}+a_3\frac{dx_2}{d\xi}+a_4\frac{dx_1}{d\xi}+a_5x_1+a_6\frac{dx_8}{d\xi}+a_7\frac{dx_7}{d\xi}+a_8\frac{dx_6}{d\xi}+a_9\frac{dx_5}{d\xi}+a_{10}x_5=0, \tag{31}$$

$$a_{11}\frac{dx_4}{d\xi}+a_{12}\frac{dx_3}{d\xi}+a_{13}\frac{dx_2}{d\xi}+a_{14}\frac{dx_1}{d\xi}+a_{15}x_1+a_{16}\frac{dx_8}{d\xi}+a_{17}\frac{dx_7}{d\xi}+a_{18}\frac{dx_6}{d\xi}+a_{19}\frac{dx_5}{d\xi}+a_{20}x_5=0, \tag{32}$$

where

$$a_1=B_{yy},\quad a_2=2\frac{dB_{yy}}{d\xi},$$
$$a_3=\frac{d^2B_{yy}}{d\xi^2}-n+\eta(\alpha^2+\Lambda^2)g_y,\quad a_4=-\frac{dn}{d\xi}+\eta(\alpha^2+\Lambda^2)\frac{dg_y}{d\xi},$$
$$a_5=-m(\alpha^2\sin^2\theta+\Lambda^2),\quad a_6=a_{11}=B_{yz},$$
$$a_7=a_{12}=2\frac{dB_{yz}}{d\xi},\quad a_8=a_{13}=\frac{d^2B_{yz}}{d\xi^2}+\eta(\alpha^2+\Lambda^2)g_x,$$
$$a_9=a_{14}=\eta(\alpha^2+\Lambda^2)\frac{dg_x}{d\xi},\quad a_{10}=a_{15}=-m\alpha^2\sin\theta\cos\theta,$$
$$a_{16}=B_{zz},\quad a_{17}=2\frac{dB_{zz}}{d\xi},\quad a_{18}=\frac{d^2B_{zz}}{d\xi^2}-n+\eta(\alpha^2+\Lambda^2)g_z,$$
$$a_{19}=-\frac{dn}{d\xi}+\eta(\alpha^2+\Lambda^2)\frac{dg_z}{d\xi},\quad a_{20}=-m(\alpha^2\cos^2\theta+\Lambda^2). \tag{33}$$

Multiplying Eq. (31) by a_{16} and Eq. (32) by a_6 and subtracting the latter from the former, one obtains

$$\frac{dx_4}{d\xi}=\sum_{j=1}^{8}c_jx_j, \tag{34}$$

where

$$c_1=-(a_5a_{16}-a_{15}a_6)/s,\quad c_2=-(a_4a_{16}-a_{14}a_6)/s,$$
$$c_3=-(a_3a_{16}-a_{13}a_6)/s,\quad c_4=-(a_2a_{16}-a_{12}a_6)/s,$$
$$c_5=-(a_{10}a_{16}-a_{20}a_6)/s,\quad c_6=-(a_9a_{16}-a_{19}a_6)/s,$$
$$c_7=-(a_8a_{16}-a_{18}a_6)/s,\quad c_8=-(a_7a_{16}-a_{17}a_6)/s, \tag{35}$$

in which $s=a_1a_{16}-a_{11}a_6$. Similarly, multiplying Eq. (31) by a_{11} and Eq. (32) by a_1 and subtracting the latter from the former, one obtains

$$\frac{dx_8}{d\xi}=\sum_{j=1}^{8}\overline{c}_jx_j, \tag{36}$$

where

$$\overline{c}_1=-(a_5a_{11}-a_{15}a_1)/\overline{s},\quad \overline{c}_2=-(a_4a_{11}-a_{14}a_1)/\overline{s},$$
$$\overline{c}_3=-(a_3a_{11}-a_{13}a_1)/\overline{s},\quad \overline{c}_4=-(a_2a_{11}-a_{12}a_1)/\overline{s},$$
$$\overline{c}_5=-(a_{10}a_{11}-a_{20}a_1)/\overline{s},\quad \overline{c}_6=-(a_9a_{11}-a_{19}a_1)/\overline{s},$$
$$\overline{c}_7=-(a_8a_{11}-a_{18}a_1)/\overline{s},\quad \overline{c}_8=-(a_7a_{11}-a_{17}a_1)/\overline{s}, \tag{37}$$

in which $\overline{s}=a_6a_{11}-a_{16}a_1$. Based on the relations (30), (34), and (36), the transformed vector characteristic governing equation can be obtained as follows:

$$\frac{d\mathbf{X}}{d\xi}=\mathbf{A}(\xi)\mathbf{X}(\xi), \tag{38}$$

where

$$X(\xi)=[x_1\ \ x_2\ \ x_3\ \ x_4\ \ x_5\ \ x_6\ \ x_7\ \ x_8]^T,$$
$$A(\xi)=\begin{bmatrix}0&1&0&0&0&0&0&0\\0&0&1&0&0&0&0&\\0&0&0&1&0&0&0&0\\c_1&c_2&c_3&c_4&c_5&c_6&c_7&c_8\\0&0&0&0&0&1&0&0\\0&0&0&0&0&0&1&0\\0&0&0&0&0&0&0&1\\\overline{c}_1&\overline{c}_2&\overline{c}_3&\overline{c}_4&\overline{c}_5&\overline{c}_6&\overline{c}_7&\overline{c}_8\end{bmatrix}, \tag{39}$$

in which the superscript "T" is the symbol of transpose of a matrix.

2.2.2 Frequency Equation. The solution of Eq. (38) can be expressed as

$$\mathbf{X}(\xi)=\mathbf{T}(\xi,0)\mathbf{X}(0), \tag{40}$$

where $\mathbf{T}(\xi,0)$ is the transition matrix from 0 to ξ, to be determined. Moreover, the state variables at $\xi=1$ can be written as

$$x_i(1)=\sum_{j=1}^{8}T_{ij}(1,0)x_j(0),\quad i=1,2,\ldots,8 \tag{41}$$

where T_{ij} is the elements of the transition matrix from 0 to 1. Expressing the boundary conditions (22)–(25) in terms of the state variables $\{x_1(0),x_2(0),\ldots,x_8(0)\}$ and substituting Eq. (41) into the boundary conditions (26)–(29), the frequency equation of the system is obtained,

$$|\chi_{ij}|_{8\times8}=0, \tag{42}$$

where

$$\chi_{11}=\chi_{14}=\chi_{15}=\chi_{16}=\chi_{18}=0,\quad \chi_{12}=-\gamma_{11},$$
$$\chi_{13}=\gamma_{12}B_{yy}(0),\quad \chi_{17}=\gamma_{12}B_{yz}(0);$$
$$\chi_{21}=\gamma_{21},\quad \chi_{22}=\gamma_{22}[\eta(\alpha^2+\Lambda^2)g_y(0)-n(0)],$$
$$\chi_{23}=\gamma_{22}B'_{yy}(0),\quad \chi_{24}=\gamma_{22}B_{yy}(0),$$
$$\chi_{25}=0,\quad \chi_{26}=\gamma_{22}\eta(\alpha^2+\Lambda^2)g_x(0),$$
$$\chi_{27}=\gamma_{22}B'_{yz}(0),\quad \chi_{28}=\gamma_{22}B_{yz}(0);$$
$$\chi_{31}=\chi_{32}=\chi_{34}=\chi_{35}=\chi_{38}=0,\quad \chi_{33}=\gamma_{32}B_{yz}(0),$$
$$\chi_{36}=-\gamma_{31},\quad \chi_{37}=\gamma_{32}B_{zz}(0);$$
$$\chi_{41}=0,\quad \chi_{42}=\gamma_{42}\eta(\alpha^2+\Lambda^2)g_x(0),$$
$$\chi_{43}=\gamma_{42}B'_{yz}(0),\quad \chi_{44}=\gamma_{42}B_{yz}(0),$$
$$\chi_{45}=\gamma_{41},\quad \chi_{46}=\gamma_{42}[\eta(\alpha^2+\Lambda^2)g_z(0)-n(0)],$$
$$\chi_{47}=\gamma_{42}B'_{zz}(0),\quad \chi_{48}=\gamma_{42}B_{zz}(0);$$
$$\chi_{5j}=B_{yy}(1)T_{3j}(1,0)+B_{yz}(1)T_{7j}(1,0),\quad j=1,2,\ldots,8;$$
$$\chi_{6j}=\eta(\alpha^2+\Lambda^2)g_y(1)T_{2j}(1,0)+B'_{yy}(1)T_{3j}(1,0)+B_{yy}(1)T_{4j}(1,0)+\eta(\alpha^2+\Lambda^2)g_x(1)T_{6j}(1,0)+B'_{yz}(1)T_{7j}(1,0)+B_{yz}(1)T_{8j}(1,0),\quad j=1,2,\ldots,8;$$
$$\chi_{7j}=B_{yz}(1)T_{3j}(1,0)+B_{zz}(1)T_{7j}(1,0),\quad j=1,2,\ldots,8;$$
$$\chi_{8j}=\eta(\alpha^2+\Lambda^2)g_x(1)T_{2j}(1,0)+B'_{yz}(1)T_{3j}(1,0)+B_{yz}(1)T_{4j}(1,0)+\eta(\alpha^2+\Lambda^2)g_z(1)T_{6j}(1,0)+B'_{zz}(1)T_{7j}(1,0)+B_{zz}(1)T_{8j}(1,0),j=1,2,\ldots,8. \quad (43)$$

Letting $\gamma_{11}=\gamma_{21}=\gamma_{31}=\gamma_{41}=1$ and $\gamma_{12}=\gamma_{22}=\gamma_{32}=\gamma_{42}=0$, the frequency equation for a cantilever beam can be obtained.

2.2.3 Semi-analytical Transition Matrix. It is well known ([21]) that the following Peano-Baker series is the closed-form transition matrix of Eq. (38)

$$\mathbf{T}(\xi,\xi_{i-1})=\mathbf{I}+\int_{\xi_{i-1}}^{\xi}\mathbf{A}(\chi_1)d\chi_1+\int_{\xi_{i-1}}^{\xi}\mathbf{A}(\chi_1)\int_{\xi_{i-1}}^{\chi_1}\mathbf{A}(\chi_2)d\chi_2 d\chi_1+\int_{\xi_{i-1}}^{\xi}\mathbf{A}(\chi_1)\int_{\xi_{i-1}}^{\chi_1}\mathbf{A}(\chi_2)\int_{\xi_{i-1}}^{\chi_2}\mathbf{A}(\chi_3)d\chi_3 d\chi_2 d\chi_1+\cdots. \quad (44)$$

However, it is impossible to determine the multiple integrals of the series analytically or numerically. Hence, an approximate transition matrix is required. In this paper, a simple and efficient algorithm is developed to find the approximate transition matrix.

By approximating the coefficient matrix $\mathbf{A}(\xi)$ by n piecewise constant coefficient matrices $\mathbf{A}(s_i)$, $i=1,2,\ldots,n$, one obtains a characteristic governing equation with constant coefficient matrix. Here s_i can be any value between $[\xi_{i-1},\xi_i]$ and ξ_i denotes the coordinate position at the end of the ith subsection. Consequently, the transition matrix of the ith subsection from ξ_{i-1} to ξ can be obtained:

$$\mathbf{T}(\xi,\xi_{i-1})=e^{\mathbf{A}(s_i)(\xi-\xi_{i-1})},\quad s_i,\quad \xi\in(\xi_{i-1},\xi_i). \quad (45)$$

After applying the composition property of the transition matrix, i.e., $\mathbf{T}(\xi_{i+1},\xi_{i-1})=\mathbf{T}(\xi_{i+1},\xi_i)\mathbf{T}(\xi_i,\xi_{i-1})$, the overall transition matrix is obtained:

$$\mathbf{T}(\xi,0)=\prod_{i=j}^{1}\mathbf{T}(s_i),\quad \xi\in(\xi_{j-1},\xi_j),\quad s_i\in(\xi_{i-1},\xi_i). \quad (46)$$

It can be observed that if the coefficient matrix $\mathbf{A}$ in the Peano-Baker series is constant, the transition matrix (44) is the same as Eq. (45). Hence, when the number of subsections approaches infinity, the approximate transition matrix becomes the exact one. It can be obtained at any desired level of accuracy by taking a suitable number of subsections. It should be noted here that while numerically determining the natural frequencies, the rate and tendency of the convergence of the solutions will be different according to the coordinate position s_i in the piecewise constant matrix selected as different values between $[\xi_{i-1},\xi_i]$. In this paper, for a better rate of convergence, s_i is taken to be $(\xi_{i-1}+\xi_i)/2$.

3 Frequency Relations

3.1 Frequency Relations of Pretwisted Beams. The relations among the setting angle θ, the rotatory inertia η, and the frequency Λ of rotating beams are studied. Meanwhile, one expects to predict the parameters of some system according to the parameters of another system. Two systems denoted as "*a*" and "*b*" have the same parameters except θ, η, and Λ. It is observed from the governing Eqs. (20) and (21) that if there exist the following relations, the two systems are similar:

$$\eta_a(\alpha^2+\Lambda_{a,i}^2)=\eta_b(\alpha^2+\Lambda_{b,i}^2), \quad (47)$$
$$\alpha^2\sin^2\theta_a+\Lambda_{a,i}^2=\alpha^2\sin^2\theta_b+\Lambda_{b,i}^2, \quad (48)$$
$$\alpha^2\cos^2\theta_a+\Lambda_{a,i}^2=\alpha^2\cos^2\theta_b+\Lambda_{b,i}^2, \quad (49)$$
$$\sin 2\theta_a=\sin 2\theta_b, \quad (50)$$

where i denotes the ith frequency. Assume that all the parameters of the system a are given and the parameters $\{\eta_b,\theta_b,\Lambda_{b,i}\}$ are unknown. It is obvious that Eqs. (48) and (49) do not be satisfied simultaneously unless $\theta_a=\theta_b$ and $\Lambda_{a,i}=\Lambda_{b,i}$. Substituting $\Lambda_{a,i}=\Lambda_{b,i}$ into Eq. (47), $\eta_a=\eta_b$. It is trivial that the two systems are the same as each other. In other words, one can't predict exactly the parameters of the system b from the parameters of the system a via the relations (47)–(50).

However, if the relation (49) is approximated and its effect is very small, the parameters of the system b can be accurately predicted from the parameters of the system a via the relations (47), (48), and (50). It is observed from Eq. (21) that the integrated parameter of the relation (49) is the coefficient for the deflection v. When the pretwisted angle is small, the deflection w is dominant and the effect of the relation (49) is very small. Moreover, the stiffer the system is, the larger the frequencies are. For a stiffer system its frequency Λ is greatly larger than the rotating speed α and the relation (49) can be approximated.

3.2.1 Frequency Relations and Mechanism of Instability of Unpretwisted Beams. Letting $V=\Phi=0$ in Eqs. (20)–(27), the governing equations and the boundary conditions of an unpretwisted Rayleigh beam can be obtained, respectively, as follows:

$$\frac{d^2}{d\xi^2}\left(B_{yy}\frac{d^2W}{d\xi^2}\right)-\frac{d}{d\xi}\left\{[n-\eta(\alpha^2+\Lambda^2)g_y]\frac{dW}{d\xi}\right\}-m(\alpha^2\sin^2\theta+\Lambda^2)W=0, \quad (51)$$

at $\xi=0$:

$$\gamma_{12}B_{yy}\frac{d^2W}{d\xi^2}-\gamma_{11}\frac{dW}{d\xi}=0, \quad (52)$$

$$\gamma_{22}\left\{\frac{d}{dx}\left(B_{yy}\frac{d^2W}{d\xi^2}\right)-[n-\eta(\alpha^2+\Lambda^2)g_y]\frac{dW}{d\xi}\right\}+\gamma_{21}W=0, \quad (53)$$

at $\xi=1$:

$$\frac{d^2W}{d\xi^2}=0, \quad (54)$$

$$\frac{d}{dx}\left(B_{yy}\frac{d^2W}{d\xi^2}\right)-[n-\eta(\alpha^2+\Lambda^2)g_y]\frac{dW}{d\xi}=0. \tag{55}$$

One can obtain from Eqs. (51)–(55) the relations (47) and (48) which can be satisfied simultaneously. Given all the parameters of the system a and the setting angle θ_b for the system b, the corresponding frequencies $\Lambda_{b,i}$ and the rotatory inertia η_b of the system b can be predicted exactly by using the relations (48) and (47), respectively.

It should be noted that the critical state of instability is $\Lambda_1^2=0$. If $\Lambda_1^2<0$, the natural frequency is imaginery and the divergent instability ([6]) occurs. Substituting $\Lambda_{a,1}$ and the associated parameters into the relations (47) and (48), one can predict whether the divergent instability will happen to the system b. Letting $\Lambda_{b,1}^2=0$, the critical rotatory inertia and the critical setting angle are obtained from Eqs. (47) and (48), respectively,

$$(\eta_b)_{\text{critical}}=\eta_a(1+\Lambda_{a,1}^2/\alpha^2), \tag{56}$$

$$(\theta_b)_{\text{critical}}=\sin^{-1}\sqrt{\sin^2\theta_a+\Lambda_{a,1}^2/\alpha^2} \tag{57}$$

under the following necessary condition of the divergent instability

$$\sin^2\theta_a+\Lambda_{a,1}^2/\alpha^2<1. \tag{58}$$

Because the effects of the rotatory inertia η and the setting angle θ are to decrease the frequencies of the system, under the condition (58) the domain of instability is $\{(\theta,\eta)|\ \sin^{-1}\sqrt{(\sin^2\theta_a+\Lambda_{a,1}^2/\alpha^2)}\leqslant\theta\leqslant\pi/2,\ \eta\geqslant\eta_a(1+\Lambda_{a,1}^2/\alpha^2)\}$.

For Bernoulli-Euler beams without taking account of the effect of the rotatory inertia η, only the relation (48) exists. The following frequency relation can be obtained by substracting the relation in the $(i+j)$th mode by that in the jth mode,

$$\Lambda_{a,i+j}^2-\Lambda_{a,i}^2=\Lambda_{b,i+j}^2-\Lambda_{b,i}^2. \tag{59}$$

It should be noted that for Bernoulli-Euler beams the condition of instability (58) is sufficient.

4 Instability of Rotating Beams

4.1 Beam With Infinite Translational Root Spring Constant.

4.1.1 Pretwisted Beam. Consider the free vibration of pretwisted Bernoulli-Euler beams with infinite translational root spring constant and without the rotational root spring, i.e., $\gamma_{12}=\gamma_{21}=\gamma_{32}=\gamma_{41}=1$ and $\gamma_{11}=\gamma_{22}=\gamma_{31}=\gamma_{42}=0$. It is assumed that there exists the free vibration of rigid-body motion and its mode shape is

$$W=w_0\xi \quad \text{and} \quad V=v_0\xi, \tag{60}$$

where w_0 and v_0 are constants. Equation (60) satisfies the boundary conditions (22)–(29). Substituting Eq. (60) into the governing Eqs. (20) and (21), one can obtain

$$\begin{aligned}&-w_0\alpha^2m(r+\xi)+m(\alpha^2\sin^2\theta+\Lambda^2)\xi w_0+m\alpha^2\sin\theta\cos\theta v_0\xi\\&\quad=0,\\&-v_0\alpha^2m(r+\xi)+m\alpha^2\sin\theta\cos\theta w_0\xi+m(\Lambda^2+\alpha^2\cos^2\theta)v_0\xi\\&\quad=0,\end{aligned} \tag{61a}$$

where the first terms of Eq. (61*a*) are derived from the second terms of Eqs. (20) and (21), respectively. Letting $r=0$, the following conditions are obtained:

$$\begin{aligned}&(\Lambda^2-\alpha^2\cos^2\theta)w_0+\alpha^2\sin\theta\cos\theta v_0=0,\\&\alpha^2\sin\theta\cos\theta w_0+(\Lambda^2-\alpha^2\sin^2\theta)v_0=0.\end{aligned} \tag{61b}$$

The first two eigenvalues are $\Lambda_1^2=0$ and $\Lambda_2^2=\alpha^2$. Because the square of fundamental frequency is zero, the instability will happen to a pretwisted Bernoulli-Euler beam. Because the effect of rotatory inertia is to decrease the frequencies, the instability will also happen to a pretwisted Rayleigh beam. However, for a pretwisted Bernoulli-Euler beam with $r>0$, $\gamma_{11}>0$, and $\gamma_{31}>0$ its fundamental frequency will be greater than the value of zero. The reason is that when the hub radius r and the rotational root spring constants γ_{11} and γ_{31} are increased from zero, the fundamental frequency of a pretwisted Bernoulli-Euler beam is increased from zero. This means that the instability will not happen to a pretwisted Bernoulli-Euler beam with $r>0$, $\gamma_{21}=\gamma_{41}=1$, $\gamma_{11}>0$, and $\gamma_{31}>0$.

4.1.2 Unpretwisted Beam. Letting $\theta=v_0=r=0$ in Eq. (61*b*), the corresponding fundamental frequency and the mode shape of an unpretwisted Bernoulli-Euler beam $\beta_2\to\infty$ are obtained, respectively,

$$\Lambda_1^2=\alpha^2, \quad W=w_0\xi. \tag{62}$$

One can predict via Eq. (48) that when $\theta_b=\pi/2$, the associated fundamental frequency $\Lambda_{b,1}=0$. When the hub radius r or the rotational root spring constant β_1 is increased, the fundamental frequency of the beam with $\theta_b=\pi/2$ is increased to be larger than zero and the instability will not happen. It is well known that when the setting angle is decreased, the frequencies are increased. Thus the instability will not happen also for the beam with $\beta_2\to\infty$, $r>0$, $\beta_1>0$ and $\theta<\pi/2$. It is concluded that in spite of the setting angle θ and the rotating speed α the instability does not happen to a Bernoulli-Euler beam with $\beta_2\to\infty$, $\beta_1>0$, and $r>0$. On the other hand, it can be observed that when $r>0$ or $\beta_1>0$, the fundamental frequency Λ_1 of the beam with $\beta_2\to\infty$ and $\theta=0$ is increased to be larger than α and the condition of instability (58) is not satisfied. This predicts also the above conclusion.

Because the frequencies of Rayleigh and Timoshenko beams taking account of the rotatory inertia η are smaller than those of Bernoulli-Euler beams under the same conditions, the fundamental frequencies of the unpretwisted Rayleigh and Timoshenko beams with $\eta>0$, $\theta=r=\beta_1=0$, and $\beta_2\to\infty$ will be less than α and the necessary condition of instability (58) is satisfied. The fundamental frequency is smaller than α and the necessary condition instability (58) is satisfied until r and β_1 are increased to be large enough. In other words, the instability will happen to the unpretwisted Rayleigh and Timoshenko beams with $\beta_2\to\infty$, $\beta_1>0$, $r>0$, and $\eta>\eta_{\text{critical}}$.

4.2 Beam With Infinite Rotational Root Spring Constants.

4.2.1 Pretwisted Beam. Consider the free vibration of a beam with infinite rotational root spring constant and without translational root spring, i.e., $\gamma_{11}=\gamma_{22}=\gamma_{31}=\gamma_{42}=1$ and $\gamma_{12}=\gamma_{21}=\gamma_{32}=\gamma_{41}=0$. It is assumed that there exists a rigid-body free-vibration motion and its mode shape is

$$W=w_0 \quad \text{and} \quad V=v_0, \tag{63}$$

where w_0 and v_0 are constants. Eq. (63) satisfies the boundary conditions (22)–(29). Substituting Eq. (63) into the governing Eqs. (20) and (21), the following conditions are obtained:

$$\begin{aligned}&(\alpha^2\sin^2\theta+\Lambda^2)w_0+\alpha^2\sin\theta\cos\theta v_0=0,\\&\alpha^2\sin\theta\cos\theta w_0+(\alpha^2\cos^2\theta+\Lambda^2)v_0=0.\end{aligned} \tag{64}$$

Equation (64) results in that the eigenvalue and the mode shape are $\Lambda^2=-\alpha^2$ and $v_0=\cot\theta w_0$. This means that the rigid-body free-vibration motion is unstable. Moreover, when the translational root spring constant is increased to a critical value from zero, the eigenvalue Λ^2 is increased to zero from the value of $-\alpha^2$. It is concluded that when the translational root spring constant is smaller than the critical value, the instability will occur.

4.2.2 Unpretwisted Beam. Consider the free vibration of rigid-body motion of a unpretwisted beam with infinite rotational

Table 1 Convergence pattern of dimensionless frequencies of a rotating pretwisted cantilever doubly tapered beam [$B_{yy}=(1-0.1\xi)^4\cos^2\xi\pi/6+4(1-0.1\xi)^4\sin^2\xi\pi/6$, $B_{zz}=4(1-0.1\xi)^4\cos^2\xi\pi/6+(1-0.1\xi)^4\sin^2\xi\pi/6$, $B_{yz}=1.5(1-0.1\xi)^4\sin\xi\pi/3$, $\alpha=3.0$, $\eta=0$]

Number of Subsections	Λ_1	Λ_2	Λ_3	Λ_4	Λ_5
5	5.100	7.791	23.747	44.036	63.632
10	5.119	7.775	23.802	43.897	63.790
20	5.124	7.771	23.817	43.861	63.836
30	5.124	7.770	23.820	43.854	63.844
40	5.125	7.770	23.821	43.851	63.848
50	5.125	7.769	23.821	43.850	63.849
60	5.125	7.769	23.822	43.850	63.850
70	5.125	7.769	23.822	43.850	63.850

root spring constant and without the translational root spring. Substituting the mode shape $W=w_0$ which satisfies the boundary conditions (52)–(55) into Eq. (51), the following condition is obtained:

$$\alpha^2\sin^2\theta+\Lambda^2=0, \tag{65}$$

which satisfies the condition of instability (58). Letting $\theta=0$, one obtains from Eq. (64) that the fundamental frequency Λ is zero. When the translational spring constant is increased, the fundamental frequency is increased from zero. The condition of instability (58) is satisfied until the translational root spring constant is larger than a critical value. This means that when the translational root spring constant is smaller than a critical value, the condition (58) will be satisfied and the instability will occur. Because for Rayleigh and Timoshenko beams which the effect of rotatory inertia is considered their fundamendal frequencies are smaller than that of a Bernoulli-Euler beam under the same parameters, the condition (58) for Rayleigh and Timoshenko beams is satisfied as soon as the condition for a Bernoulli-Euler beam is satisfied.

It is concluded that for both pretwisted and unpretwisted beams with infinite rotational root spring constants the instability will occur when the translational root spring constant is smaller than a critical value.

5 Numerical Results and Discussion

To demonstrate the efficiency and convergence of the proposed method, the first five frequencies are determined for a rotating pretwisted cantilever doubly tapered beam. In Table 1, the convergence pattern of dimensionless frequencies of the beam is shown. It shows that the natural frequencies determined by the proposed method converge very rapidly. Even when the number of subsections is only five, the differences between these solutions and the converged solutions are less than 0.5 percent.

For comparison, a uniformly pretwisted cantilever beam with constant cross section is considered. The natural frequencies obtained by the proposed method as well as those given by Subrahmanyam and Kaza [14] and Lin [12] are tabulated in Table 2.

Table 2 Effect of inertia constant η on the dimensionless frequencies of a rotating pretwisted cantilever beam [$B_{yy}=\cos^2\xi\Phi+4\sin^2\xi\Phi$, $B_{zz}=4\cos^2\xi\Phi+\sin^2\xi\Phi$, $B_{yz}=1.5\sin 2\xi\Phi$, $\alpha^*=\alpha/3.51602$]

			$\eta=0$			$\eta=0.0001$	$\eta=0.001$
Φ	α^*	Mode Number	#	##	present	present	present
30 deg	0	1	3.5245	3.5245	3.5245	3.5235	3.5149
		2	6.9585	6.9585	6.9586	6.9526	6.8994
		3	22.339	22.338	22.339	22.298	21.945
		4	42.896	42.896	42.898	42.649	40.576
		5	63.423	63.419	63.423	63.138	60.758
	1	1	5.1824	-	5.1824	5.1804	5.1632
		2	7.1461	-	7.1462	7.1386	7.0705
		3	24.055	-	24.055	24.010	23.618
		4	43.735	-	43.737	43.479	41.335
		5	65.103	-	65.104	64.811	62.367
	3	1	8.2156	-	8.2156	8.1990	8.0502
		2	11.749	-	11.748	11.743	11.694
		3	34.834	-	34.834	34.763	34.136
		4	49.804	-	49.805	49.488	46.845
		5	77.191	-	77.193	76.843	73.907
90 deg	0	1	3.5900	3.5899	3.5900	3.5882	3.5716
		2	6.4847	6.4849	6.4850	6.4815	6.4500
		3	24.531	24.530	24.530	24.457	23.833
		4	37.457	37.459	37.460	37.317	36.096
		5	72.973	72.962	72.965	72.470	68.460
	1	1	5.1120	-	5.1121	5.1086	5.0780
		2	6.8250	-	6.8253	6.8202	6.7753
		3	26.041	-	26.039	25.960	25.281
		4	38.533	-	38.536	38.385	37.102
		5	74.400	-	74.392	73.887	69.798
	3	1	7.9774	-	7.9776	7.9688	7.8908
		2	11.804	-	11.804	11.792	11.688
		3	35.872	-	35.871	35.755	34.741
		4	46.044	-	46.047	45.841	44.101
		5	84.936	-	84.929	84.353	79.672

#: given by Subrahmanyam and Kaza [14]; ##: given by Lin [12]

Table 3 The frequency relations between rotating unpretwisted Bernoulli-Euler beams [$\eta=0$, $r=0$, $B_{yy}=(1-0.2\xi)^3$, $m=(1-0.2\xi)$]

	α	θ	Λ_1^2	Λ_2^2	Λ_3^2	$\Lambda_2^2-\Lambda_1^2$	$\Lambda_3^2-\Lambda_2^2$
		0 deg	17.8707	450.0783	3223.7197	432.2076	2773.6414
	2	45 deg	15.8707	448.0783	3221.7197	432.2076	2773.6414
$\beta_{TL}\to\infty$		90 deg	13.8707	446.0783	3219.7197	432.2076	2773.6414
$\beta_{\theta L}\to\infty$		0 deg	55.5119	648.9802	3750.9751	593.4683	3101.9949
	6	45 deg	37.5119	630.9802	3732.9751	593.4683	3101.9949
		90 deg	19.5119	612.9802	3714.9751	593.4683	3101.9949
		0 deg	16.8900	421.6602	3023.3622	404.7702	2601.7020
	2	45 deg	14.8900	419.6602	3021.3622	404.7702	2601.7020
$\beta_{TL}\to\infty$		90 deg	12.8900	417.6602	3019.3622	404.7702	2601.7020
$\beta_{\theta L}=50$		0 deg	53.6052	616.3647	3540.1596	562.7595	2923.7949
	6	45 deg	35.6052	598.3647	3522.1596	562.7595	2923.7949
		90 deg	17.6052	580.3647	3504.1596	562.7595	2923.7949

Subrahmanyam and Kaza [14] studied the vibration of a rotating pretwisted cantilever beam by using the finite difference method and the Ritz method. Lin [12] studied the vibration of a nonrotating nonuniform pretwisted beam by using the modified transfer matrix method. Subrahmanyam and Kaza [14] did not consider the effect of the rotatory inertia and the coupling effect of the rotating speed and the mass moment of inertia. Without considering these effects, i.e., $\eta=0$, excellent agreement is obtained between the previous numerical results and those by the proposed method. Moreover, the effect of the inertia constant η will decrease greatly the natural frequencies. The effect of the inertia constant η on the natural frequencies of higher modes is relatively greater than that on the natural frequencies of lower modes. As the rotating speed α increases, the effect of the inertia constant η on the natural frequencies increases. The reason is that the coupling effect includes the product of the rotating speed α and the rotatory inertia η.

The frequency relations (48) and (59) between rotating unpretwisted Bernoulli-Euler beams is proved numerically in Table 3. The frequency relations (47)–(50) among rotating pretwisted beams are proved numerically in Table 4. A pretwisted cantilever beam with a small pretwisted angle is considered in Table 4. It is shown that the prediction of frequency via the relations (47), (48), and (50) is very accurate.

Figure 2 verifies the facts revealed in Sections 4.1.1 and 4.2.1 that the instability will happen to a pretwisted Rayleigh beam with infinite translational root spring constants, but not to a pretwisted Bernoulli-Euler beam with $r>0$, $\theta<\pi/4$ and $\gamma_{21}=\gamma_{41}=1$. Moreover, the instability will happen to the pretwisted Rayleigh and Bernoulli-Euler beams with infinite rotational root spring constants.

The influence of the rotating speed on the first three natural frequencies of doubly tapered beams with nonuniform pretwists is shown in Fig. 3. It is observed that the effect of the rotating speed on the first two frequencies are almost the same for all three systems. However, the effect on the higher mode frequencies are greatly different.

Figure 4 shows the influence of the total pretwist angle Φ on the first four frequencies of cantilever beams with different ratio of area moment inertia in the z and y-directions $I_{ZZ}(0)/I_{YY}(0)$. If the cross section of the beam is almost square, e.g., $I_{ZZ}(0)/I_{YY}(0)=2$, the influence of the total pretwist angle Φ on the frequencies is small. However, when $I_{ZZ}(0)/I_{YY}(0)=100$, the influence of the total pretwist angle Φ on the frequencies is great. The influence on the frequencies of higher modes is greater than that on the frequencies of lower modes.

6 Conclusion

A solution procedure for the bending-bending vibration of a rotating nonuniform beam with arbitrary pretwist and an elastically restrained root is derived. A simple and efficient algorithm for deriving the semianalytical transition matrix of the general system with nonuniform pretwist is proposed. The algorithm can be applied to linear control systems. The divergence in the Frobenius method does not exist in the proposed method. The frequency

Table 4 The prediction of the fundamental frequency Λ_b of pretwisted cantilever beams [$\alpha=0.1$, $\eta_a=0.001$, $r=1$, $B_{yy}=(1-0.1\xi)\cos^2\Phi\xi+1000(1-0.1\xi)^3\sin^2\Phi\xi$, $B_{zz}=1000(1-0.1\xi)^3\cos^2\Phi\xi+(1-0.1\xi)\sin^2\Phi\xi$, $B_{yz}=(5000(1-0.1\xi)^3-0.5(1-0.1\xi))\sin 2\Phi\xi$]

Φ	θ_a	Λ_a	θ_b	η_b	Λ_b	$\overline{\Lambda_b}$
	0 deg	3.62623	90 deg	0.00100076	3.62485	3.62485
0.1 deg	20 deg	3.62607	70 deg	0.00100058	3.62501	3.62501
	40 deg	3.62566	50 deg	0.00100013	3.62543	3.62543
	60 deg	3.62520	30 deg	0.00099942	3.62589	3.62589
	0 deg	3.61501	90 deg	0.00100077	3.61363	3.61415
5 deg	20 deg	3.61493	70 deg	0.00100059	3.61387	3.61426
	40 deg	3.61468	50 deg	0.00100013	3.61444	3.61453
	60 deg	3.61439	30 deg	0.00099962	3.61509	3.61483
	0 deg	3.53790	90 deg	0.00100080	3.53648	3.54079
15 deg	20 deg	3.53829	70 deg	0.00100061	3.53721	3.54051
	40 deg	3.53920	50 deg	0.00100014	3.53895	3.53970
	60 deg	3.54019	30 deg	0.00099960	3.54090	3.53870
	0 deg	3.44536	90 deg	0.00100084	3.44391	3.45405
25 deg	20 deg	3.44647	70 deg	0.00100064	3.44536	3.45312
	40 deg	3.44914	50 deg	0.00100015	3.44889	3.45065
	60 deg	3.45212	30 deg	0.00099958	3.45285	3.44778

Λ_b : determined by using Eq. (48)
$\overline{\Lambda_b}$: substituting Λ_b into Eq. (47), η_b is obtained. Further, determine $\overline{\Lambda_b}$ by using the proposed method for the general system.

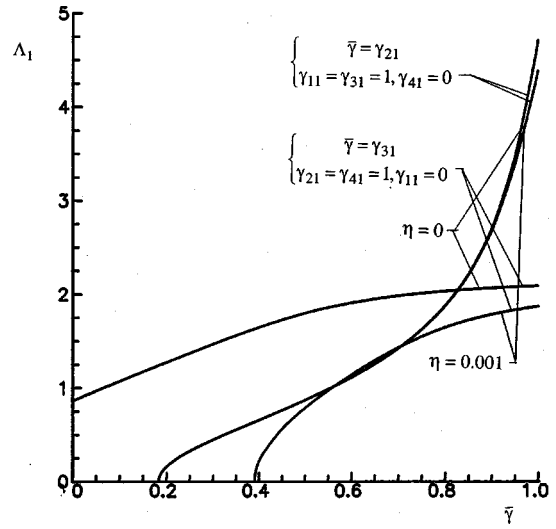

Fig. 2 The influence of the root spring constants on the instability of a pretwisted tapered beam [$B_{yy}=(1-0.1\xi)\cos^2\pi\xi/4+100(1-0.1\xi)^3\sin^2\pi\xi/4$, $B_{zz}=100(1-0.1\xi)^3\cos^2\pi\xi/4+(1-0.1\xi)\sin^2\pi\xi/4$, $B_{yz}=[50(1-0.1\xi)^3-0.5(1-0.1\xi)]\sin\pi\xi/2$, $\alpha=2$, $\theta=30$ deg, $r=0.1$]

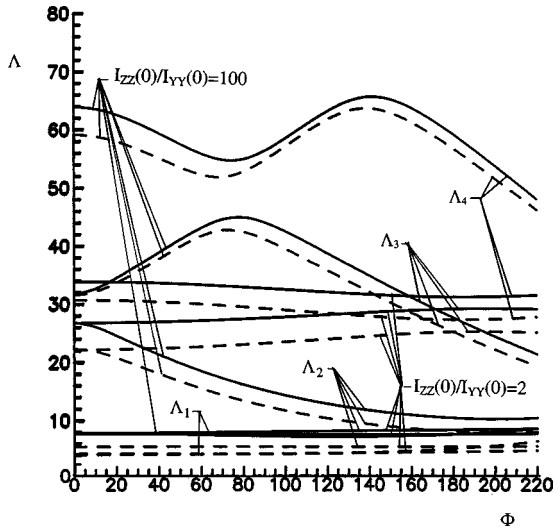

Fig. 4 The influence of the total pretwist angle Φ on the first four natural frequencies of cantilever doubly tapered beams [$B_{yy}=(1-0.1\xi)^4\cos^2\xi\Phi+I_{ZZ}(0)/I_{YY}(0)(1-0.1\xi)^4\sin^2\xi\Phi$, $B_{zz}=I_{ZZ}(0)/I_{YY}(0)(1-0.1\xi)^4\cos^2\xi\Phi+(1-0.1\xi)^4\sin^2\xi\Phi$, $B_{yz}=I_{ZZ}(0)/(2I_{YY}(0))(1-0.1\xi)^4\sin^2\xi\Phi$, $\eta=0.001$, $\theta=0$, $r=1$; ——: $\alpha=4$; — — —: $\alpha=1$]

relations among different systems are revealed. The mechanisms of instability is discovered. The effects of several parameters on the instability of rotating beams is investigated. It is shown that

1 due to the coupling effect of the rotational speed and the rotatory inertia, when the rotating speed α increases, the effect of the inertia constant η on the natural frequencies increases.

2 the effect of the rotatory inertia on the natural frequencies of higher modes is relatively greater than that on the natural frequencies of lower modes.

3 the instability does not happen to a unpretwisted Bernoulli-Euler beam with infinite translational root spring constant and $r>0$. However, if the rotational root spring constant is smaller than a critical value, the instability will happen to the Rayleigh and Timoshenko unpretwisted beams with infinite translational spring root constant, $r>0$ and $\theta>0$.

4 if the translational root spring constant is smaller than a critical value, the instability will happen to Bernoulli-Euler, Rayleigh, and Timoshenko unpretwisted and pretwisted beams with infinite rotational root spring constant.

5 the instability will not happen to a pretwisted Bernoulli-Euler beam with $r>0$, $\gamma_{21}=\gamma_{41}=1$, $\gamma_{11}>0$, and $\gamma_{31}>0$. The instability will happen to pretwisted Rayleigh and Timoshenko pretwisted beams.

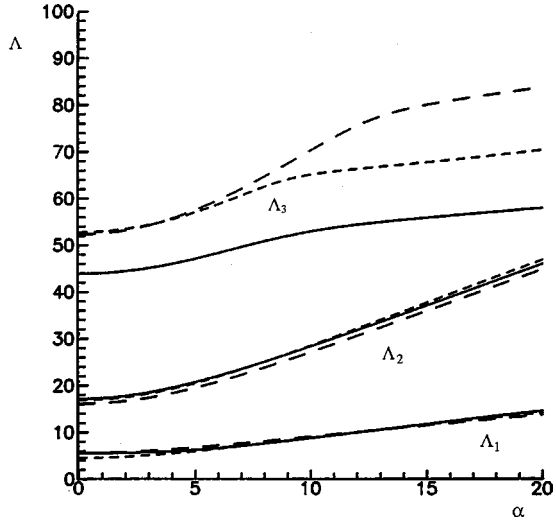

Fig. 3 The influence of the rotating speed α on the first three natural frequencies of cantilever doubly tapered beams with uniform and nonuniform pretwists [$B_{yy}=(1-0.1\xi)^4\cos^2\varphi+100(1-0.1\xi)^4\sin^2\varphi$, $B_{zz}=100(1-0.1\xi)^4\cos^2\varphi+(1-0.1\xi)^4\sin^2\varphi$, $B_{yz}=49.5(1-0.1\xi)^4\sin^2\varphi$, $\eta=0.001$, $\theta=\pi/3$, $r=0.2$; ——: $\varphi=\pi\xi^2/2$; — — —: $\varphi=\pi/2\sin(\xi\pi/2)$; — — —: $\varphi=\pi\xi/2$]

Acknowledgment

The support of the National Science Council of Taiwan, R.O.C., is gratefully acknowledged (Grant number: Nsc89-2212-E-168-002).

References

[1] Leissa, A., 1981, "Vibrational Aspects of Rotating Turbomachinery Blades," Appl. Mech. Rev., **34**, pp. 629–635.

[2] Ramamurti, V., and Balasubramanian, P., 1984, "Analysis of Turbomachine Blades: A Review," Shock Vib. Dig., **16**, pp. 13–28.

[3] Rosen, A., 1991, "Structural and Dynamic Behavior of Pretwisted Rods and Beams," Appl. Mech. Rev., **44**, pp. 483–515.

[4] Lin, S. M., 1999, "Dynamic Analysis of Rotating Nonuniform Timoshenko Beams With an Elastically Restrained Root," ASME J. Appl. Mech., **66**, pp. 742–749.

[5] Lee, S. Y., and Kuo, Y. H., 1992, "Bending Vibrations of a Rotating Nonuniform Beams With an Elastically Restrained Root," ASME J. Appl. Mech., **154**, pp. 441–451.

[6] Lee, S. Y., and Lin, S. M., 1994, "Bending Vibrations of Rotating Nonuniform Timoshenko Beams With an Elastically Restrained Root," ASME J. Appl. Mech., **61**, pp. 949–955.

[7] Gupta, R. S., and Rao, J. S., 1978, "Finite Element Eigenvalue Analysis of Tapered and Twisted Timoshenko Beams," J. Sound Vib., **56**, No. 2, pp. 187–200.

[8] Carnegie, W., and Thomas, J., 1972, "The Coupled Bending-Bending Vibration of Pre-twisted Tapered Blading," ASME J. Eng. Ind., **94**, pp. 255–266.

[9] Subrahmanyam, K. B., and Rao, J. S., 1982, "Coupled Bending-Bending Cantilever Beams Treated by the Reissner Method," J. Sound Vib., **82**, No. 4, pp. 577–592.

[10] Celep, Z., and Turhan, D., 1986, "On the Influence of Pretwisting on the Vibration of Beams Including the Shear and Rotatory Inertia Effects," J. Sound Vib., **110**, No. 3, pp. 523–528.

[11] Rosard, D. D., and Lester, P. A., 1953, ''Natural Frequencies of Twisted Cantilever Beams,'' ASME J. Appl. Mech., **20**, pp. 241–244.
[12] Lin, S. M., 1997, ''Vibrations of Elastically Restrained Nonuniform Beams With Arbitrary Pretwist,'' AIAA J., **35**, No. 11, pp. 1681–1687.
[13] Rao, J. S., and Carnegie, W., 1973, ''A Numerical Procedure for the Determination of the Frequencies and Mode Shapes of Lateral Vibration of Blades Allowing for the Effect of Pre-twist and Rotation,'' International Journal of Mechanical Engineering Education **1**, No. 1, pp. 37–47.
[14] Subrahmanyam, K. B., and Kaza, K. R. V., 1986, ''Vibration and Buckling of Rotating, Pretwisted, Preconed Beams Including Coriolis Effects,'' ASME J. Vib., Acoust., Stress, Reliab. Des. **108**, pp. 140–149.
[15] Subrahmanyam, K. B., Kulkarni, S. V., and Rao, J. S., 1982, ''Application of the Reissner Method to Derive the Coupled Bending-Torsion Equations of Dynamic Motion of Rotating Pretwisted Cantilever Blading With Allowance for Shear Deflection, Rotary Inertia, Warping and Thermal Effects,'' J. Sound Vib., **84**, No. 2, pp. 223–240.
[16] Sisto, F., and Chang, A. T., 1984, ''A Finite Element for Vibration Analysis of Twisted Blades Based on Beam Theory,'' AIAA J. **21**, No. 11, pp. 1646–1651.
[17] Young, T. H., and Lin, T. M., 1998, ''Stability of Rotating Pretwisted, Tapered Beams With Randomly Varying Speed,'' ASME J. Vibr. Acoust., **120**, pp. 784–790.
[18] Kar, R. C., and Neogy, S., 1989, ''Stability of a Rotating, Pretwisted, Nonuniform Cantilever Beam With Tip Mass and Thermal Gradient Subjected to a Non-conservative Force,'' Comput. Struct., **33**, No. 2, pp. 499–507.
[19] Hernried, A. G., 1991, ''Forced Vibration Response of a Twisted Non-uniform Rotating Blade,'' Comput. Struct., **41**, No. 2, pp. 207–212.
[20] Surace, G., Anghel, V., and Mares, C., 1997, ''Coupled Bending-Bending-Torsion Vibration Analysis of Rotating Pretwisted Blades: An Integral Formulation and Numerical Examples,'' J. Sound Vib., **206**, No. 4, pp. 473–486.
[21] Rugh, W. J., 1996, *Linear System Theory*, Prentice-Hall, Englewood Cliffs, NJ, pp. 41–44.
[22] Rao, J. S., 1987, ''Turbomachine Blade Vibration,'' Shock Vib. Dig., **19**, No. 5, pp. 3–10.

On the Internal Resonance of a Spinning Disk Under Space-Fixed Pulsating Edge Loads

Jen-San Chen
Professor,
Department of Mechanical Engineering,
National Taiwan University,
Taipei, Taiwan 10617

Internal resonance between a pair of forward and backward modes of a spinning disk under space-fixed pulsating edge loads is investigated by means of multiple scale method. It is found that internal resonance can occur only at certain rotation speeds at which the natural frequency of the forward mode is close to three times the natural frequency of the backward mode and the excitation frequency is close to twice the frequency of the backward mode. For a light damping case the trivial solution can lose stability via both pitchfork as well as Hopf bifurcations when frequency detuning of the edge load is varied. On the other hand, nontrivial solutions experience both saddle-node and Hopf bifurcations. When the damping is increased, the Hopf bifurcations along the trivial solution path disappear. Furthermore, there exists a certain value of damping beyond which no nontrivial solution is possible. Single-mode resonance is also briefly discussed for comparison. [DOI: 10.1115/1.1408616]

Introduction

The vibration analysis of a spinning disk under space-fixed edge loads attracts attention because of its possible application in such fields as circular saw cutting and grind wheel operation. Carlin and his co-workers' investigation [1] appears to be the first paper attempting to calculate the natural frequencies of a spinning disk under a concentrated radial edge load. Radcliffe and Mote [2] extended the work of [1] by considering a general concentrated edge load with both radial and tangential components. Chen [3,4] reformulated the problem with emphasis on the effects of relative motion between the disk and the edge load on the stability and natural frequencies of the loaded disk. Recently Chen [5] extended these analyses by considering the parametric resonance of a spinning disk under space-fixed pulsating edge loads.

The plate model employed in [5] ignored the effect of membrane stretching. As a consequence the equation of motion is linear in terms of the transverse deflection and the stiffness term involves a periodic coefficient which is due to the pulsating edge load. This linearized model imposes two limits on the applicability of the parametric resonance theory presented in [5]. First of all, while the linearized model can predict the onset of parametric resonance, it cannot predict the amplitude of steady-state vibration after parametric resonance occurs. Secondly, it cannot account for the complicated internal resonance phenomenon which is due to interaction between modes coupled by the nonlinear effect.

In this paper we extend our previous work [5] to consider the nonlinear parametric resonance of a spinning disk under space-fixed pulsating edge loads. Membrane stretching effect is taken into account by employing von Karman's plate model. We focus our attention on the internal resonance between a pair of forward and backward traveling waves with the same number of nodal diameters and nodal circles. Galerkin's procedure is used to discretize the equations of motion. The multiple scale method is then used to study the steady-state behavior and the stability of the response. Both static and dynamic bifurcation phenomena are discussed. The effects of damping on the bifurcation points are also studied in detail.

Contributed by the Applied Mechanics Division of THE AMERICAN SOCIETY OF MECHANICAL ENGINEERS for publication in the ASME JOURNAL OF APPLIED MECHANICS. Manuscript received by the ASME Applied Mechanics Division, May 15, 2000; final revision, May 31, 2001. Associate Editor: R. C. Benson. Discussion on the paper should be addressed to the Editor, Professor Lewis T. Wheeler, Department of Mechanical Engineering, University of Houston, Houston, TX 77204-4792, and will be accepted until four months after final publication of the paper itself in the ASME JOURNAL OF APPLIED MECHANICS.

Equations of Motion

We consider an elastic circular disk spinning with constant speed Ω. The disk is ''partially'' clamped [6] at the inner radius $r=a$ and is subjected to a periodic radial load at the outer radius $r=b$. In circular saw and grinding wheel operations the radial load is applied on a small sector of the outer edge. We assume that this space-fixed edge load can be expanded in a Fourier series $\cos \gamma t \Sigma_{k=0}^{\infty} P_k \cos k\theta$. P_k has the dimension of stress, and γ is the excitation frequency of the in-plane edge load. The direction of the edge load remains unchanged when the disk vibrates laterally. The equations of motion of the spinning disk in terms of transverse displacement w and stress function ϕ can be written as [7]

$$\rho h(w_{,tt}+2\Omega w_{,t\theta}+\Omega^2 w_{,\theta\theta})+c_f w_{,t}+D\nabla^4 w = h\left\{ w_{,rr}(r^{-1}\phi_{,r}+r^{-2}\phi_{,\theta\theta})+(r^{-1}w_{,r}+r^{-2}w_{,\theta\theta})\phi_{,rr} -2(r^{-1}w_{,\theta})_{,r}(r^{-1}\phi_{,\theta})_{,r}-\rho\Omega^2 r\left(\frac{r}{2}\nabla^2 w+w_{,r}\right)\right\} \quad (1)$$

$$\nabla^4\phi=-E[w_{,rr}(r^{-1}w_{,r}+r^{-2}w_{,\theta\theta}) +2r^{-3}w_{,r\theta}w_{,\theta}-r^{-2}(w_{,r\theta})^2-r^{-4}(w_{,\theta})^2] +2(1-\nu)\rho\Omega^2 \quad (2)$$

(r, θ) are space-fixed polar coordinates. The parameters ρ, h, E, ν, and D are the mass density, thickness, Young's modulus, Poisson ratio, and flexural rigidity of the disk, respectively. c_f represents a space-fixed homogeneous damping due to the surrounding air. In writing Eq. (2) the in-plane inertia is neglected. These two equations are based on the famous von Karman's plate model, which accounts for the membrane stretching due to bending.

It is noted that the total deflection of the disk cannot be deemed as the sum of the deflection components due to each Fourier component in the series because the edge load affects the stiffness operator instead of the forcing term. However, in Chen's previous work [4,5] on linear response in a similar loading situation he

observed through numerical simulation that the effects of each Fourier component on the stability properties of the spinning disk are additive. In other words, if a Fourier component causes unstable vibration, then so does the general loading containing this particular Fourier component. As a consequence, it is possible to predict the behavior of the loaded disk by considering the effect of the general edge load as the combined effects of its individual components. Along this line of thought we focus on the response of a spinning disk under a Fourier component $\cos \gamma t P_k \cos k\theta$ in the following discussion.

The partially clamped boundary conditions for transverse deflection w at $r=a$ are

$$w=0 \tag{3}$$

$$w_{,r}=0. \tag{4}$$

The boundary conditions at $r=b$ are

$$(\nabla^2 w)_{,r}+r^{-2}(1-\nu)(w_{,r\theta\theta}-r^{-1}w_{,\theta\theta})+\frac{hP_k}{D}\cos\gamma t\cos k\theta w_{,r}=0 \tag{5}$$

$$w_{,rr}+\nu r^{-1}(w_{,r}+r^{-1}w_{,\theta\theta})=0. \tag{6}$$

The in-plane boundary conditions at $r=b$ are

$$\sigma_{r\theta}=0, \tag{7}$$

$$\sigma_r=P_k\cos\gamma t\cos k\theta. \tag{8}$$

We also require that

$$\phi<\infty \quad \text{at} \quad r=0. \tag{9}$$

It is noted that while Eqs. (1) and (2) are nonlinear in terms of w, they are linear in ϕ. Therefore we can divide the stress function ϕ in Eq. (2) into three parts:

$$\phi=\phi_1+\phi_2+\phi_3. \tag{10}$$

The first part ϕ_1 accounts for the stretching effect due to the centrifugal force. The second part ϕ_2 accounts for the edge load effect. The corresponding stress fields σ_{rk}, $\sigma_{\theta k}$, and $\sigma_{r\theta k}$ can be found in a standard elasticity monograph [8]. The third part ϕ_3 involves nonlinear terms of w. After substituting Eq. (10) in Eqs. (1) and (2) and introducing the following dimensionless quantities,

$$t^*=\frac{t}{b^2}\sqrt{\frac{D}{\rho h}},\quad \Omega^*=\Omega b^2\sqrt{\frac{\rho h}{D}},$$

$$\gamma^*=\gamma b^2\sqrt{\frac{\rho h}{D}},\quad r^*=\frac{r}{b},\quad w^*=w\sqrt{\frac{b}{h^3}},$$

$$\phi^*=\phi\frac{h}{D},\quad c_f^*=c_f\frac{b^3}{24(1-\nu^2)\sqrt{\rho h^3 D}},$$

$$\varepsilon=12(1-\nu^2)\frac{h}{b},\quad \eta=\frac{a}{b},$$

$$\sigma_r^*=\frac{hb^2}{D}\sigma_r,\quad P_k^*=\frac{b^3}{12(1-\nu^2)D}P_k,$$

we can rewrite the equations of motion in the dimensionless form after dropping the asterisks for simplicity,

$$\begin{aligned} w_{,tt}+2\Omega w_{,t\theta}+\Omega^2 w_{,\theta\theta}+\nabla^4 w+Lw+2\varepsilon c_f w_{,t}+\varepsilon P_k\cos\gamma t L_k w \\ =w_{,rr}(r^{-1}\phi_{3,r}+r^{-2}\phi_{3,\theta\theta})+(r^{-1}w_{,r}+r^{-2}w_{,\theta\theta})\phi_{3,rr} \\ -2(r^{-1}w_{,\theta})_{,r}(r^{-1}\phi_{3,\theta})_{,r} \end{aligned} \tag{11}$$

$$\begin{aligned} \nabla^4\phi_3=-\varepsilon[w_{,rr}(r^{-1}w_{,r}+r^{-2}w_{,\theta\theta}) \\ +2r^{-3}w_{,r\theta}w_{,\theta}-r^{-2}(w_{,r\theta})^2-r^{-4}(w_{,\theta})^2]. \end{aligned} \tag{12}$$

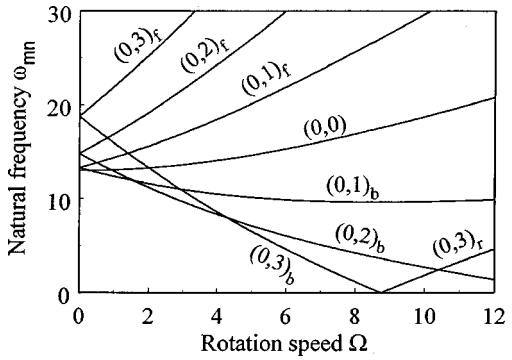

Fig. 1 Natural frequency loci of a freely spinning disk

L_k is the membrane operator associated with the stress field due to the edge load, and L is associated with the axisymmetrical stress field due to the centrifugal force,

$$L_k\equiv-\frac{1}{r}\left[\frac{\partial}{\partial r}\left(r\sigma_{rk}\frac{\partial}{\partial r}+\sigma_{r\theta k}\frac{\partial}{\partial\theta}\right)+\frac{\partial}{\partial\theta}\left(\sigma_{r\theta k}\frac{\partial}{\partial r}+\frac{1}{r}\sigma_{\theta k}\frac{\partial}{\partial\theta}\right)\right] \tag{13}$$

$$L\equiv-\frac{1}{r}\left[\frac{\partial}{\partial r}\left(r\sigma_{1r}\frac{\partial}{\partial r}\right)+\frac{\partial}{\partial\theta}\left(\frac{1}{r}\sigma_{1\theta}\frac{\partial}{\partial\theta}\right)\right] \tag{14}$$

where

$$\sigma_{1r}=\frac{3+\nu}{8}\Omega^2(1-r^2) \tag{15}$$

$$\sigma_{1\theta}=\frac{1}{8}\Omega^2[(3+\nu)-(1+3\nu)r^2]. \tag{16}$$

When the nonlinear terms of w are neglected in Eqs. (11) and (12), the equations reduce to the one considered in [5].

In the special case when $\varepsilon=0$, the solution ϕ_3 in Eq. (12) is identically zero, and as a consequence Eq. (11) is reduced to

$$w_{,tt}+2\Omega w_{,t\theta}+\Omega^2 w_{,\theta\theta}+\nabla^4 w+Lw=0. \tag{17}$$

Equation (17) is the equation of motion of a freely spinning disk. The natural frequency of a mode with n nodal diameters and m nodal circles is denoted by ω_{mn}. The corresponding eigenfunction is complex and assumes the form

$$w_{mn}(r,\theta)=R_{mn}(r)e^{in\theta}. \tag{18}$$

It is also noted that the eigenfunctions w_{mn} are orthonormal.

Figure 1 shows the natural frequency loci of a spinning disk as the rotation speed varies. The clamping ratio η is 0.5, and the Poisson ratio ν is 0.27. Only the modes with less than four nodal diameters are shown here. The subscripts f, b, and r of the mode label (m, n) represents forward, backward, and reflected modes, respectively [5].

Discretization

The linear analysis in [5] predicts that when the spinning disk is subject to a space-fixed distributed edge load $P_{2n}\cos\gamma t\cos 2n\theta$, single-mode parametric resonance can occur when the excitation frequency γ is twice the natural frequency of an (m, n) mode. Combination resonance involving two modes (m, n) and (p, q) can also occur when the numbers of nodal diameters n and q satisfy certain relations. In this paper we focus on the internal resonance between a pair of forward and backward (m, n) modes excited by the in-plane edge load. We assume that solution $w(r,\theta,t)$ of Eqs. (11) and (12) can be approximated in terms of eigenfunctions $w_{mn}(r,\theta)$ as

$$w(r,\theta,t)=c_{mn}(t)w_{mn}+\overline{c}_{mn}(t)\overline{w}_{mn}. \tag{19}$$

Both $c_{mn}(t)$ and $w_{mn}(r,\theta)$ in Eq. (19) are complex functions, while the displacement $w(r,\theta,t)$ is a real function. $\overline{w}_{mn}$ represents the complex conjugate of w_{mn}. In order to solve ϕ_3 in Eq. (12) we introduce a set of eigenfunctions ϕ_{mn} satisfying the following differential equation:

$$\nabla^4\phi_{mn}-\beta_{mn}^4\phi_{mn}=0. \tag{20}$$

ϕ_{mn} satisfy the same boundary conditions as ϕ_3 does. After expressing ϕ_3 in terms of eigenfunction series ϕ_{mn} and following Galerkin's procedure, we can discretize Eqs. (11) and (12) into

$$\ddot{c}_{mn}+2in\Omega\dot{c}_{mn}+\kappa_{mn}c_{mn}+2\varepsilon c_f\dot{c}_{mn}+\varepsilon\mu\overline{c}_{mn}\cos\gamma t+\varepsilon\alpha|c_{mn}|^2c_{mn}=0 \tag{21}$$

where

$$\kappa_{mn}=\omega_{mn}\omega_{m\bar{n}} \tag{22}$$

$$\mu=\pi\int_\eta^1\left[r\sigma_{r(2n)}(R_{mn,r})^2+\left(\frac{n^2\sigma_{\theta(2n)}}{r}-n\sigma_{r\theta(2n),r}\right)(R_{mn})^2\right]dr. \tag{23}$$

ω_{mn} and $\omega_{m\bar{n}}$ are the natural frequencies of the backward and the forward modes, respectively. It is noted that $\omega_{m\bar{n}}$ is equal to $\omega_{mn}+2n\Omega$. Constant α can be obtained via numerical integration involving eigenfunctions w_{mn} and ϕ_{mn}. $|c_{mn}|$ represents the absolute value of complex number c_{mn}.

Multiple Scale Method

We apply the method of multiple scale [9] to analyze the solution of Eq. (21). The method of multiple scale assumes an expansion of the solution in the form

$$c_{mn}(t)=c_{mn}^{(0)}(t,T_1)+\varepsilon c_{mn}^{(1)}(t,T_1)+O(\varepsilon^2) \tag{24}$$

where $T_1\equiv\epsilon t$. Substituting (24) into (21) and equating coefficients of like powers of ϵ yields

$$\varepsilon^0:\quad D_0^2c_{mn}^{(0)}+2in\Omega D_0c_{mn}^{(0)}+\kappa_{mn}c_{mn}^{(0)}=0 \tag{25}$$

$$\varepsilon^1:\quad D_0^2c_{mn}^{(1)}+2in\Omega D_0c_{mn}^{(1)}+\kappa_{mn}c_{mn}^{(1)}=-2D_1D_0c_{mn}^{(0)}-2in\Omega D_1c_{mn}^{(0)}-2c_fD_0c_{mn}^{(0)}-\alpha|c_{mn}^{(0)}|^2c_{mn}^{(0)}-\mu\overline{c}_{mn}^{(0)}\cos\gamma t \tag{26}$$

where $D_0\equiv\partial/\partial t$, and $D_1\equiv\partial/\partial T_1$. The general solution of Eq. (25) can be written in the form

$$c_{mn}^{(0)}=d_1(T_1)e^{i\omega_{mn}T_0}+d_2(T_1)e^{-i\omega_{m\bar{n}}T_0}. \tag{27}$$

Substituting (27) into the right-hand side of (26) we observe that there exist secular terms in three different cases. In the first case when $\omega_{m\bar{n}}$ is close to $3\omega_{mn}$ and γ is close to $2\omega_{mn}$ internal resonance involving both modes will occur. In the second case when $\omega_{m\bar{n}}$ is close to $3\omega_{mn}$ and γ is close to $2\omega_{m\bar{n}}$, only single-mode resonance will be induced. In the third case when $\omega_{m\bar{n}}$ is away from $3\omega_{mn}$ and γ is close to $2\omega_{mn}$ or $2\omega_{m\bar{n}}$, again only single-mode resonance is possible. The second and the third cases are the same in essence. No combination resonance of the sum or difference type is possible when only this pair of modes are considered [5]. In the following we focus on the internal resonance case.

Internal Resonance: $\omega_{m\bar{n}}$ is close to $3\omega_{mn}$ and γ is close to $2\omega_{mn}$

In this case we assume that

$$\gamma=2\omega_{mn}+\varepsilon\varsigma_1$$

$$\omega_{m\bar{n}}=3\omega_{mn}+\varepsilon\varsigma_2$$

where ς_1 and ς_2 are two independent detuning parameters. The secular terms of Eq. (26) can be eliminated if

$$2i\hat{\omega}_{mn}D_1d_1+i2\omega_{mn}c_fd_1+\alpha d_1(|d_1|^2+2|d_2|^2)-\frac{\mu}{2}(\overline{d}_1e^{i\varsigma_1T_1}+\overline{d}_2e^{i(\varsigma_2-\varsigma_1)T_1})=0 \tag{28}$$

$$2i\hat{\omega}_{mn}D_1d_2+i2\omega_{m\bar{n}}c_fd_2-\alpha d_2(|d_2|^2+2|d_1|^2)+\frac{\mu}{2}\overline{d}_1e^{i(\varsigma_2-\varsigma_1)T_1}=0 \tag{29}$$

where $\hat{\omega}_{mn}=1/2(\omega_{mn}+\omega_{m\bar{n}})$. We express d_1 and d_2 in the forms

$$d_1(T_1)=\frac{1}{2}a_1(T_1)e^{i\beta_1(T_1)} \tag{30}$$

$$d_2(T_1)=\frac{1}{2}a_2(T_1)e^{i\beta_2(T_1)}. \tag{31}$$

After substituting Eqs. (30) and (31) into Eqs. (28) and (29) we can conclude that the nontrivial steady-state solutions of a_1, β_1, a_2, and β_2 must satisfy the following equations:

$$4\hat{\omega}_{mn}\varsigma_1a_1-\alpha a_1(a_1^2+2a_2^2)+2\mu(a_1\cos\psi_1+a_2\cos\psi_2)=0 \tag{32}$$

$$4c_f\omega_{mn}a_1-\mu(a_1\sin\psi_1+a_2\sin\psi_2)=0 \tag{33}$$

$$4\hat{\omega}_{mn}(2\varsigma_2-3\varsigma_1)a_2+\alpha a_2(a_2^2+2a_1^2)-2\mu a_1\cos\psi_2=0 \tag{34}$$

$$4c_f\omega_{m\bar{n}}a_2+\mu a_1\sin\psi_2=0 \tag{35}$$

where

$$\psi_1=\varsigma_1T_1-2\beta_1 \tag{36}$$

$$\psi_2=(\varsigma_2-\varsigma_1)T_1-\beta_1-\beta_2. \tag{37}$$

It is noted that single-mode resonance is not possible in this case. A straightforward solution procedure to solve Eqs. (32) to (35) for nontrivial solutions a_1, a_2, ψ_1, and ψ_2 is described briefly in the Appendix. The steady-state vibration of the spinning disk is then

$$w(r,\theta,t)=R_{mn}(r)\left[a_1\cos\left(\frac{\gamma t}{2}-\frac{\psi_1}{2}+n\theta\right)+a_2\cos\left(\frac{3\gamma t}{2}-\frac{\psi_1}{2}+\psi_2-n\theta\right)\right]+O(\varepsilon), \tag{38}$$

which represents the superposition of two waves traveling in opposite directions. It is noted that the first term with a_1 in Eq. (38) is excited directly by the edge load, while the second term with a_2 is excited internally in a super-harmonic manner.

Stability Analysis

The stability of the steady-state solutions can be analyzed by expressing $d_1(T_1)$ and $d_2(T_1)$ as

$$d_1(T_1)=d_1^{(s)}+\hat{d}_1(T_1) \tag{39}$$

$$d_2(T_1)=d_2^{(s)}+\hat{d}_2(T_1). \tag{40}$$

$d_1^{(s)}$ and $d_2^{(s)}$ are the steady-state solutions. After substituting Eqs. (39) and (40) into Eqs. (28) and (29) and linearizing with respect to the variations $\hat{d}_1(T_1)$ and $\hat{d}_2(T_1)$ we can study the stability of the steady-state solutions. For instance, in order to study the stability of the trivial solutions we substitute

$$d_1(T_1)=[\hat{\alpha}_1(T_1)+i\hat{\beta}_1(T_1)]e^{(i\varsigma_1/2)T_1} \tag{41}$$

$$d_2(T_1)=[\hat{\alpha}_2(T_1)+i\hat{\beta}_2(T_1)]e^{(-i3\varsigma_1/2+i\varsigma_2)T_1} \tag{42}$$

into Eqs. (28) and (29) to obtain the Jacobian matrix $[J]$ of the linearized equations as

$$[J]=\begin{bmatrix} 4c_f\omega_{mn} & \mu-2\varsigma_1\hat{\omega}_{mn} & 0 & \mu \\ \mu+2\varsigma_1\hat{\omega}_{mn} & 4c_f\omega_{mn} & \mu & 0 \\ 0 & -\mu & 4c_f\omega_{mn^-} & \hat{\omega}_{mn}(6\varsigma_1-4\varsigma_2) \\ -\mu & 0 & -\hat{\omega}_{mn}(6\varsigma_1-4\varsigma_2) & 4c_f\omega_{mn^-} \end{bmatrix}. \tag{43}$$

By calculating the eigenvalues of the Jacobian matrix, we can determine the stability of the trivial solutions. The stability of the nontrivial solutions can be analyzed in a similar manner.

Steady-State Solutions

Figure 2 shows the amplitudes and phases of the steady-state solutions as functions of detuning parameter ς_1 for the internal resonance between a pair of (0, 3) modes at $\Omega=3.3$. The parameters used in the calculation are $\varepsilon=0.01$, $\omega_{03}=9.9$, $\omega_{03^-}=29.7$, $\mu=100$, $c_f=0.5$, and $\alpha=0.4$. The excitation frequency $\gamma=2\omega_{03}+\varepsilon\varsigma_1$. The solid and dashed curves represent stable and unstable solutions, respectively. The stable trivial solution undergoes a supercritical pitchfork bifurcation at $\varsigma_1=-3.11$ (point A). From point A the nontrivial solution branch is stable and undergoes a saddle-node bifurcation at point H($\varsigma_1=0.90$). On the other hand, the unstable trivial solution from point A undergoes a subcritical pitchfork bifurcation at point B ($\varsigma_1=-0.64$), creating an unstable nontrivial branch BH and a stable trivial branch BC. This stable trivial solution then loses stability via a supercritical Hopf bifurcation at $\varsigma_1=-0.33$ (point C), creating a quasi-periodic solution c_{03} which cannot be shown in Fig. 2. The unstable branch CD undergoes a supercritical Hopf bifurcation at point D ($\varsigma_1=0.33$) and creates a stable trivial branch DE. The branch DE then undergoes a supercritical bifurcation at point E creating a stable nontrivial branch EG and unstable trivial branch EF. The stable branch EG then loses stability via a supercritical Hopf bifurcation at point G creating a stable quasi-periodic solution (which again cannot be shown in Fig. 2) and an unstable periodic solution. The trivial branch EF undergoes a subcritical pitchfork bifurcation at point F creating an unstable nontrivial branch and a stable trivial branch.

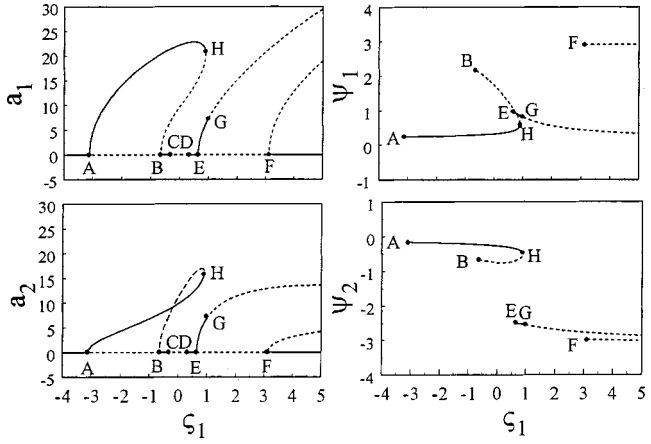

Fig. 2 Amplitudes and phases of the steady-state response. $\varepsilon=0.01$, $\Omega=3.3$, $\omega_{03}=9.9$, $\omega_{03^-}=29.7$, $\gamma=2\omega_{03}+\varepsilon\varsigma_1$, $\mu=100$, $\alpha=0.4$, and $c_f=0.5$.

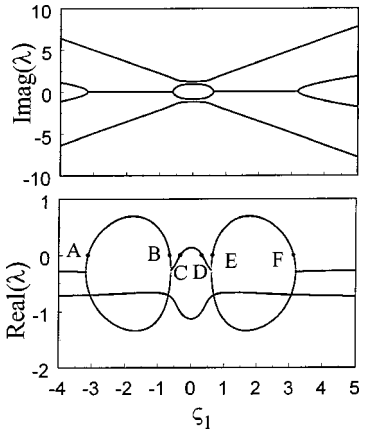

Fig. 3 Eigenvalues of the Jacobian matrix along the trivial solution path of Fig. 2

The bifurcation points along the trivial solution path can be verified by observing the eigenvalues λ of the Jacobian matrix $[J]$ in Eq. (43) in Fig. 3. At points A, B, E, and F there exists a zero eigenvalue, which implies a pitchfork bifurcation. On the other hand at points C and D there exist a pair of purely imaginary eigenvalues and the real part loci of the eigenvalues cross the zero line ''transversely,'' which implies a Hopf bifurcation [10].

To demonstrate the existence of quasiperiodic solutions predicted by the multiple scale analysis we use Runge-Kutta method to integrate Eq. (21) at $\varsigma_1=-0.32$ (a point slightly to the right of point C in Fig. 2) with initial conditions $c_{03}=0.1$ and $\dot{c}_{03}=0$. Figure 4(*a*) shows the response history of the real part of c_{03} after a long period of time. Figure 4(*b*) shows its Poincare map recorded from $t=10{,}000$ to 12,000 with the sampling rate equal to the excitation frequency. The sampling points fill up a small strip

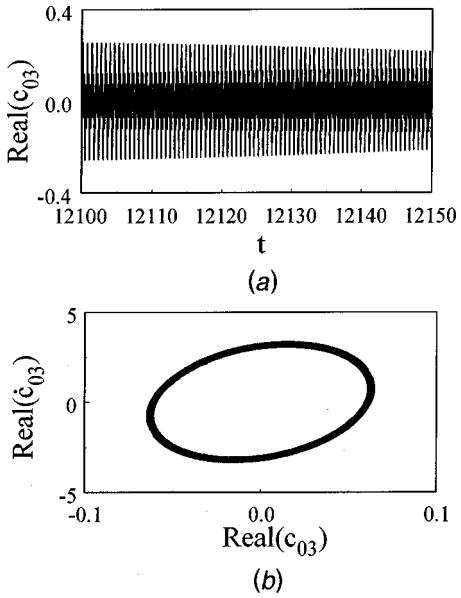

Fig. 4 (*a*) Quasi-periodic response and (*b*) the corresponding Poincare map for $\varsigma_1=-0.32$ with initial conditions $c_{03}=0.1$ and $\dot{c}_{03}=0$

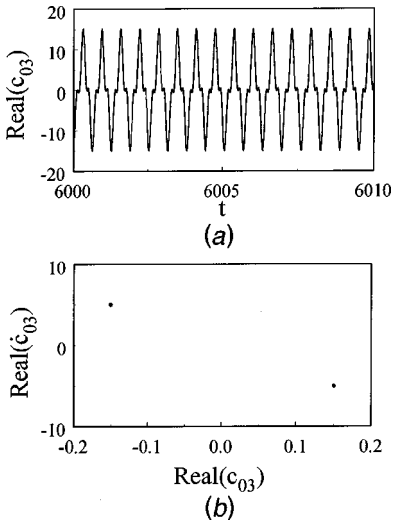

Fig. 5 (*a*) Periodic response and (*b*) the corresponding Poincare map for $\varsigma_1=-0.32$ with initial conditions $c_{03}=20$ and $\dot{c}_{03}=0$

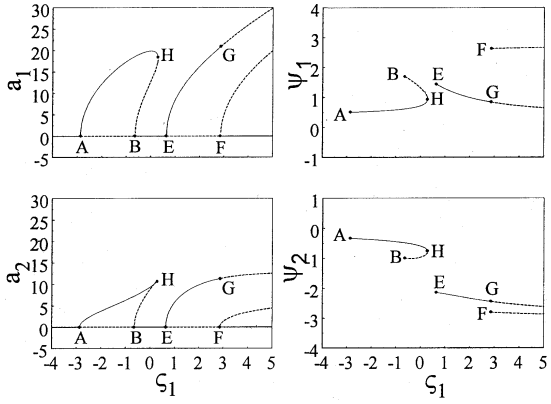

Fig. 6 Amplitudes and phases of the steady-state response. $\varepsilon=0.01$, $\Omega=3.3$, $\omega_{03}=9.9$, $\omega_{03}^{-}=29.7$, $\gamma=2\omega_{03}+\varepsilon\varsigma_1$, $\mu=100$, $\alpha=0.4$, and $c_f=1.0$.

around a closed curve, which implies the quasi-periodic feature of the response. If the initial condition of c_{03} is changed from 0.1 to 20, the response then settles to the stable branch AH in Fig. 2, as shown in Fig. 5. The Poincare map in Fig. 5(*b*) records the sampling points from $t=4000$ to 6000.

To observe the effects of damping we use the same parameters as those in Fig. 2 but change the damping c_f from 0.5 to 1. The amplitudes and phases of the steady-state solutions are shown in Fig. 6. We observe that the two Hopf bifurcation points C and D approach each other until they coalesce and disappear. Furthermore the Hopf bifurcation point G on the nontrivial solution branch moves to the right resulting in a longer stable branch EG.

Bifurcation Points

The observations on the eigenvalue loci in Fig. 3 allow us to predict the bifurcation points on the trivial solution path analytically. For the Hopf bifurcation to occur a pair of the eigenvalues of the Jacobian matrix (43) must be purely imaginary. By Routh-Hurwitz criterion we conclude that the detuning parameter ς_{1H} must satisfy the equation

$$A_{2H}\varsigma_{1H}^4+A_{1H}\varsigma_{1H}^2+A_{0H}=0 \tag{44}$$

where

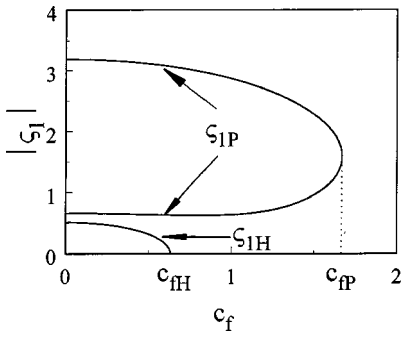

Fig. 7 Pitchfork and Hopf bifurcation points along the trivial solution path as functions of damping c_f

$$A_{2H}=1024\hat{\omega}_{mn}^4\omega_{mn}\omega_{mn}^{-}$$

$$A_{1H}=64\hat{\omega}_{mn}^2[80c_f^2\omega_{mn}\omega_{mn}^{-}\hat{\omega}_{mn}^2+\mu(4\hat{\omega}_{mn}^2+\omega_{mn}\omega_{mn}^{-})]$$

$$A_{0H}=4096c_f^4\omega_{mn}\omega_{mn}^{-}\hat{\omega}_{mn}^4+64c_f^2\mu^2\hat{\omega}_{mn}^2(\omega_{mn}^2+\omega_{mn}^{2-})-\mu^4(4\hat{\omega}_{mn}^2-\omega_{mn}\omega_{mn}^{-}).$$

The roots of Eq. (44) correspond to points C and D in Fig. 2. Similarly, the detuning parameter ς_{1P} for pitchfork bifurcation must satisfy

$$A_{2P}\varsigma_{1P}^4+A_{1P}\varsigma_{1P}^2+A_{0P}=0 \tag{45}$$

where

$$A_{2P}=144\hat{\omega}_{mn}^4$$

$$A_{1P}=4\hat{\omega}_{mn}^2[16c_f^2(8\omega_{mn}^2+\omega_{mn}^{2-})-15\mu^2]$$

$$A_{0P}=256c_f^4\omega_{mn}^2\omega_{mn}^{2-}+16c_f^2\mu^2\omega_{mn}^{-}(2\omega_{mn}-\omega_{mn}^{-})+\mu^4.$$

The roots of Eq. (45) correspond to points A, B, E, and F in Fig. 2. In Fig. 7 we plot the absolute values of the roots of Eqs. (44) and (45) as functions of damping c_f. It is observed that Hopf bifurcation ceases to exist as c_f exceeds 0.63, while pitchfork bifurcation ceases to exist as c_f exceeds 1.67. In other words, no nontrivial solution is possible when c_f is greater than 1.67. These two special dampings, denoted by c_{fH} and c_{fP}, respectively, are proportional to μ, and can be obtained by solving

$$A_{0H}=0 \tag{46}$$

$$A_{1P}^2-4A_{2P}A_{0P}=0, \tag{47}$$

respectively. Both Eqs. (46) and (47) are quadratic equations of c_f^2.

Single Mode Resonance: ω_{mn}^{-} is close to $3\omega_{mn}$ and γ is close to $2\omega_{mn}^{-}$

In this case we assume that

$$\gamma=2\omega_{mn}^{-}+\varepsilon\varsigma_1. \tag{48}$$

The secular terms of Eq. (26) can be eliminated if

$$2i\hat{\omega}_{mn}D_1d_1+i2\omega_{mn}c_fd_1+\alpha d_1(|d_1|^2+2|d_2|^2)=0 \tag{49}$$

$$2i\hat{\omega}_{mn}D_1d_2+i2\omega_{mn}^{-}c_fd_2-\alpha d_2(|d_1|^2+2|d_2|^2)+\frac{\mu}{2}\bar{d}_2e^{-i\varsigma_1T_1}=0. \tag{50}$$

Following a similar procedure as in the internal resonance case we can conclude that the steady-state solution of a_1 is zero and the nontrivial steady-state solution of a_2 and β_2 satisfy the following conditions:

$$4c_f\omega_{mn}^{-}-\mu\sin\psi_2=0 \tag{51}$$

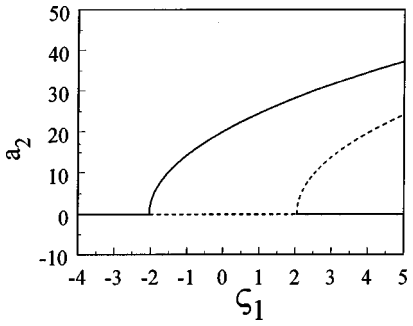

Fig. 8 Amplitude of the single-mode resonance. $\varepsilon=0.01$, $\Omega=3.3$, $\omega_{03}=9.9$, $\omega_{03}^{-}=29.7$, $\gamma=2\omega_{03}^{-}+\varepsilon\varsigma_1$, $\mu=100$, $\alpha=0.4$, and $c_f=0.5$.

$$-\alpha a_2^2+2\mu\cos\psi_2+4\hat{\omega}_{mn}\varsigma_1=0 \tag{52}$$

where

$$\psi_2=\varsigma_1 T_1+2\beta_2. \tag{53}$$

Therefore, only single-mode resonance is possible in this case. After eliminating ψ_2 from Eqs. (51) and (52), we derive the square of the steady-state amplitude a_2 as

$$a_2^2=\frac{2}{\alpha}[2\varsigma_1\hat{\omega}_{mn}\pm(\mu^2-16c_f^2\omega_{mn}^{-2})^{1/2}]. \tag{54}$$

Nontrivial steady-state vibration begins to exist when

$$\varsigma_1^2\leqslant\frac{\mu^2-16c_f^2\omega_{mn}^{-2}}{4\hat{\omega}_{mn}^2}. \tag{55}$$

Equation (55) can also be predicted by the linear analysis in [5]. Figure 8 shows the amplitude a_2 of the steady-state vibration as a function of ς_1 when the excitation frequency γ is close to twice the natural frequency of mode $(0,3)_f$. The parameters used in the calculation are the same as those used in plotting Fig. 2.

Conclusions

In this paper we use multiple scale method to study the internal resonance between a pair of forward and backward modes of a spinning disk under space-fixed pulsating edge loads. Linear analysis in [5] predicts that only single-mode parametric resonance can occur when the excitation frequency is twice the natural frequency of the mode of interest. By considering the nonlinear effect resulting from von Karman's plate model, however, internal resonance is predicted in some special cases. Several conclusions are summarized as follows:

(a) Internal resonance can occur when the natural frequency of the forward mode is close to three times the natural frequency of the backward mode and the excitation frequency is close to twice the frequency of the backward mode. In the case when the excitation frequency is close to twice the frequency of the forward mode, on the other hand, only single-mode parametric resonance is possible.

(b) For light damping case the trivial solution can lose stability via both pitchfork as well as Hopf bifurcations when frequency detuning parameter is varied. On the other hand, nontrivial solutions experience both saddle-node and Hopf bifurcations.

(c) When the damping is increased the Hopf bifurcations along the trivial solution path disappear. There also exists a certain damping value beyond which no nontrivial solution is possible.

Appendix

By eliminating ψ_1 from Eqs. (34) and (35) we can derive an equation involving only $g=a_1^2$ and $f=a_2^2$ in the form

$$p_2(f)g^2+p_1(f)g+p_0(f)=0. \tag{A1}$$

With use of Eqs. (34) and (35), Eqs. (32) and (33) can be reduced to

$$q_4(f)g^4+q_3(f)g^3+q_2(f)g^2+q_1(f)g+q_0(f)=0 \tag{A2}$$

p_i and q_i are functions of f only. Equations (*A*1) and (*A*2) can then be reduced to the following equation in terms of f:

$$(m_2p_0-m_0p_2)^2+(m_2p_1-m_1p_2)(m_0p_1-m_1p_0)=0 \tag{A3}$$

where

$$m_2=p_0(p_2q_3-p_1q_4)$$

$$m_1=p_0(p_2q_2-p_0q_4)-p_2^2q_0$$

$$m_0=p_0p_2q_1-p_1p_2q_0.$$

After solving a_2 from Eq. (*A*3), we can obtain a_1 from (*A*1).

References

[1] Carlin, J. F., Appl, F. C., Bridwell, H. C., and Dubois, R. P., 1975, "Effects of Tensioning on Buckling and Vibration of Circular Saw Blades," ASME J. Eng. Ind., **2**, pp. 37–48.

[2] Radcliffe, C. J., and Mote, C. D., Jr., 1977, "Stability of Stationary and Rotating Discs Under Edge Load," Int. J. Mech. Sci., **19**, pp. 567–574.

[3] Chen, J.-S., 1994, "Stability Analysis of a Spinning Elastic Disk Under a Stationary Concentrated Edge Load," ASME J. Appl. Mech., **61**, pp. 788–792.

[4] Chen, J.-S., 1996, "Vibration and Stability of a Spinning Disk Under Stationary Distributed Edge Loads," ASME J. Appl. Mech., **63**, pp. 439–444.

[5] Chen, J.-S., 1997, "Parametric Resonance of a Spinning Disk Under Space-Fixed Pulsating Edge Loads," ASME J. Appl. Mech., **64**, pp. 139–143.

[6] Benson, R. C., and Bogy, D. B., 1978, "Deflection of a Very Flexible Spinning Disk due to a Stationary Transverse Load," ASME J. Appl. Mech., **45**, pp. 636–642.

[7] Nowinski, J. L., 1964, "Nonlinear Transverse Vibrations of a Spinning Disk," ASME J. Appl. Mech., **31**, pp. 72–78.

[8] Coker, E. G., and Filon, L. N. G., 1957, *A Treatise on Photo-Elasticity*, Cambridge University Press, London.

[9] Nayfeh, A. H., and Mook, D. T., 1977, "Parametric Excitations of Linear Systems Having Many Degrees of Freedom," J. Acoust. Soc. Am., **62**, pp. 375–381.

[10] Nayfeh, A. H., and Balachandran, B., 1994, *Applied Nonlinear Dynamics*, John Wiley and Sons, New York.

On the Optimal Shape of a Rotating Rod

T. M. Atanackovic
Professor,
Faculty of Technical Sciences,
University of Novi Sad,
21000 Novi Sad, Yugoslavia

By using Pontryagin's maximum principle we determine the shape of the lightest rotating rod, stable against buckling. It is shown that the cross-sectional area function is determined from the solution of a nonlinear boundary value problem. Three variational principles for this boundary value problem are formulated and a first integral is constructed. The optimal shape of a rod is determined by numerical integration.
[DOI: 10.1115/1.1409938]

1 Introduction

Consider an elastic rod BC of length L, fixed at end B and free at the other end. Suppose that the rod has a circular cross section, that its axis is straight, and that it rotates with the constant angular velocity ω about its axis. Let x-B-y be the rectangular Cartesian coordinate system with the axis x oriented along the rod axis in the undeformed state. Let Π be a plane defined by the system x-B-y that rotates with the angular velocity ω about the x-axis. At a certain velocity the rod loses stability so that it could be bent under the action of centrifugal forces. If the rod is bent it will assume a relative (with respect to the rotating plane Π), equilibrium configuration (see Fig. 1). Note, however, that during the *motion* between two relative equilibrium configurations (one corresponding to the initial state in which the rod axis is straight and one in which the rod axis is bent) the axis of the rod is, in general, *not* a plane curve. The problem of determining the critical rotation speed and the post-critical behavior of the rod described has been the subject of many investigations. The first result for critical rotation speed, for prismatic rods with constant cross section, was presented by Stodola [1]. He credits Dunkerley for the first critical speed calculation performed in 1895. Later the problem of determining critical rotation speed was treated by many authors. We mention the work of Odeh and Tadjbakhsh [2] that became classic, Bazely and Zwahlen [3], Parter [4], Atanackovic [5,6], and Clément and Descloux [7]. In all of these works the classical Bernoulli-Euler theory of rods was used. For a review of generalized rod theories used in stability analysis of rotating rods, see Antman [8] and Atanackovic [9].

Our intention in this work is to formulate an optimization problem for a rotating rod by using the procedure presented in Atanackovic and Simic [10]. Suppose that the angular velocity with which the rod rotates $\omega=\omega_0=$ const. and length of the rod L are given. Let S be the arc length of the rod axis, so that $S\in[0,L]$. We define *the optimal rotating rod* as the rod so shaped that it will lose stability for $\omega>\omega_0$ while any other rod of the same length (in our case equal to L) and equal or smaller volume will lose stability for $\omega\leqslant\omega_0$.

Thus, the optimal rotating rod will be the lightest rod of length L that is stable against buckling for $0\leqslant\omega\leqslant\omega_0$. Similar problems for a centrally compressed column were treated by many authors. We mention the works of Clausen [11], Blasius [12], Ratzersdorfer [13], and Keller [14] where the most complete analysis is given. For a historical account on the problem of a compressed optimal column see Cox [15] and the discussion following that paper.

In solving the problem of determining the shape of an optimal rotating rod we shall use the procedure based on Pontryagin's maximum principle with the special identification of the ''state'' and ''costate'' variables as in Atanackovic and Simic [10]. For the relevant equations describing the optimal rotating rod, that we believe are new, we formulate three variational principles. On the basis of these variational principles we shall find a first integral corresponding to Euler-Lagrange equations. This first integral is used to check the accuracy of numerical integration.

2 Model

The equilibrium, geometrical, and constitutive equations for the rotating rod are

$$H'=0,\quad V'=-\rho_0\omega^2\bar{y},\quad M'=V\cos\theta-H\sin\theta, \tag{1a}$$

$$\bar{x}'=\cos\theta,\quad \bar{y}'=\sin\theta, \tag{1b}$$

$$\theta'=-\frac{M}{EI}, \tag{1c}$$

where H and V are components of the contact force in an arbitrary cross section, M is the bending moment, θ is the angle between the axis of rotation and tangent to the rod axis, and $\bar{x}$ and $\bar{y}$ are coordinates of an arbitrary point with respect to the rotating Cartesian frame x-B-y. Also in (1) we use ρ_0 to denote line density of the rod (mass per unit length of the rod axis), E is modulus of elasticity, I is the second moment of the cross-sectional area of the rod, and $(\cdot)'=d(\cdot)/dS$. Note that $\rho_0=\rho A$ where ρ is the density of the rod (mass per unit volume). We assume that the cross section of the rod is circular, so that

$$I=\alpha A^2, \tag{2}$$

where A is the cross-sectional area and $\alpha=(1/4\pi)$. With this notation, the volume of the rod is

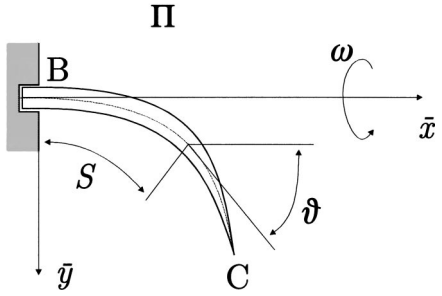

Fig. 1 Coordinate system used

Contributed by the Applied Mechanics Division of THE AMERICAN SOCIETY OF MECHANICAL ENGINEERS for publication in the ASME JOURNAL OF APPLIED MECHANICS. Manuscript received by the ASME Applied Mechanics Division, September 26, 2000; final revision, April 15, 2001. Associate Editor: N. C. Perkins. Discussion on the paper should be addressed to the Editor, Professor Lewis T. Wheeler, Department of Mechanical Engineering, University of Houston, Houston, TX 77204-4792, and will be accepted until four months after final publication of the paper itself in the ASME JOURNAL OF APPLIED MECHANICS.

$$W=\int_0^L A(S)dS. \tag{3}$$

By using the dimensionless variables and parameters

$$t=\frac{S}{L},\quad a=\frac{A}{L^2},\quad y=\frac{\overline{y}}{L},\quad w=\frac{W}{L^3}, \tag{4a}$$

$$m=\frac{M}{E\alpha L^3},\quad v=\frac{V}{E\alpha L^2},\quad \lambda^2=\frac{\rho\omega^2L^2}{E\alpha}, \tag{4b}$$

and a new dependent variable

$$u=-\frac{v}{\lambda}, \tag{5}$$

we obtain from (1*a*)–(1*c*)

$$\dot{u}=\lambda a y,\quad \dot{m}=-\lambda u\cos\theta,\quad \dot{y}=\sin\theta,\quad \dot{\theta}=-\frac{m}{a^2}. \tag{6}$$

The boundary conditions corresponding to the rod shown in Fig. 1 are

$$u(1)=0,\quad m(1)=0,\quad y(0)=0,\quad \theta(0)=0. \tag{7}$$

The system (6), (7) possesses a trivial solution, in which the axis of the rod remains straight for any value of the dimensionless rotation speed λ, in the form

$$u_0=0,\quad m_0=0,\quad y_0=0,\quad \theta_0=0. \tag{8}$$

To examine stability of the equilibrium configuration (8) we use the Euler method. Thus, we assume that

$$u=u_0+\Delta u,\quad m=m_0+\Delta m,\ \ldots,\quad \theta=\theta_0+\Delta\theta, \tag{9}$$

where $\Delta u,\ldots\Delta\theta$, denote perturbations of the corresponding variables. Then, by substituting (9) into (6) and linearizing the resulting expressions, we obtain (omitting Δ in front of perturbed variables)

$$\left(\frac{\dot{u}}{a}\right)^{\cdot}=\lambda\theta,\quad (\dot{\theta}a^2)^{\cdot}=\lambda u,\quad \dot{y}=\theta, \tag{10a}$$

subject to

$$u(1)=0,\quad \dot{u}(0)=0,\quad \theta(0)=0,\quad \dot{\theta}(1)a^2(1)=0,\quad y(0)=0. \tag{10b}$$

For the bifurcation it is enough to consider

$$\left(\frac{\dot{u}}{a}\right)^{\cdot}=\lambda\theta,\quad (\dot{\theta}a^2)^{\cdot}=\lambda u, \tag{10c}$$

subject to

$$u(1)=0,\quad \dot{u}(0)=0,\quad \theta(0)=0,\quad \lim_{t\to1}\dot{\theta}(t)a^2(t)=0. \tag{10d}$$

By introducing new variables $u=w_1$, $\dot{u}=w_2$, $\theta=w_3$, $\dot{\theta}=w_4$ and the vector $\mathbf{w}=[w_1,w_2,w_3,w_4]$, the system (10*c*), (10*d*) can be written in compact form as

$$\mathbf{F}(\lambda)\mathbf{w}=\frac{d}{dt}\left[\mathbf{A}\frac{d}{dt}\mathbf{w}\right]+\lambda\mathbf{B}\mathbf{w}=0, \tag{10e}$$

where $\mathbf{A}$ and $\mathbf{B}$ are given as

$$\mathbf{A}=\begin{bmatrix}0&1/a&0&0\\0&0&0&0\\0&0&0&0\\0&0&0&a^2\end{bmatrix};\quad \mathbf{B}=\begin{bmatrix}0&0&1&0\\0&0&0&0\\0&0&0&0\\1&0&0&0\end{bmatrix}. \tag{10f}$$

Note that the boundary condition $(10d)_4$ that corresponds to $m(1)=0$ is equivalent to $\dot{\theta}(1)=0$ if $a(1)\neq0$. However, if $a(1)=0$ (as will be in our analysis) the condition $m(1)=0$ can be satisfied with $\dot{\theta}(1)\neq0$. For fixed λ the existence of a nontrivial solution of (10*c*), (10*d*) is a necessary condition for the loss of stability.[1] The dimensionless volume of the rod is given as

$$w=\int_0^1 a(t)dt. \tag{11}$$

We state now the following optimization problem:

Given λ determine $a(t)>0$ for $t\in(0,1)$ so that λ is the smallest eigenvalue of (10*c*), (10*d*) and that at the same time w given by (11) is minimal.

We call the rod with such $a(t)$ the *optimal rod*. Thus, the optimal rod is so shaped that any other rod with smaller volume w will buckle at a rotation speed that is smaller than λ.

We coment on the boundary value problem (10*a*)–(10*f*). In it λ must be an isolated eigenvalue in order that nonlinear equilibrium equations have bifurcation point at λ and we assume this to be true. However, the boundary condition $(10b)_4$ is not standard and is of the type analyzed by Keller and Niordson [17]. Cox and McCarty [18] pointed out that the assumption about isolated eigenvalue may be violated if the cross-sectional area $a(t)$ vanishes too severe when $t\to1$. Thus, in principle, our assumption may be checked by the method similar to the one presented in [18]. This rather delicate analysis is outside the scope of the paper.

3 The Optimization Problem and Its Solution

Let $x_1,\ldots x_4$ be a set of dependent variables defined by

$$u=x_1,\quad (\dot{u}/a)=x_2,\quad \theta=x_3,\quad (a^2\dot{\theta})=x_4. \tag{12}$$

Then, the system (10*a*), (10*b*) becomes

$$\dot{x}_1=ax_2,\quad \dot{x}_2=\lambda x_3,\quad \dot{x}_3=\frac{x_4}{a^2},\quad \dot{x}_4=\lambda x_1, \tag{13a}$$

subject to

$$x_1(1)=0,\quad x_2(0)=0,\quad x_3(0)=0,\quad x_4(1)=0. \tag{13b}$$

The problem of determining the shape $a(t)$ of the optimal rod may be stated, in terms of the optimal control theory, as determine the "control" function $a(t)>0$, $t\in(0,1)$ that minimizes the functional

$$I=\int_0^1 a(t)dt, \tag{14}$$

when the system is described by (13). To solve the optimization problem we use Pontryagin's maximum principle (see Sage and White [19] and [20]). For other applications of Pontryagin's principle for design problems see Pierson [21] and Carmichael [22,23].

For system (13) the Hamiltonian function $\mathcal{H}$ is

$$\mathcal{H}=a+p_1ax_2+p_2\lambda x_3+p_3\frac{x_4}{a^2}+p_4\lambda x_1, \tag{15}$$

where the costate variables $p_1,\ldots p_4$ satisfy

$$\dot{p}_1=-\frac{\partial\mathcal{H}}{\partial x_1}=-\lambda p_4,\quad \dot{p}_2=-\frac{\partial\mathcal{H}}{\partial x_2}=-p_1a,$$

$$\dot{p}_3=-\frac{\partial\mathcal{H}}{\partial x_3}=-\lambda p_2,\quad \dot{p}_4=-\frac{\partial\mathcal{H}}{\partial x_4}=-\frac{p_3}{a^2}, \tag{16a}$$

subject to

[1] In fact a necessary condition for bifurcation at the point (u_0,m_0,y_0,λ) for the nonlinear system of Eqs. (6), (7) is that λ belongs to the spectrum of the linear differential operator $\mathbf{F}(\lambda)$. Thus, if λ is an eigenvalue of $\mathbf{F}(\lambda)$ the point (u_0,m_0,y_0,λ) is a latent bifurcation point (see [8]). The sufficient condition for bifurcation at an eigenvalue of $\mathbf{F}(\lambda)$ are given in Chow and Hale [16].

$$p_1(0)=0, \quad p_2(1)=0, \quad p_3(1)=0, \quad p_4(0)=0. \quad (16b)$$

The optimality condition $\min_u \mathcal{H}(t,x_1,x_2,p_1,p_2,a)$ leads to

$$\frac{\partial \mathcal{H}}{\partial a}=1+p_1x_2-2p_3\frac{x_4}{a^3}=0. \quad (17)$$

By solving (17) for a we obtain

$$a=\left\{\frac{2p_3x_4}{1+p_1x_2}\right\}^{1/3}. \quad (18)$$

A further procedure simplifies significantly if we make the following observation (used in a similar context in [10]): The solution of the boundary value problem (13) leads to a solution of the boundary value problem (16) if we make the following identification:[2]

$$p_1(t)=x_2(t); \quad p_2(t)=-x_1(t), \quad p_3=x_4, \quad p_4=-x_3. \quad (19)$$

By using (19) the control variable $a(t)$ given by (18) becomes

$$a=\left\{\frac{2(x_4)^2}{1+(x_2)^2}\right\}^{1/3}. \quad (20)$$

Note that with (19) substituted in (17) we have $(\partial^2\mathcal{H}/\partial a^2)>0$ so that the necessary condition for minimum of $\mathcal{H}$ is satisfied. From (20) and the boundary condition $(13b)_4$ we conclude that

$$a(1)=0. \quad (21)$$

Thus, *the optimal rod is tapered so that it has zero cross-sectional area and zero moment of inertia at its free end*. Also, when the original variables (see (12)) are used in (20) we obtain

$$\frac{a^3\dot\theta^2}{a^2+\dot u^2}=\frac{1}{2}. \quad (22a)$$

By using the boundary condition (10*b*) in (22) we get

$$a(0)\dot\theta^2(0)=\frac{1}{2}. \quad (22b)$$

We now transform the conditions of optimality (20). First we write it in the form

$$1+(x_2)^2=\frac{2(x_4)^2}{a^3}=\frac{2a^4\dot\theta^2}{a^3}=2a\dot\theta^2. \quad (23)$$

Note that from (23) we conclude that $a(t)\neq 0$ for $t\in(0,1)$. Thus, the eigenvalue in (10*e*) is simple, if it exists. Next by differentiating (23) and by using (12), (13) we get

$$(a\dot\theta^2)^{\cdot}=\lambda\theta\left(\frac{\dot u}{a}\right), \quad (24)$$

as the optimality condition. Now we transform the system (10*a*) as follows: Integrate $(10a)_1$ to obtain

$$\left(\frac{\dot u}{a}\right)=\lambda\int_0^t\theta(\xi)d\xi, \quad (25)$$

where we used the fact that $\dot u(0)=0$ and $a(0)\neq 0$ (see $(10b)_2$ and (22*b*)). Substituting (25) into (24), integrating and using (22*b*), we get

$$a\dot\theta^2=\lambda^2\int_0^t\left[\theta(\xi)\int_0^\xi\theta(\zeta)d\zeta\right]d\xi+\frac{1}{2}. \quad (26)$$

Since $\dot y=\theta$ (see $(10a)_3$) the Eq. (26) that represents the condition of optimality, may be written as

$$a\ddot y^2=\frac{1}{2}[1+\lambda^2y^2]. \quad (27)$$

Finally by differentiating $(10a)_2$ and by using (25) we get

$$(\dot\theta a^2)^{\cdot\cdot}=(\ddot y a^2)^{\cdot\cdot}=\lambda\dot u=\lambda^2a\int_0^t\theta(\xi)d\xi=\lambda^2ay. \quad (28)$$

Therefore the optimal shape $a(t)$ of the rotating rod is determined from the solution of the system (27), (28):

$$(\ddot y a^2)^{\cdot\cdot}=\lambda^2ay \quad a\ddot y^2=\frac{1}{2}[1+\lambda^2y^2], \quad (29a)$$

subject to

$$y(0)=0, \quad \dot y(0)=0, \quad \lim_{t\to 1}\ddot y(t)a^2(t)=0, \quad \lim_{t\to 1}\{[\ddot y(t)a^2(t)]^{\cdot}\}=0. \quad (29b)$$

We analyze next system (29).

4 Variational Principles for the System (29)

In this section we shall formulate three different variational principles corresponding to the system (29). Also we shall construct a conservation law (the first integral) corresponding to (29).

(a) The Variational Principle With Two Arguments. Let $\mathbf{W}_1$ be the linear function space defined as

$$\mathbf{W}_1=\{\mathbf{w}=(y,a): y\in C^4(0,1); y(0)=\dot y(0)=0; \; a\in C^2(0,1); a\geqslant 0,\ a(1)=0\}. \quad (30)$$

Consider the functional

$$I_1(y,a)=\int_0^1 F_1dt, \quad (31a)$$

with the Lagrangian function

$$F_1=a^2\ddot y^2-\lambda^2ay^2-1. \quad (31b)$$

Suppose further that we want to determine the minimum of I_1 on $\mathbf{W}_1$. We claim that I_1 is stationary on the solution of (29). To prove this note that the condition of stationarity, i.e., vanishing of the first variation δI_1, leads to the following Euler-Lagrange equations:

$$(\ddot y a^2)^{\cdot\cdot}=\lambda^2ay, \quad a\ddot y^2-\frac{\lambda^2}{2}y^2-\frac{1}{2}=0, \quad (32a)$$

and natural boundary conditions

$$\ddot y(1)a^2(1)=0, \quad \{[\ddot y(t)a^2(t)]^{\cdot}\}_{t=1}=0. \quad (32b)$$

The system (32) is equivalent to (29).

(b) The Variational Principle With one Argument. We can write system (29) as a single differential equation of fourth order if we calculate a from $(29a)_2$ and then substitute the result in $(29a)_1$. Thus we obtain

$$\left[\frac{1}{\ddot y^3}(1+\lambda^2y^2)^2\right]^{\cdot\cdot}-2\lambda^2y\frac{(1+\lambda^2y^2)}{\ddot y^2}=0, \quad (33a)$$

subject to

$$y(0)=0, \quad \dot y(0)=0,$$

$$\frac{1}{4\ddot y^3(1)}[1+\lambda^2y^2(1)]^2=0, \quad \left(\left\{\frac{1}{4\ddot y^3(t)}[1+\lambda^2y^2(t)]^2\right\}^{\cdot}\right)_{t=1}=0. \quad (33b)$$

Consider the space

$$\mathbf{W}_2=\{y: y\in C^4(0,1); y(0)=\dot y(0)=0\}, \quad (34)$$

[2]There is one more possibility to connect the solutions of (13) and (16). This is given by the following identification of dependent variables: $p_1=-x_2$, $p_2=x_1$, $p_3=-x_4$, $p_4=x_3$. However, this identification is not of interest since it does not provide $a(t)\geqslant 0$ in (18) and $(\partial^2\mathcal{H}/\partial a^2)>0$ with $\mathcal{H}$ given by (15).

and the functional

$$I_2=\int_0^1 F_2 dt, \tag{35a}$$

with Lagrangian function

$$F_2=\frac{(1+\lambda^2 y^2)^2}{\ddot{y}^2}. \tag{35b}$$

Then the Euler-Lagrange equation corresponding to $\delta I_2=0$ is equivalent to (33). Note that the natural boundary conditions for the minimization of I_2 on the set (34) are identical to (33*b*).

(c) The Canonical Formalism. The variational principle $\delta I_2=0$ could be used to write (29) in canonical form. We define a variable (a "momentum") p as

$$p=\frac{\partial F_2}{\partial \ddot{y}}=-2\frac{(1+\lambda^2 y^2)^2}{\ddot{y}^3}. \tag{36}$$

Then, the Hamiltonian function is

$$H_2=p\ddot{y}-F_2=-\frac{3}{2^{2/3}}p^{2/3}(1+\lambda^2 y^2)^{2/3}. \tag{37}$$

With (37) the canonical equations

$$\dot{y}=\frac{\partial H_2}{\partial p}, \quad \dot{p}=\frac{\partial H_2}{\partial y}, \tag{38}$$

become

$$\dot{y}=-\left[2\frac{(1+\lambda^2 y^2)^2}{p}\right]^{1/3}, \quad \dot{p}=-2^{4/3}\lambda^2 y\left[2\frac{p^2}{(1+\lambda^2 y^2)}\right]^{1/3},$$
$$t\in(0,1). \tag{39a}$$

From (29*b*) and (36) we obtain the boundary conditions corresponding to the system (38*a*) as

$$y(0)=0, \quad \dot{y}(0)=0, \quad p(1)=0, \quad p(1)=0. \tag{39b}$$

Consider the space $\mathbf{W}_3$

$$\mathbf{W}_3=\{\mathbf{w}=(y,p): y\in C^2(0,1); y(0)=\dot{y}(0)=0;$$
$$p\in C^2(0,1); p(1)=0, \ \dot{p}(1)=0\} \tag{40}$$

and the problem of determining the minimum on $\mathbf{W}_3$ of the functional

$$I_3=\int_0^1 F_3 dt, \tag{41}$$

with

$$F_3=\dot{y}\dot{p}-\frac{3}{2^{2/3}}p^{2/3}(1+\lambda^2 y^2)^{2/3}. \tag{42}$$

It is easy to see that the condition $\delta I_3=0$ reproduces the system (39). However, since F_3 does not depend explicitly on t we have a Jacobi type of first integral for (39) in the form

$$\dot{y}\dot{p}+\frac{3}{2^{2/3}}p^{2/3}(1+\lambda^2 y^2)^{2/3}=\text{const}. \tag{43}$$

We determine now the constant in (43). By using the boundary conditions (39*b*) it follows that

$$\dot{y}\dot{p}+\frac{3}{2^{2/3}}p^{2/3}(1+\lambda^2 y^2)^{2/3}=C=\frac{3}{2^{2/3}}[p(0)]^{2/3}. \tag{44}$$

We shall use (44) to check numerical integration of the system (39). Namely we shall, in each step of numerical integration, calculate the left-hand side of (44) and compare so obtained value with the constant on the right-hand side.

Finally we note that with (y, p) known, the cross-sectional area $a(t)$ is determined from Eqs. (27) and (36) so that

$$a=a(t)=\left[\frac{p^2}{2^5(1+\lambda^2 y^2)}\right]^{1/3}. \tag{45}$$

5 Numerical Results

The system (39) is integrated by using the Runge-Kutta double precision procedure. Note that the point $t=1$ is a singular point for the system (39) so that the equation $(39a)_1$ cannot be satisfied at $t=1$. Thus we proceeded as follows: We constructed a sequence of numerical solutions (y_n, p_n), $n=1,2,\ldots$ with $y_n(0)=\dot{y}_n(0)=0$ and $y_n(t)>0$, $\dot{y}_n(t)>0$, $p_n(t)<0$, $\dot{p}_n(t)>0$ for $t\in(0,1)$ and $p_n(1)=-\varepsilon_n$, $\dot{p}(1)=\delta_n$ with the constants $\varepsilon_n>0$, $\delta_n>0$. For each solution (y_n, p_n) the values of variables $p_n(0)$ and $\dot{p}_n(0)$ and the cross-sectional area $a_n=a_n(\varepsilon_n, \delta_n)$ and are determined (a_n is determined according to (45)). Then, the optimal cross-sectional area $a(t)$ and corresponding initial values $p(0)$ and $\dot{p}(0)$ are obtained as $\lim a_n$, $\lim p_n(0)$, and $\lim \dot{p}_n(0)$ when $\varepsilon_n \to 0$, $\delta_n \to 0$, respectively.

We performed the calculations for $\lambda=\sqrt{10}$ and obtained $p(0)=-0.195077$ and $\dot{p}(0)=0.379104$. In Fig. 2 we show the solution of $a(t)$ calculated according to (45). The accuracy of integration was controlled by evaluation of the first integral (44) in each step of integration. The left-hand side in (44) was constant and equal to $(3/2^{2/3})[0.195077^2]^{1/3}=0.6356$ up to 10^{-6}.

From (45) we obtain $a(0)=(p^2(0)/2^5)^{1/3}=0.10595$. The dimensionless volume w of the optimal rod is determined by using (11) and (45). For $\lambda=\sqrt[2]{10}$ we obtain

$$w=\int_0^1 a(t)dt=0.03712. \tag{47}$$

We show next that with the solution of (39) for single λ we can determine the solution for any λ. Let (y, p) be the solution of the problem (39) and let $a(t)$ be corresponding cross section area determined for the specified value of the dimensionless rotation λ. Let $(\hat{y}, \hat{p})$ and $\hat{a}(t)$ be the corresponding functions determined for the dimensionless rotation speed $\Lambda=\beta\lambda$, with the constant β given. By using (39) and (45) it is easy to show that the following relations hold:

$$\hat{y}=\frac{1}{\beta}y; \quad \hat{p}=\beta^3 p; \quad \hat{a}=\beta^2 a. \tag{48}$$

Thus, with the solution for single λ we have solution for any Λ.

We compare now the volume of the optimal rod and the rod with constant circular cross section if both are stable up to the same angular velocity ω. Suppose that both rods are made of the same material, i.e., E, ρ are the same. Also we assume that both rods lose stability at the same angular velocity ω. For the rod with constant circular cross section we have (see [6])

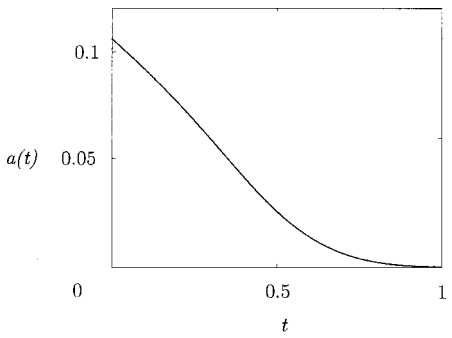

Fig. 2 The optimal cross-sectional area

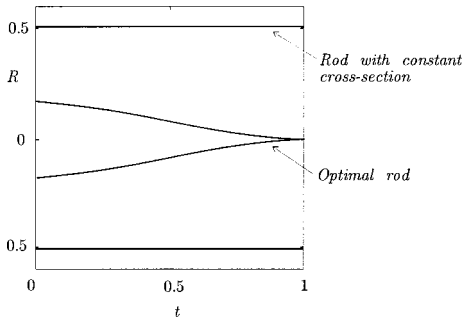

Fig. 3 Optimal rod and rod with constant cross section

$$\hat{\lambda} = \frac{\rho A \omega^2 L^4}{EI} = 12.362, \tag{49}$$

where $I = \alpha A^2$ with $A = \text{const}$. From (4*b*) we have

$$\lambda^2 = \frac{\rho \omega^2 L^2}{E\alpha} = 10. \tag{50}$$

With (49), (50) we obtain

$$\frac{\lambda^2}{\hat{\lambda}} = \frac{A}{L^2}. \tag{51}$$

Rod with constant cross section A has the volume $W_{\text{const.}} = AL$ while the volume of the optimal rod is $W_{\text{optimal}} = wL^3$. By using (50) we obtain

$$W_{\text{const.}} = \frac{\lambda^2}{\hat{\lambda}} L^3, \tag{52}$$

so that

$$\frac{W_{\text{optimal}}}{W_{\text{const.}}} = \frac{\hat{\lambda}}{\lambda^2} w = 0.04589. \tag{53}$$

Therefore, the volume of the optimal rotating rod is just 4.59 percent of the volume of the rod that has the same length and with constant cross section! Note also that from (51) the dimensionless cross-sectional area of the rod with constant cross section becomes $a_{\text{const.}} = 0.80893L^2$. Therefore for the circular cross section the ratio of the radius of the optimal rod for $t = 0$, i.e., $r(0)$ and the radius of the rod with constant cross section R is $(r_l(0)/R) = 0.362$. In Fig. 3 we show the radius of the optimal rod and rod of the constant cross section that lose stability at the same angular speed.

6 Conclusions

In this paper we analyzed the problem of determining the shape lightest rotating rod. Our main results are as follows:

1 We derived the system of differential Eqs. (29) that determine the optimal cross section $a(t)$ and the shape of the rod in the first buckling mode $y(t)$. For this system we derived three different variational principles. Then we transformed the system (29) in the canonical form (39). Finally we derived a first integral for the (39) in the form (43).

2 From Eq. (21) we concluded that the optimal rod is tapered at the free end. By numerical integration we determined the optimal shape of the rod.

3 The optimal rod has the volume of only 4.59 percent of the rod with constant cross section that loses stability at the same rotation speed.

References

[1] Stodola, A., 1906, *Steam Turbines*, D. Van Nostrand, New York.
[2] Odeh, F., and Tadjbakhsh, I., 1965, "A Nonlinear Eigenvalue Problem for Rotating Rods," Arch. Ration. Mech. Anal., **20**, pp. 81–94.
[3] Bazely, N., and Zwahlen, B., 1968, "Remarks on the Bifurcation of Solutions of a Non-linear Eigenvalue problem," Arch. Ration. Mech. Anal., **28**, pp. 51–58.
[4] Parter, S. V., 1970, "Nonlinear Eigenvalue Problems for Some Fourth Order Equations: I—Maximal Solutions," SIAM (Soc. Ind. Appl. Math.) J. Math. Anal., **1**, pp. 437–457, and "II—Fixed-Point Methods," 1, pp. 458–478.
[5] Atanackovic, T. M., 1987, "Stability of Rotating Compressed Rod With Imperfections," Math. Proc. Cambridge Philos. Soc., **101**, pp. 593–607.
[6] Atanackovic, T. M., 1997, "On the Rotating Rod With Variable Cross Section," Archive Appl. Mechnics, **67**, pp. 447–456.
[7] Clément, Ph., and Descloux, J., 1991, "A Variational Approach to a Problem of Rotating Rods," Arch. Ration. Mech. Anal., **114**, pp. 1–13.
[8] Antman, S. S., 1995, *Nonlinear Problems of Elasticity*, Springer, New York.
[9] Atanackovic, T. M., 1997, *Stability Theory of Elastic Rods*, World Scientific, Singapore.
[10] Atanackovic, T. M., and Simic, S. S., 1999, "On the Optimal Shape of a Pflüger Column," Eur. J. Mech. A/Solids, **18**, pp. 903–913.
[11] Clausen, T., 1851, "Über die Form architektonischer Säulen," Bull. cl, physico math. Acad. St. Pétersbourg, **9**, pp. 369–380.
[12] Blasius, H., 1914, "Träger kleinster Durchbiegung und Stäbe großter Knickfestigkeit bei gegebenem Materialverbrauch," Zeitsch. Math. Physik, **62**, pp. 182–197.
[13] Ratzersdorfer, J., 1936, *Die Knickfestigkeit von Stäben und Stabwerken*, Springer, Wien.
[14] Keller, J., 1960, "The Shape of the Strongest Column," Arch. Ration. Mech. Anal., **5**, pp. 275–285.
[15] Cox, S. J., 1992, "The Shape of the ideal Column," The Mathematical Intelligencer, **14**, pp. 16–24.
[16] Chow, S.-N., and Hale, J. K., 1982, *Methods of Bifurcation Theory*, Springer, New York.
[17] Keller, J. B., and Niordson, F. I., 1966, "The Tallest Column," J. Math. Mech., **16**, pp. 433–446.
[18] Cox, S. J., and McCarthy, C. M., 1998, "The Shape of the Tallest Column," SIAM (Soc. Ind. Appl. Math.) J. Math. Anal., **29**, pp. 547–554.
[19] Sage, A. P., and White, C. C., 1977, *Optimum System Control*, Prentice-Hall, Englewood Cliffs, NJ.
[20] Alekseev, V. M., Tihomirov, V. M., and Fomin, S. V., 1979, *Optimal Control*, Nauka, Moscow (in Russian).
[21] Pierson, B. L., 1977, "An Optimal Control Approach to Minimum-Weight Vibrating Beam Design," J. Structural Mechanics, **5**, pp. 147–178.
[22] Carmichael, D., 1977, "Singular Optimal Control Problems in the Design of Vibrating Structures," J. Sound Vib., **53**, pp. 245–253.
[23] Carmichael, D., 1981, *Structural Modelling and Optimization: A General Methodology for Engineering and Control*, Ellis Horwood, Chichester, UK.

The Exact One-Dimensional Theory for End-Loaded Fully Anisotropic Beams of Narrow Rectangular Cross Section

P. Ladevèze
Laboratoire de Mécanique et Technologie,
ENS Cachan/CNRS/Universite Paris 6,
94235 Cachan, France

J. G. Simmonds
Department of Civil Engineering,
University of Virginia,
Charlottesville, VA 22903
Fellow ASME

The exact theory of linearly elastic beams developed by Ladevèze and Ladevèze and Simmonds is illustrated using the equations of plane stress for a fully anisotropic elastic body of rectangular shape. Explicit formulas are given for the cross-sectional material operators that appear in the special Saint-Venant solutions of Ladevèze and Simmonds and in the overall beamlike stress-strain relations between forces and a moment (the generalized stress) and derivatives of certain one-dimensional displacements and a rotation (the generalized displacement). A new definition is proposed for built-in boundary conditions in which the generalized displacement vanishes rather than pointwise displacements or geometric averages. [DOI: 10.1115/1.1412238]

1 Introduction

Ladevèze [1,2] and Ladevèze and Simmonds [3,4] have developed an *exact theory* of linearly elastic prismatic beams of arbitrary cross section. In [1] and [2], there are no body forces or tractions on the lateral sides of the beam, whereas in [3,4] such loads may be present. In these papers, (extended) Saint Venant solutions play a key role.

This beam theory is ''exact'' in the sense that one-dimensional beamlike equations are obtained from the three-dimensional equations of linear elasticity *without any hypotheses or approximations whatsoever*. Thus, the exact theory is not asymptotic and no appeal is made to small slenderness ratios. The *generalized stress* of the exact theory is the same as in conventional beam theory, namely, the net forces and moments acting over any cross section. The heart (and novelty) of the exact theory lies in the definition of the conjugate *generalized displacement*, which comprises displacement-like and a rotation-like quantities, defined, not as certain cross-sectional averages of three-dimensional displacements, but rather as cross-sectional integrals involving the three-dimensional displacements, the three-dimensional stresses, and elastic operators $\mathbf{A}$, $\mathbf{B}$, $\overset{0}{\mathbf{A}}$, and $\overset{0}{\mathbf{B}}$. With the aid of these definitions, any problem for a beamlike body can be decomposed exactly into an interior part, explicitly computable from the solutions of the associated one-dimensional exact beam equations, and a decaying, edge-effect part, as shown in [1–4].

The calculations in [1–4] are, at times, a bit heavy, even under the assumption of a certain degree of elastic symmetry. Moreover, the cross-sectional elastic operators are not computed explicitly.

The present paper is designed to present a relatively simple, but realistic exposition of *some* of the ideas in [1–4]. All our calculations are explicit and analytic. Moreover, we make no assumptions on elastic symmetry. Thus, by considering a beam of narrow rectangular cross section, subject to prescribed end loads and/or displacements only, we may take our reference equations as those of linear plane stress theory rather than those of more complicated three-dimensional elasticity. Our final results—one-dimensional beamlike equations relating a generalized stress, (T,Q,M), to a generalized displacement, (u,v,ω)—suggest a rational definition of built-in boundary conditions, namely, that the generalized displacement vanishes. This, in turn, implies that the corresponding displacements of plane stress theory *do not* vanish at a built-in boundary. If, on the other hand, one insists that ''built-in'' means the pointwise vanishing of these displacements, then, to derive the proper kinematic boundary conditions for the exact beam theory, one must first solve a set of auxiliary ''canonical'' plane stress problems, following Ladeeze [5], as we show.

Contributed by the Applied Mechanics Division of THE AMERICAN SOCIETY OF MECHANICAL ENGINEERS for publication in the ASME JOURNAL OF APPLIED MECHANICS. Manuscript received by the ASME Applied Mechanics Division, February 12, 2001; final revision, June 2, 2001. Associate Editor: R. C. Benson. Discussion on the paper should be addressed to the Editor, Professor Lewis T. Wheeler, Department of Mechanical Engineering, University of Houston, Houston, TX 77204-4792, and will be accepted until four months after final publication of the paper itself in the ASME JOURNAL OF APPLIED MECHANICS.

2 The Dimensionless Equations of Plane Stress Theory

Consider a rectangular beam of width W, depth $2H$, and length Hl, and let $(x_1,x_2)=(x,y)$, $0\leqslant x\leqslant l$, $-1\leqslant y\leqslant 1$, be a pair of dimensionless planar Cartesian coordinates, with x lying along the centerline of the beam. Further, with E denoting some nominal Young's modulus, let $e_{\alpha\beta}$, $E\sigma_{\alpha\beta}=E(\sigma,\tau,\sigma_y)$, and $Hu_\alpha=H(U,V)$ denote, respectively, the physical (Cartesian) components of the strains, stresses, and displacements of plane stress theory. (As the notation suggests, we shall switch between Cartesian tensor notation and conventional, extended notation, as convenient and without comment.)

The field equations of plane stress theory comprise the equilibrium equations

$$\sigma_{\alpha\beta,\beta}=0, \quad \sigma_{\alpha\beta}=\sigma_{\beta\alpha}, \tag{1}$$

and the strain-displacement-stress relations

$$e_{\alpha\beta}=1/2(u_{\alpha,\beta}+u_{\beta,\alpha})=C_{\alpha\beta\lambda\mu}\sigma_{\lambda\mu}, \tag{2}$$

where a comma followed by a subscript denotes differentiation with respect to the variable with that subscript. Here, the dimensionless elastic coefficients possess the standard symmetries,

$$C_{\alpha\beta\lambda\mu}=C_{\lambda\mu\alpha\beta}=C_{\beta\alpha\lambda\mu}. \tag{3}$$

(Our analysis could be extended to elastic coefficients that vary with depth.) The lateral sides of the beam are stress free so that

$$\tau(x,\pm 1)=\sigma_y(x,\pm 1)=0. \tag{4}$$

We take the beam to be cantilevered, but refrain at this point from being more specific about the end conditions.

3 The Saint-Venant Solution

The easiest way to define this solution in plane stress theory is to satisfy (1) identically by introducing the Airy stress function f so that

$$\sigma_{\alpha\beta}=\varepsilon_{\alpha\lambda}\varepsilon_{\beta\mu}f_{,\lambda\mu}, \tag{5}$$

where $\boldsymbol{\epsilon}_{\alpha\beta}$ is the two-dimensional alternator. On substituting (2) and (5) into the compatibility equation

$$\varepsilon_{\alpha\lambda}\varepsilon_{\beta\mu}e_{\alpha\beta,\lambda\mu}=0, \tag{6}$$

we obtain the well-known fourth-order partial differential differential equation for f. Writing out the first two terms explicitly (which is all we need) and dividing by C_{1111}, we have

$$f_{,yyyy}-kf_{,xyyy}+\cdots=0, \tag{7}$$

where

$$k\equiv 4C_{1112}/C_{1111}. \tag{8}$$

The *Saint-Venant solution for f* is now defined to be

$$f^{SV}=\overset{0}{f}(y)+x\overset{1}{f}(y), \tag{9}$$

where, from (7),

$$\overset{1}{f}=A_1y+A_2y^2+A_3y^3 \tag{10}$$

and

$$\overset{0}{f}=B_2y^2+B_3y^3+(k/4)A_3y^4. \tag{11}$$

In (10) and (11), we have discarded null-stress terms. The axial and shear stresses follows from (5) and (9)–(11) as

$$\begin{aligned}\sigma^{SV}&=2B_2+6B_{3y}+3kA_3y^2+x(2A_2+6A_3y)\\ \tau^{SV}&=-(A_1+2A_2y+3A_3y^2),\quad \sigma_y^{SV}=0.\end{aligned} \tag{12}$$

The face conditions (4) of zero traction yield

$$A_1=-3A_3,\ \ A_2=0. \tag{13}$$

The remaining unknown constants are related as follows to the net forces, $EHW(T,Q)$, and the moment, EH^2WM, acting over any cross section:

$$\begin{aligned}T&=\int_{-1}^{1}\sigma dy=4B_2+2kA_3,\quad Q=\int_{-1}^{1}\tau dy=4A_3\\ M&=-\int_{-1}^{1}y\sigma dy=-4(B_3+xA_3).\end{aligned} \tag{14}$$

The dimensionless forces and moment satisfy the overall (beamlike) equilibrium equations

$$T_{,x}=0,\quad Q_{,x}=0,\quad M_{,x}+Q=0. \tag{15}$$

Thus, Airy's stress function takes the explicit form

$$\begin{aligned}f^{SV}&=(1/4)y^2T-[(k/8)y^2-(k/16)y^4+(3/4)xy]Q\\ &\quad-(1/4)M(x)y^3.\end{aligned} \tag{16}$$

Moreover, (12) can now be written

$$\boldsymbol{\sigma}^{SV}=\overset{0}{\mathbf{A}}(y)\cdot\mathbf{T}+\overset{0}{\mathbf{B}}(y)M(x), \tag{17}$$

where

$$\boldsymbol{\sigma}^{SV}=\begin{bmatrix}\sigma^{SV}\\ \tau^{SV}\end{bmatrix},\quad \mathbf{T}=\begin{bmatrix}T\\ Q\end{bmatrix},\quad \overset{0}{\mathbf{A}}=\begin{bmatrix}1/2 & (k/4)(3y^2-1)\\ 0 & (3/4)(1-y^2)\end{bmatrix},$$

$$\overset{0}{\mathbf{B}}=\begin{bmatrix}-(3/2)y\\ 0\end{bmatrix}. \tag{18}$$

Next, we compute the Saint-Venant displacements. From (2), with $\alpha=\beta=2$, and (5), we have, on integrating with respect to y,

$$V^{SV}=\overline{v}(x)+C_{2211}f,\overset{SV}{}_{y}(x,y)-2C_{2212}f,\overset{SV}{}_{x}(x,y), \tag{19}$$

where $\overline{v}(x)$ is a function of integration. Inserting (16) into this expression, using $(15)_3$ to replace $M'(x)$ by $-Q$, setting

$$v\equiv\overline{v}(x)-(3/4)C_{2211}xV \tag{20}$$

so that $V^{SV}(x,0)=v(x)$, and noting that $C_{2211}=C_{1122}$, we find that

$$\begin{aligned}V^{SV}&=v(x)+(1/2)C_{1122}yT+[(k/4)C_{1122}(y^2-1)\\ &\quad+(1/2)C_{1222}(3-y^2)]yQ-(3/4)C_{1122}M(x)y^2\\ &\equiv v(x)+A_{21}(y)T+A_{22}(y)Q+B_2(y)M(x).\end{aligned} \tag{21}$$

Next, from (2), with $\alpha=1$, $\beta=2$, (5), $(15)_3$, and (21),

$$\begin{aligned}U,\overset{SV}{}_{y}&=-\overline{\omega}(x)-(3/4)C_{1122}y^2Q+2C_{1211}f,\overset{SV}{}_{yy}(x,y)\\ &\quad-4C_{1212}f,\overset{SV}{}_{xy}(x,y),\end{aligned} \tag{22}$$

where $\overline{\omega}=v'$. Thus, integrating with respect to y, using $(15)_3$ and (16), absorbing the term $-(3/2)C_{1211}xQ$ into the function of integration $u(x)$ that arises, and setting

$$\overline{\omega}\equiv\omega(x)+(1/2)C_{1211}T+4C_{1212}Q, \tag{23}$$

we have

$$\begin{aligned}U^{SV}&=u(x)-\omega(x)y+(1/2)C_{1211}yT-[(k/2)C_{1211}(1-y^2)\\ &\quad+C_{1212}(1+y^2)+(1/4)C_{1122}y^2]yQ-(3/2)C_{1211}M(x)y^2\\ &\equiv u(x)-\omega(x)y+A_{11}(y)T+A_{12}(y)Q+B_1(y)M(x).\end{aligned} \tag{24}$$

Thus, we may write (21) and (24) in the form

$$\mathbf{U}^{SV}=\mathbf{u}(x)-\omega(x)y\mathbf{i}+\mathbf{A}(y)\cdot\mathbf{T}+\mathbf{B}(y)M(x), \tag{25}$$

where

$$\mathbf{U}=\begin{bmatrix}U\\ V\end{bmatrix},\quad \mathbf{u}=\begin{bmatrix}u\\ v\end{bmatrix}, \tag{26}$$

and $\mathbf{A}=[A_{\alpha\beta}(y)]$, $\mathbf{B}=[B_\alpha(y)]^T$.

Finally, substituting (24) into (2), with $\alpha=\beta=1$, noting (8), and using (16), we find that

$$u'(x)-\omega'(x)y=(1/2)C_{1111}T+(1/2)C_{1112}Q-(3/2)C_{1111}M(x)y. \tag{27}$$

Thus, (20), (23), and (27) imply that

$$\begin{bmatrix}\varepsilon\\ \gamma\\ \chi\end{bmatrix}\equiv\begin{bmatrix}u'\\ v'-\omega\\ \omega'\end{bmatrix}=\boldsymbol{\Lambda}\begin{bmatrix}T\\ Q\\ M\end{bmatrix}, \tag{28}$$

where

$$\boldsymbol{\Lambda}=\begin{bmatrix}(1/2)C_{1111} & (1/2)C_{1112} & 0\\ (1/2)C_{1112} & 4C_{1212} & 0\\ 0 & 0 & (3/2)C_{1111}\end{bmatrix}. \tag{29}$$

The beamlike strain-stress relations (28) are notable because they are *identical*—not merely of the same form—as the strain-stress relations for a beam under *arbitrarily* prescribed end loads and/or displacements (consistent with global equilibrium). This is shown for general beams in [1–4] and is shown in the next section for anisotropic beams of narrow rectangular cross section. Note also that the exact beam theory is of Rankine-Timoshenko type with the added feature that, in an anisotropic beam, the axial force T also contributes to the shear strain γ. Finally, note that if we choose our nominal Young's modulus E so that $C_{1111}=1$ (as we may always do), then the material matrix $\boldsymbol{\Lambda}$ given by (29) depends on two-dimensional elastic constants only, C_{1112} and C_{1212}, the

remaining three, C_{1122}, C_{1222}, and C_{2222}, having no influence on the exact one-dimensional beam theory that emerges from plane stress theory.

4 The Betti-Rayleigh Reciprocity Principle and the Generalized Displacement

Let $\boldsymbol{\sigma}=[\sigma,\tau]^T$ and consider any two solutions $s=(\mathbf{U},\boldsymbol{\sigma})$ and $\overline{s}=(\overline{\mathbf{U}},\overline{\boldsymbol{\sigma}})$ of the field equations of plane stress, (1) and (2), that satisfy the face condition of no traction, (4). Further, let

$$[s,\overline{s}]_x\equiv\int_{-1}^{1}(\boldsymbol{\sigma}\cdot\overline{\mathbf{U}}-\overline{\boldsymbol{\sigma}}\cdot\mathbf{U})_x dy. \tag{30}$$

Then the Betti-Rayleigh Reciprocity Principle implies that

$$[s,s^{SV}]_a=[s,s^{SV}]_x\quad\forall[a,x]\subseteq[0,l] \tag{31}$$

That is, $[s,s^{SV}]_x$ is a constant.

Introducing the representations (17) and (25) into (30), we find that

$$[s,s^{SV}]_x=\mathbf{T}\cdot[\mathbf{u}(x)-\tilde{\mathbf{u}}(x)]+M(x)[\omega(x)-\tilde{\omega}(x)],\quad\forall\mathbf{T},M, \tag{32}$$

where

$$\tilde{\mathbf{u}}\equiv\int_{-1}^{1}(\overset{0}{\mathbf{A}}{}^T\cdot\mathbf{U}-\mathbf{A}^T\cdot\boldsymbol{\sigma})_x dy\ \text{ and }\ \tilde{\omega}\equiv\int_{-1}^{1}(\overset{0}{\mathbf{B}}\cdot\mathbf{U}-\mathbf{B}\cdot\boldsymbol{\sigma})_x dy. \tag{33}$$

We call the displacement-rotation pair $(\tilde{\mathbf{u}},\tilde{\omega})$ the *generalized displacement*. An essential property—Property 10 in [4]—of these quantities is that

$$\tilde{\mathbf{u}}=\mathbf{u}\ \text{ and }\ \tilde{\omega}=\omega. \tag{34}$$

To prove this, first note that (14) and (17) imply that

$$\int_{-1}^{1}\{1,y\}\overset{0}{\mathbf{A}}(y)dy=\{\mathbf{1},\mathbf{0}\},\quad\int_{-1}^{1}\{1,y\}\overset{0}{\mathbf{B}}(y)dy=\{\mathbf{0},-\mathbf{i}\}, \tag{35}$$

where $\mathbf{1}$ is the two-dimensional identity tensor and $\mathbf{i}$ is a unit vector along the x-axis. Thus, by direct calculation, (33) implies that

$$\tilde{\mathbf{u}}^{SV}=\mathbf{u}\ \text{ and }\ \tilde{\omega}^{SV}=\omega. \tag{36}$$

(This is Property 6 in [4].) Now set

$$\mathbf{U}=\mathbf{U}^{SV}+\mathbf{U}^R\ \text{ and }\ \boldsymbol{\sigma}=\boldsymbol{\sigma}^{SV}+\boldsymbol{\sigma}^R, \tag{37}$$

where the superscript "R" stands for "residual." Then, by (32), (33), and (37),

$$\mathbf{T}\cdot\tilde{\mathbf{u}}^R(x)+M(x)\tilde{\omega}^R(x)=0,\quad\forall\mathbf{T},M. \tag{38}$$

But $s^R=(\mathbf{U}^R,\boldsymbol{\sigma}^R)$ is a solution of the equations of plane stress theory for which the associated generalized stress $(\mathbf{T}^R,M^R)$ is zero. Hence, $\tilde{\mathbf{u}}^R$ and $\tilde{\omega}^R$ are *independent* of $\mathbf{T}$ and M. Thus, (38) can be satisfied if and only if $\tilde{\mathbf{u}}^R$ and $\tilde{\omega}^R$ vanish, so that (36) implies (34). Henceforth, we may drop the tildes ($\sim$) over the displacements and rotation.

5 Boundary Conditions

A major problem in so-called higher-order beam, plate, and shell theories—a problem that often goes unmentioned—is how to prescribe proper boundary conditions. Actually, there are two problems, one due to lack of data and one due to too much. For example, in classical (Euler-Bernoulli) beam theory, the boundary conditions at a built-in end are clear: Whatever the measure of the vertical deflection, w, it and its axial derivative, w', must vanish. However, in the Rankine-Timoshenko theory of shear-deformable beams, the vertical deflection w and the rotation β are independent kinematic variables and "built-in" has at least two physical interpretations, depending on whether $w=\beta=0$ or $w=w'=0$ at a wall. (See Section H in Chapter IV of [6] where these and other possibilities are discussed.)

For our rectangular, anisotropic strip, it seems reasonable and simplest *to define built-in at* $x=0$ to mean

$$\mathbf{u}(0)=\mathbf{0},\quad\omega(0)=0. \tag{39}$$

If the right end of the beam is subject to the generalized stress $(\bar{\mathbf{T}},\bar{M})$, then, by $(15)_3$ and (25), these conditions induce the *Saint-Venant* displacement boundary conditions

$$\mathbf{U}^{SV}(0,y)=\mathbf{A}(y)\cdot\bar{\mathbf{T}}+\mathbf{B}(y)(\bar{M}+l\bar{Q}). \tag{40}$$

These boundary conditions in plane stress theory are special because they produce *no* edge effect at the left end. Likewise, by (17), there will be no edge effect at the right end of the beam providing the prescribed stresses of plane stress theory are given by

$$\boldsymbol{\sigma}^{SV}(l,y)=\overset{0}{\mathbf{A}}(y)\cdot\bar{\mathbf{T}}-(3/2)y\mathbf{i}\bar{M}. \tag{41}$$

Beam Boundary Conditions Induced by More General Plane Stress Boundary Conditions. To illustrate what happens if the boundary conditions at $x=0$ (and, by analogy, at $x=l$) are more general than (40), let us consider four cases: For simplicity the boundary conditions the right end of the beam will be taken to be of the form (41) so that there will be no end effects there.

(A) Stresses Prescribed:

$$\boldsymbol{\sigma}(0,y)=\hat{\boldsymbol{\sigma}}(y). \tag{42}$$

(B) Axial Stress and Vertical Displacement Prescribed:

$$\sigma(0,y)=\hat{\sigma}(y),\quad V(0,y)=\hat{V}(y). \tag{43}$$

(C) Shear Stress and Axial Displacement Prescribed:

$$\tau(0,y)=\hat{\tau}(y),\quad U(0,y)=\hat{U}(y). \tag{44}$$

(D) Displacements Prescribed:

$$\mathbf{U}(0,y)=\hat{\mathbf{U}}(y). \tag{45}$$

In case (A), the boundary conditions for the exact beam theory follow immediately from (14) as

$$\hat{\mathbf{T}}=\bar{\mathbf{T}}=\int_{-1}^{1}\hat{\boldsymbol{\sigma}}(y)dy,\quad\hat{M}=\bar{M}+l\bar{Q}=-\int_{-1}^{1}y\hat{\sigma}(y)dy. \tag{46}$$

To determine the associated beam boundary conditions in cases (B)–(D), we introduce the technique first proposed by Ladevèze [5] and later developed by Gregory and Wan [7]. To this end, in the notation of (30), we take the Betti-Rayleigh Principle in the form

$$[s-s^{SV},s^C]_0=[s-s^{SV},s^C]_x,\quad x\in[0,l], \tag{47}$$

where s is the (unknown but unique) solution of a plane stress problem, s^{SV} is the associated (unique but unknown) Saint-Venant solution, and s^C is one of a certain set of *canonical* solutions of plane stress problems, each of which is chosen so that the left side of (47) becomes known, depending on which of the cases (B)–(D) we are considering. (This set of six canonical problems, that serve as sorts of Green's functions, may be computed once for all either by finite element methods or by the analytical-numerical projection method of Gregory and Gladwell [8].) Moreover, Saint-Venant's Principle for an anisotropic strip guarantees, modulo a rigid-body displacement (that we suppress), that $s-s^{SV}$ approaches zero as we move into the beam from the left end. (See [9] and [10] for a proof and numerical values of the rate of decay for a range of values of the dimensionless elastic constants

$C_{\alpha\beta\lambda\mu}$.) Thus, if x is sufficiently large,[1] (47) takes the more explicit form

$$\int_{-1}^{1}[(\boldsymbol{\sigma}-\boldsymbol{\sigma}^{SV})\cdot\mathbf{U}^{C}-\boldsymbol{\sigma}^{C}\cdot(\mathbf{U}-\mathbf{U}^{SV})]_{x=0}dy=0. \tag{48}$$

Finally, we take

$$u^{C}(0)=v^{C}(0)=\omega^{C}(0)=0, \tag{49}$$

since these values of the generalized displacement associated with the canonical solutions represent merely rigid-body displacements.

In case (B), $\hat{T}=\bar{\bar{T}}=\int_{-1}^{1}\hat{\sigma}(y)dy$ and $\hat{M}=\bar{\bar{M}}+l\bar{\bar{Q}}=-\int_{-1}^{1}y\hat{\sigma}(y)dy$ are known, whereas $\tau(0,y)$ and $U(x,0)$ are not, so we define s^{C} to be that solution of the equations of plane stress satisfying (4), the homogeneous face traction conditions, plus the end conditions

$$V^{C}(0,y)=\sigma^{C}(0,y)=0,\quad \boldsymbol{\sigma}^{C}(l,y)=[\overset{0}{A}_{12}(y),\overset{0}{A}_{22}]^{T}. \tag{50}$$

(This second condition implies that $\hat{Q}^{C}=\bar{\bar{Q}}^{C}=1$.) Thus, (48) reduces to

$$\int_{-1}^{1}[(\hat{\sigma}-\boldsymbol{\sigma}^{SV})U^{C}-\tau^{C}(\hat{V}-V^{SV})]_{x=0}dy=0. \tag{51}$$

But, by $(14)_2$, (17), (25), and (33),

$$\int_{-1}^{1}(\tau^{C}V^{SV}-\boldsymbol{\sigma}^{SV}U^{C})_{x=0}dy$$

$$=v(0)-[\hat{T}u^{C}(0)+Qv^{C}(0)+\hat{M}\omega^{C}(0)]. \tag{52}$$

By (49), the term in brackets vanishes so that from (51) and (52),

$$v(0)=\int_{-1}^{1}(\tau^{C}\hat{V}-\hat{\sigma}U^{C})_{x=0}dy. \tag{53}$$

In case (C) $\hat{Q}=\bar{\bar{Q}}=\int_{-1}^{1}\hat{\tau}(y)dy$ is known, but $V(0,y)$ and $\sigma(0,y)$ are not, so we need two canonical solutions, s_{u}^{C} and s_{ω}^{C}. In both subcases, the boundary conditions at the left end of the beam are identical:

$$U^{C}(0,y)=\tau^{C}(0,y)=0. \tag{54}$$

Thus, (48) reduces to

$$\int_{-1}^{1}[(\hat{\tau}-\tau^{SV})V^{C}-\sigma^{C}(\hat{U}-U^{SV})]_{x=0}dy=0. \tag{55}$$

Again, by (14), (17), (25), (33), and (49), this expression reduces to

$$T^{C}u(0)+M^{C}(0)\omega(0)=\int_{-1}^{1}(\sigma^{C}\hat{U}-\hat{\tau}V^{C})_{x=0}dy. \tag{55}$$

As $Q^{C}=0$, the two canonical subcases then correspond to taking $\{T^{C},M^{C}\}=\{1,0\}$ and $\{0,1\}$, respectively. That is, the left-end boundary conditions (54) are to be supplemented by the two sets of right-end boundary conditions

$$\boldsymbol{\sigma}_{u,\omega}^{C}(l,y)=\overset{0}{\mathbf{A}}(y)\cdot\left\{\begin{bmatrix}1\\2\end{bmatrix},\begin{bmatrix}0\\0\end{bmatrix}\right\}-(3/2)y\mathbf{i}\{0,1\}. \tag{56}$$

Thus, in addition to the known vertical force $\hat{Q}$ at the left end, the remaining two boundary conditions at the left end of the beam are

$$\{u(0),\omega(0)\}=\int_{-1}^{1}(\boldsymbol{\sigma}_{u,\omega}^{C}\hat{U}-\hat{\tau}^{C}V_{u,\omega}^{C})_{x=0}dy. \tag{57}$$

In case (D), $\sigma(0,y)$ and $\tau(0,y)$ are unknown so we must take

$$\mathbf{U}^{C}(0,y)=\mathbf{0}. \tag{58}$$

Then (48) reduces to

$$\int_{-1}^{1}[\boldsymbol{\sigma}^{C}\cdot(\hat{\mathbf{U}}-\mathbf{U}^{SV})]_{x=0}dy=0. \tag{59}$$

By (25), (33), and (49),

$$\int_{-1}^{1}(\boldsymbol{\sigma}^{C}\cdot\hat{\mathbf{U}})_{x=0}dy=\mathbf{T}^{C}\cdot\mathbf{u}(0)+M_{C}(0)\omega(0). \tag{60}$$

Here we see that we need three canonical solutions, s_{u}^{C}, s_{v}^{C}, and s_{ω}^{C}, each subject to the same boundary conditions (58) at the left end of the beam and, by (41), to the following three sets of stress boundary conditions at the right end:

$$\boldsymbol{\sigma}_{u,v,\omega}^{C}(l,y)=\overset{0}{\mathbf{A}}(y)\cdot\left\{\begin{bmatrix}1\\0\end{bmatrix},\begin{bmatrix}0\\1\end{bmatrix},\begin{bmatrix}0\\0\end{bmatrix}\right\}-(3/2)y\mathbf{i}\{0,-l,1\}. \tag{61}$$

Thus,

$$\{u(0),v(0),\omega(0)\}=\int_{-1}^{1}(\boldsymbol{\sigma}_{u,v,\omega}^{C}\cdot\hat{\mathbf{U}})_{x=0}dy. \tag{62}$$

6 Conclusions

We have derived an exact, one-dimensional theory of beams from the linear, two-dimensional theory of plane stress for an elastically anisotropic rectangular strip. Our final equations, (15) and (28), resemble those of the Rankine-Timoshenko theory of shear-deformable beams, but, unlike the latter, involve no approximations whatsoever beyond those of plane stress theory itself. In contrast to the general development of exact beam theory in [1–4], all the results herein are explicit and assume no special elastic symmetries (beyond those implies by the existence of a strain-energy density). Further, using ideas first presented by Ladevèze [5], we have worked out the boundary conditions for our exact beam theory implied by imposing various combinations of end tractions and displacements in plane stress theory. Implementing these boundary conditions requires that we solve, only once, six canonical plane stress problems.

As in [3] and [4], we can extend our analysis to beams of piecewise constant width subject to arbitrary body forces and face tractions. Furthermore, it is not difficult to develop an exact theory for beams in which the anisotropic elastic coefficients vary with depth. We leave this as a future project.

References

[1] Ladevèze, P., 1983, "Sur le principe de Saint-Venant en élasticité," J. Mec. Theor. Appl., **1**, pp. 161–184.

[2] Ladevèze, P., 1985, "On Saint-Venant's Principle in Elasticity," *Local Effects in Structures*, P. Ladevèze, ed., Elsevier, New York, pp. 3–34.

[3] Ladevèze, P., and Simmonds, J. G., 1996, "New Concepts for Linear Beam Theory With Arbitrary Geometry and Loading," Comptes Rendus Acad. Sci. Paris, **332**, Ser IIb, pp. 455–462 (partially in French).

[4] Ladevèze, P., and Simmonds, J. G., 1998, "New Concepts for Linear Beam Theory With Arbitrary Geometry and Loading," Eur. J. Mech. A/Solids, **17**, pp. 377–402.

[5] Ladevèze, P., 1982, "Principes de Saint-Venant en déplacement et en contrainte pour les poutres droites élastique semi-infinies," Z. Angew. Math. Phys., **33**, pp. 132–139.

[6] Libai, A., and Simmonds, J. G., 1998, *The Nonlinear Theory of Elastic Shells*, 2nd Ed., Cambridge University Press, Cambridge, UK.

[7] Gregory, R. D., and Wan, F. Y. M., 1984, "Decaying States of Plane Strain in a Semi-Infinite Strip and Boundary Conditions for Plate Theory," J. Elast., **14**, pp. 27–64.

[8] Gregory, R. D., and Gladwell, I., 1982, "The Cantilever Beam Under Tension, Bending, or Flexure at Infinity," J. Elast., **12**, pp. 317–343.

[9] Crafter, E. C., Heise, R. M., Horgan, C. O., and Simmonds, J. G., 1993, "The Eigenvalues for a Self-Equilibrated, Semi-Infinite, Elastically Anisotropic Strip," ASME J. Appl. Mech., **60**, pp. 276–281.

[10] Wang, M. Z., Ting, T. C. T., and Yan, G., 1993, "The Anisotropic Elastic Semi-Infinite Strip," Q. J. Mech. Appl. Math., **51**, pp. 283–297.

[1] This is the only place we require l the dimensionless length of the beam, to be sufficiently large. However, this is no way affects the exactness of our beam Eqs. (15) and (28); it merely provides a device for determining boundary conditions for the beam equations.

Higher-Order Zig-Zag Theory for Laminated Composites With Multiple Delaminations

M. Cho
Associate Professor,
School of Mechanical and Aerospace Engineering,
Seoul National University,
Seoul 151-742, Korea
e-mail: mhcho@snu.ac.kr

J.-S. Kim
Graduate Research Assistant,
Department of Aerospace Engineering,
Inha University,
Inchon 402-751, Korea

A higher-order zig-zag theory has been developed for laminated composite plates with multiple delaminations. By imposing top and bottom surface transverse shear stress-free conditions and interface continuity conditions of transverse shear stresses including delaminated interfaces, the displacement field with minimal degree-of-freedoms are obtained. This displacement field can systematically handle the number, shape, size, and locations of delaminations. Through the dynamic version of variational approach, the dynamic equilibrium equations and variationally consistent boundary conditions are obtained. The delaminated beam finite element is implemented to evaluate the performance of the newly developed theory. Linear buckling and natural frequency analysis demonstrate the accuracy and efficiency of the present theory. The present higher-order zig-zag theory should work as an efficient tool to analyze the static and dynamic behavior of the composite plates with multiple delaminations. [DOI: 10.1115/1.1406959]

1 Introduction

As the increase in the application of composite materials to the primary loading structures, the refined strength evaluations and stress predictions are required. For the enhanced analysis of laminated composite plates, three types of higher-order theory have been developed. They are smeared theory ([1]), layerwise theory ([2]), and simplified zig-zag theory ([3]). Extensive reviews up to date can be found in the review papers of Noor and Burton [4], Kapania [5], and Reddy and Robbins, Jr. [6]. Recently, so-called ''zig-zag'' theories in the third category have been paid some attentions because of their accuracy and efficiency in the ply-level analysis. Most of the theories assume that interfaces are perfectly bonded. However, in many applications, this assumption is not adequate for the prediction of the behaviors of composite laminates. Low-speed impacts by foreign objects or imperfections in the manufacturing process may generate multiple delaminations in composite laminates. Compressive strength and stiffness of composite structures with delaminations decrease significantly. Therefore, delamination buckling problem has received considerable attentions. Extensive reviews for delaminated buckling issue can be found in the review paper of Simitses [7].

Vibration problems of delamnated beam/plate were analyzed by numerous researchers. Classical beam model ([8,9]), first-order shear deformation model ([10,11]), and higher-order shear model ([11]) with piezolayers ([12,13]) are employed for the natural frequency analysis. Damage detection/health monitoring problems are also considered in the frameworks of vibration analysis ([14]).

For the analysis of laminated plates with arbitrary shaped multiple delaminations, finite element method is a suitable choice to treat the general loading, boundary conditions, layups, and geometry. Even though finite element based on layerwise plate theory ([15]) can provide an adequate framework for the delamination analysis, this theory is not computationally efficient since the number of degrees-of-freedom of this theory depend upon the number of layers. Thus to reduce the active degrees-of-freedom of the problem, a global-local approach has been proposed by Cho et al. [16–18].

In the recent study, zig-zag higher order theories have been extended to the weakened interface problem ([19,20]). But the zig-zag theory describing opening as well as slipping behavior of the delaminated parts are rare. Chattopdhyay and Gu [21] developed higher-order theory to analyze the delamination buckling problem. However, this theory is complicated and employs many primary variables. In the present study, an efficient higher-order zig-zag theory with minimal degrees-of-freedom is developed to analyze multiple delamination problems. Linear buckling and natural frequency problems are analyzed to assess the performance of the proposed zig-zag higher-order theory.

2 Displacement Model

Composite plates with multiple delaminations are considered, including an linearly elastic behavior for laminates. A schematic of laminated composite plate with multiple delaminations is shown in Fig. 1. The form of the displacement field of the perfectly bonded layers is determined by the requirements that the transverse shear stresses should vanish on the upper and lower surface of the plates, and should be continuous through the thickness of the plates, including the interface between the lamina. These conditions can be satisfied by superimposing a linear zig-zag displacement, with a different slope in each layer, on an overall cubic varying field. We neglect transverse normal strain, thus w is only function of the in-plane coordinates. To model the multiple delaminations, the assumed displacement field is supplemented with unit step-functions which allow discontinuities in the displacement field.

We start with the following displacement field for a laminated plate with multiple delaminations:

$$u_\alpha(x_\alpha,z;t)=u_\alpha^0(x_\alpha;t)+\psi_\alpha(x_\alpha;t)z+\xi_\alpha(x_\alpha;t)z^2+\phi_\alpha(x_\alpha;t)z^3+\sum_{k=1}^{N-1} S_\alpha^k(x_\alpha;t)(z-z_k)H(z-z_k)+\sum_{k=1}^{N-1} \overline{u}_\alpha^k(x_\alpha;t)H(z-z_k) \quad (1)$$

$$u_3(x_\alpha,z;t)=w(x_\alpha;t)+\sum_{k=1}^{N-1} \overline{w}^k(x_\alpha;t)H(z-z_k) \quad (2)$$

Contributed by the Applied Mechanics Division of THE AMERICAN SOCIETY OF MECHANICAL ENGINEERS for publication in the ASME JOURNAL OF APPLIED MECHANICS. Manuscript received by the ASME Applied Mechanics Division, July 12, 1999; final revision, Oct. 19, 2000. Associate Editor: A. K. Mal. Discussion on the paper should be addressed to the Editor, Professor Lewis T. Wheeler, Department of Mechanical Engineering, University of Houston, Houston, TX 77204-4792, and will be accepted until four months after final publication of the paper itself in the ASME JOURNAL OF APPLIED MECHANICS.

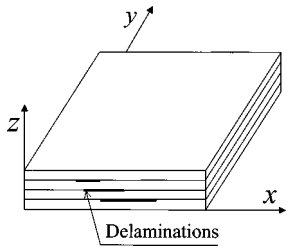

Fig. 1 Geometry of laminated composite with multiple delaminations

where u_α^0, w denote the displacement of a point (x_α) on the reference plane, ψ_α are the rotations of the normals to the reference plane about the x_α-axis, N is the number of layers, and $H(z-z_k)$ is the Heaviside unit step-function. The terms $\overline{u}_\alpha^k$, $\overline{w}^k$ represent possible jumps in the slipping and opening displacements, thus permitting incorporation of delamination for multilayered plates.

Here, we assume initially all the interfaces between the layers are delaminated. Then the number of delaminated layer interfaces are equal to the number of the whole interfaces. The perfectly bonded interfaces can be easily simulated by setting $\overline{u}_\alpha^k$, $\overline{w}^k$ to be zero.

Traction shear-free boundary conditions for the upper and lower surfaces of the plates requires that $\sigma_{\alpha 3}|_{z=0,h}=0$. For orthotropic layer, the shear stresses $\sigma_{\alpha 3}$ depend only on the transverse shear strains, so the traction-free condition can be written

$$\gamma_{\alpha 3}|_{z=0}=\psi_\alpha+w_{,\alpha}=0 \tag{3}$$

$$\gamma_{\alpha 3}|_{z=h}=\psi_\alpha+w_{,\alpha}+2\xi_\alpha h+3\phi_\alpha h^2+\sum_{k=1}^{N-1}(S_\alpha^k+\overline{w}_{,\alpha}^k)=0 \tag{4}$$

which are satisfied by

$$\psi_\alpha=-w_{,\alpha} \tag{5}$$

$$\xi_\alpha=-\left\{\frac{3h}{2}\phi_\alpha+\frac{1}{2h}\sum_{k=1}^{N-1}(S_\alpha^k+\overline{w}_{,\alpha}^k)\right\} \tag{6}$$

where $(\ )_{,\alpha}$ denotes a partial derivative with respect to the x_α-coordinate.

From the above Eqs. (5) and (6), the transverse shear strains are obtained as follows:

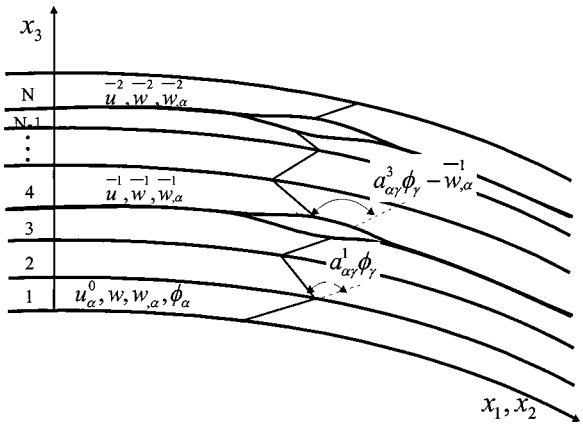

Fig. 2 Laminate deformed configurations with multiple delaminations

$$\gamma_{\alpha 3}=3(z^2-hz)\phi_\alpha+\sum_{k=1}^{N-1}(S_\alpha^k+\overline{w}_{,\alpha}^k)\left\{-\frac{z}{h}+H(z-z_k)\right\}. \tag{7}$$

At the perfectly bonded interfaces, transverse stresses are continuous. At the delaminated interfaces, transverse stresses are zero. In the present theory, at the delaminated interfaces, transverse shear stress continuity conditions are assumed to be satisfied because zero shear stresses also satisfy continuity of stresses. Thus in every interface, transverse shear stress continuity conditions are imposed. Continuity of transverse shear stresses between layers determines the change of slope S_α^k at each interface.

$$S_\alpha^k=a_{\alpha\gamma}^k\phi_\gamma-\overline{w}_{,\alpha}^k \tag{8}$$

in which the coefficient $a_{\alpha\gamma}^k$ represent the change in slope at each interface and depend only on the material properties of each layer. The term $\overline{w}_{,\alpha}^k$ represent the change in slope at each delamination interface. The deformed configuration and the kinematic variables are shown in Fig. 2.

Finally, substitution of Eqs. (5), (6), and (8) into Eqs. (1) yields

$$\begin{aligned}u_\alpha&=U_\alpha^{(0)}+U_\alpha^{(1)}z+U_\alpha^{(2)}z^2+U_\alpha^{(3)}z^3+\sum_{k=1}^{N-1}U_\alpha^k(z-z_k)H(z-z_k)\\&\quad+\sum_{k=1}^{N-1}\overline{U}_\alpha^k H(z-z_k)\\u_3&=w+\sum_{k=1}^{N-1}\overline{w}^k H(z-z_k)\end{aligned} \tag{9}$$

where

$$\begin{aligned}&U_\alpha^{(0)}=u_\alpha^0,\quad U_\alpha^{(1)}=-w_{,\alpha},\quad U_\alpha^{(2)}=-\frac{3h}{2}\phi_\alpha-\frac{z^2}{2h}\sum_{k=1}^{N-1}a_{\alpha\gamma}^k\phi_\gamma,\\&U_\alpha^{(3)}=\phi_\alpha,\quad U_\alpha^k=a_{\alpha\gamma}^k\phi_\gamma-\overline{w}_{,\alpha}^k,\quad \overline{U}_\alpha^k=\overline{u}_\alpha^k\end{aligned} \tag{10}$$

in which if we neglect the terms $\overline{u}_\alpha^k$ and $\overline{w}^k$, the displacement field is the same as that chosen by Cho and Parmerter [22,23].

The strain tensor components associated with the small-displacement theory of elasticity are given by

$$\begin{aligned}\epsilon_{\alpha\beta}&=\epsilon_{\alpha\beta}^{(0)}+z\epsilon_{\alpha\beta}^{(1)}+z^2\epsilon_{\alpha\beta}^{(2)}+z^3\epsilon_{\alpha\beta}^{(3)}\\&\quad+\sum_{k=1}^{N-1}\{\epsilon_{\alpha\beta}^k(z-z_k)+\overline{\epsilon}_{\alpha\beta}^k\}H(z-z_k)\end{aligned} \tag{11}$$

$$\gamma_{\alpha 3}=z\gamma_{\alpha 3}^{(1)}+z^2\gamma_{\alpha 3}^{(2)}+\sum_{k=1}^{N-1}\gamma_{\alpha\beta}^k H(z-z_k) \tag{12}$$

where

$$\begin{aligned}&\epsilon_{\alpha\beta}^{(0)}=\frac{1}{2}(u_{\alpha,\beta}^0+u_{\beta,\alpha}^0),\quad \epsilon_{\alpha\beta}^{(1)}=-\frac{1}{2}(w_{,\alpha\beta}+w_{,\beta\alpha}),\\&\epsilon_{\alpha\beta}^{(2)}=-\frac{3h}{4}(\phi_{\alpha,\beta}+\phi_{\beta,\alpha})-\frac{1}{4h}\sum_{k=1}^{N-1}(a_{\alpha\gamma}^k\phi_{\gamma,\beta}+a_{\beta\omega}^k\phi_{\omega,\alpha}),\\&\epsilon_{\alpha\beta}^{(3)}=\frac{1}{2}(\phi_{\alpha,\beta}+\phi_{\beta,\alpha}),\\&\epsilon_{\alpha\beta}^k=\frac{1}{2}(a_{\alpha\gamma}^k\phi_{\gamma\beta}+a_{\beta\omega}^k\phi_{\omega,\alpha}-2\overline{w}_{,\alpha\beta}^k),\quad \overline{\epsilon}_{\alpha\beta}^k=\frac{1}{2}(\overline{u}_{\alpha,\beta}^k+\overline{u}_{\beta,\alpha}^k),\\&\gamma_{\alpha 3}^{(1)}=-\left(3h\phi_\alpha+\frac{1}{h}\sum_{k=1}^{N-1}a_{\alpha\gamma}^k\phi_\gamma\right),\quad \gamma_{\alpha 3}^{(2)}=3\phi_\alpha,\quad \gamma_{\alpha 3}^k=a_{\alpha\gamma}^k\phi_\gamma.\end{aligned} \tag{13}$$

3 Equation of Motion and Boundary Conditions

The equations of motion and the variationally consistent boundary conditions are formulated in a weak form via the Hamilton's principle,

$$\int_0^t \Bigg\{ \int_V (\sigma_{\alpha\beta}\delta\epsilon_{\alpha\beta}+\sigma_{\alpha 3}\delta\gamma_{\alpha 3})dV-\int_V \rho(\dot{u}_\alpha\delta\dot{u}_\alpha+\dot{u}_3\delta\dot{u}_3)dV - \int_\Omega N^0_{\alpha\beta}u_{3,\alpha}\delta u_{3,\beta}d\Omega-\int_\Omega q\,\delta u_3 d\Omega\Bigg\}dt=0, \tag{14}$$

where a dot over quantity refers to a derivative with respect to time t, ρ is the mass density, $N^0_{\alpha\beta}$ are the constant in-plane edge loads, and q is a specified distributed transverse load. In Eqs. (14), V is the volume of the plate and Ω is the reference plane of the plate.

The equations of motion of the present theory can be derived by integrating the derivatives of the varied quantities by parts and collecting the coefficients of δu^0_α, δw, $\delta\phi_\alpha$, $\delta\overline{u}^i_\alpha$, and $\delta\overline{w}^i$,

$$\begin{gathered}
\delta u^0_\alpha: N_{\alpha\beta,\beta}=\ddot{N}_\alpha \\
\delta w: M_{\alpha\beta,\alpha\beta}+N^0_{\alpha\beta}w_{,\alpha\beta}+N^{0i}_{\alpha\beta}\overline{w}^i_{,\alpha\beta}+q=\ddot{M}_{\alpha,\alpha}+\ddot{V} \\
\delta\phi_\alpha: \hat{R}_{\alpha\beta,\beta}+\hat{V}_\alpha=\ddot{\hat{R}}_\alpha \\
\delta\overline{u}^i_\alpha: \overline{N}^i_{\alpha\beta,\beta}=\ddot{\overline{N}}^i_\alpha \\
\delta\overline{w}^i: \overline{M}^i_{\alpha\beta,\alpha\beta}+q^i+N^{0i}_{\alpha\beta}w_{,\alpha\beta}+N^{0ij}_{\alpha\beta}\overline{w}^j_{,\alpha\beta}=\ddot{\overline{M}}^i_{\alpha,\alpha}+\ddot{Q}^i,
\end{gathered} \tag{15}$$

and the associated boundary conditions are specified as

$$\begin{gathered}
N_{\alpha\beta}\nu_\beta=0 \quad \text{or} \quad \delta u^0_\alpha=0 \\
(M_{\alpha\beta,\alpha}+N^0_{\alpha\beta}w_{,\alpha}+N^{0i}_{\alpha\beta}\overline{w}^i_{,\alpha}-\ddot{M}_\beta)\nu_\beta=0 \quad \text{or} \quad \delta w=0 \\
M_{\alpha\beta}\nu_\beta=0 \quad \text{or} \quad \delta w_{,\alpha}=0 \\
\hat{R}_{\alpha\beta}\nu_\beta=0 \quad \text{or} \quad \delta\phi_\alpha=0 \\
\overline{N}^i_{\alpha\beta}\nu_\beta=0 \quad \text{or} \quad \delta\overline{u}^i_\alpha=0 \\
(\overline{M}^i_{\alpha\beta,\alpha}+N^{0i}_{\alpha\beta}w_{,\alpha}+N^{0ij}_{\alpha\beta}\overline{w}^j_{,\alpha}-\ddot{\overline{M}}^i_\beta)\nu_\beta=0 \quad \text{or} \quad \delta\overline{w}^i=0 \\
\overline{M}^i_{\alpha\beta}\nu_\beta=0 \quad \text{or} \quad \delta\overline{w}^i_{,\alpha}=0
\end{gathered} \tag{16}$$

where q^i is $qH(z-z_i)$, the stress resultants are defined as

$$\begin{aligned}
\hat{R}_{\alpha\beta}&=R^{(3)}_{\alpha\beta}-\frac{3h}{2}R^{(2)}_{\alpha\beta}+\sum_{i=1}^{N-1}a^i_{\gamma\alpha}\left(\overline{M}^i_{\gamma\beta}-\frac{1}{2h}R^{(2)}_{\gamma\beta}\right) \\
\hat{V}_\alpha&=3V^{(2)}_\alpha-3hV^{(1)}_\alpha+\sum_{i=1}^{N-1}a^i_{\gamma\alpha}\left(Q^i_\gamma-\frac{1}{h}V^{(1)}_\gamma\right)
\end{aligned} \tag{17}$$

$$\begin{aligned}
[N_{\alpha\beta},M_{\alpha\beta},R^{(2)}_{\alpha\beta},R^{(3)}_{\alpha\beta}]&=\int_0^h\sigma_{\alpha\beta}[1,z,z^2,z^3]dz \\
[\overline{N}^i_{\alpha\beta},\overline{M}^i_{\alpha\beta}]&=\int_0^h\sigma_{\alpha\beta}[1,(z-z_i)]H(z-z_i)dz \\
[V^{(1)}_\alpha,V^{(2)}_\alpha,Q^i_\alpha]&=\int_0^h\sigma_{\alpha 3}[z,z^2,H(z-z_i)]dz
\end{aligned} \tag{18}$$

and the inertia terms are defined as

$$\ddot{\hat{R}}_\alpha=\ddot{R}^{(3)}_\alpha-\frac{3h}{2}\ddot{R}^{(2)}_\alpha+\sum_{i=1}^{N-1}a^i_{\gamma\alpha}\left(\ddot{\overline{M}}^i_\gamma-\frac{1}{2h}\ddot{R}^{(2)}_\gamma\right) \tag{19}$$

$$\begin{aligned}
[\ddot{N}_\alpha,\ddot{M}_\alpha,\ddot{R}^{(2)}_\alpha,\ddot{R}^{(3)}_\alpha]&=\int_0^h\rho\ddot{u}_\alpha[1,z,z^2,z^3]dz \\
[\ddot{\overline{N}}^i_\alpha,\ddot{\overline{M}}^i_\alpha]&=\int_0^h\rho\ddot{u}_\alpha[1,(z-z_i)]H(z-z_i)dz \\
[\ddot{V},\ddot{Q}^i]&=\int_0^h\rho\ddot{u}_3[1,H(z-z_i)]dz.
\end{aligned} \tag{20}$$

In Eq. (15), as defined by Lee et al. [15], $N^0_{\alpha\beta}$, $N^{0i}_{\alpha\beta}$, $N^{0ij}_{\alpha\beta}$ are the constant in-plane edge loads defined, respectively, by the following:

$$N^0_{\alpha\beta}=-\lambda n_{\alpha\beta}, \quad N^{0i}_{\alpha\beta}=-\lambda n^i_{\alpha\beta}, \quad N^{0ij}_{\alpha\beta}=-\lambda n^{ij}_{\alpha\beta}, \tag{21}$$

where λ is a buckling parameter, $n_{\alpha\beta}$ is the specified value of the compressive or shear in-plane force, and $n^i_{\alpha\beta}$ and $n^{ij}_{\alpha\beta}$ are given as

$$n^i_{\alpha\beta}=\frac{\Sigma_{k=1}^N\int_{z_k}^{z_{k+1}}H(z-z_i)dz}{\Sigma_{k=1}^N\int_{z_k}^{z_{k+1}}dz}n_{\alpha\beta} \tag{22}$$

$$n^{ij}_{\alpha\beta}=\frac{\Sigma_{k=1}^N\int_{z_k}^{z_{k+1}}H(z-z_i)H(z-z_j)dz}{\Sigma_{k=1}^N\int_{z_k}^{z_{k+1}}dz}n_{\alpha\beta}. \tag{23}$$

4 Constitutive Equations and Inertia Coefficients

The constitutive equations of the kth orthotropic lamina in the laminate coordinate system are given by

$$\sigma^{(k)}_{\alpha\beta}=\overline{Q}^{(k)}_{\alpha\beta\gamma\omega}\epsilon^{(k)}_{\gamma\omega}, \quad \sigma^{(k)}_{\alpha 3}=\overline{Q}^{(k)}_{\alpha 3\beta 3}\gamma^{(k)}_{\beta 3} \tag{24}$$

where $\overline{Q}^{(k)}_{\alpha\beta\gamma\omega}$ is the transformed reduced stiffness of the kth lamina.

Using the definition of the strain tensor Eqs. (11) and (12), substitution of Eqs. (24) into Eqs. (18) yields the constitutive equations of the laminate:

$$\begin{Bmatrix} N_{\alpha\beta} \\ M_{\alpha\beta} \\ R^{(2)}_{\alpha\beta} \\ R^{(3)}_{\alpha\beta} \\ \overline{M}^i{}_{\alpha\beta} \\ \overline{N}^i_{\alpha\beta} \end{Bmatrix} = \begin{bmatrix} A^{(0)}_{\alpha\beta\gamma\omega} & A^{(1)}_{\alpha\beta\gamma\omega} & A^{(2)}_{\alpha\beta\gamma\omega} & A^{(3)}_{\alpha\beta\gamma\omega} & B^{j(0)}_{\alpha\beta\gamma\omega} & E^{j(0)}_{\alpha\beta\gamma\omega} \\ A^{(1)}_{\alpha\beta\gamma\omega} & A^{(2)}_{\alpha\beta\gamma\omega} & A^{(3)}_{\alpha\beta\gamma\omega} & A^{(4)}_{\alpha\beta\gamma\omega} & B^{j(1)}_{\alpha\beta\gamma\omega} & E^{j(1)}_{\alpha\beta\gamma\omega} \\ A^{(2)}_{\alpha\beta\gamma\omega} & A^{(3)}_{\alpha\beta\gamma\omega} & A^{(4)}_{\alpha\beta\gamma\omega} & A^{(5)}_{\alpha\beta\gamma\omega} & B^{j(2)}_{\alpha\beta\gamma\omega} & E^{j(2)}_{\alpha\beta\gamma\omega} \\ A^{(3)}_{\alpha\beta\gamma\omega} & A^{(4)}_{\alpha\beta\gamma\omega} & A^{(5)}_{\alpha\beta\gamma\omega} & A^{(6)}_{\alpha\beta\gamma\omega} & B^{j(3)}_{\alpha\beta\gamma\omega} & E^{j(3)}_{\alpha\beta\gamma\omega} \\ B^{i(0)}_{\alpha\beta\gamma\omega} & B^{i(1)}_{\alpha\beta\gamma\omega} & B^{i(2)}_{\alpha\beta\gamma\omega} & B^{i(3)}_{\alpha\beta\gamma\omega} & D^{ij}_{\alpha\beta\gamma\omega} & F^{ij}_{\alpha\beta\gamma\omega} \\ E^{i(0)}_{\alpha\beta\gamma\omega} & E^{i(1)}_{\alpha\beta\gamma\omega} & E^{i(2)}_{\alpha\beta\gamma\omega} & E^{i(3)}_{\alpha\beta\gamma\omega} & F^{ij}_{\alpha\beta\gamma\omega} & E^{ij}_{\alpha\beta\gamma\omega} \end{bmatrix} \begin{Bmatrix} \epsilon^{(0)}_{\gamma\omega} \\ \epsilon^{(1)}_{\gamma\omega} \\ \epsilon^{(2)}_{\gamma\omega} \\ \epsilon^{(3)}_{\gamma\omega} \\ \epsilon^{j}_{\gamma\omega} \\ \overline{\epsilon}^{j}_{\gamma\omega} \end{Bmatrix} \tag{25}$$

$$\begin{Bmatrix} V^{(1)}_\alpha \\ V^{(2)}_\alpha \\ Q^i_\alpha \end{Bmatrix} = \begin{bmatrix} A^{(2)}_{\alpha 3\beta 3} & A^{(3)}_{\alpha 3\beta 3} & E^{j(1)}_{\alpha 3\beta 3} \\ A^{(3)}_{\alpha 3\beta 3} & A^{(4)}_{\alpha 3\beta 3} & E^{j(2)}_{\alpha 3\beta 3} \\ E^{i(1)}_{\alpha 3\beta 3} & E^{i(2)}_{\alpha 3\beta 3} & E^{ij}_{\alpha 3\beta 3} \end{bmatrix} \begin{Bmatrix} \gamma^{(1)}_{\beta 3} \\ \gamma^{(2)}_{\beta 3} \\ \gamma^{j}_{\beta 3} \end{Bmatrix} \tag{26}$$

where

$$A^{(m)}_{\alpha\beta\gamma\omega}=\sum_{k=1}^{N}\int_{z_k}^{z_{k+1}}\overline{Q}^k_{\alpha\beta\gamma\omega}z^m dz,\quad (m=0,1,2,3,4,5,6)$$

$$B^{j(m)}_{\alpha\beta\gamma\omega}=\sum_{k=1}^{N}\int_{z_k}^{z_{k+1}}\overline{Q}^k_{\alpha\beta\gamma\omega}(z-z_j)H(z-z_j)z^m dz,\quad (m=0,1,2,3)$$

$$E^{j(m)}_{\alpha\beta\gamma\omega}=\sum_{k=1}^{N}\int_{z_k}^{z_{k+1}}\overline{Q}^k_{\alpha\beta\gamma\omega}H(z-z_j)z^m dz,\quad (m=0,1,2,3)$$

$$E^{ij}_{\alpha\beta\gamma\omega}=\sum_{k=1}^{N}\int_{z_k}^{z_{k+1}}\overline{Q}^k_{\alpha\beta\gamma\omega}H(z-z_i)H(z-z_j)dz$$

$$F^{ij}_{\alpha\beta\gamma\omega}=\sum_{k=1}^{N}\int_{z_k}^{z_{k+1}}\overline{Q}^k_{\alpha\beta\gamma\omega}(z-z_i)H(z-z_i)H(z-z_j)dz \quad (27)$$

$$D^{ij}_{\alpha\beta\gamma\omega}=\sum_{k=1}^{N}\int_{z_k}^{z_{k+1}}\overline{Q}^k_{\alpha\beta\gamma\omega}(z-z_i)(z-z_j)H(z-z_i)H(z-z_j)dz$$

$$A^{(m)}_{\alpha3\gamma3}=\sum_{k=1}^{N}\int_{z_k}^{z_{k+1}}\overline{Q}^k_{\alpha3\gamma3}z^m dz,\quad (m=2,3,4)$$

$$E^{j(m)}_{\alpha3\gamma3}=\sum_{k=1}^{N}\int_{z_k}^{z_{k+1}}\overline{Q}^k_{\alpha3\gamma3}H(z-z_j)z^m dz,\quad (m=1,2)$$

$$E^{ij}_{\alpha3\gamma3}=\sum_{k=1}^{N}\int_{z_k}^{z_{k+1}}\overline{Q}^k_{\alpha3\gamma3}H(z-z_i)H(z-z_j)dz$$

and substitution Eqs. (9) into Eqs. (20) yields the inertia coefficients as follows:

$$\begin{Bmatrix}\ddot{N}_\alpha\\ \ddot{M}_\alpha\\ \ddot{R}^{(2)}_\alpha\\ \ddot{R}^{(3)}_\alpha\\ \ddot{M}^i_\alpha\\ \ddot{N}^i_\alpha\end{Bmatrix}=\begin{bmatrix}I^{(0)}_0 & I^{(1)}_0 & I^{(2)}_0 & I^{(3)}_0 & I^{j(0)}_1 & I^{j(0)}_2\\ I^{(1)}_0 & I^{(2)}_0 & I^{(3)}_0 & I^{(4)}_0 & I^{j(1)}_1 & I^{j(1)}_2\\ I^{(2)}_0 & I^{(3)}_0 & I^{(4)}_0 & I^{(5)}_0 & I^{j(2)}_1 & I^{j(2)}_2\\ I^{(3)}_0 & I^{(4)}_0 & I^{(5)}_0 & I^{(6)}_0 & I^{j(3)}_1 & I^{j(3)}_2\\ I^{i(0)}_1 & I^{i(1)}_1 & I^{i(2)}_1 & I^{i(3)}_1 & I^{ij}_3 & I^{ij}_4\\ I^{i(0)}_2 & I^{i(1)}_2 & I^{i(2)}_2 & I^{i(3)}_2 & I^{ij}_4 & I^{ij}_5\end{bmatrix}\begin{Bmatrix}\ddot{U}^{(0)}_\alpha\\ \ddot{U}^{(1)}_\alpha\\ \ddot{U}^{(2)}_\alpha\\ \ddot{U}^{(3)}_\alpha\\ \ddot{U}^j_\alpha\\ \ddot{U}^j_\alpha\end{Bmatrix} \quad (28)$$

$$\begin{Bmatrix}\ddot{V}\\ \ddot{Q}^i\end{Bmatrix}=\begin{bmatrix}I^{(0)}_0 & I^{j(0)}_2\\ I^{i(0)}_2 & I^{ij}_5\end{bmatrix}\begin{Bmatrix}\ddot{w}\\ \ddot{w}^j\end{Bmatrix} \quad (29)$$

where

$$I^{(m)}_0=\sum_{k=1}^{N}\int_{z_k}^{z_{k+1}}\rho z^m dz,\quad (m=0,1,2,3,4,5,6)$$

$$I^{j(m)}_1=\sum_{k=1}^{N}\int_{z_k}^{z_{k+1}}\rho(z-z_j)H(z-z_j)z^m dz,\quad (m=0,1,2,3)$$

$$I^{j(m)}_2=\sum_{k=1}^{N}\int_{z_k}^{z_{k+1}}\rho H(z-z_j)z^m dz,\quad (m=0,1,2,3) \quad (30)$$

$$I^{ij}_3=\sum_{k=1}^{N}\int_{z_k}^{z_{k+1}}\rho(z-z_i)(z-z_j)H(z-z_i)H(z-z_j)dz$$

$$I^{ij}_4=\sum_{k=1}^{N}\int_{z_k}^{z_{k+1}}\rho(z-z_i)H(z-z_i)H(z-z_j)dz$$

$$I^{ij}_5=\sum_{k=1}^{N}\int_{z_k}^{z_{k+1}}\rho H(z-z_i)H(z-z_j)dz.$$

5 Finite Element Model

To assess the validity of the proposed theory, a finite element is developed for one-dimensional problems. The primary displacement unknowns are expressed in terms of nodal values and shape functions as follows:

$$(u^0_\alpha,\phi_\alpha,\overline{u^l_\alpha})=\sum_{m=1}^{n}N_m[(u^0_\alpha)_m,(\phi_\alpha)_m,(\overline{u^l_\alpha})_m]$$

$$w=\sum_{m=1}^{n}\{P_m(w)_m+H_{xm}(w_{,x})_m+H_{ym}(w_{,y})_m\} \quad (31)$$

$$\overline{w^j}=\sum_{m=1}^{n}\{P_m(\overline{w^j})_m+H_{xm}(\overline{w^j_{,x}})_m+H_{ym}(\overline{w^j_{,y}})_m\}$$

where n is the number of nodes in a typical finite element. N_m is a Lagrangian interpolation function and P_m, H_{xm}, H_{ym} are Hermite interpolation functions. In this study, we used a two-noded beam element with one-dimensional linear Lagrangian interpolation functions for u^0_α, ϕ_α, $\overline{u^l_\alpha}$ and Hermite interpolation functions for w, w^j.

The finite element model of the linear buckling and natural vibration problem can be expressed as follows:

$$([\mathbf{K}]-\lambda[\mathbf{S}])\{\mathbf{u}\}=\{\mathbf{0}\},\quad \text{and } ([\mathbf{K}]-\omega^2[\mathbf{M}])\{\mathbf{u}\}=\{\mathbf{0}\} \quad (32)$$

where $[\mathbf{K}]$, $[\mathbf{S}]$, and $[\mathbf{M}]$ are the stiffness matrix, the geometric stiffness matrix, and the mass matrix. The parameters λ, ω, and $\{\mathbf{u}\}$ denote the buckling load, the natural frequency, and the eigenvector of nodal displacements corresponding to an eigenvalue, respectively.

The strains are defined from the approximation of kinemtic variables

$$\{\epsilon_{\alpha\beta}\}=[B]_b\{u_n\},\quad \{\gamma_{\alpha3}\}=[B]_s\{u_n\} \quad (33)$$

$$\{\epsilon_{\alpha\beta}\}=\{\epsilon^{(0)}_{\alpha\beta},\epsilon^{(1)}_{\alpha\beta},\epsilon^{(2)}_{\alpha\beta},\epsilon^{(3)}_{\alpha\beta},\epsilon^{j}_{\alpha\beta},\overline{\epsilon^j}_{\alpha\beta},\}^T$$

$$\{\gamma_{\alpha3}\}=\{\gamma^{(1)}_{\alpha3},\gamma^{(2)}_{\alpha3},\gamma^{j}_{\alpha3},\}^T \quad (34)$$

$$\{u_n\}=\{u^0_\alpha,w,w_{,\alpha},\phi_\alpha,\overline{u^l_\alpha},\overline{w^j},\overline{w^j_\alpha}\}^T$$

where $[B]_b$, $[B]_s$, and $\{u_n\}$ denote the in-plane strain-displacement matrix, transverse shear strain-displacement matrix, and nodal displacements, respectively.

In the beginning of the construction of the displacement field of the present theory, we assumed that the delaminations exist at each interface of laminates, but reduced the presented delaminations using the following strain-displacement matrix relationships for the one-dimensional case

$$[B]_b=[B_{b1},\ldots,B_{bn}],\quad [B]_s=[B_{s1},\ldots,B_{sn}] \tag{35}$$

in which

$$B_{bi}=\begin{bmatrix} N_{i,x} & 0 & 0 & 0 & \lfloor\mathbf{0}\rfloor_D & \lfloor\mathbf{0}\rfloor_D & \lfloor\mathbf{0}\rfloor_D \\ 0 & -P_{i,xx} & -H_{xi,xx} & 0 & \lfloor\mathbf{0}\rfloor_D & \lfloor\mathbf{0}\rfloor_D & \lfloor\mathbf{0}\rfloor_D \\ 0 & 0 & 0 & A_cN_{i,x} & \lfloor\mathbf{0}\rfloor_D & \lfloor\mathbf{0}\rfloor_D & \lfloor\mathbf{0}\rfloor_D \\ 0 & 0 & 0 & N_{i,x} & \lfloor\mathbf{0}\rfloor_D & \lfloor\mathbf{0}\rfloor_D & \lfloor\mathbf{0}\rfloor_D \\ 0 & 0 & 0 & a_{11}^1N_{i,x} & \lfloor\mathbf{0}\rfloor_D & & \\ \vdots & \vdots & \vdots & \vdots & \vdots & [\mathbf{P}_{i,xx}] & [\mathbf{H}_{xi,xx}] \\ 0 & 0 & 0 & a_{11}^{N-1}N_{i,x} & \lfloor\mathbf{0}\rfloor_D & & \\ \{\mathbf{0}\}_{N-1} & \{\mathbf{0}\}_{N-1} & \{\mathbf{0}\}_{N-1} & \{\mathbf{0}\}_{N-1} & [\mathbf{N}_{i,x}] & [\mathbf{0}]_{N-1\times D} & [\mathbf{0}]_{N-1\times D} \end{bmatrix} \tag{36}$$

$$B_{si}=\begin{bmatrix} 0 & 0 & 0 & 2A_cN_i & \\ 0 & 0 & 0 & 3N_i & \\ 0 & 0 & 0 & a_{11}^1N_i & [\mathbf{0}]_{2+(N-1)\times 3D} \\ \vdots & \vdots & \vdots & \vdots & \\ 0 & 0 & 0 & a_{11}^{N-1}N_i & \end{bmatrix} \tag{37}$$

where

$$A_c=-\frac{1}{2}\left(3h+\frac{1}{h}\sum_{k=1}^{N-1}a_{11}^k\right),\quad [\mathbf{N}_{i,x}]=\begin{bmatrix} N_{i,x} & & \\ & \ddots & \end{bmatrix}_{N-1\times D}, \tag{38}$$

$$[\mathbf{P}_{i,xx}]=\begin{bmatrix} -P_{i,xx} & & \\ & \ddots & \end{bmatrix}_{N-1\times D},$$

$$[\mathbf{H}_{xi,xx}]=\begin{bmatrix} -H_{xi,xx} & & \\ & \ddots & \end{bmatrix}_{N-1\times D}. \tag{39}$$

N is the total number of layers, and D is the total number of delaminations. $\{\mathbf{0}\}_m$, $\lfloor\mathbf{0}\rfloor_m$, and $[\mathbf{0}]_{m\times n}$ is the $m\times 1$ null vector, the $1\times m$ null row vector, and $m\times n$ the null matrix, respectively. Thus, the size of the element stiffness matrix is $(4+3D)\times(4+3D)$, independent of the number of layers, and only dependent upon the number of delaminations.

6 Numerical Examples

To examine the accuracy of the present theory, buckling and vibration eigenvalue problems for laminated composite beam with multiple delaminations were considered: first, the buckling of the delaminated composite beam and, second, the vibration of the delaminated composite beam. Some of the results of the present theory are compared with the exact elasticity solutions when they are available.

Table 1 Comparison of Nondimensional Buckling Load for Various Length of Delamination

a/L	Simitses	Chen	Lee Symmetric	Anti-symmetric	Present Symmetric	Anti-symmetric
0.1	0.9999	0.9999	0.9999	1.9481	0.9999	1.9494
0.2	0.9956	0.9956	0.9956	1.4360	0.9956	1.4371
0.3	0.9638	0.9638	0.9639	1.0245	0.9641	1.0251
0.4	0.8481	0.8561	0.8562	0.8482	0.8566	0.8485
0.5	0.6896	0.6896	0.6898	0.7967	0.6901	0.7971
0.6	0.5411	0.5411	0.5413	0.7928	0.5415	0.7933
0.7	0.4310	0.4310	0.4311	0.7629	0.4312	0.7635
0.8	0.3514	0.3514	0.3515	0.6857	0.3516	0.6863
0.9	0.2923	0.2933	0.2934	0.5947	0.2934	0.5951

6.1 Example 1: A Delaminated Composite Beam-Plate Under Axial Compression. The first example analyzed by the present theory is the linear buckling problem. First, a specially orthotropic composite laminate containing one centrally located midplane delamination is considered. The results are compared with those reported by other researchers. The material properties in crossply beam-plate examples are given as follows:

$$E_{11}=26.25\times 10^6\ \text{psi},\quad E_{22}=1.49\times 10^6\ \text{psi},$$
$$G_{12}=1.04\times 10^6\ \text{psi},\quad \nu_{12}=0.28 \tag{40}$$

where E_{11} is the Young's modulus in the fiber direction, E_{22} is the Young's modulus in the transverse direction, G_{12} is the shear modulus, and ν_{12} is the Poisson's ratio.

The results of this typical example are reproduced from Lee et al. [15]. The thickness-to-span length ratio (L/h) is assumed to be very small and equal to 400. The numerical results of the nondimensional buckling loads with changing delamination length from the present theory shows good agreement with those from Simitses et al. [24], Chen [25], and Lee et al. [15]. They are shown in Table 1.

Second, a simply supported composite beam-plate is considered. The elasticity solution for this delamination buckling problem of a beam-plate was proposed by Gu and Chattopadhyay [26]. The configuration of a simply-supported beam-plate with a single delamination is given in Fig. 3. The material used in this example is as follows:

$$E_L=25\times 10^6\ \text{psi},\quad E_T=1\times 10^6\ \text{psi},\quad G_{LT}=0.5\times 10^6\ \text{psi}$$
$$G_{TT}=0.2\times 10^6\ \text{psi},\quad \nu_{LT}=\nu_{TT}=0.25 \tag{41}$$

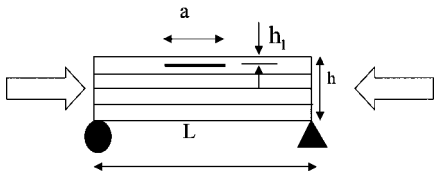

Fig. 3 Configuration of a simply supported beam-plate with a single delamination

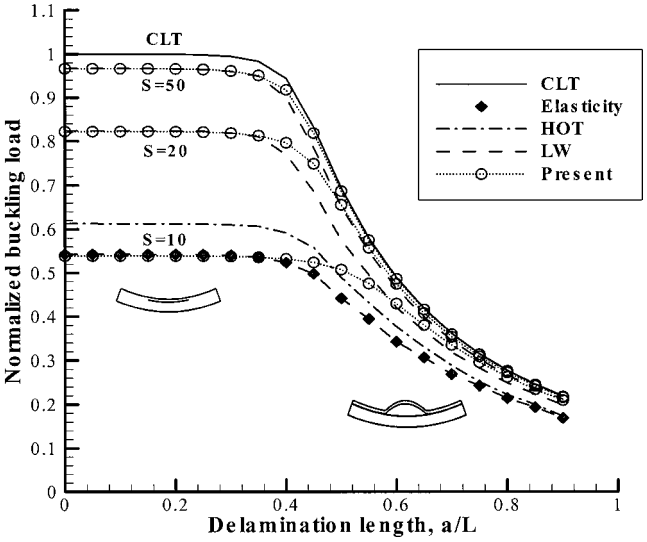

Fig. 4 Nondimensionalized buckling load versus delamination length

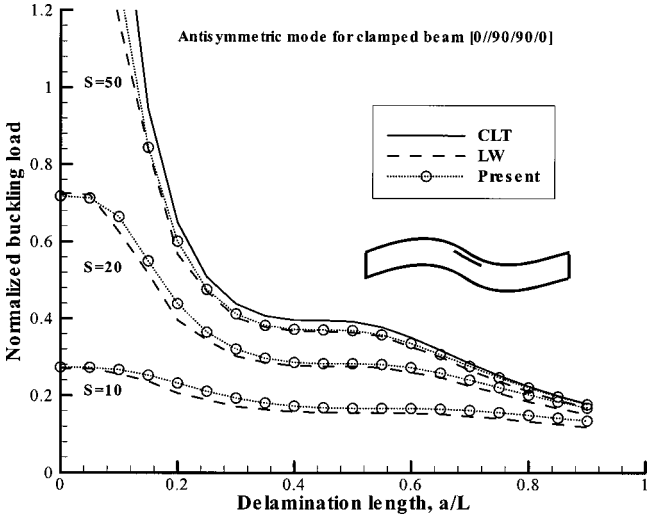

Fig. 7 Normalized buckling load versus delamination length for [0//90/90/0] composite, antisymmetric mode

where E, G, and ν represent the Young's modulus, the shear modulus, and the Poisson's ratio of the material, respectively. L denotes the fiber direction and T denotes the direction perpendicular to the fiber.

The plate is thick ($L/h=10$) and the delaminated layer is relatively thin ($h_1/h=0.8$). Figure 4 presents the critical loads normalized by the value calculated by the classical laminated theory (CLT). The results obtained for $[0_5/90_{10}/0_5]$ composite laminates are compared with those of CLT, the elasticity solution, and the layerwise theory. The results of the present theory show good correlation with the elasticity solutions in the small-sized delamination. However, in the mixed-mode range, that is, in case of the large-sized delaminations, the present theory provides stiffer buckling loads compared to those of elasticity and other higher order theories, especially for thicker cases ($S=10$). This situation is due to the fact that the deformation of the present theory cannot provide a sign change of the shear strains at the delamination interfaces. This makes the buckling load higher than that of elasticity and closer to that of the classical plate theory.

Third, a clamped beam-plate containing one centrally located delamination is considered (Fig. 5). In this example, the stacking sequence of the delaminated composite is [0//90/90/0] symmetric and [0//90/0/90] antisymmetric layup. Figures 6 and 7 present the normalized buckling loads for symmetric and antisymmetric buckling mode with symmetric layups. The results of the present theory are compared with those of CLT and those of layerwise theory for various length-to-thickness ratio ($S=L/h$). As can be seen, the numerical results of the nondimensional buckling loads with changing delamination length from the present theory shows good agreements with the results of layerwise theory. Figure 8 present the normalized buckling loads for various length-to-thickness ra-

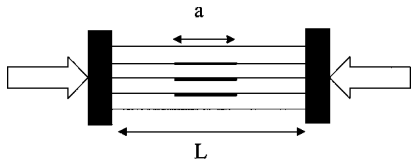

Fig. 5 Configuration of a clamped beam-plate with centrally located delaminations

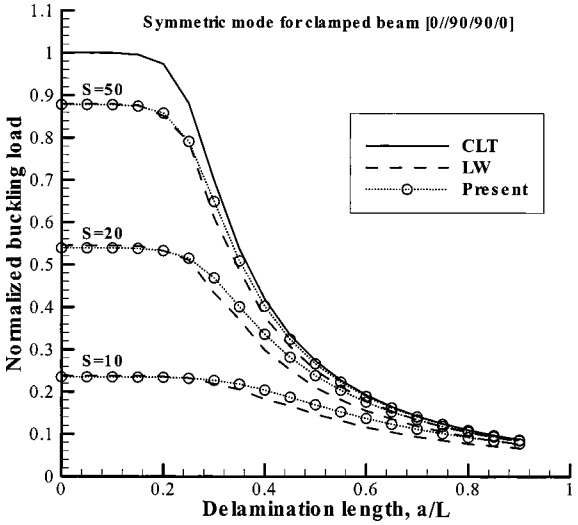

Fig. 6 Normalized buckling load versus delamination length for [0//90/90/0] composite, symmetric mode

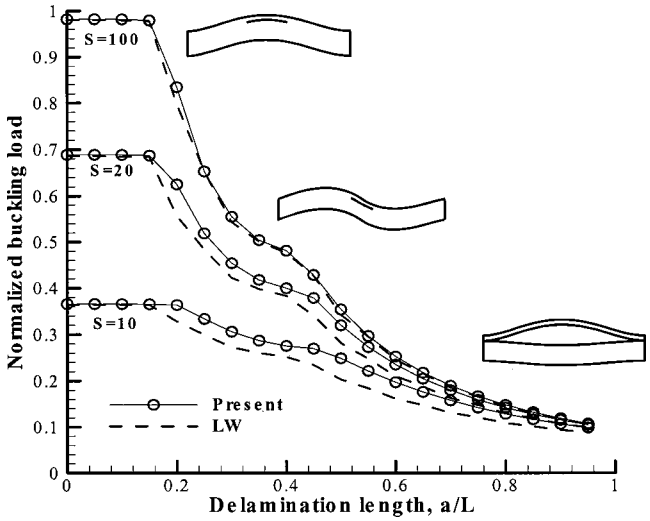

Fig. 8 Normalized buckling load versus delamination length for [0//90/0/90] composite

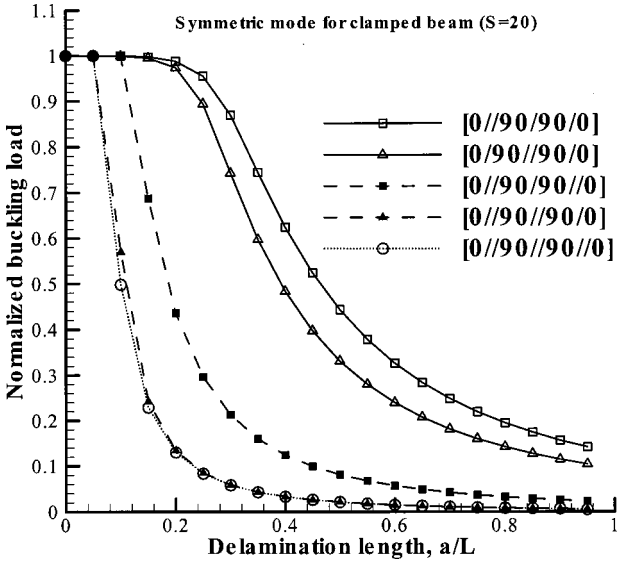

Fig. 9 Normalized buckling load versus delamination length for [0/90/90/0] composite with $S=20$, symmetric mode

tio and delamination size with an antisymmetric layup. In this case, as the size of the delamination (a/L) increases, the buckling modes of beam-plate have all the three possible buckling modes, i.e., global symmetric, antisymmetric, and local symmetric modes. Then, the range of antisymmetric modes increase as S decreases. Even in the antisymmetric layup case, the present theory gives

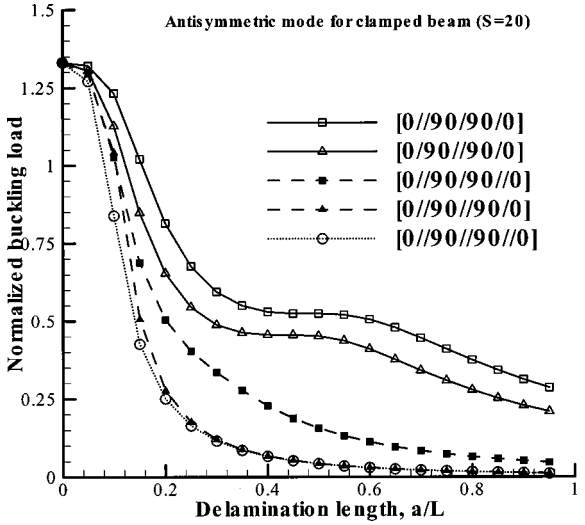

Fig. 10 Normalized buckling load versus delamination length for [0/90/90/0] composite with $S=20$, antisymmetric mode

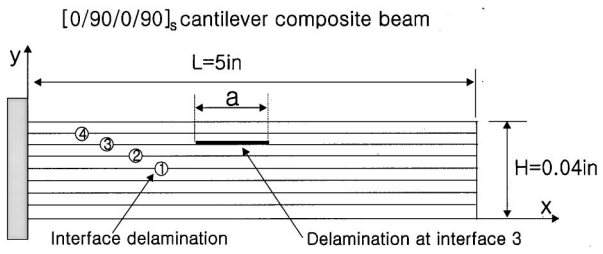

Fig. 11 Configuration of cantilevered $[0/90]_{2s}$ composite beam with a single delamination

Table 2 Fundamental Frequency for Delamination Along Interface 1

a in	Experiment[a] Specimen 1	Specimen 2	Specimen 3	Analytical Model[b]	Present
0.0	79.875	79.875	79.750	82.042	81.898
1.0	78.376	79.126	77.001	80.133	81.197
2.0	74.375	75.000	76.751	75.285	76.594
3.0	68.250	66.250	66.375	66.936	67.453
4.0	57.623	57.502	57.501	57.239	57.784

Table 3 Fundamental Frequency for Delamination Along Interface 2

a in	Experiment[a] Specimen 1	Specimen 2	Specimen 3	Analytical Model[b]	Present
0.0	79.875	79.875	79.750	82.042	81.893
1.0	78.375	78.375	76.626	81.385	81.248
2.0	75.126	75.250	75.001	78.103	76.963
3.0	64.001	70.001	69.876	71.159	68.303
4.0	45.752	49.751	49.502	62.121	57.953

comparable results to those of layerwise theory for the buckling loads for various delamination sizes and length-to-thickness ratios.

The next analysis is performed for a beam-plate with various delaminations and each ply having the same thickness. The buckling load has been normalized with respect to the critical buckling load for the undelaminated composite. The length-to-thickness ratio is assumed to be 20. The nondimensional buckling load of a [0/90/90/0] beam-plate is presented in Figs. 9 and 10 for various delaminations and the size of delamination. Figures 9 and 10 show the normalized buckling loads for the symmetric and antisymmetric buckling modes, respectively. Once more, the results of the present theory show good agreements with those of layerwise theory.

6.2 Example 2: Free Vibration of Cantilevered Composite Beam With Multiple Delaminations. The second example analyzed by the present theory is the free vibration problem. First, there is a cantilever crossply composites beam with embedded delaminations of varying size and at several different locations. The material properties in this example are given as follows:

$$E_{11}=19.6\times10^{6}\ \text{psi},\quad E_{22}=1.5\times10^{6}\ \text{psi},$$
$$G_{12}=0.725\times10^{6}\ \text{psi}$$
$$\nu_{12}=0.33,\quad \rho=1.3821\times10^{-4}\ \text{lb.}-\text{s}^2/\text{in.}^4 \tag{42}$$

where ρ is a mass density.

The configuration of this example is shown in Fig. 11. In this example, the stacking sequence of the delaminated composite is $[0/90]_{2s}$ and the thickness of the individual plies is 0.04 in. The results of the present theory are compared with those of Shen

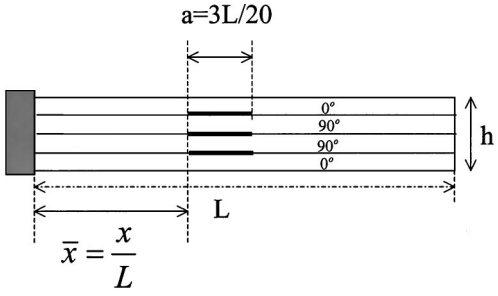

Fig. 12 Configuration of cantilevered [0/90/90/0] composite beam with multiple delaminations

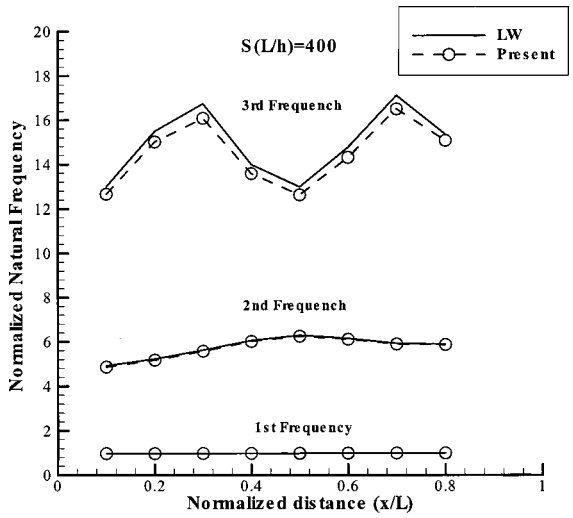

Fig. 13 Normalized natural frequency versus normalized distance for [0/90/90/0] composite with $S=400$

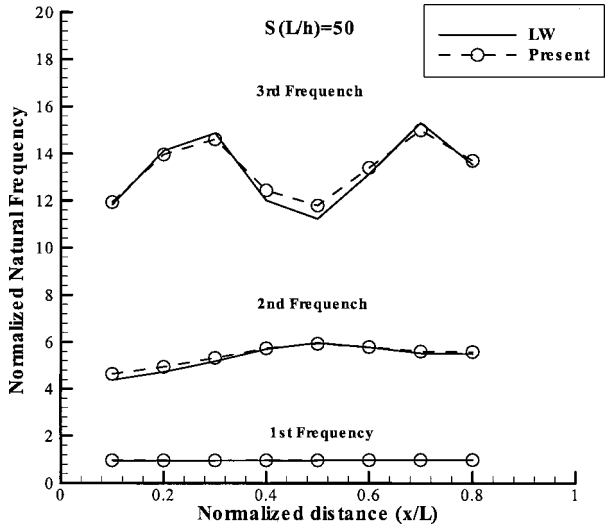

Fig. 14 Normalized natural frequency versus normalized distance for [0/90/90/0] composite with $S=50$

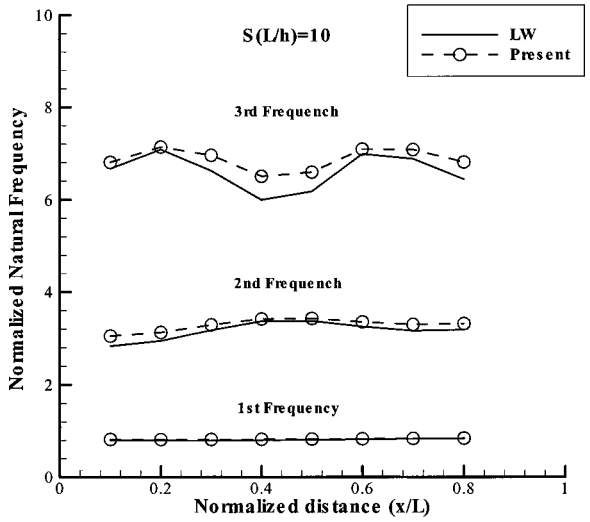

Fig. 15 Normalized natural frequency versus normalized distance for [0/90/90/0] composite with $S=10$

et al. [10] in Tables 2 and 3. Tables 2 and 3 show the effect of delamination size and interface location on the fundamental natural frequencies of the beam. As it is shown, the results of the present theory show good agreements with those of experiment and the analytical results by Shen et al. [10].

Next, a cantilever beam-plate containing three delaminations is considered. In this example, the stacking sequence of the delaminated composite is [0//90//90//0] symmetric layup. The configuration of a cantilever beam-plate with three delaminations is given in Fig. 12. Figures 13, 14, and 15 present the normalized natural frequencies with respect to the first natural frequency of the classical lamination theory for perfectly bonded composites. As shown, the present theory gives comparable results with the layerwise theory for the natural frequencies for various delamination sizes and length-to-thickness ratios. However, in the case of the thick plate ($S=10$), as shown in Fig. 15, the third natural frequency predicted by the present theory is higher than those of the layerwise theory. This is due to the displacement field of the present theory which cannot allow the sign change of the shear angle at the delamination interfaces.

7 Conclusions

A higher-order zig-zag theory has been developed to study the laminated composite plates with multiple delaminations. The present theory can provide accurate predictions of buckling loads and natural frequencies for various types of delaminations in the moderate thick plate range. The present theory determines the number of degrees-of-freedom of an undelaminated zone independently of both the number of layers and the number of delaminations. In the delaminated zone, the minimal number of degrees-of-freedom are still retained. Thus this theory can be applied to the problems with many layers and multiple delaminations. However, the present theory has its own drawbacks. In the case of a thick plate with large-sized delaminations, the prediction of buckling loads is overestimated compared to the elasticity solutions. In this case, the mixed buckling mode is dominant and it requires opposite signs of transverse shear strains of delaminated upper and lower parts. However, the present displacement field provides stiffer solutions than those of elasticity since the displacement field of the present theory does not allow sign changes of the transverse shear strain at the delamination interfaces.

Acknowledgment

This work was supported by Brain Korea 21 Project.

References

[1] Lo, K. H., Christensen, R. M., and Wu, E. M., 1977, "A Higher-Order Theory of Plate Deformation, Part 2: Laminated Plates," ASME J. Appl. Mech., **44**, pp. 669–676.
[2] Reddy, J. N., 1987, "A Generalization of Two-Dimensional Theories of Laminated Plates," Commun. Appl. Numer. Methods, **3**, pp. 173–180.
[3] Di Sciuva, M., 1986, "Bending, Vibration and Buckling of Simply Supported Thick Multilayered Orthotropic Plates: An Evaluation of a New Displacement Model," J. Sound Vib., **105**, pp. 425–442.
[4] Noor, A. K., and Burton, W. S., 1989, "Assessment of Shear Deformation Theories for Multilayered Composite Plates," Appl. Mech. Rev., **42**, pp. 1–13.
[5] Kapania, R. K., and Raciti, S., 1989, "Recent Advanced in Analysis of Laminated Beams and Plates," AIAA J., **27**, pp. 923–946.
[6] Reddy, J. N., and Robbins, D. H. Jr., 1994, "Theories and Computational Models for Composite Laminates," Appl. Mech. Rev., **47**, pp. 147–169.
[7] Simitses, G. J., 1995, "Delamination Buckling of Flat Laminates," *Buckling and Postbuckling of Composite Plates*, G. J. Turvey and I. H. Marshall, eds., Chapman & Hall, London, pp. 299–328.
[8] Wang, J. T. S., Liu, Y. Y., and Gibby, J. A., 1982, "Vibrations of Split Beams," J. Sound Vib., **84**, pp. 491–502.
[9] Wang, J. T. S., and Lin, C. C., 1995, "Vibration of Beam-Plates Having Multiple Delaminations," *Proceedings of the AIAA/ASME/ASCE/AHS/ASC 36th Structures, Structural Dynamics and Materials Conference*, New Orleans, LA, AIAA, Reston, VA, pp. 3126–3133.
[10] Shen, M.-H. H., and Grady, J. E., 1992, "Free Vibration of Delaminated Beams," AIAA J., **30**, pp. 1361–1370.
[11] Gummadi, L. N. B., and Hanagud, S., 1995, "Vibration Characteristics of Beams With Multiple Delaminations," *Proceedings of the AIAA/ASME/ASCE/*

AHS/ASC 36th Structures, Structural Dynamics and Materials Conference, New Orleans, LA, AIAA, Reston, VA, pp. 140–150.
[12] Chattopadhyay, A., Dragomir-Daescu, D., and Gu, H., 1999, ''Dynamics of Delaminated Smart Composite Cross-Ply Beams,'' Smart Mater. Struct., **8**, pp. 92–99.
[13] Seeley, C. E., and Chattopadhyay, A., 1999, ''Modeling of Adaptive Composites Including Debonding,'' Int. J. Solids Struct., **36**, pp. 1823–1843.
[14] Islam, A. S., and Craig, K. C., 1994, ''Damage Detection in Composite Structures Using Piezoelectric Materials,'' Smart Mater. Struct., **3**, pp. 318–328.
[15] Lee, J., Gürdal, Z., and Griffin, O. H., 1993, ''Layer-Wise Approach for the Bifurcation Problem in Laminated Composites With Delaminations,'' AIAA J., **31**, pp. 331–338.
[16] Cho, M., and Kim, J.-S., 1997, ''Bifurcation Buckling Analysis of Delaminated Composites Using Global-Local Approach,'' AIAA J., **35**, pp. 1673–1676.
[17] Cho, M., and Lee, S.-G., 1998, ''Global/Local Analysis of Laminated Composites With Multiple Delaminations of Various Shapes,'' *Proceedings of the AIAA/ASME/ASCE/AHS/ASC 39th Structures, Structural Dynamics and Materials Conference*, Long Beach, CA, AIAA, Reston, VA, pp. 76–86.
[18] Kim, J.-S., and Cho, M., 1999, ''Postbuckling of Delaminated Composites Under Compressive Loads Using Global-Local Approach,'' AIAA J., **37**, pp. 774–777.
[19] Cheng, Z-q., Jemah, A. K., and Williams, F. W., 1996, ''Theory for Multilayered Anisotropic Plates With Weakened Interfaces,'' ASME J. Appl. Mech., **63**, pp. 1019–1026.
[20] Di Sciuva, M., 1997, ''Geometrically Nonlinear Theory of Multilayered Plates With Interlayer Slips,'' AIAA J., **35**, pp. 1753–1759.
[21] Chattopadhyay, A., and Gu, H., 1994, ''New Higher Order Theory in Modeling Delamination Buckling of Composite Laminates,'' AIAA J., **32**, pp. 1709–1716.
[22] Cho, M., and Parmerter, R. R., 1992, ''An Efficient Higher-Order Plate Theory for Laminated Composites,'' Composite Structures, **20**, pp. 113–123.
[23] Cho, M., and Parmerter, R. R., 1993, ''Efficient Higher Order Composite Plate Theory for General Lamination Configurations,'' AIAA J., **31**, pp. 1299–1306.
[24] Simitses, G. J., Sallam, S., and Yin, W. L., 1985, ''Effect of Delamination of Axially Loaded Homogeneous Laminated Plates,'' AIAA J., **23**, pp. 1437–1444.
[25] Chen, H. P., 1991, ''Shear Deformation Theory for Compressive Delamination Buckling and Growth,'' AIAA J., **29**, pp. 813–819.
[26] Gu, H., and Chattopadhyay, A., 1998, ''Elasticity Approach for Delamination Buckling of Composite Beam Plates,'' AIAA J., **36**, pp. 2543–2551.

H.-L. Yeh
Department of Civil Engineering,
I-Shou University,
Kaohsiung County, Taiwan 84008, ROC
e-mail: hlyeh@isu.edu.tw

H.-Y. Yeh[1]
Department of Mechanical
and Aerospace Engineering,
California State University,
Long Beach, CA 90840-8305
e-mail: hyyeh@csulb.edu

Effect of Transverse Moduli on Through-Thickness Hygrothermal Expansion Coefficients of Composite Laminates

In practical analysis, under a plane stress condition, a unidirectional lamina can be assumed with $E_2=E_3$ from geometrical symmetry consideration. However, from an academic point of view, it is interesting to study the case of a lamina with $E_2\neq E_3$. In this paper the preliminary results of the physical phenomenon about the effect of different transverse moduli E_2 and E_3 on the through-thickness thermal expansion coefficients α_z of quasi-isotropic composite laminates is presented. [DOI: 10.1115/1.1410937]

Introduction

Composites for airframe structures must be designed to withstand the great diversity of terrestrial environments encountered in a variety of operations. A typical environmental effect is the hot/wet condition in which the elasticity and strength design allowables of the composite may reduce as much as 10 percent to 20 percent (50 percent reduction occur in some wet layup materials). In the terrestrial environment the combined effects of temperature and humidity must be considered when assessing long-term structural integrity ([1]).

In some points of view, composite materials can be considered as a structure ([2]). Since a number of laminae consist of the fibrous composite laminate, the mechanical behavior of the laminate is dependent on the lamina material properties and stacking sequences as well as lamina hygrothermal effects.

In a quasi-isotropic laminate the extensional stiffness matrix [*A*] is isotropic, but, in general, the other coupling and bending stiffness matrices [*B*] and [*D*], respectively, may not have an isotropic form ([3–5]). Both three-ply [−60 deg/0 deg/ 60 deg] layup and four-ply [−45 deg/0 deg/45 deg/90 deg] layup have only isotropic extensional stiffness matrix [*A*], and the other stiffness matrices [*B*] and [*D*] do not have isotropic form ([3–5]).

According to Wu and Avery [6] the isotropic laminates can be obtained from certain ply orientations and sequences with at least 36 plies. Yeh et al. ([7,8]) indicated that a fairly isotropic laminate is reached if the number of arbitrary orientation plies in the laminate is 40 or more. In a recent paper, Yeh [9] presented that a quasi-isotropic and quasi-homogeneous laminate can be obtained from a dimensionless mathematical model with 40 or more plies of arbitrary orientation. In other words, this dimensionless mathematical model of an isotropic laminate has the isotropic stiffness matrix [*A*], the null coupling stiffness matrix [*B*], and the isotropic bending stiffness matrix [*D*]. Ishikawa and Chou [10] used three physical models to examine the in-plane thermal expansion coefficients and thermal bending coefficients of fabric composites. Miller [11] indicated that the thermal expansion coefficients for laminates can be obtained from invariant lamina properties. Yeh et al. [12] reported that the mean values of the through-thickness coefficients of hygrothermal expansion in a laminate with 40 random plies or more are close to those values obtained from the analytical formulation.

In this paper, the preliminary results of the physical phenomenon about the effect of different transverse moduli E_2 and E_3 on the through-thickness thermal expansion coefficients α_z of quasi-isotropic composite laminates is presented. A dimensionless mathematical model has been used to study the influence of the various transverse elastic moduli E_2 and E_3 of lamina on the through-thickness thermal expansion coefficients of the laminate.

Results and Discussions

Both three-ply [−60 deg/0 deg/60 deg] layup and four-ply [−45 deg/0 deg/45 deg/90 deg] layup have only isotropic extensional stiffness matrix [*A*], and the other stiffness matrices [*B*] and [*D*] do not have isotropic form ([3–5]).

Although the model of Fukunaga has the isotropic extensional stiffness matrix [*A*], the null coupling stiffness matrix [*B*], and the isotropic bending stiffness matrix [*D*], the model of Fukunaga is obtained from certain ply orientations and sequences with at least 36 or more plies. Therefore, the models of Fukunaga can only evaluate the values of the through-thickness thermal expansion coefficients for the real composite materials with specific orientations.

Since the dimensionless mathematical model is obtained from a simple random statistical approach, in the mathematical point of view, it is more generalized in doing the analysis of physical phenomenon and evaluation of mechanical behavior about real composite materials with general ply orientations. Therefore, the dimensionless mathematical model has the advantages of not only doing the complete investigation of physical phenomenon and mechanical behavior about general types of real composite materials but also evaluating the values of the physical parameter (i.e., the through-thickness thermal expansion coefficients) for the specific types of real composite materials.

Intuitively, if ply orientations are random, it would expect an isotropic laminate. Therefore, an analytical formulation for the through-thickness coefficient of thermal expansion of an isotropic laminate based on the hygrothermal-elastic lamination theory can be derived. The detailed derivation of this formulation can be found in [12].

In order to study the physical phenomenon about the effect of different transverse moduli E_2 and E_3 on the through-thickness thermal expansion coefficients α_z of the composite laminates, both the case of $E_2=E_3$ and the case of $E_2\neq E_3$ are considered and the dimensionless mathematical model is used.

---

[1]To whom correspondence should be addressed.

Contributed by the Applied Mechanics Division of THE AMERICAN SOCIETY OF MECHANICAL ENGINEERS for publication in the ASME JOURNAL OF APPLIED MECHANICS. Manuscript received by the ASME Applied Mechanics Division, January 3, 2001; final revision, June 23, 2001. Associate Editor: A. K. Mal. Discussion on the paper should be addressed to the Editor, Professor Lewis T. Wheeler, Department of Mechanical Engineering, University of Houston, Houston, TX 77204-4792, and will be accepted until four months after final publication of the paper itself in the ASME JOURNAL OF APPLIED MECHANICS.

The composite laminates made of plies with different transverse moduli will display various characteristics and values of the through-thickness thermal expansion coefficients α_z. It shows that in the case of $E_3=E_2$ with the fixed values of the rest parameters (such as G_{12}, ν_{31}, $\alpha_1, \ldots$ etc.) the values of α_z decrease along with the increase of the values of E_2. But, in the case of $E_2\neq E_3$ with the fixed values of the other parameters (such as G_{12}, ν_{31}, $\alpha_1, \ldots$ etc.), the values of α_z increase along with the increase of the values of E_2.

Conclusions

The preliminary results of the physical phenomenon about the effect of different transverse moduli E_2 and E_3 on the through-thickness thermal expansion coefficients α_z of quasi-isotropic composite laminates are investigated. The approach of a dimensionless mathematical model analysis has been used to study the influence of the various transverse elastic moduli E_2 and E_3 of a lamina on the through-thickness thermal expansion coefficients of the laminate. The obtained dimensionless results can be used to cover any type of real composite materials.

In practical analysis, under a plane-stress condition a unidirectional lamina can be assumed with $E_2=E_3$ from geometrical symmetry consideration. However, from academic point of view, it is interesting to study the case of a lamina with $E_2\neq E_3$. Preliminary results based on the $E_2\neq E_3$ consideration are presented in this paper and a further investigation and detail discussion about this problem will be presented in another paper.

In the case of $E_3=E_2$, with the fixed values of the rest parameters (such as G_{12}, ν_{31}, $\alpha_1, \ldots$ etc.), the values of α_z decrease along with the increase of the values of E_2. But, in the case of $E_2\neq E_3$, with the fixed values of the other parameters (such as G_{12}, ν_{31}, $\alpha_1, \ldots$ etc.), the values of α_z increase along with the increase of the values of E_2.

The results from the analysis of this dimensionless mathematical model will provide general guidelines for designing the values of the through-thickness thermal expansion coefficient of the composite laminates to fit various environmental conditions in engineering applications.

References

[1] Michael C., and Niu, Y., 1992, *Composite Airframe Structures*, Conmilit Press Ltd.

[2] Zhang, R., Yeh, H.-L., and Yeh, H.-Y., 1998, "A Preliminary Study of Negative Poisson's Ratio of Laminated Fiber Reinforced Composites," J. Reinf. Plast. Compos., **17**, No. 18, pp. 1651–1664.

[3] Jones, R. M., 1998, *Mechanics of Composite Materials*, 2nd Ed., Taylor & Francis, London.

[4] Agarwal, B. D., and Broutman, L. J., 1990, "Analysis and Performance of Fiber Composites," 2nd Ed., John Wiley and Sons, New York.

[5] Gibson, R. F., 1994, *Principles of Composite Material Mechanics*, McGraw-Hill, New York.

[6] Wu, K. M., and Avery, B. L., 1992, "Fully Isotropic Laminates and Quasi-Homogeneous Anisotropic Laminates," J. Compos. Mater., **26**, No. 14, pp. 2107–2117.

[7] Yeh, H.-L., Huang, T., and Yeh, H.-Y., 1992, "An Optimization Study of Randomly-Oriented Composite Laminate Made of Corneal Material Subjected to Plane Stress Condition," J. Reinf. Plast. Compos., **11**, No. 6, pp. 661–669.

[8] Yeh, H.-L., and Yeh, H.-Y., 1992, "A Further Investigation of the Isotropy of Randomly-Oriented Composite Laminates," J. Reinf. Plast. Compos., **11**, No. 12, pp. 1431–1445.

[9] Yeh, H.-L., 2000, "A Dimensionless Mathematical Model for Studying the Physical Parameters of Composite Laminates—Part I," Int. J. Solids Struct., accepted for publication.

[10] Ishikawa, T., and Chou, T.-W., 1983, "In-Plane Thermal Expansion and Thermal Bending Coefficients of Fabric Composites," J. Compos. Mater., **17**, pp. 92–104.

[11] Miller, A. K., 1980, "Thermal Expansion Coefficients for Laminates Obtained From Invariant Lamina Properties," Fibre Sci. Technol., **13**, pp. 397–409.

[12] Yeh, H.-L., and Yeh, H.-Y., 2000, "The Variation in Through-Thickness Hygrothermal Expansion Coefficients of Laminate Composites," J. Compos. Mater., **34**, No. 14, pp. 1200–1215.

Robust Adaptive Neural Estimation of Restoring Forces in Nonlinear Structures

E. B. Kosmatopoulos
School of Engineering,
University of Southern California,
Los Angeles, CA 90089-2563

A. W. Smyth
School of Engineering and Applied Science,
Columbia University,
New York, NY 10027-6699

S. F. Masri
School of Engineering,
University of Southern California,
Los Angeles, CA 90089-2531
Mem. ASME

A. G. Chassiakos
School of Engineering,
California State University,
Long Beach, CA 90840-5602

The availability of methods for on-line estimation and identification of structures is crucial for the monitoring and active control of time-varying nonlinear structural systems. Adaptive estimation approaches that have recently appeared in the literature for on-line estimation and identification of hysteretic systems under arbitrary dynamic environments are in general model based. In these approaches, it is assumed that the unknown restoring forces are modeled by nonlinear differential equations (which can represent general nonlinear characteristics, including hysteretic phenomena). The adaptive methods estimate the parameters of the nonlinear differential equations on line. Adaptation of the parameters is done by comparing the prediction of the assumed model to the response measurement, and using the prediction error to change the system parameters. In this paper, a new methodology is presented which is not model based. The new approach solves the problem of estimating/identifying the restoring forces without assuming any model of the restoring forces dynamics, and without postulating any structure on the form of the underlying nonlinear dynamics. The new approach uses the Volterra/Wiener neural networks (VWNN) which are capable of learning input/output nonlinear dynamics, in combination with adaptive filtering and estimation techniques. Simulations and experimental results from a steel structure and from a reinforced-concrete structure illustrate the power and efficiency of the proposed method. [DOI: 10.1115/1.1408614]

1 Introduction

1.1 Motivation. Developing robust adaptive strategies for the control of structures (including real-world civil structures) has been a topic of recent interest ([1]). The modeling and identification of nonlinear hysteretic systems are problems widely encountered in the structural dynamics field. Nonlinear hysteretic behavior is commonly seen in structures experiencing strong earthquake excitation, in aerospace structures incorporating joints, and in various micro-mechanics problems. Noteworthy studies of this problem are reported in the works of Caughey [2], Jennings [3], Iwan [4], Bouc [5], Iwan and Lutes [6], Masri [7], Wen [8], Masri and Caughey [9], Baber and Wen [10], Spanos [11], Toussi and Yao [12], Andronikou and Bekey [13], Spencer and Bergman [14], Vinogradov and Pivovarov [15], Iwan and Cifuentes [16], Jayakumar and Beck [17], Peng and Iwan [18], Yar and Hammond [19,20], Roberts and Spanos [21], Masri et al. [22], Loh and Chung [23], Benedettini et al. [24], Chassiakos et al. [25,26], Sato and Qi [27], and most recently Smyth et al. [28].

The motivation for exploring adaptive techniques in the context of structural control comes from the recognition that since structures behave nonlinearly when excited by strong motions, the implementation of conventional fixed controller strategies may prove to be naive. Often, the governing response properties only exhibit themselves for the first time when subjected to strong shaking. As a result of this, control strategies should incorporate flexible adaptive identification schemes which can quickly capture and emulate the essential response signature of a structural system and react accordingly. Of course, another key feature of adaptive techniques is that they can model time-varying behavior, such as structural deterioration which is often observed in civil structures during the course of strong ground excitation.

Although adaptive identification schemes have been investigated with this in mind ([25,26]), the work was limited to identifying certain classes of nonlinearities. Also the aforementioned approaches impose the assumption that the restoring forces are available for measurement. In this paper, the authors apply an adaptive artificial neural network identification technique, which can cope with a much broader family of unknown nonlinear response behaviors and does not assume that the restoring forces are available from measurements.

1.2 Scope. With the above discussion in mind, the authors have developed an efficient identification algorithm for handling general structural systems incorporating severe nonlinearities, including elements with time-varying hysteretic characteristics. Section 2 provides some background of adaptive estimation techniques and formulates the problem so that the proposed neural estimator can be applied to general structural systems using only acceleration measurements; Section 3 presents an application of the proposed method to a simulated structural model incorporating hysteretic elements; Section 4 presents experimental identification results from two representative systems; and Section 5 discusses and evaluates the performance of the method presented herein.

2 Problem Formulation and Neural Estimators

2.1 General Problem Formulation. Consider the generic complex structural system shown in Fig. 1. Assume that the structure can be subjected to support excitations $x_{01},\cdots,x_{0_{n_0}}$, force excitations $f_1,\cdots,f_{n_1}$, and control forces $u_1,\cdots,u_{n_1}$. The f's and the u's are applied directly to nodes on the structure at which response sensors are located. In other words, the acceleration response at locations $1,\cdots,n_1$ will be available for measurement. The internodal connections often behave nonlinearly, and their

Contributed by the Applied Mechanics Division of THE AMERICAN SOCIETY OF MECHANICAL ENGINEERS for publication in the ASME JOURNAL OF APPLIED MECHANICS. Manuscript received by the ASME Applied Mechanics Division, May 4, 2000; final revision, June 8, 2001. Associate Editor: J. W. Ju. Discussion on the paper should be addressed to the Editor, Prof. Lewis T. Wheeler, Department of Mechanical Engineering, University of Houston, Houston, TX 77204-4792, and will be accepted until four months after final publication of the paper itself in the ASME JOURNAL OF APPLIED MECHANICS.

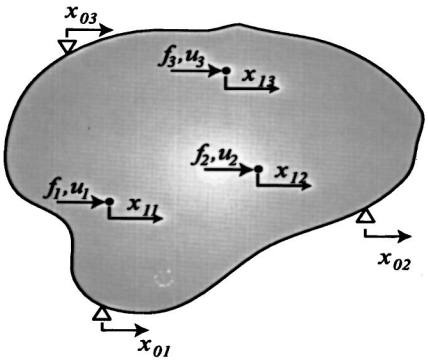

Fig. 1 General structural system, with discrete response measurement locations. The system can experience force excitation, and multiple support motions.

restoring force is denoted as $r_j(t)$ for the jth restoring element, $j=1,\cdots,n_e$. The reduced-order equation of motion for each active degree-of-freedom may be written as

$$m_i\ddot{x}_i+\sum_{j=1,\ldots,n_e}\pi_{ij}^r r_j=f_i+u_i \quad i=1,\cdots,n_1 \tag{1}$$

where n_e is the number of interconnections which could be made between active degrees-of-freedom $1,\cdots,n_1$ and support degrees-of-freedom $1,\cdots,n_0$. In the case of a completely general structure shown in Fig. 1, $n_e=(n_0+n_1)(n_0+n_1-1)/2$. The numbers π_{ij}^r are defined as follows:

$$\pi_{ij}^r=\begin{cases}+1 & \text{if the } j\text{th restoring element applies a positive force to the } i\text{ th degree-of-freedom}\\ 0 & \text{if the } j\text{th restoring element applies no force to the } i\text{ th degree-of-freedom}\\ -1 & \text{if the } j\text{th restoring element applies a negative force to the } i\text{ th degree-of-freedom}\end{cases}$$

Typically, from inspection of the topology of a structure, one may quickly disregard certain interconnections between nodal locations. If, for example, the discrete three-degree-of-freedom model shown in Fig. 2 is considered, then the equation of motion for this system may be written as follows:

$$\begin{aligned}m_1\ddot{x}_1+r_1-r_2-r_3&=f_1+u_1\\ m_2\ddot{x}_2+r_2-r_4+r_6&=f_2+u_2\\ m_3\ddot{x}_3+r_3-r_5+r_4&=f_3+u_3.\end{aligned} \tag{2}$$

In this case, using the notation of Eq. (1), the π_{ij}^r are defined by the following matrix (which is of order 3×6 or $n_1\times n_e$)

$$\pi^r=\begin{bmatrix}+1 & -1 & -1 & 0 & 0 & 0\\ 0 & +1 & 0 & -1 & 0 & +1\\ 0 & 0 & +1 & +1 & -1 & 0\end{bmatrix}. \tag{3}$$

In general, the internodal (element) relative displacements for each element j, can be written together in a vector form as the product of a connectivity matrix $\mathbf{C}$ and a vector containing the displacements of the active degrees-of-freedom and the support motions:

$$\mathbf{q}=\mathbf{C}\mathbf{x}=[(\pi^r)^T\vdots(\pi^s)^T]\begin{bmatrix}x_{11}\\ x_{12}\\ \vdots\\ x_{1n_1}\\ \cdots\\ x_{01}\\ x_{02}\\ \vdots\\ x_{0_{n_0}}\end{bmatrix} \tag{4}$$

where $\mathbf{q}$ is the vector of internodal relative displacements, of order $(n_e\times 1)$, $\mathbf{C}$ is of order $(n_e\times(n_1+n_0))$, $(\pi^r)^T$ is of order $(n_e\times n_1)$, and $(\pi^s)^T$ is of order $(n_e\times n_0)$. For example, for the three-degree-of-freedom problem in Fig. 2 this would be

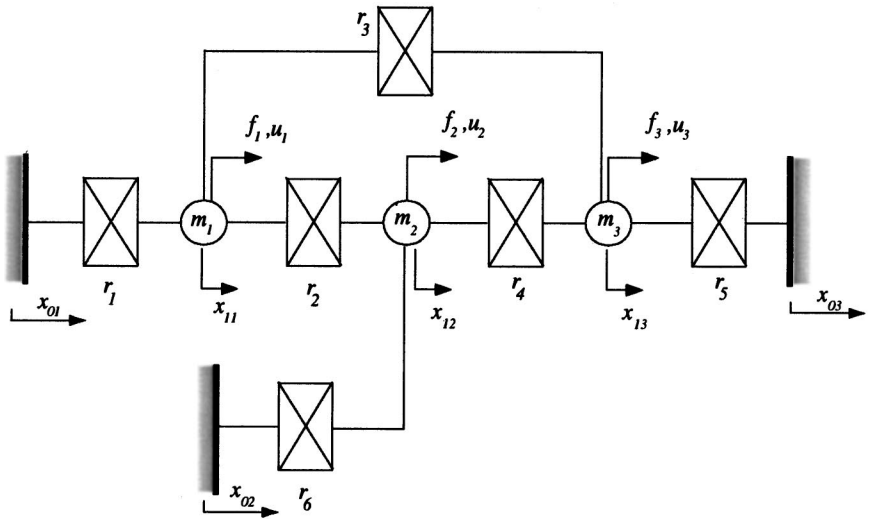

Fig. 2 Three-degree-of-freedom structural system, with discrete response measurement locations. The system can experience force excitation, and multiple support motions.

$$\begin{bmatrix} q_1 \\ q_2 \\ q_3 \\ q_4 \\ q_5 \\ q_6 \end{bmatrix} = \left[\begin{array}{ccc|ccc} 1 & 0 & 0 & -1 & 0 & 0 \\ -1 & 1 & 0 & 0 & 0 & 0 \\ -1 & 0 & 1 & 0 & 0 & 0 \\ 0 & -1 & 1 & 0 & 0 & 0 \\ 0 & 0 & -1 & 0 & 0 & 1 \\ 0 & 1 & 0 & 0 & -1 & 0 \end{array}\right] \begin{bmatrix} x_{11} \\ x_{12} \\ x_{13} \\ x_{01} \\ x_{02} \\ x_{03} \end{bmatrix}. \tag{5}$$

The objective of any control design is to select the control forces u_i such that some measures of displacements and velocities are kept small. In this study, two commonly encountered excitation scenarios will be considered:

- Excitation Scenario 1: Multiple independent support motions with or without multiple force excitation.
- Excitation Scenario 2: Single support motion with or without multiple force excitation. (Note: this could be all supports moving in unison, or could also be all supports fixed.)

For Scenario 1, which is the most general situation, the quantities to be minimized (labeled generically as the y_j's and $\dot{y}_j$'s) will be the internodal displacements and their velocities, i.e., the q_j's and $\dot{q}_j$'s. For this case then

$$\begin{aligned} y_j &= \mathbf{C}_j \mathbf{x} = q_j \\ \dot{y}_j &= \mathbf{C}_j \dot{\mathbf{x}} = \dot{q}_j \end{aligned} \tag{6}$$

where $\mathbf{C}_j$ is just the jth row of $\mathbf{C}$. Notice also that $\mathbf{y}$ is of order n_e in this case.

For Scenario 2, which involves a single support motion excitation, one can simplify the previous situation and minimize the displacements and velocities relative to the (single) support motion, in other words

$$\begin{aligned} y_j &= x_j - x_{01} \\ \dot{y}_j &= \dot{x}_j - \dot{x}_{01}. \end{aligned} \tag{7}$$

Notice that $\mathbf{y}$ is only of order n_1 in this case. Notice also that, because the support motions are all the same, any x_0 can be used to determine the relative motions. For the special case when the supports are fixed (i.e., $x_{01}=0$), Eq. (7) simplifies to minimizing the absolute displacements and velocities of the active degrees-of-freedom:

$$\begin{aligned} y_j &= x_j \\ \dot{y}_j &= \dot{x}_j. \end{aligned} \tag{8}$$

As it can be seen from the system equations in Eq. (1), knowledge of the effect of the restoring forces r_j is essential for the development of efficient control algorithms. In many realistic situations, the restoring forces are not available for measurement. In this case, we need an appropriate estimation/identification algorithm for estimating these forces. The purpose of this paper is to develop and evaluate such an algorithm.

2.2 Filtered Error. Let us define the filtered error $y_{f,i}$ as follows:

$$y_{f,i} = \dot{y}_i + \overline{\kappa} y_i \tag{9}$$

where $\overline{\kappa}$ is a positive design constant. It can be shown ([29]) that the definition (9) has two properties: (i) if $y_{f,i}=0$ then the $y_i, \dot{y}_i$ converge to zero exponentially; and (ii) if $|y_{f,i}| \leq \mathcal{C}$ for some positive constant $\mathcal{C}$, then $y_i, \dot{y}_i$ converge exponentially to the sets $\{y_i(t): |y_i(t)| \leq 1/\overline{\kappa}\mathcal{C}\}$ and $\{\dot{y}_i(t): |\dot{y}_i(t)| \leq 2\mathcal{C}\}$ respectively. In other words, if the filtered error $y_{f,i}$ is small and bounded by a constant C, then $y_i, \dot{y}_i$ converge to a residual set whose radius is proportional to $\mathcal{C}$ and inversely proportional to the design constant $\overline{\kappa}$. Thus, instead of designing control algorithms to keep $y_i, \dot{y}_i$ small, they can be designed to keep the filtered error $y_{f,i}$ small.

2.2.1 Filtered Error for Excitation Scenario 1. For the most general case, defined above as Excitation Scenario 1, there will be two kinds of filtered error expressions: one which comes from the relative motion between two active degrees-of-freedom and the second which comes from the relative motion between an active degree-of-freedom and a support degree-of-freedom. In general, differentiating $y_{f,i}$, with respect to time and taking into account Eqs. (1), (6), and (9), results in

$$\begin{aligned} \dot{y}_{f,i} &= \ddot{y}_i + \overline{\kappa} \dot{y}_i \\ &= \mathbf{C}_i \ddot{\mathbf{x}} + \overline{\kappa} \mathbf{C}_i \dot{\mathbf{x}} \end{aligned} \tag{10}$$

If $\mathbf{C}_i$ only combines active degrees-of-freedom say x_{1l} and x_{1k}, then the derivative of the filtered error becomes

$$\begin{aligned} \dot{y}_{f,i} &= c_{il}\ddot{x}_{1l} + c_{ik}\ddot{x}_{1k} + \overline{\kappa}(c_{il}\dot{x}_{1l} + c_{ik}\dot{x}_{1k}) \\ &= \frac{c_{il}}{m_l}(-\pi_l^r \mathbf{r} + f_l + u_l) + \frac{c_{ik}}{m_k}(-\pi_k^r \mathbf{r} + f_k + u_k) \\ &\quad + \overline{\kappa}(c_{il}\dot{x}_{1l} + c_{ik}\dot{x}_{1k}) \\ &= \frac{c_{il}}{m_l}(u_l) + \frac{c_{ik}}{m_k}(u_k) + \chi_i \end{aligned} \tag{11}$$

where π_l^r and π_k^r are, respectively, the lth and kth row of matrix π^r, and χ_i denotes the *combined effect* of restoring forces and the direct force excitations in Eq. (11), defined as

$$\chi_i = \frac{c_{il}}{m_l}(-\pi_l^r \mathbf{r} + f_l) + \frac{c_{ik}}{m_k}(-\pi_k^r \mathbf{r} + f_k) + \overline{\kappa}(c_{il}\dot{x}_{1l} + c_{ik}\dot{x}_{1k}). \tag{12}$$

By setting $a_i \triangleq 1/m_l$, and $b_i \triangleq 1/m_k$ for notational convenience, Eq. (11) can be rewritten as follows:

$$\dot{y}_{f,i} = \chi_i + a_i(c_{il}u_l) + b_i(c_{ik}u_k). \tag{13}$$

The terms a_i, b_i, and χ_i are the unknown terms needed to be estimated.

If, however, $\mathbf{C}_i$ combines an active degree-of-freedom say x_{1l} and a support degree-of-freedom say x_{0k}, then, following the same procedure as above, the derivative of the filtered error becomes

$$\begin{aligned} \dot{y}_{f,i} &= c_{il}\ddot{x}_{1l} + c_{ik}\ddot{x}_{0k} + \overline{\kappa}(c_{il}\dot{x}_{1l} + c_{ik}\dot{x}_{0k}) \\ &= \frac{c_{il}}{m_l}(-\pi_l^r \mathbf{r} + f_l + u_l) + c_{ik}\ddot{x}_{0k} + \overline{\kappa}(c_{il}\dot{x}_{1l} + c_{ik}\dot{x}_{0k}) \\ &= \frac{c_{il}}{m_l}(u_l) + \chi_i \end{aligned} \tag{14}$$

where now

$$\chi_i = \frac{c_{il}}{m_l}(-\pi_l^r \mathbf{r} + f_l) + c_{ik}\ddot{x}_{0k} + \overline{\kappa}(c_{il}\dot{x}_{1l} + c_{ik}\dot{x}_{0k}) \tag{15}$$

and

$$\dot{y}_{f,i} = \chi_i + a_i(c_{il}u_l). \tag{16}$$

2.2.2 Filtered Error for Excitation Scenario 2. The expression for the filtered error in the case of uniform support motion is simpler than that in the more general Excitation Scenario 1 which involved the possibility of multiple support motions. Taking Eq. (7), differentiating with respect to time, and following the same procedure as before, yields

$$\begin{aligned} \dot{y}_{f,i} &= \ddot{y}_i + \overline{\kappa}\dot{y}_i \\ &= (\ddot{x}_i - \ddot{x}_{01}) + \overline{\kappa}(\dot{x}_i - \dot{x}_{01}) \\ &= \frac{1}{m_l}(-\pi_l^r \mathbf{r} + f_l + u_l) - \ddot{x}_{01} + \overline{\kappa}(\dot{x}_i - \dot{x}_{01}) \end{aligned}$$

$$= \frac{1}{m_l}(u_l) + \chi_i$$

$$= a_i(u_l) + \chi_i \tag{17}$$

where $a_i \triangleq 1/m_l$, and

$$\chi_i = \frac{1}{m_l}(-\pi_l^r \mathbf{r} + f_l) - \ddot{x}_{01} + \overline{\kappa}(\dot{x}_i - \dot{x}_{01}). \tag{18}$$

2.3 Neural Estimators. The restoring forces r_j may possess nonlinear hysteretic characteristics. In general, the dynamics of the restoring forces can be described by means of nonlinear differential equations of the form

$$\dot{r}_j = \mathcal{Q}_j(\mathbf{r}, \mathbf{x}_1, \dot{\mathbf{x}}_1, \mathbf{u}, \mathbf{x}_0, \dot{\mathbf{x}}_0) \quad j = 1, \ldots, n_e \tag{19}$$

where $\mathbf{r}$, $\mathbf{u}$, $\mathbf{x}_1$, and $\mathbf{x}_0$ are the restoring force vector, control force vector, active degree-of-freedom and support motion vectors respectively, and $\mathcal{Q}_j$ is a nonlinear continuous function, capable of capturing nonlinear hysteretic effects. Many different models for the function $\mathcal{Q}_j$ have been proposed in the literature. As an example, in Chassiakos et al. [26], an augmented Bouc-Wen model ([30]) was used:

$$r_j = kq_j + c\dot{q}_j + dq_j^3 - \int_0^t (1/\eta)[\nu(\beta)|\dot{q}_j||r_j|^{n-1} r_j - \gamma \dot{q}_j |r_j|^n] dt \tag{20}$$

where q_j is the relative displacement of element j.

In Smyth et al. [28] the parameter clusters k, c, d, $(1/\eta)\nu\beta$ and $(1/\eta)\nu\gamma$ (which determine the nonlinear and hysteretic characteristics of the restoring force) were estimated by an on-line adaptive estimation technique. In this paper, however, no particular model will be assumed for the function $\mathcal{Q}_j$, but rather it will be considered to be an *unknown* function, whose effect needs to be estimated.

Since the restoring forces r_j as well as the functions $\mathcal{Q}_j$ are assumed unknown, we need to estimate their effect on the system dynamics in Eq. (1). Instead of estimating each of the restoring forces r_j we will estimate their *combined effect* in Eqs. (11), (14), or (17), i.e., we will estimate the term χ_i. We do so, since in many cases it is very difficult, if possible at all, to estimate the effect of each of the restoring forces and unknown signals, because the number of unknowns (restoring forces and unknown signals) is larger than the number of equations in Eqs. (11), (14), or (17).

The main challenge in designing adaptive algorithms for estimating the unknown terms in Eq. (13) is the time-varying term χ_i, which depends nonlinearly and dynamically on the vectors $\mathbf{x}_1$, $\dot{\mathbf{x}}_1$, $\mathbf{u}$, $\mathbf{x}_0$, $\dot{\mathbf{x}}_0$. This unknown nonlinear time-varying term χ_i will be estimated using Volterra/Wiener neural networks (VWNN) and their approximation properties established in Kosmatopoulos [31]. The VWNN consists of a linear multi-input multi-output (MIMO) stable dynamical system connected in cascade with a linear-in-the-weights neural network, as shown in Fig. 3.

The dynamics of the linear MIMO system are given as follows:

$$\xi = H(s)\zeta \tag{21}$$

where ζ is the input vector to the VWNN, ξ is the output of the linear MIMO system, and $H(s)$ is a stable transfer function matrix (here, s denotes the Laplace operator). The linear-in-the-weights neural network is described as follows:

$$\eta = W^\tau \phi(\xi) \tag{22}$$

where η is the output of the neural network, W denotes the matrix of the synaptic weights of the neural network, ξ is the output of the linear filter in Eq. (21), and ϕ is a vector of the nonlinear activation functions of the neural network. A detailed description of linear-in-the-weights neural networks and VWNN's is given in the Appendices.

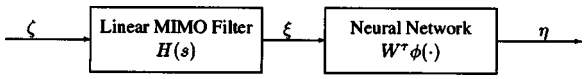

Fig. 3 Block diagram of the Volterra Wiener neural network (VWNN)

Assuming that measurements of the accelerations are available at the support locations and at the active degrees-of-freedom, the VWNN input ζ is chosen as $\zeta = [\ddot{\mathbf{x}}_1 \; \mathbf{u} \; \ddot{\mathbf{x}}_0]^T$. Using the approximation results of Kosmatopoulos [31], it can be shown that the unknown term χ_i can be approximated by a VWNN. More precisely, if the χ_i and vectors $\ddot{\mathbf{x}}_1$, $\mathbf{u}$, and $\ddot{\mathbf{x}}_0$ are bounded and the dimensions of the vectors ξ and ϕ are large, then there exists a vector θ_i such that

$$\chi_i(t) = \theta_i^\tau \phi(\xi) + \nu_i(t). \tag{23}$$

Vector θ_i contains the same values as the neural network weight matrix W, where the weights have been concatenated into a single vector for ease of development. The term $\nu_i(t)$ is the so called "modeling error," i.e., it is a measure of how closely the representation $\theta_i^\tau \phi(\xi)$ can approximate the unknown term χ_i. The modeling error satisfies the following: the magnitude of ν_i is inversely proportional to the dimensions of the vectors ξ and ϕ. In other words, the modeling error can be made arbitrarily small by increasing the dimensions of the vectors ξ and ϕ.

Equation (23) can be rewritten using the most general form of χ_i from Eq. (13) as follows:

$$\dot{y}_{f,i} = \theta_i^\tau \phi(\xi) + \nu_i + a_i(c_{il}u_l) + b_i(c_{ik}u_k). \tag{24}$$

If we now define the variables $\phi_{a,i} \triangleq c_{il}u_l$, and $\phi_{b,i} \triangleq c_{ik}u_k$, we can rewrite Eq. (24) into the following compact form:

$$\dot{y}_{f,i} = \theta_i^\tau \phi_i + a_i \phi_{a,i} + b_i \phi_{b,i} + \nu_i. \tag{25}$$

Thus, we have transformed the relative motion dynamics into the form of Eq. (25), where the filtered error velocities are written as linear combinations of unknown constant parameters and known nonlinear functions plus a modeling error term ν_i. Recall also, that the $b_i\phi_{b,i}$ term occurs only for some filtered error terms in the Scenario 1 formulation. This term can be omitted for other cases.

Since system accelerations are easily available for direct measurement, we can assume that velocity and displacement estimates are also available through integration. Equation (25) is in the standard parameter estimation form, and will be used directly in the estimation procedure. The case where system displacements are measured rather than accelerations, can be treated in a similar manner using $\zeta = [\mathbf{x}_1 \; \mathbf{u} \; \mathbf{x}_0]^T$ as the input vector, and performing some additional signal processing to obtain an estimation equation in the form of Eq. (25).

2.4 Adaptive Law and Its Properties. Although different parameter estimation algorithms exist that can be used for the estimation of θ_i, a_i, and b_i, we will use a normalized gradient adaptive law with projection ([29,32–34]). There are two reasons for this choice: (1) Such an adaptive law keeps the parameter estimates bounded regardless of the boundedness properties of the signals x_i, ϕ_i, $\phi_{a,i}$, $\phi_{b,i}$, on the one hand, and (2) it can be appropriately designed so that the estimate of $a_i = 1/m_l$ and $b_i = 1/m_k$ are always positive, on the other. The property of the adaptive law to keep the estimate of $a_i = 1/m_l$ and $b_i = 1/m_k$ always positive is very crucial for the design of active control algorithms. The adaptive law is summarized as follows:

Estimation Model:

$$\hat{z}_i = \hat{\theta}_i^\tau \phi_i + \hat{a}_i \phi_{a,i} + \hat{b}_i \phi_{b,i} \tag{26}$$

Adaptive Laws:

$$\dot{\hat{\theta}}_i = \begin{cases} \gamma \epsilon_i \phi_i & \text{if } |\hat{\theta}_i| < \mathcal{M} \\ & \text{or if } |\hat{\theta}_i| = \mathcal{M} \text{ and } (\gamma \epsilon_i \phi_i)^\tau \hat{\theta}_i \leqslant 0 \\ \left(I - \dfrac{\hat{\theta}_i \hat{\theta}_i^\tau}{\hat{\theta}_i^\tau \hat{\theta}_i} \right) \gamma \epsilon_i \phi_i & \text{otherwise} \end{cases} \tag{27}$$

$$\dot{\hat{a}}_i = \begin{cases} \gamma \epsilon_i \phi_{a,i} & \text{if } \delta_{a1} < \hat{a}_i < \delta_{a2} \\ & \text{or if } \hat{a}_i = \delta_{a2} \text{ and } (\gamma \epsilon_i \phi_{a,i})^\tau \hat{a}_i \leqslant 0 \\ & \text{or if } \hat{a}_i = \delta_{a1} \text{ and } (\gamma \epsilon_i \phi_{a,i})^\tau \hat{a}_i \geqslant 0 \\ 0 & \text{otherwise} \end{cases} \tag{28}$$

$$\dot{\hat{b}}_i = \begin{cases} \gamma \epsilon_i \phi_{b,i} & \text{if } \delta_{b1} < \hat{b}_i < \delta_{b2} \\ & \text{or if } \hat{b}_i = \delta_{b2} \text{ and } (\gamma \epsilon_i \phi_{b,i})^\tau \hat{b}_i \leqslant 0 \\ & \text{or if } \hat{b}_i = \delta_{b1} \text{ and } (\gamma \epsilon_i \phi_{b,i})^\tau \hat{b}_i \geqslant 0 \\ 0 & \text{otherwise} \end{cases} \tag{29}$$

Normalized Estimation Error:

$$\epsilon_i = (z_i - \hat{z}_i)/\lambda^2$$

$$\lambda^2 = 1 + \phi_i^\tau \phi_i + \phi_{a,i}^2 + \phi_{b,i}^2 \tag{30}$$

where $\hat{z}_i$ is the estimate of $z_i = \dot{y}_{f,i}$, and $\hat{\theta}_i$, $\hat{a}_i$, $\hat{b}_i$ are the estimates of ϕ_i, a_i, and b_i, respectively, and γ, $\mathcal{M}$, δ are design positive constants. Parameter γ is the adaptive gain; $\mathcal{M}$ is a large positive constant bounding θ_i such that $|\theta_i| < \mathcal{M}$; and δ_{a1}, δ_{a2}, δ_{b1}, δ_{b2} are positive design constants (bounds for a_i and b_i), such that $\delta_{a1} < a_i = 1/m_l < \delta_{a2}$ and $\delta_{b1} < b_i = 1/m_k < \delta_{b2}$.

The adaptive law in Eqs. (26)–(30) guarantees the following properties:

1 The estimates $\hat{\theta}_i$, $\hat{a}_i$, $\hat{b}_i$ remain bounded, provided that $\delta_{a1} < \hat{a}_i(0) < \delta_{a2}$, $\delta_{b1} < \hat{b}_i(0) < \delta_{b2}$, and $|\hat{\theta}_i(0)| < M$.
2 The normalized estimation error ϵ_i converges to a residual set whose radius is proportional to the magnitude ν_i.
3 Let $\hat{\chi}_i \triangleq \hat{\theta}_i \phi_i$ denote the estimate of χ_i. Then the error $\epsilon_\chi \triangleq \chi_i - \hat{\chi}_i$ converges to a residual set whose radius is proportional to the magnitude ν_i.
4 The errors

$$\epsilon_a \triangleq a_i \phi_{a,i} - \hat{a}_i \phi_{a,i} \equiv (a_i - \hat{a}_i) c_{il} u_l$$
$$\epsilon_b \triangleq b_i \phi_{b,i} - \hat{b}_i \phi_{b,i} \equiv (b_i - \hat{b}_i) c_{il} u_l \tag{31}$$

converge to residual sets whose radii are proportional to the magnitude $\overline{\nu_i}$.

5 Let

$$\hat{y}_{f,i} \triangleq \int_0^t [\hat{\chi}_i(\tau) + \hat{a}_i(\tau) \phi_{a,i}(\tau) + \hat{b}_i(\tau) \phi_{b,i}(\tau)] d\tau$$

denote the estimate of the filtered error $y_{f,i}$. Then, the error $\epsilon_f \triangleq y_{f,i} - \hat{y}_{f,i}$ converges to a residual set whose radius is proportional to the magnitude ν_i.

It should be noted that the linearly parameterized model in Eq. (26) can be filtered on both sides of the equation yielding $\overline{z}$ and $\overline{\phi}$'s which are filtered versions of z and the ϕ's. This was done in Smyth et al. [28] to remove measurement noise before applying the adaptive law.

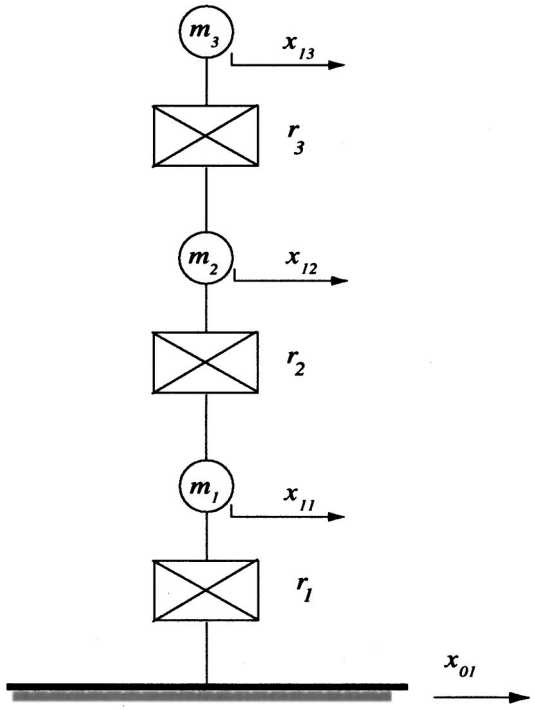

Fig. 4 Three-degree-of-freedom base excited structural system, with discrete response measurement locations

3 Application to a Nonlinear Structure

The proposed approach was tested through simulations on the base-excited three-degree-of-freedom chain-like model as in Fig. 4. This basic model can be thought of as a discrete approximation of a three-story building subjected to ground excitation. The base acceleration is chosen to be a band-limited random signal. The simulation model contains nonlinear hysteretic elements whose characteristics are considered unknown. The simulation model is based on the following system of differential equations (assuming that no control forces are applied; i.e., $u_i = 0$).

$$\begin{bmatrix} \ddot{x}_{13} \\ \dot{r}_3 \\ \ddot{x}_{12} \\ \dot{r}_2 \\ \ddot{x}_{11} \\ \dot{r}_1 \end{bmatrix} = \begin{bmatrix} (u_3 - r_3)/m_3 \\ A_3(\dot{x}_{13} - \dot{x}_{12}) + c_3((u_3 - r_3)/m_3 - (u_2 + r_3 - r_2)/m_2) + 3d_3(x_{13} - x_{12})^2(\dot{x}_{13} - \dot{x}_{12}) \\ \quad - B_3|\dot{x}_{13} - \dot{x}_{12}||r_3|^{n(3)-1} r_3 + g_3(\dot{x}_{13} - \dot{x}_{12})|r_3|^{n(3)} \\ (u_2 + r_3 - r_2)/m_2 \\ A_2(\dot{x}_{12} - \dot{x}_{11}) + c_2((u_2 + r_3 - r_2)/m_2 - (u_1 + r_2 - r_1)/m_1) + 3d_2(x_{12} - x_{11})^2(\dot{x}_{12} - \dot{x}_{11}) \\ \quad - B_2|\dot{x}_{12} - \dot{x}_{11}||r_2|^{n(2)-1} r_2 + g_2(\dot{x}_{12} - \dot{x}_{11})|r_2|^{n(2)} \\ (u_1 + r_2 - r_1)/m_1 \\ A_1(\dot{x}_{11} - \dot{x}_{01}) + c_1((u_1 + r_2 - r_1)/m_1 - \ddot{x}_{01}) + 3d_1(x_{11} - x_{01})^2(\dot{x}_{11} - \dot{x}_{01}) \\ \quad - B_1|\dot{x}_{11} - \dot{x}_{01}||r_1|^{n(1)-1} r_1 + g_1(\dot{x}_{11} - \dot{x}_{01})|r_1|^{n(1)} \end{bmatrix} \tag{32}$$

where A_i, B_i, c_i, d_i, g_i, $n_{(i)}$ are constant parameters that govern the hysteretic behavior of the restoring forces.

Assuming that acceleration measurements are available, three simulation experiments were performed:

Case 1 Using a wideband random signal as the base excitation $\ddot{x}_{01}(t)$, the system was simulated for 40 seconds. The neural estimator was also running for the entire 40-second duration. The network weights were allowed to adapt during this period. The purpose of this experiment is to simulate and test the adaptation method, and obtain the weights of the neural network that will approximate the unknown system.

Case 2 The same wideband random base excitation as in Case 1 was used, however, now the on-line adaptation is off. The weights of the neural network are fixed to the values obtained in Case 1. The purpose of this simulation is to validate the obtained neural model.

Case 3 While the neural network is still fixed to the values obtained in Case 1, a different base excitation is now used. This simulation further validates the obtained neural model. If the VWNN is indeed a good approximator of the unknown system dynamics, then it should perform well even in the case when the system is excited by a completely new random input.

Figure 5 plots the restoring forces (solid curve) and their estimates (dashed curves) produced by the neural estimator for simulation Case 1. Similarly Fig. 6 plots the accelerations (solid curve) and their estimates (dashed curves) produced by the neural estimator for simulation Case 1. The neural network weights are initially set to small random values. Although the adaptation is on from time $t=0$, it is seen from the figures that it takes about 15 seconds (a few response cycles) for the network weights to adapt and to estimate the restoring forces exactly. Figure 7 presents corresponding phase plane plots. The actual restoring forces (left subplots) and their estimates (right subplots) are plotted against the relative ''interstory'' displacements for the last 20 seconds of the simulation run, corresponding to Case 1. Only the last 20 seconds of the simulation are shown for purposes of readability (the initial transient effects of the adaptation are not plotted here).

Figure 8 plots the time-history of some representative neural estimator parameters. The VWNN parameters used for training, as well as the constants used in the adaptive law are presented in Table 1 where I_κ is the identity matrix of dimension κ, $\kappa=7$ is the dimension of the vector ζ. Note also that the value of $\bar{\kappa}=0$, in other words the derivative of the ''filtered error'' (which is being modeled) will simply consist of system response accelerations. This situation exists for a case where one is soley performing model identification, and not simultaneously applying control forces to keep the filtered error small. This is done simply because the emphasis of this paper is on the identification algorithm and performance. For a simultaneous control application a typical value of $\bar{\kappa}$ might be 1.

Figure 9 presents the results from simulation Case 2. Comparing the time history plots of Fig. 9 with those of Fig. 5, it can be seen that the neural network tracks the unknown forces from time $t=0$. This is of course expected, since adaptation is now off, i.e., there are no transient adaptation effects, and the weights have already converged to their optimal values from simulation Case 1.

Figure 10 presents plots the of time-histories of the restoring forces compared with their estimates from simulation Case 3. Now the adaptation is off, and the neural network weights are fixed to their optimal values from simulation Case 1. Although the base excitation is different than that of simulation Case 1, it is seen that the neural network approximates the unknown system dynamics very well.

In Table 2, we present the RMS of the estimation error for the three simulation runs Case 1–3. As expected, simulation Case 1 gives a higher RMS error, due to the initial adaptation transients. The RMS errors for simulations Case 2 and Case 3 are one order of magnitude smaller than those of Case 1, since the weights have now converged to their optimal values.

The same ''experiment'' was repeated by increasing the adaptive gain γ from 0.1 to 0.9. Figure 11 plots the restoring forces (solid curve) and their estimates (dashed curves) produced by the neural estimator during training and Fig. 12 plots the restoring forces (solid curve) and their estimates (dashed curves) produced by the neural estimator after training.

The value of the adaptive gain (learning rate) γ has a consider-

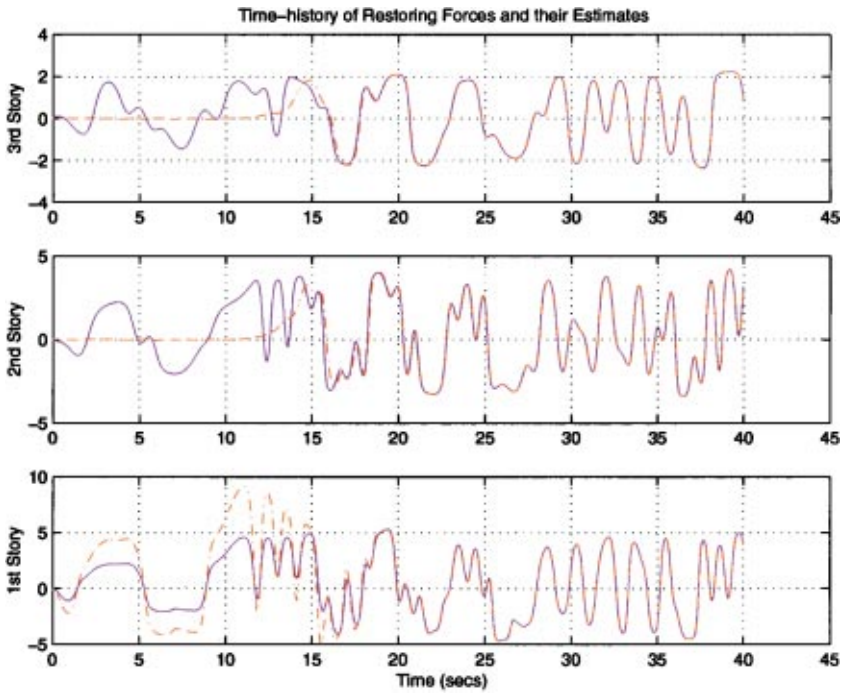

Fig. 5 Time-history of actual (solid curve) and estimated (dashed curve) restoring forces when adaptation is on

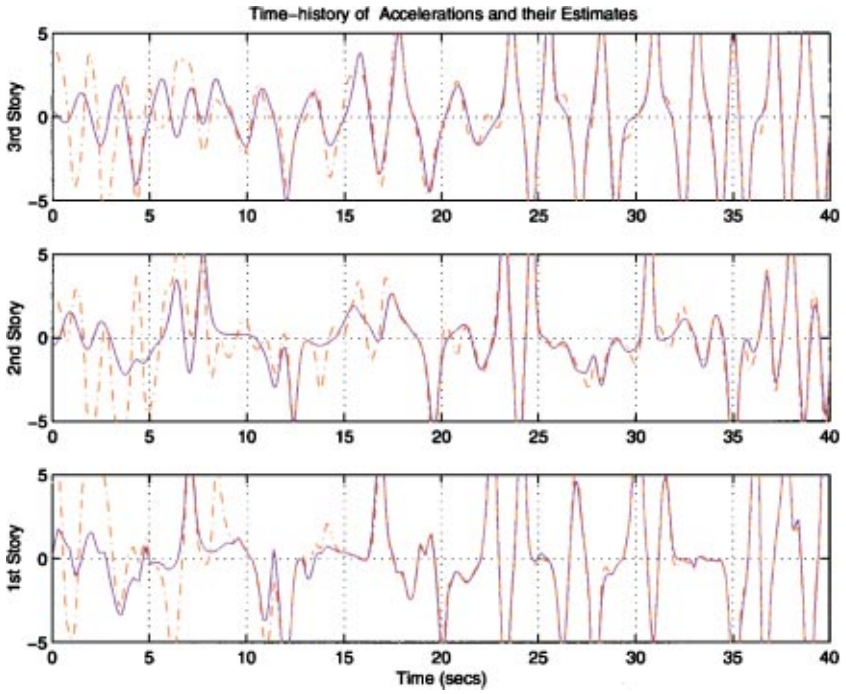

Fig. 6 Time-history of actual (solid curve) and estimated (dashed curve) accelerations when adaptation is on

able effect on the learning properties of the neural estimator. The plots in Figs. 11 and 12 are the same plots as those of simulation (1), with the exception that the learning rate has now been increased to $\gamma=0.9$, as opposed to $\gamma=0.1$ for simulation (1). A comparison between Figs. 5, 9 and Figs. 11, 12 reveals that the increase of the adaptive gain has the effect of reducing the time that the neural estimator needs to accurately predict the restoring forces from about 15 to 5 seconds during training. The tradeoff for such an improvement in the transient behavior is that the neural estimator for the larger adaptive gain case has poorer estimation capabilities after training is off. It is worth noting that, in many control applications, fast estimation error convergence during adaptation (training) is more important than good estimation after the training phase. In those cases a larger adaptive gain is suggested. It is also noted that, although theoretically the estimation error convergence can be made arbitrarily fast by increasing the

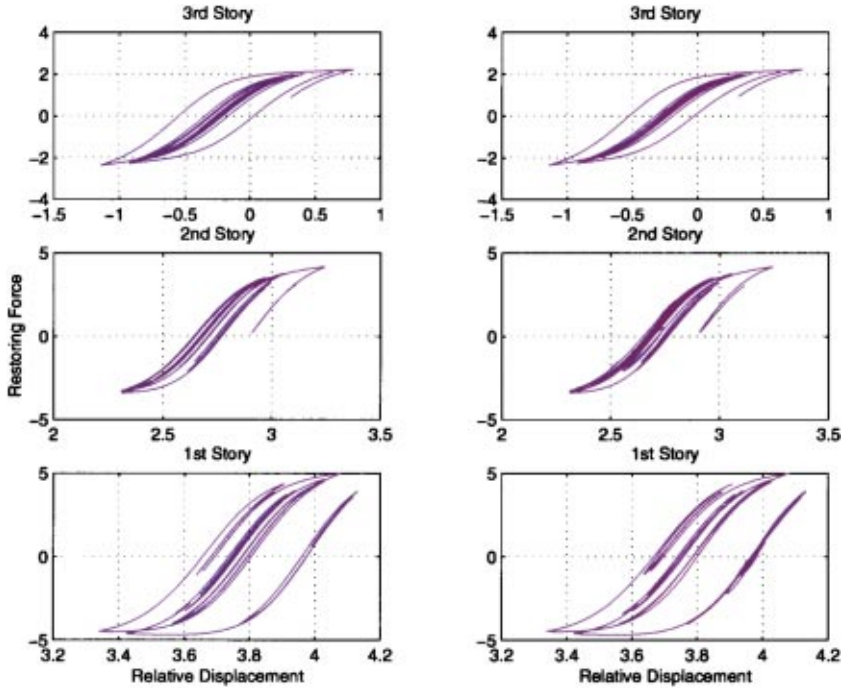

Fig. 7 Actual (left subplots) and estimated (right subplots) restoring forces versus relative displacements when adaptation is on

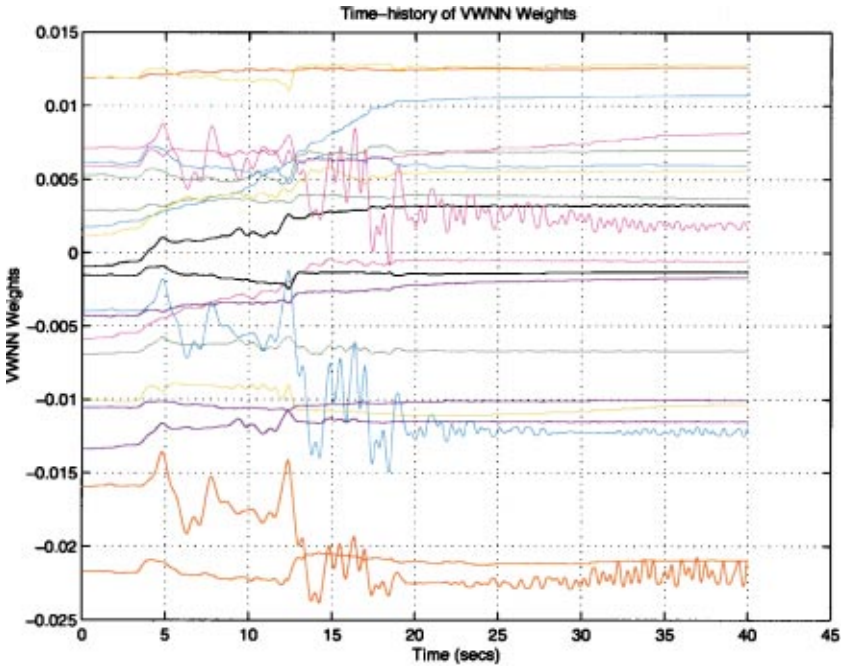

Fig. 8 Time-history of Volterra/Wiener neural network (VWNN) adjustable parameters

Table 1 Neural Network Parameters

$\overline{\kappa}$	0
$H(s)$	$\begin{bmatrix} \Lambda(s) \\ \Lambda(s)\Lambda^{\tau}(s) \end{bmatrix}$, where $\Lambda(s)=\dfrac{[I_{\kappa}s^{9},\ldots,I_{\kappa}s,I_{\kappa}]^{\tau}}{(s+10)^{10}}$
$W^{\tau}\phi(\xi)$	a third-order HONN was used ([36])
α (see Appendix B)	10
$\mathcal{M}$	10^{6}
δ_{a1}, δ_{a2} and δ_{b1}, δ_{b2}	0.1, 1000
γ	0.1

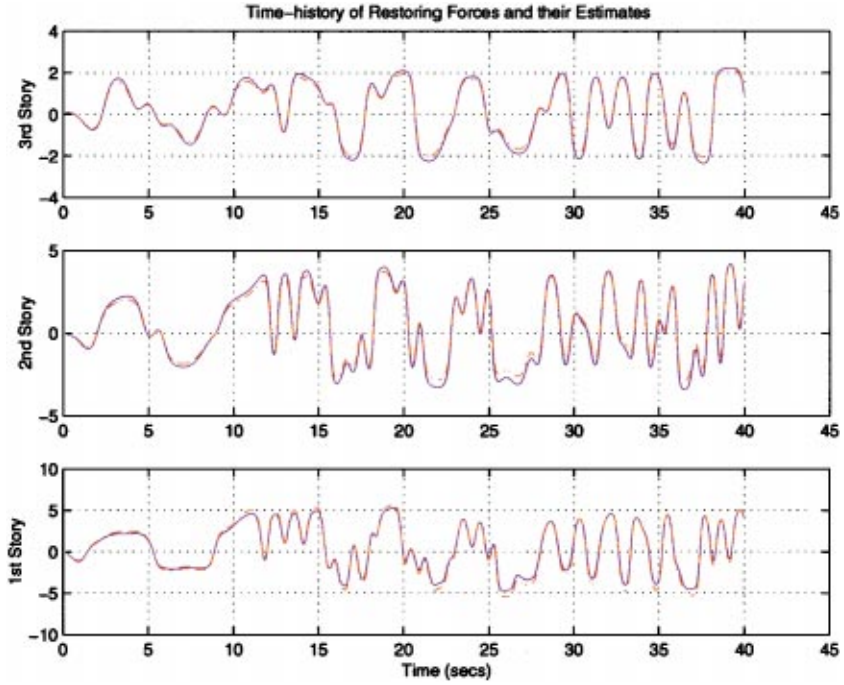

Fig. 9 Time-history of actual (solid curve) and estimated (dashed curve) restoring forces after training for the same base acceleration as in Figs. 5–8

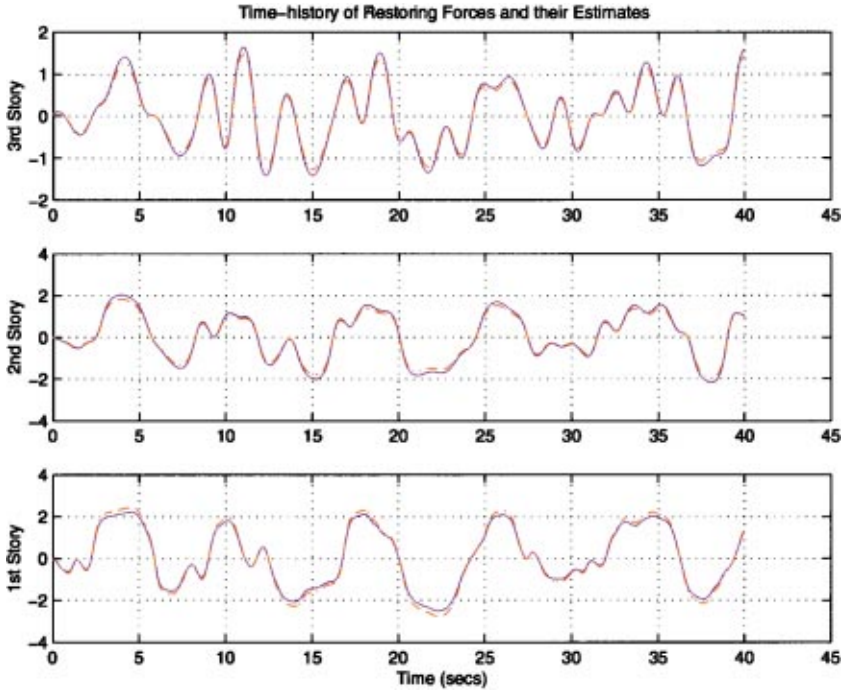

Fig. 10 Time-history of actual (solid curve) and estimated (dashed curve) restoring forces after training for different base acceleration than that of Figs. 5–8

Table 2 RMS of Estimation Error

Training Mode	RMS error
Case 1: Training On	0.0260
Case 2: Training Off	0.0066
Case 3: Training Off, Diff. Exc.	0.0029

adaptive gain, in practice there is an upper bound to the adaptive gain, since if γ is too large, then the estimation algorithm becomes numerically unstable.

4 Experimental Results

In this section, identification results using experimental data from two highly nonlinear hysteretic single-degree-of-freedom structures are presented. It is shown that our approach is success-

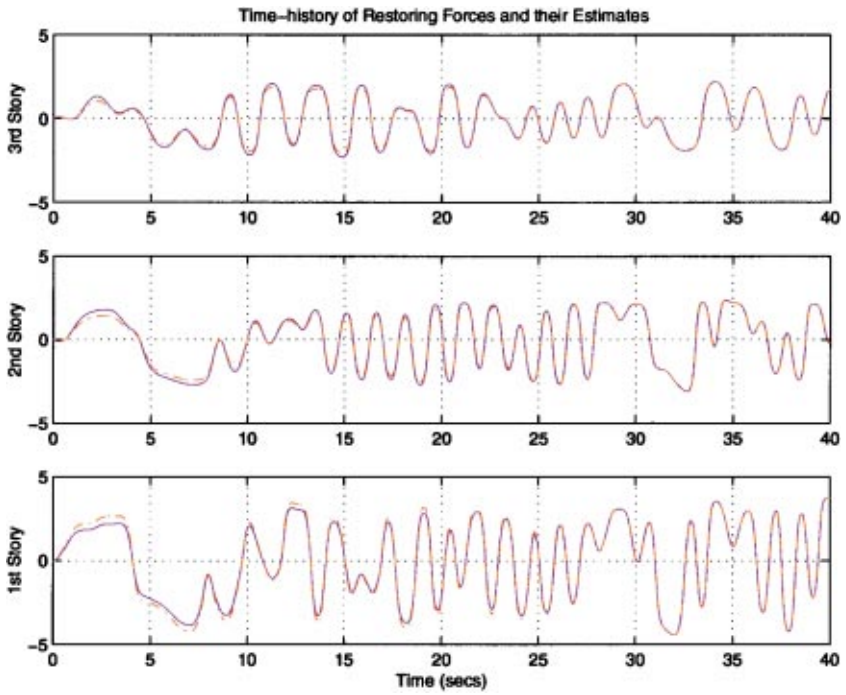

Fig. 11 Time-history of actual (solid curve) and estimated (dashed curve) restoring forces when adaptation is on, $\gamma = 0.9$

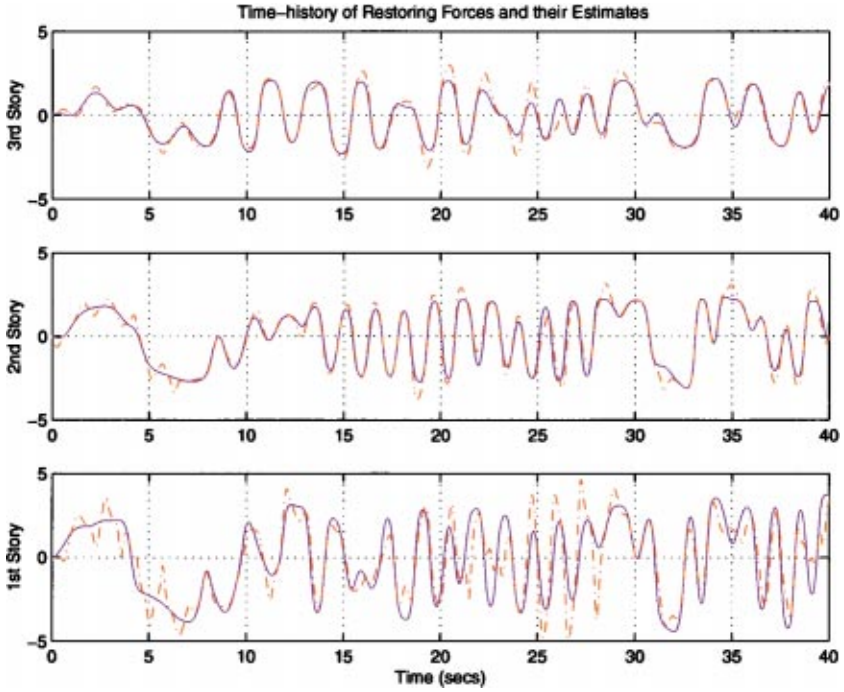

Fig. 12 Time-history of actual (solid curve) and estimated (dashed curve) restoring forces after training for different base acceleration than that of Figs. 11, $\gamma = 0.9$

Table 3 Neural Network Parameters Used for the Concrete and the Steel Structures

$\overline{\kappa}$	0
$H(s)$	$\begin{bmatrix} \Lambda(s) \\ \Lambda(s)\Lambda^{\tau}(s) \end{bmatrix}$ where $\Lambda(s) = \dfrac{[I_{\kappa}s^3, \ldots, I_{\kappa}s, I_{\kappa}]^{\tau}}{(s+10)^{10}}$
$W^{\tau}\phi(\xi)$	a second-order HONN was used ([36])
α (see Appendix B)	10
$\mathcal{M}$	10^6
δ_{a1}, δ_{a2} and δ_{b1}, δ_{b2}	0.1, 1000
γ	0.1

fully applied to the unknown nonlinear hysteretic structures. The data come from a concrete structure and a steel structure. In both cases a VWNN is used whose parameters are summarized in Table 3. Since only a limited number of data is available in both cases, the simulation policy was as follows: 50 training iterations were performed, where at the beginning of each iteration the weights from the end of the previous iteration were used where I_{κ} is the identity matrix of dimension κ, $\kappa = 2$ is the dimension of the vector ζ.

4.1 Concrete Structure. The concrete specimen was a one-third scale model of a reinforced concrete, multistory frame joint prototype. Details of the test article and a photograph of the fabricated specimen and test apparatus are available in the work of Masri et al. [35]. The concrete specimen was tested by means of a servo-hydraulic device which imposed a prescribed dynamic motion at the specimen boundary.

Figure 13 plots the actual concrete restoring force (solid curve) and its estimate (dashed curve) versus time (upper subplot) and versus the displacement (lower subplot) during the first iteration. Figure 14 plots the actual and estimated restoring forces after the training is finished (in 15 iterations). It is seen that the VWNN approximates very accurately the characteristics of the structure, even though the restoring force incorporates features associated with highly nonlinear behavior exhibited by hysteretic as well as dead-space type nonlinearities.

4.2 Steel Structure. Experimental tests were also conducted by means of a full-scale structural steel subassembly (made of ASTM A36 steel), consisting of a W16X40 wide flange beam framing into an 11-inch square box column. Because the behavior of the column wall has an important effect on the overall behavior of the connection, an axial load was applied to the column to simulate the dead and live load in an actual building column. Hydraulic actuators were used to impose the vertical loads as well as the induced moment at the connection. The applied tip loads and beam displacements were monitored by suitable force and displacement sensors. Experimental measurements were later processed to extract the value of the applied moment and the corresponding joint rotation, which were subsequently used to develop the hysteretic characteristics of the connection.

Figures 15 and 16 compare the actual (measured) restoring force with its estimated values at the first training episode, and after training is completed. Notice that the plotted nonlinear restoring force clearly exhibits degrading hysteretic properties. Note also that the estimation procedure is capable of accurately tracking this time varying nonlinear force.

5 Discussion

As has been discussed throughout this paper, and as can be seen from the very control-oriented formulation presented, the principal application for this estimation technique is in the area of adaptive control of nonlinear time-varying structural systems. Its identification and estimation performance has been demonstrated to be rather accurate, even during the first training cycle where no *a priori* model is assumed. In its present form the approach is somewhat computationally heavy for applications requiring estimates to be computed within with very small time step sizes. This is simply because of the large size of the neural network, and progressively enhanced speeds of computation will soon alleviate this problem. It is important to note, that through this gradient-based

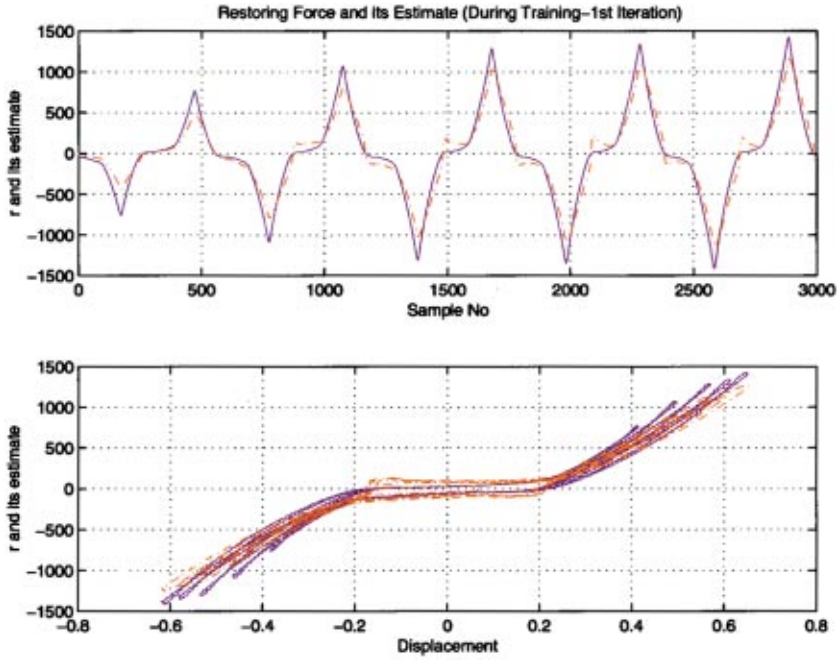

Fig. 13 Concrete structure: restoring forces and their estimates during the first training iteration

adaptive scheme, no matrix inversion is required; rather only multiplication and addition operations are called for on reasonably large matrices. In addition, it is hoped that, through further research and experience, better physical insight can be gained in order to streamline the network complexity required to model certain nonlinearities. This in turn would greatly speed up computation and model convergence.

6 Conclusions

The availability of estimation/identification techniques is crucial for the on-line control and monitoring of time-varying structural systems. The existing adaptive estimation/identification techniques suffer from two drawbacks: they assume that (1) the restoring forces applied to the system's elements are available for

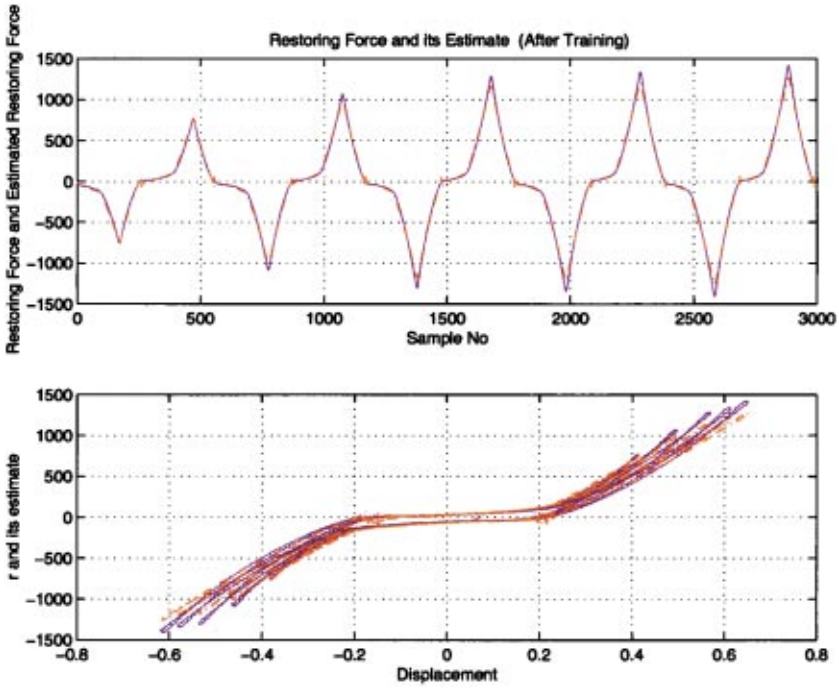

Fig. 14 Concrete structure: restoring forces and their estimates after training

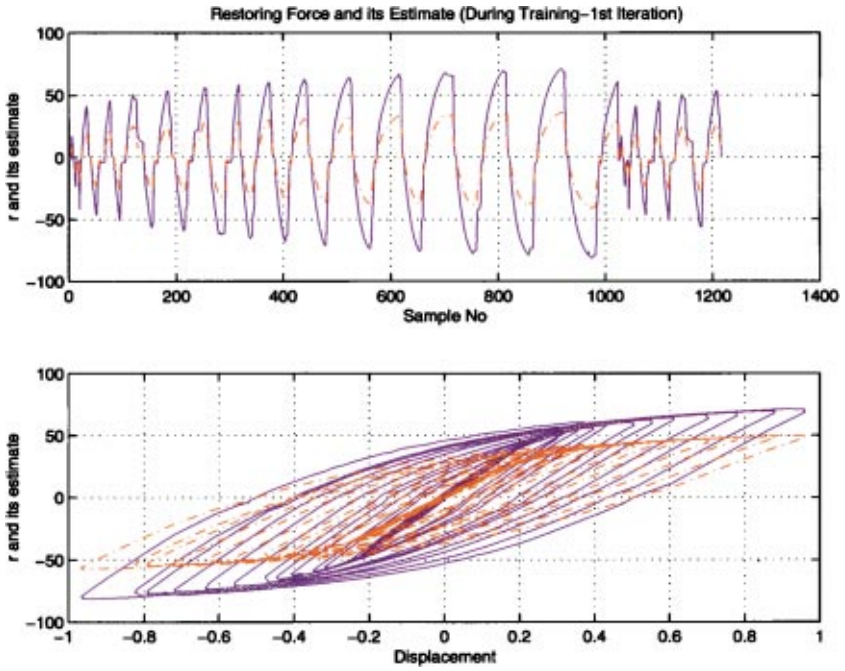

Fig. 15 Steel structure: restoring forces and their estimates during the first training iteration

measurement and that (2) the differential equation driving these restoring forces can be parameterized as a linear combination of unknown constant parameters and known nonlinear terms. In this paper, a new methodology is presented which completely overcomes the above two problems. Specifically, a new approach is presented that solves the problem of estimating/identifying the restoring forces without assuming that the restoring forces are available for measurement, or imposing any restrictions on the nature of structure of the restoring forces dynamics. The new approach uses appropriately adaptive filtering and estimation techniques and also makes use of the Volterra/Wiener neural network (VWNN) which is capable of learning input/output nonlinear dynamical behaviors.

Simulations performed on a three-story building model under earthquake excitation, as well as processing of experimental measurements from a reinforced-concrete structure as well as a steel structure, verified the efficiency of the proposed technique and demonstrated its utility.

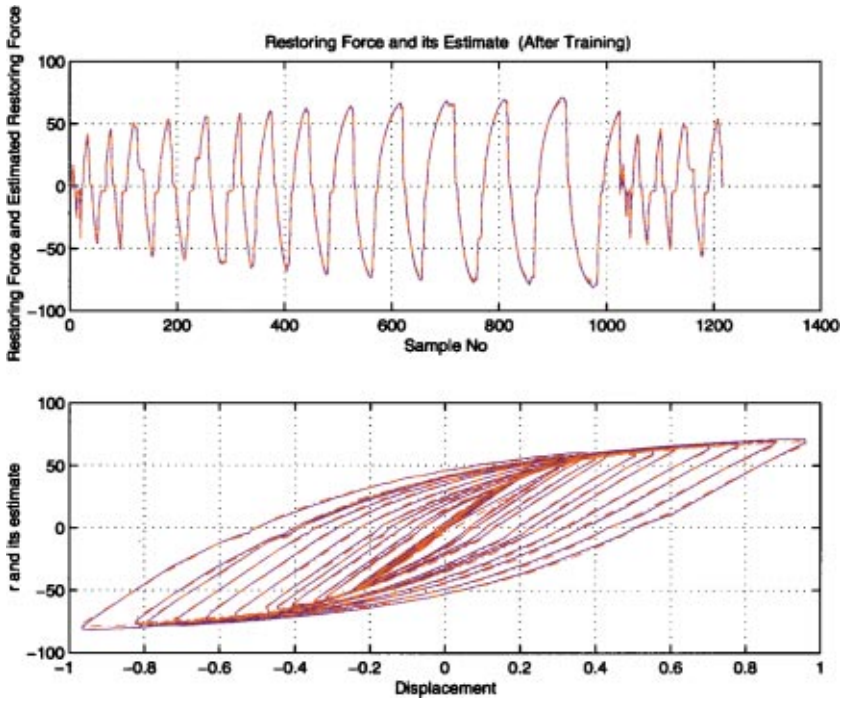

Fig. 16 Steel structure: restoring forces and their estimates after training

Acknowledgments

This study was supported in part by grants from the Air Force Office of Scientific Research, the National Science Foundation, NASA, and the Federal Emergency Management Agency.

Appendix A

Linear-in-the-Weights Neural Networks. Neural networks are known to possess powerful approximation capabilities; works by many authors (see [36] and the references therein) have shown that various neural network models are capable of approximating either functions or dynamical systems to any desired degree of accuracy. The focus of this paper is on linear-in-the-weights neural networks. In general, such neural networks are mathematically described by

$$\eta = W^{\tau}\phi(\xi) \tag{A1}$$

where $\xi \in \Re^n$ denotes the input vector, $\eta \in \Re^m$ denotes the output, $W \in \Re^{m\times L}$ denotes the synaptic matrix of the neural network and $\phi: \Re^n \mapsto \Re^L$ is a nonlinear vector function of *regressor terms* with the integer L denoting the number of regressor terms. Various neural network models belong to the class of Eq. (*A*1). For example, high-order neural networks, radial basis function networks, neural network with shifted sigmoidals and adaptive fuzzy systems have been shown to belong to the class of neural networks of Eq. (*A*1). For more details on linear-in-the-weights neural networks the reader is referred to Kosmatopoulos et al. [36].

For the readers that are not familiar with the linear-in-the-weights neural networks but are familiar with the multilayer neural networks (MNNs), they should picture a linear-in-the-weights neural network as a MNN with one input layer with as many neurons as the number of inputs, a hidden layer consisting of many neurons and one output layer with as many neurons as the number of outputs. The activation functions in the input and output layers are linear (identity) mappings while the activation functions in the hidden layer could be a variety of different nonlinear functions such as the product of the inputs, a radial basis function, etc.

An important property that the many neural network models of the form in Eq. (*A*1) satisfy is that

(**P1**) Neural networks belonging to the family described in Eq. (*A*1) are said to be *universal approximators*, if for every continuous function $\eta: \Re^n \mapsto \Re^m, \epsilon > 0$, and compact set $\chi \subset \Re^n$ there is an integer L and a matrix W^* such that the neural network with L regressor terms satisfies

$$\sup_{\xi\in\chi} |\eta(\xi) - W^{*\tau}\phi(\xi)| \leq \epsilon. \tag{A2}$$

The *optimal synaptic matrix* W^* and the *modeling error* μ w.r.t. L, ϕ, η, and χ are defined as

$$W^* \triangleq \arg\min_{W} \sup_{\xi\in\chi} |F(\xi) - W^{*\tau}\phi(\xi)|$$

and

$$\mu(\xi) \triangleq \eta(\xi) - W^{*\tau}\phi(\xi).$$

It is worth noticing that from property (**P1**) $\sup_{\xi\in\chi}\mu(\xi)$ can be made arbitrarily small by appropriately selecting L. In general, $\sup_{\xi\in\chi}\mu(\xi)$ becomes smaller whenever L increases.

Appendix B

The Volterra/Wiener Neural Network (VWNN). The Volterra/Wiener neural network consists of a linear filter interconnected in series with a linear-in-the-weights neural network as shown in Fig. 3. The linear filter has more outputs than inputs and it is used as a memory of the past history of the input signals. The two modules of the VWNN, namely, the dynamic linear module and the static neural network module are described as follows:

The Dynamic Linear Module. Let $h_i(\cdot), i=1,\ldots,N$ denote a set of stable linear transfer functions satisfying the following property:

(**P2**) For any stable transfer function $P(s)$, positive real $\omega_{\max}$ and $\epsilon > 0$, there exists a positive integer N and an N-dimensional real vector α such that

$$\sup_{\omega\in[0,\omega_{\max}]} \left\| P(j\omega) - \sum_{i=1}^{N} \alpha_i h_i(j\omega) \right\| < \epsilon.$$

An example of a family of transfer functions $h_i(s)$ that satisfy the property (**P2**) is the Laguerre polynomials $h_i(s) = \sqrt{2p}(p-s)^{i-1}/(p+s)^i$, where p is a positive design parameter ([31]).

The dynamics of the dynamic linear module are described by the following set of equations:

$$\begin{aligned} &\xi_{i_1,i} = h_{i_1}(s)\xi_i \\ &\xi_{i_k,\ldots,i_1,i} = h_{i_k}(s)\xi_{i_{k-1},\ldots,i_1,i}, \quad i \in [1,\ldots,n_1+n_e],\ i_k,\ldots,i_1 \\ &\qquad\qquad \in [1,\ldots,N],\ k \in \{1,\ldots,M\} \end{aligned} \tag{B1}$$

where $\xi \triangleq [u_1,\ldots,u_{n_1},y_1,\ldots,y_{n_e}]^{\tau}$. Let $\xi_{N,M}$ be defined as follows:

$$\begin{aligned} \xi_{N,M} = [\xi_{i_k,\ldots,i_1,i}]^{\tau},\ i \in \{1,\ldots,n_1+n_e\},\ i_k,\ldots,i_1 \\ \in \{1,\ldots,N\},\ k \in \{1,\ldots,M\}. \end{aligned} \tag{B2}$$

Let $\bar{N}_M$ denote the dimension of the vector $\xi_{N,M}$.

The vector $\xi_{N,M}$ should be thought as a signal carrying information about the past history of the input signal vector ξ.

The Static Neural Network Module. The static neural network module consists of a linear-in-the-weights neural network that satisfies property (**P1**) and is described by the following equation:

$$\eta = W^{\tau}\phi(\xi_{N,M}) \tag{B3}$$

where $\xi_{N,M} \in \Re^{\bar{N}_M}$ denotes the input vector to the neural network, $\hat{F} \in \Re^m$ denotes the output vector of the neural network, $W \in \Re^{m\times L}$ denotes the synaptic matrix of the neural network, $\phi: \Re^{\bar{N}_M} \mapsto \Re^L$ is a nonlinear vector function of *regressor terms* and the integer L denotes the number of regressor terms.

References

[1] Housner, G. W., Bergman, L. A., Caughey, T. K., Chassiakos, A. G., Claus, R. O., Masri, S. F., Skelton, R. E., Soong, T. T., Spencer, B. F., and Yao, J. T. P., 1997, "Structural Control: Past Present and Future," J. Eng. Mech. Div., Am. Soc. Civ. Eng., **123**, No. 9, pp. 897–971.
[2] Caughey, T. K., 1960, "Random Excitation of a System With Bilinear Hysteresis," ASME J. Appl. Mech., **27**, pp. 649–652.
[3] Jennings, P. C., 1964, "Periodic Response of a General Yielding Structure," J. Eng. Mech. Div., Am. Soc. Civ. Eng., **90**, No. 3m2, pp. 131–166.
[4] Iwan, W. D., 1966, "A Distributed-Element Model for Hysteresis and Its Steady-State Dynamic Response," ASME J. Appl. Mech., **33**, pp. 893–900.
[5] Bouc, R., 1967, "Forced Vibration of Mechanical Systems With Hysteresis," abstract, *Proceedings, 4th Conference on Nonlinear Oscillation*, Prague, Czechoslovakia.
[6] Iwan, W. D., and Lutes, L. D., 1968, "Response of the Bilinear Hysteretic System to Stationary Random Excitation," J. Acoust. Soc. Am., **43**, No. 3, pp. 545–552.
[7] Masri, S. F., 1975, "Forced Vibration of the Damped Bilinear Hysteretic Oscillator," J. Acoust. Soc. Am., **57**, No. 1, pp. 106–113.
[8] Wen, Y. K., 1976, "Method for Random Vibration of Hysteretic Systems," J. Eng. Mech. Div., Am. Soc. Civ. Eng., **102**, No. Em2, pp. 249–263.
[9] Masri, S. F., and Caughey, T. K., 1979, "A Nonparametric Identification Technique for Nonlinear Dynamic Problems," ASME J. Appl. Mech., **46**, No. 2, pp. 433–447.
[10] Baber, T. T., and Wen, Y. K., 1981, "Random Vibration of Hysteretic Degrading Systems," J. Eng. Mech. Div., Am. Soc. Civ. Eng., **107**, No. 3m6, pp. 1069–1087.
[11] Spanos, P. D., 1981, "Stochastic Linearization in Structural Dynamics," Appl. Mech. Rev., **34**, No. 1, pp. 1–8.
[12] Toussi, S., and Yao, J. T. P., 1983, "Hysteretic Identification of Existing Structures," J. Eng. Mech. Div., Am. Soc. Civ. Eng., **109**, No. 5, pp. 1189–1202.

[13] Andronikou, A. M., and Bekey, G. A., 1984, ''Identification of Hysteretic Systems,'' Proc. of the 18th IEEE Conf. on Decision and Control, Dec., pp. 1072–1073.
[14] Spencer, B. F., and Bergman, L. A., 1985, ''On the Reliability of a Simple Hysteretic System,'' J. Eng. Mech. Div., Am. Soc. Civ. Eng., **111**, pp. 1502–1514.
[15] Vinogradov, O., and Pivovarov, I., 1986, ''Vibrations of a System With Non-Linear Hysteresis,'' J. Sound Vib., **111**, No. 1, pp. 145–152.
[16] Iwan, W. D., and Cifuentes, A. O., 1986, ''A Model for System Identification of Degrading Structures,'' Jnl Earthquake Engineering and Structural Dynamics, **14**, No. 6, pp. 877–890.
[17] Jayakumar, P., and Beck, J. L., 1987, ''System Identification Using Nonlinear Structural Models,'' *Proceedings, Structural Safety Evaluation Based on System Identification Approaches*, Lambracht, Germany, pp. 82–102.
[18] Peng, C. Y., and Iwan, W. D., 1992, ''An Identification Methodology for a Class of Hysteretic Structures,'' Earthquake Eng. Struct. Dyn., **21**, pp. 695–712.
[19] Yar, M., and Hammond, J. K., 1987, ''Modeling and Response of Bilinear Hysteretic Systems,'' J. Eng. Mech. Div., Am. Soc. Civ. Eng., **113**, pp. 1000–1013.
[20] Yar, M., and Hammond, J. K., 1987, ''Parameter Estimation for Hysteretic Systems,'' J. Sound Vib., **117**, No. 1, pp. 161–172.
[21] Roberts, J. B., and Spanos, P. D., 1990, *Random Vibration and Statistical Linearization*, John Wiley and Sons, New York, NY.
[22] Masri, S. F., Miller, R. K., Traina, M.-I., and Caughey, T. K., 1991, ''Development of Bearing Friction Models From Experimental Measurements,'' J. Sound Vib., **148**, No. 3, pp. 455–475.
[23] Loh, C., and Chung, S., 1993, ''A Three-Stage Identification Approach for Hysteretic Systems,'' Earthquake Eng. Struct. Dyn., **22**, pp. 129–150.
[24] Benedettini, F., Capecchi, D., and Vestroni, F., 1995, ''Identification of Hysteretic Oscillators Under Earthquake Loading by Nonparametric Models,'' J. Eng. Mech., **121**, pp. 606–612.
[25] Chassiakos, A. G., Masri, S. F., Smyth, A., and Anderson, J. C., 1995, ''Adaptive Methods for Identification of Hysteretic Structures,'' *Proceedings American Control Conference*, ACC95, Seattle, WA, June, American Automatic Control Council.
[26] Chassiakos, A. G., Masri, S. F., Smyth, A. W., and Caughey, T. K., 1998, ''On-Line Identification of Hysteretic Systems,'' ASME J. Appl. Mech., **65**, pp. 194–203.
[27] Sato, T., and Qi, K., 1998, ''Adaptive H_{inf} Filter: Its Applications to Structural Identification,'' J. Eng. Mech. **124**, No. 11, pp. 1233–1240.
[28] Smyth, A. W., Masri, S. F., Chassiakos, A. G., and Caughey, T. K., 1999, ''On-Line Parametric Identification of MDOF Nonlinear Hysteretic Systems,'' J. Eng. Mech. Div., Am. Soc. Civ. Eng., **125**, No. 2.
[29] Narendra, K. S., and Annaswamy, A. M., 1989, *Stable Adaptive Systems*, Prentice-Hall, Englewood Cliffs, NJ.
[30] Wen, Y. K., 1989, ''Methods of Random Vibration for Inelastic Structures,'' Appl. Mech. Rev., **42**, No. 2, pp. 39–52.
[31] Kosmatopoulos, E. B., 1999, ''Neural Controllers for Output Feedback Control,'' IEEE Trans. Autom. Control, submitted for publication.
[32] Goodwin G. C., and Sin K. S., 1984, *Adaptive Filtering, Prediction and Control*, Prentice-Hall, Englewood Cliffs, NJ.
[33] Ioannou, P. A., and Datta, A., 1991, ''Robust Adaptive Control: A Unified Approach,'' Proc. IEEE, **79**, pp. 1736–1768.
[34] Polycarpou M. M., and Ioannou P. A., 1992, ''Neural Networks as On-line Approximators of Nonlinear Systems,'' *Proc. of the 31st IEEE CDC*, Tucson, AZ, IEEE, New York, pp. 7–12.
[35] Masri, S. F., Agbabian, M. S., Abdel-Ghaffar, A. M., Highazy, M., Claus, R. O., and de Vries, M. J., 1994, ''An Experimental Study of Embedded Fiber-Optic Strain Gauges in Concrete Structures,'' J. Eng. Mech. Div., Am. Soc. Civ. Eng., **120**, No. 8, pp. 1696–1717.
[36] Kosmatopoulos, E. B., Polycarpou, M. M., Christodoulou, M. A., and Ioannou, P. A., 1995, ''High-Order Neural Network Structures for Identification of Dynamical Systems,'' IEEE Trans. Neural Netw., **6**, No. 2, pp. 422–431.

D. Durban

G. Davidi

D. Lior

Faculty of Aerospace Engineering,
Technion,
Haifa 32000, Israel

Plastic Forming Processes Through Rotating Conical Dies[1]

Drawing and extrusion of single-phase and multilayered tubes through rotating conical dies is investigated within the framework of continuum plasticity. Large strain perfectly plastic J_2 flow theory models constitutive behavior along with a radial-helical flow pattern. The governing system for a single-layer process is reduced to three coupled nonlinear ordinary differential equations. An approximate solution is developed for long and tapered working zones with low wall friction. That solution is used to simulate the field within each layer in composite tube forming. Exact relations are derived for the n-layered tube and it is shown that wall rotation can considerably reduce the required working loads. [DOI: 10.1115/1.1382597]

Dedicated to Professor Dietmar Gross on the occasion of his 60th birthday

1 Introduction

Multilayered composite tubes offer a combination of properties suitable for a wide range of industrial applications. By comparison with single phase tubes there are obvious advantages of the composites in the practice of nuclear and chemical engineering, as well as in cryogenic applications and in aerospace engineering. Composite bi-layered cylinders are frequently encountered in heat transfer tubes (aluminum on steel) and in electrical wires (copper on steel).

Existing studies on drawing and extrusion of composite tubes through conical dies center almost exclusively on the upper bound estimation of the working load ([1,2]) with stationary dies. Durban [3] applied the Shield [4] radial flow solution to study analytically drawing and extrusion of composite tubes. His analysis—valid for long and tapered working zones with small wall friction—has been extended recently by (Alcaraz, Martinez-Espanola, and Gil-Sevillano [5]) to include large cone angles.

In this work we examine plastic forming processes of composite multilayered tubes through rotating conical dies (in opposing directions). That rotation is expected to divert the resisting radial shear stresses along the walls, thus reducing the required working load and hence increasing the efficiency of the process by allowing higher reductions. Early studies of drawing through rotating conical dies are by Brovman [6] for perfectly plastic wires, and by Durban [7] for power-law viscous tubes.

We begin, in the next section, with the formulation of the governing field equations for a single-phase tube. Material behavior is modeled by the rigid/perfectly plastic J_2 flow theory and the flow pattern is assumed to be radially helical. The resulting system consists of three coupled nonlinear ordinary differential equations with the shear stresses transverse profiles as unknowns.

Next, in section 3, we concentrate on the important case of long and tapered dies with small wall friction. A consistent approximation of the field equations admits, under these assumptions, an exact analytical solution for the stresses and velocities. This solution is briefly discussed, emphasizing the beneficial effects of wall rotation. Contact is made with the study in ([6]) for the full cylinder with one rotating wall.

The single-layer approximate solution is employed, in Section 4, to model the behavior of each phase in a composite multilayered tube. Interfacial continuity requirements along with surface boundary data lead to a closed-form solution in terms of averaged composite properties. The expressions for working stresses are on equal footing with the single layer analysis and reveal again the advantage of wall rotation. The paper concludes with a brief discussion of the solution for composite tubes, and a few examples are given to illustrate the main findings.

2 Single-Phase Formulation

With the notation of Fig. 1 we consider a steady forming process of combined extrusion/drawing of tubes through rotating conical dies. The initial dimensions of the tube are reduced by enforcing an irreversible plastic deformation within the conical working zone. The conical walls of the die have a common apex O and the flow pattern within the working zone is assumed to be axially symmetric with two velocity components; a radial component u, induced by the entry/exit loads, and a circumferential velocity w due to the rotation of the walls. The latter component is transmitted by circumferential friction along the walls.

Thus, with a fixed Eulerian triad $(\mathbf{e}_r, \mathbf{e}_\theta, \mathbf{e}_\phi)$, located at the virtual apex 0, we have the velocity vector of the working zone

$$\mathbf{v} = u\mathbf{e}_r + w\mathbf{e}_\phi \tag{2.1}$$

where both components (u, w) depend on r and θ.

Constitutive behavior is modeled by the J_2 flow theory, with rigid/perfectly plastic response,

$$\mathbf{S} = \sqrt{\frac{2}{3}}\, Y \frac{\mathbf{D}}{\sqrt{\mathbf{D}\cdot\cdot\mathbf{D}}} \tag{2.2}$$

where $\mathbf{S}$ is the stress deviator, Y—the uniaxial yield stress and $\mathbf{D}$ denotes the Eulerian strain rate tensor. It is now a matter of ease to verify that material incompressibility, implied by (2.2), dictates the radial velocity component

$$u = -\frac{f(\theta)}{r^2} \tag{2.3}$$

where $f(\theta)$ is an unknown function of θ and the negative sign indicates converging conical flow. Furthermore, to have both velocity components on equal footing (and hence all strain rate com-

[1]This work is based in part on a Master of Science thesis submitted to the Technion by G. Davidi.

Contributed by the Applied Mechanics Division of THE AMERICAN SOCIETY OF MECHANICAL ENGINEERS for publication in the ASME JOURNAL OF APPLIED MECHANICS. Manuscript received by the ASME Applied Mechanics Division, Oct. 13, 2000; final revision, Feb. 20, 2001. Associate Editor M.-J. Pindera. Discussion on the paper should be addressed to the Editor, Prof. Lewis T. Wheeler, Department of Mechanical Engineering, University of Houston, Houston, TX 77204-4792, and will be accepted until four months after final publication of the paper itself in the ASME JOURNAL OF APPLIED MECHANICS.

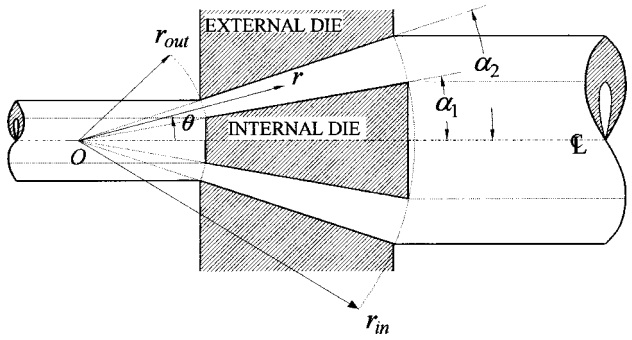

Fig. 1 Drawing or extrusion of tubes through rotating conical dies. The working zone is bounded by the radii $r_{in} \leq r \leq r_{out}$ and wall angles $\alpha_1 \leq \theta \leq \alpha_2$.

ponents with an identical algebraic weight of the radial coordinate) we take a circumferential velocity profile of the form

$$w = \frac{g(\theta)}{r^2} + \Omega_0 r \sin\theta \tag{2.4}$$

where $g(\theta)$ is again an unknown function of θ, and Ω_0 denotes a reference rigid-body rate of rotation. Accordingly, notice that the second term in (2.4) does not induce any strain rates within the working zone and, in fact, we may proceed with $\Omega_0 = 0$. The choice (2.3)–(2.4) generates, by (2.2), a deviatoric stress field which is independent of r, thus facilitating an analytical solution along the lines of ([4,8,9]).

The strain rate components that follow from (2.3)–(2.4) are, with an obvious notation,

$$\varepsilon_{rr} = \frac{2f}{r^3} \quad \varepsilon_{\theta\theta} = \varepsilon_{\phi\phi} = -\frac{f}{r^3}$$

$$\varepsilon_{r\theta} = -\frac{f'}{2r^3} \quad \varepsilon_{r\phi} = -\frac{3g}{2r^3} \quad \varepsilon_{\theta\phi} = \frac{g' - g\cot\theta}{2r^3} \tag{2.5}$$

where the prime indicates differentiation with respect to θ. A further substitution of (2.5) in (2.2) results in the deviatoric stresses

$$\Sigma_{rr} - \Sigma_{\theta\theta} = \frac{1}{\Delta} \quad \text{with} \quad \Sigma_{\theta\theta} = \Sigma_{\phi\phi}$$

$$\Sigma_{r\theta} = -\frac{\beta}{\sqrt{3}\Delta} \quad \Sigma_{r\phi} = -\frac{\gamma_1}{\sqrt{3}\Delta} \quad \Sigma_{\theta\phi} = \frac{\gamma_2}{\sqrt{3}\Delta} \tag{2.6}$$

where all stress components have been nondimensionalized with respect to Y (i.e., $\Sigma_{rr} = \sigma_{rr}/Y$, $\Sigma_{r\theta} = \sigma_{r\theta}/Y$, etc., σ_{ij} being the true stress components) and

$$\beta = \frac{\sqrt{3}f'}{6f} \quad \gamma_1 = \frac{\sqrt{3}g}{2f} \quad \gamma_2 = \frac{\sqrt{3}(g' - g\cot\theta)}{6f} \tag{2.7}$$

$$\Delta = \sqrt{1 + \beta^2 + \gamma_1^2 + \gamma_2^2}. \tag{2.8}$$

The deviatorics in (2.6) are now independent of r and contain two unknown functions (f, g) of θ. The relative strength of the three shear strain rates is expressed by β and (γ_1, γ_2).

It remains to consider the equations of equilibrium (inertia effects are neglected for low-speed processes) given by

$$\Sigma_{rr,\rho} + \frac{1}{\rho}\Sigma_{r\theta,\theta} + \frac{1}{\rho}[2(\Sigma_{rr} - \Sigma_{\theta\theta}) + \Sigma_{r\theta}\cot\theta] = 0 \tag{2.9a}$$

$$\Sigma_{r\theta,\rho} + \frac{1}{\rho}\Sigma_{\theta\theta,\theta} + \frac{3}{\rho}\Sigma_{r\theta} = 0 \tag{2.9b}$$

$$\Sigma_{r\phi,\rho} + \frac{1}{\rho}\Sigma_{\theta\phi,\theta} + \frac{1}{\rho}(3\Sigma_{r\phi} + 2\Sigma_{\theta\phi}\cot\theta) = 0 \tag{2.9c}$$

where $\rho = r/r_{out}$ is the nondimensionalized radial coordinate and a comma followed by an index denotes partial differentiation. Now, inserting the deviators $(\Sigma_{rr} - \Sigma_{\theta\theta})$ and $\Sigma_{r\theta}$, from (2.6), in (2.9a) and integrating over ρ gives

$$\Sigma_{rr} = \left[\left(\frac{\beta}{\sqrt{3}\Delta}\right)' + \left(\frac{\beta}{\sqrt{3}\Delta}\right)\cot\theta - \frac{2}{\Delta}\right] ln\rho + G(\theta) \tag{2.10}$$

where $G(\theta)$ is yet another unknown function of θ. Combining (2.10) with the first of (2.6) we obtain an expression for $\Sigma_{\theta\theta}$ which is substituted in (2.9b) together with $\Sigma_{r\theta}$ from (2.6). It follows that transverse equilibrium is maintained if

$$\left[\left(\frac{\beta}{\sqrt{3}\Delta}\right)' + \left(\frac{\beta}{\sqrt{3}\Delta}\right)\cot\theta - \frac{2}{\Delta}\right]' = 0 \tag{2.11}$$

and

$$G' = \left(\frac{1}{\Delta}\right)' + \frac{\sqrt{3}\beta}{\Delta}. \tag{2.12}$$

Finally, we substitute the shear stresses $\Sigma_{r\phi}$ and $\Sigma_{\theta\phi}$ from (2.6) in the circumferential equilibrium equation (2.9c). This gives the equation

$$\left(\frac{\gamma_2}{\Delta}\right)' + 2\left(\frac{\gamma_2}{\Delta}\right)\cot\theta - 3\left(\frac{\gamma_1}{\Delta}\right) = 0. \tag{2.13}$$

To sum up, the radial-helical flow pattern (2.3)–(2.4) can be sustained by the perfectly plastic solid (2.2) provided the Eqs. (2.11)–(2.13) are satisfied. That system of three equations is for three unknown functions (f, g, G) and can be solved along with appropriate boundary data. In fact, Eq. (2.12) can be treated separately for function G, which leaves us with the two Eqs. (2.11) and (2.13) for f and g. While no attempt is made in this study to handle the fully nonlinear system, it is worth mentioning that it is possible to extract a compatibility equation from relations (2.7) in the form

$$\gamma_1' + (2\sqrt{3}\beta - \cot\theta)\gamma_1 - 3\gamma_2 = 0. \tag{2.14}$$

Equations (2.11) and (2.13)–(2.14), along with the algebraic connection (2.8), may be regarded as a system of fourth order for $(\beta, \gamma_1, \gamma_2)$ which appears to be simpler than the original formulation.

A similar analysis for power low viscous solids has been presented by Durban [7], and an earlier version for perfectly plastic solids was given in ([6]). In the absence of rotation ($g \equiv 0$) we recover from (2.11)–(2.12), with $\Delta = \sqrt{1 + \beta^2}$, the radial flow equations first obtained by Shield [4].

3 Approximate Solution for Long and Tapered Dies With Small Wall Friction

Radial flow simulation of extrusion and drawing through conical dies is by now well established (Durban [3,9]) for long and tapered dies with small wall friction. In such configurations it is permissible to neglect the contributions of wall friction and of entry/exit transition zones to plastic yielding within the working zone. That analysis is of asymptotic value and is practically valid for long dies with small cone angles. In fact, initial experimental work, which has accompanied this study, shows that pure extrusion processes are bounded by the effect of blocking beyond certain levels of taperness.

Proceeding along similar lines in the present study we consider now the restricted case where all three shear stresses $(\sigma_{r\theta}, \sigma_{r\phi}, \sigma_{\theta\phi})$ are much smaller than the yield stress Y. This

assumption is usually met in reality since the forming processes are conducted with well lubricated dies. Thus, in nondimensionalized notation

$$\Sigma_{r\theta}^2, \Sigma_{r\phi}^2, \Sigma_{\theta\phi}^2 \ll 1 \tag{3.1}$$

implying, via (2.6) and (2.8), that

$$\beta^2, \gamma_1^2, \gamma_2^2 \ll 1 \quad \text{and} \quad \Delta \approx 1 \tag{3.2}$$

it follows that the three governing equations, (2.11) and (2.13)–(2.14), simplify to

$$(\beta' + \beta \cot\theta)' = 0 \tag{3.3}$$

$$\gamma_2' + 2\gamma_2 \cot\theta - 3\gamma_1 = 0 \tag{3.4}$$

$$\gamma_1' - \gamma_1 \cot\theta - 3\gamma_2 = 0. \tag{3.5}$$

Put differently, the system (3.3)–(3.5) is the consistent first-order linearization of the original nonlinear system, as all coupled terms have been dropped out.

Equation (3.3) admits the exact solution

$$\beta = -A \cot\theta + \frac{B}{\sin\theta} \tag{3.6}$$

where (A, B) are integration constants. Likewise, the couple (3.4)–(3.5) can be integrated exactly in terms of Legendre functions. However, for small cone angles we may use the approximation $\cot\theta \approx \theta^{-1}$ and write the solution of (3.4)–(3.5)—with $\cot\theta$ replaced by θ^{-1}—in terms of modified Bessel functions. Expanding (3.6) and the Bessel solution for (γ_1, γ_2) in powers of θ, results in the consistent small-angle approximation

$$\beta = -\sqrt{3}\,\delta\left(\theta - \frac{\alpha_s^2}{\theta}\right) \tag{3.7}$$

$$\gamma_1 = \frac{3\sqrt{3}}{4} M\left(\frac{\theta}{\alpha_k^2} - \frac{1}{\theta}\right) \tag{3.8}$$

$$\gamma_2 = \frac{\sqrt{3}}{2} M\left(\frac{1}{\theta^2}\right) \tag{3.9}$$

where $(\delta, \alpha_s, M, \alpha_k)$ are integration constants. Constants (δ, α_s) are of course related to constants (A, B) in (3.6). Solutions (3.7)–(3.9) can also be derived asymptotically from (3.3)–(3.5), as θ becomes small, by a standard expansion in powers of θ.

Within that framework, the solution of (2.12) is simply

$$G = D, \tag{3.10}$$

D being a constant, and the stresses follow from (2.10) and (2.6) as

$$\Sigma_{rr} = -2(1+\delta)\ln\rho + D \quad \Sigma_{\theta\theta} = \Sigma_{\phi\phi} = \Sigma_{rr} - 1$$
$$\Sigma_{r\theta} = \delta\left(\theta - \frac{\alpha_s^2}{\theta}\right) \quad \Sigma_{r\phi} = \frac{3}{4} M\left(\frac{1}{\theta} - \frac{\theta}{\alpha_k^2}\right) \quad \Sigma_{\theta\phi} = \frac{1}{2} M\left(\frac{1}{\theta^2}\right). \tag{3.11}$$

In the expression for Σ_{rr} we have assumed that $\alpha_s^2 \ll 1$, as will be confirmed later.

To find the radial velocity profile we integrate the first of (2.7) in the form

$$f(\theta) = U \exp(2\sqrt{3}\int \beta\, d\theta) \approx U(1 + 2\sqrt{3}\int \beta\, d\theta) \approx U \tag{3.12}$$

since both β and θ are assumed to be small. Here U is a constant, which scales the transversally uniform radial velocity (2.3). The circumferential velocity profile $g(\theta)$ in (2.4) follows from the second of (2.7) along with (3.8) and (3.12), viz

$$g(\theta) = \frac{3}{2} M\left(\frac{\theta}{\alpha_k^2} - \frac{1}{\theta}\right) U. \tag{3.13}$$

At this stage we have completed the construction of the first-order approximate solution of the field equations. The normal stresses in (3.11) vary as $ln\rho$ in the radial direction but are transversally uniform, while shear stresses vary only in the θ-direction and contribute very little to the yield stress Y. Likewise the radial velocity profile (3.12) is uniform in the transverse direction while the circumferential component's profile (3.13) varies through the thickness of the working zone.

The five integration constants that appear in the stresses (3.11) are determined from five boundary conditions, see also in ([7]). To begin with, we assume that no end couples are applied on the working piece. Thus, at the entry and at the exit

$$\int_0^{2\pi} \int_{\alpha_1}^{\alpha_2} \Sigma_{r\phi} r^3 \sin^2\theta\, d\theta\, d\phi = 0 \tag{3.14}$$

where entry/exit surfaces are assumed to be spherical. However, with $\Sigma_{r\phi}$ from (3.11) being independent of r we find that the torsional moment (3.14) vanishes over any spherical cross section along the working zone. Substituting $\Sigma_{r\phi}$ from (3.11) in (3.14), and using the small angle approximation $\sin\theta \approx \theta$, gives

$$\alpha_k^2 = \frac{1}{2}(\alpha_1^2 + \alpha_2^2). \tag{3.15}$$

Next, we consider the twisting moment M^* applied by the stresses $\Sigma_{\theta\phi}$ along the walls $\theta = \alpha_1, \alpha_2$. These moments, of equal magnitude, but in opposite directions in view of (3.14), are given by

$$M^* = \int_0^{2\pi} \int_{r_{out}}^{r_{in}} \sigma_{\theta\phi} r^2 \sin^2\theta\, dr\, d\phi \quad \text{at} \quad \theta = \alpha_1, \alpha_2. \tag{3.16}$$

Within our approximations $\sigma_{\theta\phi}$ of (3.11) is independent of r, $\sin\theta \approx \theta$, and (3.16) gives

$$M^* = \frac{\pi}{3}(r_{in}^3 - r_{out}^3) YM \tag{3.17}$$

which is in fact independent of wall angle. Observing that

$$\frac{\pi}{3}(r_{in}^3 - r_{out}^3) = V \tag{3.18}$$

is exactly one quarter of the spherical volume included between the spheres $r = r_{in}$ and $r = r_{out}$, we find that the integration constant M is related to the twisting moment M^* by

$$M = \frac{M^*}{VY}. \tag{3.19}$$

Two additional boundary conditions are imposed by surface friction data along the rotating conical walls. We assume that the resultant surface shear stress is a fraction of the effective shear stress $Y/\sqrt{3}$, namely

$$\Sigma_{r\theta}^2 + \Sigma_{\theta\phi}^2 = \frac{1}{3} m_1^2 \quad \text{at} \quad \theta = \alpha_1$$

$$\Sigma_{r\theta}^2 + \Sigma_{\theta\phi}^2 = \frac{1}{3} m_2^2 \quad \text{at} \quad \theta = \alpha_2 \tag{3.20}$$

where $m_i (i = 1,2)$ are the surface friction factors, with $m_i = 1$ for a perfectly rough wall and $m_i = 0$ for a smooth wall. Here we assume that both friction factors are much smaller than unity. From (3.11), (3.7), and (3.9), we find that conditions (3.20) become

$$\beta^2 + \gamma_2^2 = m_1^2 \quad \text{at} \quad \theta = \alpha_1$$

$$\beta^2 + \gamma_2^2 = m_2^2 \quad \text{at} \quad \theta = \alpha_2 \tag{3.21}$$

or, accounting for the appropriate signs of the shear stresses,

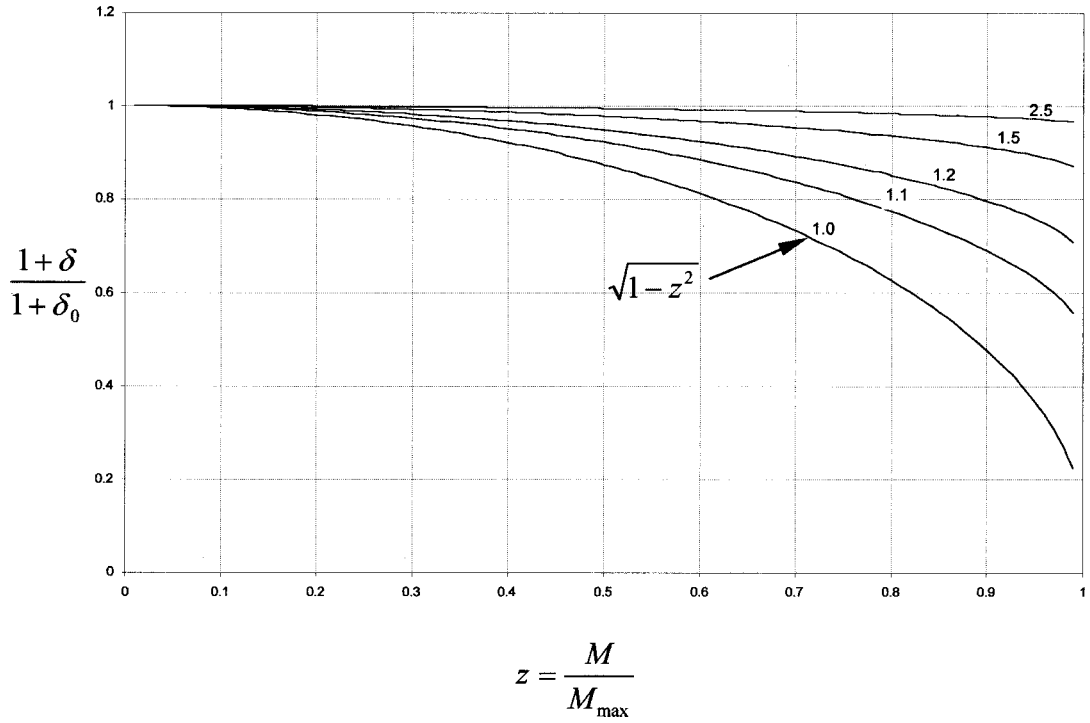

Fig. 2 Effect of walls rotation on reducing working loads. Curves are for $m_1 = m_2 = 0.05$ and $\alpha_1 = 7$deg. Here $M_{max} = 8.62 \cdot 10^{-4}$. Values of cone angles ratio α_2/α_1 are indicated over the curves. In the absence of rotation $z = 0$ and $\delta = \delta_0$. The theoretical limit for $\alpha_2/\alpha_1 \to 1$ is given by $\sqrt{1-z^2}$.

$$\alpha_s^2 = \frac{X_1\alpha_2^2 + X_2\alpha_1^2}{X_1 + X_2}$$

$$\delta = \frac{X_1 + X_2}{\alpha_2^2 - \alpha_1^2} \tag{3.22}$$

with

$$X_1 = \sqrt{\left(\frac{m_1\alpha_1}{\sqrt{3}}\right)^2 - \left(\frac{M}{2\alpha_1}\right)^2} \quad X_2 = \sqrt{\left(\frac{m_2\alpha_2}{\sqrt{3}}\right)^2 - \left(\frac{M}{2\alpha_2}\right)^2}. \tag{3.23}$$

The expression for α_s^2 confirms the earlier assumption in (3.11) that $\alpha_s^2 \ll 1$. Notice that for our flow pattern $\Sigma_{r\theta}$ is positive at $\theta = \alpha_2$ but negative at $\theta = \alpha_1$, while $\Sigma_{\theta\phi}$ is positive on both walls.

The last integration constant (D in (3.11)) is determined by specifying the entry/exit loading ratio. For long and tapered dies we can identify the extrusion pressure P and the drawing tension T (both nondimensionalized with respect to Y) with the values of the radial stress Σ_{rr} at $r = r_{in}, r_{out}$ (or $\rho = \rho_0 = r_{in}/r_{out}, 1$), respectively. Both processes can be handled together by introducing the loading parameter

$$\eta = \frac{T - P}{T + P} \tag{3.24}$$

with $\eta = 1$ in pure drawing ($P = 0$) and $\eta = -1$ in pure extrusion ($T = 0$). Thus, with $\Sigma_{rr}(\rho = 1) = T$ and $\Sigma_{rr}(\rho = \rho_0) = -P$, we find from the first of (3.11) and definition (3.24) that

$$D = (1 + \eta)(1 + \delta)ln\rho_0 \tag{3.25}$$

which concludes the solution.

A detailed analysis of this first-order solution has been made by Davidi [10], and to some extent earlier by Durban [7] for power low viscous tubes. Brovman [6] reports on the case of a perfectly plastic solid cone being extruded through a single conical die. It has been found that wall rotation can reduce significantly the working loads and thus improve the efficiency of the forming process.

Consider for example the case of pure extrusion ($\eta = -1$) with the extrusion pressure, from (3.11) and (3.25),

$$P = 2(1 + \delta)ln\rho_0 \tag{3.26}$$

with the nonuniformity parameter δ, given by (3.22)–(3.23),

$$\delta = \frac{1}{\alpha_2^2 - \alpha_1^2}\left[\sqrt{\left(\frac{m_1\alpha_1}{\sqrt{3}}\right)^2 - \left(\frac{M}{2\alpha_1}\right)^2} + \sqrt{\left(\frac{m_2\alpha_2}{\sqrt{3}}\right)^2 - \left(\frac{M}{2\alpha_2}\right)^2}\right]. \tag{3.27}$$

In the absence of friction ($m_1 = m_2 = 0$ and $M = 0$) δ vanishes and (3.26) becomes the classical uniform extrusion pressure

$$P_u = 2ln\rho_0. \tag{3.28}$$

For static walls, with $M = 0$, we recover from (3.27) the known tube extrusion formula ([8])

$$\delta_0 = \delta(M = 0) = \frac{m_1\alpha_1 + m_2\alpha_2}{\sqrt{3}(\alpha_2^2 - \alpha_1^2)}. \tag{3.29}$$

Rotation of the walls will divert the direction of the resisting shear stresses along the walls and consequently reduce the required entry/exit working loads. That phenomenon is apparent from (3.27) in pure extrusion as increasing the twisting moment M will make δ smaller. Notice that counter-rotating directions of the two conical walls minimizes torsional distortion of the product which may occur when only one die is rotating. Interestingly, there is a maximum value permissible for M given by the lower of the two quantities $(2/\sqrt{3})m_i\alpha_i^2$ $i = 1,2$. In passing, it is worth mentioning

that since the highest value of M is of $O(m\alpha^2)$ it is quite obvious that the shear stresses in (3.11) are much smaller than Y as we have assumed at the outset.

Consider the particular case of equal friction ($m_1=m_2=m$) with $M_{\max}=(2/\sqrt{3})m\alpha_1^2$. Figure 2 displays the relative reduction in the working load by showing the ratio $(1+\delta)/(1+\delta_0)$ versus $z=M/M_{\max}$ for different cone angles ratio α_2/α_1. All curves are for $m_1=m_2=m=0.05$ and $\alpha_1=7$deg. It can be seen from Fig. 2 that wall rotation can substantially lower the working loads. This beneficial effect of rotation is more pronounced for thinner tubes. In fact, at the theoretical limit of a vanishing thin tube, with $\alpha_2/\alpha_1\to 1$, we have from (3.27) that

$$\delta\to\delta_0\sqrt{1-z^2}\quad\text{with}\quad\delta_0=m/\sqrt{3}(\alpha_2-\alpha_1)\tag{3.30}$$

implying that

$$\frac{1+\delta}{1+\delta_0}\to\sqrt{1-z^2}\quad\text{as}\quad\frac{\alpha_2}{\alpha_1}\to 1.$$

An interesting observation that follows from (3.27) is that the effect of wall friction can be eliminated altogether when

$$m_1\alpha_1^2=m_2\alpha_2^2\tag{3.31}$$

since in that configuration the twisting moment $M=M_{\max}$ will make δ vanish by (3.27), as all surface friction in (3.20) is then activated by $\Sigma_{\theta\phi}$.

The level of helicity induced by wall rotation can be assessed by considering the velocity ratio

$$\xi=\left|\frac{g(\theta)}{f(\theta)}\right|=\frac{3}{2}M\left|\frac{\theta}{\alpha_k^2}-\frac{1}{\theta}\right|\tag{3.32}$$

by (3.12)–(3.13). With α_k given in (3.15) we find that ξ attains its maximum at $\theta=\alpha_1$, namely

$$\xi_{\max}=\left(\frac{3M}{2\alpha_1}\right)\frac{\alpha_2^2-\alpha_1^2}{\alpha_2^2+\alpha_1^2}.\tag{3.33}$$

For walls with equal friction, $m_1=m_2=m$, we have $M_{\max}=(2/\sqrt{3})m\alpha_1^2$ and

$$\xi_{\max}=\sqrt{3}m\alpha_1\frac{\alpha_2^2-\alpha_1^2}{\alpha_2^2+\alpha_1^2}.\tag{3.34}$$

indicating a very low rate of rotation by comparison with the radial velocity component.

While conical surface shear stresses ($\Sigma_{r\theta},\Sigma_{\theta\phi}$) are bounded by friction conditions (3.20), it is interesting to note that the spherical surface shear component $\Sigma_{r\phi}$ is much smaller than $\Sigma_{\theta\phi}$, regardless of wall friction. This is evident from (3.11) upon constructing the ratio $|\Sigma_{r\phi}/\Sigma_{\theta\phi}|$ and observing that its highest value, attained at $\theta=\alpha_2$, is $3\alpha_2(\alpha_2^2-\alpha_1^2)/2(\alpha_2^2+\alpha_1^2)$. Put differently, $|\Sigma_{r\phi}|=1/2\xi$ in view of (3.32), which to some extent justifies the averaged condition imposed in (3.14).

For the full cylinder ($0\leqslant\theta\leqslant\alpha$) the solution of Eq. (3.3)–(3.5) has to be bounded along the axis $\theta=0$. The consistent first-order approximation (3.7)–(3.9) is then replaced by

$$\beta=-\sqrt{3}\,\delta\theta\quad\gamma_1=\frac{2\sqrt{3}}{3}M\frac{\theta}{\alpha^4}\quad\gamma_2=\frac{\sqrt{3}}{2}M\frac{\theta^2}{\alpha^4}\tag{3.35}$$

where constant M is related to the twisting moment M^*, applied over the outer surface $\theta=\alpha$, by relation (3.19) as obtained from integral (3.16) at $\theta=\alpha$. The end couples (3.14) are now active, and the shear stresses within the working zone are

$$\Sigma_{r\theta}=\delta\theta\quad\Sigma_{r\phi}=-\frac{2}{3}M\frac{\theta}{\alpha^4}\quad\Sigma_{\theta\phi}=\frac{1}{2}M\frac{\theta^2}{\alpha^4}\tag{3.36}$$

with the normal components given by (3.11).

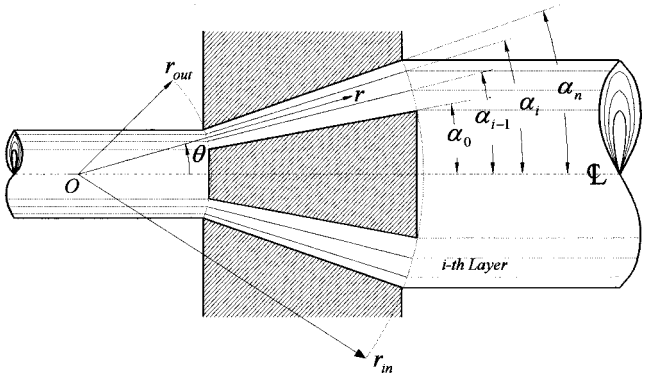

Fig. 3 Notation for composite multilayered tube drawing or extrusion. The composite consists of n layers ($i=1,2,\ldots,n$) with the ith layer bounded by the cones $\alpha_{i-1}\leqslant\theta\leqslant\alpha_i$. All layers have common entry/exit radii ($r=r_{\text{in}},r_{\text{out}}$) and wall angles are α_0,α_n.

The velocity profiles follow from (3.35) as

$$f=U\quad g=\frac{4}{3}MU\frac{\theta}{\alpha^4}\tag{3.37}$$

inducing the surface helicity

$$\xi_{\max}=\frac{4M}{3\alpha^3}.\tag{3.38}$$

The wall friction condition $\beta^2+\gamma_2^2=m^2$ at $\theta=\alpha$ gives

$$\delta=\sqrt{\left(\frac{m}{\sqrt{3}\alpha}\right)^2-\left(\frac{M}{2\alpha^3}\right)^2}=\sqrt{\left(\frac{m}{\sqrt{3}\alpha}\right)^2-\left(\frac{3}{8}\xi_{\max}\right)^2}\tag{3.39}$$

implying a maximum moment of $M_{\max}=2/\sqrt{3}\,m\alpha^2$, which is similar to the tube result (3.27), where δ vanishes.

The linear profile of radial shear stress $\Sigma_{r\theta}$ in (3.36), and the reduction in δ due to surface helicity in (3.39), compare qualitatively with the numerical results in ([6]) for small die angles and low friction.

4 Multilayered Composite Tubes

In this section we examine forming processes of multilayered tubes (Fig. 3) through rotating conical dies. The composite consists of n phases, labeled by $i=1,2,\ldots,n$, all having identical entry/exit radii ($\rho=\rho_0,1$, respectively). The walls have angles α_0 and α_n, while a representative layer i is bounded by the cones $\alpha_{i-1}\leqslant\theta\leqslant\alpha_i$. The common virtual apex is at 0 and we assume that the flow field and stresses within each layer are given with sufficient accuracy by the approximate solution (3.11) and (3.12)–(3.13). The analysis follows an earlier study by Durban [3] for drawing and extrusion of composite sheets, wires, and tubes through stationary dies.

Denoting the yield stress of each layer by Y_i it is instructive to define at the outset the volume-averaged yield stress of the entire composite by

$$Y_{av}=\frac{1}{\alpha_n^2-\alpha_0^2}\sum_{i=1}^{n}(\alpha_i^2-\alpha_{i-1}^2)Y_i\tag{4.1}$$

along with the relative yield stress of each phase

$$y_i=\frac{Y_i}{Y_{av}}\quad i=1,2,\ldots,n.\tag{4.2}$$

Now, we rewrite the single-phase stress field (3.11) for each layer, with all stress components nondimensionalized with respect to Y_{av},

$$\Sigma^i_{rr}=-2y_i(1+\delta_i)ln\rho+D_i$$

$$\Sigma^i_{\theta\theta}=\Sigma^i_{\phi\phi}=-2y_i(1+\delta_i)ln\rho+D_i-y_i$$

$$\Sigma^i_{r\theta}=y_i\delta_i\left(\theta-\frac{\alpha^2_{s,i}}{\theta}\right)\quad \Sigma^i_{r\phi}=\frac{3}{4}y_iM_i\left(\frac{1}{\theta}-\frac{\theta}{\alpha^2_{k,i}}\right)\quad \Sigma^i_{\theta\phi}=\frac{y_iM_i}{2\theta^2}. \tag{4.3}$$

There are five integration constants $(\delta_i, D_i, \alpha_{s,i}, \alpha_{k,i}, M_i)$ in each of the n layers. Also, the associated velocity field in each phase is

$$u_i=-\frac{U_i}{r^2}\quad w_i=\frac{3}{2}M_i\left(\frac{\theta}{\alpha^2_{k,i}}-\frac{1}{\theta}\right)\frac{U_i}{r^2} \tag{4.4}$$

not accounting for the rigid-body rate of rotation in (2.4). The velocity field adds one more integration constant (U_i) at each layer.

Radial velocity continuity at the interfaces implies immediately the common radial component

$$U_i=U\quad i=1,2,\ldots,n \tag{4.5}$$

while circumferential velocity continuity gives the $(n\text{-}1)$ equations

$$\frac{M_{i+1}-M_i}{\alpha^2_i}=\frac{M_{i+1}}{\alpha^2_{k,i+1}}-\frac{M_i}{\alpha^2_{k,i}}\quad i=1,2,\ldots,n-1. \tag{4.6}$$

Interfacial continuity of normal stresses results in two sets of equations

$$y_{i+1}\delta_{i+1}-y_1\delta_i=-(y_{i+1}-y_i) \tag{4.7a}$$

$$D_{i+1}-D_i=y_{i+1}-y_i \tag{4.7b}$$

both for $i=1,2,\ldots,n-1$.

Stress continuity conditions are completed with the requirement that both $\Sigma_{r\theta}$ and $\Sigma_{\theta\phi}$ pass smoothly at each interface. This gives, respectively,

$$y_{i+1}\delta_{i+1}\alpha^2_{s,i+1}-y_i\delta_i\alpha^2_{s,i}=(y_{i+1}\delta_{i+1}-y_i\delta_i)\alpha^2_i \tag{4.8}$$

$$y_{i+1}M_{i+1}=y_iM_i \tag{4.9}$$

again for $i=1,2,\ldots,n-1$.

However, the external twist relation (3.16), applied here at $\theta=\alpha_0$ and $\theta=\alpha_n$, gives the simple result

$$M^*=VY_{av}y_iM_i\quad i=1,n, \tag{4.10}$$

V being one quarter of the included spherical volume (3.18). Combining (4.10) with (4.9) we find that constants M_i are now completely determined by (with $\overline{M}$ replacing M in (3.19))

$$y_iM_i=\frac{M^*}{VY_{av}}=\overline{M}\quad i=1,2,\ldots,n. \tag{4.11}$$

Vanishing of end torsion—written in (3.14) for a single phase—takes here the form

$$\sum_{i=1}^{n} y_iM_i\int_{\alpha_{i-1}}^{\alpha_i}\left(\theta-\frac{\theta^3}{\alpha_{k,i}}\right)d\theta=0. \tag{4.12}$$

Applying the small angle approximation, integrating (4.12), using (4.11) and arranging finally gives

$$\sum_{i=1}^{n}\left(\frac{\alpha_i^4-\alpha_{i-1}^4}{\alpha^2_{k,i}}\right)=2(\alpha_n^2-\alpha_0^2). \tag{4.13}$$

Turning to the loading condition (3.24) we find, by (4.3), that end loads for multilayered tubes are given by

$$T=\frac{2}{\alpha_n^2-\alpha_0^2}\sum_{i=1}^{n}\Sigma^i_{rr}(\rho=1)\int_{\alpha_{i-1}}^{\alpha_i}\theta d\theta=\frac{1}{\alpha_n^2-\alpha_0^2}\sum_{i=1}^{n}D_i(\alpha_i^2-\alpha_{i-1}^2) \tag{4.14}$$

$$P=-\frac{2}{\alpha_n^2-\alpha_0^2}\sum_{i=1}^{n}\Sigma^i_{rr}(\rho=\rho_0)\int_{\alpha_{i-1}}^{\alpha_i}\theta d\theta=\frac{2ln\rho_0}{\alpha_n^2-\alpha_0^2}\sum_{i=1}^{n}y_i(1+\delta_i)$$
$$\times(\alpha_i^2-\alpha_{i-1}^2)-\frac{1}{\alpha_n^2-\alpha_0^2}\sum_{i=1}^{n}D_i(\alpha_i^2-\alpha_{i-1}^2). \tag{4.15}$$

Now, it is deduced from (4.7) that

$$y_i(1+\delta_i)=1+\overline{\delta}\quad\text{and}\quad D_i-y_i=\overline{D}-1 \tag{4.16}$$

where $\overline{\delta}$ and $\overline{D}$ are universal constants common for all layers. Observing the two simple identities

$$\sum_{i=1}^{n}y_i(1+\delta_i)(\alpha_i^2-\alpha_{i-1}^2)=(1+\overline{\delta})(\alpha_n^2-\alpha_0^2)$$

$$\sum_{i=1}^{n}D_i(\alpha_i^2-\alpha_{i-1}^2)=\overline{D}(\alpha_n^2-\alpha_0^2) \tag{4.17}$$

we find that the working stresses (4.14)–(4.15) become

$$T=\overline{D}\quad P=2(1+\overline{\delta})ln\rho_0-\overline{D}. \tag{4.18}$$

A further substitution of (4.18) in the loading condition (3.24) results in the connection

$$\overline{D}=(1+\eta)(1+\overline{\delta})ln\rho_0 \tag{4.19}$$

which is identical with the single-phase relation (3.25), but with (D,δ) replaced by the averaged constants $(\overline{D},\overline{\delta})$. Both constants are volume averages of D_i and $y_i\delta_i$, respectively, as is evident from (4.16).

We still have to implement the friction conditions (3.20), which for the composite tube read

$$(\Sigma^1_{r\theta})^2+(\Sigma^1_{\theta\phi})^2=\frac{1}{3}(y_1m_0)^2\quad\text{at}\quad\theta=\alpha_0$$

$$(\Sigma^n_{r\theta})^2+(\Sigma^n_{\theta\phi})^2=\frac{1}{3}(y_nm_n)^2\quad\text{at}\quad\theta=\alpha_n \tag{4.20}$$

where (m_0, m_n) are the friction factors along the external walls. Substituting the shear stresses from (4.3) in (4.20) we obtain the equations

$$-y_1\delta_1(\alpha_0^2-\alpha_{s,1}^2)=\sqrt{\left(\frac{y_1m_0\alpha_0}{\sqrt{3}}\right)^2-\left(\frac{\overline{M}}{2\alpha_0}\right)^2}=\overline{X}_1 \tag{4.21}$$

$$y_n\delta_n(\alpha_n^2-\alpha_{s,n}^2)=\sqrt{\left(\frac{y_nm_n\alpha_n}{\sqrt{3}}\right)^2-\left(\frac{\overline{M}}{2\alpha_n}\right)^2}=\overline{X}_2 \tag{4.22}$$

with due account of the shear stresses directions. The definitions of $\overline{X}_1, \overline{X}_2$ in (4.21)–(4.22) may be compared with those of X_1, X_2 in (3.23) for the single phase tube. Equations (4.21)–(4.22) are conveniently combined to give the relation

$$y_n\delta_n\alpha^2_{s,n}-y_1\delta_1\alpha^2_{s,1}=y_n\delta_n\alpha_n^2-y_1\delta_1\alpha_0^2-(\overline{X}_1+\overline{X}_2). \tag{4.23}$$

However, the l.h.s. of (4.23) can be constructed differently by summing up equations (4.8) from $i=1$ to $i=n-1$, namely

$$y_n\delta_n\alpha^2_{s,n}-y_1\delta_1\alpha^2_{s,1}=\sum_{i=1}^{n-1}(y_{i+1}\delta_{i+1}-y_1\delta_i)\alpha_i^2$$
$$=\alpha_n^2-\alpha_0^2-(y_n\alpha_n^2-y_1\alpha_0^2) \tag{4.24}$$

on account of the first of (4.16). Thus, from (4.23)–(4.24)

$$y_n\delta_n\alpha_n^2-y_1\delta_1\alpha_0^2-(\overline{X}+\overline{X}_2)=\alpha_n^2-\alpha_0^n-(y_n\alpha_n^2-y_1\alpha_0^2)$$

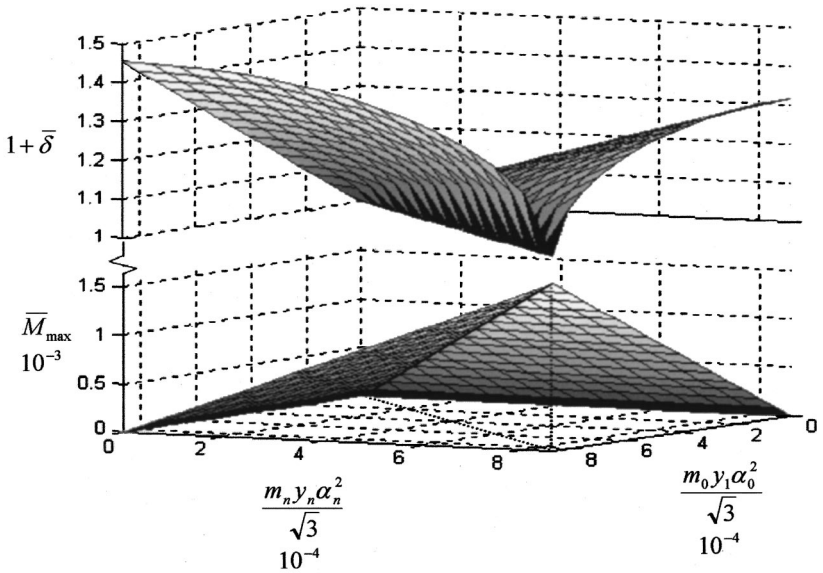

Fig. 4 Variation of $\bar{M}_{\max}$ and $1+\bar{\delta}(\bar{M}=\bar{M}_{\max})$ with wall data. Optimal design where $\bar{\delta}=0$ corresponds to the line of intersection of the $\bar{M}_{\max}$ pyramid faces where $m_0\alpha_0^2 y_1 = m_n \alpha_n^2 y_n$. Results are for composite multilayered tubes.

or, again with use of (4.16),

$$\bar{\delta}=\frac{\bar{X}_1+\bar{X}_2}{\alpha_n^2-\alpha_0^2}, \tag{4.25}$$

which may be compared with (3.22). In the absence of rotation the expression for $\bar{\delta}$ agrees with that of ([3]) for composite tubes.

Having the solution for $\bar{\delta}$ determines also constant $\bar{D}$, by (4.19), and in turn constants (δ_i, D_i) are now known from (4.16) for all layers. In fact, the working stresses (4.18) are now completely known, even without the solution for constants $\alpha_{s,i}$ and $\alpha_{k,i}$. In pure extrusion, for example, with $\eta=-1$, we have the working stress

$$P=2(1+\bar{\delta})ln\rho_0 \tag{4.26}$$

with $\bar{\delta}$ given by (4.25).

Constants $\alpha_{s,i}$ are easily found from (4.8) and (4.21). In fact, constant $\alpha_{s,1}$ is given by (4.21)—and similarly $\alpha_{s,n}$ is given by (4.22)—so if we sum up Eq. (4.8) from $i=1$ to $i=j-1$ the resulting expression

$$y_j\delta_j\alpha_{s,j}^2-y_1\delta_1\alpha_{s,1}^2=\alpha_j^2\left(\frac{Y_{av}^j}{Y_{av}}-y_j\right)-\alpha_0^2\left(\frac{Y_{av}^j}{Y_{av}}-y_1\right) \tag{4.27}$$

completely determines constants $\alpha_{s,j}$. Here, Y_{av}^j is the volume-averaged yield stress, over the first j layers, defined by

$$Y_{av}^j=\frac{1}{\alpha_j^2-\alpha_0^2}\sum_{i=1}^{j}(\alpha_i^2-\alpha_{i-1}^2)Y_i. \tag{4.28}$$

The last integration constants that need to be determined are $\alpha_{k,i}$ of Eqs. (4.6) and (4.13). This particular system is sufficient since constants M_i are given by (4.11). The solution procedure is similar to the technique we have applied in finding constants $\alpha_{s,j}$. Taking the sum of Eq. (4.6) from $i=1$ to $i=j-1$ gives each constant $\alpha_{k,j}$ in terms of $\alpha_{k,1}$ namely

$$\frac{M_j}{\alpha_{k,j}^2}-\frac{M_1}{\alpha_{k,1}^2}=-\sum_{i=1}^{j}M_i\left(\frac{1}{\alpha_i^2}-\frac{1}{\alpha_{i-1}^2}\right)+\frac{M_j}{\alpha_j^2}-\frac{M_1}{\alpha_0^2}. \tag{4.29}$$

A further substitution of $\alpha_{k,i}^{-2}$ from (4.29) in (4.13) leads to a single equation for $\alpha_{k,1}$. Solution of that equation, which is linear in $\alpha_{k,1}^{-2}$, determines all other constants $\alpha_{k,i}$ by (4.29). For future use we shall just record here the expression for $\alpha_{k,1}$ as

$$M_1\left(\frac{1}{\alpha_{k,1}^2}-\frac{1}{\alpha_0^2}\right)\sum_{j=1}^{n}\frac{\alpha_j^4-\alpha_{j-1}^4}{M_j}$$
$$=\sum_{j=1}^{n}\left(\frac{\alpha_j^4-\alpha_{j-1}^4}{M_j}\right)\left[\sum_{i=1}^{j}M_i\left(\frac{1}{\alpha_i^2}-\frac{1}{\alpha_{i-1}^2}\right)\right]$$
$$-\sum_{j=1}^{n}\frac{\alpha_j^4-\alpha_{j-1}^4}{\alpha_j^2}+2(\alpha_n^2-\alpha_0^2). \tag{4.30}$$

5 Discussion and Conclusions

As in the single-phase process, wall rotation lowers the required working stresses in composite tube forming. Taking the pure extrusion case (4.26) as an example we find from (4.25) and (4.21)–(4.22) that the value of $\bar{\delta}$ can be considerably reduced by applying torsional moment $\bar{M}$. That moment is bounded by the smaller of the quantities $(2/\sqrt{3})y_1m_0\alpha_0^2$ and $(2/\sqrt{3})y_nm_n\alpha_n^2$. Evidently, an optimal design appears to be characterized by the relation

$$y_1m_0\alpha_0^2=y_nm_n\alpha_n^2 \tag{5.1}$$

with $\bar{M}=\bar{M}_{\max}$ making $\bar{\delta}$ vanish. The extrusion pressure is then given by the uniform process relation (3.28) with the averaged yield stress of the composite (4.1). By comparison with (3.31) we find that for composite tubes (5.1) provides more degrees-of-freedom in improving the forming process by an appropriate choice of y_1 and y_n.

Figure 4 displays the variation of $\bar{M}_{\max}$, and of $1+\bar{\delta}(\bar{M}=\bar{M}_{\max})$ with wall data (values of $m\alpha^2y/\sqrt{3}$ on both boundaries) as evaluated from (4.25). The pyramid shape of $\bar{M}_{\max}$ follows immediately from (4.21)–(4.22), when either $\bar{X}_1$ or $\bar{X}_2$ vanish, with the optimal design (5.1) at the intersection of the pyramid faces. The nonuniformity parameter $\bar{\delta}$ vanishes along the optimal design line (where $\bar{X}_1=\bar{X}_2=0$) in Fig. 4 and increases monotonously with each of the wall parameters $(m\alpha^2y/\sqrt{3})$. As expected,

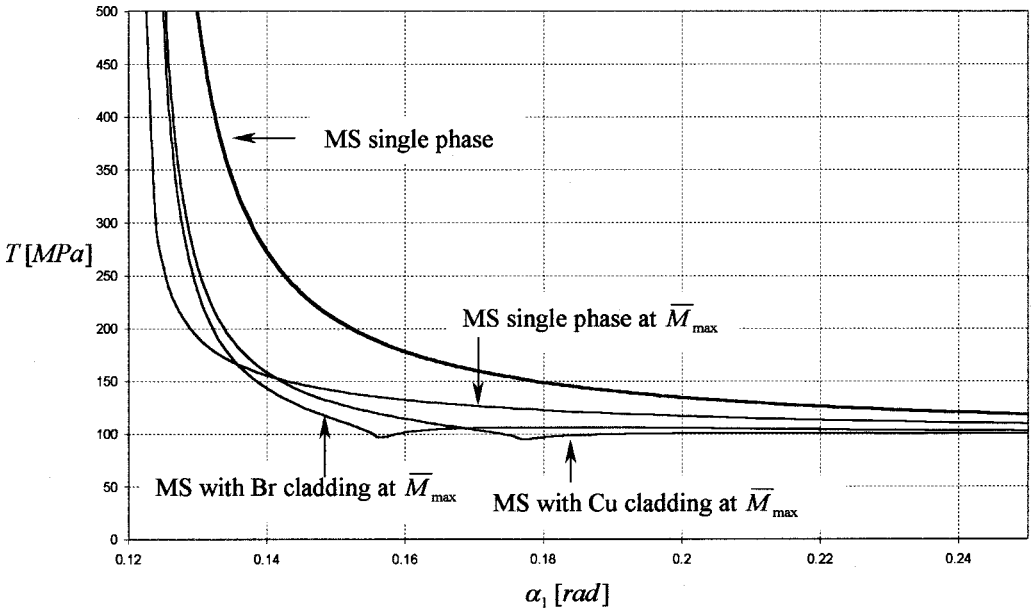

Fig. 5 Drawing stress T for mild steel (MS) tubes with fixed inner wall angle of $\alpha_0=7$deg ≈ 0.12 rad. Upper curve is for stationary dies. Lower curves are for rotating dies at $\overline{M}_{max}$. Also shown is the influence of cladding of external surface with brass (Br) or with copper (Cu). Friction factors in all cases are $m=0.06$ on both walls.

$\overline{M}_{max}$ remains small (about $O(10^{-3})$), but the working stresses, scaled by $(1+\overline{\delta})$, may increase considerably over the uniform value.

A specific example, shown in Fig. 5, illustrates the advantage of rotational forming for drawing through conical dies with inner wall angle of $\alpha_0=7\text{deg}\approx 0.12$ rad and equal friction factors $m=0.06$ on both walls. Results for a single phase tube, made of mild steel (MS) with a yield stress of 584.8 MPa, show the reduction in drawing stress T, due to wall rotation at $\overline{M}_{max}$, for various external wall angles α_1. With $\alpha_1=12$ deg≈ 0.21 rad, for example, wall rotation lowers the drawing stress by 11.5 percent. Also shown in Fig. 5 are curves for the drawing stress with cladding of the outer surface. Cladding material is brass (Br) with $Y=355.6$ MPa, or copper (Cu) with $Y=277$ MPa. The friction factors remain the same (0.06) on both walls, but the boundary parameters $(m\alpha^2 y/\sqrt{3})$ are of course different for each cladding. At $\alpha_1=12$ deg we have with the brass cladding a reduction of 19.3 percent in the drawing stress as compared to single-phase drawing without rotation. With copper cladding the reduction in T is 22.5 percent. In this example we have assumed that cladding thickness is extremely thin so that the average yield stress of the composite equals that of mild steel.

The multilayered tube forming analysis presented here is of course within the framework of the basic assumptions of long and tapered working zones and small wall friction. A further issue that should be examined here are the shear stresses induced by interfacial jumps of yield stresses across adjacent layers. Consider for example the radial component $\Sigma^i_{r\theta}$ at $\theta=\alpha_i$, from (4.3)

$$\Sigma^i_{r\theta}(\alpha_i)=\frac{\sigma^i_{r\theta}(\alpha_i)}{Y_{av}}=y_i\delta_i\left(\alpha_i-\frac{\alpha^2_{s,i}}{\alpha_i}\right). \tag{5.2}$$

Surely, the true stress component $\sigma^i_{r\theta}$ should be much smaller than the yield stress Y_i—so as to comply with our approximate solution—and in particular $\sigma^i_{r\theta}(\alpha_i)$ should be smaller than both Y_i and Y_{i+1}. To this end we rewrite (5.2) as

$$\alpha_i\sigma^i_{r\theta}(\alpha_i)=\frac{(\alpha_i^2-\alpha_0^2)(\alpha_n^2-\alpha_i^2)}{\alpha_n^2-\alpha_0^2}(Y^{n-(i+1)}_{av}-Y^i_{av})$$
$$+\frac{(\alpha_i^2-\alpha_0^2)\overline{X}_2-(\alpha_n^2-\alpha_i^2)\overline{X}_1}{\alpha_n^2-\alpha_0^2}Y_{av} \tag{5.3}$$

where $Y^{n-(i+1)}_{av}$ is the volume-averaged yield stress of all layers from $i+1$ to n. Thus, even in an optimal forming process, where $\overline{X}_1=\overline{X}_2=0$, the jump in the relative averages of yield stress $(Y^{n-(i+1)}_{av}-Y^i_{av})$ can induce considerable shear at the interfaces (and within the working zone as well). A full analysis of the complete nonlinear system of the governing equations is then needed to investigate the forming process.

We may conclude that wall rotation, in steady forming of composites through conical dies, can considerably reduce the required working loads as well as the normal pressure acting on the walls. With a judicious choice of layers constituents, particularly the external layers, it should be possible to control the process parameters and interfacial stresses. The potentially higher reductions which can be achieved through rotating dies call for a further study of this forming pattern beyond the simplifying assumptions employed in the present work.

Acknowledgment

One of us (D.D.) wishes to acknowledge the support of the Sydney Goldstein Chair in Aeronautical Engineering. Part of this study was supported by the fund for the promotion of research at the Technion.

References

[1] Matin, M., and Blazynski, T. Z., 1981, "An Upper Bound Solution of the Problem of Cold Plug Drawing of Trimetallic Implosively Prewelded Tube," J. Eng. Prod., **5**, pp. 33–39.

[2] Szulc, W., and Malinowski, Z., 1994, "Theoretical and Experimental Investigation of the Multilayer Tube Drawing," J. Mater. Process. Technol., **45**, pp. 347–352.

[3] Durban, D., 1984, ''Drawing and Extrusion of Composite Sheets, Wires and Tubes,'' Int. J. Solids Struct., **20**, pp. 469–666.
[4] Shield, R. T., 1955, ''Plastic Flow in a Converging Conical Channel,'' J. Mech. Phys. Solids, **3**, pp. 246–258.
[5] Alcaraz, J. L., Martinez-Espanola, J. M., and Gil-Sevillano, J., 1996, ''Analytical Approach to the Stress Field in the Extrusion of Bimetallic Tubes,'' Int. J. Solids Struct., **33**, pp. 2075–2093.
[6] Brovman, J. M., 1987, ''Stedy Forming Processes of Plastic Materials With Their Rotation,'' Int. J. Mech. Sci., **29**, pp. 483–489.
[7] Durban, D., 1987, ''Drawing of Viscoplastic Tubes Through Rotating Conical Dies,'' *Computational Methods for Predicting Material Processing Defects*, M. Predeleanu, ed., Elsevier, New York, pp. 93–102.
[8] Durban, D., 1980, ''Drawing of Tubes,'' ASME J. Appl. Mech., **46**, pp. 763–740.
[9] Durban, D., 1983, ''Radial Flow Simulation of Drawing and Extrusion of Rigid/Hardening Materials,'' Int. J. Mech. Sci., **25**, pp. 27–39.
[10] Davidi, G., 1999, ''Plastic Forming Processes Through Rotating Conical Dies,'' M.Sc. research thesis, Technion, Haifa, Israel.

N. Sri Namachchivaya
Department of Aeronautical and
Astronautical Engineering,
University of Illinois,
103 S. Wright Street,
Urbana, IL 61801-2935

H. J. Van Roessel
Department of Mathematical Sciences,
University of Alberta,
Edmonton AB, Canada

Moment Lyapunov Exponent and Stochastic Stability of Two Coupled Oscillators Driven by Real Noise

In a recent paper an asymptotic approximation for the moment Lyapunov exponent, $g(p)$, of two coupled oscillators driven by a small intensity real noise was obtained. The utility of that result is limited by the fact that it was obtained under the assumption that the moment p is small, a limitation which precludes, for example, the determination of the stability index. In this paper that limitation is removed and an asymptotic approximation valid for arbitrary p is obtained. The results are applied to study the moment stability of the stationary solutions of structural and mechanical systems subjected to stochastic excitation. [DOI: 10.1115/1.1387021]

1 Introduction

In the study of stability of solutions of random dynamical systems, the exponential growth rate of $\mathbf{E}\|x(t;x_0)\|^p$ is provided by the moment Lyapunov exponent defined as

$$g(p;x_0)=\lim_{t\to\infty}\frac{1}{t}\log \mathbf{E}\|x(t;x_0)\|^p,$$

where $x(t;x_0)$ is the solution process of a linear random dynamical system. If $g(p;x_0)<0$, then, by definition, $\mathbf{E}\|x(t;x_0)\|^p\to 0$ as $t\to\infty$ and this is referred to as pth moment stability. The connection between moment stability and almost-sure stability for an undamped linear oscillator under real noise excitation was established for the first time by Molčanov [1]. These results were extended for an arbitrary d-dimensional system by Arnold [2] where a concise formulation of the relation between almost-sure sample stability and pth mean stability is presented. The complete set of results on the so-called moment Lyapunov exponent, its properties and generators is obtained in two consecutive papers by Arnold et al. [3,4] for real and white noise situations, respectively.

The systems under consideration consist of parametrically excited two-degree-of-freedom models. Such models are encountered in the study of linear or nonlinear mechanical systems subjected to fluctuating loading or imposed displacements, as shown in Section 5. Consider, for example,

$$\ddot{y}_1+2\zeta\omega_1\dot{y}_1+\omega_1^2 y_1+g_1(y_1,y_2)=w(t),$$

$$\ddot{y}_2+2\zeta\omega_2\dot{y}_2+\omega_2^2 y_2+y_2 g_2(y_1,y_2)=0,$$

where $g_1(0,0)=0$, $\partial g_1/\partial y_2(y_1,0)\neq 0$, and $w(t)$ is a white noise process. The stability of the solution $(y_1=\xi(t),\ y_2=0)$ is governed by a set of variational equations of the form

$$\ddot{q}_i+\omega_i^2 q_i+2\zeta\omega_i\dot{q}_i+\sum_{j=1}^{2}\tilde{k}_{ij}(\xi(t))q_j=0,\quad i,j=1,2, \qquad (1)$$

with $\xi(t)$ defined by

$$\ddot{\xi}+2\zeta\omega_1\dot{\xi}+\omega_1^2\xi+g_1(\xi,0)=w(t). \qquad (2)$$

In many problems of practical interest, the $\tilde{k}_{ij}$'s are of the form

$$\tilde{k}_{ij}(\xi)=k_{ij}f(\xi).$$

This is the form we examine so (1) becomes

$$\ddot{q}_i+\omega_i^2 q_i+2\zeta\omega_i\dot{q}_i+\sum_{j=1}^{2}k_{ij}q_j f(\xi(t))=0,\quad i,j=1,2. \qquad (3)$$

The aim of this paper is to study the moment behavior of two-degree-of-freedom systems given by Eq. (3). The small noise expansions of the moment Lyapunov exponent for this two-degree-of-freedom system were obtained by Sri Namachchivaya et al. [5] for small p. In this paper, these results are extended to obtain an asymptotic representation of the moment Lyapunov exponent for finite p. As before we consider a real noise excitation with specific infinitesimal generator G. It is assumed that G has an isolated simple zero eigenvalue. In this paper, we have derived the generator $L(p)$, whose principal eigenvalue is the moment Lyapunov exponent, by two different procedures. The first method is based on an asymptotic expansion similar to that presented in Sri Namachchivaya et al. [5] and the second method is based on stochastic averaging. Although it has been shown that moment Lyapunov exponents are based on large deviation phenomena, the stochastic averaging scheme along with Girsanov and Feynman-Kac formulas yield the same result for $L(p)$ as the asymptotic method.

Section 2 describes the general theory of moment Lyapunov exponents for linear systems with real noise. In Section 3 we obtain the appropriate eigenvalue problem for the moment Lyapunov exponent. A small noise expansion is constructed and the moment Lyapunov exponent in terms of spectral densities is calculated in Section 3.1. In Section 3.2, the equation governing the moment Lyapunov exponent is obtained by means of stochastic averaging and some discussions on the validity of stochastic averaging in determining Lyapunov and moment Lyapunov exponents are given. An orthogonal expansion for the eigenvalue problem based on Galerkin method is presented in Section 4. Various cases of interest are obtained numerically based on this approximation. In Section 5, these results are applied to study the flexural-torsional stability of a narrow simply supported elastic beam under fluctuating end moments or a stochastic follower force.

Contributed by the Applied Mechanics Division of THE AMERICAN SOCIETY OF MECHANICAL ENGINEERS for publication in the ASME JOURNAL OF APPLIED MECHANICS. Manuscript received by the ASME Applied Mechanics Division, May 15, 2000; final revision, Feb. 26, 2001. Associate Editor: A. A. Ferri. Discussion on the paper should be addressed to the Editor, Professor Lewis T. Wheeler, Department of Mechanical Engineering, University of Houston, Houston, TX 77204-4792, and will be accepted until four months after final publication of the paper itself in the ASME JOURNAL OF APPLIED MECHANICS.

2 Real Noise Case

This section provides a summary of essential results for moment Lyapunov exponents. It is included to give an outline of the central ideas involved in the arguments. The reader is referred to Arnold et al. [3,4] for details of the theorems. The complete set of equations required for calculating the moment Lyapunov exponents is also presented.

For the real noise case, consider

$$\begin{aligned} \dot{x} &= A(\xi(t))x, \quad x \in \mathbf{R}^d, \\ d\xi &= X_0(\xi)dt + \sum_{i=1}^{r} X_i(\xi) \circ dW_i, \quad \xi \in M. \end{aligned} \tag{4}$$

In order to ensure that there is a unique smooth and positive invariant density ν on the compact manifold M, assume $\xi(t)$ is strongly elliptic in the sense that $\dim LA(X_1, \ldots, X_r)(\xi) = \dim M$ for all $\xi \in M$, where $LA(Z)$ denotes the Lie algebra generated by the set Z of vector fields. Introducing polar coordinates in $\mathbf{R}^d$ through the Khas'minskii transformation

$$s = \frac{x}{\|x\|} \in S^{d-1} \quad \text{and} \quad \|x\| \in \mathbf{R}^+$$

gives the following equations of motion:

$$\|x(t;x_0)\| = \|x_0\| \exp\left\{ \int_0^t q(\xi(\tau), s(\tau))d\tau \right\},$$

$$\dot{s} = h(\xi(t), s),$$

where

$$q(\xi(\tau), s(\tau)) = s^T A(\xi(\tau))s \quad \text{and} \quad h(\xi(t), s) = (A - qI)s.$$

The pair (ξ, s) together form a diffusion process on $M \times \mathbf{P}^{d-1}$ (obtained from S^{d-1} by identifying s and $-s$) whose generator is given by

$$\mathcal{L} = G + h\frac{\partial}{\partial s},$$

where $G = X_0 + 1/2\Sigma_{i=1}^{r} X_i^2$ is the generator of ξ written in Hörmander form. For a fixed $\xi \in M$, $h(\xi, \cdot)$ is a vector field on the projective space. To avoid degenerate situations for $\mathcal{L}$, the following ellipticity condition is imposed:

$$(H) \dim LA\left[X_0 + h + \frac{\partial}{\partial t}, X_1, \ldots, X_r \right](\xi, s, t) = \dim M + d$$
$$\forall (\xi, s, t) \in M \times \mathbf{P}^{d-1} \times \mathbf{R}.$$

Combining the above results with the definition of moment Lyapunov exponents yields

$$g(p;x_0) = \lim_{t\to\infty} \frac{1}{t} \log \mathbf{E}\left[\exp\left\{ p \int_0^t q(\xi(\tau), s(\tau))d\tau \right\} \right]$$
$$\text{for } p \in \mathbf{R}, \quad \text{and fixed } x_0 \in \mathbf{R}^d \backslash \{0\}.$$

The following was proven by Arnold et al. [3]:

THEOREM 1. *Assume (H)*:

1 Let $\lambda = \int_M \int_{\mathbf{P}^{d-1}} q(\xi, s)d\mu$ *where* μ *is the unique invariant probability measure of* (ξ, s) *on* $M \times \mathbf{P}^{d-1}$. *Then* λ *is the maximal Lyapunov exponent for (4), i.e., for* $x_0 \neq 0$

$$\lim_{t\to\infty} \frac{1}{t} \log \|x(t;x_0)\| = \lambda \quad \text{almost-surely.}$$

2 For $p \in \mathbf{R}$, *let* $g(p)$ *be the principal eigenvalue of* $L(p) = \mathcal{L} + pq(\xi, s)$ *acting on* $C(M \times \mathbf{P}^{d-1})$. *Then* $g(p)$ *is the pth moment Lyapunov exponent for (4), i.e., for* $x_0 \neq 0$

$$\lim_{t\to\infty} \frac{1}{t} \log \mathbf{E}\|x(t;x_0)\|^p = g(p).$$

Moreover, $g: \mathbf{R} \to \mathbf{R}$ *is convex and analytic,* $g(p)/p$ *is increasing,* $g(0) = 0$, $g'(0) = \lambda$, *and the corresponding eigenfunction of* $g(p)$ *is non-negative. Furthermore,* $g''(0)$ *is the variance in the central limit theorem, i.e.,*

$$\frac{1}{\sqrt{t}}(\log\|x(t;x_0)\| - \lambda t) \rightharpoonup \mathcal{N}(0, g''(0)) (t \to \infty) \quad \text{for any } x_0 \neq 0,$$

where $\mathcal{N}$ *is the normal distribution and* $\rightharpoonup$ *denotes weak convergence.*

Consider the operator $L(p)$ and its adjoint $L^*(p)$. By Theorem 1, $g(p)$ is an isolated simple eigenvalue of $L(p)$ with non-negative eigenfunction $\psi(p)$ such that $\|\psi(p)\| = 1$. The adjoint operator $L^*(p)$ has an eigenfunction $\nu(p)$ corresponding to $g(p)$ which is unique and has the property $\langle \psi(p), \nu(p) \rangle = 1$, i.e.,

$$L(p)\psi(p) = g(p)\psi(p), \quad \langle \psi(p), \nu(p) \rangle = 1 \quad \forall p \in \mathbf{R}. \tag{5}$$

3 Moment Lyapunov Exponent for Coupled Oscillators

Consider linear oscillatory systems described by equations of motion of the form

$$\ddot{q}_i + \omega_i^2 q_i + 2\varepsilon^2 \zeta \omega_i \dot{q}_i + \varepsilon \sum_{j=1}^{2} k_{ij} q_j f(\xi(t)) = 0, \quad i, j = 1,2, \tag{6}$$

where the q_i's are generalized coordinates, ω_i is the ith natural frequency, and $\varepsilon\zeta$ represents a small viscous damping coefficient. It is assumed that the natural frequencies are *noncommensurable*. The stochastic term $\xi(t)$ is a real-noise process on a smooth connected Riemannian manifold M (with or without boundary) with f a smooth nonconstant function defined on M. The associated infinitesimal generator is assumed to have the form

$$G(\xi) = \sum_{i=1}^{n} \mu_i(\xi) \frac{\partial}{\partial \xi_i} + \frac{1}{2} \sum_{k=1}^{r} \left[\sum_{i=1}^{n} \sigma_i^k(\xi) \frac{\partial}{\partial \xi_i} \right] \left[\sum_{i=1}^{n} \sigma_i^k(\xi) \frac{\partial}{\partial \xi_i} \right]. \tag{7}$$

In order to make the problem tractable, G will be assumed to have an *isolated simple zero eigenvalue*. Hence, the only solution of $Gu = 0$ is $u \equiv$ constant. It follows that the associated adjoint operator G^* also has zero as a simple, isolated eigenvalue and the normalized invariant measure $v(\xi)d\xi$ satisfies $G^*v(\xi) = 0$.

The almost-sure stability of the equilibrium state $q = \dot{q} = 0$ of Eq. (6) is to be investigated. Using the transformation $q_i = x_{2i-1}$, $\dot{q}_i = \omega_i x_{2i}$, $i = 1,2$, Eq. (6) may be represented by the following system of Stratonovich differential equations:

$$\begin{aligned} \dot{x} &= Ax + f(\xi(t))Bx, \\ d\xi &= \mu(\xi)dt + \sigma(\xi) \circ dW_t, \end{aligned} \tag{8}$$

where A and B are 4×4 constant matrices given by

$$A = \begin{bmatrix} 0 & \omega_1 & 0 & 0 \\ -\omega_1 & -2\varepsilon^2\zeta\omega_1 & 0 & 0 \\ 0 & 0 & 0 & \omega_2 \\ 0 & 0 & -\omega_2 & -2\varepsilon^2\zeta\omega_2 \end{bmatrix},$$

$$B = \varepsilon \begin{bmatrix} 0 & 0 & 0 & 0 \\ -k_{11}/\omega_1 & 0 & -k_{12}/\omega_1 & 0 \\ 0 & 0 & 0 & 0 \\ -k_{21}/\omega_2 & 0 & -k_{22}/\omega_2 & 0 \end{bmatrix}. \tag{9}$$

3.1 Asymptotic Results for Coupled Oscillators. Applying the transformations

$$x_1 = e^{\rho}\cos\phi_1\cos\theta, \quad x_2 = -e^{\rho}\sin\phi_1\cos\theta,$$
$$x_3 = e^{\rho}\cos\phi_2\sin\theta, \quad x_4 = -e^{\rho}\sin\phi_2\sin\theta, \tag{10}$$

yields the following set of equations for the logarithm of the amplitude ρ, phase variables (ϕ_1,ϕ_2,θ) and noise process ξ:

$$\dot{\rho} = \sum_{j=0}^{2} \varepsilon^j q^j(\phi_1,\phi_2,\theta,\xi), \quad \dot{\theta} = \sum_{j=0}^{2} \varepsilon^j s^j(\phi_1,\phi_2,\theta,\xi), \tag{11}$$

$$\dot{\phi}_i = \sum_{j=0}^{2} \varepsilon^j h_i^j(\phi_1,\phi_2,\theta,\xi), \quad d\xi = \mu(\xi)dt + \sigma(\xi)\circ dW_t, \tag{12}$$

where $q^0(\phi_1,\phi_2,\theta,\xi)\equiv 0$, $s^0(\phi_1,\phi_2,\theta,\xi)\equiv 0$, $h_i^0(\phi_1,\phi_2,\theta,\xi)=\omega_i$ and

$$q^1(\phi_1,\phi_2,\theta,\xi) = \frac{1}{4}f(\xi)[q_0^1(\phi_1,\phi_2) + q_c^1(\phi_1,\phi_2)\cos 2\theta + q_s^1(\phi_1,\phi_2)\sin 2\theta],$$
$$q_0^1(\phi_1,\phi_2) = p_{11}\sin 2\phi_1 + p_{22}\sin 2\phi_2,$$
$$q_c^1(\phi_1,\phi_2) = p_{11}\sin 2\phi_1 - p_{22}\sin 2\phi_2,$$
$$q_s^1(\phi_1,\phi_2) = p_{21}^{+}\sin\phi^{+} - p_{21}^{-}\sin\phi^{-},$$
$$s^1(\phi_1,\phi_2,\theta,\xi) = \frac{1}{4}f(\xi)[s_0^1(\phi_1,\phi_2) + s_c^1(\phi_1,\phi_2)\cos 2\theta + s_s^1(\phi_1,\phi_2)\sin 2\theta],$$
$$s_0^1(\phi_1,\phi_2) = p_{21}^{-}\sin\phi^{+} - p_{21}^{+}\sin\phi^{-},$$
$$s_c^1(\phi_1,\phi_2) = p_{21}^{+}\sin\phi^{+} - p_{21}^{-}\sin\phi^{-},$$
$$s_s^1(\phi_1,\phi_2) = p_{22}\sin 2\phi_2 - p_{11}\sin 2\phi_1,$$
$$h_1^1(\phi_1,\phi_2,\theta,\xi) = \frac{1}{2}f(\xi)[h_{1(0)}^1(\phi_1) + h_{1(\theta)}^1(\phi_1,\phi_2)\tan\theta],$$
$$h_2^1(\phi_1,\phi_2,\theta,\xi) = \frac{1}{2}f(\xi)[h_{2(0)}^1(\phi_2) + h_{2(\theta)}^1(\phi_1,\phi_2)\cot\theta],$$
$$h_{1(0)}^1(\phi_1) = p_{11}(1+\cos 2\phi_1),$$
$$h_{1(\theta)}^1(\phi_1,\phi_2) = p_{12}(\cos\phi^{+} + \cos\phi^{-}),$$
$$h_{2(0)}^1(\phi_2) = p_{22}(1+\cos 2\phi_2),$$
$$h_{2(\theta)}^1(\phi_1,\phi_2) = p_{21}(\cos\phi^{+} + \cos\phi^{-}),$$
$$q^2(\phi_1,\phi_2,\theta,\xi) = q_0^2(\phi_1,\phi_2) + q_c^2(\phi_1,\phi_2)\cos 2\theta,$$
$$q_0^2(\phi_1,\phi_2) = -\frac{1}{2}[\delta_1(1-\cos 2\phi_1) + \delta_2(1-\cos 2\phi_2)],$$
$$q_c^2(\phi_1,\phi_2) = -\frac{1}{2}[\delta_1(1-\cos 2\phi_1) - \delta_2(1-\cos 2\phi_2)],$$
$$s^2(\phi_1,\phi_2,\theta,\xi) = s_s^2(\phi_1,\phi_2)\sin 2\theta,$$
$$s_s^2(\phi_1,\phi_2) = \frac{1}{2}[\delta_1(1-\cos 2\phi_1) - \delta_2(1-\cos 2\phi_2)],$$
$$h_i^2(\phi_i) = -\delta_i\sin 2\phi_i.$$

In the above expressions, $p_{21}^{\pm} = p_{21} \pm p_{12}$, $\phi^{\pm} = \phi_1 \pm \phi_2$, $\delta_i = \zeta\omega_i$ and $p_{ij} = k_{ij}/\omega_i$.

Since the processes $(\phi_1,\phi_2,\theta,\xi)$ do not depend on ρ, the processes $(\phi_1,\phi_2,\theta,\xi)$ alone form a diffusive Markov process and the associated generator is given by

$$L^{\varepsilon}(p) = L^0(p) + \varepsilon L^1(p) + \varepsilon^2 L^2(p),$$

where

$$L^0(p) = G(\xi) + \sum_{i=1}^{2} \omega_i\frac{\partial}{\partial\phi_i} + pq^0(\phi_1,\phi_2,\theta,\xi) =: \mathcal{L}^0 + pq^0;$$
$$L^1(p) = s^1(\phi_1,\phi_2,\theta,\xi)\frac{\partial}{\partial\theta} + \sum_{i=1}^{2} h_i^1(\phi_1,\phi_2,\theta,\xi)\frac{\partial}{\partial\phi_i} + pq^1(\phi_1,\phi_2,\theta,\xi) =: \mathcal{L}^1 + pq^1;$$
$$L^2(p) = s^2(\phi_1,\phi_2,\theta,\xi)\frac{\partial}{\partial\theta} + \sum_{i=1}^{2} h_i^2(\phi_1,\phi_2,\theta,\xi)\frac{\partial}{\partial\phi_i} + pq^2(\phi_1,\phi_2,\theta,\xi) =: \mathcal{L}^2 + pq^2.$$

In Sri Namachchivaya et al. [5] use was made of the analyticity of $g(p)$ to Taylor expand in p. Each coefficient in the Taylor series was then further expanded in ε. With this double expansion in both ε and p an expression for $g(p)$ valid to $o(\varepsilon^2 p^2)$ was obtained. However, the restriction to small values of p limits the utility of that result, particularly with regard to the calculation of the stability index as pointed out by Khasminskii and Moshchuk [6]. Here we remove the small p restriction and consider an expansion of the moment Lyapunov exponent in powers of ε only:

$$g_{\varepsilon}(p) = g_0(p) + \varepsilon g_1(p) + \varepsilon^2 g_2(p) + \mathcal{O}(\varepsilon^2).$$

It has been shown that such an expansion is asymptotic as in Sri Namachchivaya et al. [5], Khasminskii and Moshchuk [6], Arnold et al. [7], and Pardoux and Wihstutz [8]. Insertion of these expansions into Eq. (5) leads to the following sequence of Poisson equations:

$$(L^0(p) - g_0(p))\psi_0 = 0; \tag{13}$$
$$(L^0(p) - g_0(p))\psi_1 = g_1(p)\psi_0 - L^1(p)\psi_0; \tag{14}$$
$$(L^0(p) - g_0(p))\psi_2 = g_2(p)\psi_0 + g_1(p)\psi_1 - L^2(p)\psi_0 - L^1(p)\psi_1. \tag{15}$$

3.1.1 The Solution to $\mathcal{O}(1)$. Since $q^0(\phi_1,\phi_2,\theta,\xi)\equiv 0$, it follows from the definition of $g(p)$ that $g_0(p)\equiv 0$. Thus the operator $L^0(p)$ reduces to $\mathcal{L}^0$ and Eq. (13) becomes

$$\mathcal{L}^0\psi_0 = 0.$$

Since the equations to be solved involve the differential operator $\mathcal{L}^0$ at each stage, the solution of the corresponding adjoint problem $\mathcal{L}^{0*}\Psi_0 = 0$, along with periodic boundary conditions $\Psi_0(\phi_1 + 2\pi,\phi_2,\theta,\xi) = \Psi_0(\phi_1,\phi_2 + 2\pi,\theta,\xi) = \Psi_0(\phi_1,\phi_2,\theta,\xi)$, is required. Since G has an isolated simple zero eigenvalue, and the frequencies ω_1 and ω_2 are noncommensurable it can be shown (see [9]) that the solution is

$$\Psi_0(\theta,\xi) = \frac{\nu(\xi)\mathcal{F}(\theta)}{4\pi^2},$$

where $\mathcal{F}$ is an arbitrary function. By a similar argument it follows that $\psi_0 \in \ker(\mathcal{L}^0) = \{C(\theta): C \text{ is an arbitrary function of } \theta\}$. Therefore $\psi_0 = \psi_0(\theta)$, a function of θ which has yet to be determined.

3.1.2 The Solution to $\mathcal{O}(\varepsilon)$. Inserting the above expression for ψ_0 into Eq. (14) results in

$$\mathcal{L}^0\psi_1 = -s^1(\phi_1,\phi_2,\theta,\xi)\psi_0' + [g_1(p) - pq^1(\phi_1,\phi_2,\theta,\xi)]\psi_0. \tag{16}$$

The eigenvalue $g_1(p)$ is obtained from the solvability condition. Applying the solvability condition to the above equation yields

$$g_1(p)=\langle q^1\psi_0+s^1\psi_0',\Psi_0\rangle$$
$$=\frac{1}{16\pi^2}\langle f(\xi)R_1(\phi_1,\phi_2,\theta;p),\nu(\xi)\mathcal{F}(\theta)\rangle=0, \quad (17)$$

where

$$R_1(\phi_1,\phi_2,\theta;p)=p[q_0^1(\phi_1,\phi_2)+q_c^1(\phi_1,\phi_2)\cos 2\theta + q_s^1(\phi_1,\phi_2)\sin 2\theta]\psi_0+[s_0^1(\phi_1,\phi_2) + s_c^1(\phi_1,\phi_2)\cos 2\theta + s_s^1(\phi_1,\phi_2)\sin 2\theta]\psi_0'(\theta),$$

$$\langle(\cdot),(\cdot\cdot)\rangle=\int_0^{\pi/2}\int_M\int_0^{2\pi}\int_0^{2\pi}(\cdot)(\cdot\cdot)d\phi_1 d\phi_2 d\xi d\theta.$$

The last equality in Eq. (17) follows from the fact that $R_1(\phi_1,\phi_2,\theta;p)$ is periodic in ϕ_1 and ϕ_2, and $f(\xi)$ is a zero mean process. In terms of $R_1(\phi_1,\phi_2,\theta;p)$, Eq. (14) reduces to

$$\mathcal{L}^0\psi_1=-\frac{1}{4}f(\xi)R_1(\phi_1,\phi_2,\theta;p). \quad (18)$$

The solution ψ_1 of the above equation can be expressed in terms of the Green's function $g(\xi,t;\eta,0)$ for the operator G and can be written as (see [5])

$$\psi_1(\phi_1,\phi_2,\theta,\xi;p)=\frac{1}{4}\int_0^\infty K(\xi,\tau)R_1(\phi_1+\omega_1\tau,\phi_2+\omega_2\tau,\theta;p)d\tau. \quad (19)$$

3.1.3 The Solution to $\mathcal{O}(\varepsilon^2)$. Employing the above results, Eq. (15) for ψ_2 becomes

$$\mathcal{L}^0\psi_2=[g_2(p)-pq^2(\phi_1,\phi_2,\theta,\xi)]\psi_0-s^2(\phi_1,\phi_2,\theta,\xi)\psi_0' - \mathcal{L}^1\psi_1(\phi_1,\phi_2,\theta,\xi;p). \quad (20)$$

The solvability condition for this equation is

$$\langle g_2(p)\Psi_0-pq^2\Psi_0-s^2\psi_0'-\mathcal{L}^1\psi_1,\Psi_0\rangle=0. \quad (21)$$

Making use of the correlation function of $f(\xi)$ and the cosine spectrum given, respectively, by

$$\mathcal{R}(\tau)=\int_M f(\xi)K(\xi,\tau)d\tau, \quad S(\omega)=2\int_0^\infty\mathcal{R}(\tau)\cos\omega\tau d\tau,$$

the solvability condition (21), after some calculation, reduces to

$$\int_0^{\pi/2}\left\{[g_2(p)-pQ(\theta)-\frac{1}{2}p^2\hat{Q}(\theta)]\Psi_0-[\mu(\theta)+p\hat{\mu}(\theta)]\psi_0'(\theta) - \frac{1}{2}\sigma^2(\theta)\psi_0''(\theta)\right\}\mathcal{F}(\theta)d\theta=0, \quad (22)$$

where

$$\mu(\theta)=\sigma^2(\theta)\cot 2\theta-\frac{1}{2}\Lambda\sin 2\theta,$$

$$\hat{\mu}(\theta)=\frac{1}{2}(B-E+2A\cos 2\theta)\sin 2\theta,$$

$$Q(\theta)=\sigma^2(\theta)+\frac{1}{2}\Lambda\cos 2\theta+D,$$

$$\hat{Q}(\theta)=F+E\cos 2\theta-A\cos^2 2\theta,$$

$$\sigma^2(\theta)=A\cos^2 2\theta+B\cos 2\theta+C,$$

with the constants given by

$$A=\frac{1}{32}\left\{(p_{21}+p_{12})^2S(\omega^+)+(p_{21}-p_{12})^2S(\omega^-) - \sum_{i=1}^2 p_{ii}^2S(2\omega_i)\right\},$$

$$B=\frac{1}{16}(p_{21}^2-p_{12}^2)(S(\omega^+)+S(\omega^-)),$$

$$C=\frac{1}{32}\left\{(p_{21}-p_{12})^2S(\omega^+)+(p_{21}+p_{12})^2S(\omega^-) + \sum_{i=1}^2 p_{ii}^2S(2\omega_i)\right\},$$

$$D=\frac{1}{2}(\Lambda_1+\Lambda_2)+\frac{1}{8}p_{21}p_{12}(S(\omega^+)-S(\omega^-)),$$

$$E=\frac{1}{16}\{p_{11}^2S(2\omega_1)-p_{22}^2S(2\omega_2)\},$$

$$F=\frac{1}{32}\left\{(p_{21}+p_{12})^2S(\omega^+)+(p_{21}-p_{12})^2S(\omega^-) + \sum_{i=1}^2 p_{ii}^2S(2\omega_i)\right\},$$

$$\Lambda_i=-\delta_i+\frac{1}{8}p_{ii}^2S(2\omega_i), \quad i=1,2,$$

$$\Lambda=\Lambda_1-\Lambda_2, \quad \omega^\pm=\omega_1\pm\omega_2.$$

Since Eq. (22) must hold for arbitrary $\mathcal{F}(\theta)$, the bracketed quantity must vanish identically. This leads to the following differential equation for ψ_0:

$$\tilde{L}(p)\psi_0:=\frac{1}{2}\sigma^2(\theta)\psi_0''+[\mu(\theta)+p\hat{\mu}(\theta)]\psi_0' + \left[pQ(\theta)+\frac{1}{2}p^2\hat{Q}(\theta)\right]\psi_0 = g_2(p)\psi_0. \quad (23)$$

We reiterate that Eq. (23) was derived without any restriction on the size of p. This equation along with appropriate boundary conditions forms the eigenvalue problem for which $g_2(p)$ is the principal eigenvalue. We note in passing that a Taylor series expansion of the above equation in p allows us to recover the equations in Sri Namachchivaya et al. [5]. Boundaries for the θ process are not physical, thus it is not clear what boundary conditions one should use to solve the eignenvalue problem (23). However, our earlier work ([5]) for small p suggests that the boundary behavior for $p=0$, which can be obtained by the Feller boundary classification, would be appropriate for determining the moment Lyapunov exponent $g(p)$.

The boundary conditions are determined by considering the adjoint equation with $p=0$:

$$\tilde{\mathcal{L}}^*(\tilde{m}(\theta)):=\frac{1}{2}\frac{d^2}{d\theta^2}(\sigma^2(\theta)\tilde{m}(\theta))-\frac{d}{d\theta}(\mu(\theta)\tilde{m}(\theta))=0. \quad (24)$$

Appropriate boundary conditions for $\tilde{m}(\theta)$ are based on the Feller boundary classification. This can also be justified from transformation (10), or equivalently (28) that $\theta=0$ implies $a_1=0$, and $\theta=\pi/2$ implies $a_2=0$. It is clear physically that unless the coupling coefficients p_{12} and p_{21} are both zero, it is not possible to have a solution with either a_1 or a_2 identically zero. Thus, $\tilde{m}(\theta)$

will not represent a point mass at $\theta=0$ or $\theta=\pi/2$. Moreover, this assertion can also be justified by applying the Feller classification based on scale and speed measures for the $\tilde{m}(\theta)$ process. It can be shown, as in Sri Namachchivaya and Van Roessel [9], that $\theta=0$ and $\theta=\pi/2$ are entrance boundaries. It is clear from Eq. (24) that the probability current is given by

$$A_{st}=-\mu(\theta)\tilde{m}(\theta)+\frac{1}{2}\frac{d}{d\theta}[\sigma^2(\theta)\tilde{m}(\theta)]. \tag{25}$$

The solution to the Fokker-Planck equation can be written as

$$\tilde{m}(\theta)=m(\theta)[2A_{st}S(\theta)+C], \tag{26}$$

where the scale and speed measures are defined in terms of $\mu(\theta)$ and $\sigma(\theta)$ as

$$m(\theta)=[\sigma^2(\theta)s(\theta)]^{-1},\quad s(\theta)=\exp\left\{-\int^{\theta}\frac{2\mu(\eta)}{\sigma^2(\eta)}d\eta\right\},$$

$$S(\theta)=\int^{\theta}s(\eta)d\eta,$$

and $\tilde{m}(\theta)$ satisfies boundary and normality conditions. Since $\theta=0$ and $\theta=\pi/2$ are entrance boundaries, it can be shown that the boundary conditions for $\tilde{m}(\theta)$, are given by $A_{st}=0$. Thus applying the appropriate inner product and using the above boundary condition gives

$$\int_0^{\infty}\tilde{\mathcal{L}}^*(\tilde{m}(\theta))\psi_0(\theta)d\theta$$

$$=\int_0^{\infty}\tilde{\mathcal{L}}(\psi_0(\theta))\tilde{m}(\theta)d\theta-\frac{1}{2}\sigma^2(\theta)\tilde{m}(\theta)\psi_0(\theta)\Big|_0^{\pi/2},$$

which yields zero Neumann boundary conditions for ψ_0.

THEOREM 2. *Suppose the system of Eqs. (11), (12) satisfies the condition (H), G has an isolated simple zero eigenvalue and the frequencies ω_1 and ω_2 are noncommensurable. The asymptotic expansion of the moment Lyapunov exponent of Eq. (8) is given by*

$$g_{\varepsilon}(p)=\varepsilon^2 g_2(p)+\mathcal{O}(\varepsilon^2), \tag{27}$$

where $g_2(p)$ is the largest eigenvalue of the Eqs. (23) with zero Neumann boundary conditions.

3.2 Results Based on Stochastic Averaging. In this section, we shall obtain the $\tilde{L}(p)$ operator defined in Eq. (23), using the method of stochastic averaging. The underpinning of the classical stochastic averaging method is a separation of time scales so that the state variables of fast time scales can be averaged while the equations of the slow variables are approximated. A mathematically rigorous proof of this result was given by Khasminskii [10]. Since then, several authors have developed the theory in various directions using various assumptions. Due to the fact that solutions of the original equations converge weakly to the averaged equation, it is not obvious that averaging for the purpose of obtaining results on Lyapunov and moment Lyapunov exponent is appropriate. Using Girsanov's theorem along with the Feynman-Kac formula, we will show that the method of averaging is indeed justified.

In order to apply this method we transform the equations of motion (8) to a standard form. To this end we shall make use of transformations similar to Eq. (10), i.e.,

$$\begin{aligned}&x_1=a_1\cos\Phi_1,\quad x_2=-\omega_1 a_1\sin\Phi_1,\quad \Phi_1=\omega_1 t+\phi_1,\\ &x_3=a_2\cos\Phi_2,\quad x_4=-\omega_2 a_2\sin\Phi_2,\quad \Phi_2=\omega_2 t+\phi_2,\end{aligned} \tag{28}$$

which yield the following set of equations for the amplitudes $a=(a_1,a_2)$, phase variables $\phi=(\phi_i,\phi_2)$:

$$\dot{a}_i=\varepsilon F_i^1(a,\phi,t)f(\xi(t))+\varepsilon^2 F_i^2(a,\phi,t)\zeta_i, \tag{29}$$

$$\dot{\phi}_i=\varepsilon G_i^1(a,\phi,t)f(\xi(t))+\varepsilon^2 G_i^2(a,\phi,t)\zeta_i, \tag{30}$$

where

$$F_i^1(a,\phi,t)=\frac{p_{ii}}{2}a_i\sin 2\Phi_i+\frac{p_{ij}}{2}a_j(\sin(\omega_{ij}^+t+\phi_{ij}^+)+\sin(\omega_{ij}^-t+\phi_{ij}^-)), \tag{31}$$

$$G_i^1(a,\phi,t)=\frac{p_{ii}}{2}(\cos 2\Phi_i+1)+\frac{p_{ij}}{2}\frac{a_j}{a_i}a_j(\cos(\omega_{ij}^+t+\phi_{ij}^+)+\cos(\omega_{ij}^-t+\phi_{ij}^-)), \tag{32}$$

$$F_i^2(a,\phi,t)=\omega_i a_i(1-\cos 2\Phi_i),\quad \omega_{ij}^{\pm}=\omega_i\pm\omega_j, \tag{33}$$

$$G_i^2(a,\phi,t)=\omega_i\sin 2\Phi_i,\quad \phi_{ij}^{\pm}=\phi_i\pm\phi_j. \tag{34}$$

Here the noise process $\xi(\omega,t)$ is a stationary stochastic process with mean zero whose correlation function $R(\tau)$ decays sufficiently quickly to zero as τ increases, implying $\xi(\omega,t)$ satisfies the strong mixing condition (Khasminskii [10]). According to the averaging theorem the processes $a_i(t,\varepsilon)$ and $\phi_i(t,\varepsilon)$ converge weakly on a time interval of order $1/\varepsilon^2$ to a diffuse Markov process $\bar{a}_i(t,\varepsilon)$ and $\bar{\phi}_i(t,\varepsilon)$ which is continuous w.p. 1, and satisfies the Itô stochastic differential equation

$$d\bar{a}_i=\varepsilon^2 m_i(\bar{a})dt+\varepsilon\bar{\sigma}_{ij}(\bar{a})dW_j, \tag{35}$$

$$d\bar{\phi}_i=\varepsilon^2 n_i(\bar{a})dt+\varepsilon\bar{\mu}_{ij}(\bar{a})dW_j, \tag{36}$$

where

$$m_i(\bar{a})=-\delta_i\bar{a}_i+\frac{1}{16}\left\{3p_{ii}^2\bar{a}_i S(2\omega_i)+\left(p_{ij}^2\frac{\overline{a_j^2}}{\bar{a}_i}+2p_{ij}p_{ji}\right)S(\omega^+)+\left(p_{ij}^2\frac{\overline{a_j^2}}{\bar{a}_i}-2p_{ij}p_{ji}\right)S(\omega^-)\right\},$$

$$n_i(\bar{a})=\frac{1}{8}\{p_{ii}^2\bar{a}_i\Psi(2\omega_i)+(p_{ij}p_{ji})\Psi(\omega^+)+(-1)^i\Psi(\omega^-)\},$$

$$(\overline{\sigma\sigma^T})_{ii}=\frac{1}{8}\{p_{ii}^2\overline{a_i^2}S(2\omega_i)+p_{ij}^2\overline{a_j^2}(S(\omega^+)+S(\omega^-))\},$$

$$(\overline{\sigma\sigma^T})_{ij}=\frac{1}{8}\{p_{ij}p_{ji}\bar{a}_i\bar{a}_j(S(\omega^+)-S(\omega^-))\},$$

$$(\overline{\mu\mu^T})_{ii}=\frac{1}{8}\left\{p_{ii}^2(S(2\omega_i)+2S(0))+p_{ij}^2\frac{\overline{a_j^2}}{\overline{a_i^2}}(S(\omega^+)+S(\omega^-))\right\},$$

$$(\overline{\mu\mu^T})_{ij}=\frac{1}{8}\{p_{ij}p_{ji}(S(\omega^+)+S(\omega^-))+2p_{ii}p_{jj}S(0)\}.$$

One of the advantages of the above approximate Itô equations is that the amplitudes $\bar{a}_i$ are decoupled from the phases $\bar{\phi}_i$ and they form a diffusive Markov process. To obtain the moment Lyapunov exponent we transform the Itô equations for the amplitudes in terms of the norm, $r=\|x\|$ and an angle θ using

$$\bar{a}_1=r\cos\theta,\quad \bar{a}_2=r\sin\theta,$$

which results in

$$g(p;x_0)=g(p;r_0)\lim_{t\to\infty}\frac{1}{t}\log\mathbf{E}[r^p]. \tag{37}$$

After some manipulation, the Itô equations for r and the angle θ become

$$dr=\varepsilon^2\nu(\theta)rdt+\varepsilon\chi_j(\theta)rdW_j, \tag{38}$$

$$d\theta=\varepsilon^2\mu(\theta)dt+\varepsilon\sigma_j(\theta)dW_j, \tag{39}$$

where

$$\nu(\theta)r = m_i(\bar{a})\frac{\partial r}{\partial \bar{a}_i} + \frac{1}{2}(\overline{\sigma\sigma^T})_{ij}\frac{\partial^2 r}{\partial \bar{a}_i \partial \bar{a}_j}, \quad \chi_j(\theta)r = \bar{\sigma}_{ij}\frac{\partial r}{\partial \bar{a}_i}, \tag{40}$$

$$\mu(\theta) = m_i(\bar{a})\frac{\partial \theta}{\partial \bar{a}_i} + \frac{1}{2}(\overline{\sigma\sigma^T})_{ij}\frac{\partial^2 \theta}{\partial \bar{a}_i \partial \bar{a}_j}, \quad \sigma_j(\theta) = \bar{\sigma}_{ij}\frac{\partial \theta}{\partial \bar{a}_i}, \tag{41}$$

and the solution $r^p(t;r_0)$ can be explicitly written as

$$r^p(t;r_0) = r_0^p \exp\left\{ p\int_0^t Q(\theta(s))ds + p\int_0^t \chi_j(\theta(s))dW_j(s)\right\},$$

with

$$Q(\theta) = \nu(\theta) - \frac{1}{2}|\chi(\theta)|^2.$$

Making use of the above solution, we can evaluate

$$\mathbf{E}[r^p(t;r_0)] = r_0^p \mathbf{E}\left[\exp\left\{ Z(t) + p\int_0^t Q(\theta(s))ds + \frac{p^2}{2}\int_0^t |\chi(\theta(s))|^2 ds\right\}\right],$$

where

$$Z(t) = p\int_0^t \chi_j(\theta(s))dW_j(s) - \frac{p^2}{2}\int_0^t |\chi(\theta(s))|^2 ds.$$

Now applying the Girsanov theorem yields

$$\mathbf{E}[r^p(t;r_0)] = r_0^p \mathbf{E}\left[\exp\left\{ p\int_0^t Q(\eta(s))ds + \frac{p^2}{2}\int_0^t |\chi(\eta(s))|^2 ds\right\}\right],$$

where the expectation on the right-hand side of the above expression is taken with respect to the measure associated with the Itô equation

$$d\eta = \varepsilon^2[\mu(\eta) + p\chi^T(\eta)\sigma(\eta)]dt + \varepsilon\sigma_j(\eta)dW_j.$$

According to the Feynmann-Kac formula, the expectation $\mathbf{E}[r^p(t)] = \psi(\eta,p,t)$ is the solution of

$$\left(\frac{\partial}{\partial t} - [\mu(\theta) + p\chi^T(\theta)\sigma(\theta)]\frac{\partial}{\partial \theta} - \frac{1}{2}\sigma^2(\theta)\frac{\partial^2}{\partial \theta^2} - pQ(\theta) - \frac{p^2}{2}|\chi(\theta)|^2\right)\psi = 0.$$

Making use of the results of Arnold [2] and Arnold et al. [4], the moment Lyapunov exponent is the largest eigenvalue of the stationary operator

$$\tilde{L}(p) = \tilde{\mathcal{L}} + p\left[\chi^T(\theta)\sigma(\theta)\frac{\partial}{\partial \theta} + Q(\theta)\right] + \frac{p^2}{2}|\chi(\theta)|^2,$$

where

$$|\chi|^2 r^2 = (\overline{\sigma\sigma^T})_{ij}\frac{\partial r}{\partial \bar{a}_i}\frac{\partial r}{\partial \bar{a}_j} = \hat{Q}(\theta)r^2,$$

$$|\sigma|^2 = (\overline{\sigma\sigma^T})_{ij}\frac{\partial \theta}{\partial \bar{a}_i}\frac{\partial \theta}{\partial \bar{a}_j} = \sigma^2(\theta),$$

$$(\chi^T\sigma)r = (\overline{\sigma\sigma^T})_{ij}\frac{\partial r}{\partial \bar{a}_i}\frac{\partial \theta}{\partial \bar{a}_j} = \hat{\mu}(\theta)r, \quad Q(\theta) = \nu(\theta) - \frac{1}{2}|\chi(\theta)|^2.$$

It is clear that the operator $\tilde{L}(p)$ obtained above is identical to the one in Eq. (23).

4 Solution of the Eigenvalue Problem

Except for some special cases, the general solution of Eq. (23) cannot be obtained explicitly for $g_2(p)$. In general, it is also possible to have singularities in θ, thus some justification is needed in order to ensure that $\psi(\theta)$ is bounded and positive. It is clear from the form of the diffusion term that there may be singularities in the open interval $(0,\pi/2)$, i.e., when $\Sigma_i p_{ii} S(2\omega_i) = 0$, singularities exist for $p_{12}p_{21} > 0$ if $S(\omega^-) = 0$ and $\cos 2\theta = (p_{12} - p_{21})/(p_{12} + p_{21})$, and for $p_{12}p_{21} < 0$ if $S(\omega^+) = 0$ and $\cos 2\theta = (p_{12} + p_{21})/(p_{12} - p_{21})$. *Only the nonsingular cases will be considered here.*

In order to reduce the number of cases to be evaluated, we can simplify the coefficients p_{ij} by a suitable scaling of the state variables x. It can be shown that it is always possible to take $p_{12} = \pm p_{21} = \kappa$, in which case the coefficients reduce to

$$A = \frac{1}{32}\left\{4\kappa^2 S(\omega^{\pm}) - \sum_{i=1}^{2} p_{ii}^2 S(2\omega_i)\right\}, \quad B = 0,$$

$$C = \frac{1}{32}\left\{4\kappa^2 S(\omega^{\mp}) + \sum_{i=1}^{2} p_{ii}^2 S(2\omega_i)\right\},$$

$$D = \frac{1}{2}(\Lambda_1 + \Lambda_2) \pm \frac{1}{8}\kappa^2(S(\omega^+) - S(\omega^-)),$$

$$E = \frac{1}{16}\{p_{11}^2 S(2\omega_1) - p_{22}^2 S(2\omega_2)\},$$

$$F = \frac{1}{32}\left\{4\kappa^2 S(\omega^{\pm}) + \sum_{i=1}^{2} p_{ii}^2 S(2\omega_i)\right\},$$

$$\Lambda = \Lambda_1 - \Lambda_2, \quad \Lambda_i = -\delta_i + \frac{1}{8}p_{ii}^2 S(2\omega_i), \quad i = 1,2,$$

where $\omega^{\pm} = \omega_1 \pm \omega_2$ and in the above expressions the upper sign is taken when $p_{12} = p_{21} = \kappa$ and the lower sign when $p_{12} = -p_{21} = \kappa$.

As in Wedig [11] and also in Bolotin [12], the solution of Eq. (23) can be calculated from an orthogonal expansion. The nature of the coefficients of the equation suggests that a Fourier series is appropriate. Because of the zero Neumann boundary conditions we may express ψ_0 as a Fourier cosine series. Thus, inserting

$$\psi_0(\theta) = \sum_{n=0}^{\infty} c_n \cos(2n\theta)$$

in Eq. (23) leads to the following infinite set of equations:

$$\sum_{m=0}^{\infty} a_{mn}c_m = g(p)c_n,$$

where

$$a_{mn} = \int_0^{\pi/2} \tilde{L}(p)(\cos(2m\theta))\cos(2n\theta)d\theta, \quad n = 0,1,2,\ldots.$$

The existence of a nontrivial solution for c_n requires that the determinant of the coefficients equals zero. Thus to evaluate $g(p)$, the leading eigenvalue of $A = (a_{mn})$, we construct a sequence of approximations by finding the eigenvalues of a sequence of submatrices:

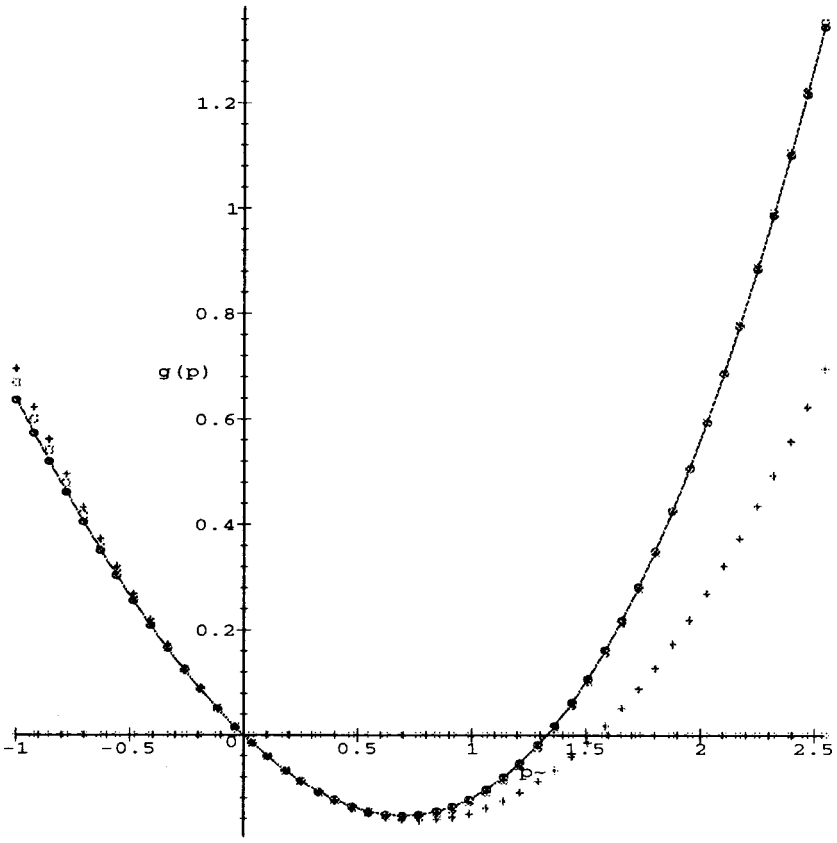

Fig. 1 Moment Lyapunov exponent for the general case $S(2\omega_1)=1$, $S(2\omega_2)=2$, $S(\omega_1+\omega_2)=2$, $S(\omega_1-\omega_2)=1$, $p_{11}=1$, $p_{22}=2$, $p_{12}=p_{21}=\kappa=1$, $\delta_1=1$, $\delta_2=2$

$$[a_{00}],\quad \begin{bmatrix} a_{00} & a_{01} \\ a_{10} & a_{11} \end{bmatrix},\quad \begin{bmatrix} a_{00} & a_{01} & a_{02} \\ a_{10} & a_{11} & a_{12} \\ a_{20} & a_{21} & a_{22} \end{bmatrix},$$

$$\cdots \begin{bmatrix} a_{00} & a_{01} & a_{02} & \cdots \\ a_{10} & a_{11} & a_{12} & \cdots \\ a_{20} & a_{21} & a_{22} & \cdots \\ a_{30} & a_{31} & a_{32} & \cdots \\ \vdots & \vdots & \vdots & \ddots \end{bmatrix}.$$

The set of approximate eigenvalues obtained by this procedure converges to the corresponding true eigenvalues as $N\to\infty$. However, the amount of calculation increases drastically with the increase in the number of terms considered. Here we present the second-order submatrix for the general cases $p_{12}=p_{21}=\kappa$ and $p_{12}=-p_{21}=\kappa$, depending on whether the coupling is symmetric or skew-symmetric. All problems of the form given in Eq. (6) can be rescaled to one of these two cases. The elements of this 2×2 submatrix are

$$a_{00}=\frac{1}{64}p(3p+10)(p_{11}^2S(2\omega_1)+p_{22}^2S(2\omega_2)) + \frac{1}{16}p\kappa^2(6+p)S(\omega^{\pm})-p(\delta_1+\delta_2)-2g_2(p),$$

$$a_{01}=\frac{1}{32}(p+2)^2(p_{11}^2S(2\omega_1)-p_{22}^2S(2\omega_2))+\frac{1}{2}(\delta_2-\delta_1)(p+2),$$

$$a_{10}=\frac{1}{64}pp_{11}^2(5p+14)S(2\omega_1)+\frac{1}{64}pp_{22}^2(6+p)S(2\omega_2) + \frac{1}{16}p\kappa^2(6+p)S(\omega^{\pm})-\frac{3}{2}p\delta_1-\frac{1}{2}p\delta_2-2g_2,$$

$$a_{11}=\frac{3}{256}p_{11}^2(18p+5p^2+8)S(2\omega_1)-\frac{1}{256}p_{22}^2(10p+p^2 +40)S(2\omega_2)+\frac{1}{64}\kappa^2(p+12)(p-2)S(\omega^{\pm})-p\delta_1 - \frac{1}{2}\kappa^2S(\omega^{\mp})-g_2-\delta_1+\delta_2,$$

where as before, the upper sign is taken when $p_{12}=p_{21}=\kappa$ and the lower sign when $p_{12}=-p_{21}=\kappa$. Now we consider some numerical results to illustrate the convergence of various orders of approximations. For this purpose consider the numerical values $S(2\omega_1)=1$, $S(2\omega_2)=2$, $S(\omega^+)=2$, $S(\omega^-)=1$, $p_{11}=1$, $p_{22}=2$, $p_{12}=1$, $p_{21}=1$, $\delta_1=1$, $\delta_2=2$ and $S(2\omega_1)=1$, $S(2\omega_2)=2$, $S(\omega^+)=2$, $S(\omega^-)=1$, $p_{11}=1$, $p_{22}=2$, $p_{12}=1$, $p_{21}=-1$, $\delta_1=1$, $\delta_2=2$. Here we consider two sets of results up to fourth-order approximations and the numerical results for these two cases are given in Fig. 1 and Fig. 2. Here the first-order approximation is

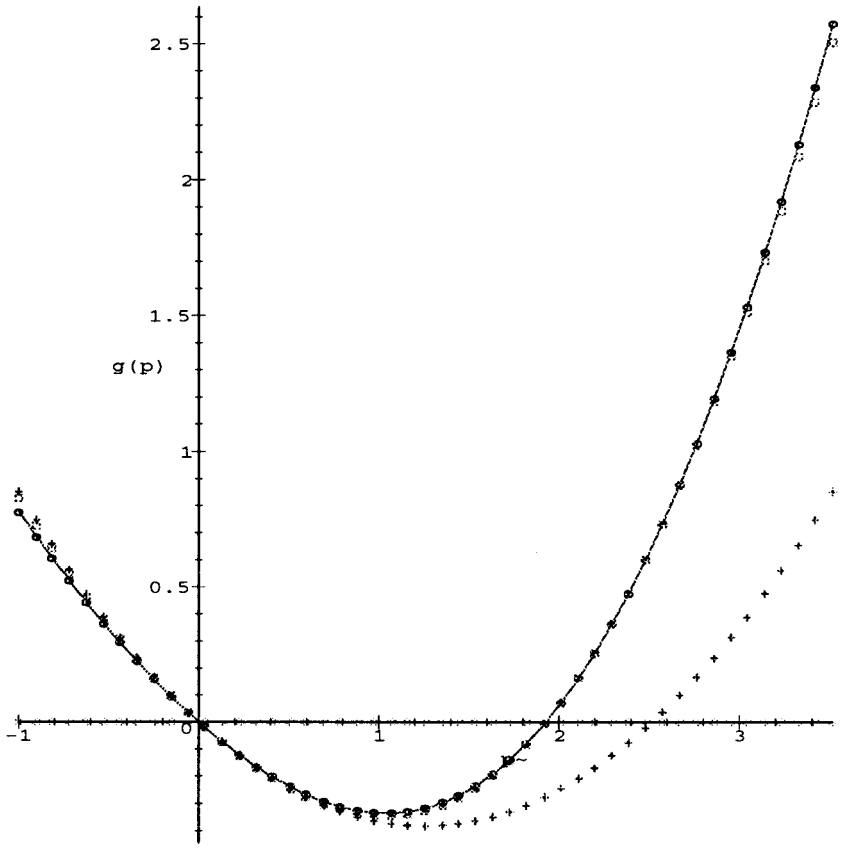

Fig. 2 Moment Lyapunov exponent for the general case $S(2\omega_1)=1$, $S(2\omega_2)=2$, $S(\omega_1+\omega_2)=2$, $S(\omega_1-\omega_2)=1$, $p_{11}=1$, $p_{22}=2$, $p_{12}=-p_{21}=\kappa=1$, $\delta_1=1$, $\delta_2=2$

indicated by the symbol+while the other three approximations virtually coincide. It is clear from these two cases that the fourth-order approximations are sufficient and the results converge. However, the second-order approximation gives an explicit formula for $g(p)$ which can provide some insight on the stability index. These figures also indicate that the oscillators may be almost-sure stable, since the slope of $g'(0)$ is negative, but unstable in the pth moment sense for sufficiently large p.

Now we shall consider some particular forms of excitation spectrums $S(\omega)$ whose values are small every where except in a neighborhood of some ω_0, i.e., the spectrum vanishes outside a bandwidth $\omega_0-\Delta\omega_0<\omega<\omega_0+\Delta\omega_0$. In the following, we shall consider the cases in which $\omega_0=2\omega_i$, $i=1, 2$, $\omega_0=\omega_1+\omega_2$, and $\omega_0=\omega_1-\omega_2$. This can simplify the moment Lyapunov exponents.

1 *Coupled oscillators under band-limited noise excitation close to* $S(2\omega_i)$, $i=1, 2$:

$$g_2^+(p)=\left(\frac{13}{512}p^2+\frac{21}{256}p-\frac{1}{64}\right)p_{ii}^2S(2\omega_i)+\left(-\frac{1}{2}(\delta_1+\delta_2)p+\left[\left(\frac{129}{262144}p^4+\frac{193}{65536}p^3+\frac{31}{8192}p+\frac{381}{65536}p^2+\frac{1}{4096}\right)p_{ii}^4S(2\omega_i)^2-\left(\frac{p}{64}(\delta_1-\delta_2)(p+2)^2\right)p_{ii}^2S(2\omega_i)+\frac{1}{8}(\delta_1-\delta_2)^2p(p+2)\right]^{1/2}=g_2^-(p).$$

2 *Coupled oscillators under band-limited noise excitation close to* $S(\omega^+)$:

$$g_2^+(p)=\left(\frac{3}{128}p^2+\frac{11}{64}p-\frac{3}{16}\right)\kappa^2S(\omega^+)-\frac{1}{2}(\delta_1+\delta_2)p+\left[\left(\frac{1}{128}p^2+\frac{1}{64}p+\frac{3}{16}\right)^2\kappa^4S(\omega^+)^2+\frac{1}{8}(\delta_1-\delta_2)^2p(p+2)\right]^{1/2},$$

$$g_2^-(p)=-\frac{1}{2}(\delta_1+\delta_2)p-\frac{1}{4}\kappa^2S(\omega^+)+\frac{1}{4}\sqrt{2p(p+2)(\delta_1-\delta_2)^2+\kappa^4S(\omega^+)^2}.$$

3 *Coupled oscillators under band-limited noise excitation close to* $S(\omega^-)$:

$$g_2^+(p)=-\frac{1}{2}(\delta_1+\delta_2)p-\frac{1}{4}\kappa^2S(\omega^-)+\frac{1}{4}\sqrt{2p(p+2)(\delta_1-\delta_2)^2+\kappa^4S(\omega^-)^2},$$

$$g_2^-(p)=\left(\frac{3}{128}p^2+\frac{11}{64}p-\frac{3}{16}\right)\kappa^2 S(\omega^-)-\frac{1}{2}(\delta_1+\delta_2)p$$
$$+\left[\left(\frac{1}{128}p^2+\frac{1}{64}p+\frac{3}{16}\right)^2\kappa^4 S(\omega^-)^2\right.$$
$$\left.+\frac{1}{8}(\delta_1-\delta_2)^2 p(p+2)\right]^{1/2}.$$

Once again the above expressions for the second-order approximations of $g(p)$ provide insight as to the qualitative behavior of stability boundary with respect to the variation in the spectral density. For example, for the *coupled oscillators under band-limited noise excitation close to* $S(\omega^+)$, the symmetric case $p_{12}=p_{21}=\kappa$ provides a stability index and a stability boundary while the skew-symmetric case $p_{12}=-p_{21}=\kappa$ has no stability index ($g(p)$ is linear in p) and the system is always stable. Similarly for the *coupled oscillators under band-limited noise excitation close to* $S(\omega^-)$, the stability index and the stability boundary exist for $p_{12}=-p_{21}=\kappa$ whereas for $p_{12}=p_{21}=\kappa$ the system is always stable.

5 Application to Beams Under Stochastic Loads

Here we apply the general results of the above section in the context of real engineering applications and show how these results can be applied to physical problems. Two simple examples, which best illustrate the theoretical results, are presented here. Consider the flexural-torsional instability of a thin rectangular elastic beam of length L subjected to (i) stochastically fluctuating end moments and (ii) a stochastic follower force. It is assumed that the boundaries are simply supported and the end moments $M(t)$ and follower force $P(t)$ are applied as shown in Figs. 3(a) and (b). The motion of the beam is governed by the partial differential equations (Bolotin [12]),

$$m\frac{\partial^2 w}{\partial t^2}+d_w\frac{\partial w}{\partial t}+EI_x\frac{\partial^4 w}{\partial z^4}=0, \tag{42}$$

$$m\frac{\partial^2 u}{\partial t^2}+d_u\frac{\partial u}{\partial t}+EI_y\frac{\partial^4 u}{\partial z^4}+\frac{\partial^2(M_x\phi)}{\partial z^2}+P\delta\left(\frac{L}{2}-z\right)\phi=0, \tag{43}$$

$$m\rho^2\frac{\partial^2\phi}{\partial t^2}+d_\phi\frac{\partial\phi}{\partial t}-GJ\frac{\partial^4\phi}{\partial z^4}+M_x\frac{\partial^2 u}{\partial z^2}=0, \tag{44}$$

where $u(z,t)$, and $w(z,t)$ denote the x, and y- components of the deflection of the beam centerline and ϕ is the angle of twist of the cross section. The delta function is *only* present in the follower force case and M_x in Eq. (43) can be taken out of the differential in the case of fluctuating end moments. The quantities EI_x, EI_y, and GJ are the flexural and torsional rigidities of the cross section and d_w, d_u, and d_ϕ are the viscous damping coefficients. In addition, m denotes the mass per unit length and ρ is the radius of gyration. In the follower force case, the function M_x can be expressed in terms of the applied stochastic load as

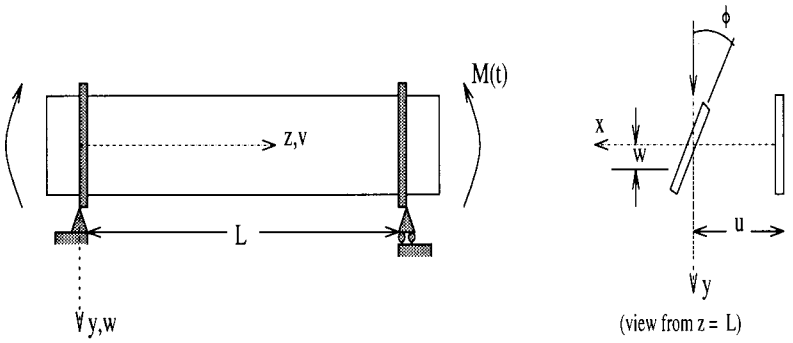

(a) stochastic end moment M(t)

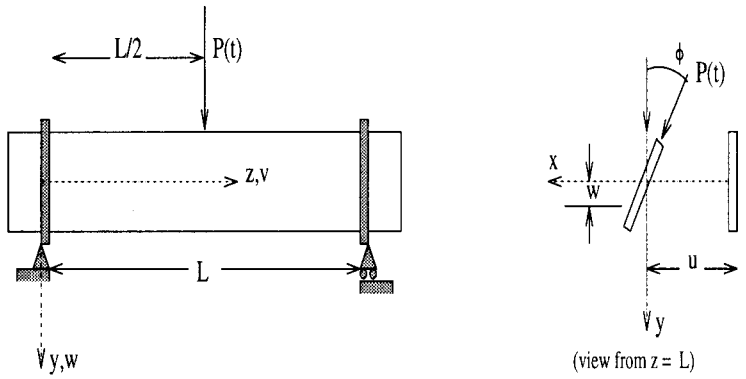

(b) stochastic follower force P(t)

Fig. 3 Thin rectangular beam subjected to stochastic excitation

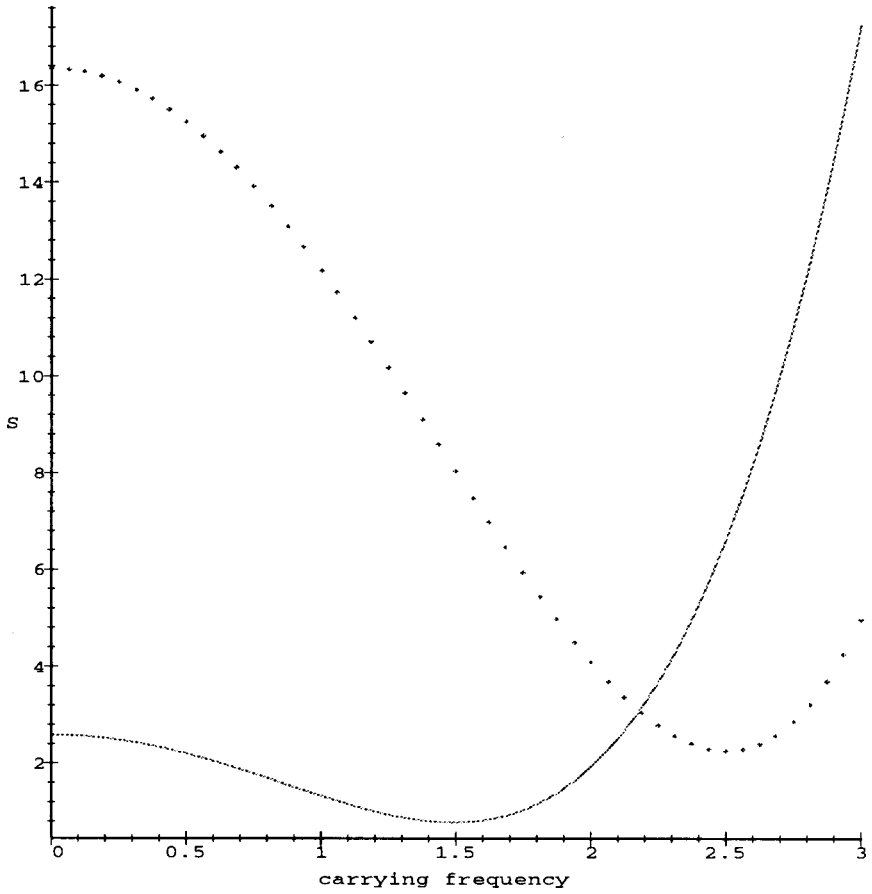

Fig. 4 Almost-sure stability boundary for follower force and end moment cases under real noise excitation, i.e., $\omega_1=0.5$, $\omega_2=2$, $\kappa=1$, $\delta_1=.001$, delta$_2=.002$, $\alpha=0.5$

$$M_x=\begin{cases}\dfrac{1}{2}Pz, & 0\leqslant z\leqslant\dfrac{L}{2},\\[2ex] \dfrac{1}{2}P(L-z), & \dfrac{L}{2}\leqslant z\leqslant L\end{cases} \tag{45}$$

where $P=P(t)$, the stochastic follower force. The first equation is uncoupled from the other two and describes the ordinary random vibration of the beam in the plane of its largest rigidity with inhomogeneous boundary conditions given by

$$EI_x\frac{\partial^2 w}{\partial z^2}(0,t)=EI_x\frac{\partial^2 w}{\partial z^2}(L,t)=-M_x=-M(t). \tag{46}$$

The other two equations form a pair of coupled partial differential equations with stochastic coefficients $M_x=M(z,t)$ given by Eq. (45) and $P=P(t)$ in the follower force case and $M_x=M(t)$ in the case of fluctuating end moments. For both the cases the two equations are subjected to homogeneous boundary conditions given by

$$u(0,t)=u(L,t)=\frac{\partial^2 u}{\partial z^2}(0,t)=\frac{\partial^2 u}{\partial z^2}(L,t)=0,$$

$$\phi(0,t)=\phi(L,t)=0.$$

Consider the shape function $\sin \pi z/L$ which satisfies the boundary conditions. For the first mode of vibration, the displacement $u(z,t)$ and twist $\phi(z,t)$ can be described by

$$u(z,t)=\rho q_1(t)\sin\left(\pi\frac{z}{L}\right),\quad \phi(z,t)=q_2(t)\sin\left(\pi\frac{z}{L}\right). \tag{47}$$

Substituting these into the partial differential Eqs. (43) and (44) and considering appropriately the two cases yields

$$\begin{aligned}&\ddot{q}_1+\omega_1^2 q_1+2\varepsilon^2\omega_1\zeta_1\dot{q}_1+\varepsilon\xi(t)k_{12}q_2=0,\\ &\ddot{q}_2+\omega_2^2 q_2+2\varepsilon^2\omega_2\zeta_2\dot{q}_2+\varepsilon\xi(t)k_{21}q_1=0,\end{aligned} \tag{48}$$

where

$$\omega_1^2=\frac{\pi^4}{mL^4}EI_y,\quad \omega_2^2=\frac{\pi^2}{m\rho^2L^2}GJ,\quad 2\varepsilon^2\omega_1\zeta_1=\frac{d_u}{m},$$

$$2\varepsilon^2\omega_2\zeta_2=\frac{d_\phi}{m\rho^2},\quad \xi(t)=\frac{P(t)}{P_{cr}}\ \text{or}\ \frac{M(t)}{M_{cr}}.$$

Here, $P(t)$ and $M(t)$ are assumed to be a stationary stochastic process and P_{cr} and M_{cr} are the critical flutter load for the follower force and critical static buckling end moments, respectively, and are given by

$$P_{cr}=\frac{4|\omega_1^2-\omega_2^2|mL\rho}{\sqrt{(28-\pi^2)(4+\pi^2)}},\quad M_{cr}=m\rho\omega_1\omega_2\frac{L^2}{\pi^2}.$$

By specifying a very thin beam, it follows that $\omega_1^2\ll\omega_2^2$. For all positive values of ζ_1 and ζ_2, the deterministic system of Eq. (48)

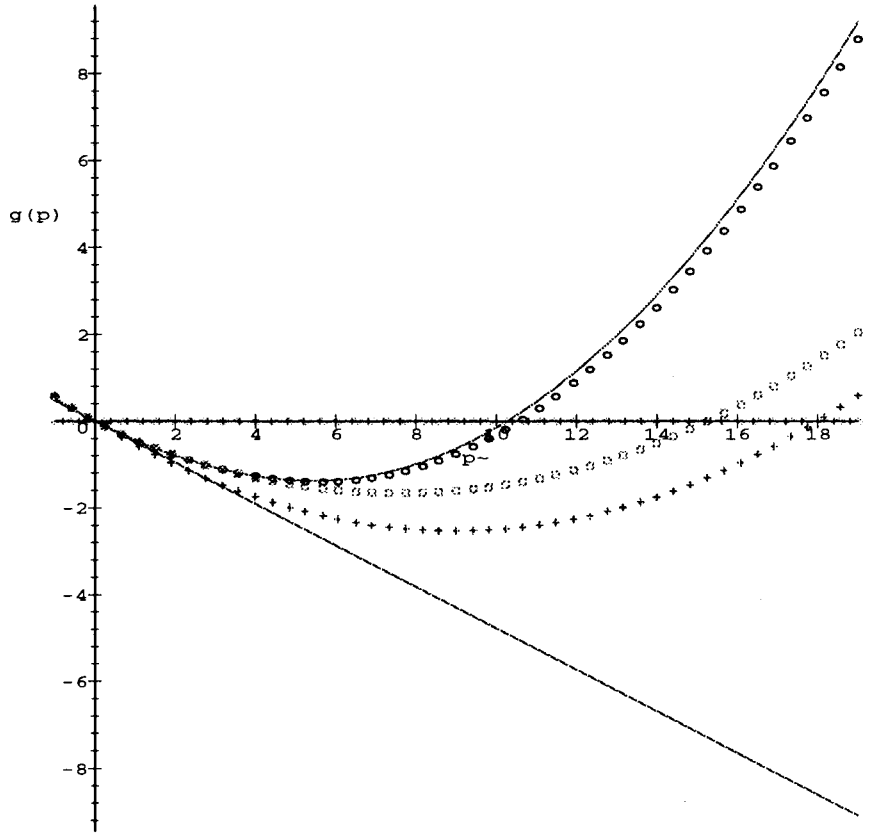

Fig. 5 Moment Lyapunov exponent for the follower force problem with $\kappa=1$, $\delta_1=0.5$, $\delta_2=1$, $S(\omega^+)=1$, $S(\omega^-)=1$

is stable. We shall consider the stochastic problem with mean fluctuation levels much less than the critical loads.

For the follower force case

$$k_{12}=P_{cr}\frac{1}{2mL\rho}\left(7-\frac{\pi^2}{4}\right)=\frac{1}{2}\sqrt{\frac{28-\pi^2}{4+\pi^2}}\,|\omega_1^2-\omega_2^2|,$$

$$k_{21}=-P_{cr}\frac{1}{2mL\rho}\left(1+\frac{\pi^2}{4}\right)=-\frac{1}{2}\sqrt{\frac{4+\pi^2}{28-\pi^2}}\,|\omega_1^2-\omega_2^2|,$$

whereas for the end moment case

$$k_{12}=k_{21}=M_{cr}\frac{1}{m\rho}\left(\frac{\pi}{L}\right)^2=\omega_1\omega_2.$$

Since $k_{ij}=p_{ij}\omega_j$, scaling the coordinates q_1 and q_2 as

$$q_1\rightarrow\sqrt{\omega_2(28-\pi^2)}q_1,\quad q_2\rightarrow\sqrt{\omega_1(4+\pi^2)}q_2$$

yields

$$\begin{aligned}&\ddot{q}_1+\omega_1^2q_1+2\varepsilon^2\omega_1\zeta_1\dot{q}_1+\varepsilon\xi(t)\omega_1\kappa q_2=0,\\&\ddot{q}_2+\omega_2^2q_2+2\varepsilon^2\omega_2\zeta_2\dot{q}_2+\varepsilon\xi(t)\omega_2\kappa q_1=0,\end{aligned}\tag{49}$$

where the lower sign corresponds to the follower force and the upper sign corresponds to the end moment force, with

$$\kappa=\begin{cases}\sqrt{\omega_1\omega_2}, & \text{for the end moment force,}\\ \dfrac{|\omega_1^2-\omega_2^2|}{2\sqrt{\omega_1\omega_2}}, & \text{for the follower force.}\end{cases}$$

The second-order moment Lyapunov exponent is given by

$$\begin{aligned}g_2(p)=&-\frac{1}{4}\kappa^2S(\omega^{\mp})+\left(\frac{3}{128}p^2+\frac{11}{64}p-\frac{3}{16}\right)\kappa^2S(\omega^{\pm})-\frac{1}{2}(\delta_1\\&+\delta_2)p+\left[\kappa^4\left(\frac{1}{4}S(\omega^{\mp})+\left(\frac{1}{128}p^2+\frac{1}{64}p+\frac{3}{16}\right)S(\omega^{\pm})\right)^2\right.\\&\left.+\frac{1}{8}(\delta_1-\delta_2)^2p(p+2)\right]^{1/2}.\end{aligned}\tag{50}$$

In addition, the maximal Lyapunov exponent for these two problems can be easily obtained from Sri Namachchivaya and Van Roessel [9] as

$$\begin{aligned}\lambda=&-\frac{(\delta_1+\delta_2)}{2}+\frac{(\delta_1-\delta_2)}{2}\coth\left[\frac{4(\delta_1-\delta_2)\tan^{-1}\left(\sqrt{\dfrac{S(\omega^{\pm})}{S(\omega^{\mp})}}\right)}{\kappa^2\sqrt{S(\omega^{\pm})S(\omega^{\mp})}}\right]\\&\pm\frac{\kappa^2}{8}(S(\omega^+)-S(\omega^-)),\end{aligned}\tag{51}$$

where, once again, lower and upper sign correspond to the beam with the stochastic follower force and stochastic end moments, respectively. We remark that it appears that the expression $g_2(p)$ given by Eq. (50) does not agree with λ given by Eq. (51). This discrepancy is due to the fact that Eq. (51) is an exact solution of the eigenvalue problem up to $\mathcal{O}(\epsilon^{\epsilon})$ while $g_2'(0)$ given by Eq. (50) is obtained by a sequence of approximate eigenvalues for the

ϵ^2 order eignenvalue problem (23). Although the analytical expressions given by Eq. (50) and Eq. (51) do not agree, their numerical values are in agreement.

Numerical results for the stability boundaries are obtained for both of these problems for the system parameters $\omega_1=0.5$, $\omega_2=2.0$, $\kappa=1$, $\delta_1=.001$, $\delta_2=.002$. The results presented in Fig. 4 are based on a real noise generated by a second order filter equation and power spectral density given, respectively, as

$$\ddot{\xi}+2\alpha\dot{\xi}+\beta^2\xi=F(t), \quad S_{\xi}(\omega)=\frac{S_0\alpha^2}{(\beta^2-\omega^2)^2+4\alpha^2\omega^2}.$$

The parameter S_0 is the power spectral density of the white noise process driving the filter equation. The peak intensity and the carrying frequency of the output process $\xi(t)$, are determined by the filter parameters α and β. In Fig. 4, the broken lines correspond to the end moment case while the solid lines represent the stability boundary for the follower force case and are calculated for the filter parameter $\alpha=0.5$. It is clear from the results that for the beam with follower force, if the noise excitation is close to $S(\omega^+)$, the system is stable even for large values of noise intensity ($S_0<5$), whereas the beam with stochastic end moments is stable for large values of noise intensity ($S_0<10$) when the noise excitation is close to $S(\omega^-)$. This stability behavior is very similar to the deterministic situation with periodic excitations where nonconservative systems with follower forces are always stable when the forcing frequency is close to ω^+, and conservative systems such as the beam with end moments are always stable when the forcing frequency is close to ω^-.

Figure 5 depicts the moment Lyapunov exponent $g_2(p)$ as a function of p for the follower force problem discussed above. It can be verified in this figure that the maximal Lyapunov exponent λ is the slope of $g_2(p)$ at $p=0$ and we compare the exact order ϵ^2 result for λ given in (51) with the slope of the first four approximations. Although the second-order approximations are not that accurate, the results seems to converge within four approximations. Similar results can be obtained for the beam with stochastic end moments. It is important to note that for $\lambda<0$, $g(p)$ is positive beyond large values of p. This indicates that, although the response of the linear system decays to zero (with probability one) at an exponential rate λ, there is a small probability that $|x(t;x_0)|$ is large. This would be the case if random oscillations cause the system response to exceed some threshold value as the mean response decays. This makes the expected value of this rare event large for large values of p and results in the pth mean instability.

In conclusion, we have obtained by two different methods the generator $\tilde{L}(p)$ given in Eq. (23) for which $g_2(p)$ is the principal eigenvalue. Except for some special cases the general solution of Eq. (23) cannot be obtained explicitly for $g_2(p)$. In this paper we have obtained certain approximate solutions based on Fourier analysis and it is shown that within four orders of approximation we obtain qualitatively good results.

Acknowledgments

The authors would like to acknowledge the support of the Office of Naval Research under grant number N00014-01-1-0647, National Science Foundation under grant number CMS 00-84944 and NSERC of Canada.

References

[1] Molčanov, S. A., 1978, "The Structure of Eigenfunctions of One-Dimensional Unordered Structures," Math. USSR Izvestija, **12**, No. 1, pp. 69–101.
[2] Arnold, L., 1984, "A Formula Connecting Sample and Moment Stability of Linear Stochastic Systems," SIAM (Soc. Ind. Appl. Math.) J. Appl. Math., **44**, No. 4, pp. 793–802.
[3] Arnold, L., Kliemann, W., and Oeljeklaus, E., 1986, *Lyapunov Exponents of Linear Stochastic Systems*, Vol. 1186 (Lecture Notes in Mathematics), Springer-Verlag, New York, pp. 85–125.
[4] Arnold, L., Oeljeklaus, E., and Pardoux, E., 1986, *Almost Sure and Moment Stability for Linear Itô Equations*, Vol. 1186 (Lecture Notes in Mathematics), Springer-Verlag, New York, pp. 129–159.
[5] Namachchivaya, N. Sri, Van Roessel, H. J., and Doyle, M. M., 1996, "Moment Lyapunov Exponent for Two Coupled Oscillators Driven by Real Noise," SIAM (Soc. Ind. Appl. Math.) J. Appl. Math., **56**, pp. 1400–1423.
[6] Khas'minskii, R. Z., and Moshchuk, N., 1998, "Moment Lyaponov Exponent and Stability Index for Linear Conservative System With Small Random Perturbation," SIAM (Soc. Ind. Appl. Math.) J. Appl. Math., **58**, No. 1, pp. 245–256.
[7] Arnold, L., Doyle, M. M., and Namachchivaya, N. Sri, 1997, "Small Noise Expansion of Moment Lyapunov Exponents for General Two Dimensional Systems," Dyn. Stab. Syst., **12**, No. 3, pp. 187–211.
[8] Pardoux, E., and Wihstutz, V., 1988, "Lyapunov Exponent and Rotation Number of Two-Dimensional Linear Stochastic Systems With Small Diffusion," SIAM (Soc. Ind. Appl. Math.) J. Appl. Math., **48**, No. 2, pp. 442–457.
[9] Namachchivaya, N. Sri, and Van Roessel, H. J., 1993, "Maximal Lyapunov Exponent and Rotation Numbers for Two Coupled Oscillators Driven by Real Noise," J. Stat. Phys., **71**, No. 3/4, pp. 549–567.
[10] Khas'minskii, R. Z., 1966, "A Limit Theorem for Solutions of Differential Equations With Random Right-Hand-Side," Theor. Probab. Appl., **11**, No. 3, pp. 390–406.
[11] Wedig, W. V., 1988, "Lyapunov Exponents of Stochastic Systems and Related Bifurcation Problems," *Stochastic Structural Dynamics: Progress in Theory and Applications*, S. T. Ariaratnam, G. I. Schuëller, and I. Elishakoff, eds., Elsevier, London.
[12] Bolotin, V. V., 1964, *The Dynamic Stability of Elastic Systems*, Holden-Day, San Francisco.

Moving Loads on an Elastic Half-Plane With Hysteretic Damping

A. Verruijt
e-mail: A.Verruijt@planet.nl

C. Cornejo Córdova
e-mail: Cornejoc@dutchpu.tudelft.nl

Department of Civil Engineering,
Delft University of Technology,
Stevinweg 1,
2628 CN Delft, The Netherlands

A closed-form solution is presented for the problem of a moving point load on an elastic half-plane with hysteretic damping. The problem has been studied in order to investigate the dynamic amplification of stresses and displacements if the velocity of the load approaches the Rayleigh wave velocity or the shear wave velocity in the elastic medium. This is relevant for the construction of high speed railway lines on relatively soft soils. Hysteretic damping is introduced as pseudo-viscous damping, assuming that the damping in a full cycle of loading and unloading is independent of the frequency.
[DOI: 10.1115/1.1410097]

1 Introduction

This paper presents an analytical solution of the problem of a vertical load moving at constant speed over the upper boundary of the half-plane $z>0$. The material is isotropic linear elastic, with hysteretic damping to represent the energy dissipated by plastic deformations. The method used is a Fourier integral method ([1]). The solution is a generalization of the solution by Cole and Huth [2] for the undamped elastic case, see also Eringen and Suhubi [3], Frýba [4], and the correction by Georgiadis and Barber [5].

The purpose of the paper is to investigate the influence of hysteretic damping on the displacements and the stresses, as it is expected that hysteretic damping may greatly reduce the large stresses and strains near the critical velocity. Solutions for the undamped case indicate that very large displacements and stresses occur for values of the velocity of the moving load in the vicinity or larger than the propagation speed of the Rayleigh wave, which has been shown to be of great importance for the analysis of the effects of high speed trains on relatively soft soils by Dieterman and Metrikine [6]. It has been suggested by Verruijt [7] that the relatively large hysteretic damping which is characteristic for soft soils may lead to a considerable reduction of the peak stresses and peak displacements. This will be investigated in this paper for the case of plane strain deformations of a half-plane. It will appear that a simple closed-form solution can be obtained for the case of a moving point load. Including hysteretic damping as an integral part of the material behavior also appears to unify the limiting case of zero damping, as there is no need to distinguish between small and large velocities.

2 Hysteretic Damping

One of the basic principles of soil mechanics is that the deformations of granular materials are not caused by deformations of the grains themselves, but are mainly caused by local rearrangements of the granular structure, with grains slipping and rolling over each other. This is one of the basic notions behind Terzaghi's principle of effective stress ([8,9]). Thus a large part of the soil deformations is of an irreversible character, even though grains may slide back into their previous position during unloading. Analysis of the micromechanics of granular materials up to failure by Van Baars [10] has shown that one of the most important deformation mechanisms of a granular material is that in an arrangement of four particles the main force transfer chain changes from horizontal to vertical, and back, see Fig. 1. Irreversible deformations due to sliding occur in both the loading and the unloading part of the cycle. A simple interpretation of the mechanism shown in Fig. 1 is that the original assembly can only carry a small vertical load, depending upon the lateral load and the friction in the inclined contact surfaces. If the vertical load is increased the assembly becomes unstable, and the top particle will be pushed through the two particles below it, until a horizontal contact plane is formed with the lower particle. From then on a large vertical force can be transmitted. If subsequently the vertical load is decreased or the horizontal load is increased, the assembly may revert to its original shape, again dissipating energy due to friction in the sliding of the grains.

Mechanisms such as the one illustrated in Fig. 1 are considered to be responsible for the stress-strain behavior obtained in a cyclic triaxial compression test on sand as shown in the left part of Fig. 2, which has been obtained for a typical Dutch sand, from the river Meuse. The main features of the stress-strain behavior relevant to dynamic loads seem to be the stiffness and the damping. In order to describe these features an equivalent viscoelastic model is introduced, with its shear behavior described by

$$\tau = G\gamma + Gt_r\dot{\gamma}, \tag{1}$$

where G is the shear modulus and t_r is a retardation constant, representing the effect of the viscous damper.

The equivalent retardation constant for cyclic hysteretic deformations as illustrated in Fig. 2 can be determined by comparing the dissipation of energy in a full cycle with the dissipation in a viscoelastic model, assuming a frequency ω. The dissipation of energy is characterized by a damping ratio ζ ([11]), defined as $\zeta = 1/2 \sin \psi$, where ψ is defined by

$$\tan \psi = \omega t_r . \tag{2}$$

Comparison of the dissipation of energy in the two models ([7]) leads to an expression for the damping ratio of the form

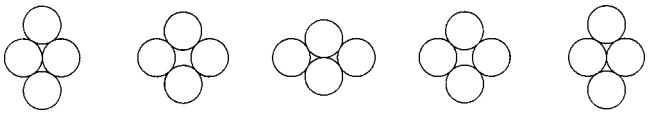

Fig. 1 A full cycle of deformations of a soil element

Contributed by the Applied Mechanics Division of THE AMERICAN SOCIETY OF MECHANICAL ENGINEERS for publication in the ASME JOURNAL OF APPLIED MECHANICS. Manuscript received by the ASME Applied Mechanics Division, July 26, 2000; final revision, June 12, 2001. Associate Editor: R. C. Benson. Discussion on the paper should be addressed to the Editor, Professor Lewis T. Wheeler, Department of Mechanical Engineering, University of Houston, Houston, TX 77204-4792, and will be accepted until four months after final publication of the paper itself in the ASME JOURNAL OF APPLIED MECHANICS.

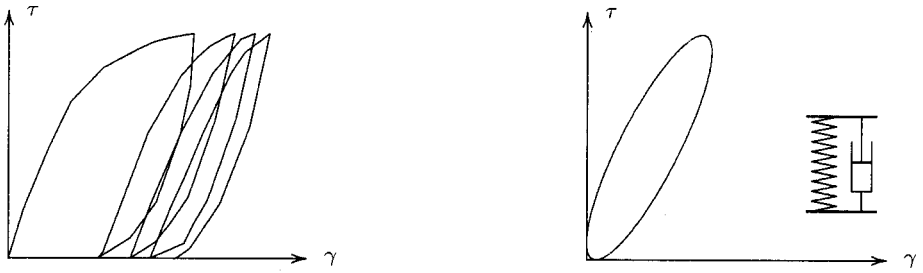

Fig. 2 Cyclic triaxial test and its representation by a viscoelastic element

$$\zeta = \frac{3}{\pi^2}\frac{\tau_0}{\tau_{\max}} = \frac{3}{\pi^2}\sqrt{\frac{\gamma_p}{\gamma_0}}, \tag{3}$$

where τ_0 is the amplitude of the cyclic shear stress, $\tau_{\max}$ is the shear strength, γ_p is the plastic (irreversible) deformation in a full cycle, and γ_0 is the amplitude of the cyclic deformation. In this paper it will be assumed that the damping ratio ζ is a constant, assuming that in the class of problems considered the average level of stress remains approximately constant. This is in agreement with the conclusion of Hardin [12], on the basis of an extensive experimental program, that a viscoelastic model can be used to describe the behavior of sand if the viscosity is assumed to be inversely proportional to the frequency.

It follows from (3) that the maximum value of the damping ratio is about $\zeta_{\max}=0.30$, on theoretical grounds. This is very close to the maximum values reported by Hardin and Drnevich [13] from an extensive review of many laboratory tests. Realistic values for the damping ratios of soft soils seem to be of the order of magnitude $\zeta=0.1$ or $\zeta=0.2$. These values correspond to $\tan\psi=0.204$ and $\tan\psi=0.436$.

It should be emphasized that for a classical viscoelastic material the damping ratio depends upon the frequency of the loading cycle, see Eq. (2), so that the higher frequencies are damped more strongly than lower frequencies. This is not a realistic description of the hysteretic damping of soils, however. For soils it can be expected that the damping will be about the same, whatever the frequency. In terms of a viscosity this means that the apparent viscosity is small for high frequencies, and large for small frequencies, so that the product ωt_r remains constant.

A small hysteretic damping ratio (say $\zeta=0.001$) is sometimes used in numerical solutions of dynamic problems in order to stabilize the solution and avoid the singular behavior for certain critical velocities ([14]). Such solutions are sometimes referred to as *viscoelastic*, although strictly speaking that is not quite correct, because the frequency dependency of the viscous damping is ignored.

It should be noted that the model used in this paper, with a constant shear modulus and a constant damping ratio as its main characteristics, is only a first approximation of the behavior of real soils. In reality soil behavior is known to be nonlinear, with the shear modulus decreasing with the strain rate, for instance, and the damping ratio increasing with the strain rate. Such a complicated type of behavior can only be taken into account in a numerical model, however. The analytical approach used here can be used as a validation of numerical models, and may also give some useful insight in the type of behavior that can be expected in real soils.

3 Solution of the Problem

The problem to be considered refers to a viscoelastic half-plane $z>0$, loaded by a moving load on its surface. The material is isotropic and linear viscoelastic, with hysteretic damping only. Hysteretic damping is defined as a special type of viscoelastic damping, the special property being that the damping ratio in each full cycle of loading is independent of the frequency of the loading. The load may be a moving strip load or a moving point load.

The basic equations are the equations of motion in plane-strain conditions for a linear viscoelastic material,

$$(\lambda+\mu)\left(1+t_r\frac{\partial}{\partial t}\right)\frac{\partial e}{\partial x}+\mu\left(1+t_r\frac{\partial}{\partial t}\right)\nabla^2 u=\rho\frac{\partial^2 u}{\partial t^2}, \tag{4}$$

$$(\lambda+\mu)\left(1+t_r\frac{\partial}{\partial t}\right)\frac{\partial e}{\partial z}+\mu\left(1+t_r\frac{\partial}{\partial t}\right)\nabla^2 w=\rho\frac{\partial^2 w}{\partial t^2}, \tag{5}$$

where u and w are the displacement components, and e is the volume strain, $e=\partial u/\partial x+\partial w/\partial z$. The material properties are the elastic coefficients λ and μ and a relaxation time t_r. For reasons of simplicity the relaxation times for the two fundamental forms of deformation, shear and compression, have been taken equal. In order to describe hysteretic damping the value of t_r should be inversely proportional to the frequency of the loading.

The Eqs. (4) and (5) are the basic differential equations for a linearly viscoelastic material, with the parameter t_r being a material constant. The generalization made in this paper is that the equations are assumed to be valid for any cyclic load, with cyclic deformations, but that the value of the parameter t_r will be different for different frequencies ω. Strictly speaking, it is assumed that the basic Eqs. (4) and (5) are valid only for a single frequency of loading, and that for a different frequency of loading the value of t_r must be adjusted so that ωt_r remains a constant. This will lead to a response to cyclic loads independent of the actual frequency, as is normally observed in cyclic testing of granular materials, and is obtained theoretically from the elastoplastic analysis of cyclic loads of soils. For each frequency a linear relation between load and deformation is assumed, and in addition it is now assumed that for a combination of two or more cyclic loads, the response will be the sum of the deformations. This enables a Fourier series approach to more general types of loading.

The problem to be considered is to determine stresses and displacements in the half-plane $z>0$, subject to the boundary conditions

$$z=0:\ \sigma_{zx}=0,\quad \sigma_{zz}=\int_0^\infty F(\alpha)\cos[\alpha(x-vt)]d\alpha, \tag{6}$$

where $F(\alpha)$ is a given real function of the positive real parameter α, and v is a given positive velocity. These boundary conditions express that the upper surface of the half-plane is free of shear stress, and that a given distribution of normal stress is traveling along this surface at a constant velocity v, in positive x-direction.

The second boundary condition can also be written in the form

$$z=0:\ \sigma_{zz}=\Re\int_0^\infty F(\alpha)\exp[i\alpha(x-vt)]d\alpha. \tag{7}$$

A possible interpretation of this boundary condition is that it consists of a superposition of harmonic loads, of frequency $\omega=\alpha v$.

For a moving strip of width $2b$, $F(\alpha)=-P\sin(\alpha b)/\pi\alpha b$, where P is the amplitude of the total load. By letting the width of the strip $b\to 0$ the case of a moving point load is obtained. In that case the loading function is simply $F(\alpha)=-P/\pi$. Although most

of the derivations in this paper will be valid for an arbitrary loading function $F(\alpha)$, all examples will apply to the special case of a moving point load.

The general solution of the problem is expressed in terms of the horizontal and vertical displacements u and w. These are represented by the Fourier integrals,

$$u=\Re\int_0^\infty \overline{u}(\alpha)\exp[i\alpha(x-vt)]\exp(-a\alpha z)d\alpha, \tag{8}$$

$$w=\Re\int_0^\infty \overline{w}(\alpha)\exp[i\alpha(x-vt)]\exp(-a\alpha z)d\alpha, \tag{9}$$

where the complex constant a is unknown in this stage. It is assumed that its real part is positive, $\Re(a)>0$, so that the solution will vanish for $z\to\infty$. It is also assumed that the imaginary part of a is negative, $\Im(a)<0$, so that waves will propagate in positive z-direction. This is the *radiation condition*, first formulated by Rayleigh [15]. If we write $a=p-iq$ the solution will contain a factor $\exp[i\alpha(x+qz-vt)]$, where q must have a positive value, to ensure that for a fixed value of x the wave is propagated in positive z-direction. The unknown functions $\overline{u}(\alpha)$ and $\overline{w}(\alpha)$ will in general be complex functions, involving the real and imaginary parts of a.

Substitution of the expressions (8) and (9) into the basic differential Eqs. (4) and (5) now leads to the following system of equations for the determination of the functions $\overline{u}(\alpha)$ and $\overline{w}(\alpha)$,

$$((m-a^2)(1-2i\zeta)-\xi^2)\overline{u}+i(m-1)(1-2i\zeta)a\overline{w}=0, \tag{10}$$

$$i(m-1)(1-2i\zeta)a\overline{u}+((1-ma^2)(1-2i\zeta)-\xi^2)\overline{w}=0, \tag{11}$$

where

$$m=\frac{\lambda+2\mu}{\mu}=\frac{2(1-\nu)}{1-2\nu}=\frac{c_p^2}{c_s^2}, \tag{12}$$

$$\xi^2=\frac{\rho v^2}{\mu}=\frac{v^2}{c_s^2}, \tag{13}$$

$$2\zeta=\omega t_r=\alpha v t_r. \tag{14}$$

Here c_p and c_s are the propagation velocities of compression waves and shear waves in the elastic material. In order to represent hysteretic damping the damping factor ζ will be considered to be a given material constant. In terms of a viscoelastic material this would mean that the relaxation time t_r is inversely proportional to the frequency $\omega=\alpha v$. It should be noted that in the description of hysteretic damping a factor sign(ω) is often included in the definition ([16]), so that ζ is always positive. In this paper a positive value of ζ is ensured by restricting v and α (and thus ω) to positive values.

The symmetric system of Eqs. (10) and (11) has a nonzero solution only if the determinant Δ is zero,

$$\Delta=m(1-a^2)^2(1-2i\zeta)^2-(m+1)(1-a^2)(1-2i\zeta)\xi^2+\xi^4=0. \tag{15}$$

This leads to the possible roots

$$a_1^2=1-\frac{\xi^2}{1-2i\zeta},\quad a_2^2=1-\frac{\xi^2/m}{1-2i\zeta}. \tag{16}$$

In order for the roots to represent finite waves traveling in positive z-direction the real parts of a_1 and a_2 must be positive, and the imaginary parts must be negative. Thus if we write

$$a_1=p_1-iq_1,\quad a_2=p_2-iq_2, \tag{17}$$

then all these constants must be positive,

$$p_1>0,\ q_1>0,\ p_2>0,\ q_2>0. \tag{18}$$

If $\zeta=0$ the squares of the roots are real, $a_1^2=1-\xi^2$ and $a_2^2=1-\xi^2/m$, in agreement with the known results for the undamped case ([2]). For small velocities the roots are real, and for very large (supersonic) velocities both roots are imaginary.

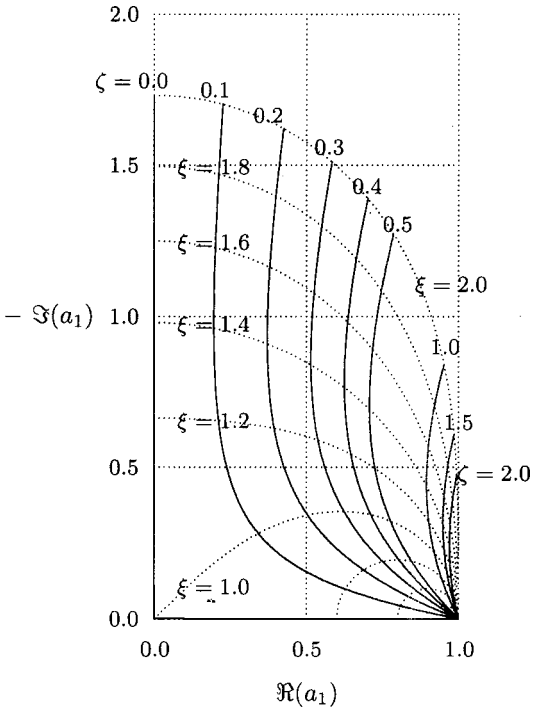

Fig. 3 First root a_1 as a function of ξ and ζ

Figure 3 shows the values of the real and imaginary parts of the root a_1, as a function of the dimensionless velocity $\xi=v/c_s$ and the damping ratio ζ. It may be noted that $a_1=1$ for $\xi=0$ and all values of ζ, and that $a_1=0$ for $\xi=1$, $\zeta=0$. The value of the other root a_2 can be obtained from the value of a_1 by substituting $\xi/\sqrt{m}$ for ξ, see (16).

The precise definitions of the constants p_1, q_1, p_2, and q_2 are

$$p_1=R_1\cos(\theta_1),\quad q_1=R_1\sin(\theta_1), \tag{19}$$

$$p_2=R_2\cos(\theta_2),\quad q_2=R_2\sin(\theta_2), \tag{20}$$

where R_1, R_2, θ_1, and θ_2 are defined by

$$R_1^4=\frac{(1-\xi^2+4\zeta^2)^2+4\zeta^2\xi^4}{(1+4\zeta^2)^2},\quad 2\theta_1=\arctan\left(\frac{2\zeta\xi^2}{1-\xi^2+4\zeta^2}\right), \tag{21}$$

$$R_2^4=\frac{(1-\xi^2/m+4\zeta^2)^2+4\zeta^2\xi^4/m^2}{(1+4\zeta^2)^2},$$

$$2\theta_2=\arctan\left(\frac{2\zeta\xi^2/m}{1-\xi^2/m+4\zeta^2}\right). \tag{22}$$

It is assumed that the angles $2\theta_1$ and $2\theta_2$ are restricted to the intervals

$$0\leqslant 2\theta_1<\pi,\quad 0\leqslant 2\theta_2<\pi. \tag{23}$$

This ensures that the values of p_1, q_1, p_2, and q_2 are always non-negative.

For each of the two solutions, characterized by the values $a=a_1$ and $a=a_2$, a pair of the Fourier transforms $\overline{u}$ and $\overline{w}$ can be established so that the basic Eqs. (10) and (11) are satisfied. Addition of these two solutions will lead to a general solution involving two unknown constants, say $\overline{u}_1$ and $\overline{u}_2$. These two constants can be determined from the two boundary conditions (6). The final expressions for the Fourier transforms of the displacements then are found to be

$$\overline{u} = -\frac{iF(\alpha)}{\mu\alpha(1-2i\zeta)} \frac{2a_1a_2\exp(-a_1\alpha z)-(1+a_1^2)\exp(-a_2\alpha z)}{4a_1a_2-(1+a_1^2)^2}, \tag{24}$$

$$\overline{w} = -\frac{F(\alpha)}{\mu\alpha(1-2i\zeta)} \frac{2a_2\exp(-a_1\alpha z)-a_2(1+a_1^2)\exp(-a_2\alpha z)}{4a_1a_2-(1+a_1^2)^2}. \tag{25}$$

The determination of the actual displacement components requires evaluation of the Fourier integrals (8) and (9). Convergence of these integrals depends upon the nature of the characteristic function $F(\alpha)$. When the resultant force of the load is nonzero the integrals are singular, but even then the derivatives of the integrals, needed for the evaluation of the stresses, may converge. Of course, the singular behavior of the displacements for problems of the elastic half-plane under the action of a given surface load is well known ([17]). It may also be noted that in the undamped case ($\zeta=0$) the denominator in the expressions (24) and (25) will be zero if the velocity equals the Rayleigh wave velocity, indicating a singularity in the displacements. In the generalized damped case, with $\zeta>0$, there are no such singularities, although the displacements may be very large if the damping ratio is small.

The Fourier transforms of the stresses are, using the transformed form of the constitutive relations,

$$\overline{\sigma_{xx}} = -F(\alpha) \times \frac{4a_1a_2\exp(-a_1\alpha z)-(1+a_1^2)(1-a_1^2+2a_2^2)\exp(-a_2\alpha z)}{4a_1a_2-(1+a_1^2)^2}, \tag{26}$$

$$\overline{\sigma_{zz}} = F(\alpha) \frac{4a_1a_2\exp(-a_1\alpha z)-(1+a_1^2)^2\exp(-a_2\alpha z)}{4a_1a_2-(1+a_1^2)^2}, \tag{27}$$

$$\overline{\sigma_{xz}} = -2ia_2(1+a_1^2)F(\alpha) \frac{\exp(-a_1\alpha z)-\exp(-a_2\alpha z)}{4a_1a_2-(1+a_1^2)^2}. \tag{28}$$

It can easily be verified that the shear stress σ_{zx} and the normal stress σ_{zz} indeed satisfy the boundary conditions (6).

4 Vertical Displacements for a Moving Point Load

One of the most interesting quantities is the vertical displacement w. The general solution for the Fourier transform of this variable has been given in Eq. (25). For the case of a moving point load this gives, with (9) and $F(\alpha)=-P/\pi$,

$$w = \frac{P}{\pi} \times \Re \int_0^\infty \frac{2a_2\exp(-a_1\alpha z)-a_2(1+a_1^2)\exp(-a_2\alpha z)}{\mu\alpha(1-2i\zeta)[4a_1a_2-(1+a_1^2)^2]} \times \exp[i\alpha(x-vt)]d\alpha. \tag{29}$$

This integral does not converge, because of the factor α in the denominator of the integrand, indicating that the displacements are infinitely large. For practical purposes this difficulty can be eliminated by considering a differential displacement Δw, defined as

$$\Delta w(x,z) = w(x,z) - w(x+l,z), \tag{30}$$

where l is a given nonzero length. Substitution of (29) into (30) gives

$$\Delta w = \frac{P}{\pi\mu(1+4\zeta^2)} \Re\{(A_1+iB_1)I_1+(A_2+iB_2)I_2\}, \tag{31}$$

where A_1, B_1, A_2, and B_2 are real constants, defined by

$$A_1+iB_1 = \frac{2(1+2i\zeta)a_2}{4a_1a_2-(1+a_1^2)^2}, \tag{32}$$

$$A_2+iB_2 = -\frac{(1+2i\zeta)a_2(1+a_1^2)}{4a_1a_2-(1+a_1^2)^2}. \tag{33}$$

and I_1 and I_2 are elementary Fourier integrals, defined by

$$I_j = \int_0^\infty \frac{\exp[i\alpha(x-vt)]-\exp[i\alpha(x+l-vt)]}{\alpha}\exp(-a_j\alpha z)d\alpha, \tag{34}$$

where $j=1$ or $j=2$. These integrals can be evaluated using standard Laplace transform tables ([18]), noting that the roots a_j can be decomposed into real and imaginary parts by $a_j=p_j-iq_j$, with both constants being positive, see (18). The result is

$$I_j = J_j + iK_j, \tag{35}$$

where

$$J_j = \frac{1}{2}\log\left\{\frac{(p_jz/l)^2+[q_jz/l+(x-vt)/l+1]^2}{(p_jz/l)^2+[q_jz/l+(x-vt)/l]^2}\right\}, \tag{36}$$

$$K_j = -\arctan\left\{\frac{p_jz/l}{(p_jz/l)^2+\left[q_jz/l+(x-vt)/l+\frac{1}{2}\right]^2-\frac{1}{4}}\right\}. \tag{37}$$

Substitution of (35) into (31) finally gives

$$\Delta w = \frac{P}{\pi\mu(1+4\zeta^2)}[A_1J_1-B_1K_1+A_2J_2-B_2K_2]. \tag{38}$$

All that remains to be done for the construction of a graphical representation of this function is to evaluate the real constants A_1, B_1, A_2, and B_2 from the definitions (32) and (33). This is a simple matter of separation of the expressions in the right-hand sides of these equations into real and imaginary parts, using the definitions of the complex parameters a_1 and a_2.

5 Examples

As a first example the vertical displacements in the field are shown in Fig. 4 for a practically undamped case ($\zeta=0.001$) and a large (supersonic) velocity ($v/c_s=2$). The figure indicates that two discontinuities are generated. The slopes of these two discontinuities are in agreement with the solution for the undamped case by Cole and Huth ([2]). Actually, in the undamped case the two discontinuities are given by $(x-vt)=-\alpha_s z$ and $(x-vt)=-\alpha_p z$, where for $\nu=0$ and $v/c_s=2$: $\alpha_s=\sqrt{3}$ and $\alpha_p=1$, which is in excellent agreement with the slopes of the two discontinuities that can be observed in Fig. 4. For values of the damping ratio smaller than 0.001 the results are found to be practically the same, with the discontinuities becoming even sharper.

The influence of a larger damping ratio is illustrated in Fig. 5, in which the damping ratio has been increased to $\zeta=0.1$, and the other parameters, Poisson's ratio and the velocity of the moving load, are the same as in Fig. 4. The two singularities can still be observed, but their effect is less pronounced. For larger values of the damping ratio the results become gradually smoother. On the other hand, for supersonic velocities a small upward displacement in front of the load may be observed. This may seem to be a surprising effect, but it occurs only if there is a considerable amount of damping, and it has also been verified that the vertical velocity directly below the point load is always in downward direction, so that a positive amount of work is done.

For very small velocities the results will approach the classical solution for a point load on an elastic half-plane (Flamant's solution ([17])). In the case of velocities close to the Rayleigh wave

velocity the displacements become very large, and there is a strong discontinuity just below the load, see Fig. 6. The velocity in this case is $v/c_s=0.874032$, which is the velocity of Rayleigh waves in an elastic medium if $\nu=0$ ([11]). Note that in Fig. 6 the scale of the displacements is a factor 50 different from the Figs. 4 and 5, indicating that the displacements are indeed very much larger for velocities near the Rayleigh wave velocity. By varying the value of the damping ratio ζ it has been found that the displacements are approximately inversely proportional to ζ, with the displacements becoming infinitely large when $\zeta\rightarrow 0$. This is illustrated in Fig. 7, which shows the product of the damping ratio ζ and the displacement difference Δw in the point $x/l=-0.1$,

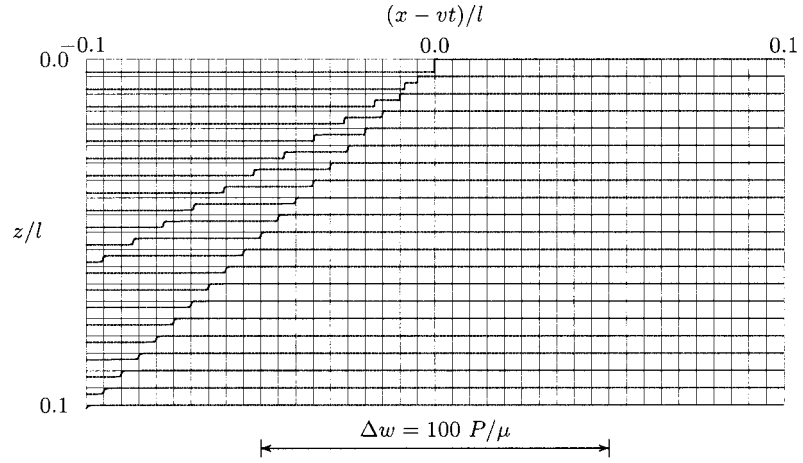

Fig. 4 Moving point load, Δw, $\nu=0.0$, $\zeta=0.001$, $v/c_s=2.0$

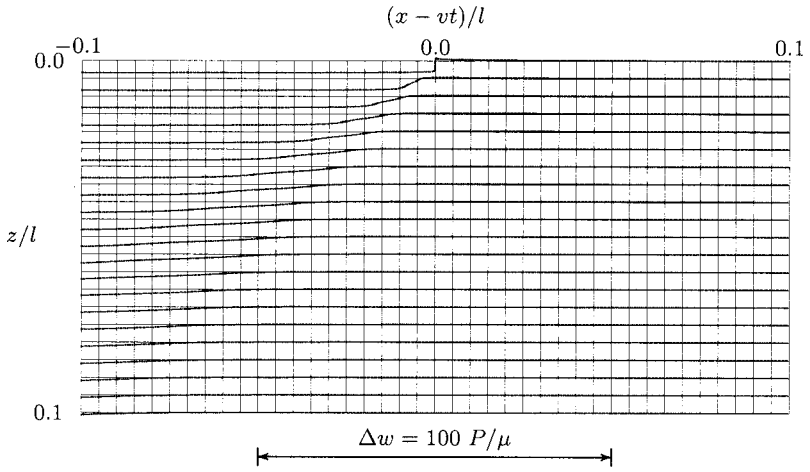

Fig. 5 Moving point load, Δw, $\nu=0.0$, $\zeta=0.1$, $v/c_s=2.0$

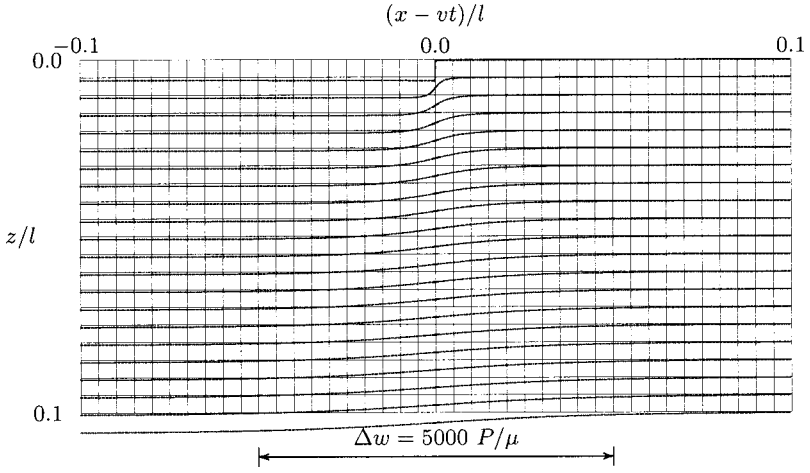

Fig. 6 Moving point load, Δw, $\nu=0.0$, $\zeta=0.1$, $v/c_s=0.874032$

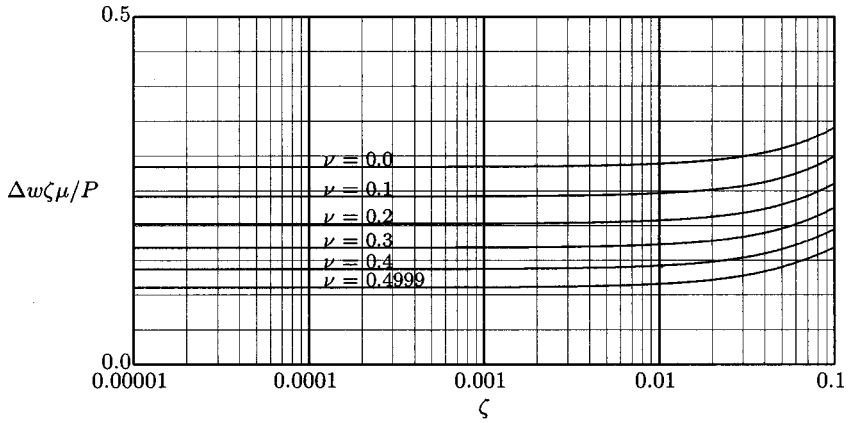

Fig. 7 Moving point load, Δw at Rayleigh wave velocity

$z/l=0.01$ as a function of ζ, for various values of Poisson's ratio ν. It appears that for small values of the damping ratio this product is practically constant.

6 Vertical Normal Stress

Some more information on the character of the solution, and the influence of damping, may be obtained when considering the stresses. For the case of a moving point load the vertical normal stresses are, with (27) and $F(\alpha)=-P/\pi$, and applying the inverse Fourier transform,

$$\sigma_{zz}=-\frac{P}{\pi}\times\Re\int_0^\infty \frac{4a_1a_2\exp(-a_1\alpha z)-(1+a_1^2)^2\exp(-a_2\alpha z)}{4a_1a_2-(1+a_1^2)^2}\times\exp[i\alpha(x-vt)]d\alpha. \tag{39}$$

Because a_1 and a_2 are complex, $a_1=p_1-iq_1$ and $a_2=p_2-iq_2$, this leads to integrals of the Laplace transform type, which can easily be evaluated. The result is

$$\sigma_{zz}=-\frac{P}{2\pi z}\left\{\frac{(1+C)p_1-D[q_1+(x-vt)/z]}{p_1^2+[q_1+(x-vt)/z]^2}+\frac{(1-C)p_2+D[q_2+(x-vt)/z]}{p_2^2+[q_2+(x-vt)/z]^2}\right\}, \tag{40}$$

where C and D are real constants, defined by

$$C+iD=\frac{4a_1a_2+(1+a_1^2)^2}{4a_1a_2-(1+a_1^2)^2}. \tag{41}$$

Using these expressions the stress distribution can easily be presented in numerical or graphical form.

A first example is shown in Fig. 8, which presents the vertical normal stresses for $\nu=0$, $\zeta=0.001$ and $v/c_s=2$, the same data as used for Fig. 4. The very large stresses along the two lines $(x-vt)=-\alpha_s z$ and $(x-vt)=-\alpha_p z$ confirm the propagation of two shock waves, in agreement with the discontinuities in the displacement field.

The influence of the hysteretic damping on the magnitude of the stresses is shown in Fig. 9, in which the damping factor is a factor 100 larger, $\zeta=0.1$. In this figure the scale for the stresses is a factor 20 smaller than in Fig. 8, and the values in the figure themselves are also much smaller. The results clearly show that the very large stresses for small values of the damping ratio are much reduced if the damping ratio increases.

The maximum value of the vertical normal stress σ_{zz} at a depth $z/l=0.1$ is shown, as a function of the velocity of the load, in Fig. 10, for five values of the damping ratio ζ, and using the maximum static value $2P/(\pi z)$ as a reference value. The influence of the damping ratio is again found to be very large. For very small values of the damping ratio the results are not shown, as the two peaks would become very large, in agreement with the results shown before, in Fig. 8.

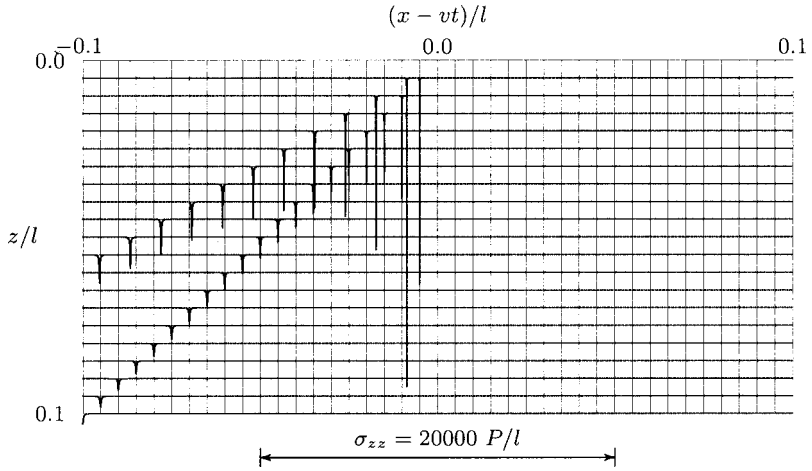

Fig. 8 Moving point load, σ_{zz}, $\nu=0.0$, $\zeta=0.001$, $v/c_s=2.0$

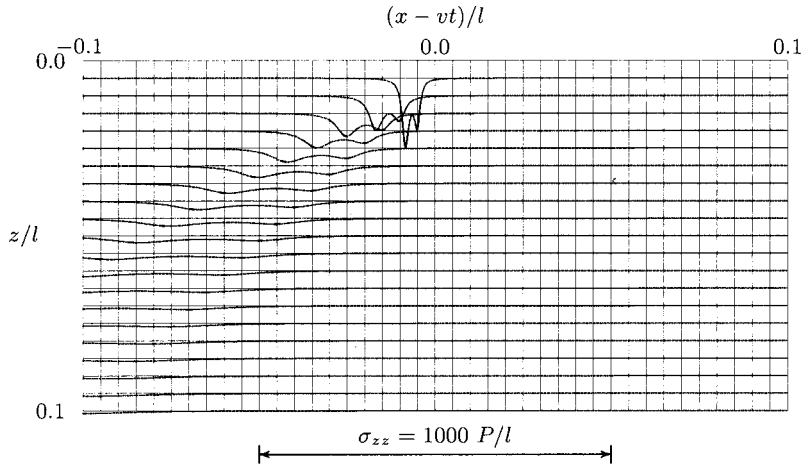

Fig. 9 Moving point load, σ_{zz}, $\nu=0.0$, $\zeta=0.1$, $v/c_s=2.0$

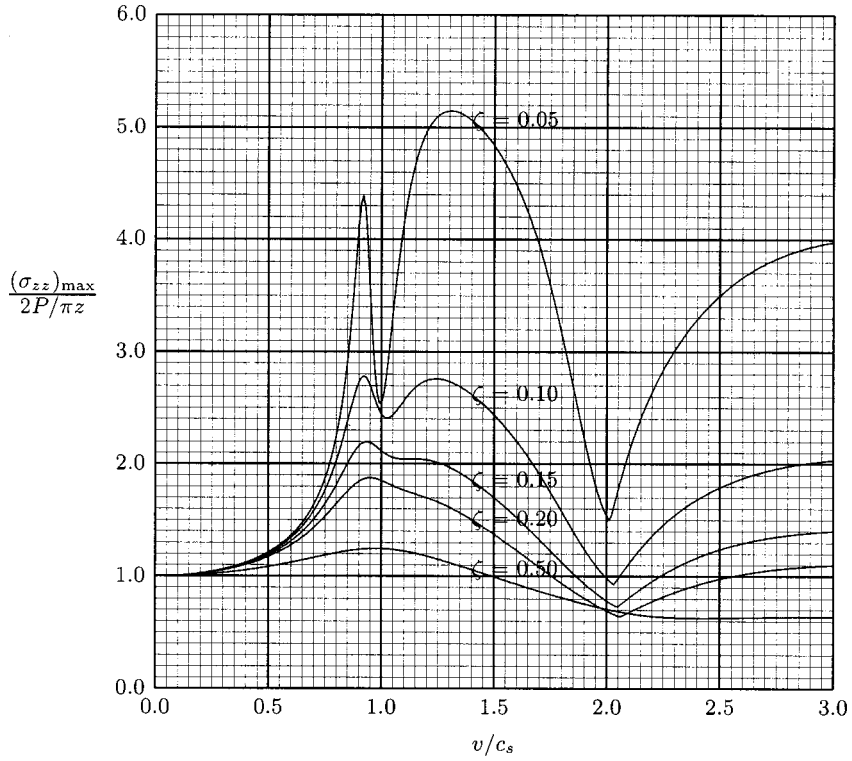

Fig. 10 Moving point load, Maximum vertical stress, $\nu=0.3333$

7. Conclusions

It has been shown that a closed-form solution can be given of the problem of an elastic half-plane with hysteretic damping, loaded by a moving load on its surface. A simple expression can be given for the stresses, which includes the static solution and the undamped dynamic solution as special cases. The solution indicates that for small values of the damping ratio, say $\zeta<0.1$, the displacements and the stresses are very large, compared to the elastostatic solution. For small values of the damping ratio, the maximum displacements, which occur if the velocity of the load approaches the Rayleigh wave velocity, are found to be inversely proportional to the damping ratio. For relatively large values of the damping ratio (say $\zeta>0.2$) the displacements and stresses are of the same order of magnitude as in the elastostatic case.

References

[1] Sneddon, I. N., 1951, *Fourier Transforms*, McGraw-Hill, New York.

[2] Cole, J., and Huth, J., 1958, "Stresses Produced in a Half Plane by Moving Loads," ASME J. Appl. Mech., **25**, pp. 433–436.

[3] Eringen, A. C., and Suhubi, E. S., 1975, *Elastodynamics*, Vol. 2, Academic Press, New York.

[4] Frýba, L., 1999, *Vibration of Solids and Structures Under Moving Loads*, 3rd Ed., Thomas Telford, London.

[5] Georgiadis, H. G., and Barber, J. R., 1993, "Steady-State Transonic Motion of a Line Load Over an Elastic Half-Space: The Corrected Cole/Huth Solution," ASME J. Appl. Mech., **60**, pp. 772–774.

[6] Dieterman, H. A., and Metrikine, A., 1997, "Critical Velocities of a Harmonic Load Moving Uniformly Along an Elastic Layer," ASME J. Appl. Mech., **64**, pp. 596–600.

[7] Verruijt, A., 1999, "Dynamics of Soils With Hysteretic Damping," *Proc. 12th Eur. Conf. Soil Mech. and Geotechnical Engineering*, Vol. 1, F. B. J. Barends et al., eds., Balkema, Rotterdam, pp. 3–14.

[8] Keverling Buisman, A. S., 1940, *Grondmechanica*, Waltman, Delft.
[9] Terzaghi, K., 1943, *Theoretical Soil Mechanics*, John Wiley and Sons, New York.
[10] Van Baars, S., 1996, ''Discrete Elements for Granular Metrials,'' Ph.D. thesis, Delft.
[11] Das, B. M., 1983, *Fundamentals of Soil Dynamics*, Elsevier, New York.
[12] Hardin, B. O., 1965, ''The Nature of Damping in Sands,'' J. Soil Mech. Found. Div., Am. Soc. Civ. Eng. **91**, pp. 63–97.
[13] Hardin, B. O., and Drnevich, V. P., 1972, ''Shear Modulus and Damping in Soils: Measurement and Parameter Effects,'' J. Soil Mech. Found. Div., Am. Soc. Civ. Eng. **98**, pp. 603–624.
[14] De Barros, F. C. P., and Luco, J. E., 1994, ''Response of a Layered Viscoelastic Half-Space to a Moving Point Load,'' Wave Motion, **19**, pp. 189–210.
[15] Rayleigh, J. W. S., 1894, *The Theory of Sound*, Macmillan, London.
[16] Wolf, J. P., 1988, *Soil-Structure Interaction Analysis in Time Domain*, Prentice-Hall, Englewood Cliffs, NJ.
[17] Timoshenko, S. P., and Goodier, J. N., 1951, *Theory of Elasticity*, 2nd Ed., McGraw-Hill, New York.
[18] Erdélyi, A., et al., 1954, *Tables of Integral Transforms*, Vol. 1, McGraw-Hill, New York.

Axial Vibration of a Padded Annulus on a Semi-Infinite Viscoelastic Medium

B. B. Guzina
Assistant Professor,
e-mail: guzina@wave.ce.umn.edu

F. Nintcheu Fata
Research Assistant,
e-mail: nint0004@tc.umn.edu

Department of Civil Engineering,
University of Minnesota,
500 Pillsbury Drive, SE
Minneapolis, MN 55455

The vibratory punch problem for a viscoelastic half-space indented by a padded annular disk is investigated. By virtue of transform methods, the problem is formulated as a set of triple integral equations which are reducible to a Fredholm integral equation of the second kind. In the formulation, the response of a thin buffer which regularizes the load transfer to the semi-infinite solid is approximated via a plane stress-type solution. A set of numerical results is included to demonstrate the effect of padding characteristics on the dynamic system response. Apart from providing an interpretation tool for the nondestructive testing methods involving buffered annular loading systems, the present solution can be used as an effective approximation to the corresponding rigid-punch problem which has so far eluded a rigorous mathematical treatment. [DOI: 10.1115/1.1410098]

1 Introduction

Dynamic interaction of an annular disk with a semi-infinite solid has been a subject of fundamental interest in applied mechanics over the past few decades because of its importance to the seismic analysis and design of structures such as cooling towers, radar stations, and liquid containment tanks. For this class of problems, the early treatments date back to El-Shafee and Gould [1] and Tassoulas and Kausel [2] who independently employed a finite element method coupled with a semi-analytic transmitting boundary to represent the radial wave propagation in a supporting elastic medium. A further insight into the nature of the problem was provided by Veletsos and Tang [3,4] via a direct boundary element solution for the vibrations of a rigid ring on a uniform elastic half-space, and Rajapakse [5] who examined the time-harmonic load transfer between a flexible annular plate and a semi-infinite viscoelastic solid using a variational principle. Owing to the complexity of the triple-integral equation systems that are intimately involved in the analytical solutions for ring-shaped contact geometries ([6]), however, dynamic interplay of an annular disk with a solid half-space has so far evaded a rigorous treatment that is attainable for the corresponding circular footing problem ([7–10]).

In the context of nondestructive testing, the subject of dynamic annulus-half-space interaction is also relevant to the proliferating class of site and material characterization techniques based on stress waves emanating from a ring-shaped loading disk ([11,12]). Owing in part to a thin rubber padding, often attached to the bottom of the source plate ([13]), the near-field waveforms stemming from such loading systems are commonly interpreted on the basis of the uniform contact-pressure assumption for the loaded area. Several elastostatic investigations concerned with the subject (e.g., [14]), however, indicate that the neglect of site-loading system interaction may be inappropriate for certain field configurations.

To provide a rational basis for quantifying near-field effects of source characteristics in nondestructive site and material characterization by wave methods, the focus of this communication is the harmonic response of a padded annular footing vibrating vertically on a uniform viscoelastic semi-infinite solid. Formulated in terms of a set of triple integral equations, the problem is reduced to a single Fredholm integral equation of the second kind which is amenable to an effective computational treatment. Numerical results are included to highlight several key aspects of the physical problem. Beyond serving as a tool for the consistent interpretation of dynamic field tests performed on profiles that are nearly uniform to a sufficient depth, the analysis developed provides the basis for extensions of the methodology to more general, multilayered systems.

2 Problem Formulation

Consider the axial vibration of a padded annular footing of internal radius a_0 and external radius a resting on a homogeneous isotropic viscoelastic half-space (see Fig. 1). The vibrating foundation is a system consisting of a massless rigid annulus underlain by a thin elastic body of thickness h, shear modulus μ_P, Poisson's ratio ν_P, and mass density ρ_P. The rigid disk is subjected to a time-harmonic vertical displacement $\Delta e^{i\omega t}$ where ω is the circular frequency of vibration. The sides of the footing and the surface of the half-space outside the contact area are free of stresses, with the axial displacements and normal stresses being continuous across both terminal sections of the buffer. With reference to the cylindrical coordinate system (r,θ,z) set at the center of the padding's bottom contact area, the semi-infinite solid $(z>0)$ is characterized by the shear modulus μ, Poisson's ratio ν, mass density ρ, and the damping ratios

$$\xi_p \equiv \frac{1}{4\pi}\frac{\Delta W_p}{W_p}, \quad \xi_s \equiv \frac{1}{4\pi}\frac{\Delta W_s}{W_s}, \tag{1}$$

for compressional and shear waves, respectively. In (1), $\Delta W_q (q=p,s)$ is the amount of energy dissipated per cycle of harmonic excitation in a representative volume, while W_q is the peak strain energy stored in the same volume of a solid subjected to compressional (p) or shear (s) body waves. In this investigation, ξ_p and ξ_s are assumed to be frequency-independent which corresponds to the case of hysteretic damping which offers a reasonable approximation of dissipative mechanisms in many frictional materials such as soils and rocks ([15]).

2.1 Response of Elastic Padding. To facilitate the solution to the load-transfer problem illustrated in Fig. 1, it will be assumed in the sequel that (i) the contacts between the rigid annulus, elastic buffer, and the half-space are frictionless, and (ii) the thickness of the padding is sufficiently small so that

Contributed by the Applied Mechanics Division of THE AMERICAN SOCIETY OF MECHANICAL ENGINEERS for publication in the ASME JOURNAL OF APPLIED MECHANICS. Manuscript received by the ASME Applied Mechanics Division, Aug. 29, 2000; final revision, June 12, 2001. Associate Editor: R. C. Benson. Discussion on the paper should be addressed to the Editor, Professor Lewis T. Wheeler, Department of Mechanical Engineering, University of Houston, Houston, TX 77204-4792, and will be accepted until four months after final publication of the paper itself in the ASME JOURNAL OF APPLIED MECHANICS.

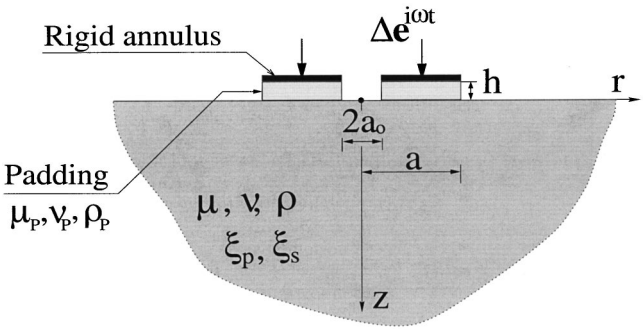

Fig. 1 Padded annulus on a uniform viscoelastic half-space

$$h \ll a, \quad h \ll \frac{2\pi}{\omega}\sqrt{\frac{\mu_P}{\rho_P}}, \quad h \ll \frac{F/\Delta}{\pi(a^2-a_0^2)\omega^2\rho_P}, \tag{2}$$

for the range of frequencies of interest where F is the resultant interfacial force between the padding and the top disk. Physically, (2*b*) postulates that the shear wave length in the pad significantly exceeds its thickness, while (2*c*) implies that the mass of the buffer has a negligible effect on the overall system response. Under such hypotheses, the shear stress component σ_{rz}^{pad} in the padding can be neglected and the variation of the axisymmetric stress field within the buffer can be approximated via a *plane stress-type*, i.e., depth-independent representation

$$\sigma_{jk}^{\text{pad}}(r,z,t) = \delta_{jk}\hat{\sigma}_{jk}^{\text{pad}}(r)e^{i\omega t}, \quad j,k=r,\theta,z, \quad \begin{matrix} -h<z<0 \\ a_0<r<a, \end{matrix} \tag{3}$$

where δ_{jk} denotes the Kronecker delta with no summation implied. On the basis of (3), the equilibrium equations governing the response of an annular padding reduce to

$$\frac{\partial\hat{\sigma}_{rr}^{\text{pad}}}{\partial r} + \frac{\hat{\sigma}_{rr}^{\text{pad}} - \hat{\sigma}_{\theta\theta}^{\text{pad}}}{r} = 0, \quad \begin{matrix} -h<z<0, \\ a_0<r<a, \end{matrix} \tag{4}$$

in the absence of inertial body forces which are, consistent with (2*c*), assumed to be insignificant relative to the stresses transmitted through the buffer. By means of the generalized Hooke's law for an isotropic solid and the compatibility conditions, (4) can be rewritten as

$$\frac{\partial}{\partial r}\left(\frac{1}{r}\frac{\partial}{\partial r}(r\hat{u}_r^{\text{pad}})\right) = -\frac{\nu_P}{2\mu_P}\frac{d\hat{\sigma}_{zz}^{\text{pad}}}{dr}, \quad \begin{matrix} -h<z<0, \\ a_0<r<a, \end{matrix} \tag{5}$$

where $u_r^{\text{pad}}(r,z,t) = \hat{u}_r^{\text{pad}}(r,z)e^{i\omega t}$ denotes the radial displacement in the padding. If the normal stress $\hat{\sigma}_{zz}^{\text{pad}}$ is further assumed to be known, (5) can be solved for the radial displacement field as

$$\hat{u}_r^{\text{pad}}(r,z) = \frac{r}{2}C_1(z) + \frac{1}{r}C_2(z) - \frac{\nu_P}{2\mu_P}\frac{1}{r}\int_{a_0}^{\tau}\tau\hat{\sigma}_{zz}^{\text{pad}}(\tau)d\tau, \quad \begin{matrix} -h<z<0, \\ a_0<r<a, \end{matrix} \tag{6}$$

where C_1 and C_2 are the constants of integration to be determined from the boundary conditions. To such end, one may invoke (3) and the requirement that the sides of the padding are stress-free, that is

$$\hat{\sigma}_{rr}^{\text{pad}}(a_0) = 0, \quad \hat{\sigma}_{rr}^{\text{pad}}(a) = 0, \tag{7}$$

which yields the depth-invariant parameters

$$C_1 = \frac{-\nu_P(1-\nu_P)}{\mu_P(1+\nu_P)(a^2-a_0^2)}\int_{a_0}^{a}\tau\hat{\sigma}_{zz}^{\text{pad}}(\tau)d\tau,$$

$$C_2 = \frac{-\nu_P a_0^2}{2\mu_P(a^2-a_0^2)}\int_{a_0}^{a}\tau\hat{\sigma}_{zz}^{\text{pad}}(\tau)d\tau. \tag{8}$$

By virtue of (6) and (8), the axial strain in the padding can be shown to admit the representation $\varepsilon_{zz}^{\text{pad}}(r,z,t) = \hat{\varepsilon}_{zz}^{\text{pad}}(r)e^{i\omega t}$ where

$$\hat{\varepsilon}_{zz}^{\text{pad}}(r) = \frac{1-2\nu_P}{2\mu_P(1-\nu_P)}\hat{\sigma}_{zz}^{\text{pad}} - \frac{\nu_P}{1-\nu_P}\frac{1}{r}\frac{d}{dr}(r\hat{u}_r^{\text{pad}}) \equiv \alpha\hat{\sigma}_{zz}^{\text{pad}}(r) + \beta, \tag{9}$$

with the parameters

$$\alpha = \frac{1-\nu_P}{2\mu_P}, \quad \beta = \frac{\nu_P^2}{\mu_P(1+\nu_P)(a^2-a_0^2)}\int_{a_0}^{a}\tau\hat{\sigma}_{zz}^{\text{pad}}(\tau)d\tau, \tag{10}$$

dependent on the properties of the buffer as well as the average normal stress transmitted through the padding. It is of interest to note that upon neglecting the Poisson's effects in the padding via setting $\nu_P = 0$, (9) reduces to the familiar one-dimensional relationship $\hat{\varepsilon}_{zz}^{\text{pad}} = \hat{\sigma}_{zz}^{\text{pad}}/E_P$ where E_P denotes the buffer's Young's modulus.

2.2 Normal Load on a Half-Space. For a general representation of the response of a lossy semi-infinite solid to time-harmonic excitation, it is convenient to employ the correspondence principle [16] which states that the damped solution in the frequency domain may be obtained from the elastic one by replacing the featured elastic constants with the corresponding complex moduli. By virtue of (1) and dissipation analysis in Findley et al. [17], the complex shear modulus and the Poisson's ratio for the half-space outlined in Fig. 1 can be written, respectively, as

$$\mu^* = \mu(1+2i\xi_s/\sqrt{1-4\xi_s^2}),$$

$$\nu^* = \frac{(1-\nu)(1+2i\xi_p/\sqrt{1-4\xi_p^2}) - (1-2\nu)(1+2i\xi_s/\sqrt{1-4\xi_s^2})}{2(1-\nu)(1+2i\xi_p/\sqrt{1-4\xi_p^2}) - (1-2\nu)(1+2i\xi_s/\sqrt{1-4\xi_s^2})}. \tag{11}$$

In dealing with the media with less pronounced intrinsic dissipation so that $\xi_p \ll 1$ and $\xi_s \ll 1$, the square-root terms in (11) may be dropped leading to the commonly used expressions for the complex isotropic viscoelastic moduli (e.g., [5]).

For the time-harmonic problem of interest, cylindrical components of the displacement and stress fields in the half-space can be conveniently expressed as

$$u_j(r,z,t) = \hat{u}_j(r,z)e^{i\omega t} \equiv a\overline{u}_j(\overline{r},\overline{z})e^{i\omega t},$$
$$\sigma_{jk}(r,z,t) = \hat{\sigma}_{jk}(r,z)e^{i\omega t} \equiv \mu^*\overline{\sigma}_{jk}(\overline{r},\overline{z})e^{i\omega t}, \quad \overline{r} \equiv \frac{r}{a} \geqslant 0, \quad \overline{z} \equiv \frac{z}{a} > 0, \tag{12}$$

respectively, where $j,k=r,\theta,z$. With such definitions, it can be shown by means of (11) and the elastodynamic solution in Pak [18] that the vertical displacement on the surface of a homogeneous viscoelastic half-space due to an arbitrary normal surface load $\hat{\sigma}_{zz}(r,0)$ permits the integral representation

$$\overline{u}_z(\overline{r},0) = \int_0^{\infty}\Omega(\zeta)\tilde{\mathfrak{R}}^0(\zeta)J_0(\overline{r}\zeta)d\zeta, \tag{13}$$

where J_0 denotes the Bessel function of order zero, and

$$\tilde{\Re}^0(\zeta)=\int_0^\infty \overline{r}\sigma_{zz}(\overline{r},0)J_0(\overline{r}\zeta)d\overline{r}, \tag{14}$$

is the zeroth-order Hankel transform of the normalized surface traction $\overline{\sigma}_{zz}$. In (13),

$$\Omega(\zeta)=\frac{\overline{k}_s^2\zeta\sqrt{\zeta^2-\overline{k}_p^2}}{(2\zeta^2-\overline{k}_s^2)^2-4\zeta^2\sqrt{\zeta^2-\overline{k}_p^2}\sqrt{\zeta^2-\overline{k}_s^2}}, \tag{15}$$

where

$$\overline{k}_s=a\omega\sqrt{\frac{\rho}{\mu^*}},\quad \overline{k}_p=\sqrt{\frac{1-2\nu^*}{2-2\nu^*}}\overline{k}_s \tag{16}$$

denote the dimensionless shear and compressional wave numbers in the half-space, respectively.

3 Mathematical Analysis of the Annular Load Transfer

On account of the premises and results derived in Section 2, the boundary conditions for the elastic buffer that are relevant to the interaction problem can be expressed as

$$\begin{gathered}\hat{u}_z^{\text{pad}}(r,-(h^-))=\Delta,\\ \hat{u}_z^{\text{pad}}(r,0^-)=\hat{u}_z(r,0^+),\quad a_0<r<a,\\ \hat{\sigma}_{zz}^{\text{pad}}(r)=\hat{\sigma}_{zz}(r,0^+),\end{gathered} \tag{17}$$

where $\hat{u}_z$ and $\hat{\sigma}_{zz}$ denote the axial displacement and stress in the half-space as examined earlier, and (17*c*) synthesizes the normal stress conditions on both terminal sections of the padding. By virtue of (9), (17), and the frictionless contact assumption, the boundary conditions on the surface of the semi-infinite medium can be written as

$$\begin{gathered}\hat{u}_z(r,0)=\Delta+(\alpha\hat{\sigma}_{zz}(r,0)+\beta)h,\quad a_0\leqslant r\leqslant a,\\ \hat{\sigma}_{zz}(r,0)=0,\quad r<a_0,\quad r>a,\\ \hat{\sigma}_{zr}(r,0)=0,\quad r\geqslant 0,\end{gathered} \tag{18}$$

with the superscript "+" dropped in view of the continuity of $\hat{u}_z$ and $\hat{\sigma}_{zz}$ in the half-space.

On the basis of (13), (14) and the theory of Hankel transforms, mixed boundary conditions (18) constituting the load-transfer problem can be conveniently recast in a dimensionless form as a set of triple integral equations

$$\begin{gathered}\int_0^\infty\left[1-\frac{a\Omega(\zeta)}{\alpha h\mu^*\zeta}\right]\zeta\tilde{\Re}^0(\zeta)J_0(\overline{r}\zeta)d\zeta=-\frac{\Delta+\beta h}{\alpha h\mu^*},\quad \frac{a_0}{a}\leqslant\overline{r}\leqslant 1,\\ \int_0^\infty\zeta\tilde{\Re}^0(\zeta)J_0(\overline{r}\zeta)d\zeta=0,\quad 0\leqslant\overline{r}<\frac{a_0}{a},\\ \int_0^\infty\zeta\tilde{\Re}^0(\zeta)J_0(\overline{r}\zeta)d\zeta=0,\quad \overline{r}>1,\end{gathered} \tag{19}$$

for the transformed contact stress $\tilde{\Re}^0$. Here, the first equation asserts the continuity of axial displacements across the annular contact area, while the latter two equalities maintain zero normal tractions on the half-space outside the loaded zone.

3.1 Reduction of Triple Integral Equations. The treatment of the governing triplet of integral equations can be facilitated by introducing an auxiliary function $\Phi(\overline{r})$ such that

$$-\frac{\Delta+\beta h}{\alpha h\mu^*}\Phi(\overline{r})=\int_0^\infty\zeta\tilde{\Re}^0(\zeta)J_0(\overline{r}\zeta)d\zeta,\quad \overline{r}\geqslant 0, \tag{20}$$

where β is a functional of the contact stress $\hat{\sigma}_{zz}(r,0)$ as given by (10*b*) and (17*c*). With the aid of (19) and the Hankel inversion theorem, (20) can be reversed via

$$\tilde{\Re}^0(\zeta)=-\frac{\Delta+\beta h}{\alpha h\mu^*}\int_{a_0/a}^1\tau\Phi(\tau)J_0(\tau\zeta)d\tau,\quad \zeta\geqslant 0. \tag{21}$$

By virtue of (10*a*), (20), and (21), it can be shown that the system of triple integral Eq. (19) leads to a Fredholm integral equation of the second kind

$$\Phi(\overline{r})-\Lambda\int_{a_0/a}^1 K(\overline{r},\tau)\Phi(\tau)d\tau=1,\quad \frac{a_0}{a}\leqslant\overline{r}\leqslant 1, \tag{22}$$

where

$$\Lambda=\frac{2}{1-\nu_P}\frac{a\mu_P}{h\mu^*}, \tag{23}$$

denotes the Fredholm integral parameter, and

$$K(\overline{r},\tau)=\tau\int_0^\infty\Omega(\zeta)J_0(\overline{r}\zeta)J_0(\tau\zeta)d\zeta,\quad \frac{a_0}{a}\leqslant\overline{r},\tau\leqslant 1. \tag{24}$$

To expose the physical meaning of Λ, it is useful to recall (i) the one-dimensional axial stiffness of a solid cylindrical column $(a_0/a=0)$ with Young's modulus $E_P=2\mu_P(1+\nu_P)$ and height h which is given by $S_P=E_P(\pi a^2)/h$, and (ii) the normal stiffness $S=4\mu a/(1-\nu)$ of an elastic half-space with shear modulus μ and Poisson's ratio ν under the action of a rigid circular punch of radius a ([19]). With such definitions, Fredholm integral parameter (23) can be recast as

$$\Lambda=\frac{S_P}{S}\left\{\frac{4\sqrt{1-4\xi_s^2}}{\pi(1-\nu)(1-\nu_P^2)(\sqrt{1-4\xi_s^2}+2i\xi_s)}\right\}, \tag{25}$$

which clearly identifies Λ as a stiffness ratio between the padding and the half-space.

For an in-depth study of the load-transfer problem, it is useful to observe the asymptotic behavior of (15) given by

$$\lim_{\zeta\to\infty}\Omega(\zeta)=\nu^*-1, \tag{26}$$

which, combined with the respective asymptotic expansions of Bessel functions in (24), reveals a logarithmic singularity of the kernel $K(\overline{r},\tau)$ in the limit as $|\overline{r}-\tau|\to 0$. To pursue a rigorous solution to (22) under such circumstances, it is useful to extract the singular part of the Fredholm kernel and integrate it in closed form so that

$$\begin{aligned}K(\overline{r},\tau)=(\nu^*-1)\frac{2\tau}{\pi(\overline{r}+\tau)}F_0\left(\frac{4\overline{r}\tau}{(\overline{r}+\tau)^2}\right)+\tau\int_0^\infty\{\Omega(\zeta)\\ -(\nu^*-1)\}J_0(\overline{r}\zeta)J_0(\tau\zeta)d\zeta,\quad \frac{a_0}{a}\leqslant\overline{r},\tau\leqslant 1,\end{aligned} \tag{27}$$

where F_0 denotes the complete elliptic integral of the first kind ([20]). One may observe that the remaining integral in (27) is now regular, thus being amenable to numerical evaluation via suitable truncation of the integration interval.

On account of (12*b*), (14), and (20), the contact stress distribution between the annular buffer and the half-space can be evaluated directly in terms of the solution to the Fredholm integral equation via

$$\hat{\sigma}_{zz}(r,0)=\gamma\Phi\left(\frac{r}{a}\right),\quad \gamma=-\frac{\Delta+\beta h}{\alpha h},\quad r\geqslant 0, \tag{28}$$

which implies that $\Phi(\bar{r})$ has a physical meaning of the normalized contact load. A careful examination of (10) and (28) also reveals that γ depends on the mean value of Φ over the contact area through the relationship

$$\beta=\frac{\Delta\nu_P\phi}{h(\alpha-\nu_P(\alpha+\phi))},$$

$$\phi=\frac{-\nu_P(1-\nu_P)a^2}{\mu_P(1+\nu_P)(a^2-a_0^2)}\int_{a_0/a}^{1}\tau\Phi(\tau)d\tau. \tag{29}$$

It is important to note that Φ and ϕ do not depend on the vibration amplitude Δ, thus rendering the linearity of the solution in (28) explicit.

To cater for engineering applications where the induced surface deflections are often used as an input to the back-calculation of ground properties, integral representation of the vertical displacement $\hat{u}_z(r,0)$ on the surface of a semi-infinite solid due to a buffered annular punch can be derived from (12*a*), (13), and (21) in the form of

$$\hat{u}_z(r,0)=\frac{a\gamma}{\mu^*}\int_{a_0/a}^{1}L(\bar{r},\tau)\Phi(\tau)d\tau,\quad r\geqslant 0, \tag{30}$$

where

$$L(\bar{r},\tau)=\tau\int_0^{\infty}\Omega(\zeta)J_0(\bar{r}\zeta)J_0(\tau\zeta)d\zeta,\quad \bar{r}\geqslant 0,\quad \frac{a_0}{a}\leqslant\tau\leqslant 1. \tag{31}$$

As can be seen from (24) and (31), $L(\bar{r},\tau)$ is the *continuation* of $K(\bar{r},\tau)$ over the strip $[0,+\infty)\times[a_0/a,1]$ which indicates that the asymptotic decomposition (27) can be employed for the evaluation of $L(\bar{r},\tau)$ as well.

4 Computational Treatment

For numerical purposes, the solution to the Fredholm integral Eq. (22) is sought via the collocation method with linear interpolation functions. To effectively deal with possible stress concentrations along the edges of the annular contact area, an open-ended discretization scheme

$$\frac{a_0}{a}<\bar{r}_1<\bar{r}_2<\cdots<\bar{r}_{n-1}<\bar{r}_n<1, \tag{32}$$

is selected where $\bar{r}_j(j=1,2,\ldots n)$ denotes the radial coordinate of the jth collocation point. Upon introducing the set of auxiliary constants via $s_1=a_0/a$, $s_k=\bar{r}_k(1<k<n)$, and $s_n=1$, an approximate solution to the Fredholm integral equation can be expressed as

$$\tilde{\Phi}(\bar{r})=\sum_{j=1}^{n}\Phi_j\psi_j(\bar{r}),\quad \frac{a_0}{a}\leqslant\bar{r}\leqslant 1 \tag{33}$$

where $\Phi_j\equiv\tilde{\Phi}(\bar{r}_j)$, and

$$\psi_k(\bar{r})=H(\bar{r}-s_{k-1})H(\bar{r}_k-\bar{r})\frac{\bar{r}-\bar{r}_{k-1}}{\bar{r}_k-\bar{r}_{k-1}}+H(\bar{r}-\bar{r}_k)\times H(s_{k+1}-\bar{r})\frac{\bar{r}_{k+1}-\bar{r}}{\bar{r}_{k+1}-\bar{r}_k},$$

$$k=2,3,\ldots n-1,$$

$$\psi_1(\bar{r})=H(\bar{r}-s_1)H(\bar{r}_2-\bar{r})\frac{\bar{r}_2-\bar{r}}{\bar{r}_2-\bar{r}_1},$$

$$\psi_n=H(\bar{r}-\bar{r}_{n-1})H(s_n-\bar{r})\frac{\bar{r}-\bar{r}_{n-1}}{\bar{r}_n-\bar{r}_{n-1}}, \tag{34}$$

with H denoting the Heaviside function. On the basis of (33), the governing integral Eq. (22) can be converted into a system of linear algebraic equations

$$\sum_{j=1}^{n}\left(\delta_{ij}-\Lambda\int_{a_0/a}^{1}K(\bar{r}_i,\tau)\psi_j(\tau)d\tau\right)\Phi_j=1,\quad i=1,2,\ldots,n, \tag{35}$$

for the nodal values Φ_j. Here, δ_{ij} denotes the Kronecker delta, Λ is given by (23), and K stands for the Fredholm kernel function evaluated via (27).

Apart from revealing the contact stress distribution between the padding and the semi-infinite solid through (28) and (33), the nodal values Φ_j of the piecewise-linear approximation can also be used as a basis for evaluation of the surface deflections in a half-space via

$$\hat{u}_z(r,0)=\frac{a\gamma}{\mu^*}\sum_{j=1}^{n}\Phi_j\int_{a_0/a}^{1}L(\bar{r},\tau)\psi_j(\tau)d\tau,\quad r\geqslant 0, \tag{36}$$

with $L(\bar{r},\tau)$ given by (31).

5 Results

By means of the foregoing mathematical analysis and computational scheme, the dynamic response of a half-space due to a padded annular punch can be evaluated numerically. In what follows, a set of illustrative results is presented with the typical values of a_0/a taken as 0.1 and 0.8 to provide benchmarks for the existing nondestructive testing configurations ([11,12]). To bring the results into a self-similar format, the dimensionless frequency is taken as

$$\bar{\omega}=\omega a\sqrt{\frac{\rho}{\mu}}. \tag{37}$$

In Fig. 2, the static contact stress distribution between the padded annulus with $a_0/a=0.1$ and an elastic half-space is plotted for several values of the stiffness ratio Λ. From the display wherein p denotes the average contact stress, it is apparent that the stress distribution varies from being nearly uniform to having pronounced edge concentrations with the increasing stiffness ratio. A close agreement between the result for $\Lambda=10^5$ and the static analytical solution for the rigid annulus ([21]) should also be observed.

The next example illustrates the dynamic response of a massless rigid ring with $a_0/a=0.8$ vibrating on a semi-infinite solid with $\nu=1/3$. The resulting dynamic compliance

$$C_{vv}(\omega)=\frac{\Delta}{F},\quad F=-2\pi\int_{a_0}^{a}r\hat{\sigma}_{zz}(r,0)dr, \tag{38}$$

where F denotes the resultant contact load is plotted in Fig. 3 for the respective cases of zero and nonzero damping. In the figure, the action of a rigid annulus is simulated by assuming $|\Lambda|=10^{10}$

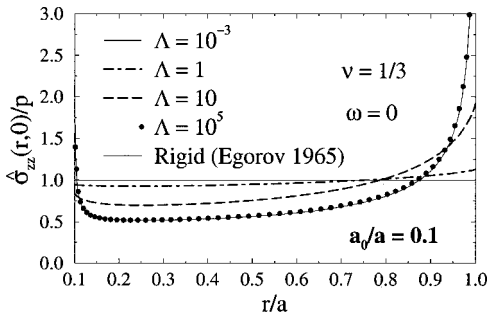

Fig. 2 Static contact stress distribution: effect of padding stiffness

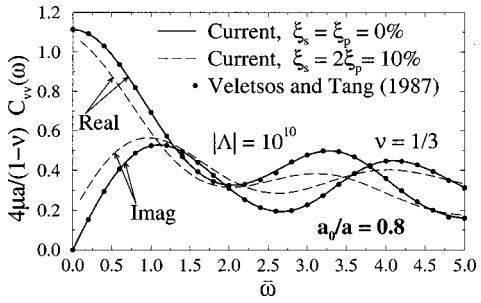

Fig. 3 Vertical dynamic compliance of a rigid annulus

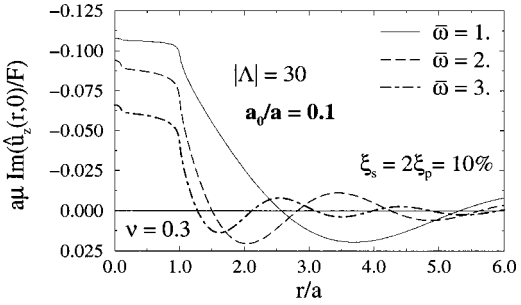

Fig. 7 Out-of-phase components of the surface motion

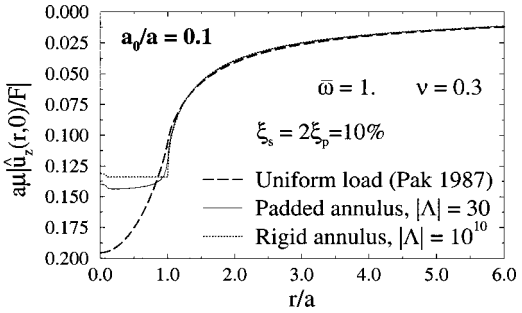

Fig. 4 Center deflection under vibratory annular punch

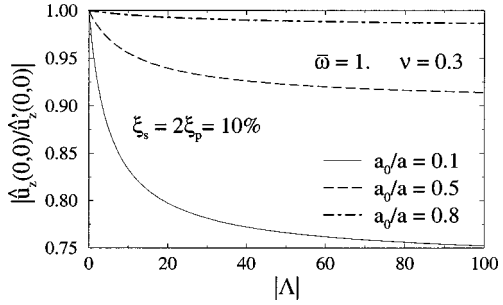

Fig. 5 Surface deflection of a half-space: effect of padding stiffness

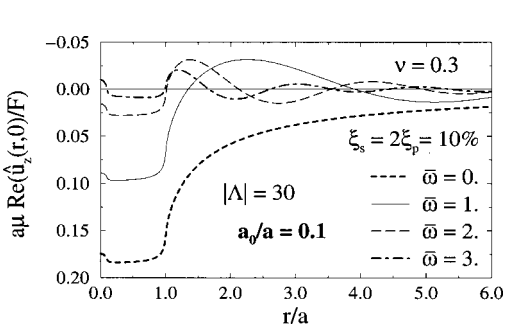

Fig. 6 In-phase components of the surface motion

for the composite model, showing a reasonable agreement with the elastodynamic boundary element solution in Veletsos and Tang [4].

Figure 4 highlights the effects of the padded annulus-half-space interaction on the amplitude of axial surface displacements (30) with $|\Lambda| = 30$ denoting a value commonly encountered in dynamic site characterization. From the display, it is evident that the uniform contact-pressure assumption which is normally employed to interpret the field data may lead to significant errors in the analysis of dynamic center deflections for moderate to high values of Λ. For engineering purposes, the interaction effects are further synthesized in Fig. 5 where the amplitude of the center deflection $\hat{u}_z(0,0)$ at $\bar{\omega} = 1$ as forecast by (30) is normalized by the approximate prediction $\hat{u}'_z(0,0)$ which assumes the *uniform* contact stress distribution

$$\hat{\sigma}'_{zz}(r,0) = \frac{2}{(a^2 - a_0^2)} \int_{a_0}^{a} \tau \hat{\sigma}_{zz}(\tau,0)\, d\tau = \text{const.}, \quad a_0 \leqslant r \leqslant a, \tag{39}$$

between the annulus and the half-space. As expected, an error introduced by the uniform contact-stress assumption amplifies with diminishing ratio a_0/a and increasing Λ. It should also be noted that $\bar{\omega} = 1$ corresponds to a vibration frequency of approximately 100 Hz in a typical field test of an unpaved subgrade. From numerical simulations, it was found that the interaction effects generally become more pronounced with increasing $\bar{\omega}$.

To provide a more complete picture of the dynamic half-space response, Figs. 6 and 7 show the variation of the respective real and imaginary components of the vertical surface displacement $\hat{u}_z(r,0)$ at several frequencies of interest. A direct comparison of the in and out-of-phase profiles at $\bar{\omega} = 1$ with Fig. 4 further reveals that the deflection amplitude profile, notwithstanding its usefulness as a tool for engineering interpretations, does not clearly convey the dynamic nature of the problem.

6 Summary

In this communication, a mathematical model is presented for the axial vibration of a padded annulus on the surface of a homogeneous viscoelastic half-space. By virtue of the Hankel integral transform, the problem is formulated as a set of triple integral equations which are reducible to a Fredholm integral equation of the second kind. In the formulation, the padding is assumed to furnish a one-dimensional load transfer from the rigid annulus to an underlying half-space via a plane stress-type hypothesis. It is shown that the contact stress between the padded annulus and the supporting semi-infinite medium may deviate significantly from the uniform pressure distribution commonly assumed in the interpretation of dynamic field measurements involving buffered annular loading systems. Beyond providing an in-depth understanding of the mechanics of the composite annulus-half-space interaction, the proposed dynamic solution can also be used as an effective approximation to the corresponding rigid-punch problem for

which the analytical solution is currently unavailable. With the aid of Fourier or Laplace transforms, the method can be readily extended to deal with transient problems.

Acknowledgments

The support provided by the National Science Foundation through CAREER Award No. CMS-9875495, the University of Minnesota Supercomputing Institute, and the University of Minnesota-IBM Shared University Research Program during the course of this investigation is gratefully acknowledged.

References

[1] El-Shafee, O. M., and Gould, P. L., 1980, ''Dynamic Axisymmetric Soil Model for a Flexible Ring Footing,'' Earthquake Eng. Struct. Dyn., **8**, pp. 479–498.
[2] Tassoulas, J. L., and Kausel, E., 1984, ''On the Dynamic Stiffness of Circular Ring Footings on an Elastic Stratum,'' Int. J. Num. Analy. Meth. Geomet., **8**, pp. 411–426.
[3] Veletsos, A. S., and Tang, Y., 1987, ''Rocking Vibration of Rigid Ring Foundations,'' J. Geotech. Eng., **113**, pp. 1019–1032.
[4] Veletsos, A. S., and Tang, Y., 1987, ''Vertical Vibration of Ring Foundations,'' Earthquake Eng. Struct. Dyn., **15**, pp. 1–21.
[5] Rajapakse, R. K. N. D., 1989, ''Dynamic Response of Elastic Plates on Viscoelastic Half-Space,'' ASCE Journal of Engineering Mechanics, **115**, pp. 1867–1881.
[6] Noble, B., 1963, ''The Solution of Bessel Function Dual Integral Equations by a Multiplying-Factor Method,'' Proc. Cambridge Philos. Soc., **59**, pp. 351–362.
[7] Bycroft, G. N., 1956, ''Forced Vibrations of a Rigid Circular Footing on a Semi-Infinite Elastic Space and on an Elastic Stratum,'' Philos. Trans. R. Soc. London, Ser. A, **A248**, pp. 327–368.
[8] Awojobi, A. O., and Grootenhius, P., 1965, ''Vibration of Rigid Bodies on Semi-Infinite Elastic Media,'' Proc. R. Soc. London, Ser. A, **A287**, pp. 27–63.
[9] Luco, J. E., and Westmann, R. A., 1971, ''Dynamic Response of Circular Footings,'' ASCE Journal of the Soil Mechanics and Foundation Division, **97**, pp. 1381–1395.
[10] Veletsos, A. S., and Wei, Y. T., 1971, ''Lateral and Rocking Vibration of Footings,'' ASCE Journal of the Soil Mechanics and Foundation Division, **97**, pp. 1227–1248.
[11] Smith, R. E., and Lytton, R. L., 1984, ''Synthesis Study of Nondestructive Testing Devices for use in Overlay Thickness Design of Flexible Pavement,'' Technical Report RD-83/097, Federal Highway Administration, Washington, DC.
[12] Siekmeier, J. A., Young, D., and Beberg, D., 2000, ''Comparison of the Dynamic Cone Penetrometer With Other Tests During Subgrade and Granular Base Characterization in Minnesota,'' ASTM Special Technical Publication, Vol. 1375, pp. 175–188.
[13] Uzan, J., Lytton, R. L., and Germann, F. P., 1989, ''General Procedure for Backcalculating Layer Moduli,'' ASTM Special Technical Publication, Vol. 1026, pp. 217–228.
[14] Boddapati, K. M., and Nazarian, S., 1994, ''Effects of Pavement-Falling Weight Deflectometer Interaction on Measured Pavement Response,'' ASTM Special Technical Publication, Vol. 1198, pp. 326–340.
[15] Ewing, W. M., Jardetzky, W. S., and Press, F., 1957, *Elastic Waves in Layered Media*, McGraw-Hill, New York.
[16] Christensen, R. M., 1971, *Theory of Viscoelasticity*, Academic Press, San Diego, CA.
[17] Findley, W. N., Lai, J. S., and Onaran, K., 1989, *Creep and Relaxation of Nonlinear Viscoelastic Materials*, Dover, New York.
[18] Pak, R. Y. S., 1987, ''Asymmetric Wave Propagation in a Half-Space by a Method of Potentials,'' ASME J. Appl. Mech., **54**, pp. 121–126.
[19] Muki, R., 1961, ''Asymmetric Problems of the Theory of Elasticity for a Semi-Infinite Solid and a Thick Plate,'' Vol. 1, *Progress in Solid Mechanics*, North-Holland, Amsterdam.
[20] Abramowitz, M., and Stegun, I. A., 1972, *Handbook of Mathematical Functions*, Dover, New York.
[21] Egorov, K. E., 1965, ''Calculation of Bed for Foundation With Ring Footing,'' *Proceedings, 6th International Conference on Soil Mechanics ands Foundation Engineering*, Vol. 2, pp. 41–45 (excerpted from Poulos, H. G. and Davis, E. H., 1974, *Elastic Solutions for Soil and Rock Mechanics*, John Wiley and Sons, New York).

S. Stramigioli
Associate Professor,
Faculty of Electrical Engineering,
Drebbel Institute,
P.O. Box 217,
NL-7500 AE Enschede, The Netherlands
e-mail: S.Stramigioli@ieee.org

Nonintrinsicity of References in Rigid-Body Motions

This paper shows that in the use of Lie groups for the study of the relative motion of rigid bodies some assumptions are not explicitly stated. A commutation diagram is shown which points out the "reference problem" and its simplification to the usual Lie group approach under certain conditions which are made explicit. [DOI: 10.1115/1.1409937]

1 Introduction

There are two main ways to describe rigid bodies motions: screw theory based on the original work of Ball [1] and then used by Lipkin [2–4] and Lie groups theory ([5,6]), which is used for kinematics in [7]. These two have been recently formally related in [8]. The reader is also addressed to the excellent book ([9]) where among others, screw systems are related to Lie subalgebras.

In the Lie group approach, the basic starting point is the isometry group $SE(3)$ of the Euclidean three-dimensional space which can be used to describe motions. Here, with $SE(3)$ it is NOT meant the set of homogeneous matrices which are commonly used in robotics, but the abstract Lie group of positive isometries of an Euclidean space.

In this setting, twists are seen as elements of the Lie algebra $se(3)$ which correspond to the Lie group $SE(3)$. Wrenches are instead defined as elements of the dual of $SE(3)$ which is indicated as $se^*(3)$. Unfortunately, in this approach, the position of a rigid body is identified by an element of $SE(3)$ after a reference position for the body has been chosen the choice of which is NOT intrinsic. Furthermore, almost everywhere, a framework with coordinates is used where usually the notation $SE(3)$ is NOT used for the abstract Lie group of positive isometries of the three dimensional space, but instead for the set of Lie group of homogeneous matrices of the form

$$\begin{pmatrix} R & p \\ 0 & 1 \end{pmatrix}$$

where R is an orthonormal matrix representing a rotation and p a translation vector, from the very start. This happens also in the excellent book of Murray et al. [7] and hides simple but important hypotheses which are clear in a coordinate free framework instead.

Only in [10,11] is the importance and necessity of a NOT intrinsic reference presented.

In this article we try to make all the assumptions explicit in order to built a clear and formally correct framework. After a coordinate-free treatment, coordinates will be added and explicit assumptions will be made. This article is of a fundamental nature and therefore suited for a mathematical-oriented reader.

For more general treatments on kinematic issues, the reader is addressed to [12] and [9]. For a very nice treatment and classification using Lie groups of motions, the reader is addressed to [13].

In Section 2 the basic definitions are reported. In Section 3 the definition of twists is reported and a commutation diagram is shown which explains the basic contribution of this paper. In Section 4 the hypothesis which bring to the standard Lie groups are announced.

2 Euclidean Systems and Configurations

The concept of an observer is very important and is coupled to the concept of space: an observer is identified with a Euclidean space in which he is rigidly connected together with all those objects which are always stationary in relation to him. A set of objects which are never changing position in relation to one another can be considered as a single entity from a kinematic point of view.

For these reasons and for more formal ones that should become clear in the sequel, we consider as many Euclidean spaces as there are bodies moving relative to one another. An object will be a subset of a Euclidean space together with a mass density function which associates a value to each of the body's points. The mass density function is relevant for dynamic considerations. For kinematic considerations, it is sufficient to define a proper body B_i as a subset of a Euclidean space $\mathcal{E}_i$ instead.

Once we have defined the geometry of bodies and spaces, we can introduce time as an absolute[1] scalar variable.

We can start by giving a formal definition of an Euclidean space:

DEFINITION 1. (Euclidean Space) *An n-dimensional Euclidean Space $\mathcal{E}_i$ is a triple (M_i, g_i, Ω_i) where (M_i, g_i) is an n-dimensional manifold with Riemannian metric g_i which is isometric to $\mathbb{R}^n$ with Riemannian metric $\langle,\rangle$, whose matrix in standard coordinates $(x_1, \ldots, x_n)$ is $\delta_{i,j}$. In other words there is a diffeomorphism $\varphi: M_i \to \mathbb{R}^n$ such that $\varphi^*\langle,\rangle = g_i$. Ω_i is a nonzero volume n-form on M_i and ω is $dx_1 \wedge \ldots \wedge dx_n$. It is also assumed that φ is orientation preserving, that is, $\varphi^*\omega = \Omega_i$.*

We can now define what we will call a Euclidean system.

DEFINITION 2. (Euclidean System) *The ordered set of m, n-dimensional Euclidean oriented manifolds*:

$$S^m(n) := \{\mathcal{E}_1, \mathcal{E}_2, \ldots, \mathcal{E}_m\}$$

is called a Euclidean system of dimension n and order m. We use the Euclidean system as the basic structure to consider relative motions. All the material which will be treated will be general and applicable to n dimensions. Clearly in three-dimensional mechanics, we will have $n=3$. The number m corresponds to the number of objects and/or observers we consider in our study of motion.

To understand the concepts intuitively, we consider the two-dimensional Euclidean system $S^3(2)$ of Fig. 1. We use a two-dimensional example for simplicity and to illustrate some concepts which will be introduced later. We can consider each of the Euclidean spaces as sheets of paper of infinite extension which

Contributed by the Applied Mechanics Division of THE AMERICAN SOCIETY OF MECHANICAL ENGINEERSfor publication in the ASME JOURNAL OF APPLIED MECHANICS. Manuscript received by the ASME Applied Mechanics Division, May 19, 2000; final revision, Apr. 25, 2001. Editor: R. C. Benson. Discussion on the paper should be addressed to the Editor, Professor Lewis T. Wheeler, Department of Mechanical Engineering, University of Houston, Houston, TX 77204-4792, and will be accepted until four months after final publication of the paper itself in the ASME JOURNAL OF APPLIED MECHANICS.

[1]The fact that we will consider time as an absolute is a consequence of the classical separation in mechanics of space and time, which is due to the Galilean hypothesis.

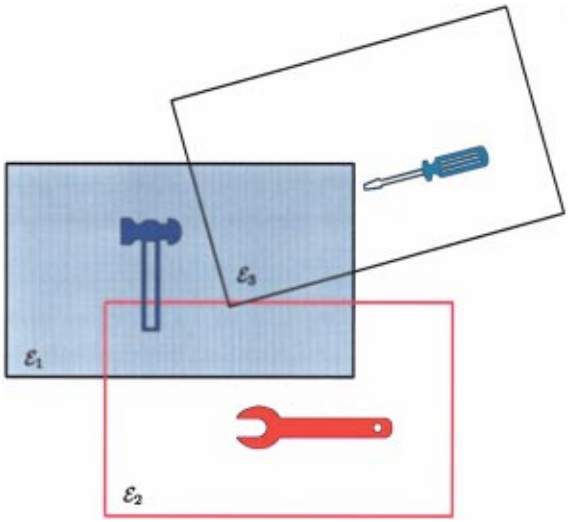

Fig. 1 An example of a two-dimensional Euclidean system

can be placed on one another. In the figures, the sheets are drawn as finite rectangles for the sake of clarity, but should be thought of as having an infinite extension.

The following definition is necessary to understand relative positions:

DEFINITION 3. (Positive Isometry) *A positive (or orientation preserving) isometry* $h_i^j:\mathcal{E}_i\rightarrow\mathcal{E}_j$ *is a diffeomorphism such that* $(h_i^j)^* g_j = g_i$ *and* $(h_i^j)^*\Omega_j = \Omega_i$. *The set of all such isometries is indicated with* $SE_i^j(n)$ *when* $i\neq j$ *and* $SE_i(n)$ *when* $i=j$.

Two considerations are now important.

First of all, the set $SE_i(n)$ corresponds to the set of positive isometries of a Euclidean space which is usually indicated as $SE(n)$. The extra index is used to discriminate between positive isometries of different Euclidean spaces. It can be found on any book on Lie groups like ([6]) that $SE_i(n)$ is indeed a Lie group. We will indicate with $se_i(n) := T_{e_i}SE_i(n)$ the Lie algebra corresponding to the Lie group $SE_i(n)$.

Second, it is possible to see that $SE_i^j(n)$ is indeed a finite dimensional smooth manifold. This can be seen by taking any orthonormal reference frame Ψ_i fixed in $\mathcal{E}_i$ and any orthonormal frame Ψ_j fixed in $\mathcal{E}_j$. Doing so, it is possible to see that $SE_i^j(n)$ is diffeomorphic to the matrix Lie group of homogeneous matrices and therefore $SE_i^j(n)$ is indeed a manifold.

To improve intuition clarity, we could consider the orientation writing the name of the Euclidean space on each of the sheets (see Fig. 2). It is then possible to see that in Fig. 2, h_1^2 is a positive isometry and this can be seen by shifting the two sheets of paper so that the two hammers coincide, as reported bottom left in the figure. Furthermore, $\tilde{h}_1^2$ is still an isometry but it is not positive since we must first turn over the sheet before all the points of one sheet correspond to those on the other sheet. This is reported bottom right of the figure. The last mapping, $\bar{h}_1^2$, is not even an isometry since it changes distances between points and there is no way to place the two sheets so that the points on one will correspond to the points on the other.

DEFINITION 4. (Relative Position) *An element* $h_i^j\in SE_i^j(n)$ *is called a relative position of* $\mathcal{E}_i$ with respect to $\mathcal{E}_j$.

It is important to reflect a moment on the previous definitions. Observers and/or objects are associated to a Euclidean space to which they are rigidly connected. We can think of all these spaces as interpenetrating. In the example, this ''interpenetration'' can be understood by considering how the sheets overlap. In each instant, all the points of one of the spaces, will have associated points on

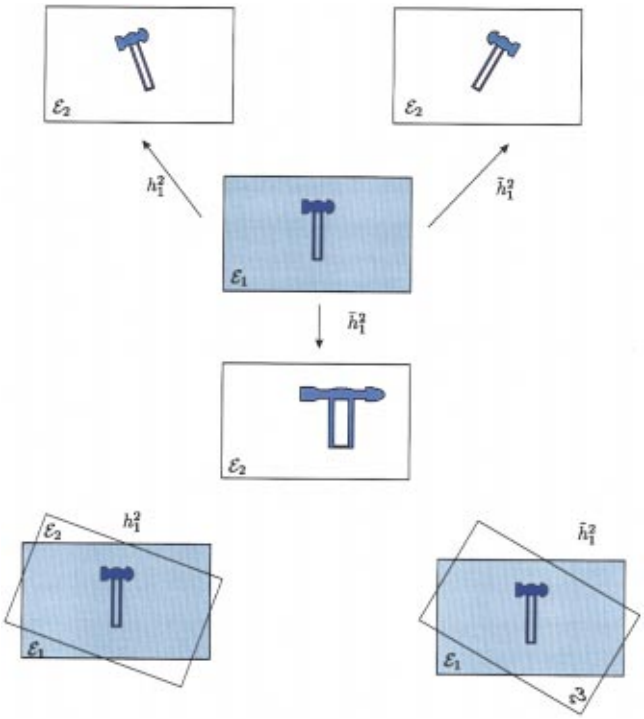

Fig. 2 Maps between Euclidean spaces

each of the other spaces. In the example ''the association'' is the one which assigns to all the points of one sheet the corresponding points underneath on another sheet. This map is represented by a positively oriented isometry. It is important at this point to reason without any use of coordinates because it enables us to define entities which are intrinsic. We can now define a *kinematic state*.

DEFINITION 5. (Kinematic State) *We call a kinematic state for a Euclidean system* $S^m(n)$ *a point*:

$$h := (h_2^1, h_3^2, \ldots, h_m^{m-1}) \in SE_2^1(n)\times SE_3^2(n)\times \ldots \times SE_m^{m-1}.$$

Most of the euclidean spaces belonging to $S^m(n)$ will represent physical bodies. These spaces have a subsets of points $B_i\subset\mathcal{E}_i$ where matter is present. This set B_i is called the *matter set* and it corresponds to the Euclidean space $\mathcal{E}_i$.

We say that a Euclidean space in $S^m(n)$ is a *pure observer* iff its matter set is the empty set. In the working example, the set B_1 will be the set of points where the hammer is, B_2 where the screw driver is and B_3 where the spanner is. These are sets in two-dimensional Euclidean spaces. In the examples there are no pure observers which could be thought of as additional sheets with no objects on it. We can now talk about a compatible kinematic state.

DEFINITION 6. (Compatible Kinematic State) *We will say that a kinematic state* h *as defined in Definition 5 is compatible iff* $h_i^j(B_i)\cap B_j = \varnothing \forall i\neq j\ i,\ j=1,\ldots,m$.

The previous definition can be used to describe object impenetrability. This is the simplest and most basic constraint which has to be satisfied at this stage: Rigid objects will not penetrate one another.[2]

The idea of compatibility of state is illustrated in Fig. 3. The relative position of $\mathcal{E}_1$ and $\mathcal{E}_2$ does not create any problem for the kinematic state compatibility, but the relative position of $\mathcal{E}_1$ and $\mathcal{E}_3$ is not compatible since it maps points of an object belonging to one space to points of another object of another space. Remember

[2]In reality, when bodies will contact each other, they will slightly deflect and generate an elastic force which will oppose the compenetration.

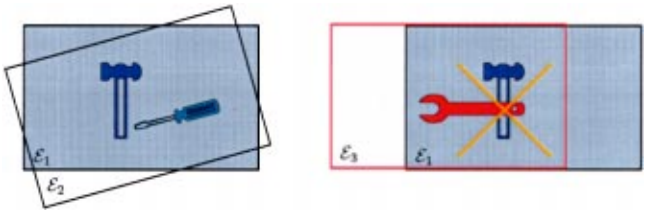

Fig. 3 Compatibility of the kinematic state

that, in the example, the previously considered map, corresponds to the one which maps points of one sheet (Euclidean space) to the points underneath on another sheet.

Here a remark is in place: At first glance the presented framework would seem unnecessarily theoretical and formal. Nevertheless, such an approach is not just fundamentally meaningful, but could be used as the basis for implementing computer tools for the analysis of mechanisms. To be able to describe a mechanism, we need to have formal and exact ways to represent information and the definitions proposed here help to give such a structure.

We can now define the corresponding left, right, and conjugation maps between two spaces. Note that if the spaces are different, these operations are neither endomorphisms nor group operations. This is why we use the adjective ''hybrid'' for the following definitions.

DEFINITION 7. (Hybrid Right and Left Maps) *We call*

$$R_{h_i^j}: SE_j(n) \to SE_i^j(n); h_j \mapsto h_j \ o \ h_i^j$$

the right hybrid map for the pair of spaces $(\mathcal{E}_i, \mathcal{E}_j)$ *at* $h_i^j \in SE_i^j(n)$ *and*

$$L_{h_i^j}: SE_i(n) \to SE_i^j(n); h_i \mapsto h_i^j \ o \ h_i$$

the left hybrid map for the pair of spaces $(\mathcal{E}_i, \mathcal{E}_j)$ *at* $h_i^j \in SE_i^j(n)$.

The ''*o*'' indicates the composition of maps. The left hybrid map can be used to create a bijection between $SE_i^j(n)$ and $SE_i(n)$ and the right hybrid map can be used to create a bijection between $SE_i^j(n)$ and $SE_j(n)$. Remember that $SE_i^j(n)$ represents the space of relative positions of *i* and *j* independent on any relative reference position. Then it is possible to consider how the corresponding representations in $SE_i(n)$ and $SE_j(n)$ are related given a reference relative position h_i^j. This is done using the hybrid conjugation map.

DEFINITION 8. (Hybrid Conjugation Map) *We will call the map* $K_{h_i^j} := R_{h_i^j}^{-1} L_{h_i^j}$, *hybrid conjugation map for the pair of spaces* $(\mathcal{E}_i, \mathcal{E}_j)$ *in* $h_i^j \in SE_i^j(n)$. *This map can be expressed as*

$$K_{h_i^j}: SE_i(n) \to SE_j(n); h_i \mapsto h_i^j \ o \ h_i \ o \ (h_i^j)^{-1}.$$

With respect to the previous definitions of hybrid right, left and conjugation maps, it is important to note that if the domain and range spaces coincide (they are the same Euclidean space), these maps become endomorphisms and correspond to the standard Lie group maps on a special isometry group ([6]).

Remark 1. (Swap Domain-Range) If in the previous definition we would swap the domain space with the range $(i \leftrightarrow j)$, the result is that $r \to r^{-1}$, $h \to h^{-1}$ and the right maps would correspond to the previous left maps and so on. This can be formally stated as follows:

$$(L_h^{-1}(r))^{-1} = (h^{-1} \ o \ r)^{-1} = (r^{-1} \ o \ h) = R_{(h^{-1})}^{-1}(r^{-1})$$

where $r, h \in SE_i^j(n)$ and the previous elements are all belonging to $SE_i(n)$, or dually,

$$(L_{(h^{-1})}^{-1}(r^{-1}))^{-1} = (h \ o \ r^{-1})^{-1} = (r \ o \ h^{-1}) = R_h^{-1}(r)$$

where $r, h \in SE_i^j(n)$ and the previous elements are all belonging to $SE_j(n)$.

This remark has important implications when twists are introduced.

It can be easily verified that $K_{h_i^j}(e_i) = e_j \forall h_i^j \in SE_i^j(n)$, where $e_k \in SE_k(n)$ is the identity element of the group $SE_k(n)$. We can consider the tangent map of $K_{h_i^j}$:

$$(K_{h_i^j})_* : TSE_i(n) \to TSE_j(n); (h_i, v_i) \mapsto \left(h_i^j \ o \ h_i \ o \ (h_i^j)^{-1}, \frac{d}{dt}(h_i^j \ o \ e^{v_i t} h_i \ o \ (h_i^j)^{-1}) \Big|_{t=0} \right) \tag{1}$$

where with $e^{v_i t} h_i$ we used the usual exponential map ([6]) to consider a curve in $SE_i(n)$ parameterized by t and passing through h_i at time $t=0$ with velocity v_i. It is now possible to define the hybrid adjoint.

DEFINITION 9. (Hybrid Adjoint) *We call hybrid adjoint from space* $se_i(n)$ *to space* $se_j(n)$ *the following map*:

$$Ad_{h_i^j}: se_i(n) \to se_j(n); t_i \mapsto \Pi((K_{h_i^j})_*(e_i, t_i))$$

where $\Pi(\cdot)$ *indicates the fiber projection* ([14]), *which in this case corresponds to the tangent space in* e_j, *the identity element of* $SE_j(n)$.

It is important to note that $se_i(n)$ and $se_j(n)$ are NOT the same and that there is no natural identification for these algebras.[3] Furthermore, if the domain and range space of $Ad_{h_i^j}$ coincide, the hybrid adjoint corresponds to the usual adjoint group operation ([6]).

We can associate an element of $SE_i(n)$ or $SE_j(n)$ to a relative position of *i* with respect to *j* corresponding to a $h_i^j \in SE_i^j(n)$ using a reference $r_i^j \in SE_i^j(n)$:

$$h_i = L_{r_i^j}^{-1}(h_i^j) = (r_i^j)^{-1} \ o \ h_i^j \tag{2}$$

$$h_j = R_{r_i^j}^{-1}(h_i^j) = h_i^j \ o \ (r_i^j)^{-1}. \tag{3}$$

Remark 2. Note that the identification of a relative position by an element of $SE_i(n)$ or an element of $SE_j(n)$ is NOT intrinsic and depends on the choice of a reference relative position r_i^j. This is often not stated in the literature, even though the use of Lie group theory for rigid body motions description depends on it!

[3]The vector spaces $se_i(n)$ and $se_j(n)$ are algebras since they have a commutator operator derived from the Lie Bracket of vector fields on $SE_i(n)$ and $SE_j(n)$. For details see [5].

3 Twists

So far we have considered relative positions without introducing motion. The latter is clearly a change of relative position. To be able to talk about change, we need to consider a time set I which will be an open interval of $\mathbb{R}$. We can then consider curves in $SE_i^j(n)$ parameterized by $t \in I$.

DEFINITION 10. (Relative Motion) *We call a differentiable function of the following form*[4]

$$h_i^j : I \to SE_i^j(n)$$

a relative motion of space $\mathcal{E}_i$ with respect to $\mathcal{E}_j$ where I is a close interval of $\mathbb{R}$.

Since relative motions are differentiable, we can consider the velocity vector of the curve at h_i^j which we indicate as

$$\dot{h}_i^j \in T_{h_i^j} SE_i^j(n).$$

The element $\dot{h}_i^j$ which is also indicated as v_i^j is called relative velocity in h_i^j.

Considering Eq. (2) (respectively Eq. (3)) we can map these relative motion velocities to elements of the tangent bundle $TSE_i(n)$ (respectively, $TSE_j(n)$):

$$(L_{r_i^j}^{-1})_* : TSE_i^j(n) \to TSE_i(n) : (h_i^j, v_i^j) \mapsto \left(L_{r_i^j}^{-1}(h_i^j), \frac{d}{dt}((L_{r_i^j}^{-1}(e^{v_i^j t} h_i^j)))\Big|_{t=0} \right) \tag{4}$$

where with $t \mapsto e^{v_i^j t} h_i^j$ we indicate any curve in $SE_i^j(n)$ passing through h_i^j at time $t=0$ with velocity v_i^j. An analogous map can be used to map to $TSE_j(n)$ using the hybrid right translation.

Remark 3. (Inverse Mapping) It is important to realize that each $h_i^j : I \to SE_i^j(n)$ is bijective to a $h_j^i : I \to SE_j^i(n)$; $t \mapsto (h_i^j(t))^{-1}$. This implies also that to each $\dot{h}_i^j \in T_{h_i^j} SE_i^j(n)$ an element $\dot{h}_j^i \in T_{h_j^i} SE_j^i(n)$ will uniquely correspond. This means that whenever we will talk about vector fields or distributions on $SE_i^j(n)$, we will uniquely also have corresponding vector fields or distributions defined on $SE_j^i(n)$.

So far, we have shown a way to map relative velocities to elements of $TSE_i(n)$ or $TSE_j(n)$. Both of these maps are not intrinsic since they depend on a choice of a reference relative position r_i^j. These elements belong to tangent bundles of Lie groups and therefore it is meaningful to transport these tangent vectors to the group identities by means of either left or right translations ([6]).

3.1 Transports to the Identity of the Domain Lie Group.

Consider the element $(L_{r_i^j}^{-1})_*(h_i^j, v_i^j)$ which is the representative in $TSE_i(n)$ of the relative motion of $\mathcal{E}_i$ with respect to $\mathcal{E}_j$ in the relative position h_i^j with a relative velocity v_i^j. We can transport this tangent vector to e_i, the identity element of $SE_i(n)$ either by left or right translation. An important result is the following:

THEOREM 1. *The left translation to the identity of the left hybrid translated tangent vector representative of a relative motion, is defined intrinsically and independent of any choice of a fixed reference r_i^j.*

Proof. Consider an element $(h_i^j, v_i^j) \in T_* SE_i^j(n)$. Consider a relative motion

$$\tilde{h}_i^j : [-a, a] \to SE_i^j(n)$$

with $a > 0$ and such that $\tilde{h}_i^j(0) = h_i^j$ and $(d/dt)(\tilde{h}_i^j(t))|_{t=0} = v_i^j$. Defining

$$(h_i, v_i) := (L_{r_i^j}^{-1})_*(h_i^j, v_i^j)$$

it is possible to see that $h_i = \tilde{h}_i(0)$ and $v_i = (d/dt)(\tilde{h}_i(t))|_{t=0}$ where $\tilde{h}_i(t) = L_{r_i^j}^{-1}(\tilde{h}_i^j(t))$.

To calculate the left translation at the identity of (h_i, v_i), we have, therefore

$$t_i^{i,j} := \Pi((L_{h_i^{-1}})_*(h_i, v_i)) = \ldots = \frac{d}{dt}((\tilde{h}_j^i(0) \;\; o \;\; \tilde{h}_i^j(t))|_{t=0}. \tag{5}$$

□

It is possible to see that the last expression is independent of r_i^j and therefore defined intrinsically. We will call the last quantity $t_i^{i,j} \in se_i(n)$ the intrinsic twist of the motion of $\mathcal{E}_i$ with respect to $\mathcal{E}_j$ expressed in the space $se_i(n)$.

Note the notation: in $t_i^{i,j}$ the subscript and the second superscript indicate the relative motion, which in this case is i with respect to j. The first superscript indicates in which algebra this motion is expressed, which in this case is $se_i(n)$. The reader could be tempted to say that $t_i^{i,j}$ is the twist that an observer sitting in $\mathcal{E}_i$ would observe. This is NOT the case as can be seen in the commutation diagram of Fig. 4: An observer sitting in $\mathcal{E}_i$ and looking to a point p_j fixed in $\mathcal{E}_j$, would observe exactly the opposite motion to the one described. To understand this consider that the observer $\mathcal{E}_i$ for whom the time increases would see a motion corresponding to a mapping from $p_i(0)$ to $p_i(t)$ with $t > 0$ which has a direction opposite to the one reported in Fig. 4 and corresponds to $(h_j^i(0) o \tilde{h}_i^j(t))$.

If instead of left translating to the identity we right translate, we do NOT get a quantity that is intrinsically defined. This is formally stated below:

THEOREM 2. *The right translation to the identity of the left hybrid translated tangent vector representative of a relative motion is NOT intrinsically defined and is equal to*

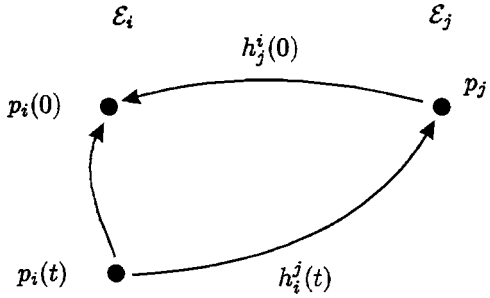

Fig. 4 Commutation diagram of the intrinsic left translations

[4]Note the abuse of notation here: h_i^j has been used both as an element of $SE_i^j(n)$ and as a function from I to $SE_i^j(n)$.

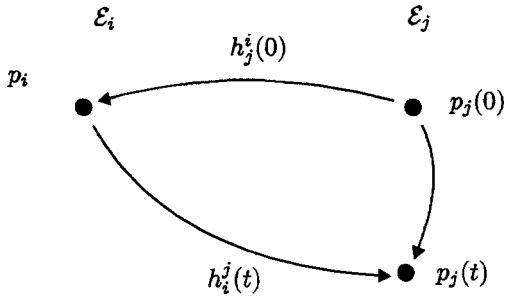

Fig. 5 Commutation diagram of the intrinsic right translations

$$\overline{t_i^{i,j}} = Ad_{r_j^i} t_i^{j,j}$$

where

$$t_i^{j,j} := \frac{d}{dt}((\tilde{h}_i^j(t) o \tilde{h}_j^i(0)))\bigg|_{t=0}. \tag{6}$$

We will indicate with the simplified notation $t_i^j = t_i^{j,j}$ when the two superscripts coincide.

Proof. With similar definitions as in the previous theorem, we show that

$$\overline{t_i^{i,j}} := \Pi((R_{h_i^{-1}})_*(h_i, v_i)) = \ldots$$

$$= \frac{d}{dt}((r_j^i o \tilde{h}_i^j(t) o \tilde{h}_j^i(0) o r_i^j))\bigg|_{t=0} = Ad_{r_i^j} t_i^j. \tag{7}$$

□

3.2 Transports to the Identity of the Range Lie Group. Like we did in the previous subsection, we can first use the hybrid right translation to map relative motions to $SE_j(n)$, and then Lie group right of left translations within $SE_j(n)$ to map to the identity. The following two theorems then correspond to the previous ones.

THEOREM 3. *The right translation to the identity of the right hybrid translated tangent vector representative of a relative motion, is defined intrinsically, independent of any choice of reference r_i^j and equal to t_i^j as defined in Eq. (6).*

Proof. See proof of Theorem 1. □

Observing the commutation diagram of Fig. 5, we can see that the twist t_i^j is indeed the twist that an observer sitting in $\mathcal{E}_j$ would observe. The diagram shows that a fixed point $p_i \in \mathcal{E}_i$ is indeed mapped from a point $p_j(0) \in \mathcal{E}_j$ to future points $p_i(t)$. This means that the right translation is somehow more representative. On the other hand, as a consequence of what was said in Remark 1, we could consider the isometries going from j to i corresponding to the inverse of what was done so far. This would result to a right translation which would give the intrinsic twist t_j^i. This will be discussed in detail later.

If instead of right translating to the identity we left translate, we do NOT get an intrinsically defined quantity. This is formally stated in what follows:

THEOREM 4. *The left translation to the identity of the right hybrid translated tangent vector representative of a relative motion is NOT defined intrinsically and is equal to*

$$\overline{t_i^j} = Ad_{r_i^j} t_i^{i,j}.$$

Proof. See proof of Theorem 2. □

In a similar way, it is also possible to find an intrinsic mapping which maps intrinsic twists of one space to the other. This is formally stated in the following theorem which can be proven along the same lines as the previous ones.

THEOREM 5. (Map Between Intrinsic Twists) *For any relative position h_i^j, a bijection exists between the intrinsic twists in $se_i(n)$ and the ones in $se_j(n)$. This map is given by*

$$t_i^j = Ad_{h_i^j} t_i^{i,j}.$$

$Ad_{h_i^j}$ is to the hybrid adjoint of Definition 9.

The thick cross-hatched lines show the intrinsic maps to and between the Lie algebras of the Lie groups of the motions of the two spaces under consideration. Only those twists are intrinsic and independent of the reference r_i^j which are obtained by following the maps to the circled se_i and se_j.

Furthermore, it has been shown that the standard adjoint maps within the Lie algebras of the two spaces are not maps between intrinsically defined quantities. This means that in a coordinate free framework, it is not correct to say that the adjoint group operation maps twists from one reference to the other since one of the two elements is not intrinsic and dependent on the reference r_i^j. We denoted these nonintrinsic elements with $\overline{t_i^j}$ and $\overline{t_i^{i,j}}$.

3.3 Relations Between Twists. It is possible to see that the complete right translation is somehow more representative than the left one since it gives the motion of $\mathcal{E}_i$ that an observer sitting in $\mathcal{E}_j$ would observe directly. From the considerations of Fig. 4 and Fig. 5, it should be clear that

$$t_i^j = \frac{d}{dt}((\tilde{h}_i^j(t) o \tilde{h}_j^i(0)))\bigg|_{t=0}$$

represents the motion of $\mathcal{E}_i$ for an observer sitting in $\mathcal{E}_j$. In exactly the same way, namely by inverting the domain and range space as explained in Remark 1, we could arrive at the definition of

$$t_j^i = \frac{d}{dt}((\tilde{h}_j^i(t) o \tilde{h}_i^j(0)))\bigg|_{t=0}$$

which would correspond again to the right translation to the identity of the right hybrid translated tangent vector of a motion, but now in the opposite direction: for the isometries from $\mathcal{E}_j$ to $\mathcal{E}_i$.

A representation of the two intrinsic right translated twists t_i^j and t_j^i is shown in Fig. 6. It is possible to see that the direction of t_1^2 is opposite to that one of t_2^1. This relation can be formally stated in the following theorem.

THEOREM 6. (Twist Relations) *With the notation used previously, the following identities hold*:

$$-t_j^{j,i} = t_i^j = Ad_{h_i^j} t_i^{i,j} = -Ad_{h_j^i} t_j^i \tag{8}$$

and

$$t_j^i = -t_i^{i,j} = -Ad_{h_j^i} t_i^j = Ad_{h_j^i} t_j^{j,i}. \tag{9}$$

Instead of giving a formal proof of the previous theorem, Fig. 7, Fig. 8, Fig. 9, and Fig. 10 can be used to understand the result. Figures 7 and 8 represent the right translated relative motion in the two directions and the bottom ones are the left translated. Figures 7 and 9 correspond to the intrinsic maps $\pi_{h_i^j}^j$ which is also denoted with $\pi_{h_i^j}$ (Fig. 7) and $\pi_{h_i^j}^i$ (Fig. 9) of Fig. 11 and Figs. 8 and 10 correspond to the intrinsic maps $\pi_{h_j^i}^i$ (Fig. 8) and $\pi_{h_j^i}^j$ (Fig. 10) of a diagram similar to Fig. 11, but now the considered isometries would belong to $SE_j^i(n)$ instead of $SE_i^j(n)$.

4 The Simplification to Lie Groups

In Section 3, we have worked in a coordinate-free manner. If we introduce coordinates, we can identify certain operations using a matrix algebra. We will see that an intelligent choice of the

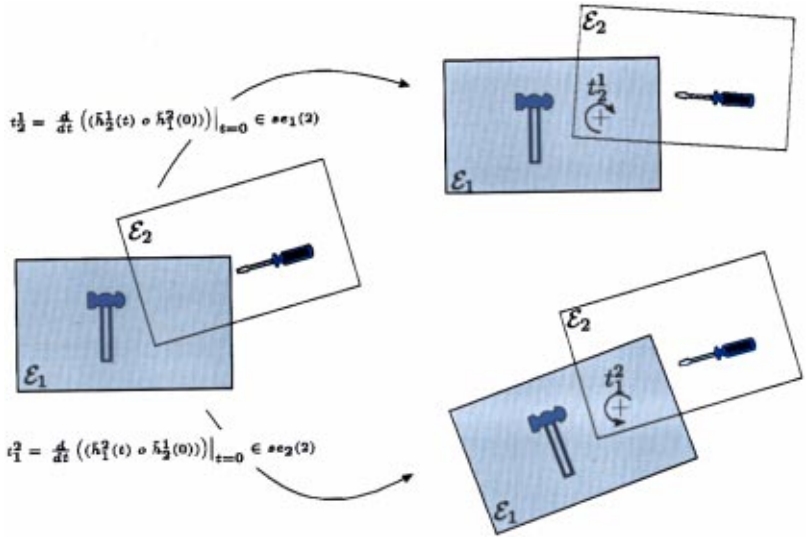

Fig. 6 Intrinsic twist maps

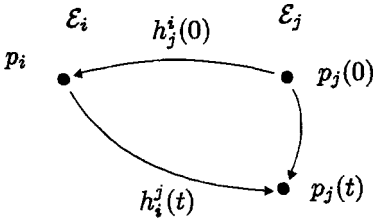

Fig. 7 $t_i^j = \frac{d}{dt}(h_i^j(t) \circ h_j^i(0))|_0$

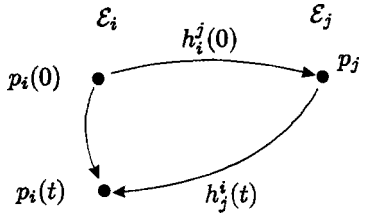

Fig. 8 $t_j^i = \frac{d}{dt}(h_j^i(t) \circ h_i^j(0))|_0$

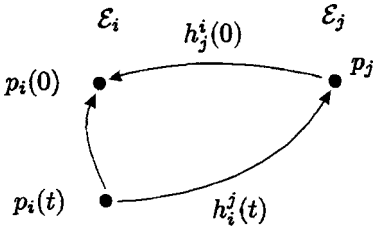

Fig. 9 $t_i^{i,j} = \frac{d}{dt}(h_j^i(0) \circ h_i^j(t))|_0$

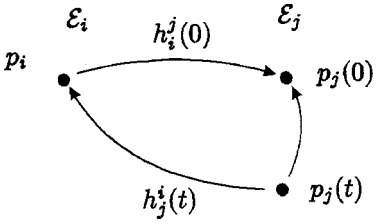

Fig. 10 $t_j^{j,i} = \frac{d}{dt}(h_i^j(0) \circ h_j^i(t))|_0$

reference r_i^j dependent on the choice of the coordinates, will yield standard Lie group operations of the matrix group $SE(n)$ as presented in [7].

First of all we need to define what we mean with "Cartesian coordinates" for a Euclidean space.

DEFINITION 11. (Cartesian Coordinates) *An isometry of the following form*:

$$\Psi_i : \mathcal{E}_i(n) \rightarrow \mathbb{R}^n$$

is called Cartesian coordinates or simply coordinates for a Euclidean space $\mathcal{E}_i(n)$, *where we consider the canonical metric in* $\mathbb{R}^n$ *represented by the identity matrix. We will call this Cartesian coordinate right handed or positive oriented iff* $\exists \lambda \in C^\infty(\mathcal{E}_i)$ *s.t.* $\lambda(\cdot) > 0$ *and* $\lambda \Omega_i = (\Psi_i)^*(dx_1 \wedge dx_2 \wedge \ldots \wedge dx_n)$, *where with* $(\Psi_i)^*$ *we indicated the pullback operator,* Ω_i *is the n-form orienting* $\mathcal{E}_i$ *and* $(dx_1 \wedge dx_2 \wedge \ldots \wedge dx_n)$ *is the canonical n-form in* $\mathbb{R}^n$.

It is possible to show that there exists a bijection between the set of right handed Cartesian coordinates and the set of $(n+1)$-tupels of the form $(p, e_1, e_2, \ldots, e_n)$ where $p \in \mathcal{E}_i, e_k \in T_p\mathcal{E}_i$ and such that $g_p(e_i, e_j) = \delta_i^j \forall i, j = 1, \ldots, n$ where δ_i^j is the Kronecker symbol and g_p is the metric of the Euclidean space in the point p. The vectors $e_1, \ldots, e_n$ attached to p would be the usual base frame which can be used to express vectors.

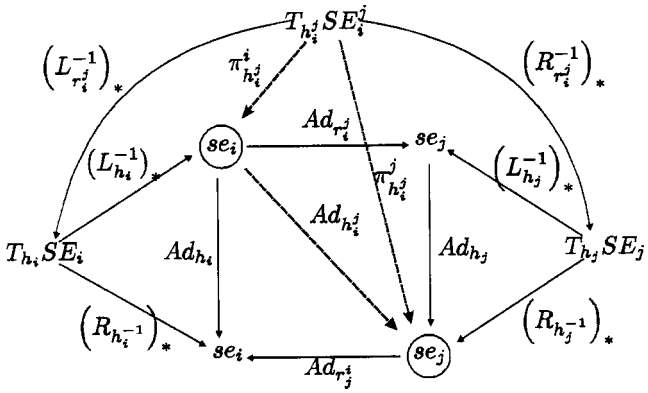

Fig. 11 The complete commutation diagram

4.1 Isometries in $\mathbb{R}^n$. The positively oriented motions in $\mathbb{R}^n$ will be essential to what follows. It is well known that this set is homeomorphic to the special isometries matrix group $SE(n)$ which is defined in the following way:

$$SE(n) := \left\{ \begin{pmatrix} R & p \\ 0 & 1 \end{pmatrix} \; s.t. \;\; R \in SO(n), p \in \mathbb{R}^n \right\} \tag{10}$$

where with $SO(n)$ we indicate the special orthonormal group of orthonormal matrices defined as

$$SO(n) := \{ R \in \mathbb{R}^{n \times n} \; s.t. \;\; \det(R) = 1, R^{-1} = R^T \}. \tag{11}$$

We see that the operation $y = h(x)$ for a positive isometry h from $\mathbb{R}^n$ to itself corresponds to a matrix multiplication of the form:

$$\begin{pmatrix} y \\ 1 \end{pmatrix} = \begin{pmatrix} R & p \\ 0 & 1 \end{pmatrix} \begin{pmatrix} x \\ 1 \end{pmatrix}$$

where the matrix belongs to $SE(n)$. This representation of points of $\mathbb{R}^n$ by means of vectors of $\mathbb{R}^{n+1}$ is the concept on which projective geometry ([15]) is based. In this framework, elements of $SE(n)$ can be seen as projective transformations which are also called homographies or collineations. These are all concepts often used in screw theory ([8]).

4.2 Representation of Relative Positions With Coordinates. Suppose we associate with each $\mathcal{E}_i \in S^m(n)$ a right-handed coordinate frame Ψ_i. We can, therefore, assign an element of $H_i^j \in SE(n)$ to each element $h_i^j \in SE_i^j(n)$ which corresponds to the following isometry of $\mathbb{R}^n$:

$$H_i^j = \Psi_j \; o \; h_i^j \; o \; \Psi_i^{-1}. \tag{12}$$

The element H_i^j is an element of $SE(n)$ because it is defined as a composition of positively oriented isometries and it is therefore a positively oriented isometry of $\mathbb{R}^n$. Note that H_i^j is actually a $(n+1) \times (n+1)$ matrix which can therefore be used as a linear mapping from $(n+1)$-tuples to $(n+1)$-tuples. From now on we will consider all these $(n+1)$-tuple as having the last component that is equal to 1. With the previous abuse of notation it is then possible to consider H_i^j as a mapping from $\mathbb{R}^n$ to $\mathbb{R}^n$.

4.3 Coordinates to Represent Twists. When looking at the expressions for t_i^j, t_j^i, $t_i^{i,j}$, and $t_j^{j,i}$, we can see straightaway that, by applying Eq. (12), their matrix representation becomes

$$T_i^j = \dot{H}_i^j H_j^i \;\; T_j^i = \dot{H}_j^i H_i^j \;\; T_i^{i,j} = H_j^i \dot{H}_i^j \;\; T_j^{j,i} = H_i^j \dot{H}_j^i. \tag{13}$$

What will be the form of these matrices? This question can be easily answered when using the following well-known results.

THEOREM 7. (Derivatives of Orthonormal Matrices) *Given an orthonormal matrix $R \in SO(n)$ that is a smooth function of time, the matrices $\dot{R}R^{-1}$ and $R^{-1}\dot{R}$ are given by antisymmetric matrices of dimension $\mathbb{R}^{n \times n}$.*

Proof. The proof follows straightaway when differentiating RR^{-1} and $R^{-1}R$. □

It is now possible to extend the result to elements of $SE(n)$.

THEOREM 8. (Derivatives of Isometries) *Given a matrix $H \in SE(n)$ that is a smooth function of time, the matrices $\dot{H}H^{-1}$ and $H^{-1}\dot{H}$ are given by matrices of the following form*:

$$\begin{pmatrix} \Omega & v \\ 0 & 0 \end{pmatrix} \tag{14}$$

where $\Omega \in \mathbb{R}^{n \times n}$ is antisymmetric[5] *and $v \in \mathbb{R}^n$.*

[5]Note that $\Omega \in SO(3)$.

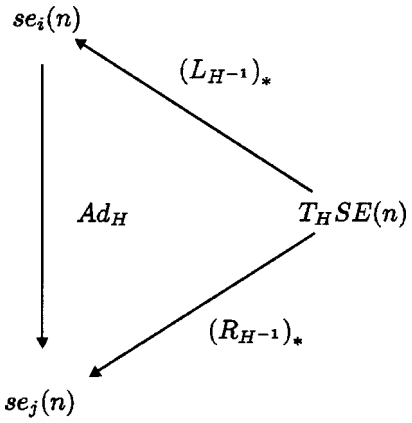

Fig. 12 The Lie group commutation diagram

Proof. The proof follows in a straightforward manner when $\dot{H}H^{-1}$ and $H^{-1}\dot{H}$ are written out as matrices of the form in Eq. (10) and the previous theorem is used. □

Since the dimension of the vector space of antisymmetric matrices belonging to $\mathbb{R}^{n \times n}$ is $n(n-1)/2$ for the three-dimensional case, we can associate a three-dimensional vector ω to the matrix Ω in Eq. (14) such that $\omega \wedge x = \Omega x \; \forall x \in \mathbb{R}^3$. The six-dimensional vector (ω, v) can therefore be considered to be the numerical representation of the intrinsic twist for the chosen coordinates Ψ_i and Ψ_j. These are closely related to the *Plücker coordinates* in screw theory ([3, 8]).

4.4 The Link With Standard Lie Groups. It is now possible to link the presented material to the standard Lie group approach.

THEOREM 9. *If we choose as reference $r_i^j = \Psi_j^{-1} \, o \, \Psi_i$, with the coordinate functions $\Psi_k \; k = 1,...,n$ then, $Ad_{r_i^j}$, $Ad_{r_j^i}$ will be represented by the identity, and all the maps on the right side of the diagram in Fig. 11 will have the same representations as the symmetrically corresponding maps on the left.*

Proof. Can be shown by using a representation with coordinates.□

Note that the choice of $r_i^j = \Psi_j^{-1} \, o \, \Psi_i$ has a very straightforward explanation: We consider as a reference relative position that position in which the coordinate frames $(p, e_1, \ldots, e_n)$, which are the n vectors $e_1, \ldots, e_n$ attached to p and represent the Cartesian coordinates Ψ_i and Ψ_j, coincide. This choice is useful for practice but NOT intrinsic and depends on the choice of coordinate frames for an initial relative position.

By using coordinates, we achieve that the commutation diagram of Fig. 11 ''folds'' its right and left parts on one another to give the standard Lie group commutation diagram reported in Fig. 12 where $H = \Psi_j o \, h_j \, o \, \Psi_j^{-1} = \Psi_i o \, h_i \, o \, \Psi_i^{-1} = \Psi_i o \, h_i^j \, o \, \Psi_j^{-1}$.

5 Conclusions

This article has shown that behind the use of Lie groups for rigid-body motions, there are implicit assumptions that, even if more or less ''natural,'' are not intrinsic and just dependent on a choice of relative reference between spaces (see Remark 2).

It is always important to pinpoint those assumptions which are not intrinsic: Any hypothesis which is not intrinsic can in fact be considered a modeling hypothesis and should be made explicit as such.

Twists have been analyzed in detail and their mappings and relations have been shown. The intrinsic mappings using right translations are the ones which give the motion of a space with respect to an observer space directly and have been denoted with only one subscript and one superscript: t_i^j or t_j^i.

Acknowledgments

The author wants to acknowledge the interesting discussions with Prof. Ernest Fasse of the University of Arizona which have started the interest for this research and the useful comments and remarks of anonymous reviewers.

References

[1] Ball, R. S., 1900, *A Treatise on the Theory of Screws*, Cambridge University Press, Cambridge, UK.
[2] Lipkin, H., 1985, ''Geometry and Mappings of Screws With Applications to the Hybrid Control of Robotic Manipulators,'' Ph.D. thesis, University of Florida.
[3] Lipkin, H., and Duffy, J., 1985, ''The Elliptic Polarity of Screws,'' ASME J. Mech., Transm., Autom. Des., **107**, pp. 377–387.
[4] Lipkin, H., and Duffy, J., 1988, ''Hybrid Twist and Wrench Control for a Robotic Manipulator,'' ASME J. Mech. Des., **110**, pp. 138–144.
[5] Olver, P. J., 1993, *Applications of Lie Groups to Differential Equations*, Vol. 107 (Graduate Texts in Mathematics) 2nd Ed., Springer-Verlag, New York.
[6] Gilmore, R., 1974, *Lie Groups, Lie Algebras, and Some of Their Applications*, John Wiley and Sons, New York.
[7] Murray, R. M., Li, Z., and Shankar Sastry, S., 1994, *A Mathematical Introduction to Robotic Manipulation*, CRC Press, Boca Raton, FL.
[8] Stramigioli, S., Maschke, B., and Bidard, C. 2000, ''Hamiltonian Formulation of the Dynamics of Spatial Mechanisms Using Lie Groups and Screw Theory,'' *Proceedings of the Symposium Commemorating the Legacy, Works, and Life of Sir Robert Stawell Ball* H. Lipkin, ed., Cambridge University Press, Cambridge, UK.
[9] Selig, J. M., 1996, *Geometric Methods in Robotics* (Monographs in Computer Sciences), Springer-Verlag, New York.
[10] Maschke, B. M. J., 1996, *Modeling and Control of Mechanisms and Robots*, World Scientific, Singapore, pp. 1–38.
[11] Stramigioli, S., 2001, *Modeling and Interactive Mechanical Systems: A Coordinate Free Approach*, Springer, Berlin.
[12] Karger, A., and Novak, J., 1978, *Space Kinematics and Lie Groups*, Gordon and Breach, New York.
[13] Herve, J. M., 1999, ''The Lie Group of Rigid Body Displacements, a Fundamental Tool for Mechanism Design,'' Mech. Mach. Theory, **34**, pp. 719–730.
[14] Abraham, R., and Marsden, J. E., 1994, *Foundations of Mechanics*, 2nd Ed., Addison-Wesley, Reading, MA.
[15] Samuel, P., 1988, *Projective Geometry* (Undergraduate Texts in Mathematics, Readings in Mathematics), Springer-Verlag, New York.

K. Bearden
Captain,
Department of Engineering Mechanics,
U.S. Air Force Academy
USADA, CO 80840

J. W. Dally
Glenn L. Martin Institute
Professor of Engineering,
Emeritus

R. J. Sanford
Professor Emeritus

Department of Mechanical Engineering,
University of Maryland,
College Park, MD 20742

Experimental Determination of K_I for Short Internal Cracks

Since the pioneering discussion by Irwin, a significant effort has been devoted to determining stress intensity factors (K) using experimental methods. Techniques have been developed to determine stress intensity factors from photoelastic, strain gage, caustics, and moiré data. All of these methods apply to a relatively long single-ended-edge crack. To date, the determination of K for internal cracks that are double-ended by experimental methods has not been addressed. This paper describes a photoelastic study of tension panels with both central and eccentric internal cracks. The data recorded in the experiments was analyzed using a new series solution for the opening-mode stress intensity factor for an internal crack. The data was also analyzed using the edge-crack series solution, which is currently employed in experimental studies. Results indicated that the experimental methods usually provided results accurate to within three to five percent if the series solution for the internal crack was employed in an overdeterministic numerical analysis of the data. Comparison of experimental results using the new series for the internal crack and the series for an edge crack showed the superiority of the new series.
[DOI: 10.1115/1.1381004]

Introduction

When applying fracture mechanics to the analysis of the safety of structures containing flaws, it is necessary to determine fracture parameters such as stress intensity factors. In some of these analyses the opening mode stress intensity factor, K_I, and/or the forward shear mode stress intensity factor, K_{II}, may be determined from existing theoretical solutions to well-defined boundary value problems. However, when theoretical solutions are not available, stress intensity factors are often obtained by numerical analysis, but again the structure and the material are usually idealized and the loading must be known.

If the structure cannot be idealized or the nominal stresses are not known in the region of the structure containing the crack, experimental methods are used to determine K_I and/or K_{II}. These experimental methods include photoelasticity, strain gages, moiré, and caustics applied to either a model or to the actual structure. A method for the experimental determination of K_I and σ_{ox}[1] from isochromatic fringe patterns was first outlined by Irwin [1] in a discussion of a paper by Wells and Post [2]. In the years following Irwin's pioneering contribution, a number of investigators ([3–8]) extended his method to improve the accuracy of the predictions and to include the simultaneous determination of K_I and K_{II} and σ_{ox}. However, all of these techniques were based on a small number of measurements of the field parameters (fringe order, N, and position, r and θ); consequently, the accuracy of the determination of the stress intensity factors often suffered. Later, Sanford and Dally [9] introduced a general method for determining K_I, K_{II}, and σ_{ox} based on an overdeterministic analysis of data taken from a large number of points in the local neighborhood surrounding the tip of the crack. The use of full-field data permitted a significant improvement in the accuracy of the determination of K_I, K_{II}, and σ_{ox}. The overdeterministic approach of reference ([9]), originally developed for analysis of photoelastic data, was extended to other experimental techniques for measuring stress intensity factors ([10–12]).

All of the experimental methods for determining stress intensity factors in finite bodies employ data taken from the intermediate region defined in Fig. 1. In the intermediate region, a singular term plus a small number of higher order terms accurately describes the stress field. Data taken from the near field, also defined in Fig. 1, do not yield accurate results because of the stress field is three-dimensional (neither plane stress or plane strain) in this region ([13]). Also, if the data points are located very close to the crack tip, errors in measuring r and θ are often excessive. Data from the far field are not useful because excessively large numbers of terms in the general solution is required to yield accurate results. Also, far-field terms are insensitive to K values.

For long edge cracks (single-ended), data from the intermediate region provide an accurate means for determining either K_I or K_{II} or a combination of both in the case of mixed mode loading. For short edge cracks, the single-ended solution augmented with a series containing several higher order terms provides an adequate approximation. For internal cracks (double-ended), current practice is to employ the same augmented single-ended solution and to ignore the effect of the second singularity. This practice for determining the stress intensity factors data is an adequate approximation that may be used with confidence if the internal crack is sufficiently long. On the other hand, if the crack is sufficiently short, it is clear that the influence of the singularity from both ends of the crack affects the stress field in the intermediate region, and consequently techniques based on the augmented near field equations may lead to significant errors.

Recently, Sanford and Drude [14] published a series solution for an internal crack giving the relations for the mode 1 stresses in the intermediate region. This solution, which accounts for the stress singularities at both ends of the crack, was employed in this study to determine K_I for both symmetric and eccentric internal cracks of various lengths located in a tension panel. Photoelastic methods were used to collect approximately 200 data points from a broad region surrounding both crack tips as shown in Fig. 2. An iterative, overdeterministic method was employed to estimate the coefficients in the two different series describing the stress field in the region near the crack tips. This approach is a generalization of the method proposed by Sanford and Dally [9]. Although the numerical analysis of the experimental data is nonlinear, the solution

[1] σ_{ox} is a uniform stress in the direction of the crack, which is also referred to as the *T*-stress.

Contributed by the Applied Mechanics Division of THE AMERICAN SOCIETY OF MECHANICAL ENGINEERS for publication in the ASME JOURNAL OF APPLIED MECHANICS. Manuscript received by the ASME Applied Mechanics Division, July 26, 2000; final revision, Jan. 18, 2001. Associate Editor: K. Ravi-Chandar. Discussion on the paper should be addressed to the Editor, Prof. Lewis. T. Wheeler, Department of Mechanical Engineering, University of Houston, Houston, TX 77204-4792, and will be accepted until four months after final publication of the paper itself in the ASME JOURNAL OF APPLIED MECHANICS.

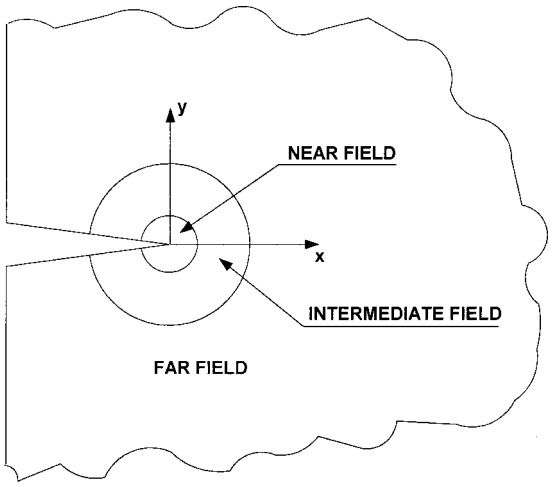

Fig. 1 Illustration of the near, intermediate, and far-field regions near the single-ended crack tip

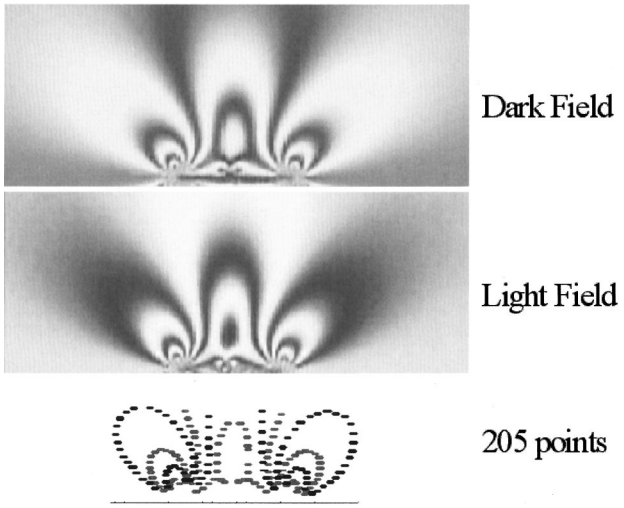

Fig. 2 Light and dark field isochromatic fringe patterns yield a set of data points for numerical analysis

converges rapidly. Since the values of K_I are determined at both crack tips, the method may be employed for both symmetrical and unsymmetrical geometries in a single analysis.

Results from ten experiments with center cracks in several tension panels are presented showing K_I determined using both the single and double-ended solutions in analyzing the same data set. The results from both methods of data analysis are compared with theoretical results and the errors for both approaches are illustrated as a function of crack length.

Results from five experiments involving tension panels with eccentric cracks are also are presented. In this series of experiments, the data were analyzed using only the theory for the internal crack. The experimental results for cracks with different eccentricity ratios were compared with theoretical results from Isida's [15] series solution for K_I.

Theory

For edge cracks with a single crack tip in a finite body, Sanford [16] has shown that the Airy's stress function for the opening mode is given by

$$\phi = \mathrm{Re}\ \tilde{\tilde{Z}}(z) + y\ \mathrm{Im}\ \tilde{Z}(z) + y\ \mathrm{Im}\ \tilde{Y}(z) \tag{1}$$

where

$$Z(z) = \frac{d\tilde{Z}(z)}{dz} = \frac{d^2\tilde{\tilde{Z}}(z)}{dz^2}, \quad Y(z) = \frac{d\tilde{Y}(z)}{dz}$$

and

$$z = x + iy = \mathrm{Re}(z) + i\ \mathrm{Im}(z) = re^{(i\theta)}.$$

The stresses in terms of these functions are expressed as

$$\begin{aligned}
\sigma_x &= \frac{\partial^2\phi}{\partial y^2} = \mathrm{Re}\ Z(z) - y[\mathrm{Im}\ Z'(z) + \mathrm{Im}\ Y'(z)] + 2\mathrm{Re}\ Y(z) \\
\sigma_y &= \frac{\partial^2\phi}{\partial x^2} = \mathrm{Re}\ Z(z) + y[\mathrm{Im}\ Z'(z) + \mathrm{Im}\ Y'(z)] \\
\tau_{xy} &= -\frac{\partial^2\phi}{\partial x\,\partial y} = -\mathrm{Im}\ Y(Z) - y[\mathrm{Re}\ Z'(z) + \mathrm{Re}\ Y'(z)]
\end{aligned} \tag{2}$$

$$\text{where } Z'(z) = \frac{dZ(z)}{dz} \text{ and } Y'(z) = \frac{dY(z)}{dz}.$$

The complex functions $Z(z)$ and $Y(z)$ for a body containing an edge crack are

$$\begin{aligned}
Z(z) &= \sum_{n=0}^{N} A_n Z^{n-1/2} \\
Y(z) &= \sum_{m=0}^{M} B_m Z^m
\end{aligned} \tag{3}$$

where A_n and B_m are coefficients to be determined by a numerical analysis of experimental data. The opening mode stress intensity factor, K_I, and the uniform stress, σ_{ox}, are related to only A_0 and B_0 by

$$\begin{aligned}
K_I &= \sqrt{2\pi} A_0 \\
\sigma_{0x} &= B_0/2.
\end{aligned} \tag{4}$$

The complex functions defined in Eq. (3) are not valid for the internal crack because they accommodate only the single singularity associated with an edge crack; however, singularities exist at both ends of an internal crack. To accommodate the singularities at each of the crack tips, Sanford and Drude [14] have proposed a new stress function $Z(z)$ with singularities located at $z = a$ and $z = b$ of the form

$$Z(z) = \sum_{j=0}^{J} A_j \frac{(z - z_0)^{j+1}}{\sqrt{(z-a)(z-b)}}$$

and

$$Y(z) = \sum_{m=0}^{M} B_m (z - z_0)^m \tag{5}$$

where $z_0 = (a+b)/2$.

The coordinate system for the internal crack in a finite body is shown in Fig. 3. The stresses are determined by substituting Eq. (5) into Eq. (2) to obtain

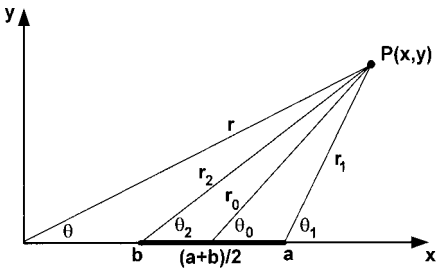

Fig. 3 Coordinate system for the internal crack

$$\sigma_x=\sum_{j=0}^{J} A_j\frac{r_0^{j+1}}{(r_1r_2)^{1/2}}\left\{\cos\left[(j+1)\theta_0-\frac{\theta_1+\theta_2}{2}\right]\right\}$$
$$-(j+1)\sin\theta_0\sin\left[j\theta_0-\frac{\theta_1+\theta_2}{2}\right]$$
$$+\frac{1}{2}\left(\frac{r_0}{r_1}\right)\sin\theta_0\sin\left[(j+1)\theta_0-\frac{3\theta_1+\theta_2}{2}\right]$$
$$+\frac{1}{2}\left(\frac{r_0}{r_2}\right)\sin\theta_0\sin\left[(j+1)\theta_0-\frac{\theta_1+3\theta_2}{2}\right]$$
$$+\sum_{m=0}^{M} B_m r_0^m[2\cos m\theta_0-\sin\theta_0\sin(m-1)\theta_0] \quad (6)$$

$$\sigma_y=\sum_{j=0}^{J} A_j\frac{r_0^{j+1}}{(r_1r_2)^{1/2}}\left\{\cos\left[(j+1)\theta_0-\frac{\theta_1+\theta_2}{2}\right]\right\}$$
$$+(j+1)\sin\theta_0\sin\left[j\theta_0-\frac{\theta_1+\theta_2}{2}\right]$$
$$-\frac{1}{2}\left(\frac{r_0}{r_1}\right)\sin\theta_0\sin\left[(j+1)\theta_0-\frac{3\theta_1+\theta_2}{2}\right]$$
$$-\frac{1}{2}\left(\frac{r_0}{r_2}\right)\sin\theta_0\sin\left[(j+1)\theta_0-\frac{\theta_1+3\theta_2}{2}\right]$$
$$+\sum_{m=0}^{M} B_m r_0^m[m\sin\theta_0\sin(m-1)\theta_0] \quad (7)$$

$$\tau_{xy}=-\sum_{j=0}^{J} A_j\frac{r_0^{j+1}}{(r_1r_2)^{1/2}}\left\{(j+1)\cos\left[j\theta_0-\frac{\theta_1+\theta_2}{2}\right]\sin\theta_0\right\}$$
$$-\frac{1}{2}\left(\frac{r_0}{r_1}\right)\sin\theta_0\cos\left[(j+1)\theta_0-\frac{3\theta_1+\theta_2}{2}\right]$$
$$-\frac{1}{2}\left(\frac{r_0}{r_2}\right)\sin\theta_0\cos\left[(j+1)\theta_0-\frac{\theta_1+3\theta_2}{2}\right]$$
$$-\sum_{m=0}^{M} B_m r_0^m[\sin m\theta_0+m\sin\theta_0\cos(m-1)\theta_0]. \quad (8)$$

The relations for the stress intensity factors are obtained for each crack tip by employing the limit definition of K at each crack tip with the limit taken from the material side.

$$K=\lim_{r\Rightarrow 0}\sigma_y|_{\theta=0,\pi}\sqrt{2\pi r} \quad (9)$$

Substituting Eq. (7) into Eq. (9) yields

$$K_a=\sum_{j=0}^{J} A_j\frac{\sqrt{2\pi}}{\sqrt{a-b}}\left(\frac{a-b}{2}\right)^{j+1} \quad (10)$$

$$K_b=\sum_{j=0}^{J} (-1)^j A_j\frac{\sqrt{2\pi}}{\sqrt{a-b}}\left(\frac{a-b}{2}\right)^{j+1}. \quad (11)$$

Examination of Eqs. (10) and (11) indicates that the stress intensity factors K_a and K_b depend on the summation of all of the unknown coefficients A_j. This is different from previous experience with edge cracks where K_1 depended only on A_0 as indicated in Eq. (4).

For boundary value problems with symmetry, such as the central crack in a tension panel, K_a and K_b are equal. To achieve this equality, it is necessary for all of the odd coefficients, A_1, A_3, A_5, etc., to vanish. Of course, for boundary value problems with eccentric crack geometries, the values of K_a and K_b differ and all terms in the series expansion must be considered.

Experimental Procedure

Photoelastic models of a tension panel, shown schematically in Fig. 4, were prepared from a 3.2-mm (0.12-in.) thick sheet of photoelastic grade polycarbonate[2] that was free of residual birefringence. The polycarbonate polymer exhibited a material fringe value of 7.00 MPa/mm/fringe (40 psi/in./fringe). Both central and eccentric cracks were introduced by first drilling a small hole on the horizontal centerline of the tension panel. A fine scroll saw was then inserted into the hole and cutting along the horizontal centerline formed a simulated crack. Several tension panels were prepared with crack lengths ($2a$) ranging from 5.46 mm (0.215 in.) to 47.3 mm (1.862 in.). The geometry of the symmetric and eccentric photoelastic models is defined in Tables 1 and 2, respectively.

The panels were loaded in tension in a screw-type universal-testing machine, and the fringes were displayed in a custom fabricated white-light diffused polariscope. The load applied to the tension panel depended upon the length of the crack with increasing load associated with decreasing crack length. At a prescribed load, photographs of the fringe patterns formed about the crack tips were recorded through a monochromatic filter (wavelength of 575 nm) using a color digital camera equipped with a 640×480 pixel array. Fringe patterns were recorded with the polariscope set for both light and dark field to double the number of fringe loops available for analysis. Typical examples of the light and dark fringe patterns were illustrated in Fig. 2.

The photographs of the isochromatic fringe patterns were post-processed with image processing software. This interactive program allowed for scaling the size of the image and determining the location and the number of the fringe order. The coordinates and the fringe order (x, y, and N) were established for about 200 data points from the pair of photographs for each photoelastic model. Data was taken from the intermediate regions near both crack tips and from the region between the crack tips. Characterizing the fringes in the region between the crack tips is important to the analysis of the data since they are unique to the internal crack problem.

[2]PSM-1 is commercially available from Micro Measurements, Photolastic Division, Raleigh, NC.

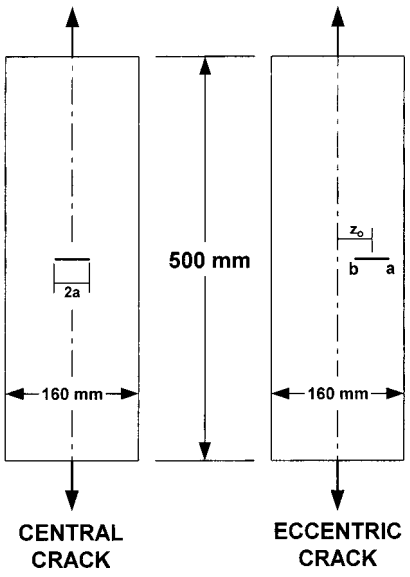

Fig. 4 Geometry of the tension panels with symmetric and eccentric cracks

Table 1 Geometry of the photoelastic models with a central crack

Model No.	Crack Length (2a) mm	(in.)	2a/W	Model No.	Crack Length (2a) mm	(in.)	2a/W
CC-1	5.46	0.215	0.034	CC-6	16.1	0.633	0.101
CC-2	5.97	0.235	0.038	CC-7	16.8	0.660	0.105
CC-3	9.96	0.392	0.063	CC-8	19.4	0.763	0.122
CC-4	12.9	0.509	0.081	CC-9	32.1	1.265	0.203
CC-5	13.3	0.524	0.084	CC-10	47.3	1.862	0.298

Table 2 Geometry of the photoelastic models with an eccentric crack

Model No.	Crack Length (2a) mm	(in.)	2a/W	z_0 mm	(in.)	z_0/W
EC-1	16.1	0.633	0.101	0.0	0.00	0.00
EC-2	15.9	0.625	0.100	15.9	0.63	0.10
EC-3	16.2	0.637	0.102	39.7	1.56	0.25
EC-4	15.9	0.626	0.100	55.4	2.18	0.35
EC-5	16.0	0.630	0.101	63.5	2.50	0.45

Numerical Analysis of the Data

The full set of data points was used as input to an iterative over deterministic method applied to the double-ended solution for the internal crack. The equations for the stresses and the application of a combined Newton-Raphson and linear-least-squares method of analysis for this nonlinear formulation were programmed in *Mathematica*™. This approach is a generalization of the method introduced by Sanford and Dally [9] and follows the same procedure described by Sanford [17] except that the internal crack solution replaces the edge crack solution used for the single ended crack studies.

The mathematical approach for the data analysis is based on minimizing the function, g, which is derived from the photoelastic stress optic law as indicated below:

$$g_k = D_k^2 + T_k^2 - (N f_\sigma / 2h)^2 \tag{12}$$

where $D = [\sigma_{yy} - \sigma_{xx})/2]$
$T = \tau_{xy}$
N is the fringe order
f_σ is the photoelastic material fringe value
h is the model thickness.

The subscript k indicates the value of g evaluated at a point (r_k, θ_k) with a fringe order of N_k located in the intermediate region. Since D and T are both dependent on coefficients A_j and B_m in Eqs. (6)–(9), the correct values for these constants will give $g_k = 0$ for all values of k. One initially estimates the coefficients A_j and B_m and computes g_k only to find $g_k \neq 0$. To correct the error in the initial estimates of the coefficients, the values of A_j and B_m are adjusted using an iterative relation based on a Taylor-series expansion of g_k as described in reference ([9]).

Although the use of photoelastic data leads to a nonlinear relation among the coefficients of the series expansion for the stresses and the fringe order, the overdeterministic solution converged rapidly. The K values at both crack tips are determined from the best-fit coefficients from Eqs. (10) and (11). Introducing additional data points produced more rapid convergence but did not affect the overall results. Convergence was excellent, achieving differences between iterations of the order of 10^{-3} in ten iterations or less. Also, the initial estimate of the coefficients in the series expansion was not a factor for the convergence of the important coefficients. In order to confirm the validity of the solution, computer generated fringe patterns were constructed using best-fit coefficients. Comparison of the computer generated fringe pattern with the original isochromatic fringe pattern, as illustrated in Fig. 5, indicates the ''goodness'' of the fit of the numerical analysis with the original photoelastic data. This comparison of the computer generated fringe pattern with the original fringe pattern is important because it provides confidence that the data was selected from the intermediate region. If some the original data points do not fall on or very near a computer generated fringe, it is an indication that these points may not be within the intermediate region where the series solution is representative.

Experimental Results

Central Cracks. The results obtained from ten different experiments with the central cracks of various lengths $(2a)$ in tension panels subjected to a normalized load of 4448 (1000 1b) are presented in Tables 3 and 4. The results presented in Table 3 were obtained by employing the series associated with an edge crack, given by Eq. (3), which neglected the influence of the singularity at the other end of the crack. The results presented in Table 4 were determined with the series for the internal crack, Eq. (5), where singularities at both ends of the crack were accommodated. The results in both Tables 3 and 4 showed that the stress intensity factors increased with crack length as anticipated. Comparisons of the experimental and theoretical results showed less than three

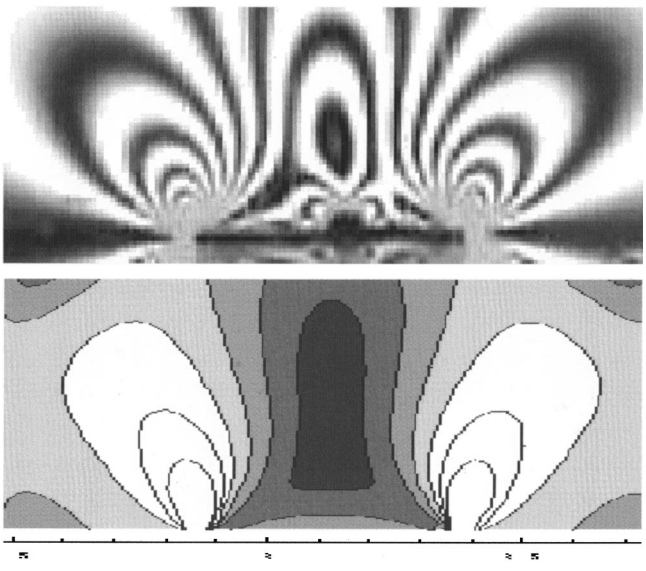

Fig. 5 Comparison of the original isochromatic fringe pattern with a computer regenerated fringe pattern for a central crack

Table 3 Opening mode stress intensity factor models with double-ended internal crack centrally located, numerical analysis with a series solution for a single-ended edge crack load of 4448 N (1000 lb)

MODEL NO.	2a/W	r_{ave}/a	K_I THEORY* ksi-in$^{1/2}$	K_I THEORY* MPa-m$^{1/2}$	K_I EXPL ksi-in$^{1/2}$	K_I EXPL MPa-m$^{1/2}$	% ERROR
CC-1	0.034	0.657	0.744	0.818	0.535	0.588	+28.1
CC-2	0.038	0.539	0.777	0.854	0.604	0.664	+22.3
CC-3	0.063	0.480	1.007	1.106	0.903	0.992	+10.3
CC-4	0.081	0.473	1.149	1.263	1.051	1.155	+8.5
CC-5	0.084	0.819	1.165	1.280	1.164	1.279	+0.1
CC-6	0.101	0.918	1.284	1.411	1.178	1.295	+8.3
CC-7	0.105	0.453	1.312	1.442	1.211	1.331	+7.7
CC-8	0.122	0.736	1.413	1.553	1.382	1.519	+2.2
CC-9	0.203	0.680	1.852	2.035	1.874	2.060	-1.2
CC-10	0.298	0.688	2.317	2.546	2.290	2.517	+1.2

*The theoretical solution is from Isida reference [15].

Table 4 Opening mode stress intensity factor models with a double-ended internal crack centrally located, numerical analysis with a series solution for a double-ended internal crack load of 1000 lb (4448 N)

MODEL NO.	2a/W	r_{ave}/a	K_I THEORY* MPa-m$^{1/2}$	K_a EXPL MPa-m$^{1/2}$	K_b EXPL MPa-m$^{1/2}$	K_{ave} EXPL MPa-m$^{1/2}$	% ERROR
CC-1	0.034	0.657	0.818	0.846	0.849	0.848	-3.7
CC-2	0.038	0.539	0.853	0.765	0.793	0.779	+8.8
CC-3	0.063	0.480	1.107	1.046	1.046	1.046	+5.5
CC-4	0.081	0.473	1.263	1.220	1.220	1.220	+3.4
CC-5	0.084	0.819	1.280	1.281	1.346	1.314	-2.7
CC-6	0.101	0.918	1.411	1.398	1.369	1.393	+1.2
CC-7	0.105	0.453	1.442	1.416	1.416	1.416	+1.7
CC-8	0.122	0.736	1.553	1.534	1.519	1.526	+1.8
CC-9	0.203	0.680	2.035	2.088	2.066	2.077	-2.1
CC-10	0.298	0.688	2.546	2.477	2.640	2.618	-2.8

* *The theoretical solution is from Isida reference [15].

Table 5 Comparison of results for the opening mode stress intensity factor, numerical analysis with series solutions for edge and internal cracks load of 4448 N (1000 lb)

MODEL NO.	2a/W	r_{ave}/a	K_I THEORY MPa-m$^{1/2}$	K_{ave} EDGE ksi-in$^{1/2}$	K_{ave} INT. MPa-m$^{1/2}$	% ERROR EDGE	% ERROR INT.
CC-1	0.034	0.657	0.818	0.588	0.848	+28.1	-3.7
CC-2	0.038	0.539	0.853	0.664	0.779	+22.3	+8.8
CC-3	0.063	0.480	1.107	0.992	1.046	+10.3	+5.5
CC-4	0.081	0.473	1.263	1.155	1.220	+8.5	+3.4
CC-5	0.084	0.819	1.280	1.279	1.314	+0.1	-2.7
CC-6	0.101	0.918	1.411	1.295	1.393	+8.3	+1.2
CC-7	0.105	0.453	1.442	1.331	1.416	+7.7	+1.7
CC-8	0.122	0.736	1.553	1.519	1.526	+2.2	+2.4
CC-9	0.203	0.680	2.035	2.060	2.077	-1.2	-2.1
CC-10	0.298	0.688	2.546	2.517	2.618	+1.2	-2.8

percent error for experiments with longer cracks (i.e., $2a/W > 0.12$). Errors increased for those experiments with shorter cracks, but were always less than ten percent if the data were analyzed using the internal crack series. For very short cracks (i.e., $2a/W < 0.06$), the errors resulting from using the series for the edge crack became excessive.

A comparison of the experimental results obtained with data analysis using the edge and internal crack series in the data analysis is presented in Table 5. This comparison shows that both the edge crack and internal crack series provide an accurate method for predicting K_1 if the cracks are sufficiently long $2a/W > 0.12$. In this group of experiments, the location of the data points expressed as r_{ave}/a was about 0.7. For all crack lengths, the internal crack series was superior to the edge crack series in the numerical analysis of the data. For intermediate length cracks, with $0.12 < 2a/W < 0.3$, the errors occurring when the internal crack series was employed ranged from 1.2 to 3.4 percent. However, when the edge crack series was utilized to evaluate the data the errors were more than twice as large. For very short cracks, $2a/W < 0.06$, the errors increased with both methods of data analysis. However, in

Table 6 Results for eccentric cracks in a tension panel, numerical analysis with internal crack series load of 4448 N (1000 lb)

MODEL No.	z_0/W	ISIDA K_b MPa-m$^{1/2}$	ISIDA K_a MPa-m$^{1/2}$	EXPL K_b MPa-m$^{1/2}$	EXPL K_a MPa-m$^{1/2}$	% ERROR K_b	% ERROR K_a
EC-1	0.00	1.411	1.411	1.389	1.398	+1.55	+0.93
EC-2	0.25	1.428	1.433	1.466	1.488	-2.62	-3.83
EC-3	0.35	1.444	1.462	1.334	1.501	+7.61	-2.71
EC-4	0.40	1.501	1.560	1.426	1.556	+4.98	+0.28

all of the three experiments with the very short cracks the internal crack series provided much more accurate results.

Eccentric Cracks. Experimental results from the photoelastic studies of eccentric cracks in tension panels are presented in Table 6. The results for all four of the experiments were normalized to 4448 N (1000 lb) applied load, and the crack lengths were nearly constant at 16 mm (0.63 in.). The crack in model EC-1 was centrally located to give the case with zero eccentricity. The eccentricity, as measured by the ratio z_0/W, increased from 0.10 to 0.40 in models EC-2 to EC-5. For model EC-5, the tip right-hand tip of the crack was only 8.0 mm (0.312 in.) from the vertical edge of the photoelastic model.

Examination of Table 6 indicates that the experimental results determined with a numerical analysis of photoelastic data using the internal crack series is (with one exception) accurate to within five percent. The comparison of the experimental results is made with the theoretical results of Isida. Another comparison is shown in Fig. 6 where the reconstructed fringe patterns are matched with the original photoelastic isochromatic fringe patterns. In making the comparison, only the region of data acquisition (shown by the dots) is germane. Over the limited region, the strong similarity in the match of the two patterns is an indication of the adequacy of the data analysis method. Based on these results and the ability of the experimental solutions to model the fringe pattern between the crack tips, is clear evidence that the internal crack series of Sanford and Drude accurately models the state of stress for internal cracks in finite models subject to remote loading.

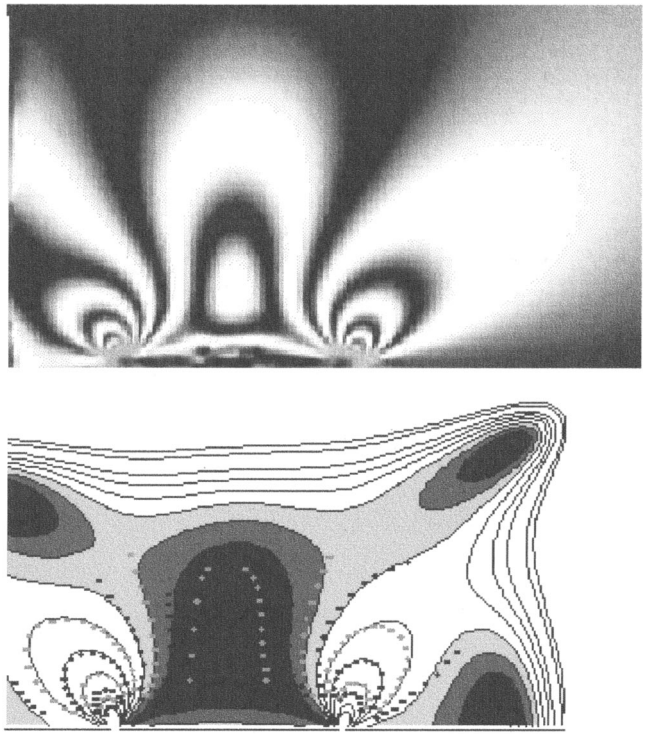

Fig. 6 Comparison of the original isochromatic fringe pattern with a computer regenerated fringe pattern for an eccentric crack

Discussion

The results from this photoelastic study of stress intensity factors K for central and eccentric cracks in a tension panel have verified the general Westergaard series solution for the internal crack. The series solution is used with the well-known overdeterministic method for numerically solving the nonlinear equations that occur when using photoelasticity for determining K. Of course, the results obtained depend on the quality of the data and the ''goodness of the fit.'' The use of a digital camera to record the data together with post processing by image analysis software enhanced the quality of the data and simplified the analysis. Equally important was establishing the fit of the solution to the data ([18]). Some data points carry error into the solution because they are outside the intermediate region for which the series solution is representative. Second, some of these data points are flawed because of inherent measurement error. By comparing the reconstructed fringe patterns with the original fringe patterns, one may qualitatively judge the ''goodness of the fit.'' The fit may also be assessed with an analysis of the sum of the squares of the cumulative error E is given by

$$E=\frac{1}{k}\sum_{i=l}^{k}\left[N_o(r,\theta)-N_s(r,\theta)\right]^2 \tag{13}$$

where N_o and N_s are the fringe orders for the experimental and reconstructed results at the locations (r, θ) of the k data points.

Comparisons were made for the experimental results obtained by performing data analysis with the edge and internal crack series solutions. In general, we found that the error was reduced significantly when the internal crack series was employed to analyze the data. The reduction in error depended on the length of the internal crack with marked reductions for the very short cracks. For short cracks the use of the internal crack series solution is imperative if results with errors of about five percent are to be achieved. For the longer cracks both approaches gave satisfactory results with errors less than three percent. For intermediate length internal cracks the superiority of the new series solution is also evident if accuracy better than four percent is expected.

The series solution for the internal crack has two other advantages. First, solutions for both ends of the crack are obtained in the same analysis. This reduces the time required for the data analysis and enables one to more effectively deal with eccentric cracks subjected to mode 1 loading. Second, the internal crack series solution effectively increases the size of the intermediate region. With the internal crack series, data may be taken from much of the region over the crack where low-order fringes form. With the edge crack series, the region over the crack must be avoided.

References

[1] Irwin, G. R., 1958, discussion of paper by Wells and Post, *Proc. SESA*, Vol. XVI, pp. 93–96.

[2] Wells, A., and Post, D., 1958, ''The Dynamic Stress Distribution Surrounding a Running Crack—A Photoelastic Analysis,'' *Proc. SESA*, Vol. XVI, pp. 69–93.

[3] Schroedl, M. A., and Smith, C. W., 1973, ''Local Stresses Near Deep Surface Flaws Under Cylindrical Bending Fields,'' *Progress in Flow Growth and Frac-*

ture Toughness Testing, ASTM STP 536, ASTM, Philadelphia, PA, pp. 45–63.
[4] Bradley, W. B., and Kobayashi, A. S., 1970, ''An Investigation of Propagating Cracks by Dynamic Photoelasticity,'' Exp. Mech., **10**, No. 3, pp. 106–113.
[5] Chisholm, D. B., and Jones, D. L., 1977, ''An Analytical and Experimental Stress Analysis of a Practical Mode II Fracture Test Specimen,'' Exp. Mech., **17**, No. 1, pp. 7–13.
[6] Smith, D. G., and Smith, C. W., 1972, ''Photoelastic Determination of Mixed Mode Stress Intensity Factors,'' Eng. Fract. Mech., **4**, No. 2, pp. 357–366.
[7] Gdoutus, E. E., and Theocaris, P. G., 1978, ''A Photoelastic Determination of Mixed Mode Stress Intensity Factors,'' Exp. Mech., **18**, No. 3, pp. 87–97.
[8] Etheridge, J. M., and Dally, J. W., 1978, ''A Three Parameter Method for Determining Stress Intensity Factors From Isochromatic Fringe Loops,'' J. Strain Anal., **13**, No. 2, pp. 91–94.
[9] Sanford, R. J., and Dally, J. W., 1979, ''A General Method for Determining Mixed Mode Stress Intensity Factors From Isochromatic Fringe Patterns,'' Eng. Fract. Mech., **11**, pp. 621–633.
[10] Berger, J. R., and Dally, J. W., 1988, ''An Overdeterministic Approach for Measuring K_1 Using Strain Gages,'' Exp. Mech., **28**, No. 2, pp. 142–145.
[11] Barker, D. B., Sanford, R. J., and Chona, R., 1985, ''Determining K and Related Stress Field Parameters From Displacement Fields,'' Exp. Mech., **25**, No. 12, pp. 399–407.
[12] Kalthoff, J. F., 1987, ''Shadow Method of Caustics,'' in *Handbook on Experimental Mechanics*, A. S. Kobayashi, ed., Prentice-Hall, Englewood Cliffs, NJ, pp. 430–500.
[13] Rosakis, A. J., and Ravi-Chandar, K., 1986, ''On the Crack-Tip Stress State: An Experimental Evaluation of Three-Dimensional Effects,'' Int. J. Solids Struct., **22**, No. 2, pp. 121–134.
[14] Sanford, R. J., and Drude, B. T., 1993, *Proc. 1993 Conf. on Exp. Mechanics*, SEM Bethel, CT.
[15] Isida, M., 1966, ''Stress Intensity Factors for the Tension of an Eccentrically Cracked Strip,'' ASME J. Appl. Mech., **33**, pp. 674–675.
[16] Sanford, R. J., 1979, ''A Critical Re-examination of the Westergaard Method for Solving Opening-Mode Crack Problems,'' Mech. Res. Commun., **6**, No. 5, pp. 289–294.
[17] Sanford, R. J., 1989, ''Determining Fracture Parameters With Full-Field Optical Methods,'' Exp. Mech., **29**, No. 3, pp. 241–247.
[18] Chona, R., Irwin, G. R., and Sanford, R. J., 1983, ''Influence of Specimen Size and Shape on the Singularity Dominated Zone,'' *Fracture Mechanics: Fourteenth Symposium —Volume: I Theory and Analysis*, ASTM STP 791, J. C. Lewis and G. Sines, eds., ASTM, Philadelphia, PA, pp. 13–23.

Journal of Applied Mechanics

Brief Notes

A Brief Note is a short paper that presents a specific solution of technical interest in mechanics but which does not necessarily contain new general methods or results. A Brief Note should not exceed 1500 words *or equivalent* (a typical one-column figure or table is equivalent to 250 words; a one line equation to 30 words). Brief Notes will be subject to the usual review procedures prior to publication. After approval such Notes will be published as soon as possible. The Notes should be submitted to the Editor of the JOURNAL OF APPLIED MECHANICS. Discussions on the Brief Notes should be addressed to the Editorial Department, ASME International, Three Park Avenue, New York, NY 10016-5990, or to the Editor of the JOURNAL OF APPLIED MECHANICS. Discussions on Brief Notes appearing in this issue will be accepted until two months after publication. Readers who need more time to prepare a Discussion should request an extension of the deadline from the Editorial Department.

Inertia Effects in a Curved Non-Newtonian Squeeze Film

R. Usha and P. Vimala
Department of Mathematics,
Indian Institute of Technology,
Madras 600 036, India

1 Introduction

In recent years, hydrodynamically lubricated bearings are used under increasingly severe conditions of high speed and heavy load. Owing to the friction, the temperature of the lubricating film rises under such operations and the viscosity of the lubricating oil decreases. Lubricating oils often contain sufficient additives of high molecular-weight polymers as a viscosity index improver in order to prevent viscosity variation with temperature change. Experimental evidence of rheological characteristics of polymer-thickened oils indicates that such lubricants behave as non-Newtonian viscous fluids such as pseudo-plastic fluids when the amount of additives is small. It has been confirmed that the non-Newtonian viscous behavior of polymer-thickened oils may be approximated by a cubic equation model relating the shear stress and the rate of shear ([1]). In the cubic equation model, the shear rate $\dot{\gamma}$ is expressed in terms of the shear stress τ as $\mu\dot{\gamma}=\tau+k\tau^3$, where $k>0$ characterizes the pseudo-plastic fluid; $k=0$, the Newtonian fluid and $k<0$, the dilatant fluid, the initial viscosity μ is equal to the viscosity of the Newtonian fluid.

The effects of fluid inertia forces in parallel circular and annular squeeze films lubricated with pseudo-plastic fluids have been theoretically examined using the cubic equation model by the method of averaged inertia by Hashimoto and Wada [2,3]. This study has been motivated by the significance of fluid inertia effects in most squeeze films, in addition to the non-Newtonian effects, where the operating speed is high or low viscosity fluids are used as lubricants ([4–7]).

The effect of a curved surface on a Newtonian squeeze film has drawn the interest of many researchers due to its importance in improving the performance of hydraulic machine elements and these studies include the investigations by Murti [8], Gupta and Kapur [9], and Hasegawa [10]. In squeeze flow problems, the gap between the approaching surfaces is small compared with the dimensions of the surfaces. Then, even if the order of waviness in the curved plates is small, the effect of nonflatness on the squeeze film flow is not necessarily negligible. Further, in the case of a small squeeze velocity, the inertia forces due to the space variations in the flow are not always small compared with the viscous and the pressure forces. In view of this, it becomes important to study the combined effects of inertia and curvature on the squeeze film performance between curved surfaces.

In this note, the combined effects of fluid inertia, curvature, and non-Newtonian characteristics on the squeeze film pressure are examined in a curved squeeze film between a flat circular disk and a curved circular disk lubricated with pseudo-plastic fluids described by a cubic equation model. The modified lubrication theory is employed to obtain the equation for the pressure gradient and the equation is solved numerically for the pressure distribution for the sinusoidal motion of the upper curved disk described by an exponential function. Further, the analytical solution for the pressure distribution is obtained using a perturbation method.

2 Theoretical Analysis

The axially symmetric laminar flow of a non-Newtonian lubricant fluid that exhibits characteristics in agreement with the cubic equation model given by

$$\mu\frac{\partial u}{\partial z}=\tau_{rz}+k\tau_{rz}^3 \tag{1}$$

between a flat circular disk located at $z=0$ and a curved circular disk at $z=H(r,t)$ is considered (Fig. 1(*a*)). The film thickness variation at radius r is assumed to be

$$H(r,t)=h(t)e^{-cr^2} \tag{2}$$

where H is axisymmetric about the z-axis and $h(t)$ denotes the central film thickness (Fig. 1(*b*)) ([8,9]). It is possible to generate different types of films for different values of c because of the dependence on c. Concave films are generated for $c>0$ and convex films are obtained for $c<0$. The top curved disk moves towards the bottom disk with velocity dh/dt and the central film thickness is maintained as constant.

Using the hydrodynamic lubrication assumptions applicable to thin films, and retaining the inertial terms, the governing equation of motion in the r-direction is given by

$$\rho\left(\frac{\partial u}{\partial t}+u\frac{\partial u}{\partial r}+w\frac{\partial u}{\partial z}\right)=-\frac{\partial p}{\partial r}+\frac{\partial r_{rz}}{\partial z} \tag{3}$$

where u and w denote the radial and axial components of velocity and τ_{rz} is the shear stress. The equation of continuity is

Contributed by the Applied Mechanics Division of THE AMERICAN SOCIETY OF MECHANICAL ENGINEERS for publication in the ASME JOURNAL OF APPLIED MECHANICS. Manuscript received by the ASME Applied Mechanics Division, August 16, 2000; final revision, April 28, 2001. Associated Editor: D. A. Siginer.

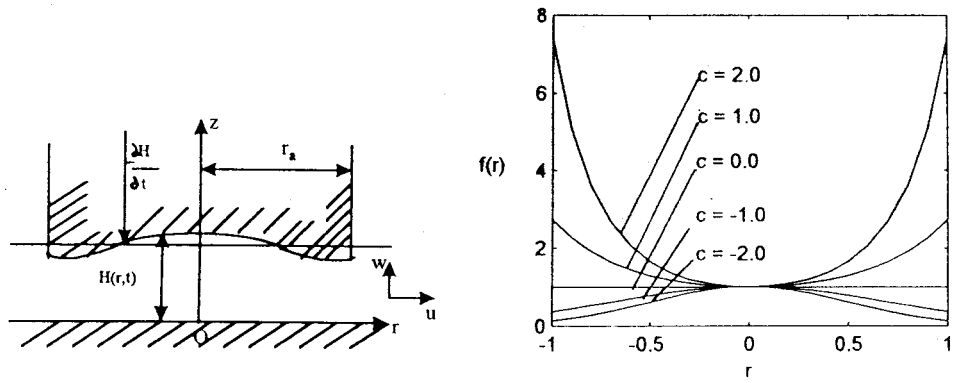

Fig. 1 (*a*) Curved squeeze film geometry, (*b*) configuration of the curved disk

$$\frac{1}{r}\frac{\partial(ru)}{\partial r}+\frac{\partial w}{\partial z}=0. \tag{4}$$

The boundary conditions are

$$u=0,\quad w=0\ \text{ on }\ z=0 \tag{5}$$

$$u=0,\quad w=\frac{dh}{dt}\ \text{ on }\ z=he^{-cr^2} \tag{6}$$

$$p=0\ \text{ on }\ r=r_a \tag{7}$$

where r_a is the radius of the circular disk. The equation for the squeeze motion is obtained from (4), (5), and (6) as

$$\int_0^{he^{-cr^2}} u\,dz=-\frac{r}{2}\frac{dh}{dt}. \tag{8}$$

As the film is thin, it is reasonable to take the inertia forces as constant across the film and hence the inertia terms in Eq. (3) are approximated by the mean value averaged across the film thickness as

$$\frac{\rho}{he^{-cr^2}}\int_0^{he^{-cr^2}}\left(\frac{\partial u}{\partial t}+u\frac{\partial u}{\partial r}+w\frac{\partial u}{\partial z}\right)dz=-\frac{\partial p}{\partial r}+\frac{\partial \tau_{rz}}{\partial z} \tag{9}$$

which is rewritten using Eqs. (4)–(6) as

$$\frac{\rho}{he^{-cr^2}}\left[\frac{\partial}{\partial t}\int_0^{he^{-cr^2}}u\,dz+\left(\frac{\partial}{\partial r}+\frac{1}{r}\right)\int_0^{he^{-cr^2}}u^2\,dz\right]$$

$$=-\frac{\partial p}{\partial r}+\frac{\partial \tau_{rz}}{\partial z}. \tag{10}$$

Introducing the modified pressure gradient f_e as

$$f_e=\frac{\partial p}{\partial r}+\frac{\rho}{he^{-cr^2}}\left[\frac{\partial}{\partial t}\int_0^{he^{-cr^2}}u\,dz+\left(\frac{\partial}{\partial r}+\frac{1}{r}\right)\int_0^{he^{-cr^2}}u^2\,dz\right], \tag{11}$$

Eq. (10) gives

$$f_e=\frac{\partial \tau_{rz}}{\partial z}. \tag{12}$$

Since f_e is independent of z, integrating Eq. (12) with respect to z and using (1), (5), and (6), the radial velocity component is obtained as

$$u=\frac{1}{\mu}\left[\frac{f_e z}{2}(z-he^{-cr^2})+\frac{kf_e^3}{8}\{2z^4-4he^{-cr^2}z^3+3h^2e^{-2cr^2}z^2-h^3e^{-3cr^2}z\}\right]. \tag{13}$$

Substituting Eq. (13) in (8), the equation satisfied by the modified pressure gradient f_e is obtained as

$$\frac{kh^5e^{-5cr^2}}{40}f_e^3+\frac{h^3e^{-3cr^2}}{6}f_e=r\frac{dh}{dt}. \tag{14}$$

In terms of the following dimensionless quantities

$$r^*=\frac{r}{r_a},\quad z^*=\frac{z}{h_0},\quad w^*=\frac{w}{W_0},$$

$$u^*=\frac{uh_0}{r_aW_0},\quad h^*=\frac{h}{h_0},\quad T=\frac{tW_0}{h_0},$$

$$f_e^*=\frac{f_eh_0^3}{\mu r_aW_0},\quad p^*=\frac{ph_0^3}{\mu r_a^2W_0},\quad \delta=k\left(\frac{\mu r_aW_0}{h_0^2}\right)^2,$$

$$\bar{c}=cr_a^2,\quad \mathrm{Re}=\frac{\rho h_0W_0}{\mu} \tag{15}$$

Eqs. (14), (13), and (11) are obtained as

$$\frac{\delta f_e^{*3}h^{*5}e^{-5\bar{c}r^{*2}}}{40}+\frac{f_e^*h^{*3}e^{-3\bar{c}r^{*2}}}{6}-r^*\frac{dh^*}{dT}=0 \tag{16}$$

$$u^*=\frac{\delta f_e^{*3}}{8}(2z^{*4}-4h^*e^{-\bar{c}r^{*2}}z^{*3}+3h^{*2}e^{-2\bar{c}r^{*2}}z^{*2}-h^{*3}e^{-3\bar{c}r^{*2}}z^*)+\frac{f_e^*}{2}(z^{*2}-h^*e^{-\bar{c}r^{*2}}z^*) \tag{17}$$

$$\frac{\partial p^*}{\partial r^*}=f_e^*-\frac{\mathrm{Re}}{h^*e^{-\bar{c}r^{*2}}}\left[\frac{\partial}{\partial T}\int_0^{h^*e^{-\bar{c}r^{*2}}}u^*\,dz^*+\left(\frac{\partial}{\partial r^*}+\frac{1}{r^*}\right)\int_0^{h^*e^{-\bar{c}r^{*2}}}u^{*2}\,dz^*\right] \tag{18}$$

where h_0 is the initial central film thickness, W_0 is the characteristic velocity of the curved plate, and Re is the Reynolds number. Substituting for u^* from (17) in (18), the dimensionless radial pressure gradient is given by

$$\frac{\partial p^*}{\partial r^*}=f_e^*-\frac{\mathrm{Re}}{h^*e^{-\bar{c}r^{*2}}}\left[-\frac{r^*}{2}\frac{d^2h^*}{dT^2}+f_e^*\frac{\partial f_e^*}{\partial r^*}h^{*5}\times e^{-5\bar{c}r^{*2}}\left(\frac{1}{60}+\frac{\delta h^{*2}e^{-2\bar{c}r^{*2}}f_e^{*2}}{105}+\frac{\delta^2h^{*4}e^{-4\bar{c}r^{*2}}f_e^{*4}}{960}\right)-\bar{c}f_e^{*2}h^{*5}e^{-5\bar{c}r^{*2}}\left(\frac{1}{12}+\frac{\delta h^{*2}e^{-2\bar{c}r^{*2}}f_e^{*2}}{30}+\frac{\delta^2h^{*4}e^{-4\bar{c}r^{*2}}f_e^{*4}}{320}\right)+\frac{f_e^{*2}h^{*5}e^{-5\bar{c}r^{*2}}}{r^*}\times\left(\frac{1}{120}+\frac{\delta h^{*2}e^{-2\bar{c}r^{*2}}f_e^{*2}}{420}+\frac{\delta^2h^{*4}e^{-4\bar{c}r^{*2}}f_e^{*4}}{5760}\right)\right] \tag{19}$$

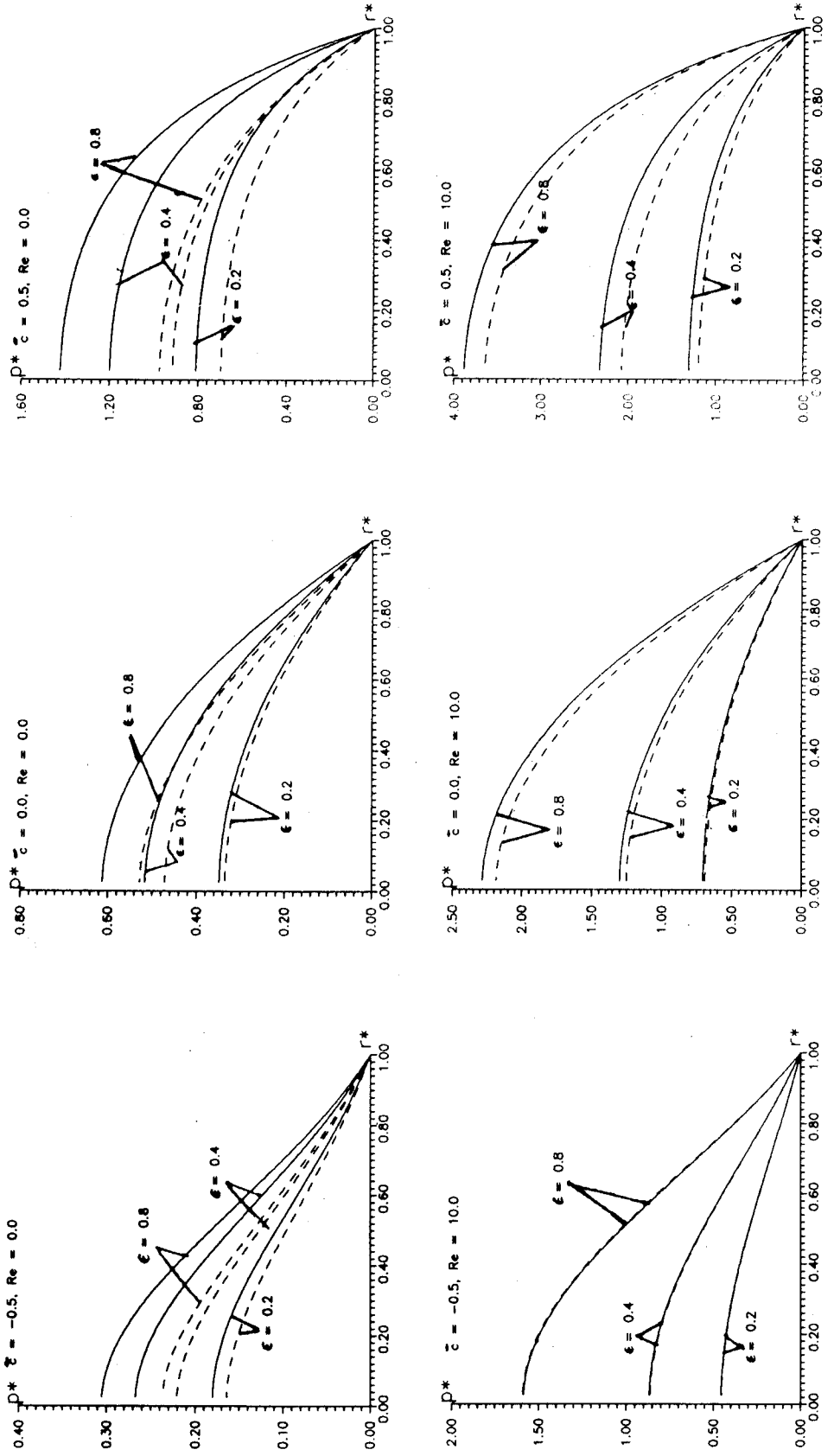

Fig. 2 Radial pressure distribution for different amplitudes of sinusoidal squeeze motion (numerical); $T=0.8$; ------ $\delta_1=1.0$; —— $\delta_1=0.0$

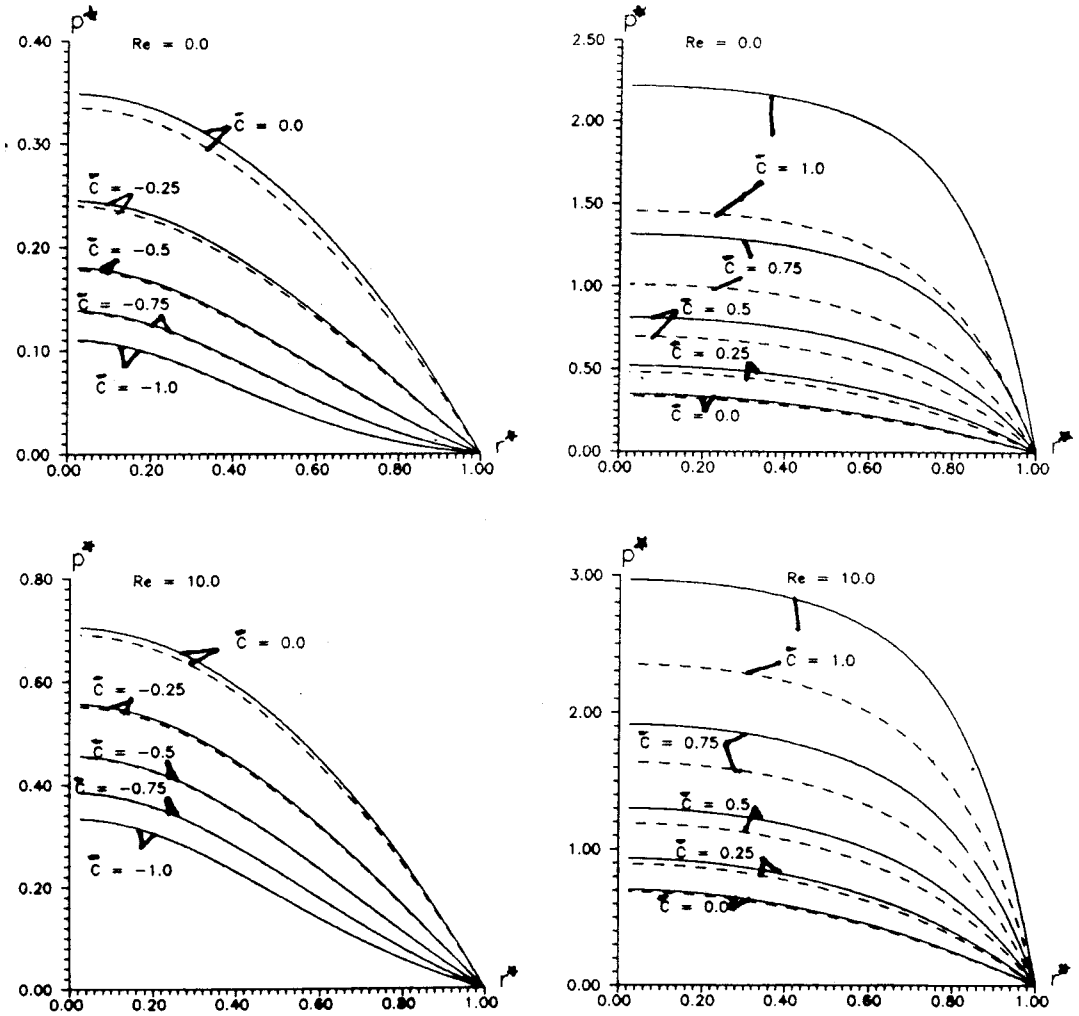

Fig. 3 Effects of curvature on radial pressure distribution (numerical) $\varepsilon=0.2$, $T=0.8$; ——$\delta_1=0.0$; — — —$\delta_1=10$

It is observed that the radial pressure gradient in the non-Newtonian squeeze film obtained from Eq. (19) for the case of a flat circular disk ($\bar{c}=0.0$) is identical to the result presented by Hashimoto and Wada [2].

The pressure distribution p^*, is obtained by integrating Eq. (19) and this requires a knowledge of the modified pressure gradient f_e^*. This is obtained by solving Eq. (16) for f_e^*. The radial and the axial velocity in the squeeze film are then obtained from (17) and (4), respectively.

3 Approximate Analytical Solution

A perturbation method is employed to determine the dimensionless squeeze film pressure. The dimensionless pressure p^*, the dimensionless modified pressure gradient f_e^* and the radial velocity component u^* are expanded for $0\leqslant \mathrm{Re}<1$ as

$$f_e^*=(f_{e00}+\delta f_{e01})+\mathrm{Re}(f_{e10}+\delta f_{e11})+O(\mathrm{Re}^2) \tag{20}$$

$$p^*=(p_{00}+\delta p_{01})+\mathrm{Re}(p_{10}+\delta p_{11})+O(\mathrm{Re}^2) \tag{21}$$

$$u^*=(u_{00}+\delta u_{01})+\mathrm{Re}(u_{10}+\delta u_{11})+O(\mathrm{Re}^2). \tag{22}$$

Substituting (20), (21) and (22) in (16) and (19) and equating the like powers of Re, and using the boundary condition on p^*, the solution under the assumption $-1<\delta<1$ is obtained as

$$f_{e00}=\frac{6r^*}{h^{*3}e^{-3\bar{c}r^{*2}}}\frac{dh^*}{dT} \tag{23}$$

$$p_{00}=\frac{(e^{3\bar{c}r^{*2}}-c^{3\bar{c}})}{\bar{c}h^{*3}}\frac{dh^*}{dT} \tag{24}$$

$$f_{e01}=-\frac{162r^{*3}}{5h^{*7}e^{-7\bar{c}r^{*2}}}\left(\frac{dh^*}{dT}\right)^3 \tag{25}$$

$$p_{01}=-\frac{81}{35h^{*7}}\left(\frac{dh^*}{dT}\right)^3\left[\frac{1}{\bar{c}}(r^{*2}e^{7\bar{c}r^{*2}}-e^{7\bar{c}})-\frac{1}{7\bar{c}^2}(e^{7\bar{c}r^{*2}}-e^{7\bar{c}})\right] \tag{26}$$

$$f_{e10}=0 \tag{27}$$

$$p_{10}=\frac{1}{4h^*}\left(\frac{e^{\bar{c}r^{*2}}-e^{\bar{c}}}{\bar{c}}\right)\left(\frac{d^2h^*}{dT^2}\right)-\frac{3}{20h^{*2}}\left(\frac{e^{2\bar{c}r^{*2}}-e^{2\bar{c}}}{\bar{c}}\right)\left(\frac{dh^*}{dT}\right)^2-\frac{3}{20h^{*2}}(r^{*2}e^{2\bar{c}r^{*2}}-e^{2\bar{c}})\left(\frac{dh^*}{dT}\right)^2 \tag{28}$$

$$f_{e11}=0 \tag{29}$$

$$p_{11}=\frac{27}{35h^{*6}}\left(\frac{dh^*}{dT}\right)^4\left\{\left(\frac{r^{*4}e^{6\bar{c}r^{*2}}-e^{6\bar{c}}}{6}\right)+\left(\frac{r^{*2}e^{6\bar{c}r^{*2}}-e^{6\bar{c}}}{36\bar{c}}\right)-\left(\frac{e^{6\bar{c}r^{*2}}-e^{6\bar{c}}}{216\bar{c}^2}\right)\right\} \tag{30}$$

Thus, the pressure distribution is obtained from (21), (24), (26), (28) and (30) as

$$\begin{aligned}p^*=&\frac{1}{h^{*3}}\left(\frac{dh^*}{dT}\right)\left(\frac{e^{3\bar{c}r^{*2}}-e^{3\bar{c}}}{\bar{c}}\right)\\&-\frac{81\delta}{35h^{*7}}\left(\frac{dh^*}{dT}\right)^3\left[\left(\frac{r^{*2}e^{7\bar{c}r^{*2}}-e^{7\bar{c}}}{\bar{c}}\right)-\left(\frac{e^{7\bar{c}r^{*2}}-e^{7\bar{c}}}{7\bar{c}^2}\right)\right]\\&+\mathrm{Re}\left[\frac{1}{4h^*}\left(\frac{d^2h^*}{dT^2}\right)\left(\frac{e^{\bar{c}r^{*2}}-e^{\bar{c}}}{\bar{c}}\right)\right.\\&-\frac{3}{20h^{*2}}\left(\frac{dh^*}{dT}\right)^2\left(\frac{e^{2\bar{c}r^{*2}}-e^{2\bar{c}}}{\bar{c}}\right)-\frac{3}{20h^{*2}}\left(\frac{dh^*}{dT}\right)^2\\&\times(r^{*2}e^{2\bar{c}r^{*2}}-e^{2\bar{c}})+\frac{27\delta}{35h^{*6}}\left(\frac{dh^*}{dT}\right)^4\left\{\left(\frac{r^{*4}e^{6\bar{c}r^{*2}}-e^{6\bar{c}}}{6}\right)\right.\\&\left.\left.+\left(\frac{r^{*2}e^{6\bar{c}r^{*2}}-e^{6\bar{c}}}{36\bar{c}}\right)-\left(\frac{e^{6\bar{c}r^{*2}}-e^{6\bar{c}}}{216\bar{c}^2}\right)\right\}\right]+O(\mathrm{Re}^2)\end{aligned} \tag{31}$$

For a given motion of the upper curved disk, equation (31) gives the pressure distribution in the curved squeeze film for small values of the parameter δ (characterizing the non-Newtonian behavior of the liquid lubricant) and the squeeze Reynolds number Re.

4 Results and Discussion

The approximate analytical solution presented above is valid for small values of the parameters δ and the squeeze Reynolds number Re. For other values of these parameters, the equations (16) and (19) are solved numerically for radial pressure distribution for given sinusoidal motion of the upper curved disk ($h^*(T)=1+\epsilon\sin T$). It is observed that (Figures 2, 3)

(i) the pressure distribution for pseudoplastic fluids is less than that for Newtonian fluids for both flat and curved squeeze films,

(ii) with the increase of the curvature parameter, the pressure distribution increases for the concave disk and the reverse trend is noted for convex disks,

(iii) the changes in pressure due to inertia effects, though small are not negligible,

(iv) film pressure increases with the increase in amplitude and this increase is enhanced by the fluid inertia effects.

It is worth mentioning that the paper combines elegantly the method of averaged inertia or modified lubrication theory for non-Newtonian squeeze films and the small perturbation method to treat lubricant inertia and presents the general solution for the velocity components and the radial pressure gradient in a non-Newtonian curved squeeze film, for a given motion of the upper curved moving surface. The numerical results indicate a marked influence of fluid inertia, pseudoplasticity of the lubricant and the curvature of the upper curved disk on the pressure distribution in the squeeze film.

Acknowledgments

The authors thank both the referees for their very useful suggestions and comments. The authors also wish to thank the Associate Editor Prof. Dennis Siginer for his very encouraging remarks.

References

[1] Wada, S., and Hayashi, H., 1971, "Hydrodynamic Lubrication of Journal Bearings by Pseudoplastic Lubricants Part II: Experimental Studies," Bull. JSME, **14**, pp. 279–286.

[2] Hashimoto, H., and Wada, S., 1986, "The Effects of Fluid Inertia Forces in Parallel Circular Squeeze Film Bearings Lubricated With Pseudoplastic Fluids," ASME J. Tribol., **108**, pp. 282–287.

[3] Hashimoto, H., and Wada, S., 1986, "The Effects of Fluid Inertia Forces in Squeeze Film Bearings Lubricated With Pseudoplastic Fluids (2nd Report, Annular Parallel Plate Squeeze Film Bearings)," Bull. JSME, **29**, pp. 1913–1918.

[4] Tichy, J. A., and Skinkle, M. E., 1979, "An Analysis of the Flow of a Viscoelastic Fluid Between Arbitrary Two Dimensional Surface Subject to Normal High Frequency Oscillations," ASME J. Lubr. Technol., **101**, pp. 145–151.

[5] Tichy, J. A., 1982, "Effects of Fluid Inertia and Viscoelasticity on Squeeze Film Bearing Forces," ASLE Trans., **25**, pp. 125–132.

[6] Tichy, J. A., 1982, "Effects of Fluid Inertia and Viscoelasticity on Squeeze Film Bearing Forces at Large Vibration Amplitudes," Wear, **76**, pp. 69–89.

[7] Tichy, J. A., 1996, "Non-Newtonian Lubrication With the Convected Maxwell Model," ASME J. Tribol., **118**, pp. 344–348.

[8] Murti, P. R. K., 1975, "Squeeze Films in Curved Circular Plates," Trans. ASME, **97**, pp. 650–652.

[9] Gupta, R. S., and Kapur, V. K., 1980, "The Simultaneous Effects of Thermal and Inertia in Curved Circular Squeeze Films," ASME J. Lubr. Technol., **102**, pp. 501–504.

[10] Hasegawa, E., 1985, "On Squeeze Film of a Curved Circular Plate," Bull. JSME, **28**, pp. 951–958.

Large Deflection Analysis of a Biomimetic Lobster Robot Antenna due to Contact and Flow

T. G. Barnes

T. Q. Truong

G. G. Adams
Fellow ASME

Department of Mechanical, Industrial, and Manufacturing Engineering, Northeastern University, Boston, MA 02115

N. E. McGruer
Department of Electrical and Computer Engineering, Northeastern University, Boston, MA 02115

Lobsters use their antennae to navigate among obstacles along the ocean floor. Effective ambulation requires that the lobster, or a biomimetic lobster robot whose behavior is patterned after a real lobster, must distinguish between antenna bending due to contact and bending due to flow. The analysis presented here shows that the key feature appears to be the taper of the antennae. The curvature of a tapered antenna due to an end-load is nearly constant whereas the curvature distribution due to flow is nearly a quadratic function of the arc-length measured from the tip of the antenna. [DOI: 10.1115/1.1406955]

Introduction

Biomimetics is an emerging branch of science and technology in which synthetic systems are developed using information obtained from biological systems. The authors are part of a research

Contributed by the Applied Mechanics Division of THE AMERICAN SOCIETY OF MECHANICAL ENGINEERS for publication in the ASME JOURNAL OF APPLIED MECHANICS. Manuscript received by the ASME Applied Mechanics Division, Nov. 6, 2000; final revision, June 12, 2001. Associate Editor: R. C. Benson.

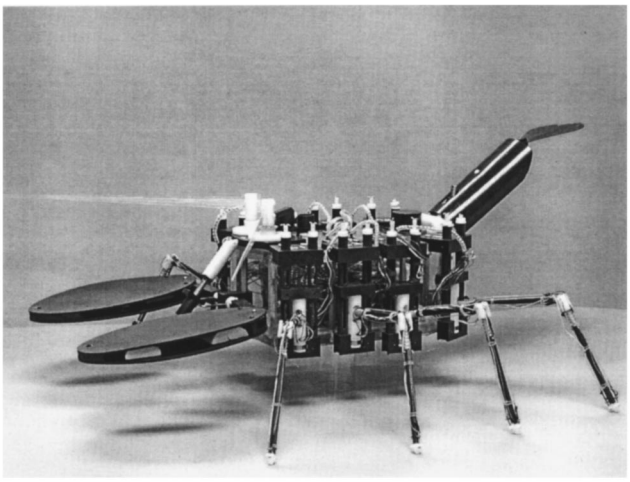

Fig. 1 A biomimetic lobster robot

effort to design and construct a biomimetic lobster robot (Fig. 1). These underwater ambulatory vehicles are to be used to search for and destroy mines in the littoral zone. The robot design and its behavior mimics those of lobsters which have evolved over many hundreds of thousands of years to optimize their search for food on the ocean floor. Lobsters use both their sight and their antennae in order to navigate the rocky and uneven sea floor in the coastal area. However, experiments have shown that blindfolded lobsters can navigate well by using their antennae alone ([1]). When the end of an antenna touches an obstacle, the contact force causes the antenna to bend. *It is the bending of the antenna which the lobster uses to sense the nearby obstruction*. On the other hand, water flow due to surf or currents will also cause these flexible antennae to bend, often to the same degree as when contacting an obstacle. How then does a lobster distinguish antenna bending due to contact and bending due to flow? How do we design the biomimetic lobster robot so that it can distinguish between contact and flow? It was an attempt to answer these questions which motivated this investigation.

Antenna Design

The design of the lobster robot antenna is based on that of a real lobster antenna, specifically the function that it serves as a sensing device to detect contact with an obstacle. Each antenna is composed of two halves of machined PVC sheets, each of which is 20 mils thick with a milled slot 10 mils deep ([2]). The bending sensors and flexible circuit are sandwiched in the slot between the two halves which serves as a housing to isolate the sensors and circuit from the sea water (Fig. 2). The antenna design has a tapered width in order to mimic the antennae of a real lobster. As will be shown later in this note, it is the taper which is the crucial feature which allows the lobster to distinguish between bending due to contact and bending due to flow. There are three bending sensors, one at each of three points on the antenna axis (Fig. 2).

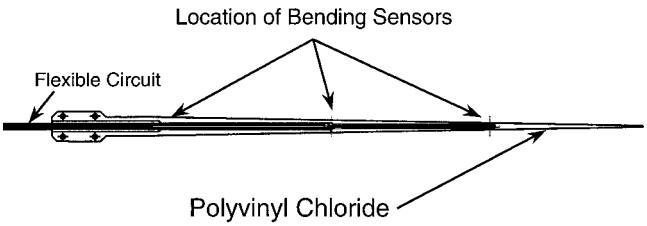

Fig. 2 PVC antenna with bending sensors and a flexible circuit

Each sensor is a simple switch which is either open or closed depending upon whether or not the local curvature exceeds a threshold value.

Analysis

The slope of the bent antenna can be quite large and so an analysis of the antenna deformation requires the use of the large deflection and small material strain theory known as the *elastica* ([3]). These calculations will determine the relationship between the antenna curvature and the magnitude and direction of the end-load and water flow. In order to simplify the analysis and numerical computations, an x-y coordinate system (with arc-length coordinate s) is placed at the tip of the antenna as shown in Fig. 3, whereas the X-Y-axes are attached to the fixed end. In Fig. 3, α is the angle between the end-load P and the Y-axis, β is the angle between the direction of water flow and the Y-axis, $\phi(s)$ is the angle between the tangent to the curve and the x-direction (tangent to the free end), and ϕ_L is the angle of rotation of the free end of the antenna.

From Frisch-Fay [3] the moment-curvature equation for the elastica is given by

$$EI\frac{d\phi}{ds}=M \tag{1}$$

in which E is the Young's modulus, I is the second moment of the cross-sectional area, and M is the internal bending moment. Taking the derivative of (1) with respect to the arc-length coordinate gives

$$EI\frac{d^2\phi}{ds^2}+E\frac{dI}{ds}\frac{d\phi}{ds}=\frac{dM}{ds}=V \tag{2}$$

in which V is the internal shearing force, $I=\frac{1}{12}wt^3$, where $w=w(s)$ and t are the width and thickness respectively of the antenna cross section. For this uniformly tapered antenna dI/ds is constant. Equation (2) is subject to the boundary conditions of zero angular rotation and vanishing bending moment, i.e.,

$$\phi(0)=0,\quad \frac{d\phi}{ds}(0)=\frac{P\cos(\alpha-\phi_L)}{EdI/ds}. \tag{3}$$

It is noted that the first of these conditions is a consequence of the choice of the x-y coordinate system. The second condition gives a nonzero curvature at the free end due to the vanishing values of both the moment and the second moment of the area at that point. It is noted that the lobster moves slowly (several cm/s) and its antennae are very flexible and highly damped due to the surrounding sea water. Thus the effect of antennae vibration induced by sudden contact with an obstacle is negligible.

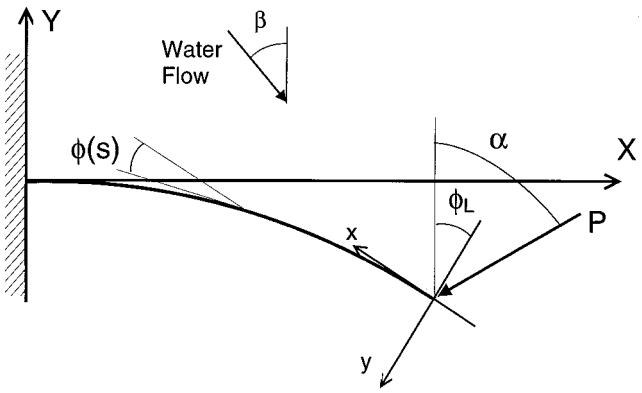

Fig. 3 An antenna acted upon by an end-load and by water flow

It is now necessary to relate the internal shear force (V) to the contact force and pressure due to the water flow using equilibrium and a simplified description of the water flow. The use of a drag coefficient ([4]) for the component of the flow normal to the antenna leads to the force per unit length acting perpendicular to the antennae ($\frac{1}{2}C_D\rho[U\cos(\phi'-\phi_L-\beta)]^2w'$) at $s=s'$. This quantity is then integrated and combined with the shear force contribution due to the end-load in order to obtain

$$V(s)=P\cos(\alpha-\phi_L+\phi)+\frac{1}{2}C_D\rho U^2 \times\int_0^s w'\cos^2(\phi'-\phi_L-\beta)\cos(\phi-\phi')ds' \qquad (4)$$

where C_D is the drag coefficient, ρ is the water density, U is the flow speed, β is the flow angle, $\phi'=\phi(s')$, and $w'=w(s')$. Equations (2) and (4) can be readily combined in order to obtain a second-order nonlinear differential equation for ϕ which is subject to the two boundary conditions (3). These equations were solved numerically using standard software for the solution of ordinary differential equations. Note that the choice of the x-y coordinate system has allowed this equation to be solved as an initial value problem, rather than as a boundary value problem. After determining $\phi(s)$ it is a simple matter to determine the curvature $d\phi/ds$ at any point.

Results and Discussion

The antenna is 11.12 mm wide at the base, 0.327 m long, and 1.016 mm thick. The Young's modulus of PVC is 2.2 GPa. Results are shown in Fig. 4 for the tip angle (ϕ_L) as a function of the end-load angle (α), for various values of the end-load (P) and with zero flow velocity. The tip angle vanishes for $\alpha=-90$ deg which corresponds to an axial tensile load. The tip angle also vanishes for $\alpha=90$ deg which corresponds to an axial compressive load provided that P is less than the buckling load (P_{cr}). Thus for sufficiently large P, the results are multivalued if $\alpha>90$ deg with the upper branch representing stable equilibrium. Note that for small P the maximum tip angle occurs when α is close to zero, i.e., when the load is perpendicular to the initial beam configuration. However, as the load increases the maximum value of ϕ_L occurs for progressively larger values of α due to the effect of the tip rotation on the deflection.

Results are shown in Fig. 5 for the tip angle (ϕ_L) as a function of the flow angle (β), for various values of the flow-speed (U) and with a vanishing end-load. Again the tip angle vanishes when $\beta=\pm90$ deg with an instability occurring now for large flow speeds and β near -90 deg. For low flow speeds the maximum tip angle occurs when β is close to zero, but due to the nonlinearity the maximum tip angle occurs for increasingly negative values of β.

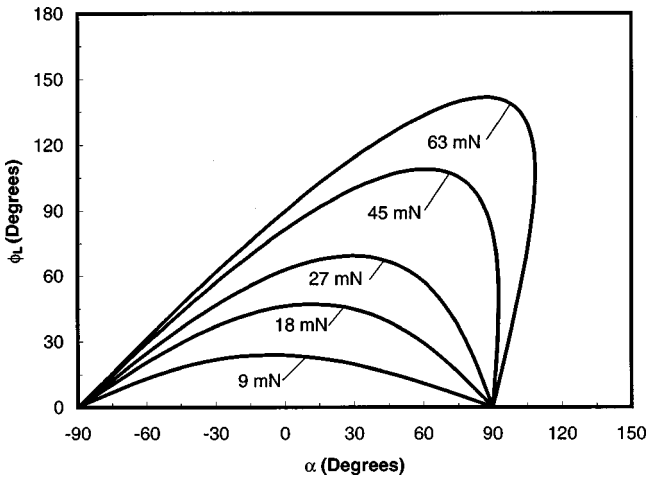

Fig. 4 Maximum deflection angle versus angle of applied load for various values of the applied load and with zero flow

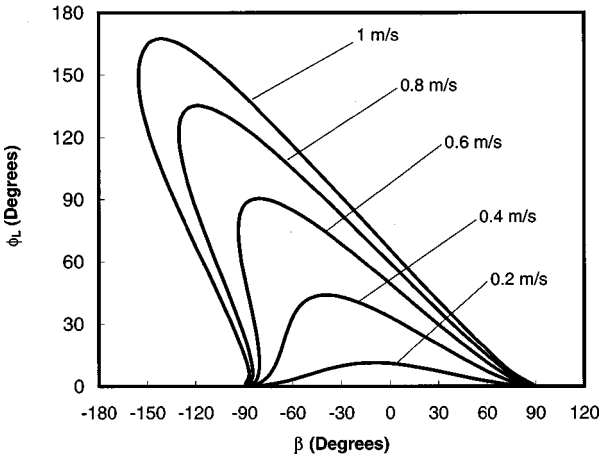

Fig. 5 Maximum angle of deflection versus angle of flow for various flow speeds and with vanishing end-load

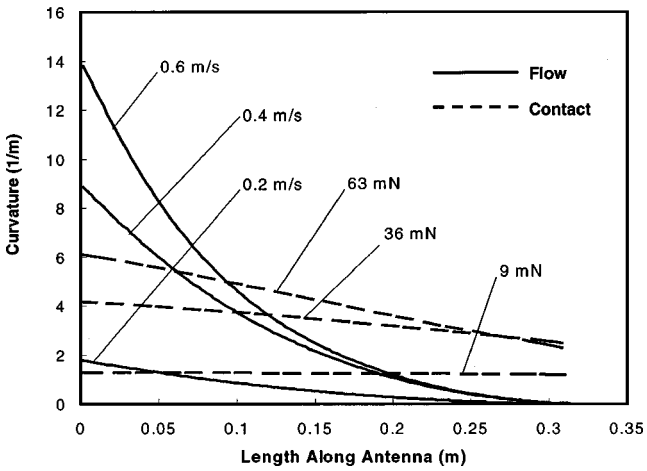

Fig. 6 Curvature along the antennae for various flow rates and applied end loads

It is the curvature of the antenna, at the locations of the three sensors, which will activate the sensors. Thus Fig. 6 shows the variation of the antenna curvature with arc-length coordinate s (measured from the fixed end) for various flow speeds (with $\beta=0$ and $P=0$) and contact forces (with $\alpha=0$ and $U=0$). Under the action of an end-load, the curvature at the free end is not zero as previously discussed and is not monotonic with the applied load. The latter result is due to the nonlinear effect associated with the rotation of the end under increasing applied load. An increase in the applied load does not produce a proportional increase in curvature because the angle of rotation (ϕ_L) also increases $(3)_2$. It is noted that it is possible to use a prescribed displacement boundary condition or a prescribed end-load condition. Either family of curves would contain the same essential information. Also note the dramatic difference in curvature distribution for contact and for flow. For contact the curvature distribution is nearly constant. For flow the curvature is zero at the free end and increases nearly quadratically to a maximum at the fixed end.

A simple linear analysis for a transverse end-load shows that the curvature ($d\phi/ds$ in Eq. (1)) for a *tapered* beam is exactly constant because both the bending moment (M) and the second moment of the area (I) increase linearly with distance from the

free end. However, for flow the linear analysis gives a linearly varying load per unit length which yields a cubic distribution of internal moment and a quadratic distribution of curvature. Now consider a *constant* cross-section antenna. The curvature and internal moment are linear functions of position for the end-load and quadratic functions of position for flow. Hence the tapered antenna is more capable of distinguishing between deformation due to contact and deformation due to flow, than is the uniform antenna. The nonlinear theory used in this paper is necessary due to the large angles of rotation. Nonetheless it is still true that, for a tapered antenna, the distribution of curvatures due to contact and flow differ greatly and allows the lobster robot to distinguish between antenna deflections due to contact and deflections due to flow.

Acknowledgments

The authors are grateful to the Controlled Biological Systems Program of DARPA for their support of this work under Grant N00014-98-1-0381.

References

[1] Ayers, J., 1995, "A Reactive Ambulatory Robot Architecture for Operation in Current and Surge," *Proceedings of the Autonomous Vehicles in Mines Countermeasures Symposium*, pp. 15–31.

[2] Truong, T. Q., Barnes, T. G., Lu, X., Adams, G. G., and McGruer, N. E., 1999, "Design, Analysis, Fabrication, and Testing of a MEMS Contact/Bending Sensor With Improved Dynamics Range," *Micro-Electro-Mechanical Systems (MEMS) 1999*, MEMS-Vol. 1, ASME, New York.

[3] Frisch-Fay, R., 1962, *Flexible Bars*, Butterworths, London.

[4] Munson, B. R., Young, D. F., and Okiishi, T. H., 1998, *Fundamentals of Fluid Mechanics*, 3rd Ed., John Wiley and Sons, New York.

A New Approach to Nonlinear Oscillations

B. Wu
e-mail: bswu@public.cc.jl.cn

P. Li

Department of Mathematics, Jilin University,
Changchun 130012, P. R. China

This paper deals with nonlinear oscillation of a general single-degree-of-freedom system. By combining the linearization of the governing equation with the method of harmonic balance, we establish two analytical approximate formulas for the period. These two formulas are valid for small as well as large amplitudes of oscillation. [DOI: 10.1115/1.1406960]

Introduction

The widest used analytical techniques to solve nonlinear oscillations are the perturbation methods (Nayfeh [1] and Mickens [2]). However, an analytical approximate solution given by the perturbation methods has, in most cases, a small range of validity. In some cases, one may apply the method of harmonic balance to obtain an analytic approximate solution ([1–3]), which is valid even for strongly nonlinear systems. But it is difficult to give high-order analytical approximate formulas by applying the method. Therefore one needs to develop some analytical techniques which can overcome the above-mentioned difficulties.

Consider a single-degree-of-freedom system governed by

$$\frac{d^2u}{dt^2}+f(u)=0, \quad u(0)=\beta, \quad \frac{du}{dt}(0)=0. \tag{1}$$

Let $F(u)=\int f(u)du$ be the potential energy of the system and suppose it arrives at its minimum at $u=u_0$, called a center. We may assume $u_0=0$. For the special case of $f(u)$ being odd function of u, Agrwal and Denman [4] and Liao and Chwang [5] applied the weighted linearization method and the homotopy analysis method, respectively, to establish analytical approximate formulas for the period. In this paper we consider the case of $f(u)$ being a general function of u, then the system will oscillate between asymmetric limits $[\alpha,\beta]$ where both α and β have the same energy level, i.e., $F(\alpha)=F(\beta)$.

A new approximate method will be presented to solve Eq. (1). By combining the linearization of governing equation with the method of harmonic balance, we establish two analytical approximate formulas for the period. These two formulas are valid for small as well as large amplitudes of oscillation.

Solution Method

A new independent variable, $\tau=pt$, is introduced, Eq. (1) becomes

$$p^2u''+f(u)=0, \quad u(0)=\beta, \quad u'(0)=0 \tag{2}$$

where a prime denotes differentiation with respect to τ. The new independent variable τ is chosen in such a way that the solution of Eq. (2) is a periodic function of τ, of period 2π. The corresponding period is given by $T=2\pi/p$.

Let $u_0(\tau)$ be an approximation to $u(\tau)$, which is a periodic function of τ, of period 2π, and satisfies initial conditions in Eq. (2). The idea is to express the periodic solution of Eq. (2) with the assigned initial conditions in the form $u_0(\tau)+v(\tau)$, which is composed of the harmonics of the motion. Here, $u_0(\tau)$ is the main part and $v(\tau)$ is the correction part. Then $v(\tau)$ is assumed to satisfy, via linearization of Eq. (2), the following equation:

$$p^2u_0''+f(u_0)+p^2v''+f_u(u_0)v=0, \quad v(0)=0, \quad v'(0)=0. \tag{3}$$

Solving the resulting linear Eq. (3) in v, by the method of harmonic balance, will give the approximate period and corresponding periodic solution.

Note that the trajectories around the center are not necessarily symmetric with respect to the center. Thus the motion appears to drift as the amplitude increases: The midpoint of the motion is not the center. Following the fact above, a reasonable and simple initial approximation satisfying initial conditions in Eq. (2) is given by

$$u_0(\tau)=\frac{\beta+\alpha}{2}+\frac{\beta-\alpha}{2}\cos\tau \tag{4}$$

where for $\tau=\pi$, $u_0(\tau)$ arrives at the minimum α of $u(\tau)$. Based on the selection of $u_0(\tau)$, $v(\tau)$ should satisfy, in addition initial conditions in Eq. (3), $v(\pi)=0$. We expand $f[u_0(\tau)]$ and $f_u[u_0(\tau)]$, respectively, into the Fourier series of τ:

$$f[u_0(\tau)]=\frac{a_0}{2}+\sum_{i=1}^{\infty}a_i\cos(i\tau),$$
$$f_u[u_0(\tau)]=\frac{b_0}{2}+\sum_{i=1}^{\infty}b_i\cos(i\tau). \tag{5}$$

First, we take

Contributed by the Applied Mechanics Division of THE AMERICAN SOCIETY OF MECHANICAL ENGINEERS for publication in the ASME JOURNAL OF APPLIED MECHANICS. Manuscript received by the ASME Applied Mechanics Division, June 7, 2000; final revision, June 10, 2001. Associate Editor: D. A. Siginer.

$$v(\tau)=c_0[1-\cos(2\tau)]. \tag{6}$$

Substituting Eqs. (5) and (6) into Eq. (3), equating the constant term and the coefficient of $\cos\tau$ to zeros, respectively, and solving the set of resulting equations for p and c_0, we can obtain the first approximation to period T:

$$T_1=2\pi\left\{\frac{2}{\beta-\alpha}\left[a_1-\frac{a_0(b_1-b_3)}{2(b_0-b_2)}\right]\right\}^{-1/2}. \tag{7}$$

Next, we take

$$v(\tau)=c_0[1-\cos(2\tau)]+c_1[\cos\tau-\cos(3\tau)]. \tag{8}$$

Substituting Eqs. (5) and (8) into Eq. (3), equating the constant term, the coefficients of $\cos\tau$ and $\cos 2\tau$ to zeros, respectively, and solving the set of resulting equations for p, c_0, and c_1, leads to the second approximation to period T:

$$T_2=2\pi\left[\frac{-B\pm(B^2-4AC)^{1/2}}{2A}\right]^{-1/2} \tag{9}$$

where

$$A=8[(\beta-\alpha)(b_1-b_3)-2a_0],$$

$$B=[(b_0-b_2)(b_3-b_5)-(2b_2-b_0-b_4)(b_1-b_3)](\alpha-\beta)$$
$$-16a_1(b_1-b_3)+2a_0(5b_0-2b_2-3b_4)+4a_2(b_0-b_2),$$

$$C=2a_1(b_0-b_2)(b_3-b_5)+(b_0-b_4)[a_0(2b_2-b_0-b_4)$$
$$-2a_2(b_0-b_2)]+(b_1-b_3)[a_0(b_3-b_5)+2a_1(2b_2-b_0-b_4)$$
$$+2a_2(b_1-b_3)].$$

The sign before $\sqrt{B^2-4AC}$ in Eq. (9) should be determined by the condition that the ratio T_2/T_1 is near 1 as β tends to 0. High-order approximations for period T can be established in a similar way.

Example

We take the oscillator with second-order nonlinearity as an example to illustrate the use and the effectiveness of the proposed approach. The motion equation is

$$\frac{d^2u}{dt^2}+u+u^2=0,\ u(0)=\beta,\quad \frac{du}{dt}(0)=0. \tag{10}$$

For this problem, $f(u)=u+u^2$, $f_u(u)=1+2u$. The Fourier series expansions of $f[u_0(\tau)]$ and $f_u[u_0(\tau)]$ are given in Eq. (5) where $a_0=\beta+\alpha+(\beta+\alpha)^2/2+(\beta-\alpha)^2/4$; $a_1=(\beta-\alpha)(1+\beta+\alpha)/2$; $a_2=-(\beta-\alpha)^2/8$; $b_0=2(1+\beta+\alpha)$; $b_1=\beta-\alpha$; $a_{i+1}=b_i=0(i=2,3,\ldots)$. Substitution of the these coefficients into Eqs. (7) and (9), respectively, gives two analytical approximate formulas to the period T:

$$T_1=2\pi\left[\frac{8+12\alpha+12\beta+5\alpha^2+14\alpha\beta+5\beta^2}{8(1+\alpha+\beta)}\right]^{-1/2} \tag{11}$$

and

$$T_2=2\pi\left[\frac{-B_0+(B_0^2-4A_0C_0)^{1/2}}{2A_0}\right]^{-1/2} \tag{12}$$

where

$$A_0=-4(\alpha^2+6\alpha\beta+\beta^2+4\alpha+4\beta),$$

$$B_0=2(1+\alpha+\beta)(3\alpha^2+14\alpha\beta+3\beta^2+10\alpha+10\beta),$$

$$C_0=(\beta-\alpha)^4/4-2(1+\alpha+\beta)(\alpha^2+2\alpha\beta+\beta^2+2\alpha+2\beta).$$

For the oscillation equation, the approximate periods obtained by the perturbation method and the method of harmonic balance using single-mode approximation are, respectively,

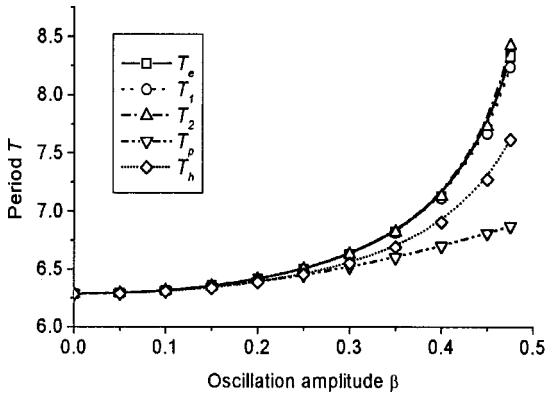

Fig. 1 Comparison of the approximate periods with the exact one

$$T_p=2\pi\left(1+\frac{5}{12}\beta^2\right) \tag{13}$$

and

$$T_h=2\pi\left(1+\alpha+\beta\right)^{-1/2}. \tag{14}$$

The exact period is

$$T_e=2\int_\alpha^\beta\left[\beta^2-u^2+\frac{2}{3}(\beta^3-u^3)\right]^{-1/2}du. \tag{15}$$

For comparison, the exact period in Eq. (15) and the approximate periods computed, respectively, by Eqs. (11), (12), (13), and (14) are pictured in Fig. 1. For the oscillator, the maximum oscillation amplitude should satisfy $\beta<0.5$ (for $\beta=0.5$, Eq. (10) has a homoclinic orbit with period $+\infty$). Figure 1 indicates that formulas (11) and (12) are more exact than formulas (13) and (14), and can give very good approximate periods for both small and large values of β.

Conclusions

We have presented a new method to solve nonlinear oscillation of a general single-degree-of-freedom system. The equation of motion need not contain a small parameter. Unlike the classical harmonic balance method, linearization is performed prior to proceeding with harmonic balancing thus resulting in linear algebraic equations instead of nonlinear algebraic equations. Hence, we are able to establish these approximate analytic formulas for the exact solution. These approximate solutions are valid for small as well as large amplitudes of oscillation.

Acknowledgments

This work was supported by the National Natural Science Foundation of P. R. China, under grant number 19972023, and the excellent youth's teacher fund of the Educational Ministry of P.R. China.

References

[1] Nayfeh, A. H., 1993, *Introduction to Perturbation Techniques*, John Wiley and Sons, New York.

[2] Mickens, R. E., 1996, *Oscillations in Planar Dynamic Systems*, World Scientific, Singapore.

[3] Delamotte, B., 1993, "Nonperterbative Method for Solving Differential Equations and Finding Limit Cycles," Phys. Rev. Lett., **70**, pp. 3361–3364.

[4] Agrwal, V. P., and Denman, H., 1985, "Weighted Linearization Technique for Period Approximation in Large Amplitude Nonlinear Oscillations," J. Sound Vib., **99**, pp. 463–473.

[5] Liao, S. J., and Chwang, A. T., 1998, "Application of Homotopy Analysis Method in Nonlinear Oscillations," ASME J. Appl. Mech., **65**, pp. 914–922.

Three-Dimensional Field Equations of Motion, and Energy Functionals for Thick Shells of Revolution With Arbitrary Curvature and Variable Thickness

J.-H. Kang
Department of Architecture, Chung-Ang University, Seoul, South Korea

A. W. Leissa
Professor, Fellow ASME, Department of Mechanical Engineering, The Ohio State University, Columbus, OH 43210-1154

Equations of motion and energy functionals are derived for a three-dimensional coordinate system especially useful for analyzing the static and dynamic behavior of arbitrarily thick shells of revolution having variable thickness. The field equations are utilized to express them in terms of displacement components.
[DOI: 10.1115/1.1406961]

Introduction

Dozens of books (cf. Leissa [1]) and scores of published papers exist which derive field equations, equations of motion, and/or energy functionals for thin or moderately thick shells of revolution. Such derivations typically make simple kinematic assumptions about the variation of the displacements through the thickness. This reduces the three-dimensional theory to a two-dimensional one characterized by the middle surface displacements. But for thicker shells or higher frequencies (short wave lengths), a three-dimensional analysis is necessary.

This work presents a summary of applicable equations for the three-dimensional analysis of shells of revolution with arbitrary curvature and arbitrary, variable thickness. They are expressed in terms of a curvilinear (ϕ,ζ,θ) coordinate system, as shown in Fig. 1, which is a particularly useful one. They were derived by tensor analysis, relating all quantities to the shell middle surface $(\zeta=0)$. Much of the relevant derivation is available in the dissertation of the first author (Kang [2]). And they have been used successfully to obtain accurate results for some three-dimensional vibration problems (Kang and Leissa [3,4]).

Equations of Motion

Utilizing the general equations in tensorial form, and relating them to the shell midsurface, the equations of motion in terms of the stress components (σ_{ij}) are found to be (Kang [2])

$$\sigma_{\phi\zeta,\zeta}+\frac{1}{r_\zeta}[\sigma_{\phi\theta,\theta}+\sigma_{\phi\zeta}\sin\phi+(\sigma_{\phi\phi}-\sigma_{\theta\theta})\cos\phi]+\frac{1}{\rho_\zeta}(\sigma_{\phi\phi,\phi}+2\sigma_{\phi\zeta})+f_\phi=\rho\ddot{u}_\phi, \tag{1a}$$

$$\sigma_{\zeta\zeta,\zeta}+\frac{1}{r_\zeta}[\sigma_{\zeta\theta,\theta}+(\sigma_{\zeta\zeta}-\sigma_{\theta\theta})\sin\phi+\sigma_{\phi\zeta}\cos\phi]+\frac{1}{\rho_\zeta}(\sigma_{\phi\zeta,\phi}-\sigma_{\phi\phi}+\sigma_{\zeta\zeta})+f_\zeta=\rho\ddot{u}_\zeta, \tag{1b}$$

$$\sigma_{\zeta\theta,\zeta}+\frac{1}{r_\zeta}(\sigma_{\theta\theta,\theta}+2\sigma_{\zeta\theta}\sin\phi+2\sigma_{\phi\theta}\cos\phi)+\frac{1}{\rho_\zeta}(\sigma_{\phi\theta,\phi}+\sigma_{\zeta\theta})+f_\theta=\rho\ddot{u}_\theta \tag{1c}$$

where u_ϕ, u_ζ, and u_θ (circumferential) are displacement components; $\rho_\zeta\equiv\rho_1+\zeta$ and $r_\zeta\equiv(\rho_2+\zeta)\sin\phi$, with ρ_1 and ρ_2 being the principal radii of curvature of the midsurface (Fig. 1); and ρ is mass density per unit volume. The commas and dots are the conventional space and time derivatives.

Assuming a linearly elastic, isotropic material, the stress-strain equations are

$$\sigma_{\phi\phi}=\lambda\varepsilon+2G\varepsilon_{\phi\phi},\quad \sigma_{\zeta\zeta}=\lambda\varepsilon+2G\varepsilon_{\zeta\zeta},\quad \sigma_{\theta\theta}=\lambda\varepsilon+2G\varepsilon_{\theta\theta},\quad \sigma_{\phi\zeta}=2G\varepsilon_{\phi\zeta},\quad \sigma_{\phi\theta}=2G\varepsilon_{\phi\theta},\quad \sigma_{\zeta\theta}=2G\varepsilon_{\zeta\theta}, \tag{2}$$

where λ and G are the Lamé coefficients, and $\varepsilon\equiv\varepsilon_{\phi\phi}+\varepsilon_{\zeta\zeta}+\varepsilon_{\theta\theta}$. The strain-displacement equations are found to be

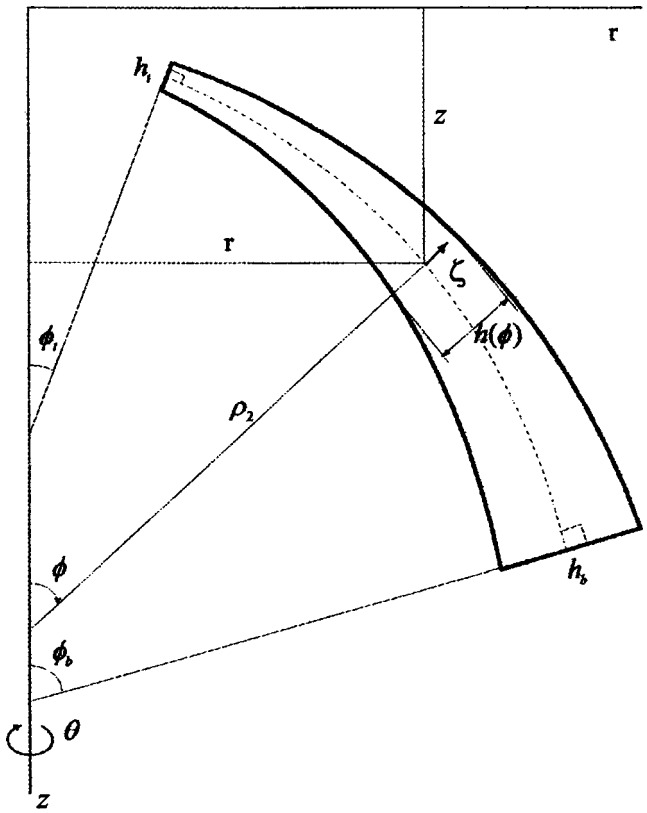

Fig. 1 Cross section of an arbitrary shell of revolution with variable thickness in the meridional direction ϕ and positive Gaussian curvature, and the curvilinear coordinate system (ϕ,ζ,θ)

Contributed by the Applied Mechanics Division of THE AMERICAN SOCIETY OF MECHANICAL ENGINEERS for publication in the ASME JOURNAL OF APPLIED MECHANICS. Manuscript received by the ASME Applied Mechanics Division, June 15, 2000; final revision, May 24, 2001. Associate Editor: R. C. Benson.

$$\varepsilon_{\phi\phi}=\frac{1}{\rho_\zeta}(u_{\phi,\phi}+u_\zeta),\quad \varepsilon_{\zeta\zeta}=u_{\zeta,\zeta},$$

$$\varepsilon_{\theta\theta}=\frac{1}{r_\zeta}(u_{\theta,\theta}+u_\phi\cos\phi+u_\zeta\sin\phi),$$

$$\varepsilon_{\phi\zeta}=\frac{1}{2}\left[u_{\phi,\zeta}-\frac{1}{\rho_\zeta}(u_\phi-u_{\zeta,\phi})\right],\qquad(3)$$

$$\varepsilon_{\phi\theta}=\frac{1}{2}\left[\frac{1}{r_\zeta}(u_{\phi,\theta}-u_\theta\cos\phi)+\frac{u_{\theta,\phi}}{\rho_\zeta}\right],$$

$$\varepsilon_{\zeta\theta}=\frac{1}{2}\left[\frac{1}{r_\zeta}(u_{\zeta,\theta}-u_\theta\sin\phi)+u_{\theta,\zeta}\right].$$

Assuming the material to be homogeneous, and substituting Eqs. (2) and (3) into (1) yields the equations of motion in terms of displacement components:

$$\lambda\left[\frac{u_{\zeta,\phi\zeta}}{\rho_\zeta}+\frac{1}{\rho_\zeta^2}(u_{\zeta,\phi}+u_{\phi,\phi\phi})-\frac{\rho_{1,\phi}}{\rho_\zeta^3}(u_{\phi,\phi}+u_\zeta)+\frac{1}{r_\zeta\rho_\zeta}\{u_{\theta,\phi\theta}+(u_{\zeta,\phi}-u_\phi)\sin\phi+(u_{\phi,\phi}+u_\zeta)\cos\phi\}\right.$$
$$\left.-\frac{\cos\phi}{r_\zeta^2}(u_{\theta,\theta}+u_\zeta\sin\phi+u_\phi\cos\phi)\right]+G\left[u_{\phi,\zeta\zeta}+\frac{u_{\phi,\zeta}\sin\phi}{r_\zeta}-\frac{1}{r_\zeta^2}\{(3u_{\theta,\theta}+2u_\zeta\sin\phi+2u_\phi\cos\phi)\cos\phi-u_{\phi,\theta\theta}\}\right.$$
$$+\frac{1}{r_\zeta\rho_\zeta}\{u_{\theta,\phi\theta}+(u_{\zeta,\phi}-u_\phi)\sin\phi+2(u_{\phi,\phi}+u_\zeta)\cos\phi\}+\frac{1}{\rho_\zeta}(u_{\zeta,\phi\zeta}+u_{\phi,\zeta})$$
$$\left.+\frac{1}{\rho_\zeta^2}(3u_{\zeta,\phi}-u_\phi+2u_{\phi,\phi\phi})-\frac{2\rho_{1,\phi}}{\rho_\zeta^3}(u_{\phi,\phi}+u_\zeta)\right]+f_\phi=\rho\ddot{u}_\phi,\qquad(4a)$$

$$\lambda\left[u_{\zeta,\zeta\zeta}+\frac{1}{r_\zeta}(u_{\theta,\zeta\theta}+u_{\zeta,\zeta}\sin\phi+u_{\phi,\zeta}\cos\phi)-\frac{\sin\phi}{r_\zeta^2}(u_{\theta,\theta}+u_\zeta\sin\phi+u_\phi\cos\phi)+\frac{1}{\rho_\zeta}(u_{\phi,\phi\zeta}+u_{\zeta,\zeta})-\frac{1}{\rho_\zeta^2}(u_{\phi,\phi}+u_\zeta)\right]$$
$$+G\left[2u_{\zeta,\zeta\zeta}+\frac{1}{r_\zeta}(u_{\theta,\zeta\theta}+2u_{\zeta,\zeta}\sin\phi+u_{\phi,\zeta}\cos\phi)+\frac{1}{r_\zeta^2}\{u_{\zeta,\theta\theta}-(3u_{\theta,\theta}+2u_\zeta\sin\phi+2u_\phi\cos\phi)\sin\phi\}+\frac{\cos\phi}{r_\zeta\rho_\zeta}(u_{\zeta,\phi}-u_\phi)\right.$$
$$\left.+\frac{1}{\rho_\zeta}(2u_{\zeta,\zeta}+u_{\phi,\phi\zeta})+\frac{1}{\rho_\zeta^2}(u_{\zeta,\phi\phi}-3u_{\phi,\phi}-2u_\zeta)+\frac{\rho_{1,\phi}}{\rho_\zeta^3}(u_\phi-u_{\zeta,\phi})\right]+f_\zeta=\rho\ddot{u}_\zeta,\qquad(4b)$$

$$\lambda\left[\frac{u_{\zeta,\zeta\theta}}{r_\zeta}+\frac{1}{r_\zeta^2}(u_{\theta,\theta\theta}+u_{\zeta,\theta}\sin\phi+u_{\phi,\theta}\cos\phi)+\frac{1}{r_\zeta\rho_\zeta}(u_{\phi,\phi\theta}+u_{\zeta,\theta})\right]+G\left[u_{\phi,\zeta\zeta}+\frac{u_{\theta,\zeta}}{\rho_\zeta}+\frac{u_{\theta,\phi\phi}}{\rho_\zeta^2}-\frac{\rho_{1,\phi}}{\rho_\zeta^3}u_{\theta,\phi}+\frac{1}{r_\zeta\rho_\zeta}(u_{\zeta,\theta}+u_{\phi,\phi\theta}\right.$$
$$\left.+u_{\theta,\phi}\cos\phi)+\frac{1}{r_\zeta}(u_{\zeta,\zeta\theta}+u_{\theta,\zeta}\sin\phi)+\frac{1}{r_\zeta^2}\{2u_{\theta,\theta\theta}+(3u_{\zeta,\theta}-u_\theta\sin\phi)\sin\phi+(3u_{\phi,\theta}-u_\theta\cos\phi)\cos\phi\}\right]+f_\theta=\rho\ddot{u}_\theta.\qquad(4c)$$

The correctness of Eq. (4) was verified by means of Maple, a symbolic logic computer program. Exact solutions of Eq. (4) are possible for some constant or variable thickness shell configurations, such as circular cylindrical or conical. They may also be useful in using some approximate methods (e.g., Galerkin, finite differences).

Energy Functionals

For other approaches to the problem (e.g., Ritz, finite element) it is desirable to have the energy functionals corresponding to Eq. (4). The strain energy due to deformation is the volume intergral

$$V=\frac{1}{2}\int_\Omega(\sigma_{\phi\phi}\varepsilon_{\phi\phi}+\sigma_{\zeta\zeta}\varepsilon_{\zeta\zeta}+\sigma_{\theta\theta}\varepsilon_{\theta\theta}+2\sigma_{\phi\zeta}\varepsilon_{\phi\zeta}+2\sigma_{\phi\theta}\varepsilon_{\phi\theta}$$
$$+2\sigma_{\zeta\theta}\varepsilon_{\zeta\theta})\rho_\zeta r_\zeta d\phi d\zeta d\theta\qquad(5)$$

with ρ_ζ and r_ζ given previously. Substituting Eqs. (2) and (3) into (5) results in

$$V=\frac{1}{2}\int_\Omega[\lambda(\kappa_1+\kappa_2+\kappa_3)^2+G\{2(\kappa_1^2+\kappa_2^2+\kappa_3^2)$$
$$+\kappa_4^2+\kappa_5^2+\kappa_6^2\}]\rho_\zeta r_\zeta d\phi d\zeta d\theta,\qquad(6)$$

where

$$\kappa_1\equiv\frac{u_\phi\cos\phi+u_\zeta\sin\phi+u_{\theta,\theta}}{r_\zeta},\quad \kappa_2\equiv\frac{u_\zeta+u_{\phi,\phi}}{\rho_\zeta},$$

$$\kappa_3\equiv u_{\zeta,\zeta},\quad \kappa_4\equiv\frac{u_\phi-u_{\zeta,\phi}}{\rho_\zeta}-u_{\phi,\zeta},$$

$$\kappa_5\equiv\frac{u_{\zeta,\theta}-u_\theta\sin\phi}{r_\zeta}+u_{\theta,\zeta},\quad \kappa_6\equiv\frac{u_{\phi,\theta}-u_\theta\cos\phi}{r_\zeta}+\frac{u_{\theta,\phi}}{\rho_\zeta}.$$

The kinetic energy (T) is simply

$$T=\frac{1}{2}\int_\Omega\rho(\dot{u}_\phi^2+\dot{u}_\zeta^2+\dot{u}_\theta^2)\rho_\zeta r_\zeta d\phi d\zeta d\theta.\qquad(7)$$

References

[1] Leissa, A. W., 1971, *Vibration of Shells*, U.S. Government Printing Office; 1993 reprinted by The Acoustical Society of America.

[2] Kang, J.-H., 1997, ''Three-Dimensional Vibration Analysis of Thick Shells of Revolution With Arbitrary Curvature and Variable Thickness,'' Ph.D. dissertation, The Ohio State University.

[3] Kang, J.-H., and Leissa, A. W., 1999, ''Three-Dimensional Vibrations of Hollow Cones and Cylinders With Linear Thickness Variations,'' J. Acoust. Soc. Am., **106**, pp. 748–755.

[4] Kang, J.-H., and Leissa, A. W., 2000, ''Three-Dimensional Vibrations of Thick Spherical Shell Segments With Variable Thickness,'' Int. J. Solids Struct., **37**, pp. 4811–4823.

Torsion of a Circular Compound Bar With Imperfect Interface

T. Chen
e-mail: tchen@mail.ncku.edu.tw

I. S. Weng

Department of Civil Engineering, National Cheng Kung University, Tainan 70101, Taiwan

The Saint-Venant torsion problem of a circular cylinder reinforced by a nonconcentric circular bar of a different material with an imperfect interface is studied. Conformal mapping together with a Laurent series expansion are employed to analyze the problem. The jump condition in either the warping function or the shear traction, characterizing the imperfect interface, is simulated in the transformed domain in an exact manner. Unlike the problem with perfectly bonded interface, the series solution has to be resolved by a truncation. Numerical illustrations are provided for the torsional rigidity of the cross section. In the case of perfect bonding case, our results agree with that reported in Muskhelishvili.
[DOI: 10.1115/1.1406962]

1 Introduction

Benveniste and Chen [1] recently proved that, in Saint-Venant's torsion problem of compound bars, thin interphases with either low or high stiffness between the phases lead to two different types of imperfect interface conditions. The first type involves a jump in the warping displacement, the other in the shear traction. The jump quantity is characterized by a scalar interface parameter which measures the degree of the imperfect bond. Understanding the degree of imperfect bonding on the torsional rigidity is essential in designing compound bars under torsion. The study of the effect of imperfect interface in torsion problems seems to be first explored by Lipton [2], in which the spring-type interface, describing a jump in the warping displacement, was employed to find the optimal fiber configurations for the torsional rigidity. Benveniste and Chen [1] later showed that imperfect interfaces can be used to design so-called ''neutral inhomogeneities'' in torsion problems. These are cylindrical inhomogeneities which can be introduced in a host bar without disturbing the warping function and possibly the torsional stiffness of the host bar. The present work is concerned in providing a most typical benchmark solution: an eccentric reinforcing bar with an imperfect interface in a circular cylinder. The solution of the same boundary value problem with perfect bonding conditions was first obtained by Vekua and Rukhadze [3] (see also [4]). We mention that in the context of heat conduction, rigorous derivations of the interface conditions have been given by Sanchez-Palencia [5] and Pham Huy and Sanchez-Palencia [6].

The displacement field of the Saint-Venant torsion is characterized by $u_x=-\vartheta yz$, $u_y=\vartheta xz$, and $u_z=\vartheta\varphi(x,y)$, where ϑ is the angle of twist per unit length of the bar and φ is the warping function to be determined. Equilibrium condition suggests that φ is harmonic throughout the cross section of the cylinder. A Traction-free boundary condition on the lateral surface of the cylinder gives

$$\frac{d\varphi}{dn}=-\mathbf{v}\cdot\mathbf{n}\ \text{ on }\ C \tag{1}$$

where $\mathbf{v}=-y\mathbf{i}+x\mathbf{j}$ and $\mathbf{n}$ denotes the outward normal to the boundary C of the cross section S. There are two types of interface conditions. The first kind, referred to as the LS type, is characterized by ([1])

$$\Delta\{\mu(\nabla\varphi+\mathbf{v})\cdot\mathbf{n}\}|_\Gamma=0,\quad \mu_1(\nabla\varphi_1+\mathbf{v})\cdot\mathbf{n}|_\Gamma=-\xi\Delta\varphi|_\Gamma, \tag{2}$$

where $\Delta q=q_1-q_2$ denotes the jump in a quantity q across Γ, μ is the shear modulus, $\mathbf{n}$ is the unit normal of the interface pointing from phase 1 to 2, and ξ is the interface parameter. The other type of interface is called the HS type, in which on the interface Γ it follows that ([1])

$$\Delta\varphi|_\Gamma=0,\quad \Delta\{\mu(\nabla\varphi+\mathbf{v})\cdot\mathbf{n}\}|_\Gamma=\nabla_s[\,\eta(\nabla_s\varphi+\mathbf{v}\cdot\mathbf{s})]|_\Gamma, \tag{3}$$

where η is the interface parameter and $\nabla_s\varphi=\nabla\varphi\cdot\mathbf{s}$, $\mathbf{s}$ is the unit tangential vector to Γ chosen as being rotated counterclockwise from the normal vector $\mathbf{n}$. Perfect bonding interfaces correspond to the limiting value of $\xi\to\infty$ or $\eta\to0$.

2 Torsion of a Circular Cylinder Reinforced by a Longitudinal Round Bar of a Different Material

To begin with, we define the cross section as S, consisting of the region S_1 bounded by the circle Γ, and the region S_2, bounded by the same circle Γ and a circle C (Fig. 1). The circles Γ and C need not be concentric. Let the moduli of rigidity of the component bars be μ_1 and μ_2 in S_1 and S_2, respectively. Suppose the radii of the circles Γ and C are respectively given by r_1 and r_2, and the quantity l denotes the distance between their centers ($l<r_2-r_1$). As in ([4]), we introduce the bilinear mapping function

$$z=\omega(\zeta)=\frac{\zeta}{1-a\zeta},\quad a=\frac{l}{\sqrt{(r_1^2-r_2^2)^2-2l^2(r_1^2+r_2^2)+l^4}} \tag{4}$$

in which $z=x+iy$ and $\zeta=\rho e^{i\theta}$. The mapping function (4) will map the circles Γ and C in the z-plane onto concentric circles γ_1 and γ_2 in the ζ plane with radii ρ_1 and $\rho_2(\rho_1<\rho_2)$. Specifically, the region S_1 will correspond to the circle $\sigma_1:|\zeta|<\rho_1$ and S_2 to the circular ring $\sigma_2:\rho_1<|\zeta|<\rho_2$ (Fig. 1), where

$$\rho_1=\frac{\sqrt{1+4r_1^2a^2}-1}{2r_1a^2},\quad \rho_2=\frac{\sqrt{1+4r_2^2a^2}-1}{2r_2a^2}. \tag{5}$$

2.1 An LS-type Interface. For the LS-type interface, the boundary and interface conditions need to be fulfilled by φ_1 and φ_2 are (1) and (2). Let ψ be the function conjugate to φ so that

$$\frac{d\varphi}{dn}=\frac{d\psi}{ds},\quad \frac{d\varphi}{ds}=-\frac{d\psi}{dn} \tag{6}$$

hold on the contour Γ and C. In terms of conjugate functions, Eqs. (1) and (2) become

$$\psi_2=g+\text{const.}|_C,\quad \mu_2\psi_2-\mu_1\psi_1=(\mu_2-\mu_1)g+\text{const.}|_\Gamma, \tag{7}$$
$$\mu_1\frac{d^2}{ds^2}(\psi_1-g)=-\xi\left(\frac{d\psi_2}{dn}-\frac{d\psi_1}{dn}\right)\Bigg|_\Gamma,$$

where the function g is defined as

$$g\equiv\frac{1}{2}(x^2+y^2),\quad -\mathbf{v}\cdot\mathbf{n}=\frac{dg}{ds}. \tag{8}$$

Let $F(z)=\varphi+i\psi$ be the complex torsion function and let $f(\zeta)=\varphi+i\psi$ be the same function in the ζ plane. Let f_1 and f_2 be the values of this functions in σ_1 and σ_2. Then one will have

Contributed by the Applied Mechanics Division of THE AMERICAN SOCIETY OF MECHANICAL ENGINEERS for publication in the ASME JOURNAL OF APPLIED MECHANICS. Manuscript received and accepted by the ASME Applied Mechanics Division, Oct. 4, 2000. Associate Editor: D. A. Kouris.

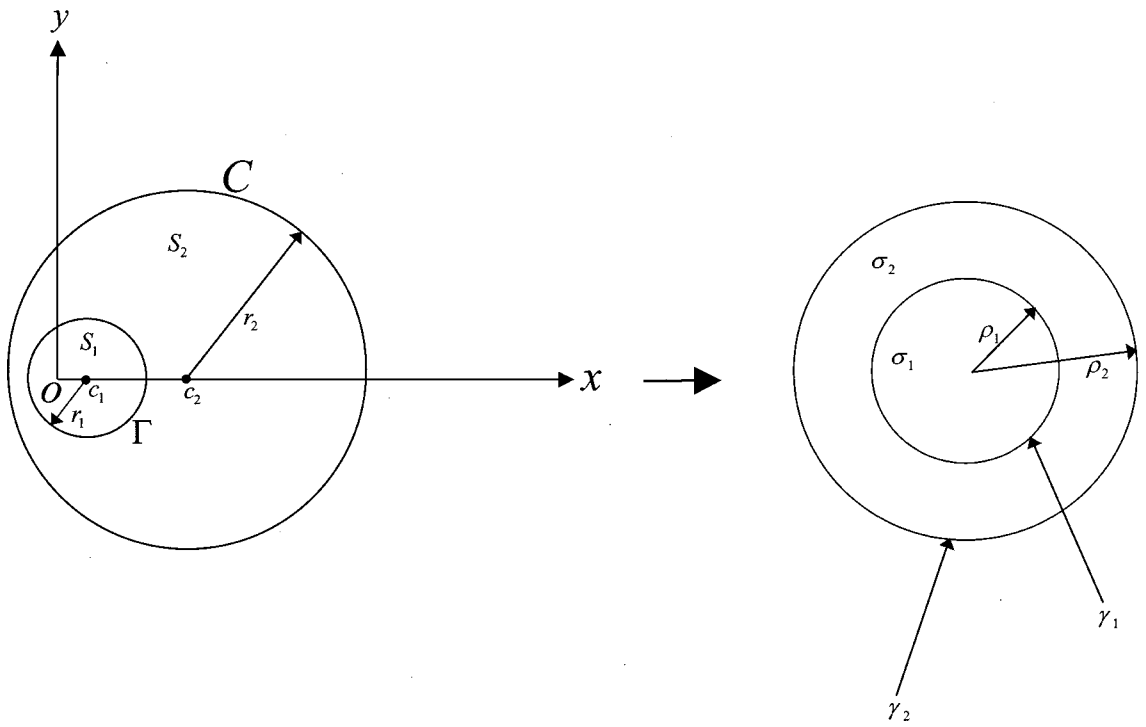

Fig. 1 Mapping from the eccentric cylinder to a circular compound cylinder

$$f_1(\zeta)=\sum_{k=0}^{\infty}(a_k'+ib_k')\zeta^k,\ \text{in}\ \sigma_1,$$
$$f_2(\zeta)=\sum_{k=-\infty}^{\infty}(a_k''+ib_k'')\zeta^k,\ \text{in}\ \sigma_2, \tag{9}$$

where a_k', b_k', a_k'', and b_k'' are some unknown real constants to be determined. Letting $\zeta=\rho e^{i\theta}$ in (9) one finds

$$\psi_1=b_0'+\sum_{k=1}^{\infty}(a_k'\sin k\theta+b_k'\cos k\theta)\rho^k,\ \text{in}\ \sigma_1,$$
$$\psi_2=b_0''+\sum_{k=1}^{\infty}[(\rho^k a_k''-\rho^{-k}a_{-k}'')\sin k\theta + (\rho^k b_k''+\rho^{-k}b_{-k}'')\cos k\theta],\ \text{in}\ \sigma_2. \tag{10}$$

To proceed, we note that due to the conformality of the mapping function there follows

$$\left.\frac{d}{ds}\right|_z=\left|\frac{d\zeta}{dz}\right|\left.\frac{d}{\rho d\theta}\right|_\zeta,\quad \left.\frac{d}{dn}\right|_z=\left|\frac{d\zeta}{dz}\right|\left.\frac{d}{d\rho}\right|_\zeta, \tag{11}$$

where, by virtue of (4), one can show that

$$\left|\frac{d\zeta}{dz}\right|=1-2a\rho\cos\theta+a^2\rho^2. \tag{12}$$

Further, it was shown that the series converges absolutely for $\rho<1/a$ ([1])

$$g=\frac{\rho^2}{1-a^2\rho^2}\left[\frac{1}{2}+\sum_{k=1}^{\infty}a^k\rho^k\cos k\theta\right]\equiv w(\rho,\theta). \tag{13}$$

Now substituting (10) and (13) into (7), using (11) and (12), provides constraints for the determination of the unknown coefficients. Specifically, we found that $a_k'=a_k''=a_{-k}''=0$, $a_0'=a_0''=b_0'=b_0''=0$ and

$$b_k''=\frac{[c_2-(1-\lambda)c_1\alpha^k]a^{k-1}-\lambda\alpha^k b_k'}{1-\alpha^k},$$
$$b_{-k}''=-\frac{[c_2-(1-\lambda)c_1]a^{k-1}-\lambda b_k'}{1-\alpha^k}\rho_1^{2k}, \tag{14}$$

where $\lambda=\mu_1/\mu_2$, $\alpha=(\rho_1/\rho_2)^2$ and c_1 and c_2 are the distances of the centers of Γ and C from the origin given by

$$c_1=\frac{a\rho_1^2}{1-a^2\rho_1^2},\quad c_2=\frac{a\rho_2^2}{1-a^2\rho_2^2}, \tag{15}$$

so that $l=c_2-c_1$. In summary, one obtains

$$\varphi_1(\rho,\theta)=-\sum_{k=1}^{\infty}b_k'\rho^k\sin k\theta, \tag{16}$$

in σ_1 and

$$\varphi_2(\rho,\theta)=\sum_{k=1}^{\infty}(b_{-k}''/\rho^{2k}-b_k'')\rho^k\sin k\theta, \tag{17}$$

in σ_2. The only unknown coefficients b_k' are determined from the relations

$$-a[(k+1)b_{k+1}'+(k-1)\rho_1^{-2}b_{k-1}']\mu_1\rho_1/\xi + \left[k\rho_1^{-1}(1+a^2\rho_1^2)\mu_1/\xi+(1+\lambda)\frac{1-\nu\alpha^k}{1-\alpha^k}\right]b_k' = a^k\rho_1\mu_1/\xi+(1+\lambda)\left[\frac{1-\nu\alpha^k}{1-\alpha^k}c_2+\nu l\frac{1+\alpha^k}{1-\alpha^k}\right]a^{k-1},\quad k\geq 1, \tag{18}$$

where $\nu=(\mu_2-\mu_1)/(\mu_2+\mu_1)$. The recurrence relation of (18) constitutes a linear set of algebraic equations with an infinite number of unknowns, which can be resolved by truncation at any

desired order. By letting $1/\xi \to 0$, the system can be exactly solved without any trunction. In this case, the coefficients b_k' reduce to the simple form

$$b_k' = c_2 a^{k-1} + l\nu \frac{1+\alpha^k}{1-\nu\alpha^k} a^{k-1}, \quad k \geqslant 1 \tag{19}$$

which exactly agrees with the result of Muskhelishvili [4].

2.2 An HS-Type Interface. For the HS-type interface, the conditions satisfied by φ_1 and φ_2 are (1) and (3). In terms of conjugate functions these can be written as

$$\begin{aligned} &\psi_2 = g + \text{const.}|_C, \quad \frac{d\psi_1}{dn} = \frac{d\psi_2}{dn}\bigg|_\Gamma, \\ &\mu_1\psi_1 - \mu_2\psi_2 + (\mu_2 - \mu_1)g = \eta\frac{d}{dn}(g-\psi) + \text{const.}\bigg|_\Gamma. \end{aligned} \tag{20}$$

Again we employ the Laurent series (10) in (20), using the relations (13) and (11). This will provide conditions for the determination of the unknown coefficients. The final expression for the warping function φ_1 remains the same as (16) in σ_1, and φ_2 as

$$\varphi_2(\rho,\theta) = \sum_{k=1}^{\infty} \frac{c_2 a^{k-1}[(\rho_1/\rho)^{2k} - 1] - [(\rho_1/\rho)^{2k} + \alpha^k b_k']}{1+\alpha^k} \rho^k \times \sin k\theta, \tag{21}$$

in σ_2. The unknown coefficients b_k' are determined from the relation

$$\begin{aligned} &\left[\eta k(\rho_1^{-2} + a^2)\rho_1/\mu_2 + (\lambda+1)\frac{1-\nu\alpha^k}{1+\alpha^k}\right] b_k' - \eta a[(k-1)\rho_1^{-2} b_{k-1}' \\ &\quad + (k+1)b_{k+1}']\rho_1/\mu_2 \\ &\quad = \eta\rho_1 a^k/\mu_2 + (\lambda+1)\left(c_2\frac{1-\nu\alpha^k}{1+\alpha^k} + \nu l\right) a^{k-1}, \quad k \geqslant 1. \end{aligned} \tag{22}$$

Again, the system of (22) constitutes a linear set of equations for the unknowns b_k' that need to be solved by a truncation. For the perfect bonding case ($\eta = 0$), the unknowns b_k' can be exactly solved which again recover the form (19).

3 Torsional Rigidity and Numerical Illustration

To illustrate the effect of imperfect interface we evaluate the torsional rigidity of the compound section. The torsional rigidity T of the cross section can be shown as ([1])

$$T = \sum_{k=1}^{2} \mu_k (I_k + D_0^{(k)}) + T_c, \tag{23}$$

where $T_c = 0$ for an LS-type interface and

$$T_c = \int_\Gamma \eta[(\nabla\varphi\cdot\mathbf{s} + \mathbf{v}\cdot\mathbf{s})(\mathbf{v}\cdot\mathbf{s})]ds, \tag{24}$$

for an HS-type interface. In (23), I_k is the polar moment of intertia of the region S_k with respect to the origin O, and

$$D_0^{(k)} = \int\int_{S_k} \left(x\frac{\partial\varphi_k}{\partial y} - y\frac{\partial\varphi_k}{\partial x}\right) dxdy. \tag{25}$$

To proceed, one may rewrite (25) as, applying the Green's theorem,

Table 1 The value T/T_P versus the interface parameter ξ or η

ξ or η	T_{LS}/T_P	T_{HS}/T_P
0	.726985	1.0
0.01	.738333	1.00091
0.1	.809527	1.00897
0.5	.913686	1.04196
1.0	.948702	1.07813
5.0	.987909	1.27869
10	.993816	1.45879
100	.999369	4.04919
∞	1.0	∞

$$\begin{aligned} D_0^{(1)} &= -\oint_\Gamma \varphi_1(x\,dx + y\,dy) \\ &= -\frac{1}{2}\oint_\Gamma \varphi_1 d(x^2+y^2) = -\oint_{\gamma_1} \varphi_1(\rho_1,\theta)dw(\rho_1,\theta), \\ D_0^{(2)} &= -\oint_{\gamma_2} \varphi_2(\rho_2,\theta)dw(\rho_2,\theta) + \oint_{\gamma_1} \varphi_2(\rho_1,\theta)dw(\rho_1,\theta), \end{aligned} \tag{26}$$

which can be evaluated using (10), (16), (17), and (21). Particularly, for the LS type of interface, the torsional rigidity of the compound bar is

$$\begin{aligned} T_{LS} &= \frac{\pi\mu_2}{2}[r_2^4 + (\lambda-1)r_1^2(r_1^2 + 4c_1^2)] \\ &\quad + 2\pi\mu_2\rho_1^{2k}\left[\lambda l\sum_{k=1}^{\infty} a^{k-1}\frac{kb_k'}{1-\alpha^k} - l(l+\lambda c_1)\right. \\ &\quad \left.\times\sum_{k=1}^{\infty} a^{2k-2}\frac{k}{1-\alpha^k} - \frac{(\lambda-1)}{(a^2-1)^2}c_1^2\right]. \end{aligned} \tag{27}$$

For the HS type of interface, one additional term T_c needs to be evaluated. In doing this, one rewrites T_c in term of conjugate function as, using $(8)_2$

$$T_c = \eta\oint_\Gamma \frac{d(g-\psi)}{dn}\cdot\frac{dg}{dn}ds. \tag{28}$$

Using the relations (10)–(11) we can show that

$$\begin{aligned} T_c &= -2\eta\pi\rho_1(c_1^2 + c_1/a)(ab_1' + 1) + \eta\pi c_1\sum_{k=1}^{\infty}(2 + k \\ &\quad + 2c_1 a)a^{k-1}\rho_1^{2k-1}\{k\rho_1(1+a^2\rho_1^2)(c_1 a^{k-1} - b_k') - a[(k-1) \\ &\quad \times(c_1 a^{k-2} - b_{k-1}') + \rho_1^2(k+1)(c_1 a^k - b_{k+1}')]\}. \end{aligned} \tag{29}$$

The torsional rigidity of the compound bar with HS interface can be derived as

$$\begin{aligned} T_{HS} &= T_c + \pi\mu_2\left\{(r_2^4/2 + 2c_2^2 r_2^2) + (\lambda-1)(r_1^4/2 + c_1^2 r_1^2)\right. \\ &\quad -(1+\lambda)\sum_{k=1}^{\infty}\left(c_2\frac{1-\nu\alpha^k}{1+\alpha^k} + \nu l\right)ka^{k-1}\rho_1^{2k}b_k' \\ &\quad \left.-2c_2^2\sum_{k=1}^{\infty}\frac{ka^{2k-2}\rho_2^{2k}}{1+\alpha^k}\right\}. \end{aligned} \tag{30}$$

As a numerical illustration, we consider the following example in which $r_1 = 2.0$, $r_2 = 5.0$, $\mu_1 = 1.0$, $\mu_2 = 2.0$, $l = 2.8$. In the case that the interface is perfectly bonded, the torsional rigidity is given in Muskhelishvili ([4], Eq. (140a.14)). For convenience, we denote the quantity by T_P. For $\xi = \infty$ or $\eta = 0$, our converged result for a 20-term approximation gives $T_P = 1789.63$, which agrees

with that of [4]. As expected, the warping displacement is antisymmetric with respect to the horizontal line and thus $\varphi=0$ on the horizontal axis. To illustrate the influence of the interface parameter on the effective torsional rigidity, numerical values of the factors T_{LS}/T_P and T_{HS}/T_P are given in Table 1. The numbers indicate that for the totally debonded case $\xi=0$ the torsional rigidity is 27 percent less than that of the perfect one, whereas for $\eta > 10^2$ the torsional rigidity will increase drastically to infinity. The physical behavior and mathematical explanation of the latter phenomena was given in([1]). Finally, it is mentioned that our result is also verified with a recently proven theorem by Lipton ([2], Eq. (1.7)) and Benvensite and Chen ([1], Eqs. (4.19,4.20)). Specifically, the theorem states that for the considered compound cross-section, if the interface is of LS type and that the interface parameter has a certain constant value, then the torsional rigidity remains a constant quantity valid for any position of the circular bar.

References

[1] Benveniste, Y., and Chen, T., 2001, ''On Saint-Venant Torsion of Composite Bars With Imperfect Interfaces,'' Proc. R. Soc. London, Ser. A, **457**, pp. 231–255.

[2] Lipton, R., 1998, ''Optimal Configurations for Maximum Torsional Rigidity,'' Arch. Ration. Mech. Anal., **144**, pp. 79–106.

[3] Vekua, I. N., and Rukhadze, A. K., 1933, ''The Problem of Torsion of a Circular Cylinder, Reinforced by Additional Circular Rods,'' Izv. A. N. SSSR, **3**, pp. 373–386.

[4] Muskhelishvili, N. I., 1953, *Some Basic Problems of the Mathematical Theory of Elasticity*, Noordhoff, Groningen.

[5] Sanchez-Palencia, E., 1970, ''Comportement Limite d'un Probleme de Transmission a Travers une Palque Faiblement Conductrice,'' Comp. Rend. Acad. Sci. Paris, **A270**, 1026–1028.

[6] Pham Huy, H., and Sanchez-Palencia, E., 1974, ''Phenomenes de Transmission a Travers des Couches Minces de Conductivite Elevee,'' J. Math. Anal. Appl., **47**, pp. 284–309.

Journal of Applied Mechanics

Discussion

Discussion: "Shear Coefficients for Timoshenko Beam Theory" (Hutchinson, J. R., 2001, ASME J. Appl. Mech., 68, pp. 87–92)

N. G. Stephen
School of Engineering Sciences, Mechanical Engineering, University of Southampton, Highfield, Southampton SO17 1BJ, England

In a recent article, Hutchinson [1] employed the Hellinger-Reissner variational principle to construct a beam theory of Timoshenko type, together with a new expression for the inherent shear coefficient κ, as

$$\kappa=\frac{-2(1+\nu)}{\frac{A}{I_y^2}C_4+\nu\left(1-\frac{I_x}{I_y}\right)} \tag{1}$$

where

$$C_4=-\int\int\{\nu(x^2-y^2)f_1+2\nu\,x\,y\,f_2+2(1+\nu)(f_1^2+f_2^2)\}dx\,d\,y \tag{2a}$$

$$f_1=\frac{-1}{2(1+\nu)}\left(\frac{\partial\chi}{\partial x}+\frac{\nu\,x^2}{2}+\left(\frac{2-\nu}{2}\right)y^2\right) \tag{2b}$$

$$f_2=\frac{-1}{2(1+\nu)}\left(\frac{\partial\chi}{\partial y}+(2+\nu)xy\right). \tag{2c}$$

In the above, the notation is largely the same as that of Hutchinson except that Love's notation ([2]) has been employed for the beam cross-sectional coordinates, by replacing y by x, and z by y, in [1]; z is then the beam axial coordinate. The motivation of Hutchinson appears to be the construction of a theory in which the shear coefficient takes on the "best" value; for beams of circular and thin rectangular cross section, these are widely accepted to be $\kappa=6(1+\nu)^2/(7+12\nu+4\nu^2)$, and $\kappa=5(1+\nu)/(6+5\nu)$, respectively. The evidence to suggest that these values are "best" comes from comparison with available "exact" elastodynamic analyses and, to a lesser degree, from experiment, and is discussed in [1,3,4].

Expression (1) derived by Hutchinson is exactly equivalent to one derived by the present author and Prof. Mark Levinson [3,4] some two decades ago, which is (Ref. [3], Eq. (20))

$$\kappa=\frac{-4(1+\nu)^2\,I_y^2}{2(1+\nu)A\int\int x(\chi+xy^2)dx\,dy+2\nu(1+\nu)I_y(I_y-I_x)+\nu A\int\int\left\{\left(\frac{x^2-y^2}{2}\right)\left(\frac{\partial\chi}{\partial x}+\frac{\nu x^2}{2}+\left(\frac{2-\nu}{2}\right)y^2\right)+xy\left(\frac{\partial\chi}{\partial y}+(2+\nu)xy\right)\right\}dx\,dy}. \tag{3}$$

It is remarkable that three quite different approaches should lead to the same expression for the coefficient. Hutchinson's use of Hellinger-Reissner overcomes the compromises inevitable in a beam theory, allowing "best" choices for both stress and displacement fields, which may be incompatible. In [4], Stephen and Levinson adapted the procedure of Cowper [5], but argued that the stress distribution within a beam performing long wavelength flexural vibration would be approximated better by gravity force body loading (see Love [2], Chapter 16), rather than tip loading of a cantilevered beam, as assumed in [5]. The former has shearing force varying linearly with axial coordinate, while for the latter shearing force is constant. In [3], the coefficient was obtained from the curvature correction during bending, again due to gravity loading (again see Chapter 16 of Love).

Demonstration of the equivalence of the two formulas is somewhat lengthy, and is based upon usage of Green's formula

$$\int\int\left(\frac{\partial g}{\partial x}-\frac{\partial f}{\partial y}\right)dx\,dy=\oint(f\,dx+g\,dy), \tag{4}$$

and a knowledge of the normal derivative of the (harmonic) flexure function χ on the boundary of the cross section, that is

$$\frac{d\chi}{dn}=-\left(\frac{\nu x^2}{2}+\left(\frac{2-\nu}{2}\right)y^2\right)\cos(x,n)-(2+\nu)xy\cos(y,n). \tag{5}$$

The key step is recognition that the term within Hutchinson's coefficient C_4 involving the area integral of the sum of the squares of the terms f_1 and f_2, in turn involves the area integral of the sum $(\partial\chi/\partial x)^2+(\partial\chi/\partial y)^2$. Transformation of such terms within potential theory is well documented; see, for example, Sokolnikoff [6]. For the present problem an outline of the procedure is as follows:

construct

$$\frac{\partial}{\partial x}\left[(\chi+xy^2)\frac{\partial \chi}{\partial x}\right]=(\chi+xy^2)\frac{\partial^2 \chi}{\partial x^2}+\left(\frac{\partial \chi}{\partial x}+y^2\right)\frac{\partial \chi}{\partial x} \quad (6a)$$

$$\frac{\partial}{\partial y}\left[(\chi+xy^2)\frac{\partial \chi}{\partial y}\right]=(\chi+xy^2)\frac{\partial^2 \chi}{\partial y^2}+\left(\frac{\partial \chi}{\partial y}+2xy\right)\frac{\partial \chi}{\partial y} \quad (6b)$$

and add, noting that χ is harmonic, to give

$$\frac{\partial}{\partial x}\left[(\chi+xy^2)\frac{\partial \chi}{\partial x}\right]+\frac{\partial}{\partial y}\left[(\chi+xy^2)\frac{\partial \chi}{\partial y}\right]=\left(\frac{\partial \chi}{\partial x}\right)^2+\left(\frac{\partial \chi}{\partial y}\right)^2+y^2\frac{\partial \chi}{\partial x}+2xy\frac{\partial \chi}{\partial y}. \quad (7)$$

Integrate over the cross section, and transform the left-hand side (LHS) of the above using Green's formula, to give

$$\text{LHS}=\oint(\chi+xy^2)\frac{d\chi}{dn}ds \quad (8)$$

where direction cosines $\cos(x,n)=dx/dn=dy/ds$, and $\cos(y,n)=dy/dn=-dx/ds$ have been employed.

Substitute for the normal derivative of χ according to (5), and convert back to an area integral to give

$$\begin{aligned}\int\int\left\{\left(\frac{\partial \chi}{\partial x}\right)^2+\left(\frac{\partial \chi}{\partial y}\right)^2\right\}dx\,dy+\int\int\left(y^2\frac{\partial \chi}{\partial x}+2xy\frac{\partial \chi}{\partial y}\right)dx\,dy&\\ =-\int\int 2(1+\nu)x(\chi+xy^2)dx\,dy&\\ -\int\int(2+\nu)xy\frac{\partial \chi}{\partial y}dx\,dy&\\ -\int\int\left(\frac{\nu x^2}{2}+\left(\frac{2-\nu}{2}\right)y^2\right)\frac{\partial \chi}{\partial x}dx\,dy&\\ -\int\int\left(\left(4+\frac{5\nu}{2}\right)x^2y^2+\left(\frac{2-\nu}{2}\right)y^4\right)dx\,dy.&\end{aligned} \quad (9)$$

Next, expand Hutchinson's expression for coefficient C_4, and substitute the above, when one finds

$$\begin{aligned}C_4=\int\int x(\chi+xy^2)dx\,dy&\\ +\int\int\frac{\nu(x^2-y^2)}{4(1+\nu)}\left(\frac{\partial \chi}{\partial x}+\frac{\nu x^2}{2}+\left(\frac{2-\nu}{2}\right)y^2\right)dx\,dy&\\ +\int\int\frac{\nu xy}{2(1+\nu)}\left(\frac{\partial \chi}{\partial y}+(2+\nu)xy\right)dx\,dy.&\end{aligned} \quad (10)$$

Lastly substitute the above into Eq. (1) to give expression (3). Not surprisingly, the values of the coefficient for the circular cross section, both solid, hollow and thin-walled, and for the elliptic cross section calculated in [1], are identical to those given in [3,4]. Similarly, Hutchinson's expression for the rectangular cross section reduces to the "best" value of $\kappa=5(1+\nu)/(6+5\nu)$ as one approaches plane stress conditions.

A further very interesting feature of [1], Figs. 3 and 4, is the possibility of the shear coefficient taking a negative value for the combination of large width to depth ratio, and for large Poisson's ratio. The effect of a negative coefficient would be to stiffen the structure, leading to a natural frequency higher than that predicted by Euler-Bernoulli theory. However, as one would not normally employ Timoshenko theory for a beam having a large width to depth ratio, this result may turn out to be of little importance. Nevertheless, the physical implication of a possible negative coefficient requires further consideration.

Finally, it is noted that while the above values for the coefficient may be widely accepted as the best, paradoxically Cowper's values appear to be the more widely used; it is to be hoped that investigators will in future make greater use of these "best" values.

References

[1] Hutchinson, J. R., 2001, "Shear Coefficients for Timoshenko Beam Theory," ASME J. Appl. Mech., **68**, pp. 87–92.
[2] Love, A. E. H., 1944, *A Treatise on the Mathematical Theory of Elasticity*, Dover, New York.
[3] Stephen, N. G., 1980, "Timoshenko's Shear Coefficient from a Beam Subjected to Gravity Loading," ASME J. Appl. Mech., **47**, pp. 121–127.
[4] Stephen, N. G., and Levinson, M., 1979, "A Second Order Beam Theory," Journal of Sound and Vibration, **67**, pp. 293–305.
[5] Cowper, G. R., 1966, "The Shear Coefficient in Timoshenko Beam Theory," ASME J. Appl. Mech., **33**, pp. 335–340.
[6] Sokolnikoff, I. S., 1956, *Mathematical Theory of Elasticity*, McGraw-Hill, New York.

Closure to "On Shear Coefficients for Timoshenko Beam Theory" (2001, ASME J. Appl. Mech., 68, p. 959)

J. R. Hutchinson
Department of Civil and Environmental Engineering,
College of Engineering, University of California,
One Shields Avenue, Davis, CA 95616-5294

In his most important point Professor Stephen is completely correct. That is, his shear coefficient and mine are identical. I was aware of his work when it first came out and discounted it because it was derived by solving a static problem for a specific type of loading. It implied that the shear coefficient for the static problem was a function of the type of loading and, further, that by choosing the right type of static loading one could find the best value of the shear coefficient for dynamic loads. As it turns out both of these implications are correct.

Professor Stephen states, "The motivation of Hutchinson appears to be the construction of a theory in which the shear coefficient takes on the 'best' value." I did not mean to convey that impression. My motivation was simply to construct a simple, consistent, dynamic theory which did not require guessing a shear coefficient. This simple consistent theory allowed me to find an expression for the shear coefficient in the Timoshenko beam theory. That this shear coefficient agreed with the "best" values simply validated my approach.

Professor Stephen states, "the values of the coefficient for the circular cross section, both solid, hollow and thin-walled, and for the elliptic cross section calculated in [1], are identical to those given in [3,4]." What he doesn't note is that the expressions for the rectangular cross section in both his and my paper also produce identical results. He further comments on the fact that the shear coefficient goes to zero for the rectangular cross section. Actually, as shown in my Fig. 4, it is the reciprocal of the shear coefficient that goes to zero which means the shear coefficient would have a pole at that point. Professor Stephen's conclusion that the beam is stiffened with an increase in width is correct. I do not understand, however, his remark that, "one would not normally employ Timoshenko theory for a beam having large width to depth ratio." For a Poisson's ratio of 0.3 the reciprocal of the shear coefficient goes to zero at a width to depth ratio of about 3. This is definitely within the range I would expect Timoshenko theory to be applied. Also the lowest natural frequency would

probably occur (depending on boundary conditions) about a neutral axis in the width direction. I should probably also note that the shear coefficient is very sensitive to the assumed shear stress distribution. If one were to assume a simple parabolic shear stress distribution through the thickness of the rectangular beam one would get a shear stress of $5(1+\nu)/6+5\nu)$ independent of the aspect ratio.

In my paper I also had a small section on static problems. In that section I found expressions for a static shear coefficient found by comparing solution of my equations with the elementary beam solution including shear deformation. The comparison was done for a tip loaded cantilever. Since Professor Stephen's work indicates that the coefficient depends on loading I decided to investigate a beam loaded under it's own weight. To accomplish this I inserted a new term γv into the integral in my Eq. (28) and dropped all the time dependent terms. The term γ is the specific weight of the beam and v is the displacement in the y-direction. Proceeding in the same way as in the paper, I came up with the following set of equations,

$$\psi''' + \frac{\gamma A}{EI_z} = 0 \tag{1}$$

$$\psi' - \varphi'' + \frac{C_4}{I_z}\psi''' - \frac{\gamma\nu}{2EI_z}(I_z - I_y) = 0. \tag{2}$$

These equations are solved by integrating the first three times and inserting the result into the second and integrating two more times. The boundary conditions for a cantilever fixed at $x=0$ and free at $x=L$ are $\psi(0)=0$, $\varphi(0)=0$, $\psi'(L)=0$ and $\psi''(L)=0$. Since there are five constants of integration another condition is needed. That condition is, for the axial location at which the shear is zero, the slope ψ equals the slope of the center line deflection φ'. Thus $\psi(L)=\varphi'(L)$. The expression for the center line displacement is then

$$\varphi = \frac{\gamma A}{EI_z}\left(-\frac{x^4}{24} + \frac{Lx^3}{6} - \frac{L^2x^2}{4}\right) + \left[\frac{\gamma A}{EI_z^2}c_4 + \frac{\gamma\nu}{2EI_z}(I_z - I_y)\right] \times \left(Lx - \frac{x^2}{2}\right). \tag{3}$$

The first group of terms in Eq. (3) corresponds to the Euler-Bernoulli beam solution and the second group of terms corresponds to the shear deformation solution. This is the same expression that would result from simple beam theory with shear deformation if the shear coefficient were the expression shown in my paper as Eq. (57). If one uses the integrated average displacement, as was done by Professor Stephen, instead of the center line displacement then one gets the shear coefficient which he found, that is, my Eq. (41) and his comment Eqs. (1) and (3). Thus, even in my approach the shear coefficient is a function of the loading, and for a gravity load the resulting shear coefficient is the same as the dynamic coefficient. Similar equations to (1) and (2) above could be developed for any type of loading on a beam and thus eliminate the need for a shear coefficient entirely.

I recently presented a paper entitled ''Shear Coefficients for Thin-Walled Timoshenko Beams'' at the Third International Symposium on the Vibrations of Continuous Systems, July 23–27, 2001 at Jackson Lake Lodge, WY. In that paper I considered all the thin-walled cases treated by Cowper plus two additional cases. As in all other cases the ''best'' shear coefficient agreed with Cowper's values only for Poisson's ratio equal zero.

As to Professor Stephen's final remark, ''it is noted that while the above values for the coefficient may be widely accepted as best, paradoxically Cowper's values appear to be more widely used; it is hoped the investigators will in the future make greater use of these 'best' values,'' I fully agree.